DROPLET COMBUSTION OF SURROGATE AND REAL FUEL SYSTEMS IN A LOW CONVECTION CONDITION: GROUND-BASED AND SPACE-BASED EXPERIMENTS

A Dissertation

Presented to the Faculty of the Graduate School

of Cornell University

In Partial Fulfillment of the Requirements for the Degree of

Doctor of Philosophy

by

Yu-Cheng Liu

August 2013

DROPLET COMBUSTION OF SURROGATE AND REAL FUEL SYSTEMS IN A LOW CONVECTION CONDITION: GROUND-BASED AND SPACE-BASED EXPERIMENTS

Yu-Cheng Liu, Ph. D.

Cornell University 2013

The droplet burning characteristics of aviation (Jet-A) and ground transportation (gasoline) fuels, a standard reference gasoline (indolene), three and four component surrogate fuels, several biodiesel surrogates (methyl butanoate (MB) and decanoate (MD)), and three single component fuels (heptane, octane and decane) were examined from the perspective of the spherically symmetric droplet flame promoted by a low gravity environment in the standard atmosphere. The parameters included the initial droplet diameter (D_o) and the fuel composition.

Access to the experimental times required to observe the complete droplet burning history was obtained by carrying out the experiments in a drop tower that provided about 1 s of experimental time ($D_o < \sim 1$ mm), and the orbiting International Space Station (ISS) using an experimental design on the ISS that could produce both freely-floating and fiber-supported droplets with essentially any D_o and unlimited experimental times. For some of the results reported (those for n-heptane, n-octane, n-decane) D_o was varied over the widest range ever reported (0.5 mm to 5 mm) across which radiative and sooting processes were considered to either influence burning (for $D_o > \sim 1.5$ mm) or have a minimal affect (for $D_o < \sim 1$ mm). For the other fuel

systems investigated, D_o was fixed at between 0.5 mm and 0.6 mm. Also discussed is a new imaging analysis method to automate data extraction from digital video records of the droplet burning history.

The results showed the following: indolene droplets replicated reasonably well gasoline droplet burning; the three and four component blends examined performed closely to Jet-A; n-heptane and iso-octane mixture droplets did not replicate the burning characteristics of gasoline unless toluene was added to the mixture; the droplet burning rate decreases through the range of D_o examined that spanned the ground-based and ISS data; and the ground based facility for studying fiber-supported droplet burning replicates quite well the burning characteristics of free-floating droplets of the same size and method of ignition. The value of the spherical droplet flame as a canonical liquid fuel burning configuration is shown for the complex fuel systems investigated.

BIOGRAPHICAL SKETCH

Yu-Cheng Liu was born in Taipei County, Taiwan in 1983. He received his B.S. in Chemical Engineering from National Taiwan University in 2005. With a particular interest in both fluids and material sciences, he then pursued graduate studies under Professor Chung-Wen Lan in Chemical Engineering of NTU with research concentration focus on crystal growth and thermo-fluids. During his master studies, he published 5 journal articles and 1 international conference paper on flow and solutal segregation control of crystal growth. After acquiring his M.S. in 2007, he worked as a full-time teaching assistant in the Department of Chemical Engineering in NTU. During this one year duty of teaching assistantship, he found himself enjoying teaching and solving various engineering problems.

In 2008, motivated by the interests in combustion sciences, he joined the Ph.D./M.S. program of the Sibley School of Mechanical and Aerospace Engineering and was advised by Professor C. Thomas Avedisian on the project of low gravity droplet combustion. The topics studied include using spherically symmetric droplet flame to benchmark conventional fuels (e.g. gasoline, Jet-A), surrogate fuels, and new generation biofuels and their potential surrogates. His research focus at Cornell also involved with multi-phase and multi-component phenomena and the thermal combustion physics associated with the length scale of a spherically droplet flame. He acquired the M.S. on Mechanical Engineering from Cornell in 2010. His research outcome at Cornell includes 7 journal articles and 8 conference papers on the topic of droplet combustion and image analysis by July, 2013

ACKNOWLEDGMENTS

First I would like to thank my parents, Yu-Shian Liu and Lan-Teng Chen, as well as my fiancée I-Chen Chiang for being supportive of my decision to pursue a Ph.D. at Cornell and for all the countless conciliation during my tough times.

I would like to thank the National Aeronautics and Space Administration (NASA) for their financial support for my Cornell tuition and the research grant over the 2008 to 2013 period, under the grant No. NNX08AI51G. I thank Dr. Daniel Dietrich and Michael C. Hicks of NASA for monitoring this project and along with Dr. Vedha Nayagam and Paul Ferkul for their assistances during the ISS experiments. I thank Professor Frederick L. Dryer from Princeton University and Professor Tanvir Farouk from University of South Carolina for co-authoring two journal articles that include their numerical predictions for the droplet combustion experiments performed at Cornell.

Dr. Tim Edwards who provided the Jet-A (POSF4658), Camelina HRJ (POSF6152), and Tallow HRJ (POSF6308) as well as Dr. Brad Zigler who provided the reference gasoline, indolene, and discussion regarding the gasoline compositions are very much appreciated. Special thanks are given to Dr. Xia Zheng of Human Ecology of Cornell for his help with all the GC/MS analyses in this study and John Hunt of Material Science Engineering for his help with the SEM imaging for the support fibers.

I thank all the students at Cornell who have worked with me: James Roll, Mark Fuller, Chris Dembia, Anthony Savas, Koffi Trenou, and Jeff Rah. They provided their great assistance during the drop tower experiments (and some ISS experiments)

and data analyses. I am thankful that lab colleagues, Dr. Sung Ryel Choi, John Evangelista, Wei-Chih Kuo, Robert Chen, Eric Ching, Iris Choi, Jeremy Horwitz, and James Young, who worked on different projects, shared interesting things and their lives with me and that had been some delightful distractions for my research.

Warm and frequent regards from my good friends from college and high school who went to the U.S. for graduate studies in the same year as I did, Ken-Hsuan Liao, Kung-Po Chao, Wei-Jiun Yuan have been very cheerful. Good friends in Taiwan, Chi-Chieh Fei, Wen-Chieh Lan, who offered their supports overseas whenever I need, are very much appreciated. I thank my master advisor Professor Chung-Wen Lan for his enlightening words towards the direction and attitude of my academic career after leaving NTU.

During the past five year, I met several friends in Ithaca who shared their professional knowledge and living experiences with me. I thank Po-Hsun Lin, James Young, Pi-Yu Young, Chen-Pey Huang, Jonathan Shaw, Ally Chang, Amy Hsiao, Jeffery Yu, Adrian Tung, Kai-Yuan Chen, I-Fan Wu, Yu-Chao Chen, Chao-Chen Yuan, Chun-Po Wang, Lillian Hsu, for their company during all the relaxable weekends. The good times with them in Ithaca helped me adjust my pace towards the next science challenges.

Finally, I would like to devote my sincerest appreciation to my Ph.D. advisor, Professor C. Thomas Avedisian. He provided me much support and freedom for my independent research and shared his logics of how to approach a problem when needed. I thank him for unselfishly fostering me towards an academic success.

TABLE OF CONTENTS

LIST OF FIGURES

LIST OF TABLES

ABBREVIATIONS

AC	Alternating current
AKI	Anti-knocking Index (= (RON + MON)/2)
AOI	Area of interest
BNC	Bayonet Neil-Concelman (connector)
BW	Black-and-white
CCD	Charged-coupled device
CFF	Counterflow flame
CI	Compression ignition
CIR	Combustion Integrated Rack
CMOS	Complementary metal-oxide semiconductor
CPU	Central processing unit
CRT	Cathode ray tube
DC	Direct current
DCN	Derived cetane number
EEE	Exhaust, Evaporative and Emissions
fps	Frame per second
FR	Flow reactor
FSR	Flame standoff ratio (=D_f/D)
FTP	Federal Test Procedure
GB	Ground-based
GC/MS	Gas chromatography/mass spectrometry
GLS	Global least squares
H/C	Hydrogen to carbon ratio
HCCI	Homogeneous charger compression ignition
HEFA	Hydroprocessed ester and fatty acids
HHV	Higher heating value
HRJ	Hydroprocessed renewable jet
ID	Inner diameter
IPSU	Image processing and storage unit
ISS	International Space Station
JSR	Jet-stirred reactor
LED	Light emitting diode
LHV	Lower heating value
LLLUV	Low-light-level ultraviolet (camera)
MB	Methyl butanoate
MD	Methyl decanoate
MDCA	Multiuse Droplet Combustion Apparatus
MON	Motor Octane Number
MP	Mega pixels
MTBE	Methyl-tert-butyl ether
MW	Molecular weight, g/mole
NAAQSs	National Ambient Air Quality Standards

NASA	National Administration of Space and Aeronautics
NMR	nuclear magnetic resonance
nH	n-heptane
OD	Outer diameter
PAHs	Polycyclic aromatic hydrocarbons
PC	Personal computer
PCI	Peripheral Component Interconnect
PFR	Premixed flow reactor
PM	Particulate matter
PRF	Primary reference fuel
PS	Point sampling
PTFE	Polytetrafluoroethylene
R-C	Resistor-capacitor
RAM	Random-access memory
RGB	Red-Green-Blue
ROI	Region of Interest
RON	Research Octane Number
SEM	Scanning electron microscope
SI	Spark ignition
SPK	Synthetic paraffinic kerosene
SSR	Soot standoff ratio ($=D_s/D$)
ST	Shock tube
TBA	Tert-butyl alcohol
TSI	Threshold sooting index
USB	Universal Serial Bus

NOMENCLATURE

A	Pre-exponential factor in the Arrhenius's equation
a	Empirical coefficient for Eq. (1.5)
a_e	Major axis of an ellipse, pixel
Bi	Biot number
B	Spalding transfer number
b	Empirical coefficient for Eq. (1.5)
b_e	Minor axis of an ellipse, pixel
C_i	Roy-Thodos structural constant
c	Empirical coefficient for Eq. (1.5)
$c_{1\text{-}5}$	Coefficients for the equations that describe a circle or an ellipse in the automated image analysis
c_{pg}	Gas specific heat at constant pressure, J/kg K
$c_{p,L}$	Liquid specific heat at constant pressure, J/kg K
D	Droplet diameter, mm, m, or pixel
$\mathcal{D}$	Diffusion coefficient, m^2/s
D_{auto}	Droplet diameter obtained from an automated analysis, pixel
D_{ball}	Diameter of the calibration ball bearing, mm or pixel
D_{ext}	Droplet extinction diameter, mm
D_f	Droplet flame diameter, mm, m, or pixel
D_{fiber}	Fiber diameter, mm or μm
D_{final}	Final droplet diameter in a evaporation process, mm
D_{init}	Initial droplet diameter in a evaporation process, mm
D_{flame}	Flame diameter from simulation, mm
D_{man}	Droplet diameter obtained from a manual image analysis, pixel
D_o	Initial droplet diameter, mm, m, or pixel
D_s	Soot shell diameter, mm, m, or pixel
d	Empirical coefficient for Eq. (1.5)
F	Aperture parameter, f-stop
f	A proportionality constant in the adaptive threshold method
f_i	Temperature-dependent function for species i in Roy-Thodos method
g	Earth's normal gravity ($9.8\ m/s^2$)
H	Height of an elliptical AOI, pixel
h_{fg}	Latent heat of vaporization, J/g
h_g	Gas heat transfer coefficient, W/m^2K
I_t	Adaptive intensity threshold value (from 0 to 255)
I_k	Color intensity at the k-th point along the scan lines in the automated image analysis
K	Droplet burning rate, mm^2/s

$K_{i,\Delta x}$	Droplet burning rate computed from a finite difference method using Δx as the interval for point i, mm^2/s
$K_{i,5\Delta x}$	Droplet burning rate computed from a finite difference method using $5\Delta x$ as the interval for point i, mm^2/s
K_o	Theoretical droplet burning rate, mm^2/s
k_{fiber}	Thermal conductivity of support fiber, W/m K
k_g	Gas thermal conductivity, W/m K
k_L	Liquid thermal conductivity, W/m K
L_c	Characteristic length, m
N	Total number of points along scan lines in the automated image analysis
N_1	Mole number of species 1 in the evaporation model, mole
N_2	Mole number of species 2 in the evaporation model, mole
Nu	Nusselt number
n	Molar density, $mole/m^3$
p	Criterion for elimination of sampling points in the automated image analysis (=0.1)
Pr	Prandtl number
P_c	Critical pressure, atm
P_{sat}	Saturation pressure, Pa
P_{total}	Total pressure, Pa
Q_r	Radiative heat transfer rate, W
Q_v	Droplet vaporization rate, W
q_{i-L}	Heat transfer into the droplet interior per mass, J/kg
R	Ideal gas constant (= 8.314 J/K mol)
R_{cur}	Resistance that determines the spark current, Ω
R_{vol}	Resistance that determines the spark voltage, Ω
Ra_D	Rayleigh number
Re_D	Reynolds number
r_o	Initial droplet radius, mm
r_d	Droplet radius, mm or m
r_e	Effective radius of an ellipse, pixel
r_f	Flame radius, mm or m
r_{fiber}	Fiber radius, mm
r_i	Radius of the circle fit in the i-th iteration in the automated image analysis, pixel
r_{i+1}	Radius of the circle fit in the (i+1)-th iteration in the automated image analysis, pixel
r_{si}	Droplet radius of soot inception, mm or m
Sp	Sphericitu number (Struk et al. (1996))
s	A length that determines the size of ROI, pixel
s_1	The first value of s selected for initialization in the automated image analysis (= 300), pixel
T	Temperature, K or ^oC
T_{ad}	Adiabatic flame temperature, K
T_b	Boiling temperature, K or ^oC

T_c	Critical temperature, K
T_d	Droplet temperature, K
T_f	Flame temperature, K
T_{flash}	Flash point, K or ^oC
T_{freeze}	Freezing point of a mixture fuel, K or ^oC
T_m	Melting point, K or ^oC
T_{max}	Maximum gas temperature, K
T_p	Property temperature, K
T_r	Reduced temperature ($=T/T_c$)
T_s	Droplet surface temperature, K
T_{si}	Soot inception temperature, K
T_∞	Ambient temperature, K
t	Time, s
t_0	arbitrary time datum at which the "run" button on the QC-9618 is pressed, s
t_{evp}	Evaporation time, s
t_{expo}	Exposure time for imaging systems, s
t_h	Thermal diffusion time ($\sim D_o^2/\alpha_L$), s
t_{pd}	Signal delay for package release, s
t_{sd}	Spark delay, s
t_r	Retraction time, s
t_{rd}	Retraction delay, s
t_b	Total droplet burning time, s
t_{res}	Residence time, s
t_s	Spark duration, s
u	Gas velocity, m/s
V_1	Liquid volume of species 1 in the evaporation model, m^3
V_2	Liquid volume of species 2 in the evaporation model, m^3
V_x	Droplet velocity in the direction of x, m/s
V_y	Droplet velocity in the direction of y, m/s
W	Width of an elliptical AOI, pixel
W_i	Molecular weight of species i
W_F	Fuel molecular weight, g/mole
W_1	Molecular weight of species 1 in the evaporation model, g/mole
W_2	Molecular weight of species 2 in the evaporation model, g/mole
X_i	Liquid mole fraction of species i
X_1	Liquid mole fraction of species 1 in the evaporation model
X_2	Liquid mole fraction of species 2 in the evaporation model
x	Gas mole fraction
$x_{1\text{-}N}$	x coordinate of the first to the N-th point that construct a boundary fitting
x_i	Value of time data at point i for the finite difference method, s/mm^2
x_c	x coordinate of the center of a fitted circle in the automated image analysis
x_{ce}	x coordinate of the center of a fitted ellipse in the automated image analysis

x_{i+1}	Value of time data at point i+1 for the finite difference method, s/mm^2
x_{i+2}	Value of time data at point i+2 for the finite difference method, s/mm^2
Y_i	Gas mole fraction of species i
Y_1	Gas mole fraction of species 1 in the evaporation model
Y_2	Gas mole fraction of species 2 in the evaporation model
$y_{1\text{-}N}$	y coordinate of the first to the N-th point that construct a boundary fitting
y_c	y coordinate of the center of a fitted circle in the automated image analysis
y_{ce}	y coordinate of the center of a fitted ellipse in the automated image analysis
y_i	Value of D^2 data at point i for the finite difference method
y_{i+1}	Value of D^2 data at point i+1 for the finite difference method
y_{i+2}	Value of D^2 data at point i+2 for the finite difference method
$Y_{O\infty}$	Oxidizer mole fraction in far field

Greek Symbols

α	Gas thermal diffusivity ($=k_g/\rho_g c_{pg}$), m^2/s
α_L	Liquid thermal diffusivity ($=k_g/\rho_g c_{pg}$), m^2/s
β	Thermal expansion coefficient, 1/K
Δh_c	Heat of combustion, J/g
Δ_i	distance between the boundary point and the center of the droplet, pixel
Δm	Mass of a liquid shell in the evaporation model ($=10^{-7}$), g
$\Delta N_{1,2L}$	Mole numbers of species 1 or 2 removed from the liquid droplet in the evaporation model in Chapter 5, mole
$\Delta N_{1,2v}$	Mole numbers of species 1 or 2 vaporized to the gas phase in the evaporation model in Chapter 5, mole
ΔT	Temperature difference, K
Δt	Time difference, s
Δt_{magnet}	Magnet delay time, s
Δx	Time interval for computing the burning rate, s/mm^2
ε	A constant defined in Nayagam et al. (2008) ($=RT_{si}/E_a$)
ε_{auto}	Relative error between automated and manual droplet measurements
ε_d	Droplet emissivity
ε_f	Flame emissivity
ε_{tol}	Error tolerance for shape fitting iteration in the automated image analysis ($=10^{-4}$)
ϕ_1	Volume faction of species 1 in the evaporation model
ϕ_2	Volume faction of species 2 in the evaporation model
Γ_i	Defined parameter for species i in Roy-Thodos method
γ_1	Activity coefficient for species 1 in at phase equilibrium
γ_2	Activity coefficient for species 2 in at phase equilibrium
$\kappa_{droplet}$	Droplet curvature ($= 1/r_o$)

κ_{fiber}	Fiber curvature (= $1/r_{fiber}$)
μ	Gas viscosity, kg/s m
ν	Gas kinematic viscosity (=μ_g/ρ_g), m^2/s
ν_c	Stoichiometric air to fuel ratio
Θ	FSR ratio for different fuels defined in Eq. (5.4)
ρ	Gas density, kg/m^3
ρ_1	Liquid density of species 1 in the evaporation model, kg/m^3
ρ_2	Liquid density of species 1 in the evaporation model, kg/m^3
ρ_L	Liquid density, kg/m^3
σ	Stefan-Boltzman constant for thermal radiation, (= 5.67×10^{-8}), W/m^2K^4
ξ	Proportional factor in the burning rate formula (=$k_g/\rho_L c_{pg}$), m^2/s
ξ_h	A ratio defined for droplet heating time and total burning time (=t_h/t_b)
ξ_r	A ratio defined in Eq. (1.11) for radiation and vaporization (=Q_r/Q_v)
ξ_{rc}	Relative curvature ratio (= D_o/D_{fiber})
ξ_{soot}	A ratio defined in Eq. (1.10) for soot residence time and total burning time (=t_{res}/t_b)
$\upsilon_{c,i}$	Molar volume of species i at critical point

CHAPTER 1

INTRODUCTION

1.1 Background

Liquid fuels have powered transportation systems for over a century and demand will be sustained for decades to come (Edwards (2003), "Transforming Combustion Research Through Cyberinfrastructure" (2011)). Within the U.S. alone, almost 12 million barrels of oil are consumed per day in ground transportation vehicles which are powered by the internal combustion engine. Sustainable energy produced from wind, solar, geothermal and electric technologies are not yet at the stage where they will significantly impact petroleum use and the emissions they produce (e.g., Service (2008), Ramanathan and Carmichael (2008)). While these alternatives are being developed to the point where they can have a significant impact on petroleum consumption and the climate, more immediate benefits can be derived from improving the understanding of the combustion performance of systems powered by conventional liquid fuels.

The complexity of fossil or bio-based fuels makes it difficult to develop oxidation schemes and physical property estimates needed to carry out numerical analysis of combustion processes (Chakravarthy et al. (2007), Ra et al. (2008)), and a thorough knowledge of fuel property and combustion chemistry effects is needed. Surrogates are an attractive, if not necessary, alternative to alleviating these concerns. Surrogates are blends of well-characterized components that represent broad chemical classes of a real fuel, with the fractional amounts of the constituents chosen to

replicate certain combustion “targets” of the real fuel (Dooley et al. (2010), Anand et al. (2011)).

While engine testing can provide useful information under realistic conditions specific to the engine design, the combustion dynamics, characterized by highly turbulent and swirling transport around the droplets, create a significant challenge in modeling (Reitz (2013)). The characterization of real transportation fuels in a well controlled and modelable environment is important for validating some of the ingredients to predicting performance under more realistic conditions. For example, the combustion chemistry itself is independent of the transport dynamics and may be determined in a much simplified environment. Pre-vaporized (gaseous) fuels have particularly benefited from being developed in a combustion configuration for which the gas transport dynamics were well characterized.

Gaseous combustion configurations that feature one or zero dimensional fluid/thermal transport processes have been used for fuel benchmark and surrogate development. For example, shock tubes (Gauthier et al. (2004), Yahyaoui et al. (2007)) give quantitative measurements of ignition delay. Counter flow flames (CFF) (Bieleveld et al. (2009), Choi et al. (2011)) characterizes extinction strain rates. Jet-stirred (Dagaut and Togbé (2008)) and premixed flow reactors (Chaos et al. (2007)) (JSR and PFR) have provided species concentration data from the combustion process of pre-vaporized fuels in configurations that may be considered as "canonical" in the sense of the flow field being greatly simplified compared to the engine environment. The results still have much wider applicability.

Regarding a suitable combustion configuration for liquid fuels, at one extreme

is the stochastic real engine environment (see Fig. 1.1). Sprays set the initial conditions for engine combustion but modeling a burning spray is currently beyond the scope of detailed numerical simulation owing to multiphase and moving boundary behavior and interaction effects among the constituent droplets.

At the other extreme is a combustion configuration that incorporates a tractable fundamental geometry and laminar conditions so as to permit detailed simulations of the combustion event. If we consider that each droplet of a spray is a sub-grid element, the complex problem of a spray could be studied from the perspective of isolated droplet that incorpoarates many of the same elements of fuel evaporation, sooting dynamics, unsteady effects, and combustion kinetics, but from a 1-D configuration. This configuration is promoted by eliminating the droplet interactions as well as minimizing the force and natural convection effects by reducing Reynolds and Rayleigh numbers ((cf. Fig. 1.1),

$$\mathrm{Re}_D = \frac{\rho u D}{\mu} = \frac{u D}{\nu} \tag{1.1}$$

$$\mathrm{Ra}_D = \frac{g\beta(T_s - T_\infty)D^3}{\nu\alpha} \tag{1.2}$$

(e.g., $\mathrm{Re}_D \sim 0.1$ and $\mathrm{Ra}_D \sim 10^{-4}$) or alternatively, the spherocity number by Struk et al. (1996) as

$$\mathrm{Sp} \equiv \frac{\sqrt{\mathrm{Pr}\,\mathrm{Ra}_{D_f}}}{\ln(1 + Y_{O\infty}\nu)}. \tag{1.3}$$

The corresponding canonical geometry for liquid fuels is that of an isolated droplet burning under conditions where there is no relative velocity (u in Eq. (1.1)) between the droplet and surrounding gas, and for which the flow is created entirely by

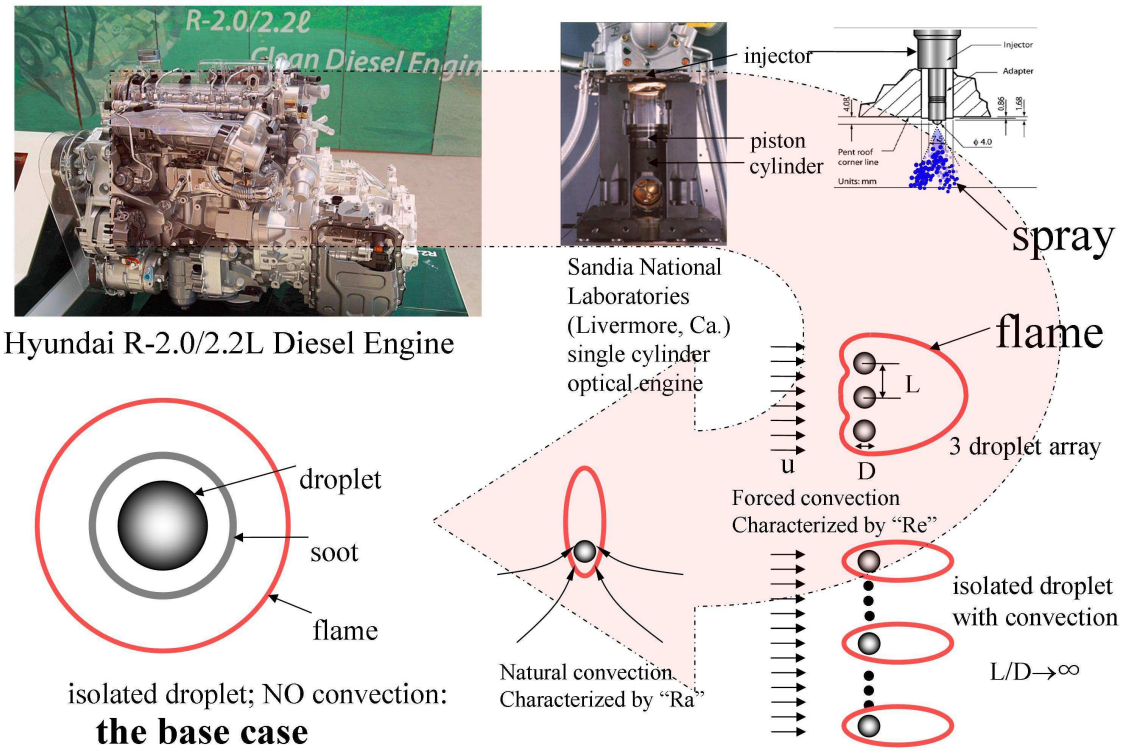

Fig. 1.1. Combustion configurations for liquid fuels: from the most complex: a real engine to the base case: spherically symmetric droplet burning.

the evaporation process. Under these conditions, the streamlines of the flow will be radial and a one-dimensional gas phase symmetric condition will be created. The flame will then be spherical and concentric with the droplet. Figure 1.2 shows this configuration.

Combustion properties for the configuration depicted in Fig. 1.2 include the evolution of flame, droplet diameter, and burning rate (Sirignano (1999)). If the fuel under consideration produces soot, the proximity of the soot shell (owing to the Stefan drag, diffusion- and thermophoresis (Knight and Williams (1980), Ben-Dor et al. (2003))) to the droplet provides another combustion characteristic. If the flame extinguishes, the droplet diameter at extinction (Chao and Law (1991)) is an important metric to identify extinction mechanisms. Moreover, the problem of soot formation during droplet combustion has not yet been fully simulated (Avedisian et al. (1988), Kumar et al. (2002)), thus placing a high reliance on experiments in the meantime to develop the understanding of combustion performance of conventional fuels, biofuels, and surrogate fuels that contain components which produce soot.

The classical droplet combustion theory (Godsave (1953), Spalding (1953), Turns (2006)), i.e. the D^2 law, describes such a one-dimensional problem:

$$D^2 = D_o{}^2 - K_o \cdot t \tag{1.4}$$

where

$$K_o = \frac{8k_g}{\rho_L c_{pg}} \ln(1+B) \neq f(D_o, t) \tag{1.5}$$

and the B is the transfer number defined by the follows:

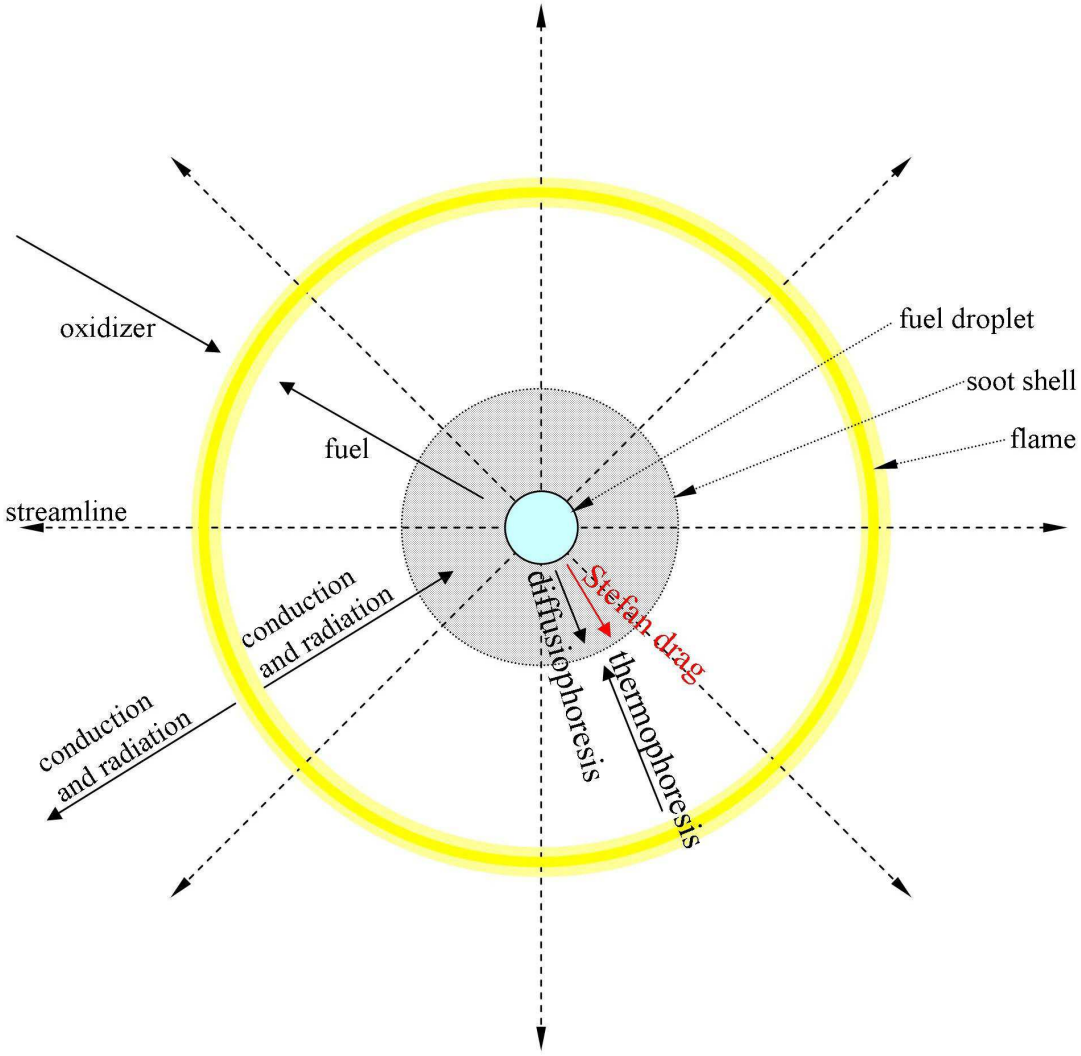

Fig. 1.2. Schematic of a spherically symmetric droplet flame.

$$B = \frac{\Delta h_c / \nu + c_{pg}(T_\infty - T_s)}{q_{i-L} + h_{fg}} \tag{1.6}$$

The D^2 law suggests that the burning rate K_o is independent of D_o and t. The dotted lines in Fig. 1.3a and 1.3b show the D^2 and K over time in this ideal situation. Also predicted by the classical droplet combustion theory is the flame standoff ratio (FSR), the relative distance of the flame away from the droplet surface, remaining constant (Turns (2006)):

$$FSR \equiv D_f / D = \frac{\ln[1 + B_{o,q}]}{\ln[(\nu + 1)/\nu]} \neq f(D_o, t) \tag{1.7}$$

The dotted line in Fig. 1.3c illustrates this prediction.

In several previous studies on spherically symmetric droplet flames, data were found inconsistent with the classical droplet combustion theory. The red solid lines in Fig. 1.3a through 1.3c illustrate the trends from experimental observations. These trends suggested that burning rate K is dependent on t and D_o and FSR was found to increase during a droplet burning process.

The mechanisms that influence the relationship between D_o and K appear to be due to soot and radiation that were not considered in the theory (i.e., Eqs. (1.4) to (1.5)). Soot formation within a droplet flame was also thought to be linked to temperature (Vranos and Liscinsky (1984)) that allows soot to form (T_{si} ~ 1650 K (Dobbins (2002)) and the residence time (t_{res}) of fuel molecules transported between the droplet and flame (Jackson and Avedisian (1992)):

$$t_{res} \sim \frac{r_d^{\,2}}{(K\rho_L)^2}\rho^2 \mathcal{D} \ . \tag{1.8}$$

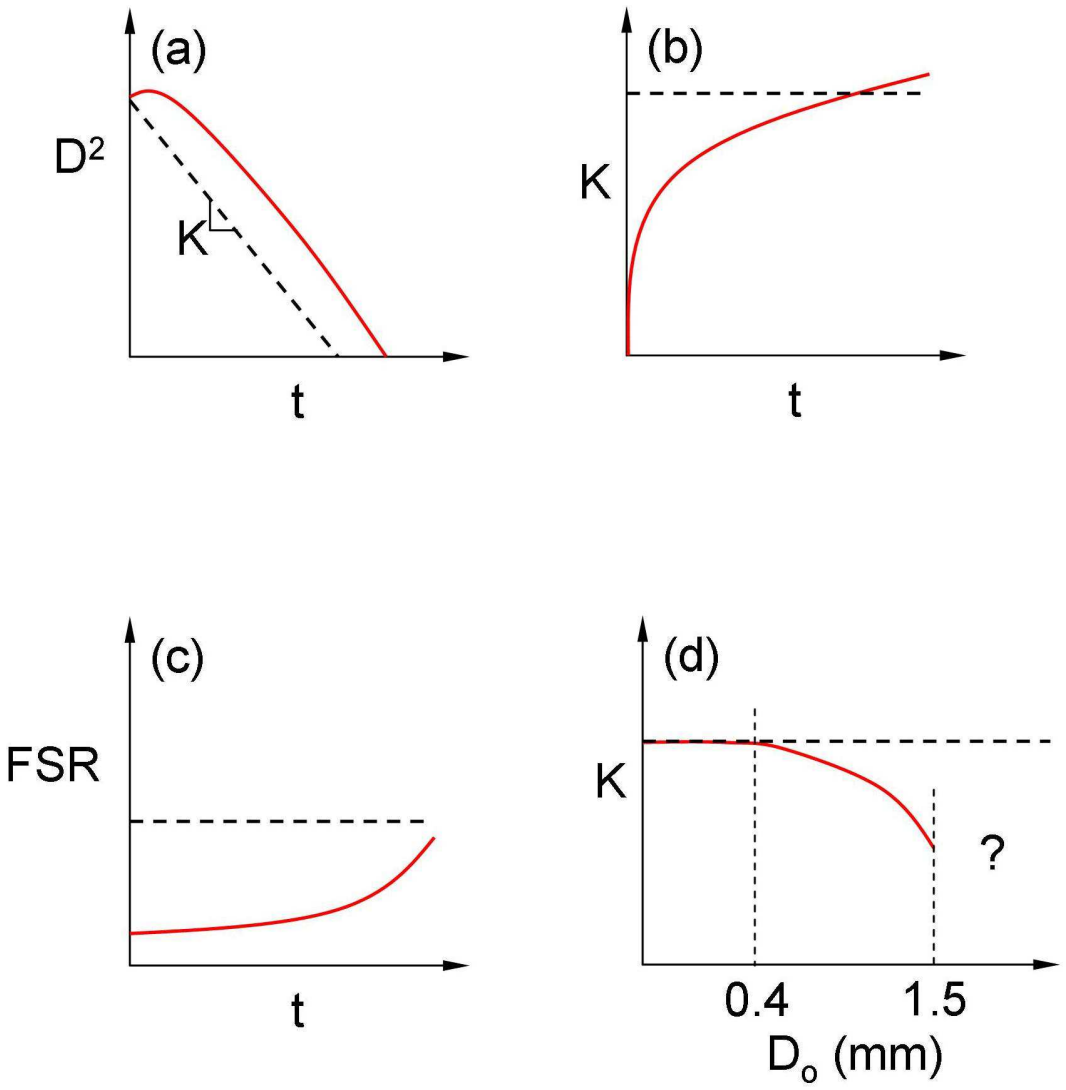

Fig. 1.3. Schematic of theoretical prediction (black dotted line) and experimentally observed trend (red solid line) for (a) D^2 vs. t; (b) K vs. t; (c) FSR vs. t; (d) K vs. D_o.

Whether or not soot may form during in the droplet burning history may be assessed using the ratio of t_{res} to the droplet burning time $t_b = D_o^2/K$ (cf. Eq. (1.1)):

$$\xi_{soot} = \frac{t_{res}}{t_b} \sim \frac{\alpha_g}{K}\left(\frac{\rho}{\rho_L}\right)^2 \tag{1.9}$$

where a small value of ξ_{soot} favors soot formation. The meaning of this scaling is that if fuel molecules move too quickly through the fuel rich side of the droplet flame, compared to the burning time, soot will not form. The droplet diameter is not explicit in this scaling. The influence of D_o on ξ_{soot} is implicit in K. Trends that will decrease K are more likely to favor soot formation.

In addition, soot aggregates in a spherical droplet flame (Hara and Kumagai (1991), Jackson and Avedisian (1994), Avedisian and Callahan (2000), Xu et al. (2003, 2004a), Bae and Avedisian (2004a, 2006, 2007, 2009)) were speculated to affect the burning rate in several ways. Though the soot particles are considered as highly porous (Kumar et al. (2002)), it could still potentially change the effective transport properties of the mixture vapor and obstacle the fuel transport (Shaw et al. (1988), Jackson et al. (1992)). Since carbon particles have a much higher heat capacity compared to vapor mixture, it could behave like a heat sink (Jackson and Avedisian (1994)) in the transient burning process such that less heat is transferred from the flame to the droplet leading to a lowered burning rate.

The fact that soot is produced indicates incomplete combustion where the heat of combustion is not completely released from the fuel (Vranos and Liscinsky (1984)). Soot aggregates also create surfaces that could potentially allow for more luminous radiative heat losses from the flame ball (Kumar et al. (2002)).

Regarding radiation, the scaling of radiative affects with D_o can be obtained by a simple model that assumes the physical geometry is as shown in Fig. 1.2, and gases surrounding the droplet are not absorbing. The radiative heat transfer rate (Q_r) is expressed (i.e., with a number of additional assumptions such as $T_f^4 >> T_d^4$, $\varepsilon_d \sim 0.8$, $\varepsilon_f \sim 0.2$, $(D/D_f)^2 \sim 0.04$ and $\frac{\varepsilon_d}{\varepsilon_f}\left(\frac{D}{D_f}\right)^2\left(1-\varepsilon_f\right) < 1$) to be $Q_r \approx D^2\varepsilon_d\sigma T_f^4$. The heat transfer rate for droplet vaporization is approximately $Q_v \sim \rho_L K D h_{fg}$. The ratio of these two energies expresses the relative importance of radiation to vaporize the liquid:

$$\xi_r \sim \frac{D\varepsilon_d\sigma T_f^4}{\rho_L K h_{fg}}. \tag{1.10}$$

The presence of droplet diameter here indicates that the importance of radiation will depend on the size of the droplet.

Detailed numerical modeling (Marchese and Dryer (1997)) has shown a diameter affect on the radiative contribution such that for "small" droplets (D_o< 1 mm) the importance of radiation for typical hydrocarbon fuels is negligible while for "large" droplets, D_o > 1.5 mm (or so) it is important. On this basis, we will expect a different set of physics to be operative when considering the influence of scale (droplet size) on the overall burning process.

Droplet flame temperatures can be reduced by as much as 300 K (Marchese et al. (1999)) due to radiative heat losses to the surroundings. As the flame temperature decreases due to radiation, soot formation is significantly inhibited. The excessive radiative heat losses can also lead to "radiative flame extinction" (Chao and Law (1991), Marchese et al. (1998), Nayagam et al. (1998), Kazakov et al. (2003), Farouk

and Dryer (2012b)), which is to be contrasted to "diffusive flame extinction" that occurs when droplet is small and the fuel or oxidizer is depleted (Avedisian et al. (1988), Hara and Kumagai (1991), Farouk and Dryer (2012b)).

Radiative extinction in a droplet burning process is signified by the disappearance of the visible flame. Recent literature (Nayagam et al. (2012), Farouk and Dryer (2013)) suggests that after radiative extinction, low temperature (600-900 K) chemical kinetics can still be sustained by the remaining hot vapor though the heat is gradually dissipating. The droplet evaporation rate (or burning rate) is evidently higher than pure evaporation until the low temperature chemistry is terminated due to heat dissipation.

Regarding the time dependency of K, a standard practice was to linearize D^2 data and obtain a single value for K. However, the time dependency appears to be a real phenomenon associated with unsteady droplet heating (a transient heating region was experimentally observed to lapse 10-20 % of the entire burning time (Hubbard et al. (1975), Glassman (2008))). Though Eq. (1.4) is not predictive, it does capture the influence of thermophysical properties on the total burning time, $t_b = D_o^2/K$. The significance of transient heating can be estimated by characteristic time for thermal diffusion, $t_h \sim D_o^2/\alpha_L$. Therefore the importance of transient droplet heating processes relative to the total burning time is the ratio of these two times, $\xi_h = t_h/t_b \sim K/\alpha_L$, which shows that (at least according to the classical theory where K is constant) droplet heating affects are not dependent on the initial droplet diameter. With representative properties ($\alpha_L \sim 10^{-8}$ m^2/s and $K \sim 10^{-6}$ m^2/s), $\xi_h >> 1$. Hence, the thermal diffusion time

is long relative to the burning time irrespective of the droplet size. It should be expected that K is time dependent throughout.

As a result of the combined effects addressed above, burning rates can also be dependent on the initial droplet diameter as illustrated by the red solid line in Fig. 1.3d. The question mark in Fig. 1.3d indicates that there has been a lack of data that explore that soot and radiation related combustion physics for larger droplets (D_o > 1.5 mm) while existing data only encompass the asymptotic burning rate region (D_o < 0.4) and the intermediate droplet diameter region (0.4 mm < D_o < 1.5 mm) (Nayagam et al. (2008)).

Figure 1.4 categorizes the mechanisms of soot and radiation for various D_o regions. The D_o values that detemine the boundary of each region come from Nayagam et al. (2008) for heptane. For D_o < 0.4 mm, the flame size is small such that t_{res} is insufficient for soot to form. Soot formation becomes significant for 0.4 mm < D_o < 1.5 mm because the tres is long enough in this region. When D_o > 1.5 mm, soot formation in this region could either be enhanced due to a longer t_{res} with larger flames or inhibited by the low flame temperatures due to radiative heat losses to the surroundings.

As mentioned earlier, spherically symmetric droplet flame is the base case among all liquid combustion configurations. The interests in observing the spherically symmetric droplet burning behaviors of conventional fuels (e.g., gasoline and Jet-A), biofuels (e.g., camelina and tallow biofuels), and the surrogates that provide fundamental information that are not seen in the gaseous phase configurations motivates part of this study. Also, a lack of droplet combustion physics that have not

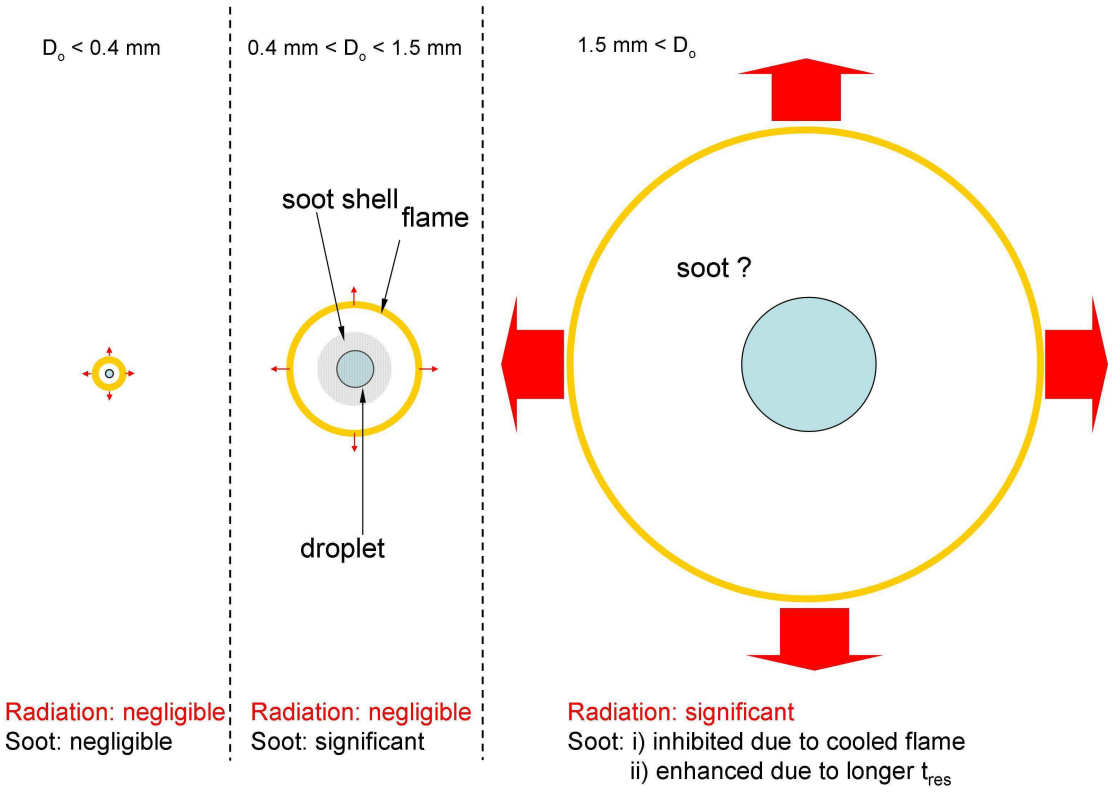

Fig. 1.4. Summary of anticipated length scale effects on soot formation and radiation of a spherical droplet flame for different regimes of droplet diameter (cf. Fig. 1.3d).

been described by the classical droplet combustion theory, e.g. effects of transient burning, soot and radiation, motivates the investigation for the droplet combustion experiments with a wide range of D_o.

1.2 Literature Review

1.2.1 Experiments on Low Gravity Droplet Combustion

To experimentally create a spherical droplet flame, minimizing Re_D and Ra_D is necessary. A reasonable approach is to control the suite of variables in these non-dimensional groups. With a given fuel and ambient condition of interest, properties like ν, β, T_s, and T_∞ (cf. Eqs. (1.1) and (1.2)) are less likely to adjust. Reducing gravity level or the droplet size is the most efficient and commonly used approach to generate spherical droplet flames. This section reviews the efforts of isolated single droplet combustion experiments carried out under low gravity. At the end of this section a literature table (Table 1.1) developed since Jackson (1994) was updated for all the literature of droplet combustion experiments carried out in low gravity before July, 2013.

The earliest low gravity droplet combustion experiments were documented by Kumagai and coworkers (Kumagai (1956) and Kumagai and Isoda (1957)). A nearly 1 mm n-heptane droplet was anchored on a single vertical silica fiber filament and ignited using sparks inside a falling chamber. The low gravity period (i.e., 1.0 s) is insufficient for droplets with this size so only fractions of the burning were observed. The droplet flames were found distorted either due to residual gravity or the support fiber. To isolate the effect of fiber on the flame distortion, Kumagai and coworkers

(Isoda and Kumagai (1958), Kumagai et al. (1971)) employed a streamline-shaped combustion chamber to reduce the drag effects and improve the spherical symmetry of the droplet flame during free fall.

Okajima and Kumagai (1975) first showed evidence of burning rate variation of n-heptane droplets with the D_o and t. Though a straight line is used to outline the D^2 data, a curvature in the early burning was noticeable but not discussed. The trend suggested that the burning rate slightly increases with D_o for 0.8 mm < D_o < 1.8 mm. A soot shell structure was first experimentally shown in this study but with only few notes on the carbon particle formation. n-Heptane later became a "calibration" fuel for further investigation of burning rate variations.

In the study of Okajima and Kumagai (1975), only partial burns were reported due to the limited experimental times. Potentially important phenomena such as extinction, micro-explosive burning and nonlinear trends were not accessible from these studies. Furthermore, no mention was made of the potential importance of soot formation even though the fuels examined were those that ostensibly would be expected to form soot. Later studies (Yang et al. (1991), Jackson et al. (1992), Jackson and Avedisian (1994) Hara and Kumagai (1994), Lee et al. (1998), Xu et al. (2003, 2004a, 2004b)) presented the influence of D_o on K in which the complete burning history was observed and some of these studies did show extinction and micro-explosive processes.

The reported data for conditions where the complete burning history could be observed and spherical symmetry was promoted were obtained for D_o less than about 1.8 mm. Values as low as 0.070 mm were reported (Hara and Kumagai (1994)). In this

range, burning in a "cold" ambience K_o is generally found to decrease with increasing D_o (Lee et al. (1998), Manzello et al. (2000)), Xu et al. (2003, 2004a, 2004b)), with the trends suggesting an asymptotic value for the alkanes and chlorinated hydrocarbons examined (Jackson et al. (1992), Jackson and Avedisian (1994)), as D_o is reduced.

Regarding the use of support fibers and its effect, Kumagai et al. (1971) first compare the results from free droplet and fiber supported (using a vertical beaded silica filament (0.15 mm)). The fiber supported droplet burning rate was noted to be slight "slower" compared to free droplet.

Avedisian and coworkers (Jackson et al. (1992), Jackson and Avedisian (1994), Avedisian and Jackson (2000)) used a single vertical quartz fiber (with various D_{fiber} ranging from 30 and 330 μm) with a beaded tip in their study of heptane. Figure 1.5 shows the photographs of free droplet (a) and fiber-supported droplet burning (b to d, for different fiber sizes) from Avedisian and Jackson (2000). Though it significantly reduced droplet distortion and burning rate discrepancies between fiber-supported (with the 30 μm fiber) and free droplet experiments, the vertical quartz fiber was found to introduce asymmetry of the soot shell at the end of the burning process (i.e., when the droplet is small), especially for the slightly larger fiber ($D_{fiber} > 50$ μm). This effect was concluded to be the lack of symmetry for Stefan drag and thermophoresis exerts on the soot particles as well as for the fuel vaporization due to the presence of the fiber.

The vertical beaded fiber arrangement (shown in Fig. 1.6a) was also used by Sato et al. (1990), Mikami et al. (1993), Xu et al. (2003, 2004a, 2004b), Dietrich et al.

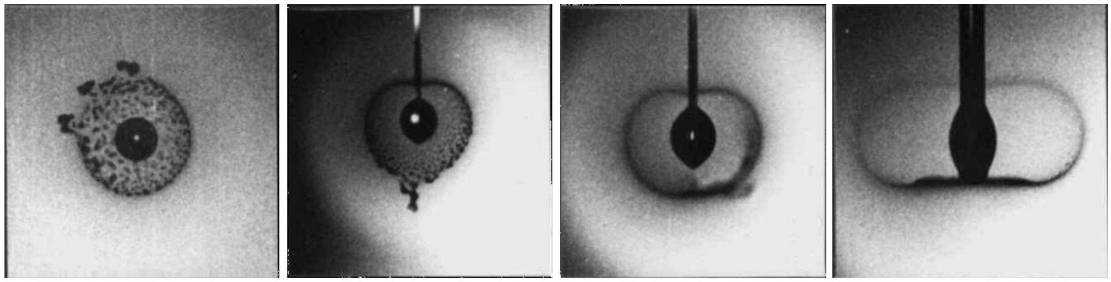

(a) (b) (c) (d)

Fig. 1.5. Photographs adapted from Avedisian and Jackson (2000) showing the effect of vertical quartz fiber sizes on the droplet shape and the soot shell formed during the combustion process (at t = 0.35 s) of a n-heptane droplet; (a) free-droplet experiment: D_o = 0.694 mm; (b) D_o = 0.697 mm, D_{fiber} = 0.057 mm; (c) D_o = 0.765 mm, D_{fiber} = 0.110 mm; (d) D_o = 0.614 mm, D_{fiber} = 0.330 mm.

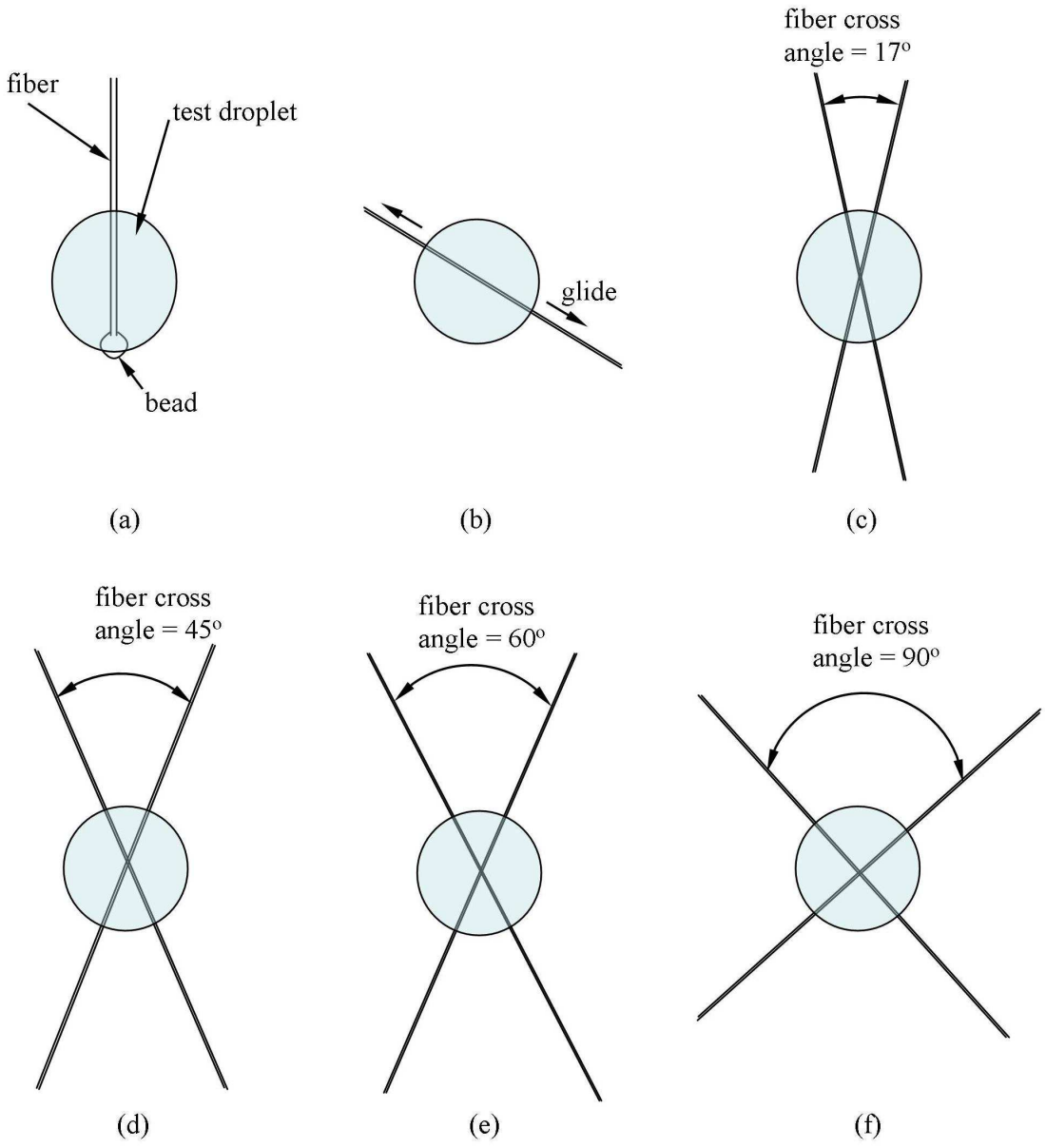

Fig. 1.6. Fiber setups that were considered for droplet combustion experiments: a single vertical fiber (a); a single stretched horizontal fiber (b); two horizontal stretched fibers crossed at 17^{o} (c), 45^{o} (d), 60^{o} (e), and 90^{o} (f).

(2005), Dattarajan et al. (2006), Jangi et al. (2009), Ogami et al. (2009), Nakaya et al. (2011) in their low gravity single droplet combustion experiments (see Table 1.1). Later development of support fiber configuration includes "stretched horizontal single fiber" (see Fig. 1.6b) first used by Lebedev and Marchenko (1979) and later adopted in several studies (Dietrich and Huggard (1992), Dietrich et al. (1996), Choi and Lee (1996), Aharon and Shaw (1998), Nayagam et al. (1998), Manzello et al. (2000), Dee and Shaw (2004), Ackerman et al. (2005), Mikami et al. (2006), Hicks et al. (2007), Manzello et al. (2009), Dzik et al. (2010), Shaw and Wei (2011, 2012), Aharon et al. (2013)).

The issue of test droplet gliding on a stretched fiber was improved by using two stretched fibers in an X shape. Avedisian and Callahan (2000) choose 17^o (see fig. 1.6c) as the crossing angle for their two 12 μm SiC fibers. This arrangement was later found to create noticeable droplet distortion from the top view (Bae (2005)). Larger fiber cross angles were pursued in later studies, e.g. 45^o (Bae and Avedisian (2002, 2004) with 12 μm SiC fibers) (cf. Fig. 1.6d), 60^o (Bae and Avedisian (2006, 2007, 2009) (cf. Fig. 1.6e), and 90^o (Pan et al. (2009) with 7 μm carbon fibers, Pan and Chiu (2013) with 2.5 μm ceramic fibers) (cf. Fig. 1.6f). Bae and Avedisian (2004) showed that using two 12 μm SiC fibers did not alter the burning rates of n-nonane droplets (D_o ~0.5 mm). Nonetheless, there have been very few literature reported comparisons between unsupported and supported droplet burning and addressed the cause of fiber effects on spherically droplet burning (if any).

There are a variety of facilities that create low gravity experimental environments. At one extreme, as discussed above, free fall facilities (or so-called

"drop towers") have a low gravity time ranging from about 1 s up to 10 s. At the other extreme are orbital craft, e.g. the International Space Station. The "free-fall" time is essentially unlimited and the quality of the on-board gravity level is high, less than 10^{-6} of earth's value with minimal disturbance associated with cabin disturbances. In between these extremes of available experimental time include aircraft flying parabolic trajectories (Gökalp et al. (1988)) and rockets launched in sub-orbital trajectories (Dietrich et al. (1996), Moesel et al. (2009, 2011), Kikuchi et al. (2011)).

For aircraft the gravity levels relative to the earth's value are on the order of 10^{-3} which is too high to entirely remove the affects of buoyancy in the droplet burning process. The presence of turbulence also degrades the gravity by the fluctuations that are introduced by turbulence. Facilities aboard sounding rockets have been successfully employed to study combustion of droplet arrays anchored to support fibers (Moesl et al. (2009, 2011), Kikuchi et al. (2011)), though they can be cumbersome to use (Nayagam et al. (1998)).

The environment of the ISS is ideal for droplet combustion experimentation because of its unlimited experimental time and physical internal space to house a novel design for forming, deploying and igniting test droplets without the need for mounting droplets on support structures to restrict their motion (though such a capability does exist on the ISS). The available time for low gravity must be longer than the droplet burning time.

For the straight chain hydrocarbons of interest, typical burning rates range from 0.5 mm^2/s to 0.7 mm^2/s (i.e., averaged over the life of the burning event). Figure 1.7 shows the variation of D_o with t_b from the classical theory for these two burning

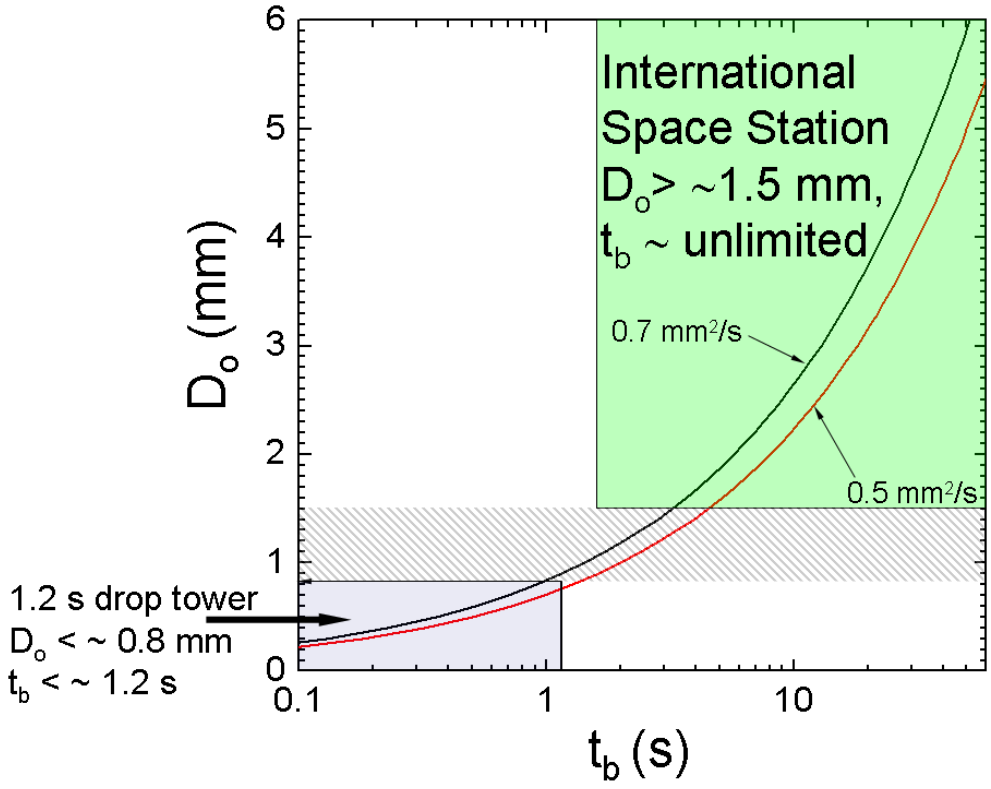

Fig. 1.7. Initial droplet diameter D_o vs. burning time t_b estimated using (K = 0.5 and 0.7 mm^2/s) with possible facilities that provide sufficient low gravity time.

rates. For a 1.2 s drop tower (Avedisian et al. (1988)), the complete burning history can be recorded for $D_o < 0.8$ mm while the complete burning history is accessible for all droplets greater than 1.5 mm in the ISS. Lower values of D_o cannot (easily) be studied in the ISS owing to difficulties with deploying droplets with minimum drift during burning with the experimental design. The cross-hatched zone signifies the range of D_o that was inaccessible with a 1.2 s drop tower and the ISS apparatus.

Table 1.1 includes the literature for droplet combustion experiments performed under low gravity condition from 1956 to 2013. This table was last updated by Bae (2005). Literature for different subjects in the following sections is reviewed in a narrative fashion.

Table 1.1. List of previously reported droplet combustion experiments in low gravity

fuel	configuration	ambience	initial diameter	g/g_o	reference
ethanol, heptane	suspended	0.1 MPa	0.9 - 1.3 mm	-	Kumagai 1956, Kumagai and Isoda 1957, Isoda and Kumagai 1959
benzene, heptane, hexadecane, iso-octane	suspended	0.1-0.4 MPa	0.7 - 1.8 mm	-	Faeth and Olson 1968 Faeth et al. 1969, Lazar and Faeth 1971
heptane	free & suspended	0.1 MPa	0.8 - 1.8 mm	-	Kumagai et al. 1971
ethanol, heptane	free	0.1 MPa	0.8 - 1.8 mm	$\sim 10^{-4}$	Okajima and Kumagai 1975, 1976
benzene, heptane, octane	free, array	0.1 MPa	1.2 - 2.2 mm	-	Brzustowski et al. 1979, 1981
decane, heptane	free	0.1 MPa & reduced, (variable O_2)	1.1 - 1.2 mm	$\sim 10^{-6}$	Knight and Williams 1980
benzene, heptane	suspended	0.1 MPa	1.3 - 1.4 mm	$\sim 10^{-5}$	Okajima and Kumagai 1982
benzene, ethanol, heptane	suspended, array	0.1-0.5 MPa	1.5 - 1.8 mm	$\sim 10^{-5}$	Okajima 1985, Okajima and Hara 1988
hydrazine/oil, water/oil	suspended	0.1 MPa	0.8 - 1.3 mm	$\sim 10^{-5}$	Okajima et al. 1985, Kimura et al. 1986
decane	free	0.1 MPa	0.9 - 1.5 mm	$\sim 10^{-5}$	Shaw et al. 1986, 1988, Haggard and Kropp 1987
heptane, toluene	free	0.1 MPa	0.4 - 0.5 mm	$\sim 10^{-3}$	Yang et al. 1987, 1989, Avedisian et al. 1988

Table 1.1. (continued) List of previously reported droplet combustion experiments in low gravity

methanol	free	0.1 MPa, (variable O_2)	0.8-1.1 mm	$\sim 10^{-6}$	Choi et al. 1988a, 1989, Cho et al. 1990
heptane	suspended	0.1 MPa	1.1-1.4 mm	$\sim 10^{-2}$	Gökalp et al. 1988, 1989, Chauveau and Gökalp 1989, Chauveau and Monsallier 1989
n-alkanes, ethanol	free	0.1 MPa	0.07-0.9 mm	$\sim 10^{-5}$	Hara and Kumagai 1988, 1989, 1991, 1994
heptane/hexadecane	free	0.1 MPa	0.4-0.5 mm	$\sim 10^{-3}$	Yang and Avedisian 1988
heptane	free	0.1 MPa	1.7-1.8 mm	-	Ristau et al. 1989
decane, heptane	free	0.1 MPa & reduced, (variable O_2)	0.7-2.5 mm	$\sim 10^{-6}$	Haggard et al. 1989, 1990, 1991, Card and Choi 1990
heptane, octane	suspended	0.1-10 MPa	1.0 mm	$\sim 10^{-5}$	Sato et al. 1989, 1990
n-alkanes, benzene	free	0.1 MPa	0.1-0.5 mm	$\sim 10^{-3}$	Sung and Wang 1989
heptane	suspended	0.1 MPa	1.0-1.1 mm	$\sim 10^{-3}$	Chandra and Avedisian 1990
decane, heptane	free	0.1 MPa & reduced, (variable O_2)	0.8-1.5 mm	$\sim 10^{-6}$	Choi et al. 1990, 1992, 1993
methanol/toluene	free	0.1 MPa	0.4-0.6 mm	$\sim 10^{-3}$	Jackson et al. 1990, 1991
octane	suspended	0.1-3.8 MPa	0.6-1.0 mm	$\sim 10^{-5}$	Sato et al. 1990
methanol/dodecanol	free	0.1 MPa	0.4-0.6 mm	$\sim 10^{-3}$	Yang et al. 1990
chloro-alkanes, heptane, their mixtures	free & suspended	0.1 MPa	0.4-1.1 mm	$\sim 10^{-3}$	Jackson & Avedisian 1991, Jackson et al. 1992
heptane	suspended	0.1 MPa	1.0-2.0 mm	$\sim 10^{-2}$	Chauveau et al. 1993
chloro-octane, heptane	free & suspended	0.1 MPa	0.4-1.1 mm	$\sim 10^{-5}$	Jackson and Avedisian 1994, Avedisian and Jackson 2000

Table 1.1. (continued) List of previously reported droplet combustion experiments in low gravity

heptane/hexadecane	suspended	0.4-3.0 MPa, N_2/O_2 (12, 13% O_2)	1.0 mm	$\sim 10^{-5}$	Mikami et al. 1993
decane, ethanol, heptane, hexadecane, methanol, octane	suspended	0.1-10 MPa, air & N_2/O_2 (12% O_2)	0.8 - 1.0 mm	-	Sato 1993
heptane/hexadecane	unsupported	0.1 MPa	1.0 mm	$\sim 10^{-6}$	Shaw and Aharon 1993
heptane	suspended, array	0.1 MPa	1.4 mm	-	Dietrich et al. 1994a
decane	free	0.1 MPa	1.0 - 4.0 mm	-	Dietrich et al. 1994b
heptane, hexadecane	free & suspended, array	0.1 MPa	0.8 mm	-	Kono 1994
binary and ternary mixtures of various alkanes & alcohols	suspended	0.033-0.3 MPa	0.4 - 1.8 mm	$\sim 10^{-6}$	Shaw et al. 1995
methanol	suspended	0.1-5 MPa	1.5 mm	$\sim 10^{-2}$	Chauveau et al. 1995
heptane/ethanol, heptane/methanol	suspended	0.1 MPa	0.6 - 1.15 mm	$\sim 10^{-6}$	Aharon and Shaw 1996
heptane, hexane, methanol, octane	suspended	0.1-12 MPa	1.5 mm	$\sim 10^{-2}$	Chauveau et al. 1996
heptane/hexadecane, methanol, methanol/dodecanol, methanol/water	suspended	0.1 MPa	2.0 - 5.0 mm	$\sim 10^{-6}$	Dietrich et al. 1996

Table 1.1. (continued) List of previously reported droplet combustion experiments in low gravity

methanol, methanol/water	suspended	0.1 MPa, N_2/O_2 (18-35% O_2)	1.0 - 1.5 mm	$\sim 10^{-6}$	Marchese et al. 1996
decane	porous	0.025 - 0.1 MPa	3.7 - 6.1 mm	$10^{-2} \sim 10^{-4}$	Struk et al. 1996
dodecane, dodecane/water	suspended	0.1 MPa	2.0 mm	10^{-5}	Tsue et al. 1996
ethanol, heptane, hexane, methanol, octane	suspended	0.1-12 MPa	~ 1.5 mm	$\sim 10^{-2}$	Vieille et al. 1996
heptane/hexadecane	suspended,	1.0 - 6.0 MPa	1.0 mm	$\sim 10^{-5}$	Mikami et al. 1997, 1998
heptane/hexadecane	suspended	0.033 - 0.3 MPa	0.47 - 1.5 mm	$\sim 10^{-6}$	Aharon and Shaw 1998
heptane/water	free	0.1 MPa	0.58 - 0.74 mm	$\sim 10^{-5}$	Jackson and Avedisian 1998
octadecanol	suspended	1.4 MPa	1.0 - 2.5 mm	10^{-2}, 10^{-4}	Kadota et al. 1998
methanol, methanol/water	suspended	0.1 MPa	2.0 - 7.0 mm	$\sim 10^{-6}$	Marchese et al. 1998
heptane	suspended	0.1 MPa, He/O_2 (variable O_2)	2.0 - 5.0 mm	$\sim 10^{-6}$	Nayagam et al. 1998
heptane, hexadecane, their mixtures	suspended, single & array	1.0 - 3.5 MPa, N_2/O_2 (12% O_2)	0.8 - 1.0 mm	$\sim 10^{-4}$	Okai et al. 1998, Okai et al. 2000a
nonane	free	0.1 MPa	0.55 - 0.57 mm	$\sim 10^{-4}$	Callahan and Avedisian 1999

Table 1.1. (continued) List of previously reported droplet combustion experiments in low gravity

decane,heptane	suspended	0.075 MPa	1.5 mm	~10^{-6}	Manzello et al. 1999
heptane	free	0.1 MPa, air & N_2/O_2 (25, 30% O_2)	2.9 - 4.0 mm	~10^{-6}	Marchese et al. 1999
decane	suspended, single & array	0.5 MPa & reduced	1.0 - 1.7 mm	~10^{-6}	Struk et al. 1999, 2002
nonane/hexanol	suspended	0.1 MPa	0.46 - 0.57 mm	~10^{-4}	Avedisian and Callahan 2000
methanol	suspended	0.1 - 14 MPa	~1.5 mm	~10^{-2}, 10^{-4}	Chauveau et al. 2000
heptane, heptane/hexadecane	suspended	0.1 MPa	1.0 mm	~10^{-6}	Chen and Shaw 2000
heptane	suspended	0.1 MPa	2.6 - 2.9 mm	~10^{-5}	Manzello et al. 2000
methanol, methanol/dodecanol	suspended, single & array	0.1 - 9.0 MPa	0.9 mm	~10^{-5}	Okai et al. 2000b
octadecanol, octadecane	suspended	0.1 - 20 MPa, N_2/O_2 & CO_2/O_2 (variable O_2)	1.0 mm	~10^{-5}, 10^{-2}	Segawa et al. 2000a
hexadecane/water	suspended	0.1 MPa	2.5 mm	~10^{-5}	Segawa et al. 2000b
nonane, hexanol	suspended	0.1 MPa, air & He/O_2 (30% O_2)	0.4 - 0.9 mm	~10^{-4}, 1	Avedisian and Bae 2001 Bae and Avedisian 2001a, 2001b, 2003a
decane	suspended	0.1 - 1.5 MPa	1.5 mm	-	Bolik et al. 2001
ethanol	suspended	0.1-0.2 MPa, N_2/O_2 (21 - 31% O_2)	1.9 - 3.0 mm	~10^{-4}	Choi et al. 2001, Yozgatligil et al. 2003

Table 1.1. (continued) List of previously reported droplet combustion experiments in low gravity

propanol/glycerol	suspended	0.1 MPa	~ 1 mm	10^{-6}	Dee and Shaw 2001, 2004
heptane, heptane/hexadecane	suspended	0.1 MPa	0.25 - 5.2 mm	$\sim 10^{-5}$	Shaw et al. 2001a, Shaw and Harrison 2002
ethanol/dodecanol, methanol/dodecanol	suspended	0.1 MPa	0.8 - 1.2 mm, 4.2 - 5.4 mm	$\sim 10^{-6}$	Shaw et al. 2001b
JP8, JP8+100	suspended	0.1 - 0.3 MPa, air & He/O_2 (30% O_2)	0.44 - 0.49 mm	$\sim 10^{-4}$, 1	Bae and Avedisian 2002, 2003b, 2003c
decane	suspended, array	0.1 - 5.0 MPa	1.0 mm	10^{-5}	Kobayashi et al. 2002
decane	free, spray	0.1 MPa	0.001 - 1.0 mm	10^{-5}	Nunome et al. 2002
ethanol, octane, toluene	suspended, array	0.1 MPa	0.7 - 0.8 mm	$\sim 10^{-4}$	Ueda et al. 2002
light diesel oil (LO), light cycle oil (LCO)	suspended	0.1 MPa, (variable T_∞)	0.6 - 1.7 mm	$\sim 10^{-5}$	Xu et al. 2002
JP8, JP8/TPGME	suspended	0.1 MPa	0.4 - 0.5 mm	$\sim 10^{-4}$	Bae and Avedisian 2003d, 2004b, 2005
decane	suspended	0.1 MPa, (variable T_∞)	0.8 - 1.6 mm	$\sim 10^{-5}$	Xu et al. 2003, 2004a, 2004b
JP8, JP8+100, JP8/hexanol, nonane	free, suspended	0.1 MPa, air & He/O_2 (30% O_2)	~ 0.5 mm	$\sim 10^{-4}$	Bae and Avedisian 2004a
propanol	suspended	0.1 - 1.0 MPa	~ 1 mm	10^{-4}	Dakka and Shaw 2004
decane	suspended	0.1 MPa	1.5 mm	10^{-6},1	Dattarajan et al. 2004

Table 1.1. (continued) List of previously reported droplet combustion experiments in low gravity

hexane	suspended	0.1 MPa	1.44 mm	10^{-6}	Manzello et al. 2004
ethanol	free, suspended	0.1-0.2 MPa variable O_2	1.5, 3 mm	10^{-6}	Urban et al. 2004
ethanol	suspended	0.1 MPa 21- 50 % O_2	0.9 – 2.0 mm	10^{-6}	Yozgatligil et al. 2004
hydroxylammonium nitrate/methanol/water	suspended	0.1 - 1.0 MPa	~1 mm	10^{-4}	Wei and Shaw 2004, 2006
methanol, heptane	suspended v= 3,5,10 cm/s	0.1 MPa,	2.17 mm, 1.03 mm	10^{-6}	Ackerman and Williams 2005
methanol, heptane	suspended, v=0.125 – 4 cm/s a=-10 to 10 cm/s^2	0.1 MPa	1.8 - 2.5 mm	10^{-6}	Ackerman et al. 2005
decane	suspended	0.013 - 1 MPa X_{O2} = 0.15, 0.17, 0.19	0.9, 1.7 mm	10^{-6}	Dietrich et al. 2005
heptane/hexadecane	suspended	0.1- 2.5 MPa 600, 700 ^oC	1.1 - 1.3 mm	-	Ghassemi et al. 2005
ethanol, octane, toluene	Suspended, electric field	0.1 MPa	0.8, 1.07-1.46 mm	-	Imamura et al. 2005a, 2005b, 2005c
decane	suspended	0.1 MPa 300,650,750 K	0.86, 1.0 mm	10^{-5}	Kikuchi et al. 2005, Mikami et al. 2006
nonane,ethanol	suspended, 1,2 droplets v= 10,20 cm/s	0.1 - 2 MPa	~1.2 mm	10^{-6},1	Kobayashi et al. 2005, Mitsuya et al. 2005

Table 1.1. (continued) List of previously reported droplet combustion experiments in low gravity

decane	suspended, array	0.1 MPa	~ 0.86, 1, 1.5 mm	10^{-6}	Mikami et al. 2005
1-octadecanol	suspended, array	0.1 MPa	1.0, 1.2 mm	10^{-5}	Segawa et al. 2005a
1-octadecanol, hexadecane	suspended, 2D and 3D droplet cluster	0.1 MPa	0.8 mm	10^{-5}	Segawa et al. 2005b
decane/hexadecane	suspended	0.1 MPa	~1 mm	10^{-4}	Shaw and Dee 2005
decane	suspended, acoustic field	0.1, 0.5 MPa	1.5 mm	10^{-5}	Tanabe et al. 2005
decane	suspended, array	0.1 MPa	~1 mm	10^{-4}	Wakashima et al. 2005
nonane	suspended	0.1 – 1 MPa	0.56 – 0.62 mm	10^{-4}	Bae and Avedisian 2006
1-propanol	suspended	0.1 – 1.0 MPa	~1 mm	10^{-4}	Dakka and Shaw 2006
methanol	suspended, acoustic field	0.1 MPa	~1 mm	10^{-6},1	Dattarajan et al. 2006
nonane	suspended	0.1 MPa 30% O_2/ 70% inert (He/N_2)	0.4 – 0.8 mm	10^{-4}	Bae and Avedisian 2007
methanol, heptane	suspended	0.1,0.3,0.5 MPa 21% O_2/ 0-70% CO_2/79-9%N_2	1.81 – 2.24 mm	10^{-6}	Hicks et al. 2007
eicosane	suspended, 3D droplet cluster	90 kPa, 820 K	0.6 – 1.2 mm	3×10^{-2}	Segawa et al. 2007

Table 1.1. (continued) List of previously reported droplet combustion experiments in low gravity

propanol	suspended	0.03,0.1, 0.3MPa Air/He,Xe,CO_2	1.2 – 1.3 mm	10^{-4}, 1	Shaw and Wei 2007 Wei and Shaw, 2009
methanol, methyl butanoate	suspended	0.1 MPa ~1273 K	1.2, 1.7 mm	-	Vaughn et al. 2007
ethanol	suspended	0.10 – 0.24 MPa 30% O_2/ 70%He, Ar, H_2	1.6 – 2.2 mm	10^{-6}	Park et al. 2008
ethanol	suspended, electric field	0.1 MPa	0.73 mm	10^{-4}	Yamashita et al. 2008a
octane	suspended, electric field	0.1 MPa	1.0 mm	10^{-4}	Yamashita et al. 2008b
nonane	suspended	0.1 MPa Air 30% O_2/70%He	0.4 – 0.95 mm	10^{-4}, 1	Bae and Avedisian 2009
1-butanol	suspended, v = 10 – 40 cm/s	0.4 MPa	~ 1 mm	10^{-6}	Jangi et al. 2009
hexane, heptane nonane, decane	suspended	75.9,101.3 kPa	1.46 – 1.53	10^{-6}	Manzello et al. 2009
decane	suspended	0.1 MPa 300 - 500 K	1.0, 1.2, 1.5 mm	-	Moesl et al. 2009
heptane	suspended, array	0.1 MPa	0.8 mm	10^{-4}	Nomura et al. 2009

Table 1.1. (continued) List of previously reported droplet combustion experiments in low gravity

decane	suspended, array	0.1 MPa	1.0 mm	10^{-5}	Oyagi et al. 2009
dodecane/hexadecane, biodiesel	suspended	0.1 MPa	~ 0.5 mm	10^{-2}-10^{-4}	Pan et al. 2009
ethanol	suspended	0.24 MPa 30% O_2/70%Ar 35% O_2/64%He	1.6 – 2.2 mm	10^{-6}	Park and Choi 2009, Park et al. 2009
methanol	suspended	0.1 MPa 21%O_2/ 79%(CO_2/N_2)	1.25 – 1.72 mm	10^{-5}	Hicks et al. 2010
1-butanol	suspended, v = 2,10,40 cm/s	0.1 – 1.0 MPa	1.25 mm	-	Jangi and Kobayashi 2010
decane	suspended, acoustic field	0.1, 0.5 MPa	-	10^{-5}	Tanabe 2010
ethanol	suspended, electric field	0.1 MPa	~1 mm	-	Imamura et al. 2011a, 2011b
octane	suspended, array, electric field	0.1 MPa	0.84 – 1.12 mm	-	Imamura et al. 2011c
decane	suspended, array	0.1 MPa 500 K	1.5 mm	-	Kikuchi et al. 2011, Moesl et al. 2011
soy methyl ester methyl oleate methyl decanoate	suspended	0.1 MPa 1300 K	1.0 – 1.2 mm	-	Marchase et al. 2011

Table 1.1. (continued) List of previously reported droplet combustion experiments in low gravity

ethanol, decane	suspended	0.1 MPa 21%O_2/0-60%CO_2/ 79-19%N_2	0.30 – 0.80 mm	-	Nakaya et al. 2011
decane	suspended, array	0.1 MPa Φ_g = 0.5 - 2	0.8 mm	10^{-4}	Nomura et al. 2011
1-propanol, heptane	suspended	0.1,0.3 MPa He,CO_2,Xe	~ 1 mm	10^{-4},1	Shaw and Wei 2011
iso-octane/heptane /toluene gasoline	suspended	0.1 MPa	0.50 – 0.53 mm	10^{-4}	Liu and Avedisian 2012*
gasoline, indolene	suspended	0.1 MPa	0.47 – 0.59 mm	10^{-4}	Liu et al. 2012a*
Jet-A, decane/iso-octane/toluene dodecane/iso-octane/ 1,3,5-trimethyl benzene/ propylbenzene	suspended	0.1 MPa	0.52 – 0.61 mm	10^{-4}	Liu et al. 2012b* Liu et al. 2013a*
heptane	free, suspended	0.07,0.1,0.2 MPa Variable O_2,CO_2	2.49 - 4.05 mm	- (ISS)	Nayagam et al. 2012
methanol, 1-propanol	suspended	0.1 MPa He,CO_2,Xe	~ 1 mm	10^{-4},1	Shaw and Wei 2012

Table 1.1. (continued) List of previously reported droplet combustion experiments in low gravity

heptane/methanol, heptane/ethanol	suspended	0.1 MPa variable O_2,He	0.67 – 0.92 mm	10^{-4}	Aharon et al. 2013
methyl butanoate	suspended	0.1 MPa	0.53 – 0.55 mm	10^{-4}	Farouk et al. 2013*
methyl decanoate	suspended	0.1 MPa	0.53 – 0.57 mm	10^{-4}	Liu et al. 2013b*
Jet-A, Camelina HRJ Tallow HRJ	suspended	0.1 MPa	0.54 – 0.63 mm	10^{-4}	Liu et al. 2013c*
decane	suspended, array	0.1,0.3 MPa 600-720 K	1 mm	-	Moriue et al. 2013
ethanol, 1-butanol, decane	suspended	0.1 MPa Air, CO_2,Ar	0.41 – 0.82 mm	10^{-4}	Nakaya et al. 2013
decane	suspended, array	0.1 MPa Φ_g=0 – 0.5	0.8 mm	10^{-4}	Nomura et al. 2013
methanol, ethanol, 2-propanol biodiesel/diesel	suspended	0.1 MPa	0.46 – 0.53 mm	10^{-2}-10^{-4}	Pan and Chiu 2013

The references with an asterisk (*) form chapters in this thesis.

1.2.2. Surrogate Development for Conventional Transportation Fuels

Conventional transportation fuels usually consist of hundreds of different compounds because they are derived from petroleum. The term "surrogate" is used in the field of combustion to refer to a model fuel that represents certain properties of a complex fuel (a target fuel) (Curran et al. (1998), Kyne et al. (1999), Edwards and Maurice (2001), Cooke et al. (2005)), e.g. conventional transportation fuels. A surrogate can consist of one or multiple components depending on the extent of combustion details to which it is designed to emulate for the target fuel (Edwards and Maurice (2001)). For example, a binary mixture of n-heptane and iso-octane ("primary reference fuel" (PRF) of gasoline) has been used to scale the knocking behavior of gasoline while octene (C_8H_{16}) alone has been used to represent the averaged formula of gasoline in simple emission calculations (Cooper and Alley (2002)).

More sophisticated surrogates are developed to match detailed species concentrations (PRF+ toluene (PRF+1), Chaos et al. (2007)) during the combustion of the target fuel as well as other combustion behaviors at the same time. A developed surrogate fuel is purely for modeling purposes. It is different from a "replacement" fuel that is actually used in the engine systems.

Existing guidelines for surrogate development include Edwards and Maurice (2001), Violi et al. (2002), Tsang and Hudgens (2003), Pitz et al. (2007), Colket et al. (2007), and Farrell et al. (2007). To summarize the general methodology, the first step in surrogate development is to determine the target fuel (e.g. gasoline), and the target combustion properties or objective functions (Smith et al. (1985), Hakansson et al. (2001), Williams (2001), Zhang et al. (2007)) to be mimicked by the surrogate (e.g.,

ignition delay, flame speed, emission, droplet burning rate,…etc.). The selected combustion properties should be "experimentally measurable" owing to a lack of target fuel properties in general. The surrogate components are then identified basing on the similarity of carbon number and the fragment groups between the target fuel and the surrogate mixture. More importantly, the physical and chemical properties as well as the combustion kinetics for the surrogate components should be available for the surrogate model.

With the chosen surrogate compounds, the concentration of each component in the surrogate mixture (if multi-component) is adjusted such that the measured combustion properties of the surrogate match that of the target fuel. The essence of surrogate development is to "mix" one or more modellable surrogate compounds and "match" the measurable combustion properties between the surrogate and the target fuel- "mix and match." This concept also applies for the surrogate developed to match the physical properties (in contrast with combustion properties) of the target fuel, e.g. liquid density, viscosity, dielectric constant.

Dooley et al. (2010, 2012a) proposed a methodology for surrogate development that uses four identified combustion properties (hydrogen to carbon (H/C) ratio, derived cetane number (DCN), molecular weight (MW), and threshold sooting index (TSI)) that are important for gas phase combustion processes to attempt to cover all the combustion properties. Intentions for selecting these properties are to comprehensively represent flame temperature (by H/C ratio), chemical kinetics (by DCN), molecular transport (by MW) (Holley et al. (2009)), and sooting (by TSI) at the same time for the target fuel. The formulated 3 and 4 component surrogates show very

good agreement with the target fuel, Jet-A (POSF4658) in several gaseous combustion experiments. However, it is also shown in their work that the formulated surrogates do a poor job on emulating the density and viscosity of Jet-A. This methodology was also applied to developing surrogates for synthetic paraffinc jet aviation fuel (S-8 (POSF4734)) (Dooley et al. (2012b)).

Mueller et al. (2012) proposed a methodology for formulating diesel surrogates that employs only fuel composition, ignition quality, volatility, and density as the combustion properties. By directly matching the fuel composition (through nuclear magnetic resonance (NMR) spectrometry), the H/C ratio, lower heating value, and smoke point, which are not explicitly matched, are fairly close to the target fuel values. Volatility is used instead of MW due to its potential to cover vaporization characteristics.

At this point, we see no study using a canonical multi-phase configuration like spherically symmetric droplet flame for surrogate testing. Moreover, whether or not a surrogate developed based on gaseous combustion can represent the combustion behaviors of its target fuel in a configuration involved with phase equilibrium and liquid gas unsteadiness is of interest.

1.2.3 Standard Gasoline- Indolene

Indolene is a federal certification fuel that was developed to reproduce gasoline's emission qualities in practical engine tests. The importance of using indolene for engine tests is due to the fact that the composition of gasoline varies with

regions and seasons. On the other hand, indolene was formulated to mitigate this effect, thereby leading to more uniform bases of comparison. The word "indolene" originated from the trade name for a test fuel manufactured by Standard Oil Company (Johnson and Riley (1978)) and it was later adopted by Amoco/BP (United States patent and Trademark Office (1926)).

In the U.S., indolene is more commonly referred to as a certification fuel that has passed the U.S. Federal Test Procedure (FTP) and can be used as a standard reference gasoline for engine emission testing. Like commercial gasoline, indolene is also produced from a petroleum refinery stream and thus consists of various hydrocarbons. In order to be certified as "indolene", the fuel has to pass a series of specification tests for physical and combustion properties (Haltermann Solutions (2010)), e.g. distillation temperatures, density, Reid vapor pressure, sulfur content, aromatic and olefins contents, octane number, and net heating value.

According to these specification regulations, manufacturers such as Amoco, Haltermann Solutions, or Chevron Phillips Chemical Company make certification fuels (Amoco/BP Indolene, TIER II EEE (HF-0437; EEE stands for Exhaust, Evaporative and Emissions), and Unleaded Gasoline (UTG-96) (Specification of UTG 96 (2008)), respectively) that all meet the regulated properties. Cromas (2012) compared the properties and particulate matter emissions of Amoco Indolene and Haltermann EEE fuel using a two-stroke direct-injection single cylinder research engine and the results show that these two fuels are identical. Recognizing that many synonyms for indolene do exist, we hereafter use the term "indolene" to refer to this federal certification fuel. Figure 1.8 shows the compositional differences between

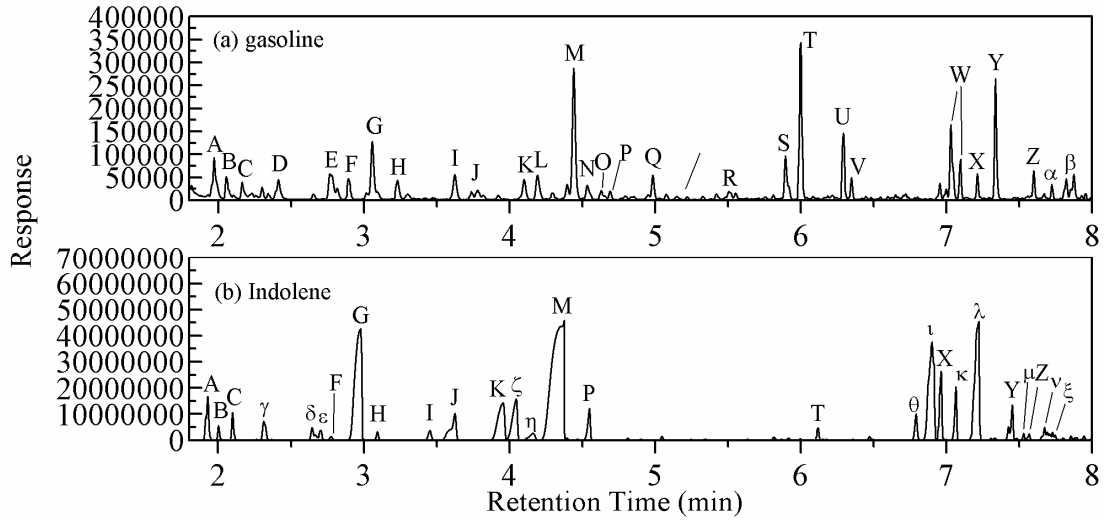

Fig. 1.8. GC/MS traces and analysis for (a) gasoline (octane 87) and (b) indolene: A, 2-methylpentane; B, 3-methylpentane; C, hexane; D, methylcyclopentane, E, benzene; F, 3-methylhexane; G, iso-octane; H, n-heptane; I, methylcyclohexane; J, 2,4-dimethylhexane; K, 2,3,4-trimethylpentane; L, 3,3-dimethylhexane; M, toluene; N, 3-methylheptane; O, 1,3-dimethyl-cis-cyclohexane; P, 2,2,5-trimethylhexane; Q, n-octane; R, ethylcyclohexane; S, ethylbenzene; T, 1,3-dimethylbenzene; U, p-xylene; V, nonane; W, 1-ethyl-2-methyl-benzene; X, 1,2,3-trimethylbenzene; Y, 1,3,5-trimethylbenzene; Z: indane; α, 1-ethyl-3,5-dimethybenzene; β, 1-methyl-2-(1-methylethyl)benzene; γ: 2,4-dimethylpentane; δ: cyclohexane; ε: 2,3-dimethylpentane; ζ: 2,3,3-trimethylpentane; η: 4-methylheptane; θ: propylbenzene; ι: 1-ethyl-3-methylbenzene; κ: 1-ethyl-4-methylbenzene; λ: 1,2,4-trimethylbenzene; μ: 3,7-dimethylnonane; ν: 1,3-diethylbenzene; ξ: 2-ethyl-1,3-dimethylbenzene.

gasoline and indolene.

A number of studies have been reported on combustion of indolene in both spark ignition (SI) and compression ignition (CI) engines. For SI studies, the effect of additives (e.g., tert-butyl alcohol (TBA) (Bykowski and Garbe (1981)), methyl-tert-butyl ether (MTBE) (Bykowski and Garbe (1981), Kayes and Hochgreb (1999)), methanol (Johnson and Riley (1978)), and ethanol (Dimou (2011), Hibert (2011), Kar and Cheng (2011)) on emissions has been examined. For CI engines, performance of indolene in a homogeneous charge compression ignition (HCCI) engine has also been studied (Daw et al. (2008), Farrell and Bunting (2006), Zigler et al. (2008)). Andersen et al. (2010a,b) used indolene (referred to as "EEE" gasoline) to investigate the effect of ethanol addition in gasoline on the distillation curve and vapor pressure. Metghalchi and Keck (1982) studied the flame velocity of indolene (research fuel RMFD-303); Abu-Isa (1983) used indolene (HO-III) to evaluate the effect of adding ethanol and MTBE to gasoline on elastomer swelling; and Ganley and Springer (1974) used leaded (HO 30) and unleaded (HO 0, clear) indolene to examine the effect of various engine parameters (e.g., spark timing, engine speed, air-fuel ratio) on particulate emission.

As indolene is considered a reference fuel for gasoline emission, we know of no study that has used a canonical multi-phase configuration, e.g. spherical symmetric droplet flame, to compare the burning processes of indolene and gasoline and show the effects of their intrinsic compositional differences.

1.2.4 Hydroprocessed Renewable Jet Fuels

Bio-based synthetic paraffinic kerosene (Bio-SPK) (derived from such

feedstocks as jatropha curcas, camelina, algae, and beef tallow) is a promising replacement for conventional jet fuels, with the most desired of such fuels being "drop-in" replacements (Blackey et al. (2011)). To produce Bio-SPK, chemically bonded oxygen is removed from animal fats (usually consisting of triglycerides and free fatty acids) or plant oil to produce a fuel with a higher heat of combustion, and the olefins are converted to paraffins (with carbon numbers in the jet range) for better thermal stability (Kinder and Rahmes (2009)). The resulting fuel is also termed a "Hydroprocessed Renewable Jet" (HRJ) fuel or "Hydroprocessed Ester and Fatty Acids" (HEFA) fuel (Hui et al. (2012)).

The composition of HRJs is less dependent on the bio-mass sources. Figure 1.9 shows the compositions of Jet-A (POSF4658) and HRJs derived from camelina (CHRJ, POSF6152) and tallow (THRJ). Jet-A has a comparatively high aromatic content while the HRJs consist of mostly paraffins and have virtually no aromatics (Fig. 1.9b). As such, we expect soot formation to be less for the biofuels compared to Jet-A, which would be manifested by thicker Jet-A soot shells compared to the biofuels. Moreover, CHRJ has 10% of cyclo-paraffins compared to 2% for tallow (see Fig. 1.9b) so we anticipate that CHRJ should be slightly more sooty than THRJ.

The potential for Bio-SPK fuels to reduce use of conventional fossil-based jet fuels is the basis for advocating that synthetic jet fuels comprise 50% of domestic aviation fuel usage by 2016 (Blackwell (2007)) for U.S. Air Force and reduce 50% of carbon emissions by 2050 for global aviation (Air Transportation Action Group).

The performance of sustainable jet fuels in military and civilian aircraft has been a subject of recent interest. Assessments of the efficacy of the fuels in flight tests

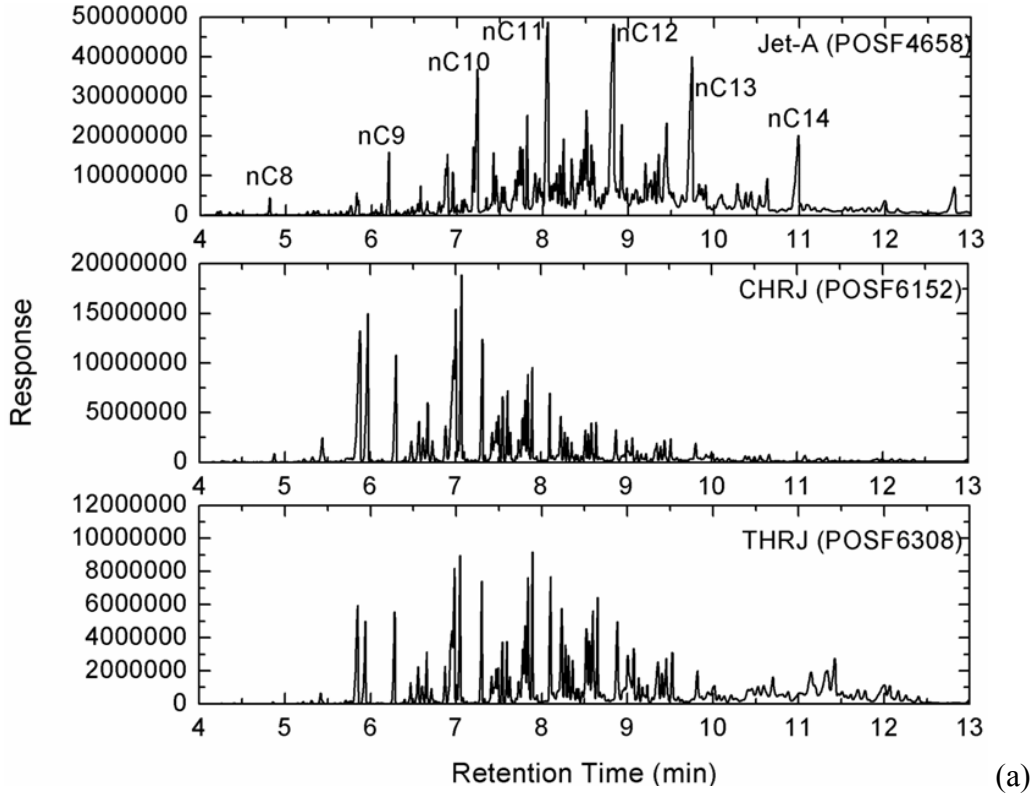

Fig. 1.9. (a) GC/MS peaks for Jet-A (POSF4658), CHRJ (POSF6152), and THRJ (POSF6308); (b) Hydrocarbon class distribution for Jet-A (Voili et al. (2002)), CHRJ, and THRJ (Corporan et al. (2011)) with numbers provided.

have often been qualitative and dependent to some extent on the specific aircraft being evaluated. For example, reports of full scale flight tests using equal-volume blends of JP8 and camelina to fuel FA/18 Super Hornet, C17 Globemaster, and A-10C Thunderbolt II aircraft indicated few differences compared to performance using neat JP8 (Corporan et al. (2011), IATA (2010)). On the other hand, aircraft fueled with Jet-A1 and jatropha blends showed differences in sooting and fuel efficiency in Air New Zealand, Continental Airlines and KML B747-400, and Japan Air Lines B747-300 aircraft (Rahmes et al. (2009), Blackey et al. (2011)). The reduced aromatic content of the biofuel was thought to be responsible for the reduced emissions. The various transport conditions experienced by fuels in different aircraft engines, or the differing blends themselves, could also be responsible for the results noted.

Provided the good agreement between HRJs and conventional jet fuels in several flight and engine tests, there has still been a lack of fundamental investigation that explains the combustion physics behind it. Comparison of spherically symmetric droplet burning for Jet-A and HRJs would provide more fundamental insights regarding the effects of fuel composition on a burning process.

1.2.5 Biodiesel Surrogates: Methyl Butanoate and Methyl Decanoate

Diesel power has the potential for an immediate impact on petroleum consumption, especially when conventional diesel is blended with bio-diesel fuels (Chakravarthy et al. (2007), Dagaut and Gaïl (2007), Pan et al. (2009)). First generation biodiesels derived from vegetable oils such as soybean and rapeseed oils are typically produced by reaction of the bio-oil with an alcohol (e.g., methanol,

ethanol, etc.) to form methyl ester mixtures (the "biodiesel") and glycerol (Agarwal (2007), Pagliaro and Rossi (2010)). Considering as an example rapeseed oil as the biofeedstock, the rapeseed methyl ester (RME) biodiesel that results from this process is considered to be comprised of five mostly unsaturated C_{17} to C_{19} (Herbinet et al. (2008 and 2010) or C_{14} to C_{22} methyl esters (Dagaut et al. (2007)).

Methyl butanoate (MB, boiling point of 375 K) is a simple biodiesel surrogate with its combustion chemistry originally developed by Fisher et al. (2000). It was subsequently considered that MB is too simple to simulate biodiesel as it does not represent its autoignition characteristics, particularly at low temperatures (Gaïl et al. (2007), Seshadri et al. (2009)). Herbinet et al. (2010) noted that the larger methyl decanoate molecule (MD, boiling point of 497 K) better represented the kinetics of RME for the jet-stirred reactor (JSR) data of Dagaut et al. (2007) than did smaller methyl ester molecules (e.g., MB). Most recently, the MD combustion kinetics was improved to include both high and low temperature oxidation chemistry (Dagaut et al. (2007)).

As the combustion chemistry for MB and MD has been developed, we know of no study that reports experimental data obtained from a liquid fuel combustion process that the combustion modelers use while incorporating the multi-phase combustion physics with developed combustion kinetics.

1.3 Objectives

An overarching objective of this study is to show that droplet combustion with spherical symmetry can be used as a "tool" to assess the efficacy of a formulated surrogate, quantitatively benchmark different fuel systems, and provide useful data for combustion modeling. The followings are the fuel systems of interest and the objectives associated with them.

With the longstanding recommendation of iso-octane and n-heptane as PRF of gasoline, we are interested to know whether or not a mixture consist of only PRF can be a good surrogate that replicates the spherically symmetric droplet burning of gasoline. Also, adding toluene to a PRF mixture was shown to improve the surrogate performance in gaseous combustion configurations (Chaos et al. (2007)). Here the effects of toluene as a surrogate component of gasoline on droplet burning also need to be addressed.

Indolene is used to represent emission of gasoline. Given the intrinsic difference in composition for gasoline and indolene, we would like to know if indolene burns similarly as gasoline in the configuration of spherically symmetric droplet flame. Also interested to see is that whether or not spherically symmetric droplet burning is a good configuration for such a benchmark process.

The 3 and 4 component surrogates (3CS and 4CS) for Jet-A (Dooley et al. (2010, 2012a)) were formulated based on gaseous combustion configurations. Besides the DCN and H/C of Jet-A that are matched by the 3CS, the 4CS further matches MW and TSI of Jet-A so it is presumably a better surrogate than the 3CS. In particular, sooting tendency is tractable in a spherically symmetric droplet flame, the 4CS is

expected to have better representation of Jet-A in terms of sooting compared to the 3CS. We would like to see if the 4CS really does a better job emulating the droplet burning of Jet-A than the 3CS and the extent to which the efficacy of surrogates developed using gaseous combustion can be carried over to a liquid fuel combustion configuration.

Camelina and tallow HRJs (CHRJ and THRJ) were shown to have similar performance as Jet-A in several flight and engine test. Whether or not their "performances" are still similar in the spherically symmetric droplet combustion is of interest. Moreover, we hope to obtain more fundamental understanding regarding the combustion physics related to the performance similarity for these fuels.

As the detailed combustion kinetics of MB and MD have been developed, numerical simulations of simple biodiesel surrogates is ready for gaseous combustion. However, there has been no literature reporting on a combustion model that is incorporated with multi-phase, liquid and gas unsteadiness, and at the same time with a 1-D configuration. Spherically symmetric droplet burning provides such an opportunity for numerical modelers to use the data obtained from experiments and compare with the numerical predictions. Moreover, as state of the art soot modeling is not yet ready to be incorporated with detailed combustion model, MB and MD droplets produce no soot (within the D_o range of interest) so the conditions used in the MB and MD simulations are more closely aligned with the real experiments, compared to sooting fuels. Our objective here is to provide experimental data that are useful for developing a combustion model (by a collaborator in Princeton University) for these biodiesel surrogate.

As support fibers are used in our droplet combustion experiments, it is important to know if there is any fiber effects on the data reported. We would like to compare the data obtained from fiber-supported with free droplet (without a support fiber) experiments. This comparison would show the validity of our fiber-supported data, while the support fiber had been found to have effects on the burning in some previously studies.

By using both the ground-based (a drop tower) and the ISS, we are able to access the combustion physics associated with a wide range of initial droplet diameters (D_o = 0.5 ~ 5.0 mm). The detailed trends of burning rate and other droplet burning parameters for D_o > 1 mm were only depicted by a very small number of data. We would like to obtain data within 0.5 mm < D_o < 5.0 mm (especially for the D_o > 1 range) with a finer increment of D_o that allow us to gain more insights into the combustion physics associated with droplet or flame sizes, e.g. soot formation and radiation. n-Alkanes like n-heptane (the "calibration" fuel for D_o effects since Okajima and Kumagai (1975)), n-octane, and n-decane are of interest because they are relevant to real transportation fuels and most importantly, they produce soot during droplet burning.

A thesis option at Cornell is to submit verbatim copies of journal articles for which the student is the lead author. At least three such articles are required when using this option. The following summarizes the chapters (or appendices) that are extracted from the original manuscripts of published and unpublished journal articles. Introductions, experimental methods, and image analyses of these articles are placed in Chapter 1, 2, and 3, respectively, in a more coherent way.

Chapter 4: **Liu, Y.C.**, Rah, J.K., Trenou, K.T., Hicks, M.C., Avedisian, C.T., "An experimental study of effects of support fiber on droplet burning in a low convection environment," *Combustion and Flame* (2013).

Chapter 5: **Liu, Y.C.**, Avedisian, C.T., "A comparison of the spherical flame characteristics of sub-millimeter droplets of binary mixtures of n-heptane/iso-octane and h-heptane/toluene with a commercial unleaded gasoline," *Combustion and Flame* 159 (2012) 770-783.

Chapter 6: **Liu, Y.C.**, Savas, A.J., Avedisian, C.T., "Comparison of the burning characteristics of indolene and commercial grade gasoline droplets without convection," *Energy & Fuels* 26 (2012) 5740-5749.

Chapter 7: **Liu, Y.C.**, Savas, A.J., Avedisian, C.T., "Spherically symmetric droplet combustion of three and four component miscible mixtures as surrogates for Jet-A," *Proceedings of the Combustion Institute* 34 (2013) 1569-1576.

Chapter 8: **Liu, Y.C.**, Savas, A.J., Avedisian, C.T., "The spherically symmetric droplet burning characteristics of Jet-A and biofuels derived from camelina and tallow," *Fuel* 108 (2013) 824-832.

Chapter 9: **Liu, Y.C.**, Farouk, T., Savas, A.J., Dryer, F.L., Avedisian, C.T., "On the spherically symmetrical combustion of methyl decanoate droplets and comparisons with detailed numerical modeling," *Combustion and Flame* 160 (2013) 641-655.

Farouk, T.I., **Liu, Y.C.**, Savas, A.J., Avedisian, C.T., Dryer, F.L., "Sub-millimeter sized methyl butanoate droplet combustion: microgravity experiments and detailed numerical modeling," *Proceedings of the Combustion Institute* 34 (2013) 1609-1616.

Chapter 10: **Liu, Y.C.**, Trenou, K.T., Rah, J.K., Hicks, M.C., Avedisian, C.T., "The influence of initial diameter on convection-free burning in the standard atmosphere for n-heptane, n-octane, and n-decane droplets: International Space Station and ground-based experiments," *Combustion and Flame* (2013).

Appendix C: Dembia, C.L., **Liu, Y.C.**, Avedisian, C.T., "Automated data analysis for consecutive images from droplet combustion experiments," *Image Analysis and Stereology* 31 (2012) 137-148.

CHAPTER 2

EXPERIMENTAL METHODS

2.1 Drop Tower Experiments

The spherical symmetry of a droplet flame is achieved by burning a "stagnant" (u = 0) and small droplet (D < 1 mm) in an environment that reduces the gravity level. As such, a low convection condition can be created because Re_D and Ra_D (cf. Eq. (1.5) and (1.6)) are reduced at the same time. A drop tower is used for this purpose in the ground-based configuration. The droplet tower at Cornell University is 7.6 m high and it provides an experimentation time of 1.2 s with a low gravity environment. The low gravity environment is simply created by releasing the entire instrumentation into free fall. A test droplet is ignited by two symmetric sparks on the opposite side of the droplet and the created spherically symmetric flame is imaged during this course of period (1.2 s). A low Reynolds number condition is created by anchoring the droplet very thin fiber structures such that the relative velocity between the droplet and stagnant ambient is minimized during free fall.

Figure 2.1 provides an overview of the entire drop tower facility used in this study. An instrumentation package in which a combustion chamber, spark ignition circuits, imaging systems are mounted is released from the top of the drop tower and falls down to a deceleration facility. The signals for droplet generation, spark ignition, electrode retraction, and camera communications (all described later) are transmitted through the long signal cable. The procedures of droplet generation, package release, spark ignition, electrode retraction in a drop tower experiment described here requires

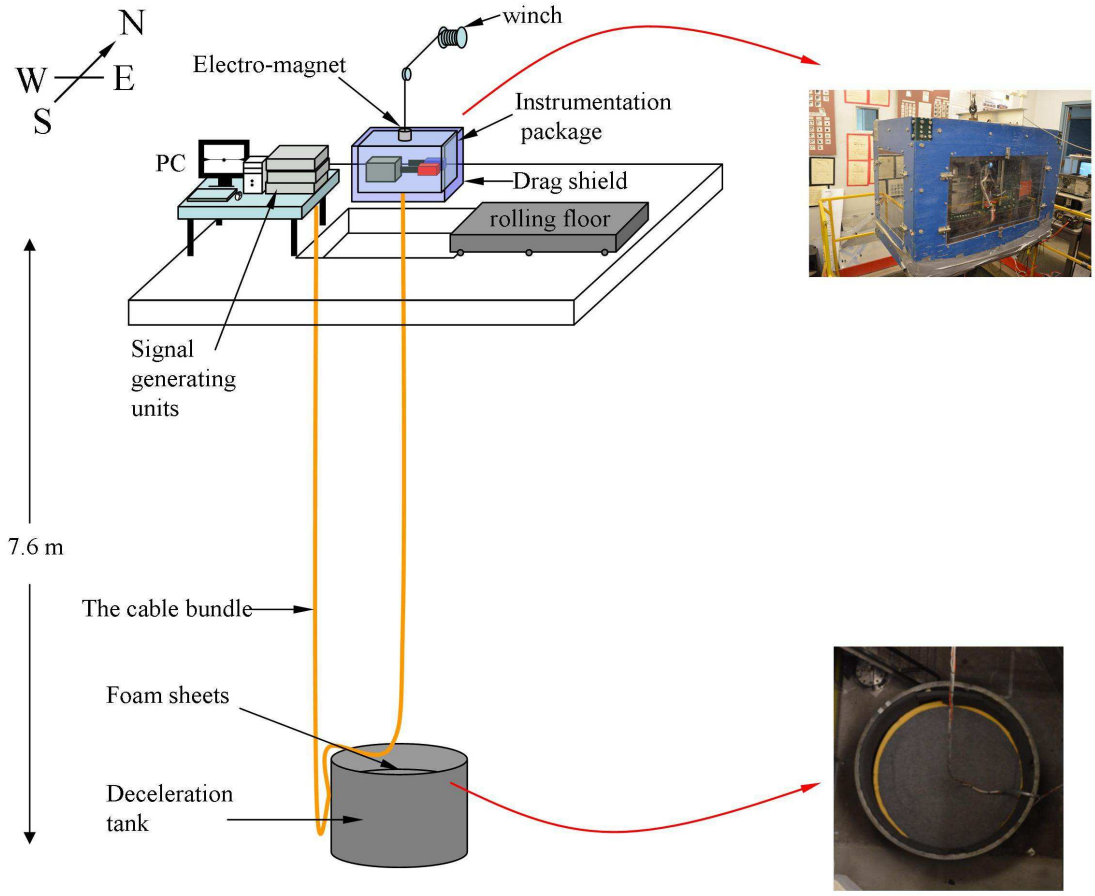

Fig. 2.1. Schematic of the drop tower facilities used in this study.

high precision of positioning and timing control. The following sub-sections describe components in the drop tower facility used in this study, including a drop package, drag shield, combustion chamber, spark circuits, droplet generator, imaging systems and electromagnet, and the challenges associated with their operations.

2.1.1 Drop Package, Drag Shield, and Deceleration Tank

The "drop package" described in this section is the instrumentation package (cf. Fig. 2.1) in which a combustion chamber, spark and retraction circuits, an onboard power supply, and two cameras are mounted. The skeleton of this inner package is adopted from the 400-lb package (18"×22"×36") described by Bae (2005). By using color video (Hitachi HV-C20, 3CCD, 30 fps, 0.4 MP) and new digital high speed black-and-white (BW) cameras (Canadian Photonic Labs, MS-80K, 200 fps, 3.9 MP) in the current it is more convenient than the effort to develop 16 mm film and digitalize them for measurement purposes, which constituted a very significant amount of time in the experiments of subsequent analysis of the images (i.e. Yang (1990), Jackson (1994), Callahan (2000), Bae (2005)). The transition from 16 mm high speed film to high speed digital imaging was made possible by commercial development of a new generation of high resolution (4MP/frame) cameras.

The challenge in the present study is to design a new layout that accommodates the digital high speed camera and all the other components within the platform of the instrumentation package. Figure 2.2 shows a top view of the component layout and Fig. 2.3 presents photographs of the actual component placement. With the layout shown in Fig. 2.2, the droplet burning process inside the combustion chamber can be

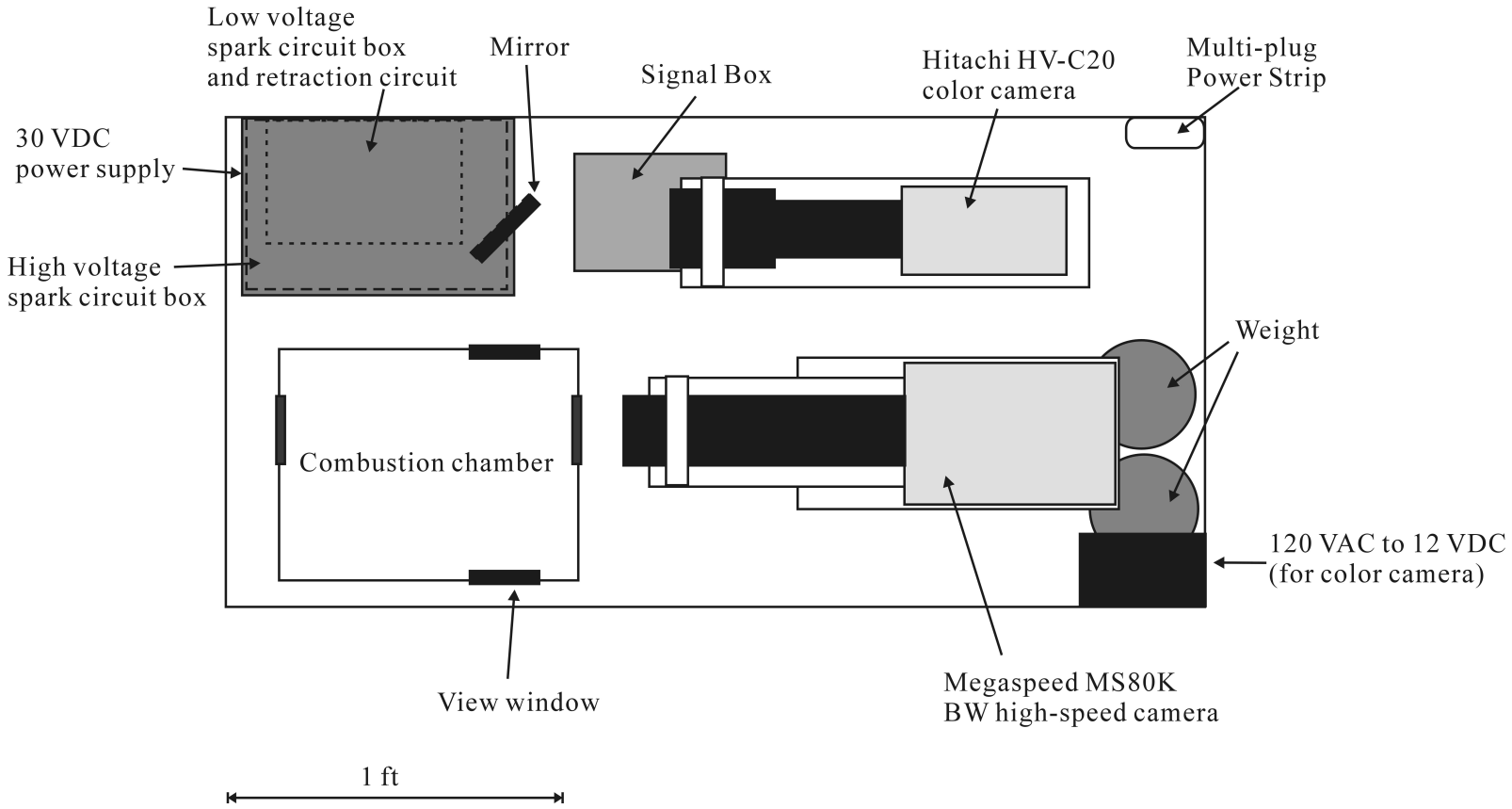

Fig. 2.2. Top view schematic of the layout arrangement for the inner instrumentation package.

documented by both BW and color cameras through the view windows on the combustion chamber.

It is found very convenient to mount the cameras and the combustion chamber on traverses (G, I, and E, respectively, in Fig. 2.3) that provides flexibility for fine-tuning the droplet position (inside the combustion chamber) relative to the two cameras. Note that the relative distances between the chamber and the cameras are slightly different for every experiment since the entire spark-fiber arrangement varies every time.

The color camera is positioned parallel to the MS-80K and recording the mirror reflection of the flame from the north window on the combustion chamber whereas the MS-80K records the flame directly from the east view window. The working distance of the lens (after adding extension tube elements) on the color camera is around 30 cm. This long working distance facilitates the recording from the mirrored images. This is to be contrast to the slight shorter working distance for the BW camera lens, which is considerably closer to the droplet flame. Details for the cameras and lenses are provided in Section 2.1.8.

A 30 VDC power supply is stacked with the spark circuits onboard the drop package (see the west-north corner of Fig. 2.2) because it is found that the 30 VDC signal degrades during transmission along the long cable. Details of the connections and working principles of these circuits are provided in Section 2.1.5.

The signals for droplet generation, spark ignition, electrode retraction, are all generated outside the package (from a pulse generator (HP 214B) and a multi-channel digital signal composer (QC-9618) respectively) and transmitted, along with the ±15

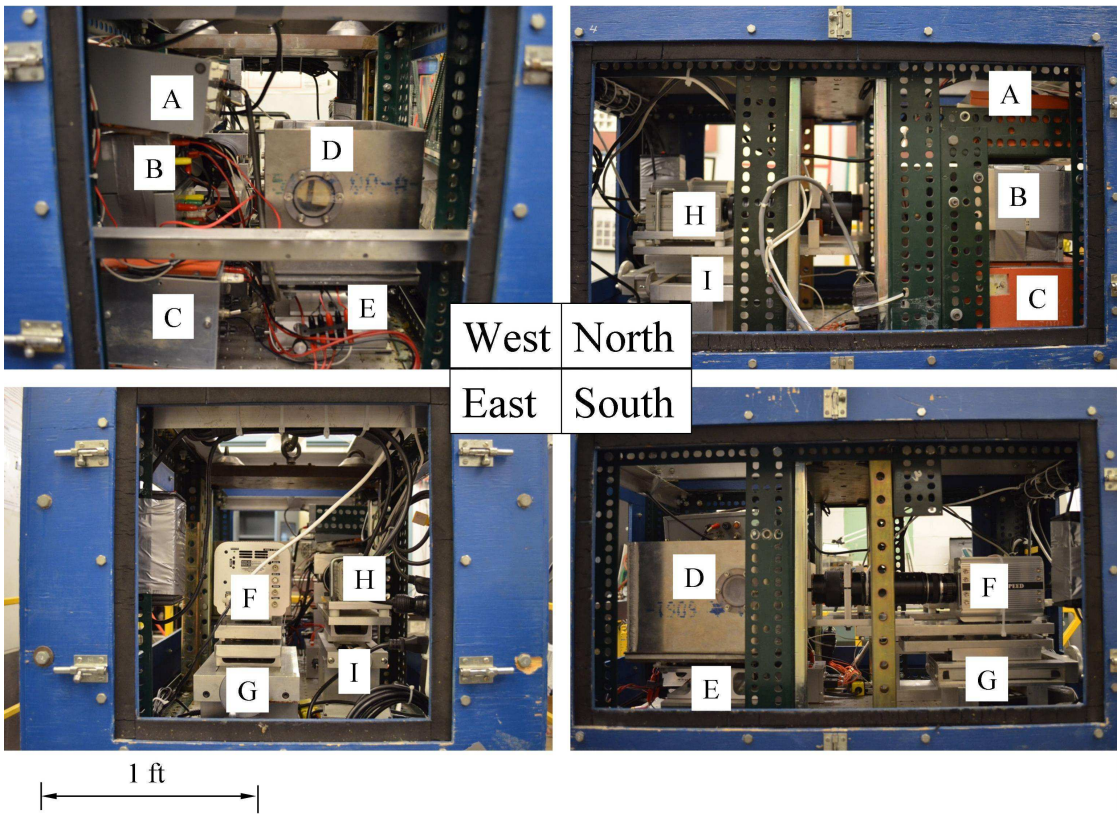

Fig. 2.3. Side views of the instrumentation package from the directions (East, West, South, and North) indicated in Fig. 2.2. A: 30 VDC power supply; B: Low voltage spark circuit; C: high voltage spark circuit; D: combustion chamber; E: 2-D traverse for the combustion chamber; F: BW camera (MS-80K); G: traverse for the BW camera; H: color camera (Hitachi HV-C20); I: traverse for the color camera.

VDC and ground connections, into the package through the main cable (16 individual wires). Outside the main cable, a 120 VAC power cord and camera signals (an Ethernet cable for the BW camera; BNC signals for the color camera) are delivered through individual cables that are braided to the main cable. We term the entire braided cable that connects the PC table (with all the associated units) and the drop package "the cable bundle or "the umbilical cable" (cf. Fig. 2.1).

The 120 V power cord goes directly to the multi-plug power strip (located at the north-east corner of the package, see Fig. 2.2) onboard the inner package that provides the power needed for the 30 VDC power supply, the BW camera, and the color camera inside the drop package. Detailed connections between the power supplies and the circuits are given in Section 2.1.5. Connections for the two cameras are in Section 2.1.8.

A falling object like an instrumentation package can be slowed down due to air drag which could increase the effective gravity level within the moving frame of reference. To reduce the air drag, a "drag shield" (see Fig. 2.1) is used to enclose the drop package. A drag shield is essentially a slightly larger package (25"×30"×43") that shields the inner package from the surroundings whereas the inner package falling within it. The drag shield employed in the present study is developed by Callahan (2000) and Bae (2005). Figure 2.4 illustrates the relative positions of the instrumentation package and the drag shield during a free fall. The current design for the drag shield allows a space (~ 7") between the bottom of the inner package and the bottom of the drag shield prior to dropping. This space is large enough so that the inner package does not make contact with the drag shield during the 7.6 mm free-fall.

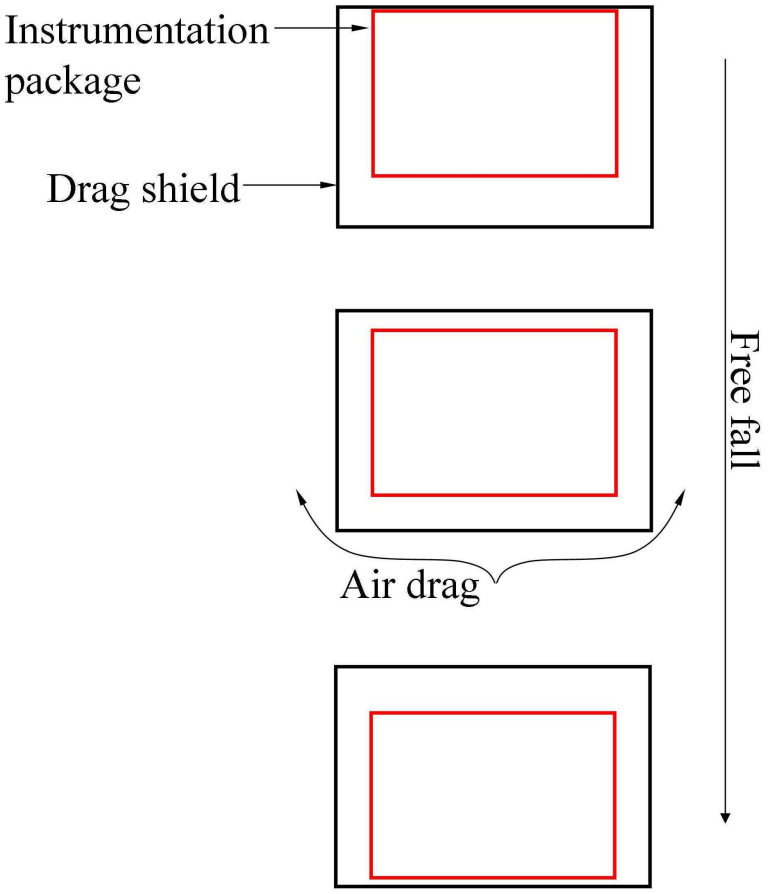

Fig. 2.4. Illustration of the relative motion of the inner and outer packages during free-fall showing how the outer package can be used as a "drag shield."

The gravity level of the inner package is therefore maintained at 10^{-4} (Callahan (2000)) of the normal earth gravity and is independent of the weight of the inner package.

There are some issues regarding the drag shield. When the entire package lands on the foam sheets (cf. Fig. 2.1), the cable bundle is typically twisted or jammed underneath the package. A particular portion of the cable bundle is often severely scratched and can be cut by the bottom sharp edges of the drag shield leading to lost of signal connections for subsequent experiments. The cable bundle that is frequently hit by the outer package should be protected. Each sharp edge at the bottom of the drag shield is protected by a row of sponges and rubber sheets. Figure 2.5a illustrates how the drop package can potentially damage the cable bundle at when it lands on the deceleration foam boards. Figure 2.5b shows how the sharp edge at the bottom of the outer package is covered that actively protect the cable bundle from drop to drop.

The deceleration system was developed by (Yang 1990). It is a cylindrical steel tank measured 6 ft in height and 6 ft in diameter being filled with 4 ft high air-tunnel foam sheets (cf. Fig. 2.1). This system is designed to protect the hardware inside the drop package from the impact at the end of free fall. Also important is that during the deceleration process, the side walls of the drag shield are uniformly enclosed. This particular feature allows the entire drop package to maintain its upright position such that the package does not bounce off or collide on the tank wall. This upright position also facilitates the later package retrieving process. A circular blanket with approximately the same size of the tank is used to reduce wearing of the foam sheets in frequent operations.

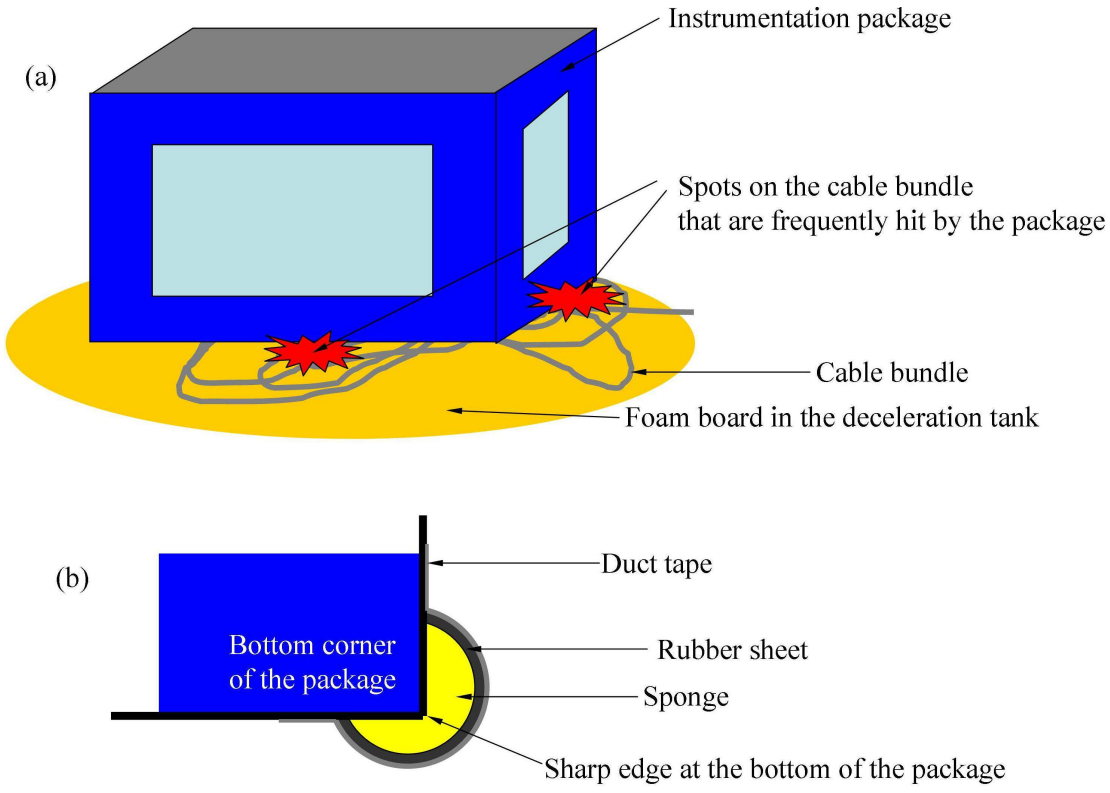

Fig. 2.5. Illustration of (a) how the package can introduce damage to the cable bundle when it lands on the deceleration foam boards and (b) how the sharp edge at the bottom of the package is covered by sponge and rubber sheets to actively protect the cable bundle.

2.1.2 Combustion Chamber

The combustion chamber used in the present study is a stainless rectangular box (8”×8”×11”). Figures 2.6a and 2.6b show photographs of the chamber and the top view of its base plate, respectively. Figure 2.7 shows the interior look of the chamber. Each side wall of the chamber has a view window that allows flame or droplet observations (see Fig. 2.7). A 10 W LED light source (Black Diamond Equipment, Ltd. Salt Lake City, UT) (cf. Fig. 2.7) is used to provide the backlighting source for the BW camera (outside of the east view window) because of its small size, low temperature, and good lighting intensity. The LED light source is installed inside the combustion chamber, on the west wall, with a piece of transparent tape. The background intensity for the BW images is adjusted merely by the camera exposure time and the lens aperture (see Section 2.1.8). We found that by varying exposure time and aperture, droplet images with various sooting levels (the least sooty (essentially no soot)- methyl butanoate; the most sooty- Jet-A) could be captured with good contrast.

As shown in Fig. 2.6b, the base plate of the combustion chamber has several small “ditches” that collect the fuel spills after a drop event. The collection of the fuel spills facilitates chamber cleaning for the preparation for the next experiment. Also can be seen in Fig. 2.6b are two rows of pin connectors (1 to 7 in Fig. 2.6b). These pins are used to transmit the signals for droplet generation, spark electrode retraction, as well as the high voltage sparks. These pin connectors are sealed from the bottom of the chamber to prevent gas leakage (for elevated pressure experiments). Figure 2.8 shows the chamber bottom where the connector sets are attached. The metal bar installed on a 2-D traverse at the south-west corner (8 in Fig. 2.6b) as well as a fixed

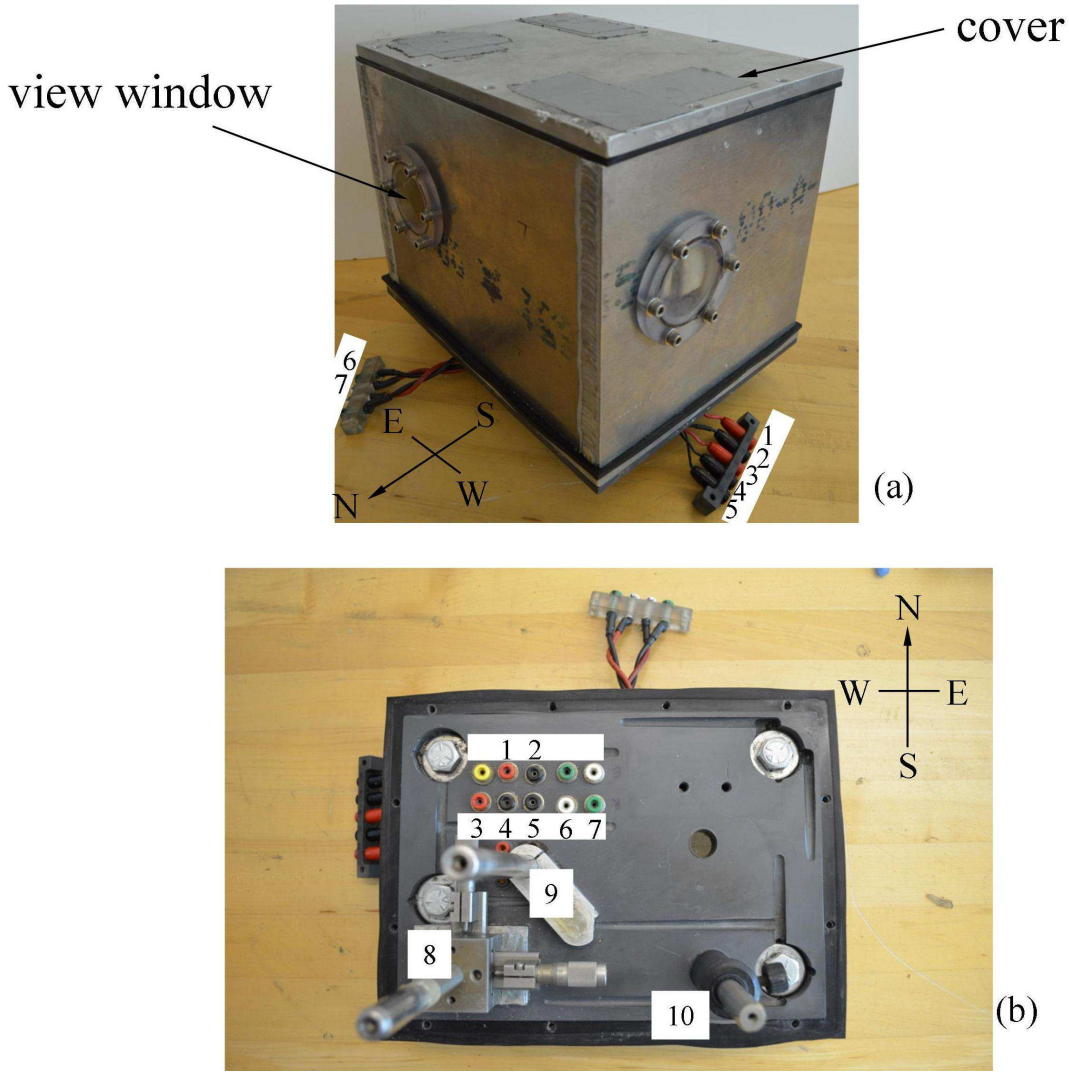

Fig. 2.6. Photographs of (a) the combustion chamber and (b) view from top with cover removed. 1 and 2 for droplet generation signal; 3-5 for spark signals; 6 and 7 for the retraction signal; 8 and 9 for the spark electrode set; 10 for the fuel reservoir. The use of these ports and supporting bars is shown in Fig. 2.7.

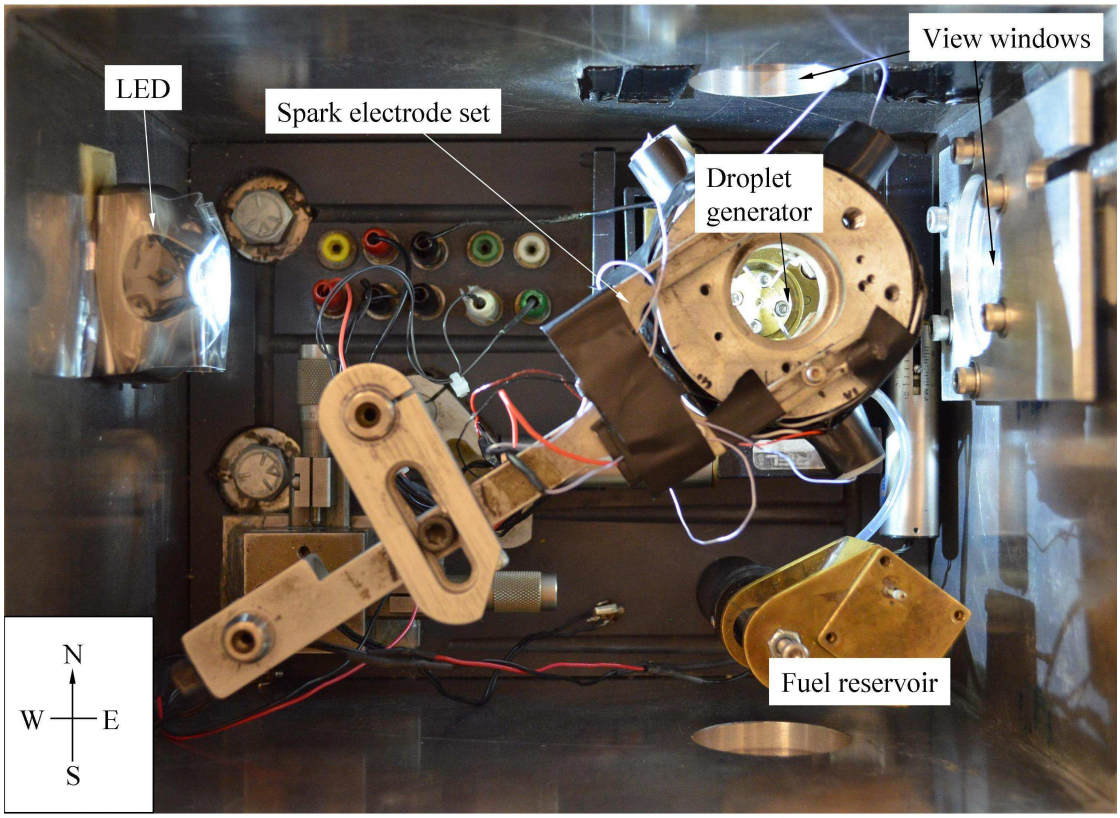

Fig. 2.7. Interior arrangement for the combustion chamber.

support (9 in Fig. 2.6b) are used to mount the spark electrode set and allow some flexibility for positioning the droplet relative to the two cameras. At the south-east corner of the base plate, a metal bar (10 in Fig. 2.6b) used as the fuel reservoir mount that provides fuel to the droplet generator that is fastened at the north-east corner of the chamber. More details about the droplet generator are provided in the next section.

2.1.3 Droplet Generation

Droplet generation is one of the most important elements of the experiments. To deploy a single droplet to a targeted location is a substantial challenge because of surface tension and wetting to other surfaces that is inherent to a liquid. The unique methodology for droplet generation used in the present study was first developed by Avedisian et al. (1988). This approach incorporates a "droplet generator" that uses a piezoelectric transducer to squeeze liquid through a nozzle with a volume that depends on electric pulse applied to it. The droplet generator used in this study is designed by Callahan (2000) based on the same working principle as Avedisian et al. (1988). Figure 2.8a and 2.8b show the assembled droplet generator and an exploded view for each component. The center of the white ceramic layer on the piezoelectric transducer (American Piezo Ceramics Inc., Mackeyville, PA, part # 352428 A) is soldered with a wire that is connected to the positive voltage pin ("10" in Fig. 2.8b) of a BNC output from the pulse generator (HP 214B). The perimeter metal part of the piezoelectric plate makes contact with the base ("9" in Fig. 2.8b) that is grounded and connected to pin 11 in Fig. 2.8b for the droplet generation signal.

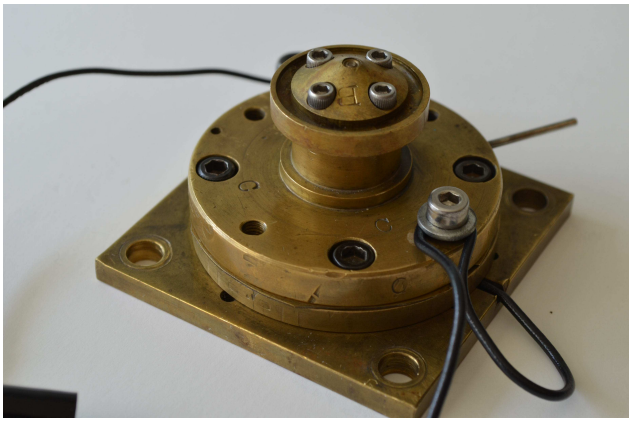

(a)

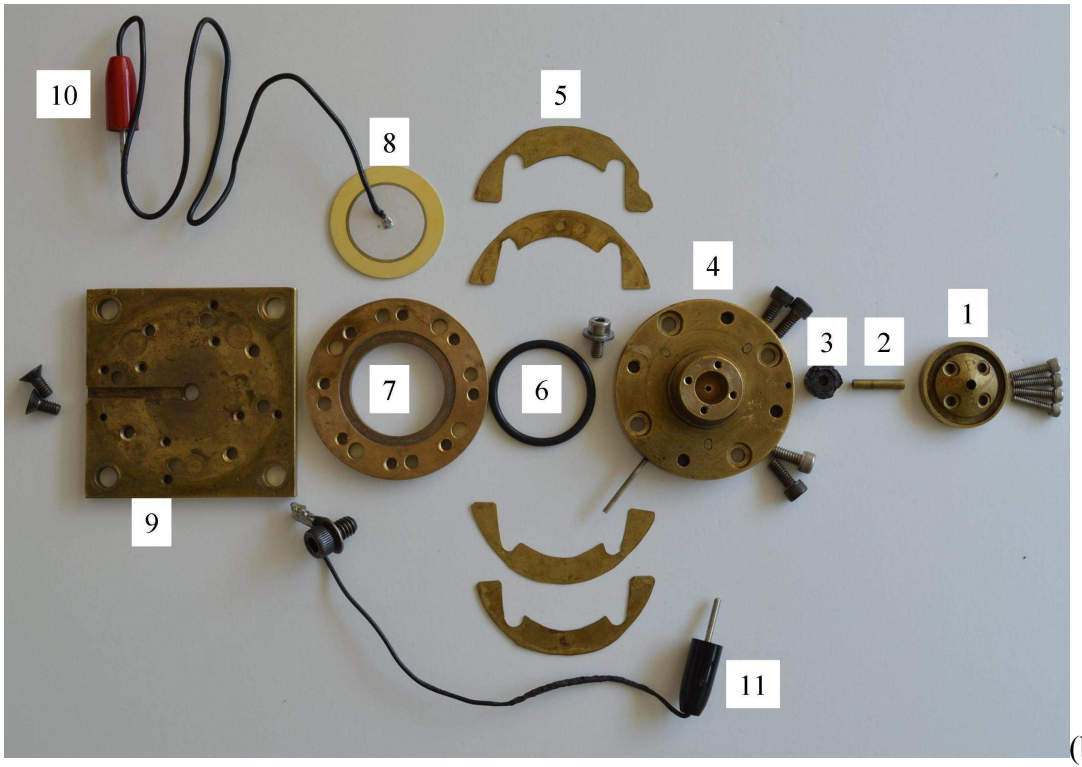

(b)

Fig. 2.8 (a) The assembled droplet generator; (b) exploded view of the droplet generator (1: top cap; 2: nozzle; 3: viton seal (1/4” OD × 1/8” ID tubing); 4: upper housing; 5: brass shims; 6: 121 viton o-ring; 7: lower housing; 8 piezoelectric diaphragm; 9: base; 10: connection pin that goes to “1” in Fig. 2.6b; 11: connection pin that goes to “2” in Fig. 2.6b.)

Although the body of the droplet generator is a design from Callahan (2000), the cap ("1" in Fig. 2.8b) is adopted from Jackson (1994) to accommodate the brass nozzle ("2" in Fig. 2.8b and Fig. 2.9b) manufactured by Schott Process Systems, Inc. (Hartville, OH) with an exit orifice made of glass. This brass nozzle facilitates droplet generation with consistent size within the range of 0.5 ~ 0.8 mm for all the fuels investigated in this study. Figure 2.9 is a photograph of a glass nozzle (a) that generated 0.5 mm droplets before the bottom was fractured due to the pressure from the cap ("1" in Fig. 2.8b) and seal ("2" in Fig. 2.8b) and a brass nozzle used in this study (b). Figure 2.9c shows how the components "1", "2", and "4" in Fig. 2.8b are assembled.

To activate the piezoelectric diaphragm, a pulse with appropriate voltage and width must be applied. These pulse parameters are sensitive to the liquid level ("h" in Fig. 2.11) in the fuel reservoir as well as to liquid properties, e.g. surface tension and viscosity. We found an optimal range of voltages for droplet generation 10 to 30 V with a pulse width of 2 to 6 ms. With the appropriate pulse adjusted using the "amplitude (V)" and "width (s)" dials on the HP 214B, the piezoelectric plate responds to the pulse and is able to squeeze a proper amount of liquid out of the nozzle. Figure 2.10 shows the front panel of the HP 214B used for droplet generation in this study. The pulse with designated voltage and width is triggered by pressing the "man" (manual) button at the bottom left corner of the panel.

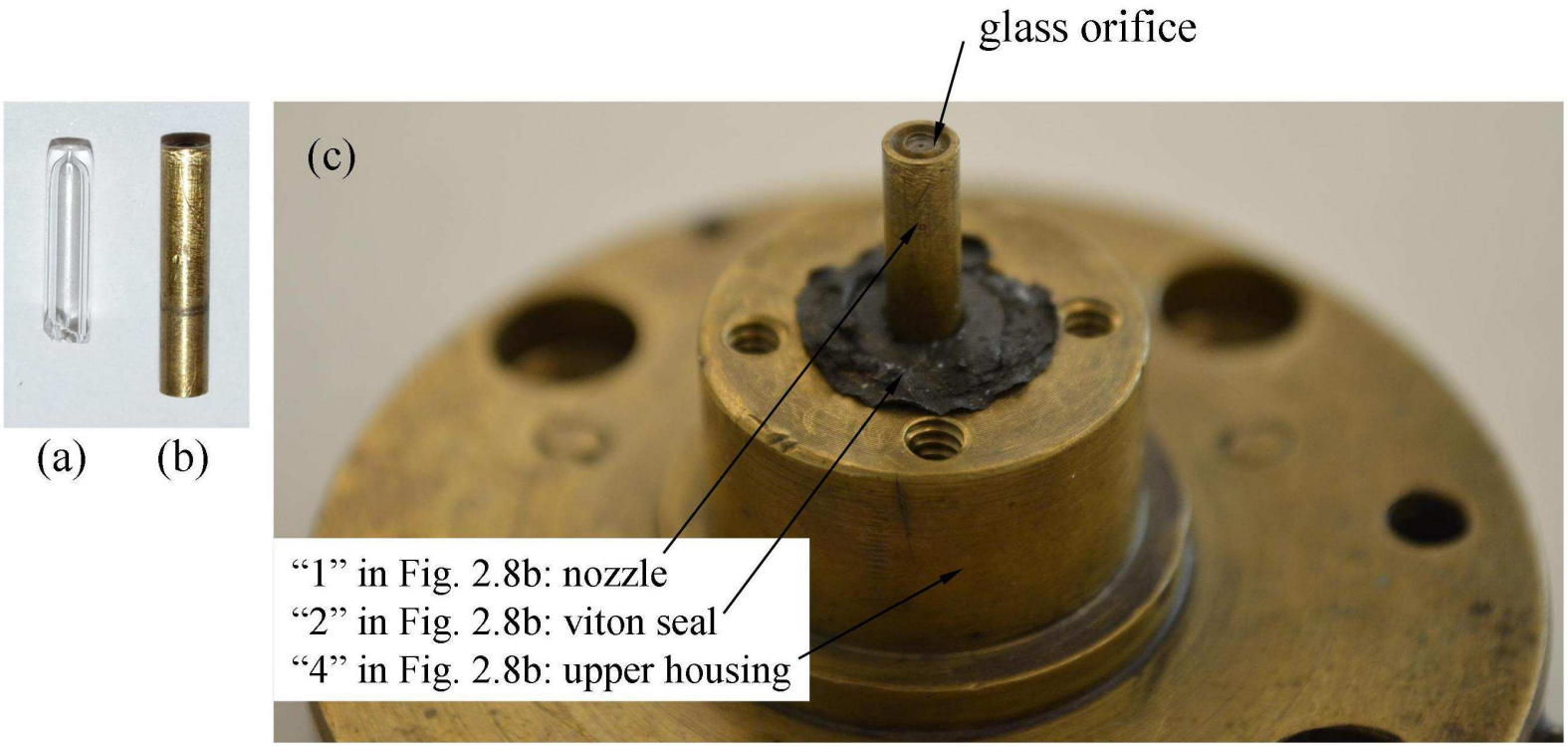

Fig. 2.9. (a) Glass nozzle (with a fractured bottom); (b) brass nozzle used in this study; (c) assemble of component "1": nozzle, "2" viton seal, and "4": upper housing from Fig. 2.8b without the cap "3".

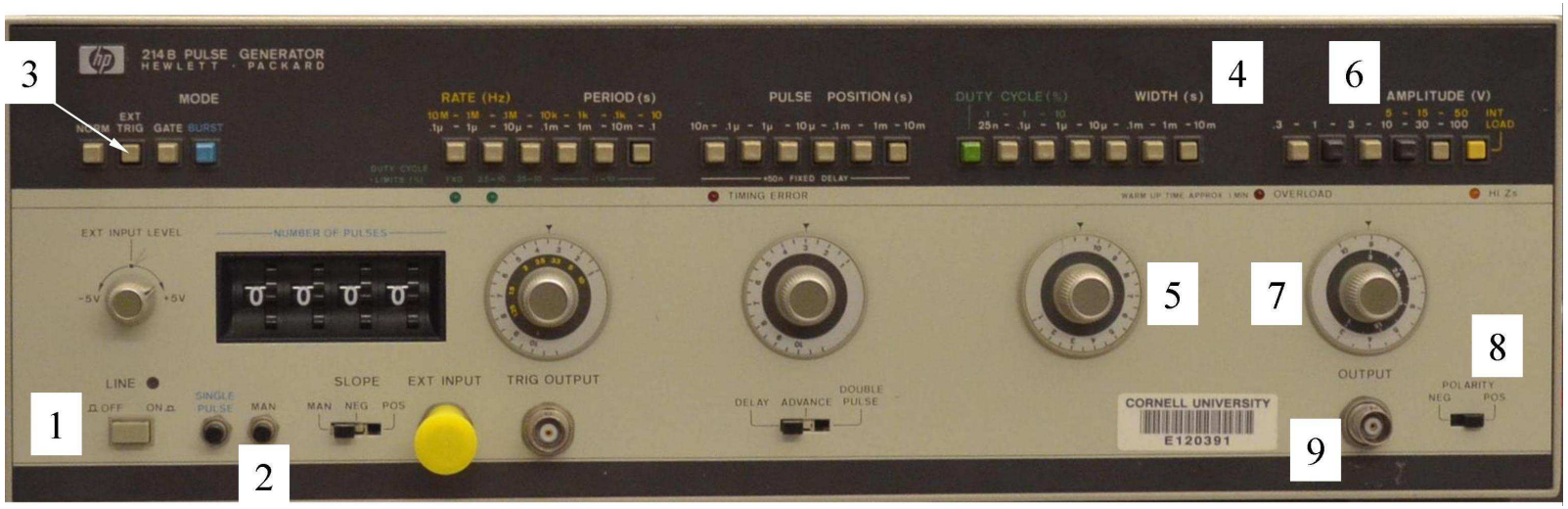

Fig. 2.10. The front panel of the HP 214B pulse generator that generates pulses for droplet generation. The functions/buttons relevant to this study are 1: power; 2: on-demand manual pulse generation; 3: pulse mode (EXT TRIG is selected for manual pulse generation; NORM is selected when one needs consecutive pulses); 4: width (s) (range of 1 ms to 10 ms is selected); 5: width dial to adjust the value within the range selected in "4"; 6: amplitude (V) (range of 10-30 V is selected); 7: amplitude dial to adjust the value within the range selected in "6"; 8: polarity (POS: positive is selected); 9: pulse output to be connected to the droplet generator (or also to QC-9618 for free-droplet experiments).

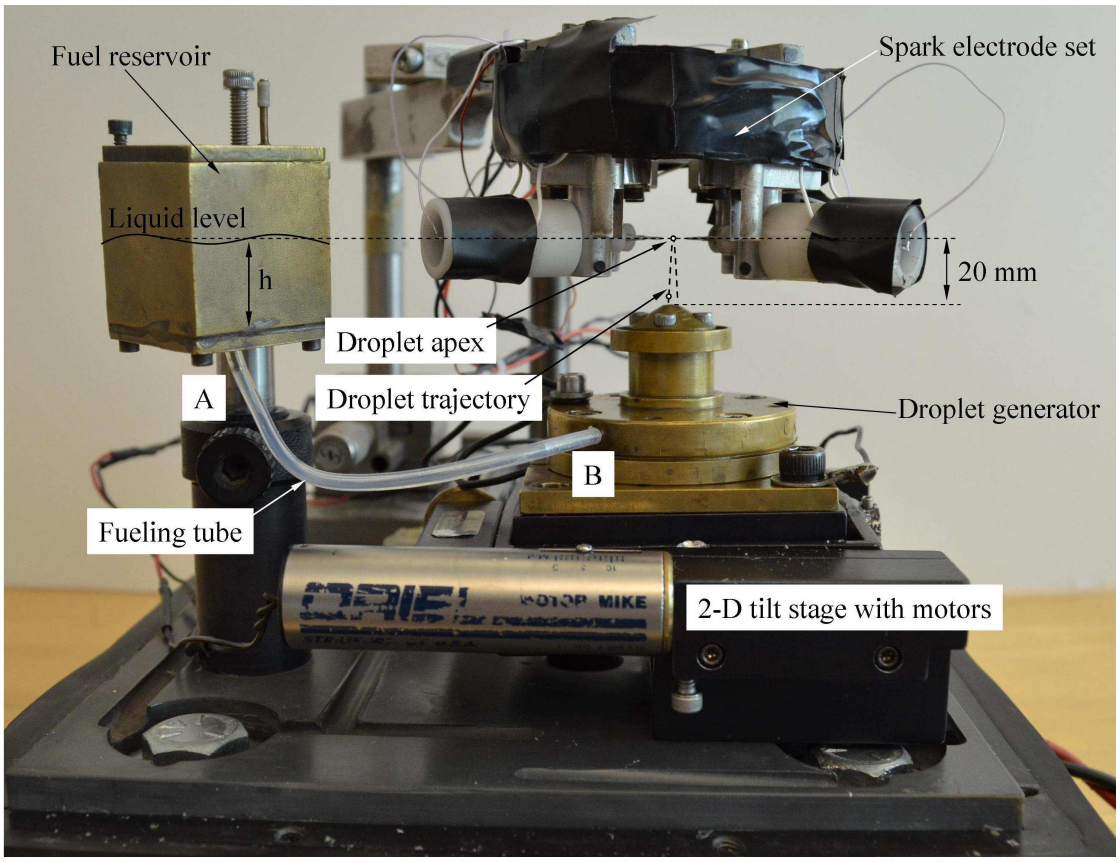

Fig. 2.11. A photograph showing the relative positions of the droplet generator, spark electrode set, and fuel reservoir. A and B indicate where the fueling tube to connected to the reservoir and the droplet generator, respectively.

In the combustion chamber, the droplet generator is installed below the spark electrode set for both free-droplet and fiber supported experiments. Figure 2.11 shows the relative positions for the spark electrode set and the droplet generator. The distance between the nozzle tip and the position where a droplet is ignited is 20 mm. With the fuel reservoir half-filled, the liquid level is also around 20 mm above the nozzle tip (see "h" in Fig. 2.11 for the liquid level).

There are several issues regarding operating the droplet generator. When the liquid initially fills the reservoir, it should smoothly flow into the inner void volume of the droplet generator due to gravity thorough a tube. However, at times air bubbles are trapped in the tube and remain during the process of liquid filling. The trapped bubbles are removed by unplugging the tube from the droplet generator ("B" in Fig. 2.11) until the bubbles are expelled by the flowing fuel liquid. At other times there are no bubbles inside the tube, but a test droplet can not be successfully generated. If the clear "popping" sound of the piezoelectric plate is not heard while pressing "man" on HP 214B, the signal for droplet generation delivered into the bottom plate of the combustion chamber should be checked using an oscilloscope (HP 54603B).

If the signal is correctly responded (with the right voltage and width), the droplet generator should be checked to see if the piezoelectric plate and the body of the droplet generator (ground) make contact with brass shims ("5" in Fig. 2.18b). The solder connection on the piezoelectric plate should also be checked because it has potential to disconnect during cleaning. If the droplet generator is responding to the signal but a droplet is not generated, there is almost likely air inside the droplet generator just below the nozzle, or air bubbles may be present in the nozzle itself. The

feed tube ("B" in Fig. 2.11) should then be moved back and forth to expel the air out of the droplet generator.

An ideal situation for droplet generation corresponds to only one droplet being generated with the desired apex (cf. Fig. 2.11). Sometimes "satellite" droplets are observed near the trajectory of the main droplet. Figure 2.12 displays three series of photographs that show the processes of generating n-decane droplets with very slightly different pulse widths that could lead to formation of satellite drops: (a) no satellites; (b) and (c) satellites. As is evident from Fig. 2.12, the tip of the nozzle is covered with liquid that forms a meniscus.

The resulting height and size of a generated droplet can be affected by the interplay of pulse voltage and width. When the pulse voltage is fixed at 25 V as in Fig. 2.12, varying only the pulse width can slightly change the droplet diameter and formation of satellites. With a pulse width of 2 ms (i.e. Fig. 2.12a, the smallest width among all three tests), the total volume of ejected liquid is smaller such that when the liquid pinches off the meniscus less liquid remains in the "necking" area compared to cases with larger pulse widths (i.e. Fig. 2.12b and 2.12c). The necking with less liquid facilitates separation of the droplet from the meniscus.

With a slightly larger pulse width, e.g. 4 ms (Fig. 2.12b), a satellite droplet forms. For 5 ms (Fig. 2.12c), the satellite droplet has a larger size compared to the droplet size at 4 ms (it is evident that the satellite droplet in Fig. 2.12b is smaller then the main droplet while the satellite droplet in Fig. 2.12c is about the same size as the main droplet. Callahan (2000) discussed several different satellite modes including a case where the satellite droplet has a larger velocity than the main droplet. The higher

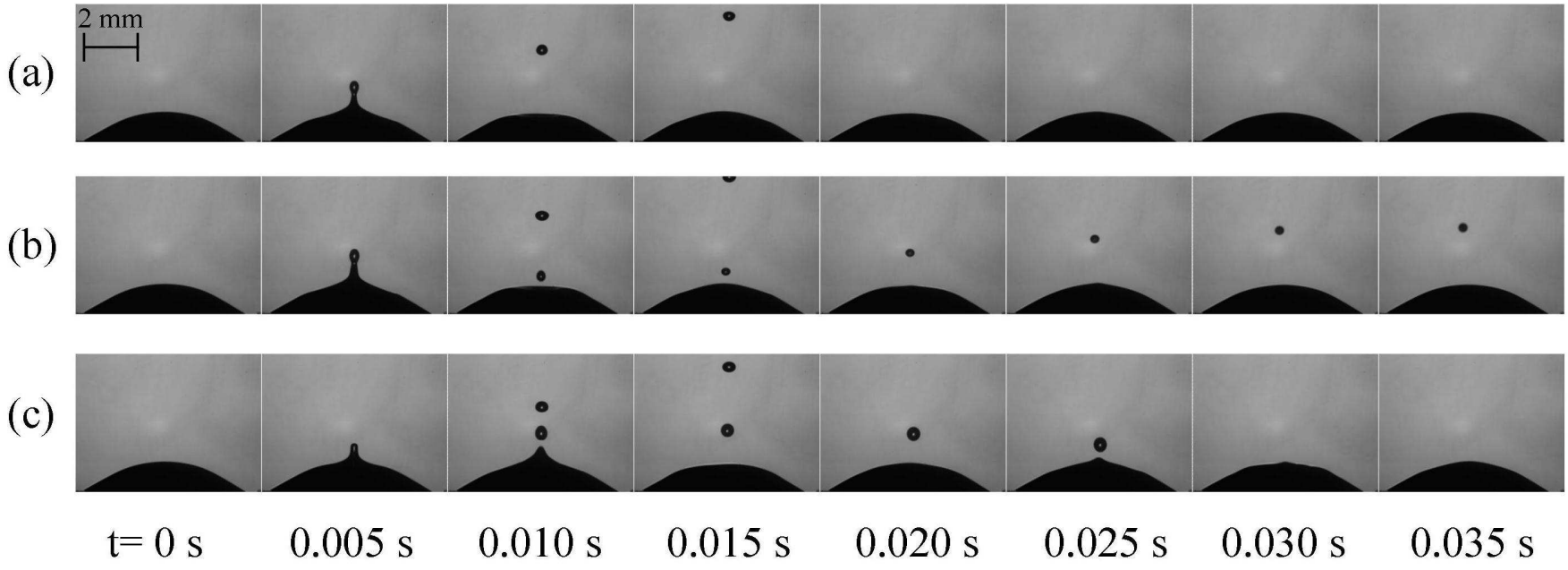

Fig. 2.12 Photographs of droplet generation with various pulse settings (a) amplitude = 25 V, width = 2 ms; (b) amplitude = 25 V, width = 4 ms; (c) amplitude = 25 V, width = 5 ms.

velocity satellite droplet will later coalesce with the main droplet and change its trajectory. This particular mode is not found in the current investigation.

Formation of satellite droplet produces smaller the main droplet. Nonetheless, the presence of satellite droplets has not been an issue for fiber-supported experiments because a satellite droplet has a smaller velocity and a lower apex compared to the apex of the main droplet (cf. Fig. 2.11). At the instant when the instrumentation package is released into free fall, only one droplet (the main droplet) is mounted on the fibers and formation of satellite droplets in the process of placing a droplet on fibers is not important. However, for free droplet experiments in which the instrumentation package must be released while a satellite droplet (if any) is still travelling, the satellite droplet can easily migrate to the main droplet flame area and ignite.

2.1.4 Electrode and Fiber Configuration

Various methods have been used to ignite fuel droplets. Common methods are spark ignition and hot-wire ignition. Although the two ignition methods appear to give the same droplet burning rate during the quasi-steady period (Bae (2005)), hot-wire ignition is not used in the present study because of its longer heating time that can change the initial size of the fuel droplet before ignition and being lack of precise timing controls. Figure 2.13 shows a top view photograph of the spark electrode set with illustration of a fuel droplet, support fiber, and sparks. It consists of four retractable electrodes, four fiber posts, retraction solenoid housings, and wires by

which the signal for firing two parallel symmetric sparks and retracting the four electrodes are transmitted from the circuits discussed later in this section.

Spark ignition is implemented by discharging high voltage electricity through a "point discharge" between the spark electrodes (cf. Fig. 2.13). When the voltage drop across the electrodes is high enough, a spark "column" forms due to ionization of the air that allows a spark to jump from one electrode to the other. The spark "column" only heats the local ambient adjacent to the spark to a very high temperature such that the fuel droplet can be ignited at a precise timing without being pre-heated. The spark temperature is expected to be very high that can melt tungsten (with a melting point of 3695 K). Figure 2.14 shows images for a tungsten needle (McCrone Microscopes & Accessories, Westmont, IL, tungsten needle (#3 ultra sharp), with a tip size of 1 μm) that is melted after discharging a moderate level of spark generated by our spark. Though small electrode sizes would benefit the localization of point discharge, the tips can be easily shattered due to physical impacts from the sparks. Moreover, from the perspective of heat transfer, a 1 μm needle tip is more likely to melt due to its small Biot number ($Bi = h_g L_c/k_L$, the L_c is the tip size of the electrode, 1 μm) that allows heat to penetrate quickly in a transient heating process. Therefore a large portion of the sharp tip area is well above its melting point making the geometry of the needle tip difficult to retain from run to run due to melting.

Customizing a conductive material that has a melting point higher than tungsten into spark electrodes might be costly. In this study, the 0.044" spark electrodes made of 304 stainless steel (Small Parts, Inc., Logansport, IN, Part# Q-SWGX-440-30, adopted from Callahan (2000) and Bae (2005)) are used for most of

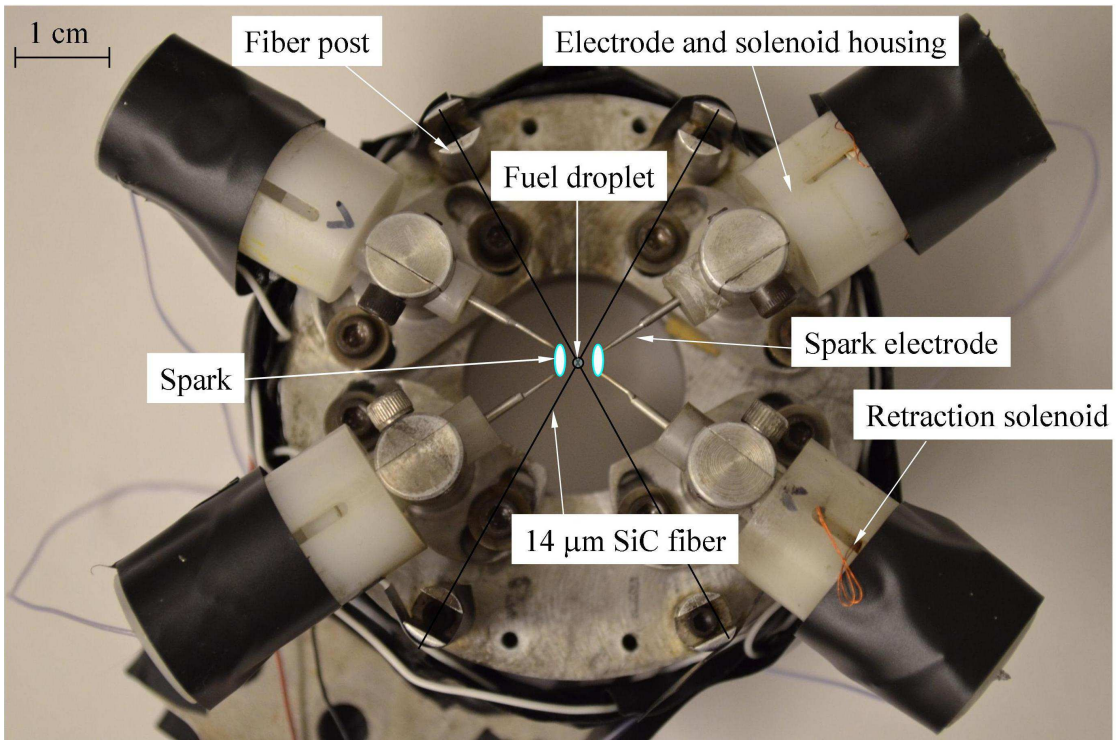

Fig. 2.13. Photograph of the spark electrode set with illustration for fuel droplet, 14 μm SiC fibers, and sparks.

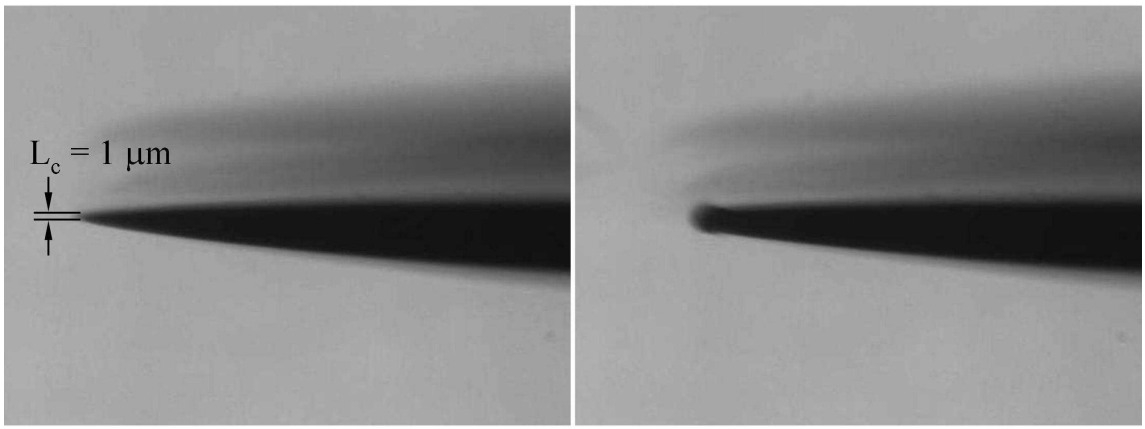

Fig. 2.14. Images of the tip of a tungsten needle (melting point = 3695 K) broken by the spark discharge.

the experiments. Smaller needles from commercial sewing needles (stainless steel, Dirtz, Prym Consumer USA Inc., Spartanburg, SC, N1-510) were also considered. The smaller sewing needles improved the spark quality because the voltage of point discharge depends on the local geometry (or curvature) of the electrode. Spark quality is particularly important for free droplet experiments since the spark disturbance that causes droplet motion needs to be minimized. It is worth noting that the melting points of these needles are lower than that of tungsten, but the sizes of their tips are large enough to maintain a consistent shape from run to run. Figure 2.15 shows the modification of a spark electrode design that uses a commercial sewing needle.

Various diameters and fiber materials were considered. For instance, 7 μm carbon fibers (Formosa Plastic Corporation, Taiwan) and 10 μm ceramic fibers (3M, Nextel 312) were tested. These fibers were found to be extremely difficult to handle due to their small size and delicacy. Moreover, the sparks usually jumped upon the carbon fibers (conductive) and broke the structure. The results from the 3M fibers (with a thermal conductivity of 2 W/m K (Wittaker et al., 1990)) show no difference compared to the SiC fibers used (comparison see Section 4.2). Since SiC fibers were much easier to handle than the 3M fibers, the majority of the fiber-supported experiments used the 12 μm SiC fibers.

2.1.5 Spark and Retraction Circuits

The spark ignition system used in the present study includes the spark electrode arrangement (cf. Fig. 2.13) and spark and retraction circuits onboard the instrumentation package that are controlled by the signal generated by QC-9618. The

spark circuits used in this study was constructed by Jackson (1994) basing on the concept of the spark circuit designed by Ronney (1985). This circuit is capable of generating two symmetric sparks with controllable voltage, current, and duration. This spark circuit was later modified by Callahan (2000) to incorporate digital signal inputs (from the QC-9318 pulse generator) for spark duration, retraction and ejection circuits for the newer spark electrode set. Note that the ejection circuit of Bae (2005) (for electrode ejection prior to spark ignition) is not used in the present study due to its potential to overheat and burn out the solenoids and the electrode housing (Bae (2005)). The electrodes are manually positioned prior to an experiment without using the ejection solenoids and circuits that were built into the system. Figure 2.16 shows the units that are needed for spark ignition with illustration of wire connections. Note that all the ground signals (shown by green connections in Fig. 2.16) are connected to each other.

Figure 2.17 is a schematic of the low voltage spark circuit (cf. Fig. 2.16) without including the retraction circuit that is also in the low voltage circuit box. As shown in Fig. 2.17, the 2N5681 NPN transistor along with a pull-up resistor takes the 5V signal generated by the QC-9618 and converts it to an inverted 15 V signal. This 15 V signal then goes to a CMOS logic circuit composed mainly of 4049B, 4538B and 4027B. The signal generated by channel 9 of 4538B (15V for 7.5 ms) was used for electrode retraction by Jackson (1994), but this function was replaced with the retraction signal from a digital pulse generator and a separate circuit by Callahan (2000).

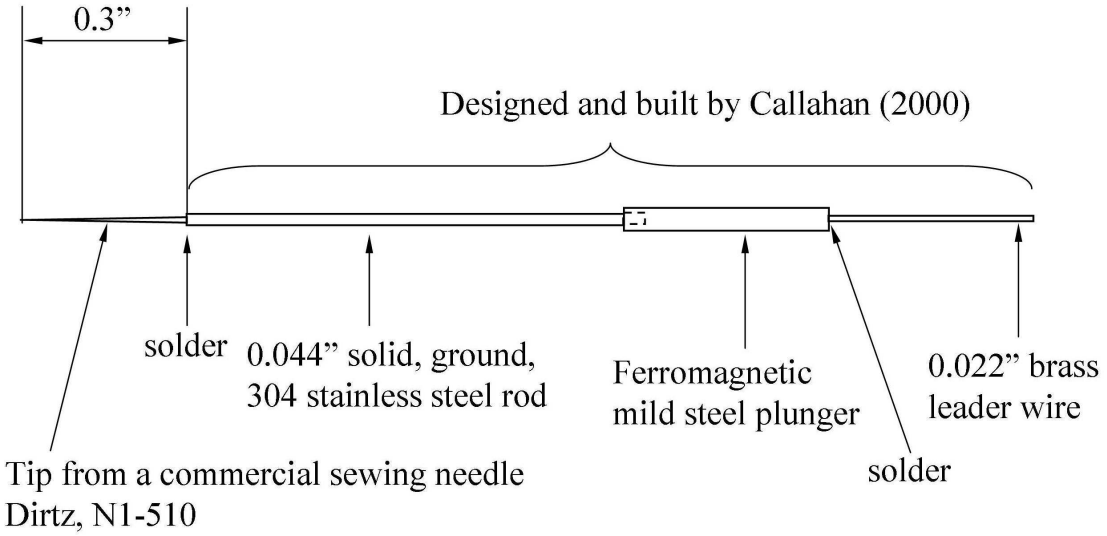

Fig. 2.15. Schematic of the spark electrode modified from Callahan (2000) and Bae (2005).

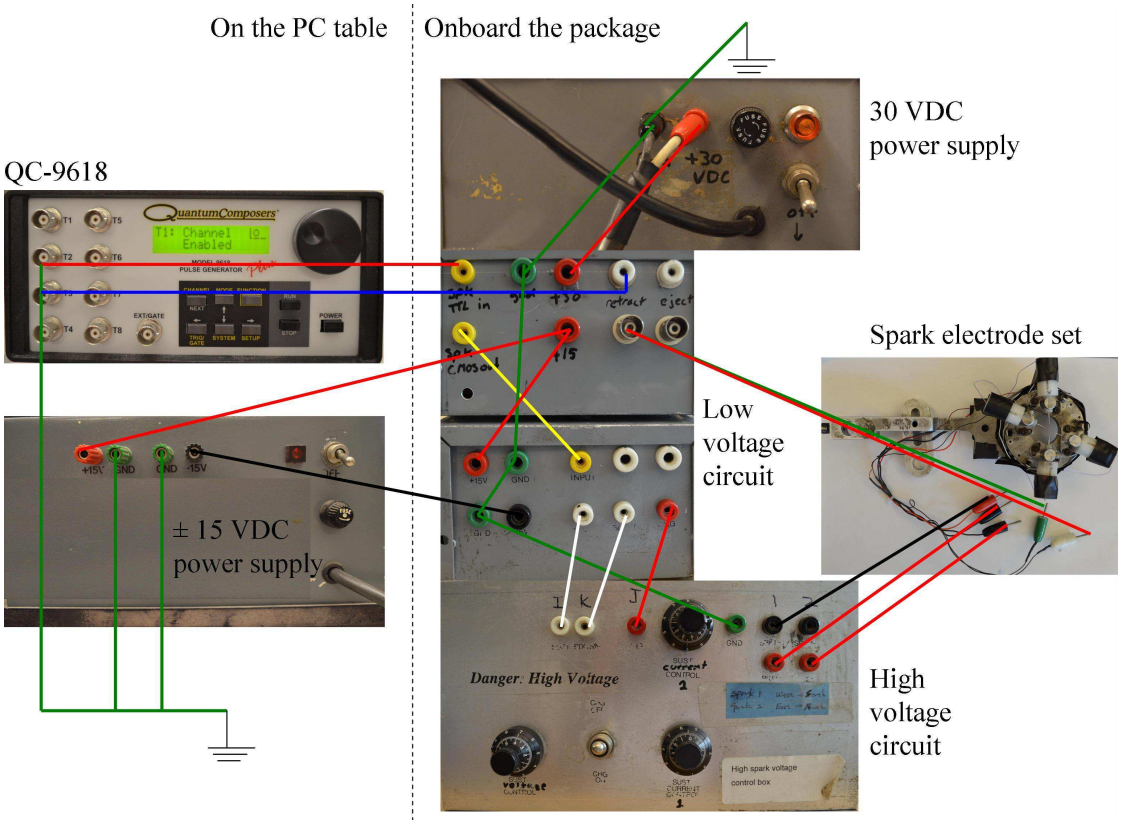

Fig. 2.16. Detailed connections between the QC-9618, ±15 VDC power supply, 30VDC power supply, low and high voltage circuit and the spark electrode set.

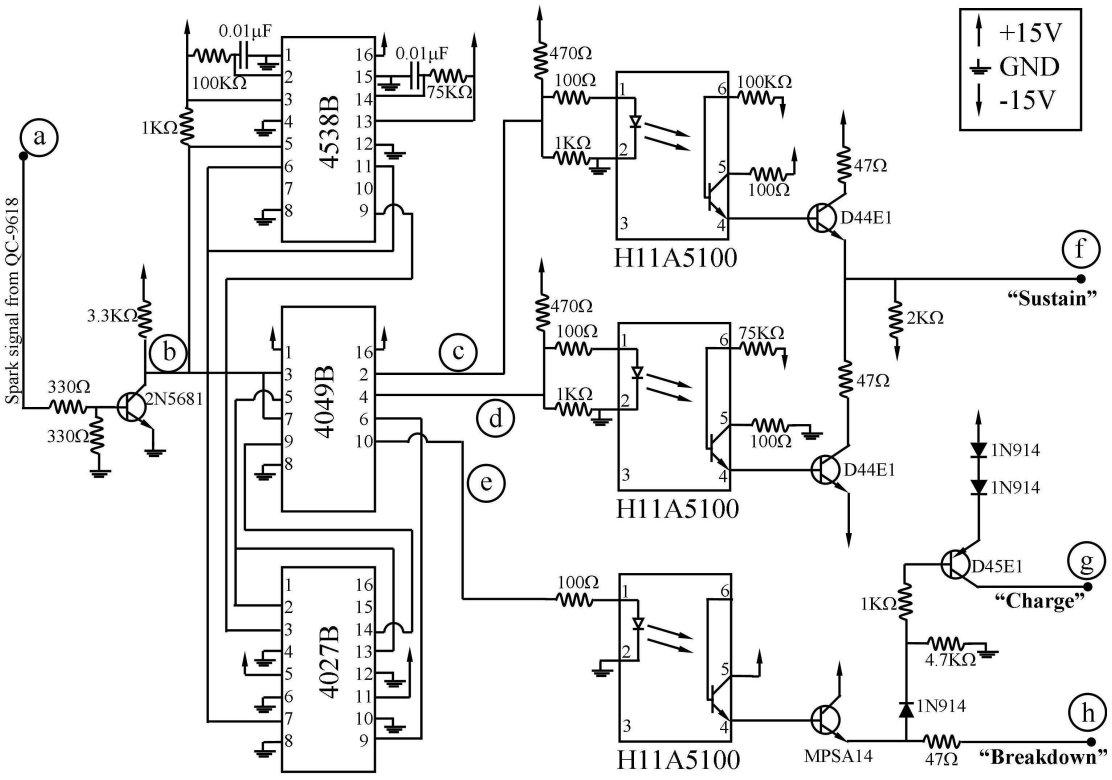

Fig. 2.17. Schematic diagram of the low voltage spark circuit use in the present study. Signals at the positions indicated by circled alphabets are shown in Fig. 2.20.

Figure 2.18 shows the high voltage spark circuit in which the “f”, “g”, and “h” designate the signals from the low voltage circuit (cf. Fig. 2.17). Figure 2.19 summarizes the signals at the positions indicated in Fig. 2.17 and 2.18. “a” is the original 5 V signal with spark duration of 800 μs generated by the QC-9618. Signal “b” is the inverted 15 V signal with the same duration as “a”. The signal from “c” is an inverted signal of “b”. The signal from “d” is an 8.5 ms long signal with a voltage of 15 V that is delayed for the spark duration as a signal to ensure the spark is turned off after the spark duration. The combination of “c” and “d” produces the “sustain” spark signal “f” that reproduces the spark duration of “a” but jumps from -15 V to ~1 V. “e” is the direct combination of “c” and “d” that signifies a duration in which capacitors are not charged because of initiation of sparks. This signal is related to the signal at “g” that switches off the charging of the high energy capacitors (1.5kV/20μF and 400V/1μF for “sustain” and “breakdown” sparks, respectively) (cf. Fig. 2.18) as well as the signal at “h” that triggers a breakdown spark through the 2N6404 thyristor (cf. Fig. 2.18).

The high voltage spark circuit uses the signal at “f”, “g”, and “h” (± 15 V) to control the current released from the capacitors for the “breakdown” and “sustain” sparks (cf. Fig. 2.17). A breakdown spark is the spark that creates the first conductive channel in the ambient between the electrodes. The energy for this breakdown spark is determined by the 200 KΩ adjustable resistor near the ER715 DC-DC converter (a compatible model to replace the old ER700 (Callahan (2000)) due to burnout), which has not been adjusted since originally set by Jackson (1994), that controls the charging voltage converted from the ER715 across the 1 μF 400V capacitors. When the 2N6404

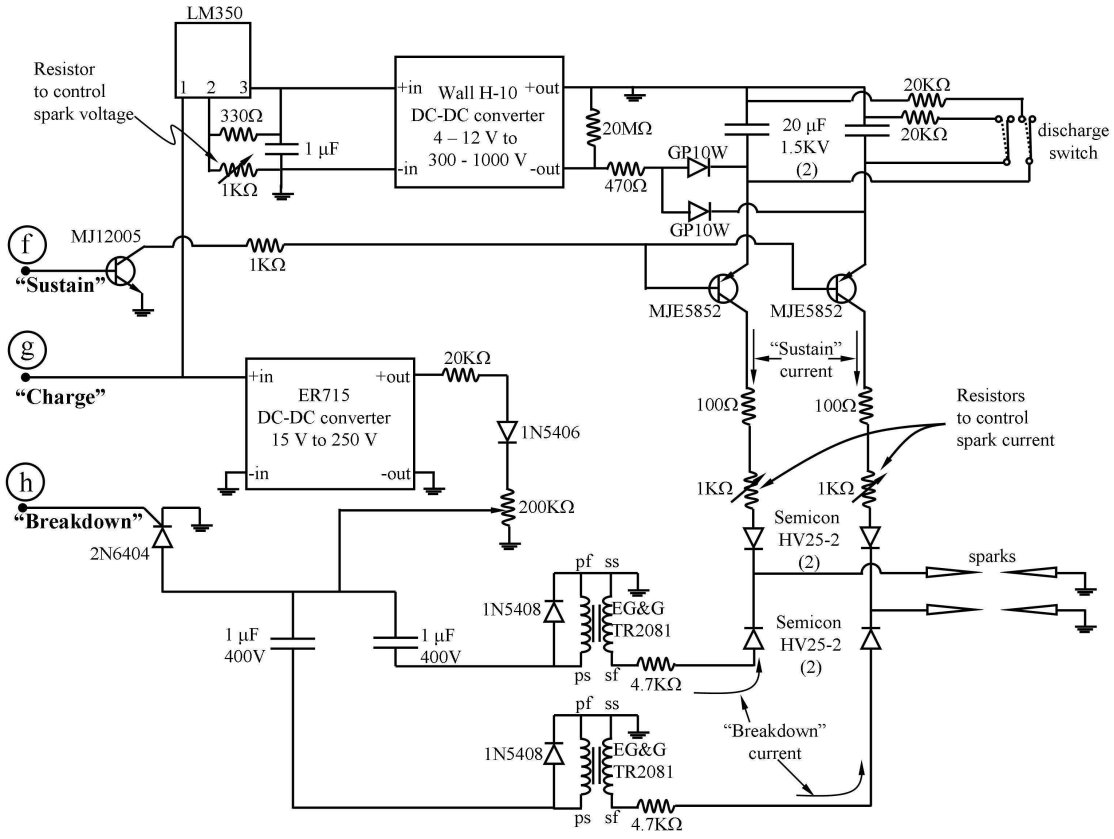

Fig. 2.18. Schematic diagram of the high voltage spark circuit use in the present study. Signals at the positions indicated by circled alphabets are shown in Fig. 2.20.

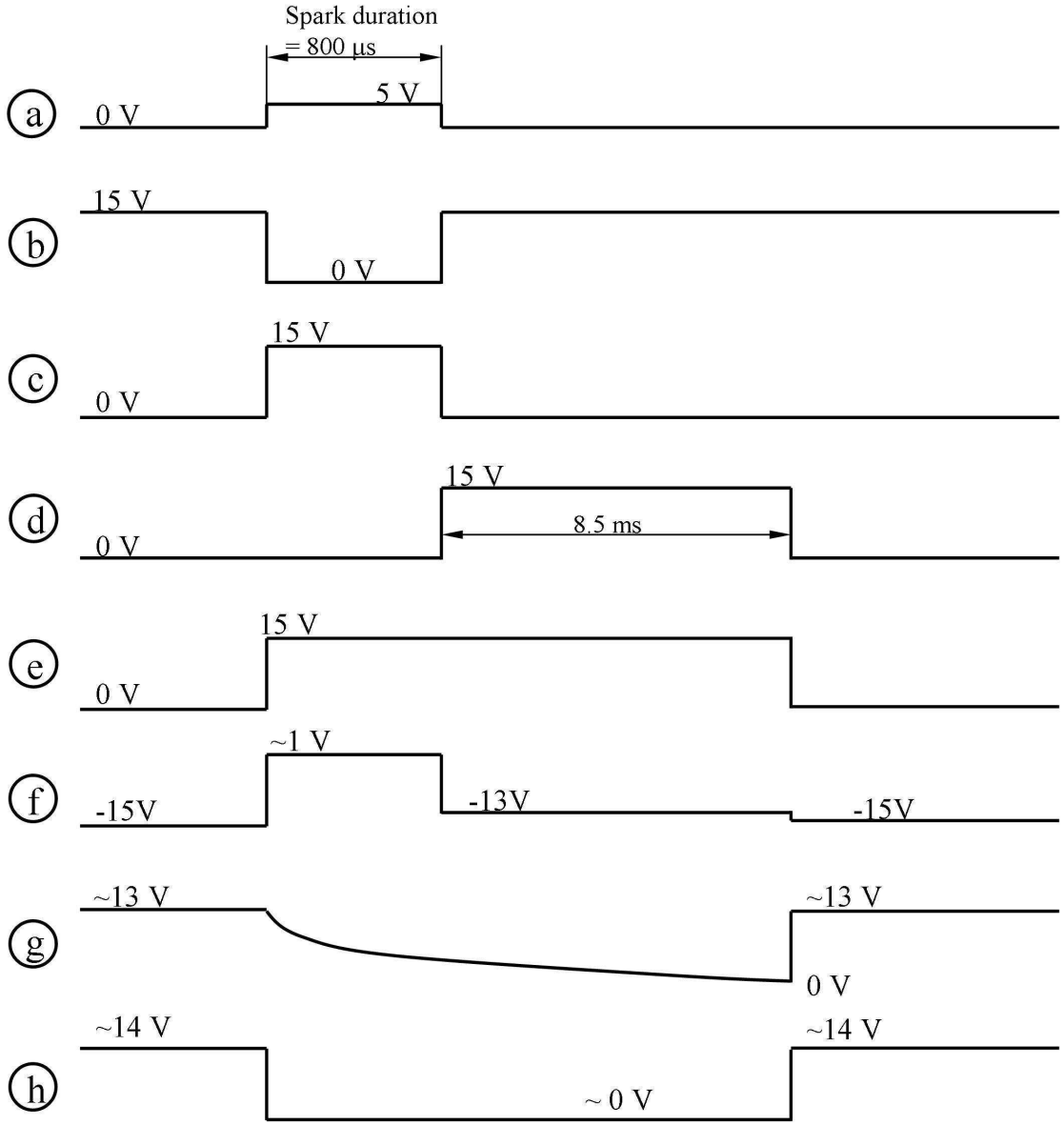

Fig. 2.19. Signals at the positions indicated in Fig. 2.17 and 2.18 for the spark circuits.

thyristor is activated by the inverted signal at "h", the current is pulled from the two 1 μF 400V capacitors to the EG&G coil transformers, then creates the breakdown spark discharge at the electrodes. The breakdown signal should last for about 1 μs and the voltage should not exceed 12 KV according to the specifications of the EG&G TR2081.

The "sustain" current (cf. Fig. 2.18) kicks in after the conductive channel is created by the "breakdown" current (cf. Fig. 2.18) between electrodes. The duration of a "sustain" spark is determined by the spark duration set on the QC-9618. The sustain spark voltage is controlled by the 1 KΩ adjustable resistor (cf. Fig. 2.18) that determines the voltage output from the LM350 voltage regulator to the Wall H-10 DC-DC voltage convertor. A 470 Ω resistor after the Wall H-10 was used by Callahan (2000) to replace the old 1 M Ω resistor (Jackson (1994)) to further increase the spark voltage. The output voltage from the Wall H-10 is used as the charging voltage across the two 1.5kV/20μF capacitors that release the energy for the "sustain" spark.

The spark current is controlled by the two 1 KΩ adjustable resistors in series with the spark electrodes. Increasing their resistances would lower the spark current. The resistance settings for the fuels of interest are listed in Table 2.1. The average energy provided by the two sparks is approximately 0.1 J (from the estimation in Jackson (1994)), though the actual number differs from fuel to fuel. By comparison, the energy released by the combustion process of the fuels examined (based on their lower heating values) is about 45 MJ/kg. For the droplet sizes examined (order of 0.5 mm diameter), the spark energy is a factor of about 20 smaller than this value. The diameter of the spark generated by the electrode pairs is similar to the initial droplet

Table 2.1. Resistance settings for the spark used for the fuels in this study.

Fuel	R_{vol} (Ω)	R_{cur} (Ω)	D_o (mm)
n-heptane	400	280	0.50
n-octane	500	50	0.52
n-octane	650	50	0.64
n-octane	700	0	0.71
n-octane	650	50	0.85
iso-octane	400	280	0.53
n-decane	600	0	0.55
n-decane (free-droplet)	600	0	0.51
Toluene	1000	0	0.52
iso-octane/n-heptane	400	280	0.52
n-heptane/toluene	700	0	0.50
Gasoline (87 unleaded)	700	300	0.53
Indolene	450	100	0.53
Jet-A (POSF4658)	300	200	0.58
3 CS surrogate for Jet-A	400	200	0.55
4 CS surrogate for Jet-A	300	200	0.61
Camelina HRJ (POSF6152)	400	200	0.57
Tallow HRJ (POSF6308)	450	100	0.54
Jet-A/Camelina HRJ	900	50	0.54
Methylbutanoate (MB)	450	100	0.54
Methyldecanoate (MD)	450	200	0.55

diameter. Detailed troubleshooting procedures for the spark circuits are provided in Appendix B.

After the sparks are triggered the electrodes are retracted in order to not affect the droplet flame. Figures 2.20 to 2.22 show schematic drawings for the components for electrode retraction. Figure 2.23 shows how the components in Figs. 2.20 to 2.22 are assembled. The solenoids in Fig. 2.23 use a 38-gage magnet wire (Belden Inc., Indianapolis, IN, model# 8085) that was wrapping 650 turns for each solenoid. The resulting total resistance (the four retraction solenoids are connected in series) is about 9 Ω. This value can be used as a reference for diagnostic purposes. The retraction solenoids are activated by the voltage output from the retraction circuit shown in Fig. 2.24.

The 2N5618 transistor and the 4049B inverter (cf. Fig. 2.24) first pull current from the ±15 VDC power supply which drives the TIP120 to draw current from the 30 VDC. This current passes through the retraction solenoids and activates the retraction. For safety considerations, an R-C circuit (dotted line portion in Fig. 2.24) is used to drain the current from the 4049B and avoid overheating of the solenoids. With the combination of a 200 μF capacitor and 80 KΩ resistor, it takes 900 ms for the R-C circuit shown in Fig. 2.24 to turn on the MPSA17 chopper transistor and draw current through the 1N4001 diode.

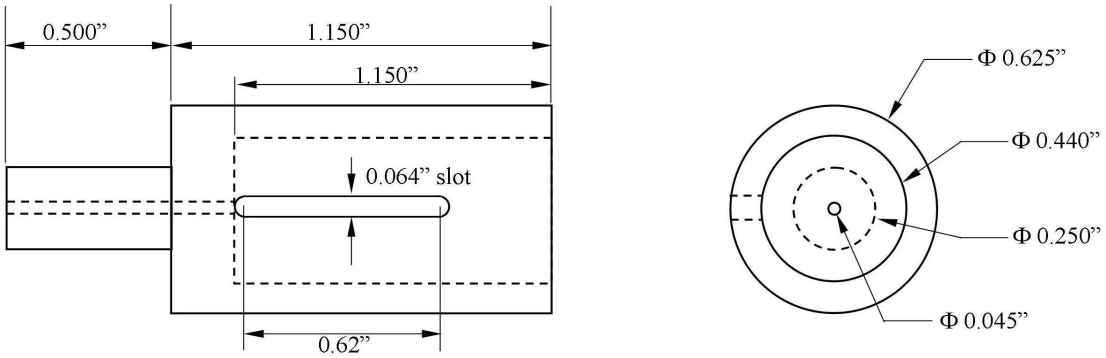

Fig. 2.20. Drawing of PTFE housing for retraction and ejection solenoids.

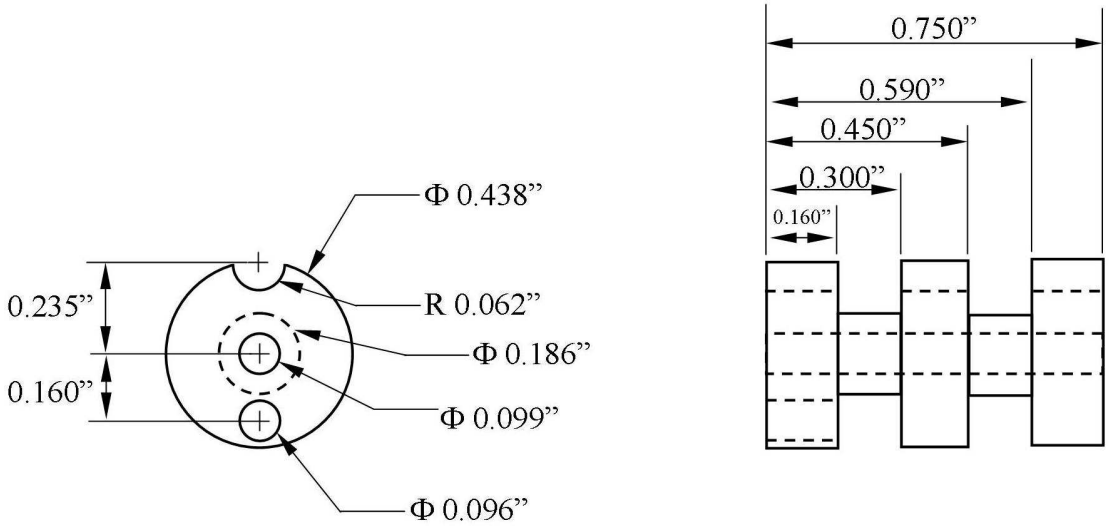

Fig. 2.21. Drawing of PTFE solenoid bobbin.

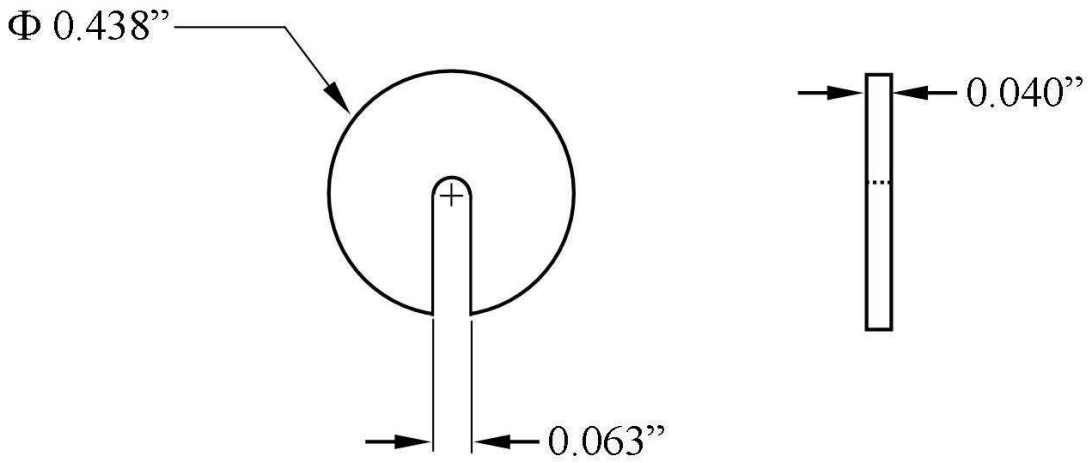

Fig. 2.22. Drawing of the PTFE plates that sandwich the solenoid bobbin (cf. Fig. 2.21) inside the solenoid housing (cf. Fig. 2.20) to retain the electrode after retraction.

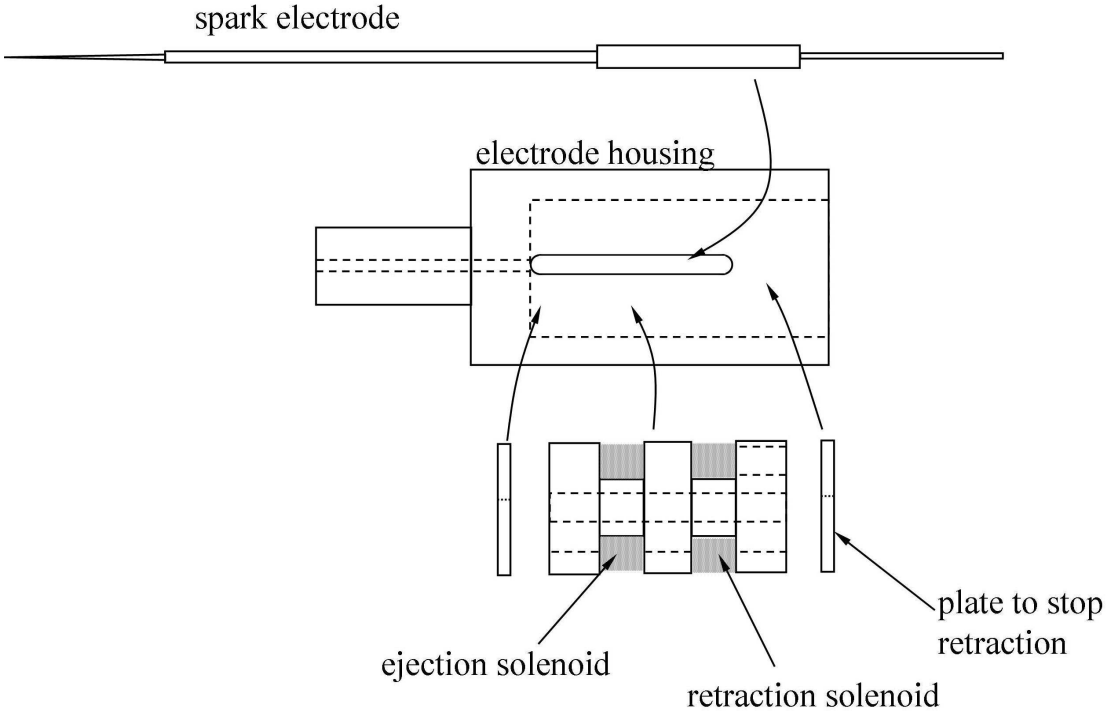

Fig. 2.23. Assembly of the spark electrode, electrode housing, solenoid bobbin, electrode retainer plate, and the solenoids.

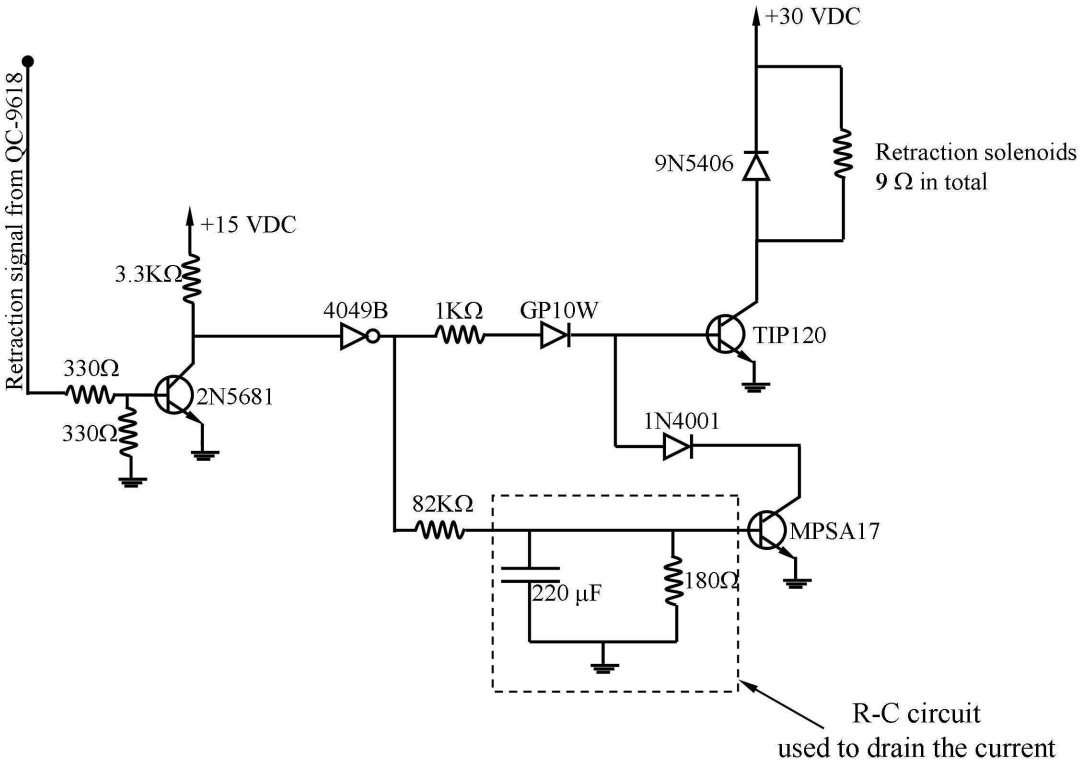

Fig. 2.24. Schematic diagram of the retraction circuit built in the low voltage circuit box.

2.1.6 Electromagnet for Package Release and Magnet Delay Measurement

The instrumentation package is released into free fall by deactivation of a 4" circular electromagnet (AEC Magnetics, Cincinnati, OH, CEA-400M-100C) that holds the package from the top center position. The power needed for the electromagnet is provided and controlled by a DC power supply (HP 6010A) and the cut-off timing is controlled by channel 1 of the QC-9618 via a separate relay circuit also made by Callahan (2000). Figure 2.25 shows the connections between the devices that are included in the electromagnet system used in the present study. The magnet circuit receives a constant 5 V signal from the QC-9618 that activates the Crydom D5D07 solid state relay in the circuit to pull current from the HP 6010A to the electromagnet. When the 5V signal (from the QC-9618) is turned off at the designated time, the power to the electromagnet is cut off and the magnet is deactivated.

Using the "constant voltage" mode on the HP 6010A, results from preliminary tests suggest that a minimum voltage applied to the magnet for suspending the 400 lb package is about 39 V (with a current of ~0.2 A showing on the front panel of the HP 6010A). For safety concerns, 100 V is used to raise the package to avoid unexpected magnet separation from the package. Prior to dropping the package, the voltage is lowered to 50 V.

Proper placement of the electromagnet on the top of the package is critical. Figure 2.26 show the positioning. A displacement as small as 0.1 mm will affect the orientation of the suspended package, which in turn will change the droplet trajectory leading to failure of deploying a droplet at the intersection of the fibers (for fiber-support experiments) or undesirable residual droplet velocity (for free-droplet

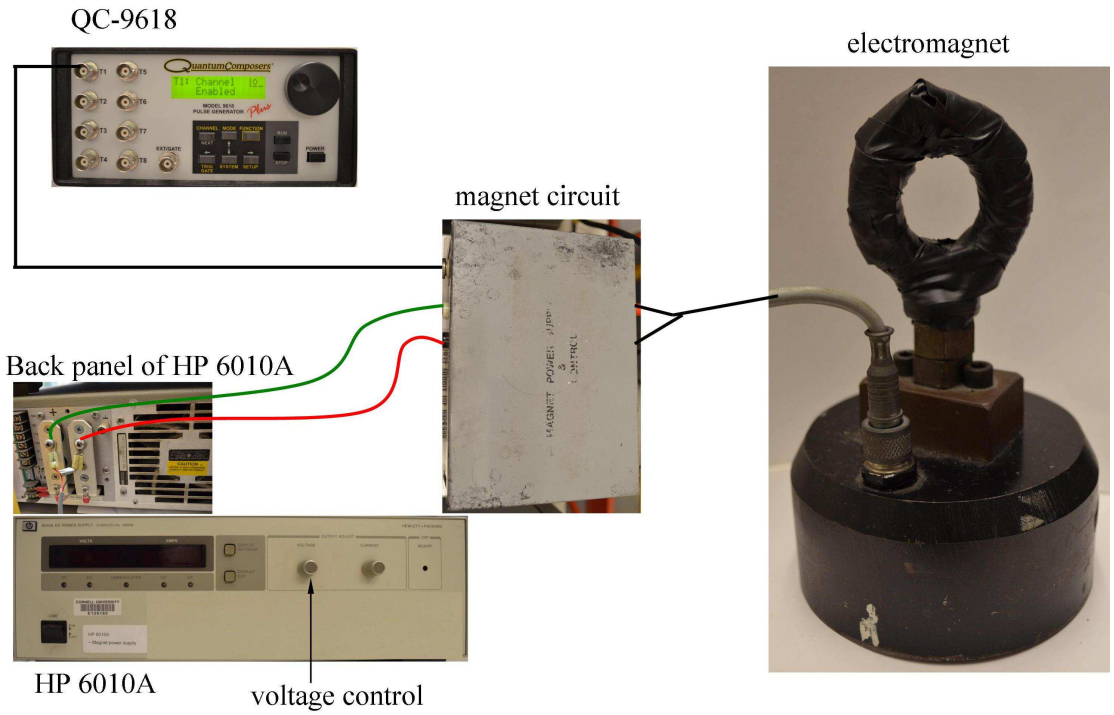

Fig. 2.25. Illustration of the connections between the devices involved with activation and deactivation of the electromagnet for package release.

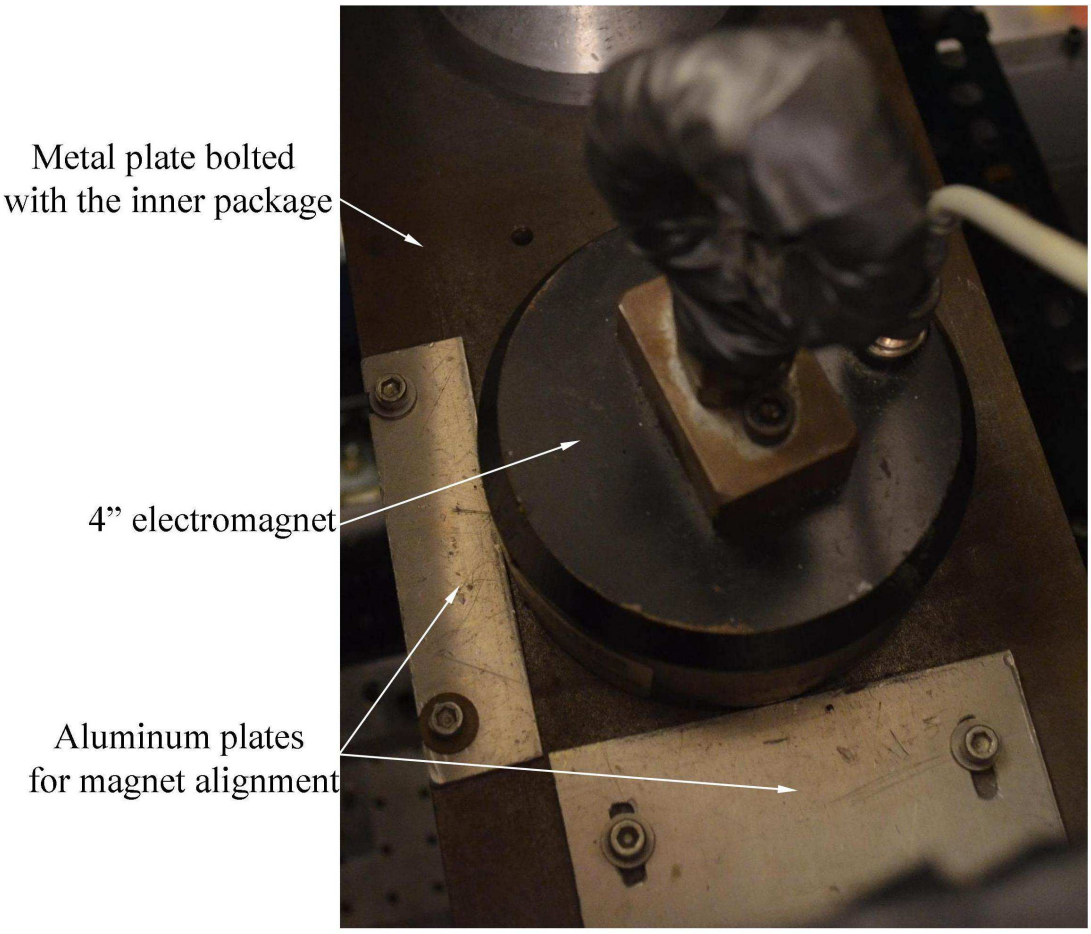

Fig. 2.26. Photograph showing how the electromagnet is aligned using two aluminum plates that are bolted on the metal plate.

experiments). Two aluminum plates (shown in Fig. 2.26) are bolted on the same metal plate on which the magnet is attached in order to reproduce the exact alignment for the magnet. It is also important to make sure the surfaces of the magnet and the metal plate are clean (they should be wiped with paper towels). Prior to each experiment the surface should be cleaned and the dust on the metal plate should be removed (using a paper towel) to avoid an unexpected package release.

Ideally, the magnet should separate from the metal plate (or the package) at the instant the power is turned off. However, there is a residual magnetism that is able to hold the package after the power to the magnet is terminated. This causes a "magnet delay", namely the magnet separates from the package sometime "after" the designated timing. A magnet delay of 35 ms was previously measured (Callahan (2000)) though for a package with a different weight. The magnet delay is not an issue for fiber-supported experiments since the droplet is anchored on the fibers and ignited after the package is released. However, the value of the magnet delay is important for free droplet experiments in which the package should be released at the same time as the droplet reaches its trajectory apex (see Section 2.1.7.2).

Figure 2.27 illustrates the approach developed to measure the magnet delay for the current system. Two symmetric devices (Fig. 2.27a) that provide signal transmission are attached to the magnet and the iron plate (Fig. 2.27b) form which the magnet holds the package. When magnet separation occurs, the 5V signal is disconnected (see Fig. 2.27c) signifying the timing of the separation. Figure 2.28 shows the signal connections between the QC-9618 (with corresponding signal settings for Channel 1-3), the magnet test devices, and a digital oscilloscope (LeCroy

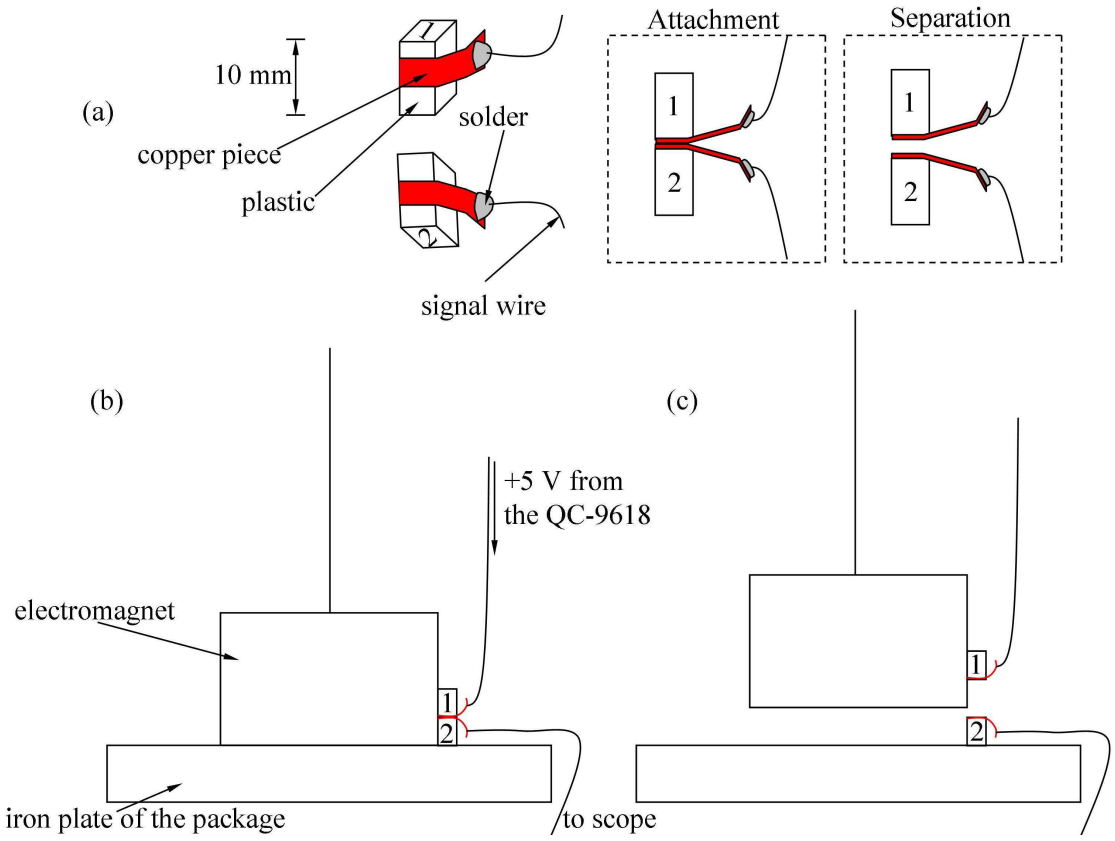

Fig. 2.27. Illustration of an approach used to obtain the magnet delay: (a) 1 and 2 are the two small plastic materials, each has a piece of copper metal that is soldered with a signal wire; (b) Schematic showing how 1 and 2 (in "a") are fastened on the electromagnet and the iron plate, respectively, letting the 5 V signal transmitted to the scope when the magnet is activated; (c) schematic showing how the 5 V signal is disconnected when the magnet is separated from the iron plate.

WaveRunner 440 MHz, Teledyne LeCroy, Chestnut Ridge, NY)) that are involved in the magnet delay tests. The connection for channel 1 of the QC-9618 is identical as in Fig. 2.25. Channel 2 of QC-9618 outputs a constant +5V signal which eventually goes to Channel 1 of the LeCroy scope. Channel 3 of QC-9618 generate an identical signal as Channel 1 as a reference signal indicating the exact time (on Channel 2 of the LeCroy scope) at which the magnet is electronically deactivated (compared to the actual separation detected on Channel 1 of the scope). This magnet delay measurement requires releasing the entire package. For these measurements the package is held by the electromagnet and hung 2 inches above the deceleration foam sheets (cf. Fig. 2.1) for magnet delay tests. Therefore the signal for Channel 2 (of QC-9618) is transmitted using the BNC connection of the color camera that is already built in the package.

Figure 2.29 shows the magnet delays as measured from Channel 1 and 2 of the LeCroy scope. The signal delay (Δt_{magnet}) represents the actual magnet delay. As shown in Fig. 2.29, as the signal that activates the electromagnet (Channel 2) quickly drops from +5 V to 0 V, the separation occurs after Δt_{magnet} with some oscillating signals potentially caused by the residual magnetism after magnet separation. This Δt_{magnet} is taken from the signal delay at 2.5 V due to the difficulty to define the actual "separation" from the noisy signal of Channel 2 (cf. Fig. 2.29). The averaged value of magnet delay time (Δt_{magnet}) was measured as 0.01575 ± 0.002 s, which is obtained from several magnet delay tests with the above described approach.

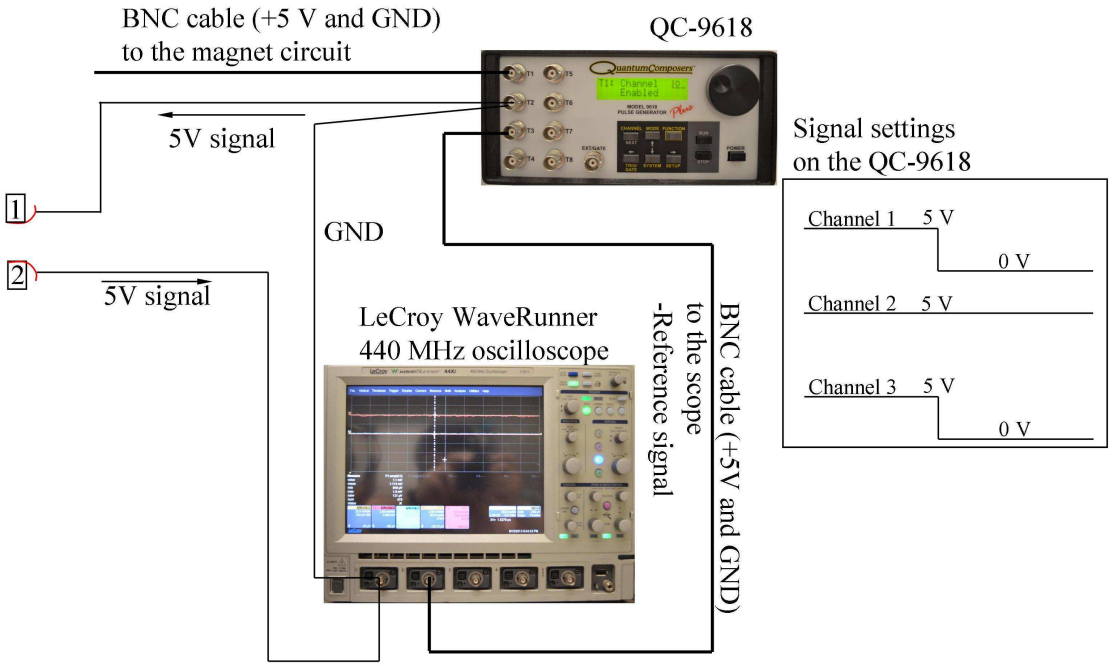

Fig. 2.28. Illustration of connections between the QC-9618, the LeCroy scope and the devices designed for magnet delay tests (see Fig. 2.27 for the installation of device 1 ad 2).

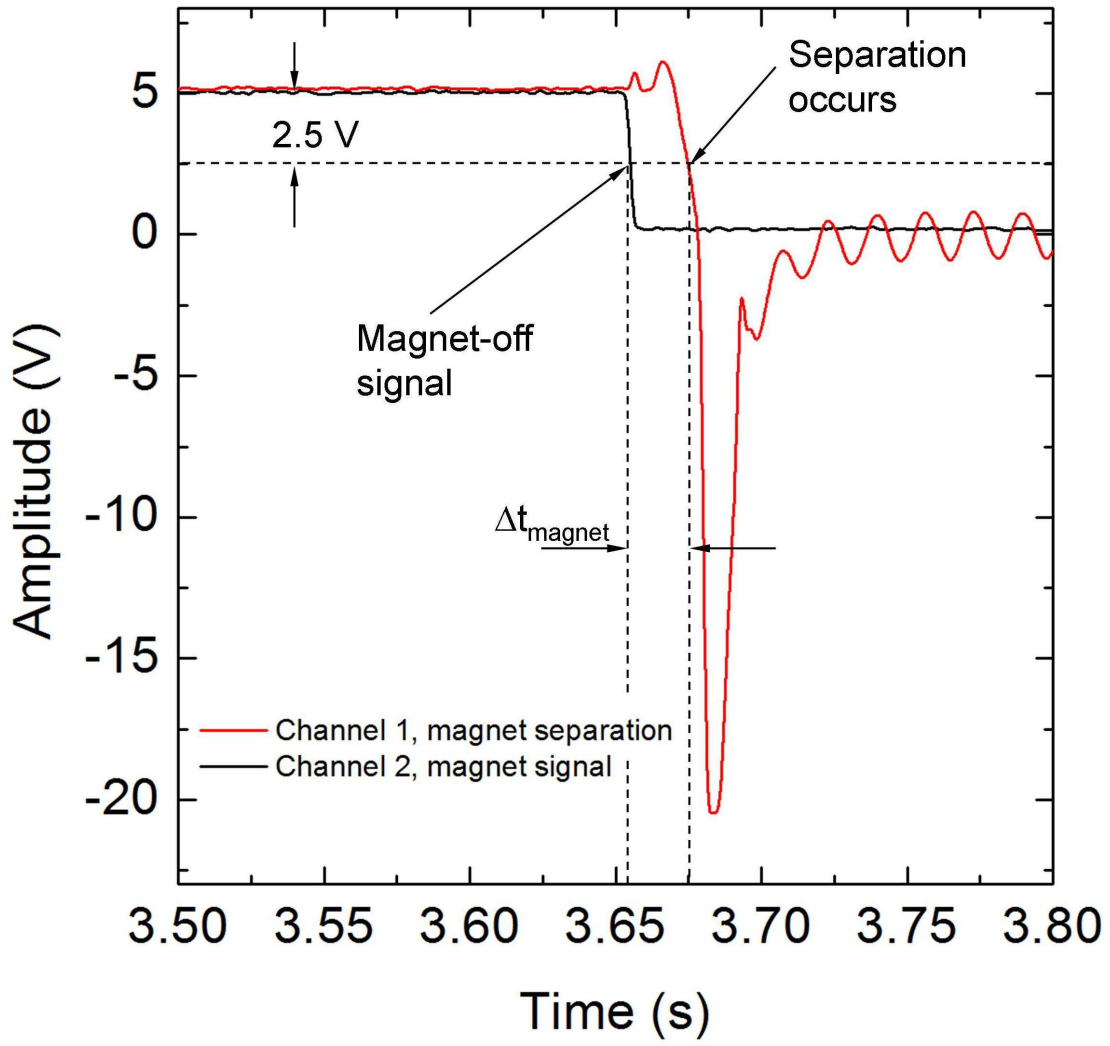

Fig. 2.29. Signals from Channel 1 (magnet separation) and Channel 2 (magnet signal) of the LeCroy scope showing the magnet delay Δt_{magnet}.

2.1.7 Experimental Procedures and Associated Timing Control

2.1.7.1 Fiber-supported Experiments

For a fiber-support droplet combustion experiment, after a test droplet is generated (as initiated by manually pressing the "man" button on the HP 214B) and anchored at the intersection of the two SiC fibers. The "run" button on the QC-9618 is pressed to initiate a series of events including package release, spark ignition, and electrode retraction mentioned in the previous sections of this chapter. Figure 2.30 shows the timeline that is required to complete the events in a fiber-supported experiment and Fig. 2.31 displays the signals generated by the QC-9618 that correspond to the events.

t_0 is an arbitrary time datum at which the "run" button on the QC-9618 is pressed. All the signal channels on the QC-9618 use this reference time and initiate the pre-programmed signals associated with it. A constant +5 V is maintained (to hold the package prior to release) for channel 1. This spark ignition delay (t_{sd}) is used to avoid the initial disturbance when the package is released. The spark duration (t_s = 0.8 ms) used for all fuels investigated in this study was obtained from an averaged value of prior work by Jackson (1994) and Callahan (2000), though it could be changed to adjust the total spark energy. Channel 3 of the QC-9618 controls the electrode retraction (mechanisms described in Section 2.1.5) immediately after the spark is generated by channel 2. The +5 V signal from channel 3 lasts for 1.0 s in order to make sure the electrodes will not pop back. Detailed settings for each channel are given in Appendix A. Note that the BW and color cameras are independently controlled from a PC (see Section 2.1.8). The cameras should start recording before

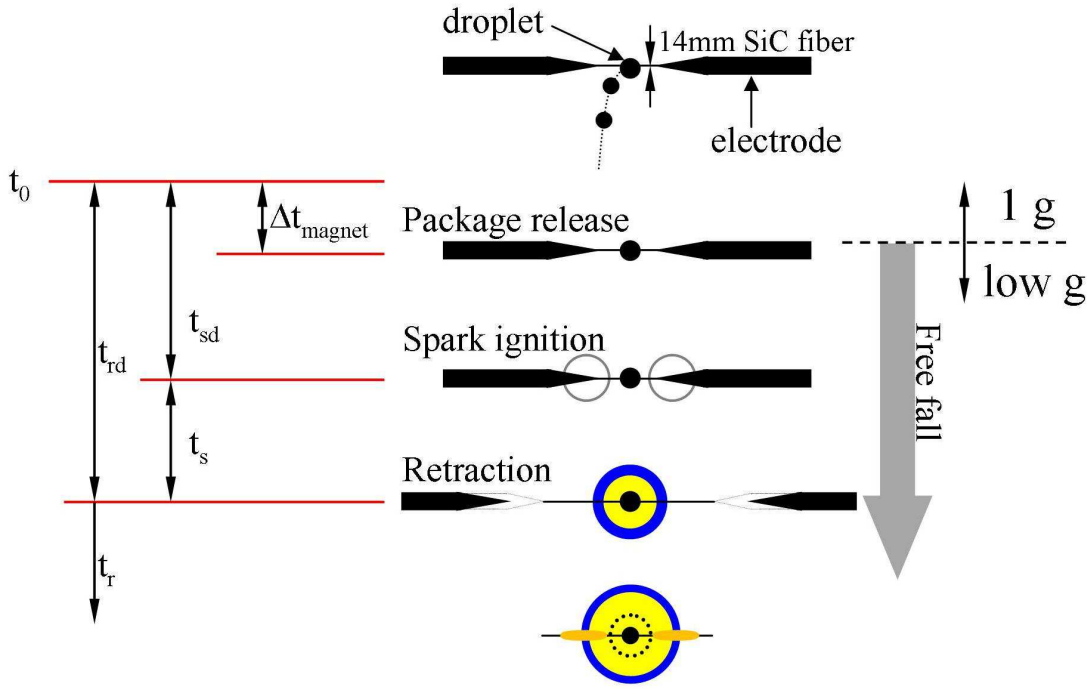

Fig. 2.30. Experimental procedure and involved timings in a fiber-support experiment.

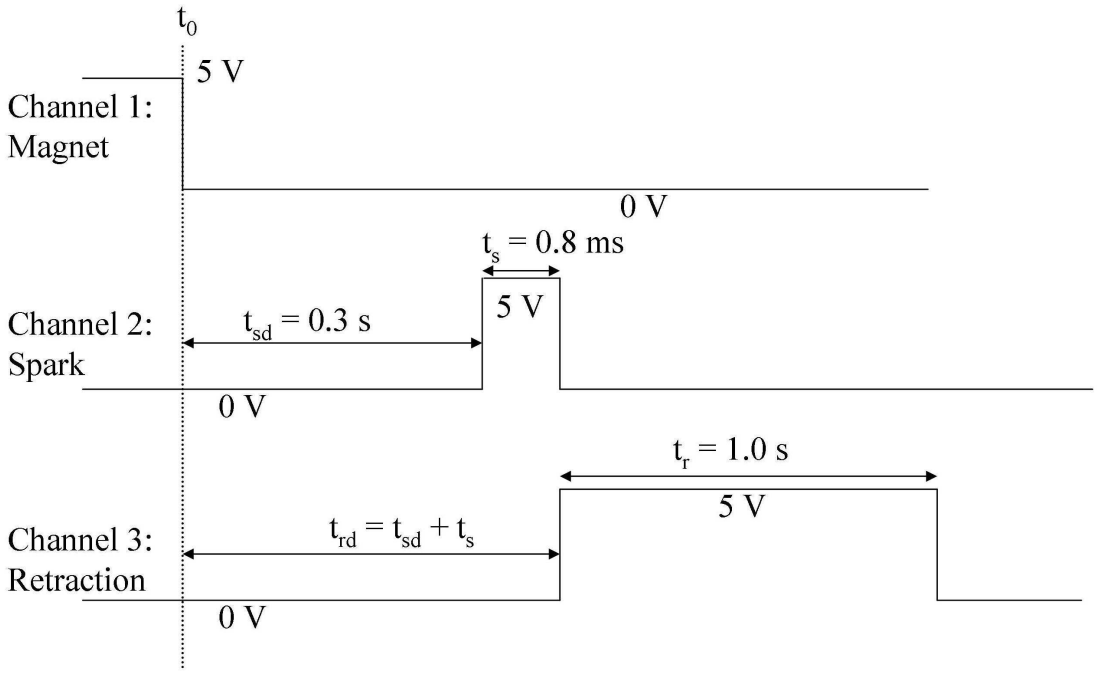

Fig. 2.31. Signal settings on the QC-9618 for the time sequence required in a fiber-supported experiment.

the “run” button on the QC-9618 is pressed and manually stop immediately after the package lands in the deceleration tank.

2.1.7.2. Free Droplet Experiments

The most challenging task in a free-droplet experiment is to obtain a freely floating droplet that does not move in the field of view for both cameras. The experimental procedure to ensure this condition uses the droplet generation signal to trigger all relevant timing pre-programmed in the QC-9618: magnet release, spark activation, and electrode retraction. Figure 2.32 shows the timings involved.

The droplet trajectory should be a vertical line from the nozzle to the droplet apex. Techniques to obtain such a vertical trajectory are described in Appendix A. Figure 2.32 shows the signal settings on the QC-9618 for a free-droplet experiment. The delay for channel 1 (t_{pd} = 0.03327 s, see Section 2.1.6) shown in Fig. 2.33 allows the package to be released when the droplet travels to its trajectory apex. This signal delay represents the time difference between magnet delay and droplet delay as illustrated in Fig. 2.32 and is obtained from trial and error of several experiments. The signal delay in channel 2 (cf. Fig. 2.33, t_{sd} = 0.06 s) is an arbitrary time that is larger than t_{pd}. The free droplet could also be ignited immediately after t_{pd} (i.e., $t_{pd} = t_{sd}$). The spark duration and associated retraction signal are similar to those in the fiber-supported setup. In contrast to a fiber-supported experiment where t_0 is arbitrary instant when the “run” button on the QC-9618 is pressed, here the t_0 for a free-droplet experiment is the precise time at which all signals from the QC-9618 are triggered by the HP 214B.

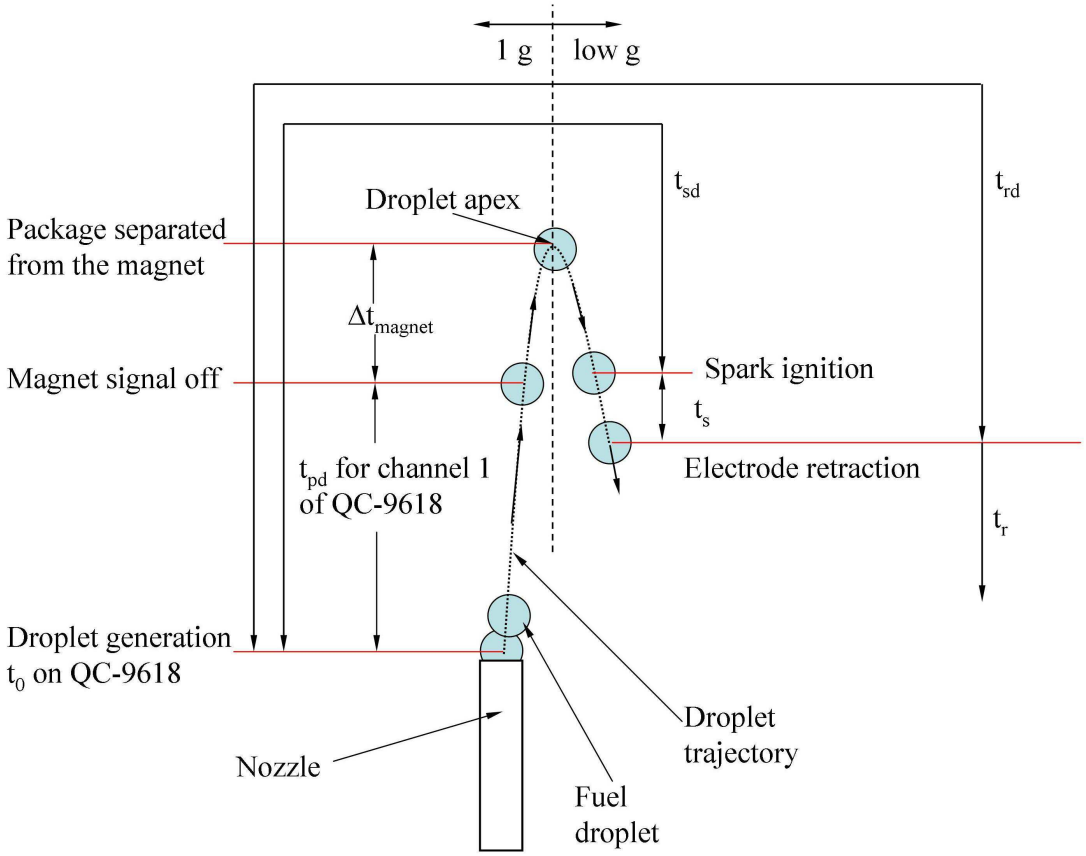

Fig. 2.32. Events during the upward flight of a fuel droplet in a free-droplet experiment.

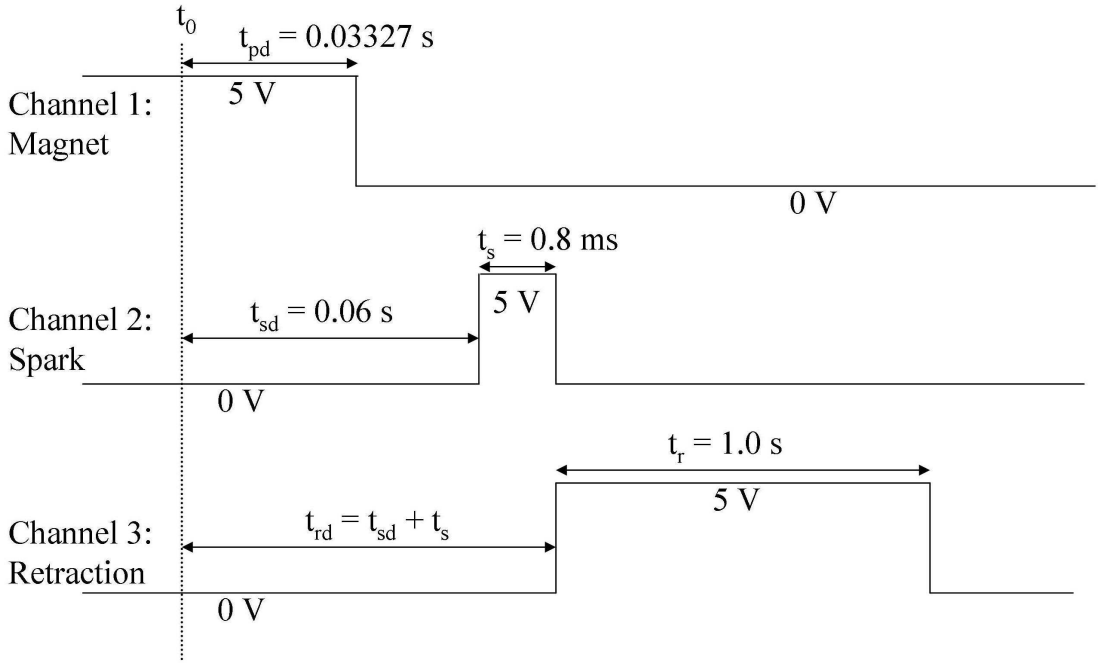

Fig. 2.33. Signal settings on the QC-9618 for the time sequence required in a free-droplet experiment.

2.1.8 Imaging Systems

2.1.8.1 High Speed Digital Black-and-white Camera

The BW camera ("F" in Fig. 2.3) is manufactured by the Canadian Photonic Labs (Manitoba, Canada, model number: Mega Speed 80K (or MS-80K), see Instruction Manual, High-Speed B/W & Color CMOS Camera Model # MS80K S2, v. 2.4). This BW camera features high speed recording (up to 200 fps) with a high photo quality for the magnification of interest here (2320 × 1722 pixels (3.9 MP) at 200 fps). This camera replaced the 16 mm cine camera (Redlake Locam-II 16mm high speed movie camera) used previously (Callahan (2000), Bae (2005)) for which the framing rate was controlled by a motor inside the cinema camera that determines the rotational speed of the film (Kodak Eastman #7278 black and white films (ASA 125)). More importantly, the digital BW camera facilitates fast diagnostics and data development for each experiment. With the previous 16 mm camera, the recorded images would not be available until the films were developed- a time consuming operation.

The BW camera is fitted with an Olympus Zuiko 90mm F/2.0 lens, an Olympus OM Telescopic Extension Tube (65–116 mm, fixed at 100 mm), and a Vivitar MC 2X teleconverter using a C-mount adapter. The MS-80K camera captures the images using a CMOS sensor and temporarily stores the images in the onboard memory. Those images are later downloaded to the PC hard drive after an experiment through an ethernet cable using the software (Camera Control) provided by the manufacturer. The ethernet cable is connected to the back panel of the camera with a Gigabit PCI Card installed on the PC.

Figure 2.34 is a screen-shot of the software interface of the Camera Control software that is installed on the PC (with Windows Vista). Operations of the BW camera are controlled by this software. As shown in Fig. 2.34, parameters/commands associated with the experiments include “start recording” (), “stop recording” (), “download images” (), and “settings” ().

When the camera is turned on and the ethernet cable is connected, the software shows ”Ready to Caputre to Camera RAM.” By clicking the “start recording” button, the BW camera starts writing recorded images into its onboard memory until either the “stop recording” is clicked or the 10 min overtime limit (shown by the green block in Fig. 2.34) is achieved. During recording, the software displays real time images that are recorded in the “capture window”. If the recording speed is as high as 200 fps, the capture window only shows arbitrary images due to the speed of Ethernet transmission. Therefore for start time events (e.g. droplet generation), the capture window will display few images. The full image sequence can be seen by clicking “download images” and reviewing the images stored in the onboard memory.

The memory storage onboard the BW camera only allows a “10 second” (10.640 s, see Fig. 2.34) recording time with the highest recording speed (200 fps) and image resolution (3.9 MP). However, for our experiments, this “10-second” recording time is sufficient because the experiment lasts only 1.2 s. After 10 second, the camera automatically erases the previous images in the memory and continues to store new images such that recording is not stopped. The user should stop the camera immediately after the experiment to prevent the recorded images from being erased.

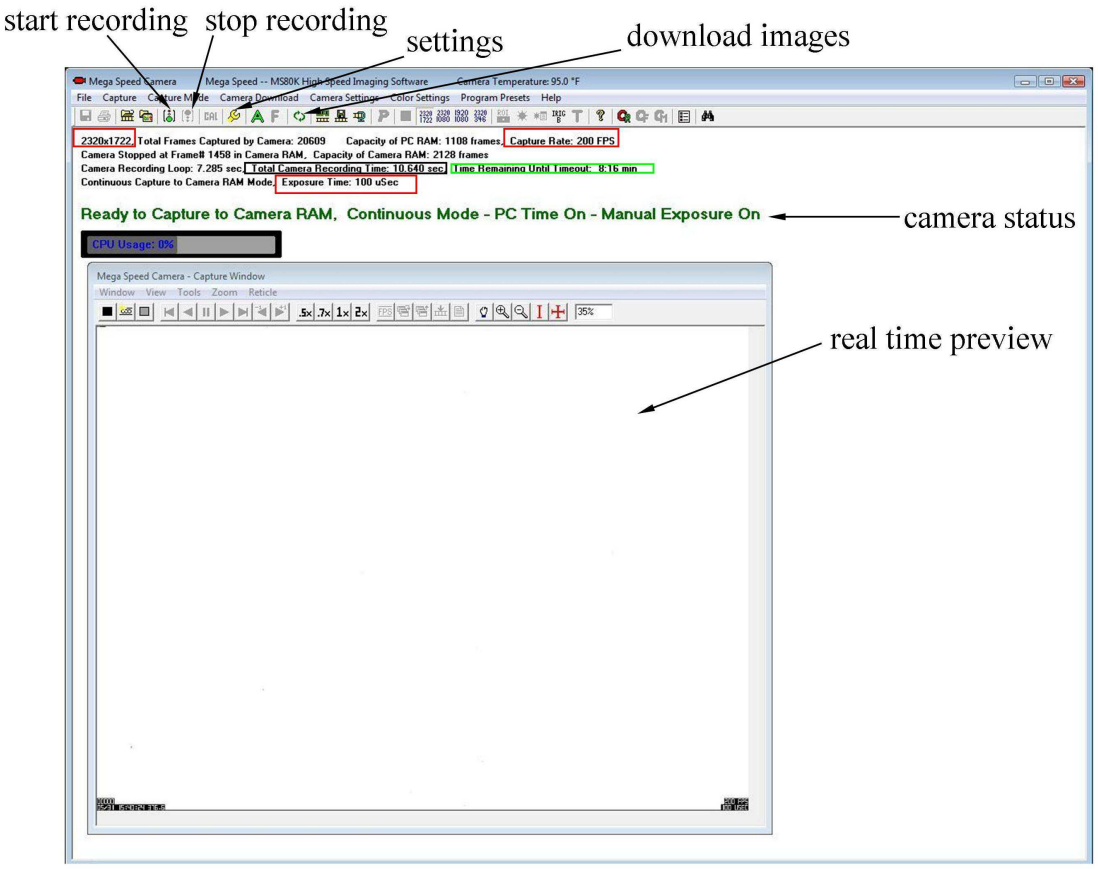

Fig. 2.34. Interface of the Camera Control software for the BW camera; the red blocks indicate the recording parameters (2320×1722 pixels, 200 fps, and 100 μs exposure time); the black blocks indicate a 10.640 s recording limit due to the temporary memory space; the green block indicates the 10 minute overtime that is default to the software to turn off the BW camera is recording for more than 10 minutes.

While recording, the framing speed, exposure time (t_{expo}) and gain value are adjusted through "setting" on the PC. The gain value here was fixed at 800 for all fuels. The framing speed used for the droplet combustion in the present study is 200 fps (i.e., 5 ms per frame) though the actual exposure time is governed by the shutter speed (or exposure time, t_{expo}). The selected t_{expo} ranges from 30 to 200 μs (or 1/33333 to 1/5000 s), also depending on the lens aperture (or f-stop value on the Olympus Zuiko 90mm f/2.0 lens) chosen for a fuel.

For sooty fuels like Jet-A and toluene, a more intensive image background (or backlight) is required to see the droplet through the soot cloud formed during the combustion process. A brighter image background is achieved by increasing the t_{expo} or reducing the f-stop. When using higher f-stops (> F/16) it is difficult to obtain a uniform background due to "vignetting" as a result of using a small aperture size. With a fixed LED intensity, t_{expo} =200 μs is used for Jet-A or toluene with F/8.0. For fuels that do not form soot shells (MB and MD), a brighter background is used in order to obtain the optimal contrast for the droplet boundary. For intermediate sooting fuels, (e.g., n- and iso-alkanes), t_{expo} and f are adjusted until a uniform background (not as bright as for very sooty fuels) and visibility of soot shells are obtained. Table 2.2 shows the exposure time and f-stop values for the fuel investigated.

After an experiment, the images are downloaded from the onboard memory to the PC hard drive in JPEG format using the "download images" function (cf. Fig. 2.34). This function also allows the user to select a specific section of images (defined by the start frame and the end frame) and download the images with a selected downloading speed (from 5 to 15 fps, 19.05 MB/s). For a typical experiment, there are

Table 2.2. Exposure time (t_{expo}) and aperture setting (F) for the fuel investigated.

	MS-80K		Hitachi HV-C20	
Fuel	t_{expo} (μs)	F	t_{expo} (μs)	F
n-heptane	50	2.8	4000	5.6
n-octane (D_o = 0.52 mm)	200	8	4000	2.8
n-octane (D_o = 0.63 mm)	200	8	4000	2.8
n-octane (D_o = 0.71 mm)	200	8	4000	2.8
n-octane (D_o = 0.85 mm)	250	8	4000	2.8
iso-octane	70	2.8	4000	5.6
n-decane	120	8	4000	2.8
n-decane (free-droplet)	30	2.8	4000	2.8
toluene	200	8	4000	4
iso-octane/n-heptane	70	2.8	4000	4
n-heptane/toluene	200	8	4000	4
Gasoline (87 unleaded)	80	4	4000	4
Indolene	80	4	4000	4
Jet-A (POSF4658)	200	8	4000	4
3 CS surrogate for Jet-A	200	8	4000	4
4 CS surrogate for Jet-A	200	8	4000	4
Camelina HRJ (POSF6152)	200	8	4000	4
Tallow HRJ (POSF6308)	200	8	4000	4
Jet-A/Camelina HRJ	200	8	4000	4
Methylbutanoate (MB)	120	5.6	4000	2.8
Methyldecanoate (MD)	200	5.6	4000	2.8

Note: the conditions are fiber-supported with D_o = 0.5 ~ 0.6 mm unless particularly specified; the free-droplet n-decane experiment uses no 2X teleconverter for the BW camera.

about 300 individual images to be downloaded (that covers the 1 g stationary and the entire free fall periods). With the RAMs (8G) currently installed on the PC, the minimum downloading speed (5 fps) is recommended because if the hard drive writing speed can not catch up with the downloading speed (which is usually the case), images would be stored temporarily in the PC RAM until the download is completed. Failure of image downloading usually occurs when the PC RAM is full such that the remaining images cannot be entirely downloaded to the PC (to the hard drive or the RAM).

2.1.8.2. Color Video Camera

Droplet flames are recorded using a color video camera (Hitachi, HV-C20, see Operation Manual, Hitachi 3-CCD Color Camera, Model HV-C20/C20M) at 30 fps without backlighting. This camera is fitted with a Nikkor 135 mm F/2.0 lens and two Kenko 36 mm extension tubes. The HV-C20 camera features a 3-CCD sensor element. This sensor captures “Red”, “Green”, and “Blue” (known as RGB) colors using three individual CCDs so that the final image has better color presentation (in terms of capturing distinct yellow and blue flames) compared to, say, the Cohu 8295 CCD color video camera used previously (Callahan (2000) and Bae (2005)). Also, the Sentech (Intertest) STC-HD133DV and the color version of MS-80K (all with 1-CCD) were considered. Figure 2.35 shows the images of Jet-A droplet flames (in normal gravity) recorded by a Hitachi HV-C20 (a) and a Sentech STC-HD133DV (b to e with various f-stop). Note that the color performance of the STC-HD133DV is better than Cohu 8295 and MS-80K (color version). As shown in Fig. 2.35, it is obvious that the

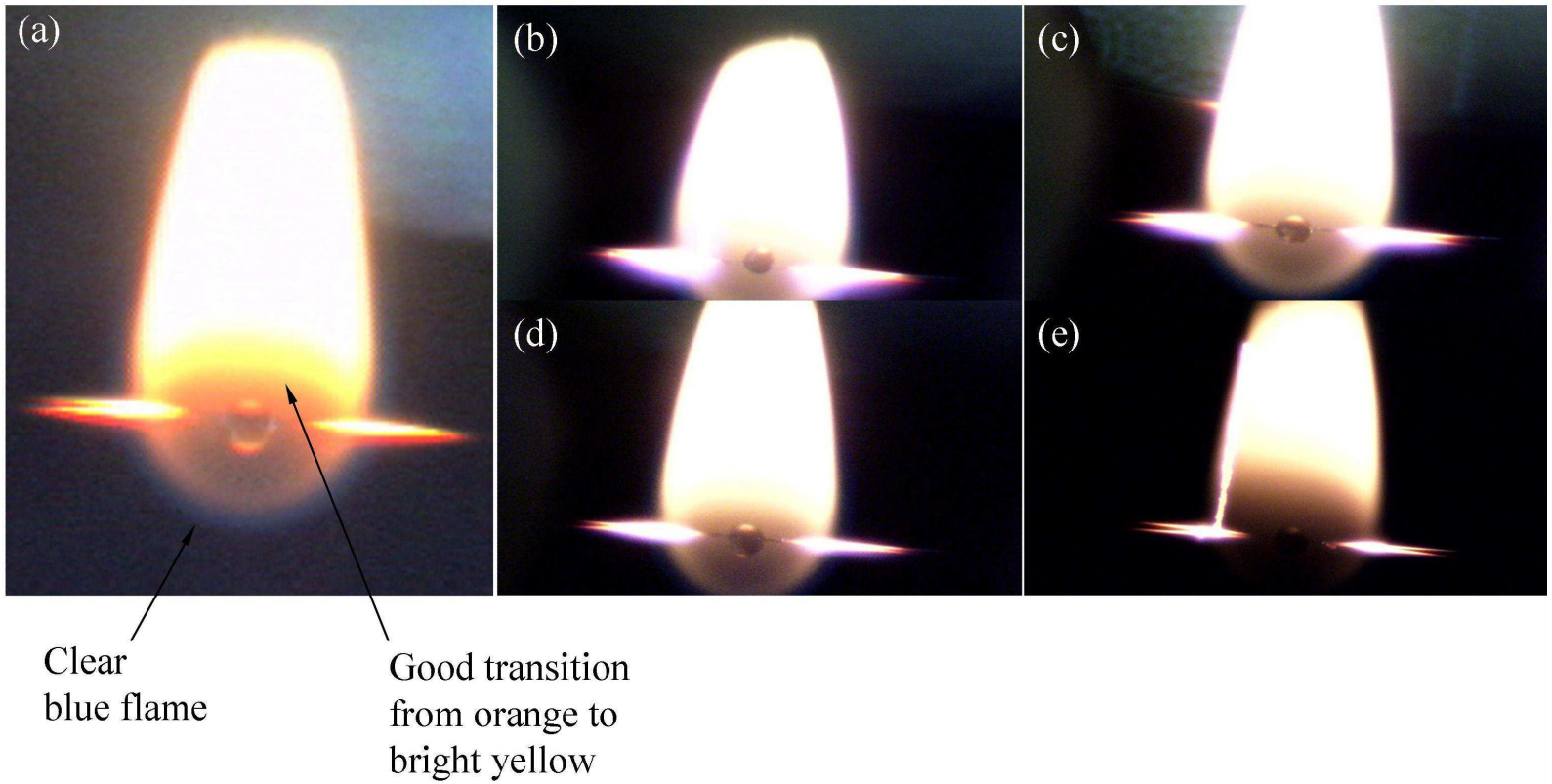

Fig. 2.35. Color images of Jet-A flames (in normal gravity) obtained from the Hitachi HV-C20 with F/4 (a), and a Sentech STC-HD133DV with F/2.8 (b), F/4.0 (c), F/5.6 (d), and F/8.0 (e) that compare the color performance.

images obtained from the HV-C20 have a much better color contrast than those from the STC-HD133DV. The blue flame boundary is clear and the color transition from orange to yellow is well-resolved by the HV-C20, which can not be achieved by the Sentach camera with any lens settings.

The HV-C20 color camera outputs video signals from a BNC connector. This BNC signal is connected to a video capturing device (Pinnacle box (Corel Inc., Mountain View, CA)) and a CRT TV (Electrohome Electronics LTD., Model no.: 38-V19NQA-AP). The Pinnacle box outputs the USB signals of the video that finally goes to the PC. The software used to capture and store videos on the PC is the Pinnacle Studio 12 (Corel Inc., Mountain View, CA). Figure 2.36 illustrates the connections between the color camera, Pinnacle box, CRT TV, and PC. The reason for sharing the video feed to a CRT TV is that it allows for images in real time without having to watch it from the PC which has some delay due to the CPU or graphic card. The video recording and the frame capture are activated in the interface of Pinnacle Studio 12. Detailed procedures of how to start recording a video and save it to the PC, as well as how to grab frames from a video using Pinnacle Studio 12 are discussed in Appendix A.

The t_{expo} of the HV-C20 camera is adjusted from the "menu" button on the back panel. For all the fuels investigated in this study, the t_{expo} is fixed at 1/250 s (i.e. 4 ms). In order to obtain optimal brightness for the droplet flames, the f-stop on the Nikkor 135 mm F/2.0 lens is adjusted for various fuels. Table 2.2 shows the f values used for the fuels of interest. In general, a smaller aperture (e.g. F/4.0) is used for soot fuels like Jet-A and toluene because their flames are brighter. A larger aperture (e.g.

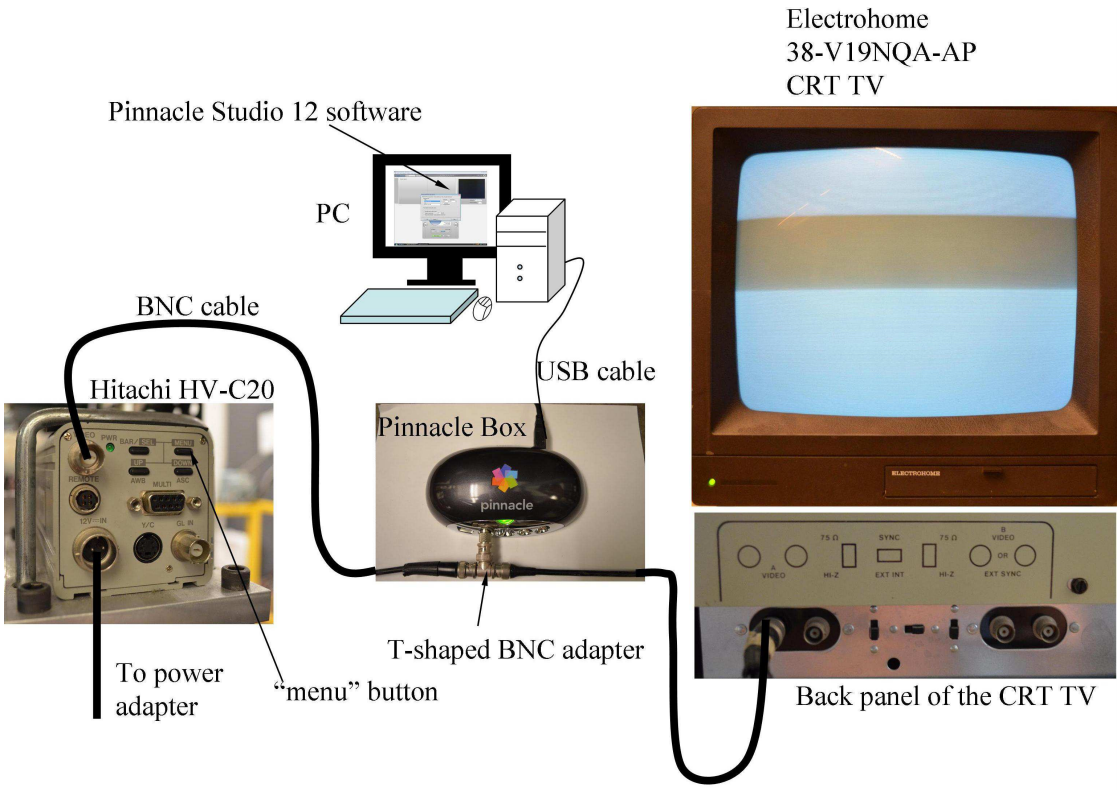

Fig. 2.36. Illustration of connections between the Hitachi HV-C20 color video camera, the Pinnacle Box, the CRT TV, and the PC for droplet flame capturing.

F/2.8) is used for non-sooting fuel like MB and MD. It is worth noting that F/5.6 was found to be large for n-heptane and iso-octane flames; F/2.8 that better shows the blue flame boundary for n-octane and n-decane could have been more suitable for them.

2.2 International Space Station: Droplet Combustion Experiments

Droplet combustion experiments were carried out using the Multiuser Droplet Combustion Apparatus (MDCA) installed in the Combustion Integrated Rack (CIR) onboard the International Space Station (ISS) (Williams et al. (2005)). Detailed components and implementation of an MDCA experiment are illustrated in Fig. 2.37. Key components include a combustion chamber, imaging systems and data storage units. In the combustion chamber fuel droplets with desired sizes (> 1.5 mm up to 6 mm) are generated and freely deployed between two retractable hot-wire igniters in a low gravity environment. The MDCA also includes an option to position a fiber to anchor the droplet if desired. Unlike the drop tower experiments discussed in Section 2.1, hot-wire igniters are used in the ISS experiments due to safety considerations. Hot-wire ignition slightly reduces the transient heating period of a droplet burning process without changing the later quasi-steady burning rates (Bae (2005)).

Figure 2.37a shows hardware involved in an ISS experiment. A deployment motor transmits liquid fuels from a fuel tank to the tips of two needles. The liquid droplet is then stretched between the needles (see Fig. 2.37b) and hot-wire igniters (Fig. 2.37c). An experiment is initiated by retracting the two deployment needles (Fig. 2.37d). The LED that provides lighting for the combustion chamber is turned off and only infrared lighting is activated for a “Hi-Beam” camera. An ideal needle retraction

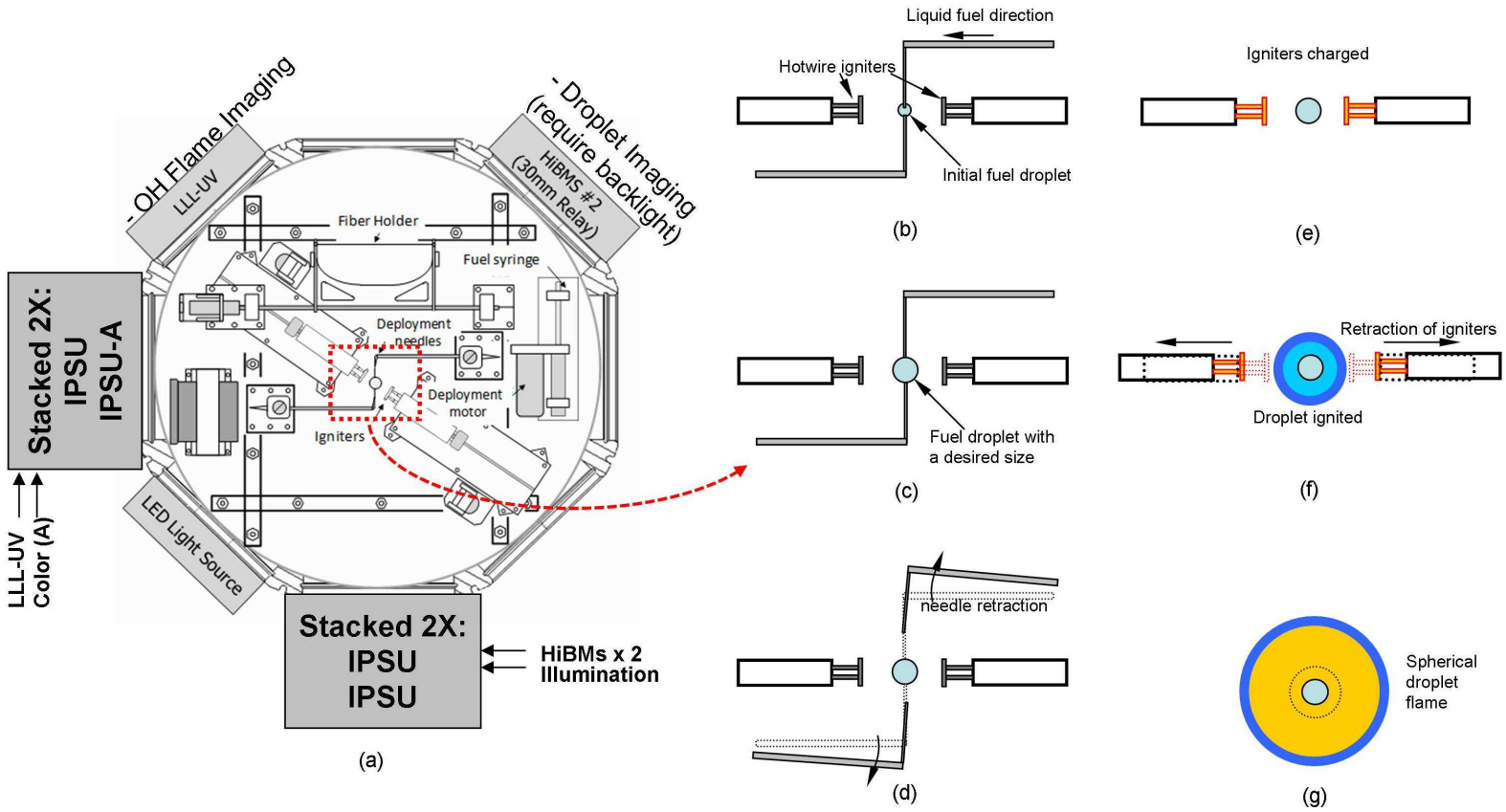

Fig. 2.37. Schematic of the Multi-user Droplet Combustion Apparatus (a) and the experimental procedure associated with it: (b) fuel droplet deployment; (c) fuel droplet sizing; (c) fuel needle retraction; (e) igniters charging; (f) droplet ignition and retraction of the two igniters; (g) a spherically symmetric droplet flame to be recorded by the imaging systems.

event allows the droplet to stay in the same position with no directional motion. The droplet shape will slightly deform but this deformation is quickly dies out.

At the moment the needles are retracted the droplet is subjected to residual owing to the liquid sticking to the deployment needles that can cause an initial velocity of the droplet (< 4 mm/s), especially for smaller droplets (D_o < 2 mm). Though small initial velocities of a droplet will not cause distortion of the spherical flame symmetry, it will lead to soot aggregates floating towards the opposite direction during the burn. A fuel droplet occasionally moves out the field of view due to poor deployment so the quality of droplet deployment is very critical to a successful ISS experiment. The largest Reynolds number associated with the residual droplet velocity for the ISS experiments reported here is around 0.1.

The droplet deployment command is followed by energizing the two hot-wire igniters (cf. Fig. 2.37e) until the droplet is ignited. Three key parameters to successful ignition are distances between the igniters and the surface of various sizes of droplets, power output from the igniters, and the igniter charging time. In general, the hot-wire igniters are moved farther away from each other to accommodate larger droplets. Fuels with a higher boiling point (e.g. n-decane) required larger power output or longer igniter charging times because a lower fuel concentration is built up around the droplet due to its lower volatility compared to lower boiling point fuels.

After the igniters are activated for the prescribed time and power, the droplet is ignited and the igniter arms are retracted by traverse motors (Fig. 2.37f). The motion of igniter retraction usually after leads to soot shell deformation. As the soot shell forms, the trace of early deformation of the shell are often observed (see Chapter 3)

that remains as two soot tails in the direction in which the igniters were retracted. This soot tail aggregates make the soot shell measurement more challenging (see the data analysis section).

While the droplet flame is freely floating in the combustion chamber (Fig. 2.37g), the Hi-Beam camera records the silhouette of the droplet and soot shell using an infrared back light. A Low-Light-Level Ultraviolet (LLLUV) camera also captures the 310 nm OH emission spectra. Furthermore, a color camera provides self-illuminated flame images during a burning event. The data from these three cameras are temporarily stored in the Image Processing and Storage Units (IPSUs) until the next scheduled downlink to earth computers. All the data with $D_o > 1$ mm in this study are obtained from the MDCA/ISS experiments described above.

The experiments are controlled from the NASA Glenn Research Center in Cleveland, OH. All commands are made by NASA Glenn in real time. Concurrently, a video feed is sent to Cornell from Marshall where we view precisely what NASA Glenn sees. A phone link between Cornell and NASA Glenn allows our real-time adjustments and recommendations to Glenn to alter such things as the ignition time and positioning of the hot wires relative to the test droplet- two crucial adjustments needed for a "successful" experiment (here "success" is defined as a free-floating drop staying in the camera field of view). Figure 3.38 shows the communication links involved.

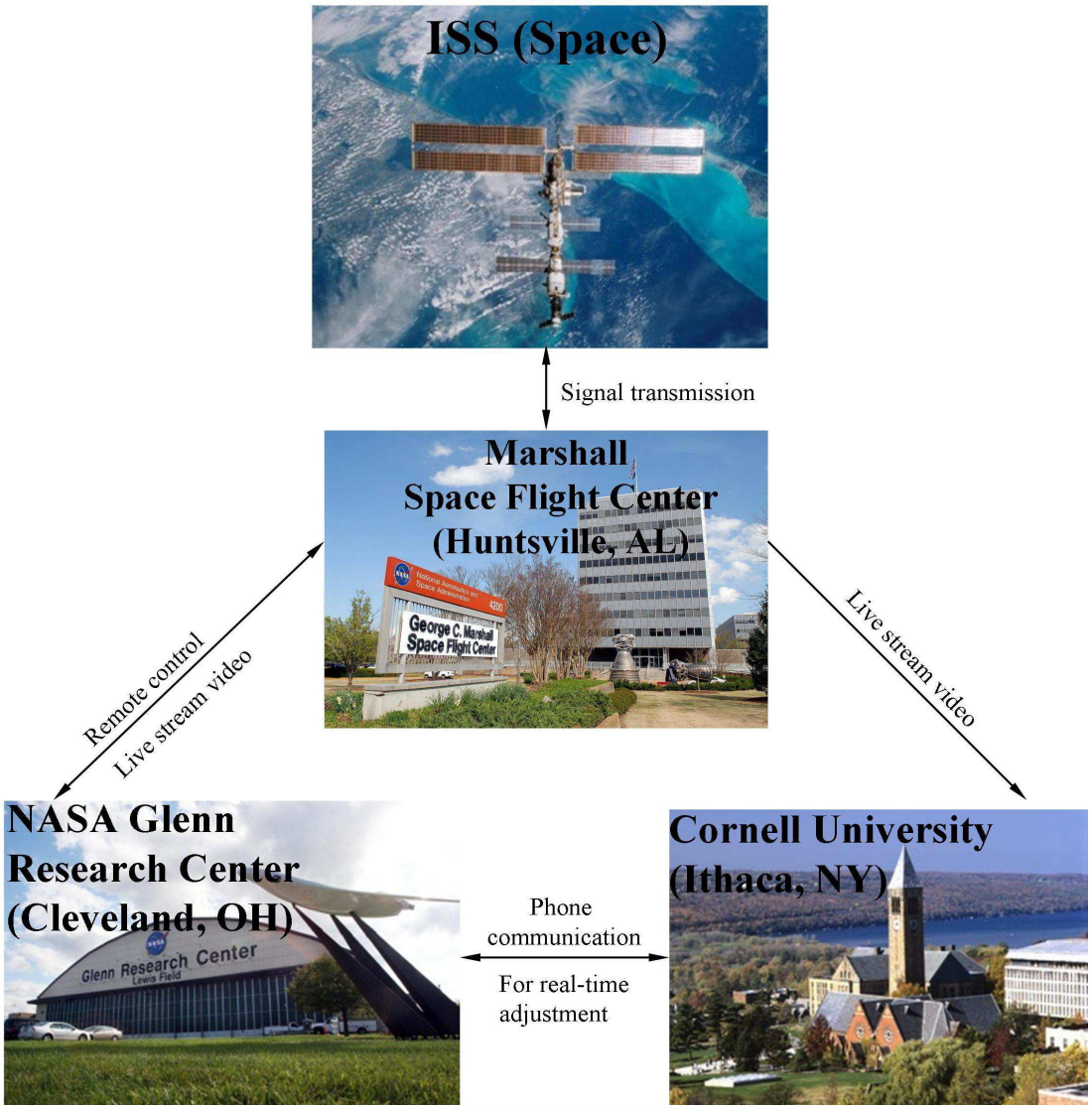

Fig. 2.38. Illustration of the communication between the ISS, Marshall Space Flight Center, NASA Glenn Research Center, and Cornell University during an ISS experiment.

CHAPTER 3

QUANTITATIVE MEASUREMENTS AND ANALYSES

3.1 Droplet Diameter Measurements

The main diagnostics of the droplet combustion experiments are the images recorded by the two cameras (see Section 2.1.8) from which the dimensions are extracted for the droplet, soot shell, and flame (cf. Fig. 1.1). By measuring the droplet diameters from the recorded droplet burning images, the evolution of droplet diameters can be examined and compared between different fuels.

The droplet diameter is measured from the image produced by the BW camera (MS-80K). Figure 3.1 shows a strip of photographs from drop tower experiments produced by the BW camera for three fuels with different sooting propensities (a: gasoline, b: iso-octane, c: methyl butanoate). The support fibers are visible in these photographs, but, no attempt was made to subtract out the diameter of the fiber protruding the diameter of the fiber was considered part of the droplet diameter. The fiber has a negligible effect in this instance when $D >> D_{fiber}$. The reliability of droplet diameter measurements breaks down at the end of burning when $D \sim D_{fiber}$. We took the condition $D < 10\ D_{fiber}$ or about 144 μm as this limit. Measurements below this threshold (down to 80 μm) were made only in a few instances when it was considered reliable to do so. The presence of soot particles and aggregates around the droplet boundary makes the droplet diameter measurement quite challenging.

Figure 3.2 shows the typical procedure of manual extraction of droplet diameter with the aid of thresholding and area of interest (AOI) functions in the

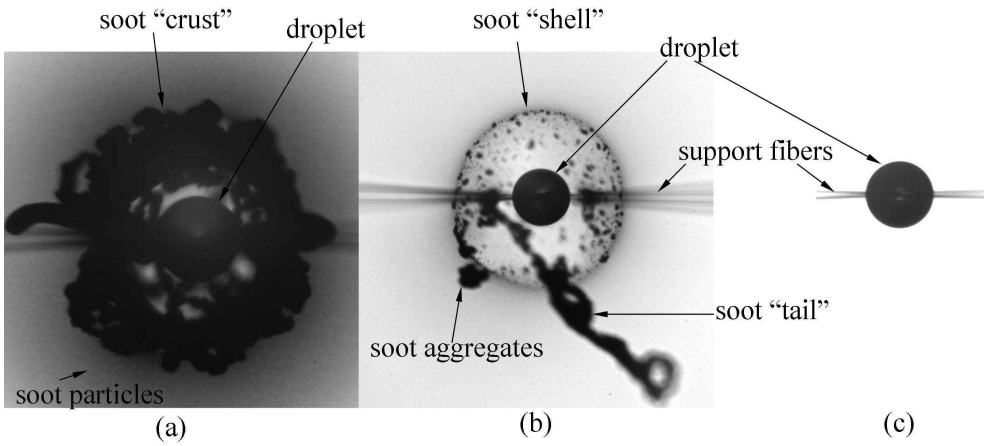

Fig. 3.1. BW images of (a) a burning gasoline droplet, (b) a burning iso-octane droplet, and (c) a burning methyl butanoate droplet, showing various level of sooting for the fuels examined in this study. Images were taken mfrom the mid portion of the burning histories as representative of the droplet and sooting configuration.

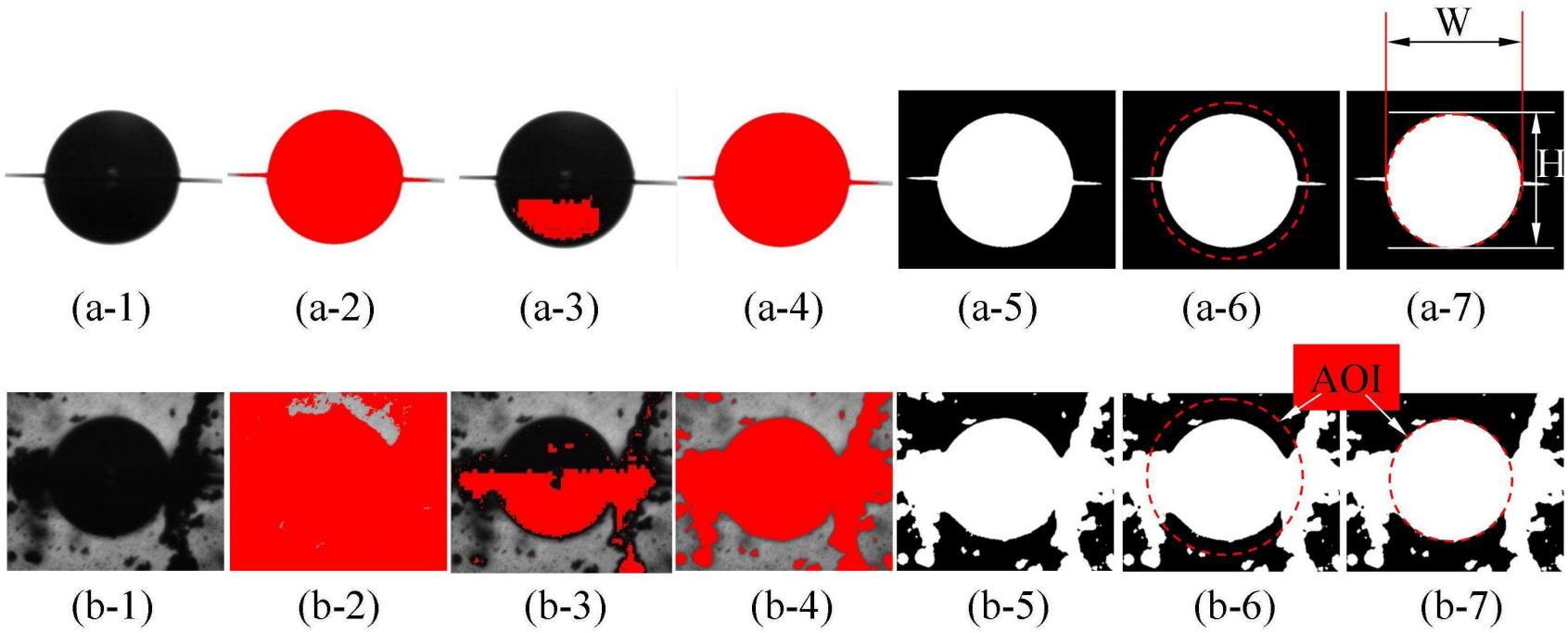

Fig. 3.2 Procedures for measuring the droplet diameter using the threshold filtering and AOI function in the Image-Pro Plus v6.3 for (a) an n-heptane image and (b) a toluene image.

Image-Pro Plus v6.3 (Media Cybernetics, Inc., Rockville, MD). Column 1 shows the original images. As can be seen, the droplet boundary for n-heptane (Fig. 3.2a-1) is quite clean compared to that for toluene (Fig. 3.2b-1) where the soot particles darken the background intensity and the soot aggregates overlap with the droplet boundary. Column 2 shows the result of auto-thresholding. When the droplet boundary is as clean as in Fig. 3.2a1, auto-thresholding can easily give accurate results for droplet diameter measurement. However, Fig. 3.2b-2 shows that when there exist considerable interference around the droplet boundary (from soot in this case), the auto-thresholding function might not be able to obtain reasonable droplet diameter measurements. Clearly, here, the auto-thresholding method is not good for toluene. Manually adjusting the threshold value until the filtered area (red in Fig. 3.2) covers the droplet boundary is necessary.

Figure 3.2a3 and 3.2b3 shows that when the threshold value is fixed at "20", the filtered area (red) poorly distinguishes the actual droplet boundary from the background for both fuels. Fig. 3.2a4 shows the when a threshold value of 160 is applied on the n-heptane image, the droplet boundary can be identified from the background after converting the image to a binary color (black or white) (Fig. 3.2a5). An AOI (dotted line in Fig. 3.2a6) is placed on the image and adjusted manually until it depicts the sharp boundary of the converted binary image.

A successful manual measurement can be obtained for toluene with a threshold value of 80 (filtered area as shown in Fig. 3.2b5) followed by a binary conversion (Fig. 3.2b6) and AOI measurement (Fig. 3.2b7). The height (H) and width (W) of the elliptical AOI can be obtained from Image-Pro, and the droplet diameter D is

computed as $D = (H \times W)^{0.5}$.

A Matlab program (Dembia et al. (2012)) that automates the processes described above for a series of consecutive images was used to complete the droplet size measurements for several fuels in this study. This program only fails to provide data that agree with the manual measurements when there is a great amount of soot surrounding the droplet boundary (e.g. Jet-A and gasoline) that will obscure part of it. This program can complete the measurements for 100 consecutive images such as Fig. 3.2a within 3 minutes (with a 3.1 GHz Intel Core i5-2400 CPU), compared to 100 minutes when done manually. The output results from this program should always be compared against manual measurements, at least, for a few selected points. Descriptions of this program are in Appendix C.

Threshold filtering with a constant value might introduce error when the background color intensity is non-uniform. This occurs for several gasoline and Jet-A droplet images in which not only the soot aggregates block the droplet boundary, the asymmetry of the trapped soot aggregates around the drop also affects the very small soot particles that darken the background. Figure 3.3 shows a case from a gasoline experiment when the background intensity was not uniform around the droplet boundary (Fig. 3.3a). Imposing a constant threshold is not the best approach here considering the threshold found for the lighter boundary does not necessarily apply to the darker boundary (Fig. 3.3c, for threshold = 20). Figures 3.3b and 3.3d show filtered areas using threshold values of 15 and 25, respectively, in which the red boundaries do not represent the actual droplet boundary. For this type of images, it is

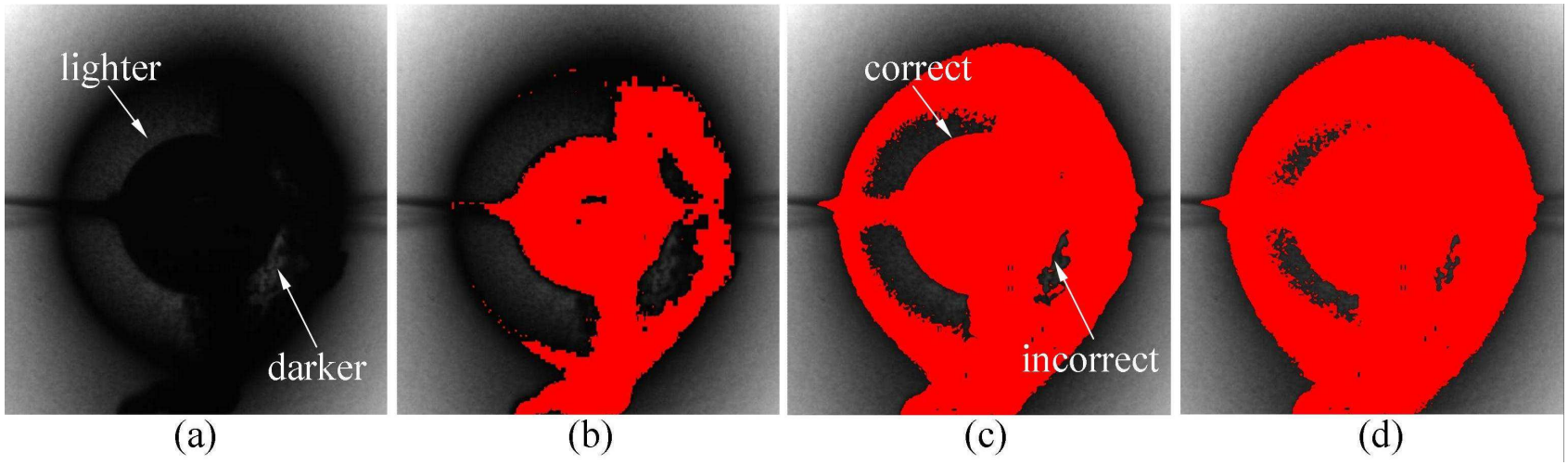

Fig. 3.3. Threshold filtering with a constant value for (a) an image obtained from the gasoline experiment; (b) with threshold value = 5; (c) with threshold value = 20; (d) with threshold value = 30.

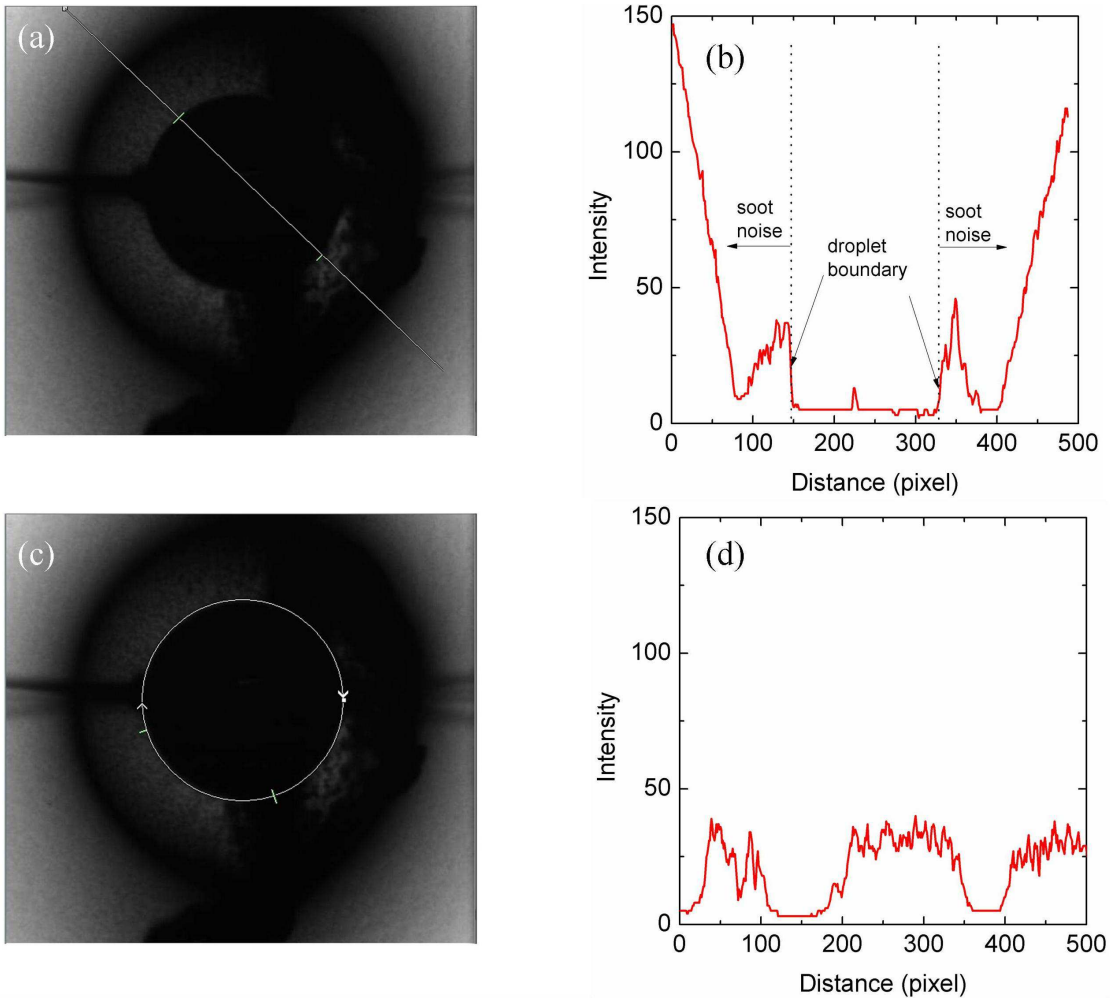

Fig. 3.4. (a) A profiling line crossing the droplet boundary and the soot noise; (b) the intensity profile along the line depicted in (a); (c) a profiling circle along the approximate droplet boundary; (d) intensity profile along the circle depicted in (c).

better to directly place an AOI on the droplet boundary for the measurement. In other words, when a manual effort is used to identify whether or not the red boundary (cf. Fig. 3.3) represents the entire droplet boundary, the measurement is actually based on where the AOI is placed (on the lighter and the darker side, cf. Fig. 3.3a).

Using the same image as Fig. 3.3, Figs. 3.4b and 3.4d are the intensity profiles along a line (a) and a circle (b) placed on the image. As shown in Fig. 3.4b, the left boundary is cleaner (and sharper) than the right one because of the presence of soot noise near the right boundary. Figure 3.4d shows that the intensity along the entire droplet boundary (the profiling boundary curve is shown as a circle in Fig. 3.4c) could vary from "5" to "40". This range makes a "constant" threshold less precise in terms of using only one value to represent the intensity along the entire droplet boundary.

To manually identify the position of a digitalized boundary without using a threshold, an elliptical AOI is placed on top of the image. The size of the AOI is determined by the width and the height of the ellipse. While using the AOI to outline the droplet boundary, the boundary of the AOI (dotted line in Fig. 3.5) is adjusted to be in the outer edge of the "grey transition area" (the color transitioning pixels are due to digitization of a definite boundary). Figure 3.5 shows the "grey transition area" at the digitized droplet boundary and where the AOI line should be placed for the measurement. When the background near the boundary is bright, this "grey transition area" is very narrow and droplet boundary can be easily identified. However, when the background near the boundary is dark (mainly due to the presence of soot particles or aggregates), the "grey transition area" can be as wide as 5 to 8 pixels, which increase the uncertainty of the measurement.

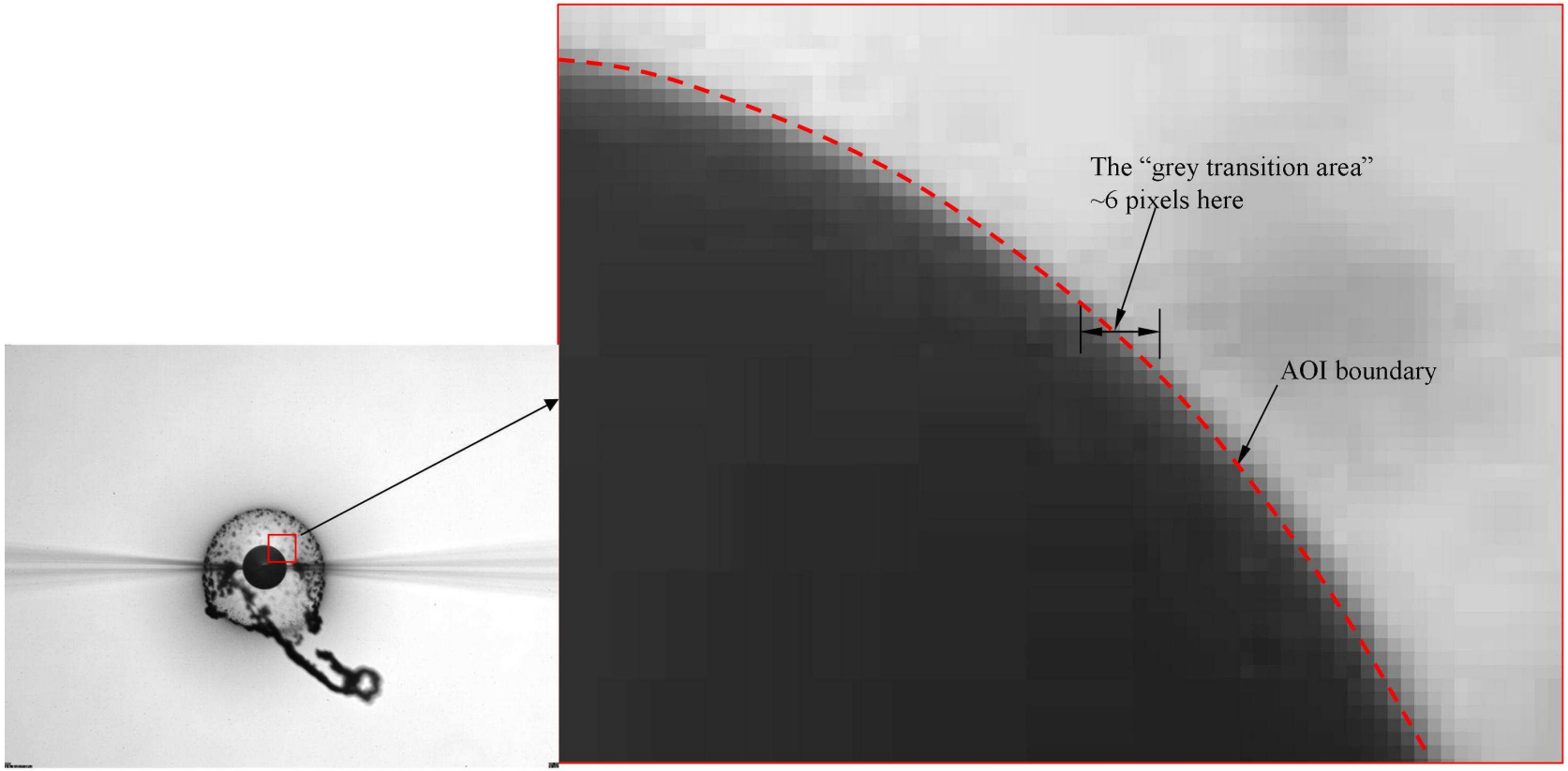

Fig. 3.5. An example image (from an iso-octane experiment) showing how the droplet boundary is identified without using the threshold method (cf. Fig. 3.2).

Figure 3.6 shows different situations where the droplet diameter can still be measured. Figure 3.6a shows an image of clean droplet boundary. This is the most common situation for the droplets before ignition, or the majority of images of a non-sooting fuel (i.e. methyl butanoate, and methyl decanoate, with D_o~ 0.5 to 0.6 mm). Figure 3.6b shows an image of an 80 μm droplet (the smallest droplet diameter reported in this study) anchored on the fibers near the end of its burn. Though the droplet boundary loses its sharpness, we can still attempt to extract the droplet diameter from this type of image with the aid of the threshold filtering. Figure 3.6c represents the most common situation that a lot of soot is produced (e.g., Jet-A, toluene, gasoline, etc.). Part of the droplet boundary is obscured by soot aggregates. Nonetheless, an AOI can still be constructed to complete the obscured droplet boundary in a measurement (see Fig. 3.6c) because more than two arcs are identified.

The droplet diameter analyses of images from the ISS experiments are similar to those for the GB experiments considering the issues with threshold filtering and soot obscuration. The Mablab program (Dembia et al. (2012)) developed originally for the GB droplet diameter measurements is modified for ISS analyses to accommodate differences in format only (ISS: 1024×1024 pixel in TIFF; GB: 2320×1722 pixel in JPEG) and filenames. The modified Matlab program can be found in Appendix E. Though this image analysis is independently developed by us, the results appear to show good agreement with the results generated by NASA Glenn.

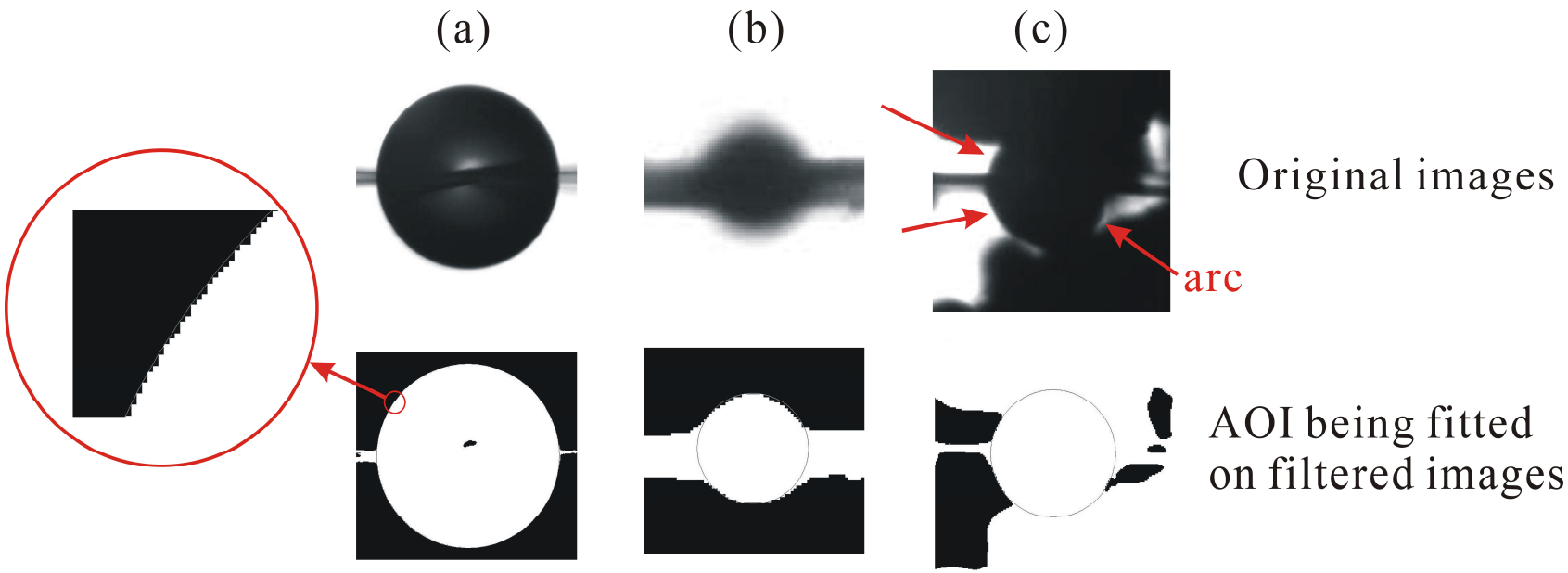

Fig. 3.6. Illustration of how to extract the droplet dimension while the droplet is big with a clean boundary (a), the droplet is small near the end of burning process (b), the droplet is partially obscured by the soot aggregates around it.

3.2 Soot Shell Diameter Measurements and Soot Standoff Ratio

From BW images soot shell (if formed) diameter must also be measured. The soot shell diameters are measured manually with the assistance of the elliptical AOI in the Image-Pro Plus v6.3. As soot particles agglomerate, the shells thicken and make the measurements more challenging. Regardless the thickness of the soot shell, the position of the mass center of the shell is of most interest. Figure 3.7 shows several BW images for the fuels examined with various sooting propensities, along with the soot shell boundary (the dotted lines) indicated for them. They cover all the situations encountered for soot shell measurements in this study.

Figure 3.7a is an image from a GB n-decane experiment (D_o = 0.55 mm). It shows a situation where "few" soot aggregates are formed so the soot shell is intact. Figure 3.7b shows the soot structure of a burning iso-octane droplet (GB, D_o = 0.53 mm) where the soot aggregates sometimes "hang" as a "tail" on the fiber though the soot shell is still intact. The presence of a soot tail does not alter the measurement of the soot shell. For a very sooty fuel, e.g. Jet-A (Figs. 3.7c and 3.7d), there is too much soot and the aggregates tend to form a thick "crust" structure with the agglomerates stuck as a hard shell. For this situation, unless the soot aggregates form a tail, only when the soot shell is still recognizable as a sphere (as in Fig. 3.7c) can the shell diameter be obtained. When the "crust" destroys the spherical symmetry (cf. Fig. 3.7d) the soot shell is not measurable.

For the ISS measurements, the distorted part of a soot shell (due to the motion of igniter retraction) should be omitted before performing measurements. Figure 3.7f shows an image for ISS n-octane droplet and its soot shell. The soot aggregates

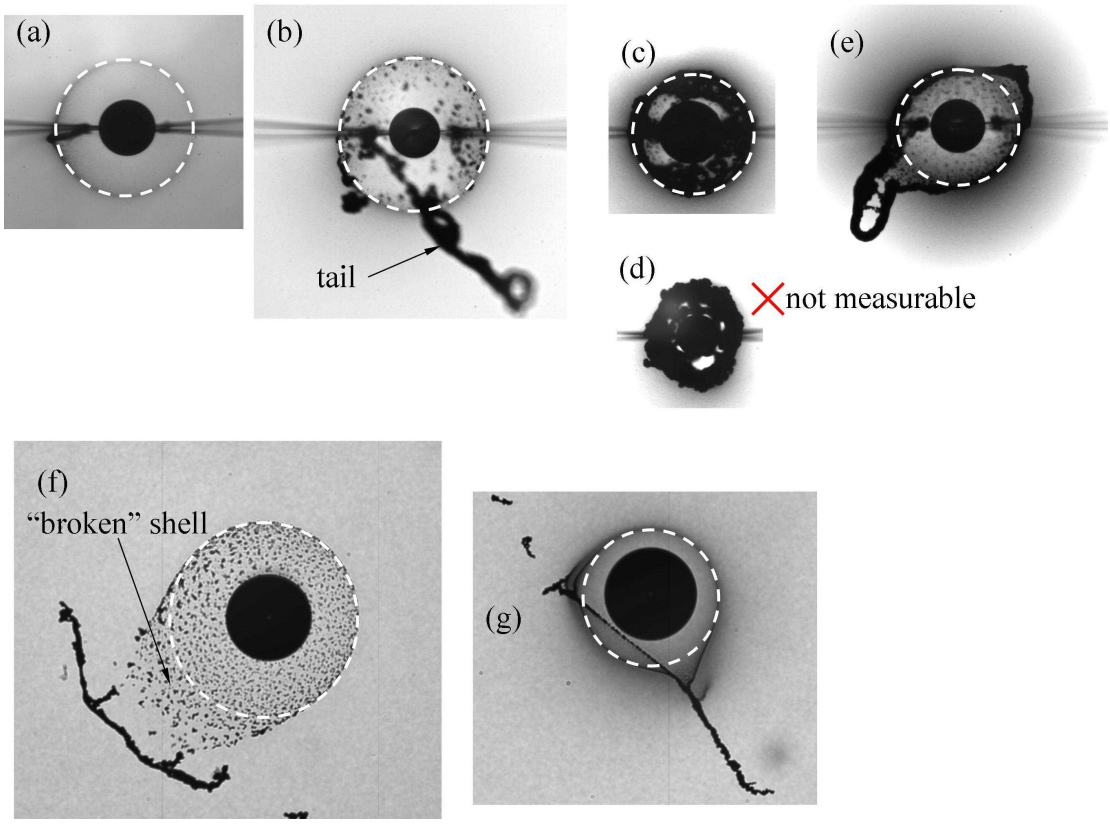

Fig. 3.7. Soot shell images and the diameter measurements indicated by the red dotted circle: (a) GB n-decane (D_o = 0.55 mm); (b) GB iso-octane (D_o = 0.53 mm); (c) GB Jet-A (D_o = 0.56 mm); (d) GB Jet-A (D_o = 0.59 mm); (e) GB gasoline (D_o = 0.53 mm); (f) ISS n-octane (D_o = 3.61 mm); (g) ISS n-octane (D_o = 3.31 mm). Images are selected to represent different soot shell structures observed.

(formed near ignition) breaks at the 8 o'clock portion of the soot shell. For this part of measurement, the shell periphery from the 10 o'clock clockwise to the 4 o'clock position constitutes the important boundary. Figure 3.7g shows an ISS n-octane droplet in the early period of burning. The spherical part of this soot shell can still be utilized for the diameter measurement. The method used in this study that determines D_s uses an elliptical AOI in Image-Pro (shown as dotted lines in Fig. 3.7) to place and overlap the soot shell periphery identified based on the criteria described above.

The soot standoff ratio (SSR = D_s/D) is plotted vs. t/D_o^2 (the normalized time). The SSR is calculated using the measured soot shell diameter and dividing it by the droplet diameter obtained from the same image.

3.3 Flame Diameter Measurements and Flame Standoff Ratio

This section explains how the flame measurements were performed for the droplet flames with various sooting propensities. The flame diameter is measured from the color images recorded by the color camera (for GB or ISS). A droplet flame consists of an inner core with a yellow or orange color and an outer faint blue flame enclosing the inner core. Figure 3.8a shows an example image of this typical flame structure from an ISS experiment. The flame boundary defined in this study is the outer edge of the blue flame.

To measure the diameter of the outer edge of the blue zone, the AOI function in Image-Pro Plus v6.3 or CorelDraw 9 is used. The blue flame has a "diffuse-like" color such that a definite boundary can be difficult to find. The issues with resolution and the nature of a blue flame boundary are evident in the enlarged blue flame

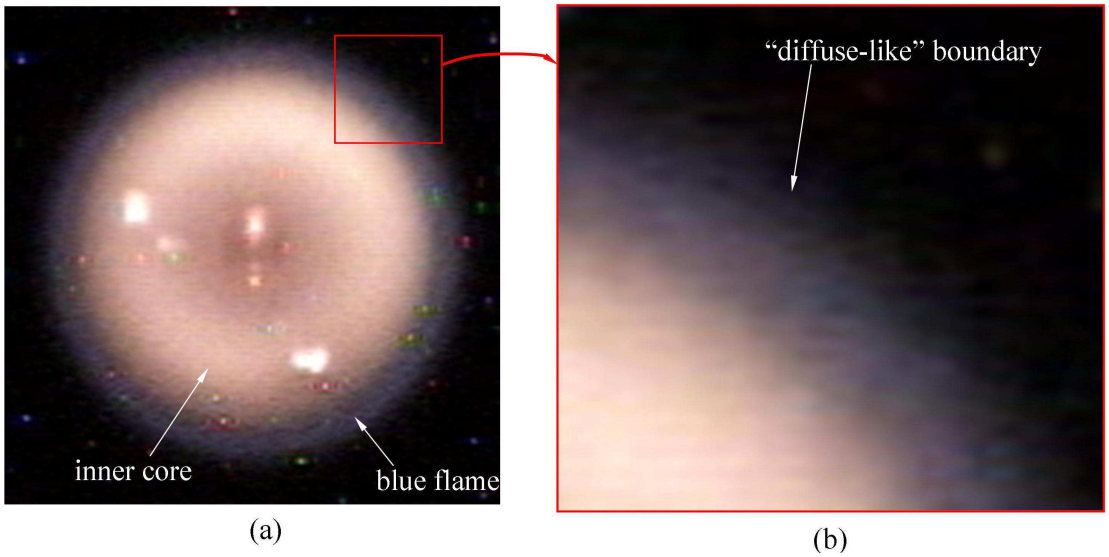

Fig. 3.8 (a) Image for a typical droplet flame with a concentric structure (from an ISS n-decane experiment (D_o = 3.97 mm); (b) enlarged image (from the red block indicated in (a)) showing the nature of the outer boundary of the blue flame. This image is taken from the mid history of burning to show the typical structure of a spherically droplet flame.

boundary shown in Fig. 3.8b. Moreover, the over-saturating inner yellow core (for very sooty fuels) sometimes further complicates the blue flame measurement.

Figure 3.9 shows several images that illustrate various flame intensities. The dotted lines in Fig. 3.9 show the AOIs that come from Image-Pro or CorelDraw for these droplet flames. Figure 3.9a shows the flame of a fiber-supported n-octane droplet. This image is typical of the flame intensities of all ~0.5 mm n- and iso-alkanes examined in this study (including n-heptane, n-octane, n-decane, iso-octane, camelina and tallow biofuels (mostly iso-alkanes)). For fiber-supported experiments (GB), the flame image has two needle-like glows on the sides. These glows are indicative of the flame-fiber interaction and can be use as a reference for the blue flame boundary. Figure 3.9b shows a droplet flame that is slightly distorted due to soot aggregates (at 7 o'clock). The inner core in this case exceeds the blue flame boundary due to the soot aggregates, which is ignored in the measurement.

Figure 3.9c shows a Jet-A droplet flame that is typical of high aromatic content fuels (e.g. gasoline, indolene, toluene, Jet-A surrogates). Despite the saturated inner core, the blue flame is still visible (outlined by the dotted line). Similarly Fig. 3.9d presents an image recorded when an ISS n-octane droplet is just ignited. The significant saturation of the inner core almost obscures the blue flame. The dotted line depicts the AOI measurement that defines the flame boundary. Note that when the flame is extremely bright, "corona effects" may emerge due to the diffraction of light produced by the flame. This phenomenon is seen in Fig. 3.9d and should not be considered for flame measurement. Figure 3.9e is an n-octane droplet flame in the middle of a burn. The inner core almost disappears and a clear blue flame is easily

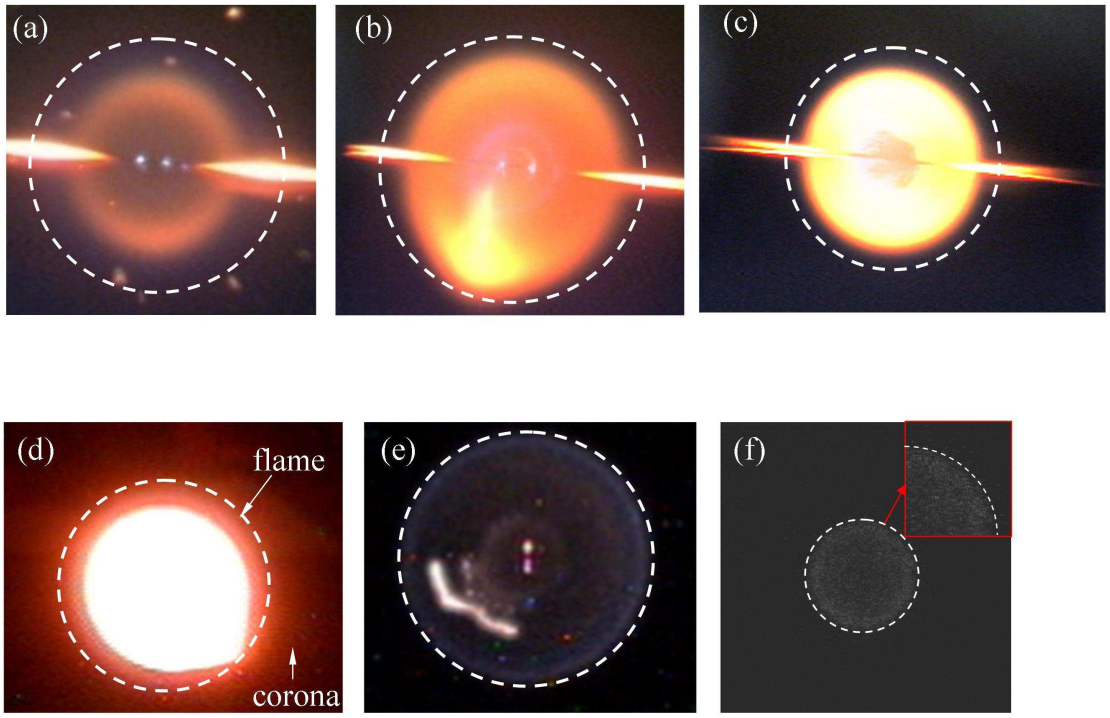

Fig. 3.9. Flame images for (a) an n-octane droplet (D_o = 0.52 mm), (b) an n-octane droplet (D_o = 0.85 mm), (c) a Jet-A droplet (D_o = 0.56 mm), (d) an n-octane droplet (D_o = 2.84 mm) near ignition, (e) an n-octane droplet (D_o = 0.52 mm) in the middle of a burn, and (f) a 2.78 mm n-octane from the LLLUV camera. Images are selected to represent different situations for flame measurements encountered in this study.

measured.

For the ISS experiments, an LLLUV camera produces images for OH emission. Figure 3.9f shows such an image. A Matlab-based program was developed to automate the OH flame measurements can be used. The measurements performed by this program are dependent on the manual measurements (similar to the blue flame measurements) as input values prior to execution. The program can be found in Appendix H.

3.4 Defining the Initial Condition and Calibration

It is now important to know which the image is in a burning sequence to establish the initial droplet diameter (D_o in Eq. (1.1)) and the t = 0 point (or the "ignition point") for the data reduction. Due to the fact that the fuel droplets are all ignited using two symmetric sparks (with a spark duration of 800 μs), the ignition point should be easy to define by noting the spark in the recorded image. However, with the current recording speed of the BW camera used (i.e. 200 fps, the time interval between two images is 5 ms, which is not synchronized to the spark circuit), if each image has an exposure time of 100 μs, an 800 μs spark duration would either only appear in one of the recorded images, or not at all. Figure 3.10 illustrates these situations. Possibility A is for a situation where the spark occurs when the shutter of the BW camera is open so that the spark can be seen in the images. Possibility B shows an ignition event between frames where the spark could not be seen. Therefore, though spark ignition can provide an accurate ignition time, spark visibility from the imaging system was not guaranteed for a given burning event. An alternative to define

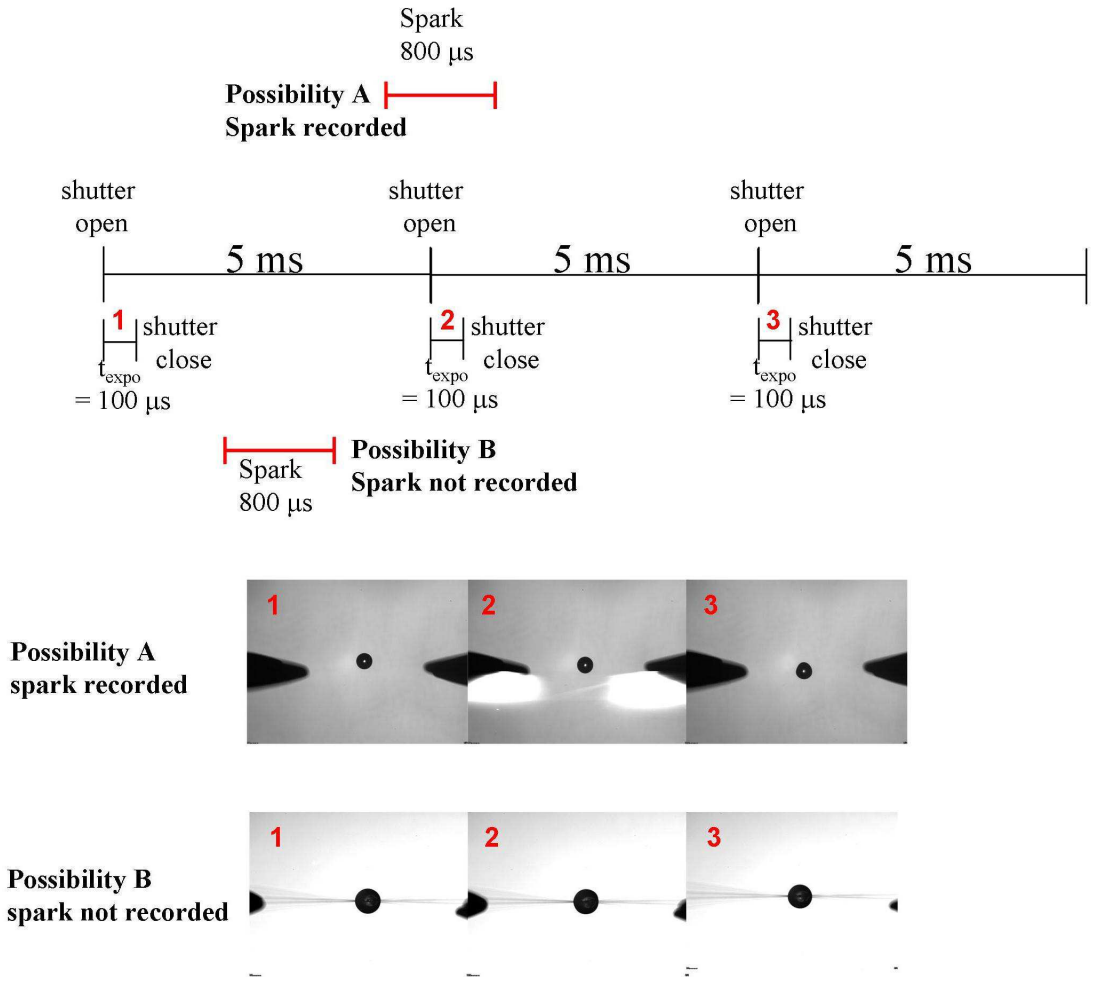

Fig. 3.10. Illustration of whether or not the sparks are recorded with the framing time interval and exposure time (t_{expo}) settings for the BW camera (MS-80K, at 200 fps). Possibility A (from a free-droplet n-decane experiment) represents the spark occurs while shutter is opened (sparks can be seen in a recorded image); possibility B (from a fiber-supported gasoline experiment) shows the spark occurs while the shutter is closed (spark can not be found in the images). The number 1, 2, and 3 (in red) label the corresponding images to the time line.

t=0 is to note possible droplet distortions.

No matter how small the spark energy, we found that the shape of the droplet was always slightly distorted due to the physical impact of the sparks on the droplet. Figure 3.11 shows such a distortion. This distortion is evidence of spark firing and it lasts slight longer than the spark itself. Therefore, the "time zero" for a D^2 history is defined here as one frame earlier than the frame in which we see droplet distortion. The uncertainty of this estimate is about the time resolution of the BW camera (5 ms). If we see droplet distortion in the current frame instead of the previous frame, the droplet distortion must have occurred between the last and current shutter close, with an uncertainty of ± 2.5 ms.

In order to convert the length from pixel to mm, a tungsten carbide ball bearing (Salem Specialty Ball Company, Canton, CT) with a diameter of 0.794 mm is recorded under the same lighting, t_{expo}, and f-stop settings as the recorded burning droplets. Figure 3.12a shows how the call bearing is mounted on a microscope slide that facilitates for photographing and Fig. 3.12b shows the recorded image. The image of the ball bearing is subjected to the identical image analysis as previously described (using the Matlab program (Dembia et al. (2012), or Image-Pro with or without the aid of threshold filtering) and the diameter of the ball bearing D_{ball} (in pixels) is obtained. Conversion between pixel and mm can thus be made using the following formula for BW images:

$$D(\text{mm}) = \frac{D(\text{pixel})}{D_{ball}(\text{pixel})} \cdot 0.794(\text{mm}) \tag{3.1}$$

It is worth noting that the calibration ball bearing should be individually recorded for

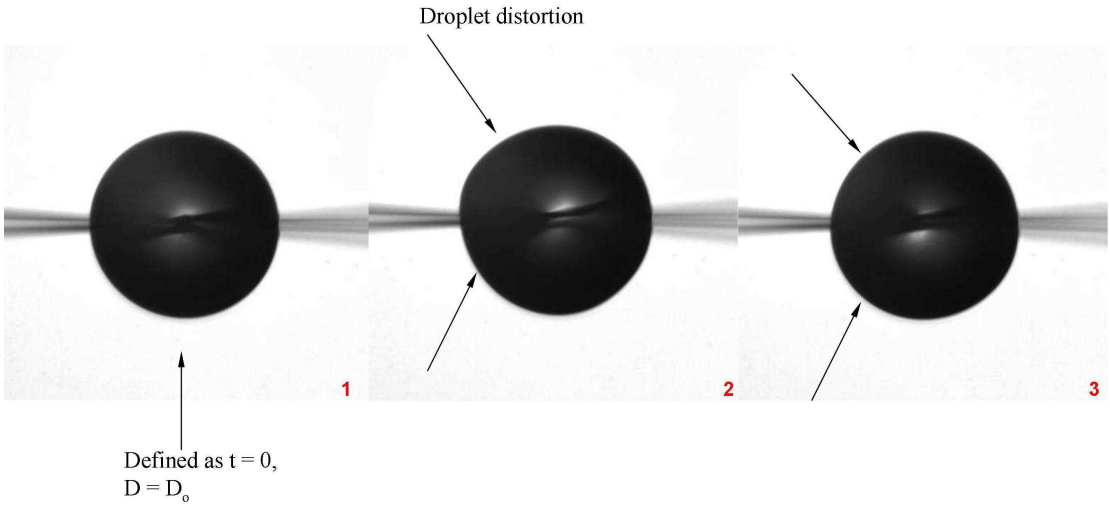

Fig. 3.11. Consecutive images from the BW camera showing the droplet distortion from which the "time zero" is defined. Images come from an iso-octane (0.53 mm) experiment for which the spark energy is small (but the droplet distortion is still noticeable) compared to all the other fuels.

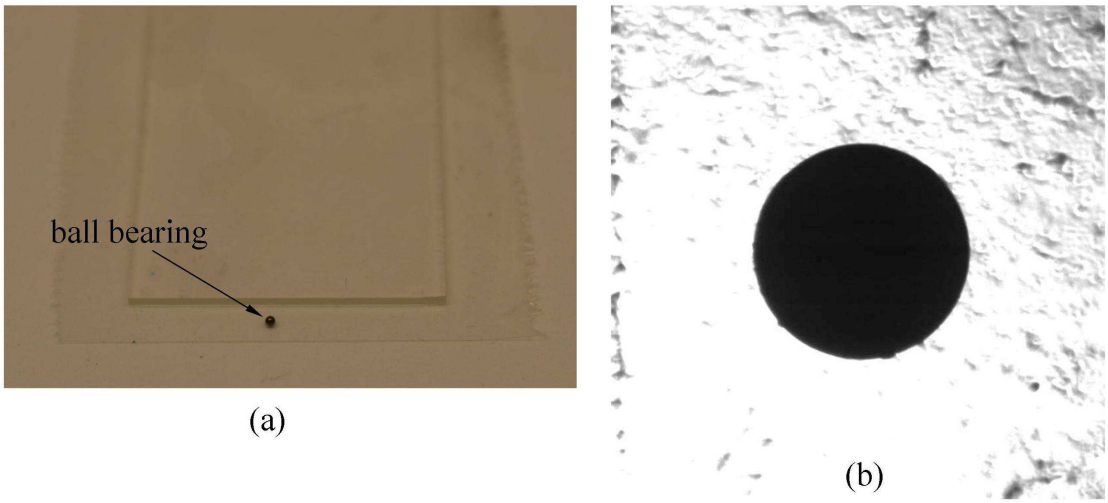

Fig. 3.12. (a) Photograph of the calibration ball bearing (0.794 mm) being taped below a microscope slide; (b) ball bearing image from the BW camera (MS-80K).

every experiment because the position of the spark electrode set and the anchored droplet might differ in each experiment.

The flame diameters are presented as the flame standoff ratio (FSR=D_f/D) vs. t/D_o^2. In the GB experiments, the color and BW cameras are not synchronized. The ignition point defined for the BW images does not carry over to the color images. The ignition point for color images in the GB framework must be independently determined. Figure 3.13 shows a series of consecutive color images near ignition of a methyl butanoate droplet (D_o = 0.53 mm). The ignition point is defined by the frame in which the flame first appears in the event. The initial "t = 0" point is assigned to the frame previous to the frame of first visibility of the flame. With the time resolution provided by the color camera, the ignition point defined here has an uncertainty of 1/30 s.

Another issue regarding the FSR is that in the GB setup, the flame and droplet diameters come from two cameras with different framing rates (color: 30 fps, BW: 200 fps). This is in contrast with the synchronized ISS cameras that have identical farming rates (30 fps). With the measured flame diameter at each time, droplet diameter values corresponding to those times are required for FSRs. However, the times from color and BW camera do not match (i.e., there is no common value from the multiples of 1/30 and 1/200 except for 1). To resolve this issue, a 4^{th} order polynomial fitted on the D^2 data that correlates D^2 with t is used to obtain D^2 (and D) values at any color image time (t = 1/30, 2/30, 3/30,…..second). Figure 3.14 illustrates how the D values from a 4^{th} order polynomial on the D^2 data are extracted for D_f.

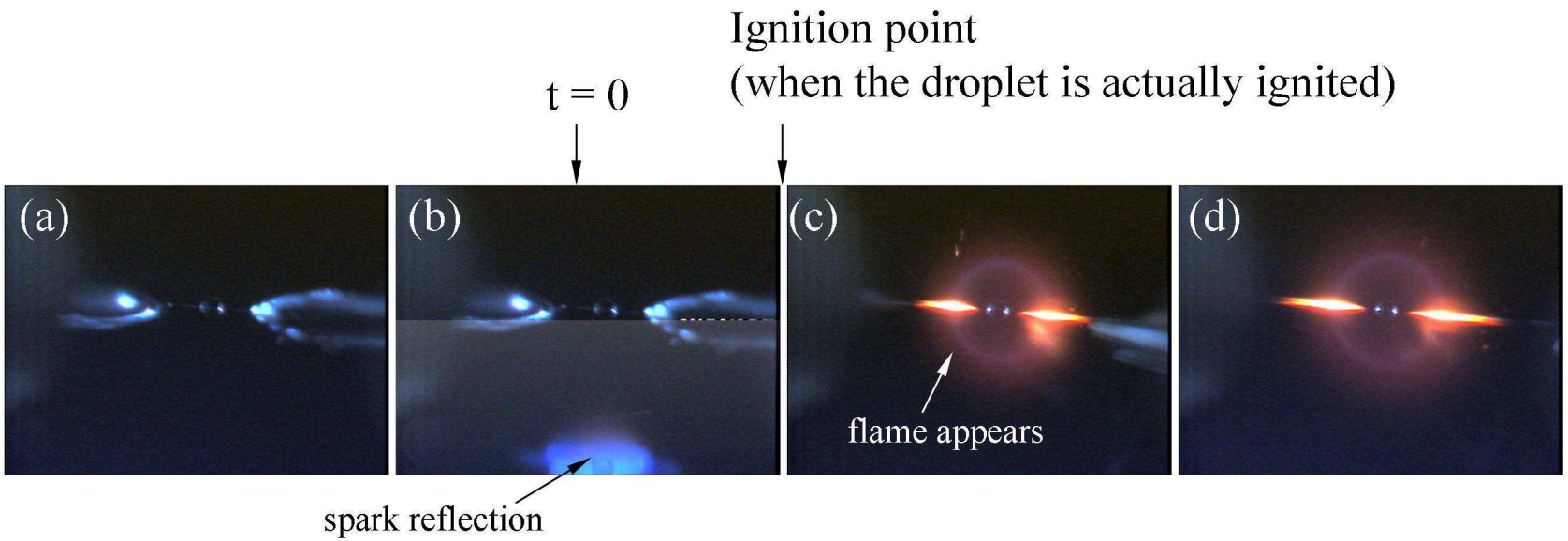

Fig. 3.13. A series of consecutive color images (recorded at 30 fps) near ignition point from a methyl butanoate experiment (D_o = 0.53 mm): (a) before spark appears; (b) spark appears but the flame is still not seen; (c) the first frame in which a flame is recognizable; (d) continual development of the droplet flame. The actual "ignition point" occurs between (b) and (c), so the t = 0 is assigned to (b) with an uncertainty of 1/30 s.

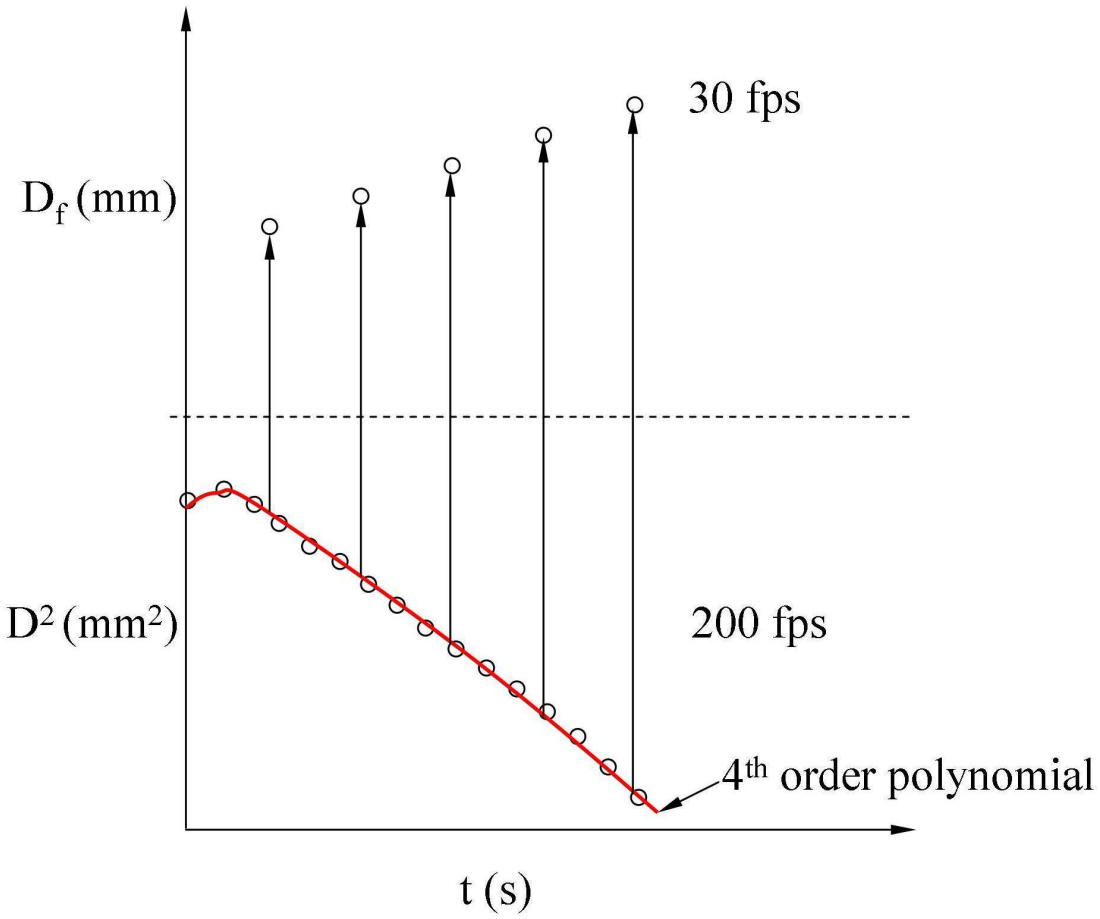

Fig. 3.14. Illustration of how to extract the droplet diameter value from a 4th order polynomial fitted on the D^2 data to facilitate calculation of FSR.

The difference between to the GB and ISS images is primarily due to the igniter setting (GB: spark; ISS: hot-wire). For hot-wire ignition, the igniters are charged and heated until the droplet is ignited. The instant when the droplet is ignited is dependent on the distance between the igniter and the droplet, as well as the energy imported to the igniters. Because, hot-wire ignition does not cause droplet distortion as in spark ignition, an alternative method is required for identification of ignition here. The "ignition point" for each ignition is between the first frame from which the flame appears (or soot cloud, if formed) and the previous frame in the view of a camera (the ISS BW and color camera record at 30 fps). Time "t = 0" where "$D = D_o$" is assigned to the frame prior to the first flame image (with an uncertainty of 1/30 s). Figure 3.15 shows how the ISS ignition point is defined from both BW and color images produced by the ISS cameras.

For GB flame measurements, the same calibration ball bearing as used for BW image analysis (see Fig. 3.12) was used for calibration. It was recorded by the color camera under the identical lighting condition, f-stop, and t_{expo} as the experiment. Figure 3.16 shows a color image of a calibration bearing. This calibration ball image should be obtained for every experiment since slight changes might be anticipated during preparation for each experiment. The calibration ball diameter (in pixels) is extracted using the same AOI method (in Image-Pro or CorelDraw). The flame diameters in pixels can then be converted to millimeters.

The length scale calibration for ISS image analyses is based on solid spheres with known materials and diameters (stainless steel: 1, 3, 4, 5 mm; glass: 3/32", 1/8", 5/32"). The spheres are recorded by the cameras under 4 different lighting conditions.

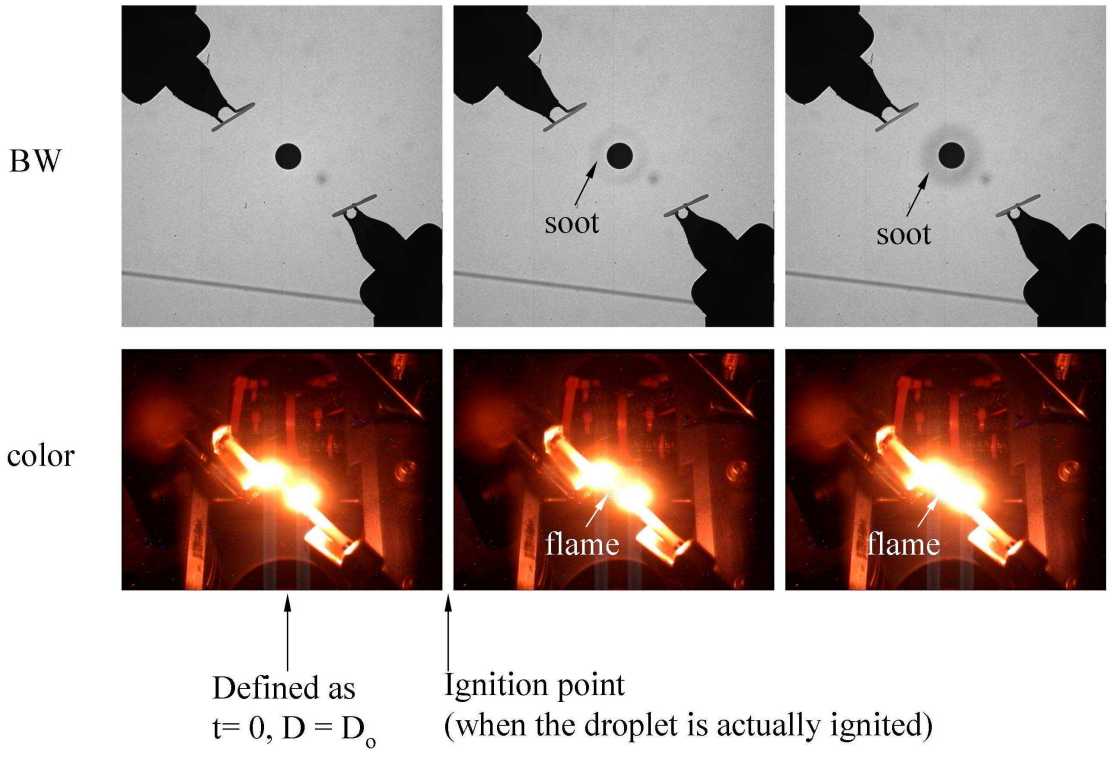

Fig. 3.15. Consecutive images (at 30 fps) from the BW and color cameras near the ignition point.

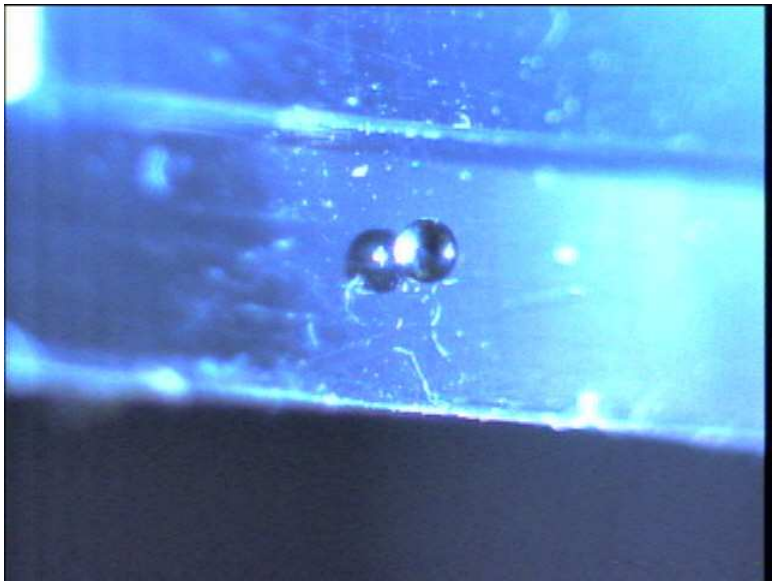

Fig. 3.16. Image of the calibration ball bearing recorded by the color camera.

Figure 3.17 shows the recorded images of the solid spheres for calibration. The scale factors (from pixels to mm) based on this method are provide by the NASA Glenn Research Center:

BW images:

x-direction: 1024 pixels = 30.22 mm

y-direction: 1024 pixels = 30.31 mm

Color camera (ISS):

640 pixels = 93.2 mm.

LLLUV camera (ISS):

x-direction: 512 pixels = 57.7 mm.

y-direction: 512 pixels = 57.9 mm.

3.5 Burning Rate Calculations

This section examines the influence of processing data like those shown in Figure 3.18a on determining the burning rate from the D^2 data. Approaches considered are akin to finite differencing the data and imposing polynomial fits of various orders on the measurements.

Plots of $(D/D_o)^2$ vs. (t/D_o^2) (normalized coordinates of D^2 vs. t) define the burning rate K according to the classical droplet combustion theory (Eq. (1.1)). In order to extract the slope of the D^2 data, the first order derivative of the fitted polynomial is calculated to give burning rate $K = - d (D/D_o)^2 /d(t/D_o^2)$.

At each time the derivative is obtained. Figure 3.18a and 3.18b show the D^2 data and the computed evolution of burning rate using a 4^{th} order polynomial for

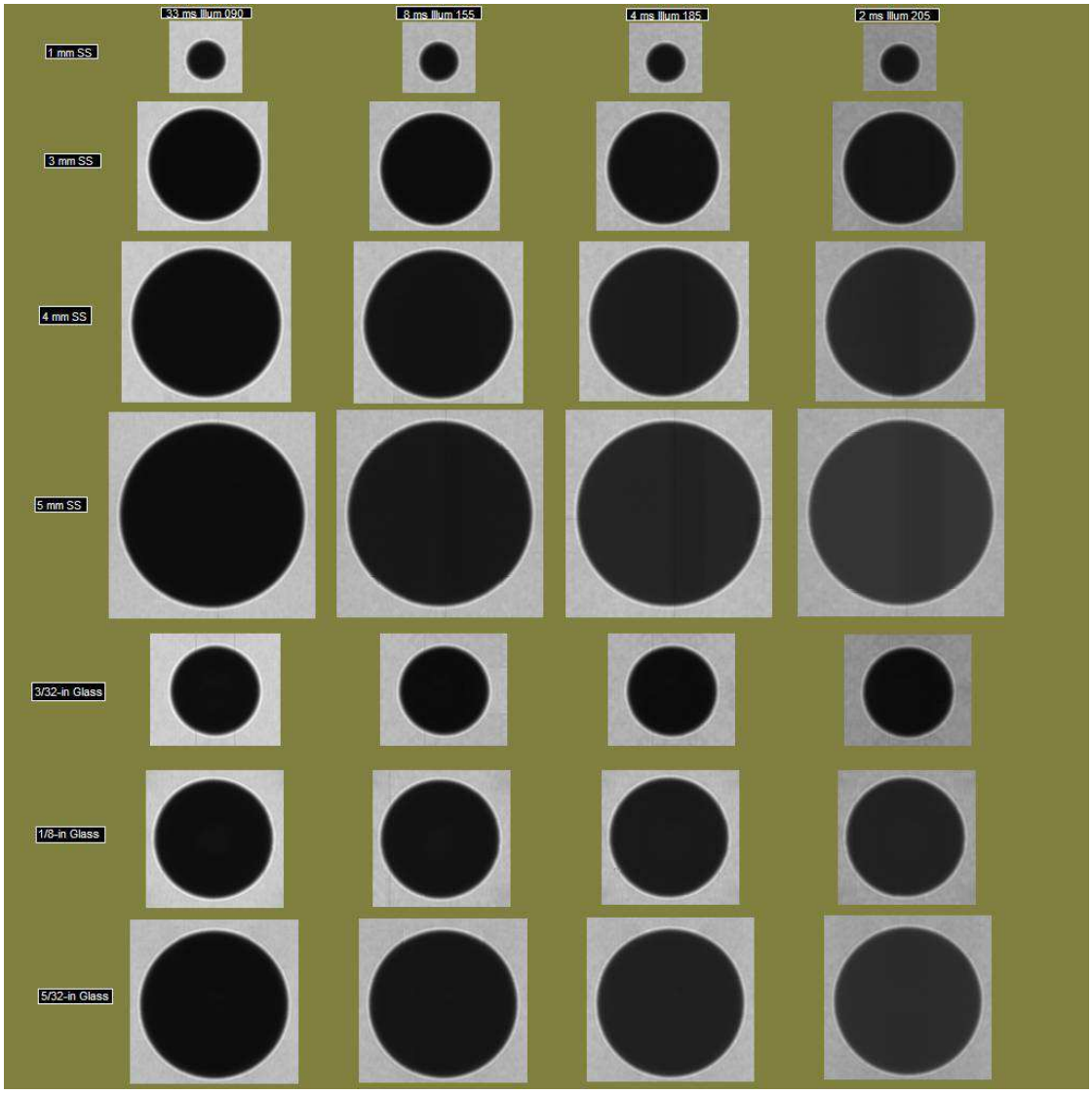

Fig. 3.17. Calibration ball images recorded by the BW camera onboard the ISS 4 different lighting conditions.

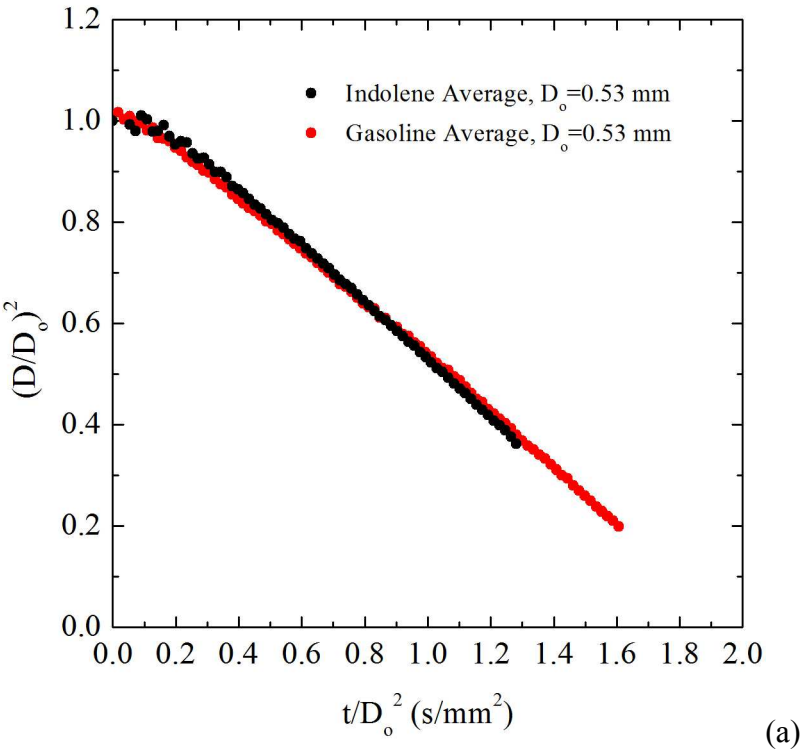

(a)

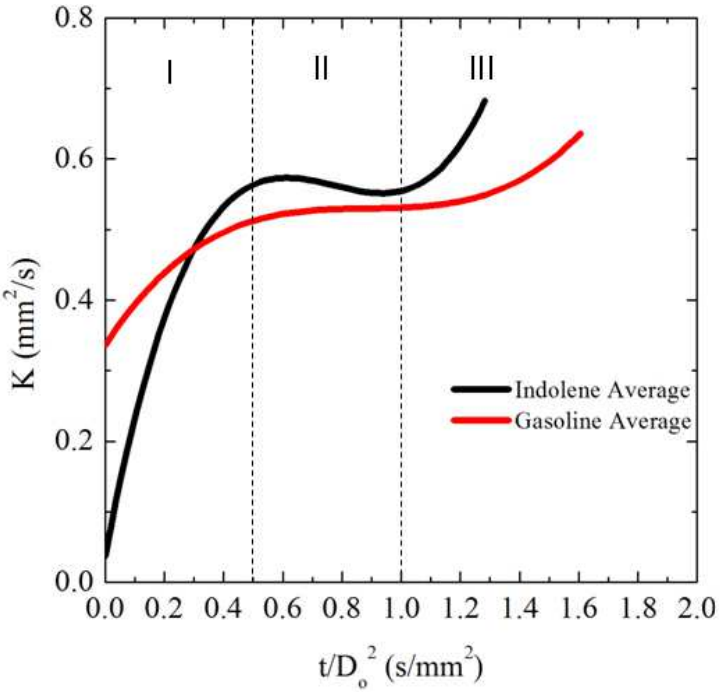

(b)

Fig. 3.18. (a) Averaged D^2 data from the gasoline and indolene experiments; (b) the burning rate K evolution calculated from the data in (a).

gasoline and indolene as an example. The Roman numerals in Fig. 3.18b indicate a transient heating region (I), an approximately the quasi-steady region (II) where K is nearly constant, and the final region (III). The following describes the efforts of assessing various methods used to obtain the slope of the D^2 data and some associated analyses using the averaged D^2 data from gasoline and indolene data.

Differentiating the data in a way analogous to a finite difference estimate of a derivative (Fig. 3.19) leads to the following expression for the burning rate:

$$K_{i,\Delta x} = -\frac{(y_{i+1} - y_i)}{(x_{i+1} - x_i)} = -\frac{(y_{i+1} - y_i)}{\Delta x} \tag{3.2}$$

This burning rate is assigned a time (cf. Fig. 3.18),

$$(t/D_o^{\,2})_{i,\Delta x} = \frac{x_{i+1} + x_i}{2}. \tag{3.3}$$

The burning rates calculated in this fashion are shown by the black data in Fig. 3.20 (black data). The resulting burning rates fluctuate significantly. This approach amplifies the physical impact of sparks on the droplet earlier in the burning and the slight errors produced by manual measurements for the droplet size. The reason the error becomes so obvious is that the time interval between each data point is very small so that K becomes sensitive to the D^2 data. A larger time spacing (e.g., $5\Delta x$) could be used to alleviate this problem,

$$K_{i,5\Delta x} = -\frac{y_{i+2} - y_{i-2}}{x_{i+2} - x_{i-2}} = -\frac{y_{i+2} - y_{i-2}}{5\Delta x} \tag{3.4}$$

for the time

$$(t/D_o^{\,2})_{i,5\Delta x} = x_i. \tag{3.5}$$

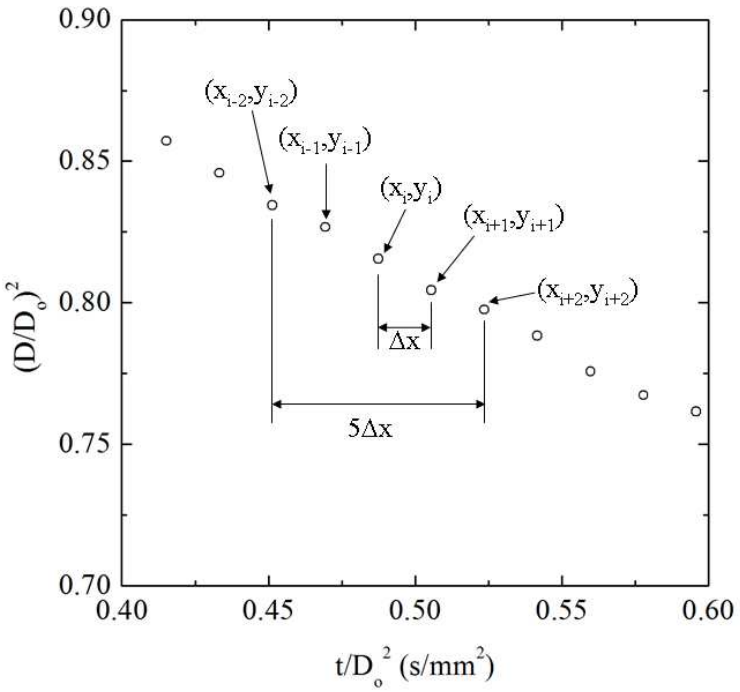

Fig. 3.19. Illustrations of various finite difference methods to obtain the burning rate K from a series of D^2 data.

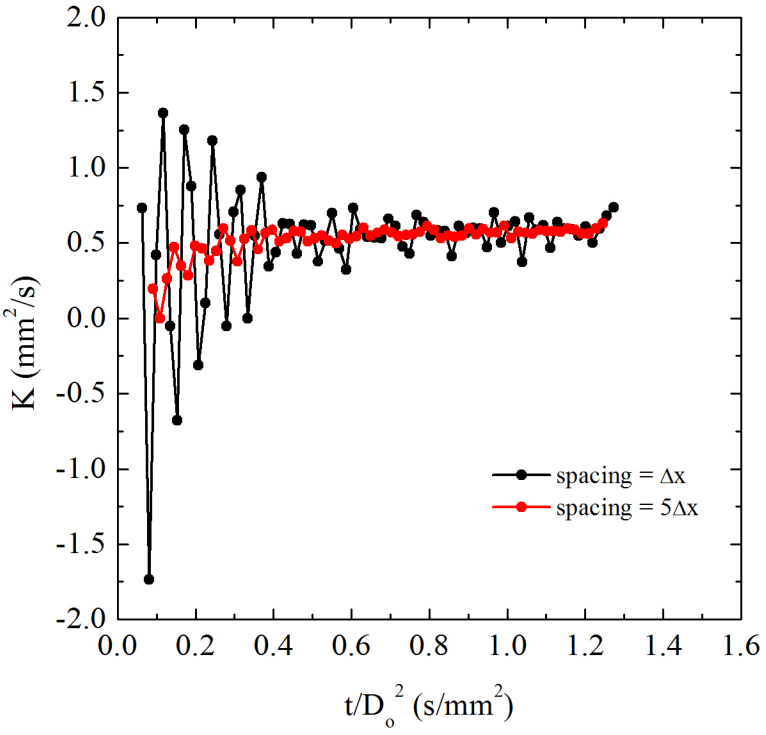

Fig. 3.20. Burning rate K calculated using the finite difference methods shown in Fig. 3.19 with different data spacing.

The red data in Fig. 3.20 show the results. The fluctuation is reduced and the quasi-steady (t/D_o^2 = 0.4~1.0 s/mm^2) burning rates do not change much compared to using a smaller time interval (black: K=0.561 mm^2/s, red: K=0.564 mm^2/s, cf. Fig. 3.20).

Since the evolution of scaled droplet diameter included in Fig. 3.19a appears to be nearly linear, a linear fit to the data may be a reasonable approximation. Figure 3.21a shows such linear fits for indolene and gasoline for the quasi-steady region ($t/D_o^2 > 0.4$ s/mm^2) in Fig. 3.18a. For the transient heating region ($t/D_o^2 < 0.4$ s/mm^2) a 2nd order polynomial is used to capture the local curvature. The burning rates calculated from the derivatives of the linear and 2nd order polynomial fits for indolene and gasoline are shown in Fig. 3.21b. Though a lower order of fitting is used in this case, this approach is still able to capture some characteristics of burning, i.e., gasoline's higher burning rate in the transient region and lower burning rate in the quasi-steady stae compared to that of indolene.

Figure 3.22a shows the efficacy of various orders of polynomials in representing the $(D/D_o)^2$ data with more nonlinearity in the transient heating region of indolene droplet burning, $t/D_o^2 < 0.3$ s/mm^2. With higher order polynomials, the curvature from 0 to 0.15 s/mm^2 is gradually improved. Both 5th and 6th order polynomials undershoot the initial diameter ($(D/D_o)^2 = 1.0$), but the 5th order fit has the closest initial value among all fits.

Figure 3.22b shows polynomial fits for indolene at $t/D_o^2 > 1.22$ s/mm^2. In this region, polynomials with an even order tend to undershoot the data whereas odd order polynomials overshoot the data. This might be due to the difference in concavity between even and odd order polynomials. Nonetheless, it is still evident that a

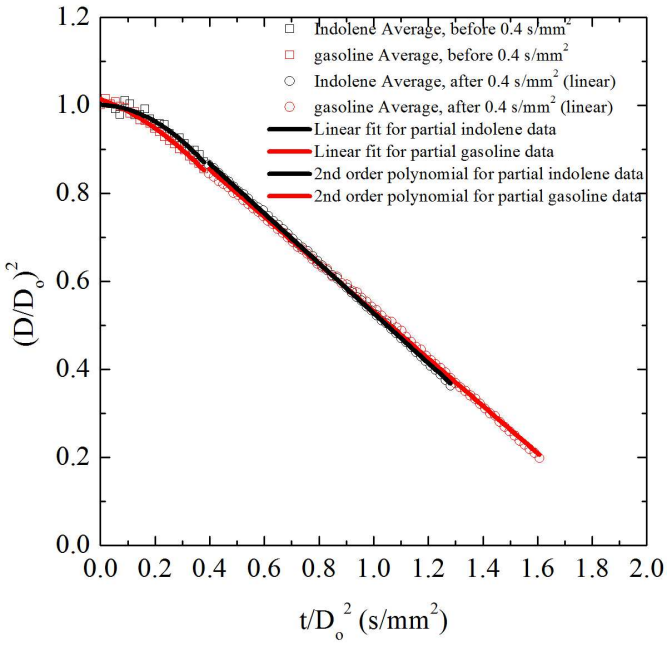

(a)

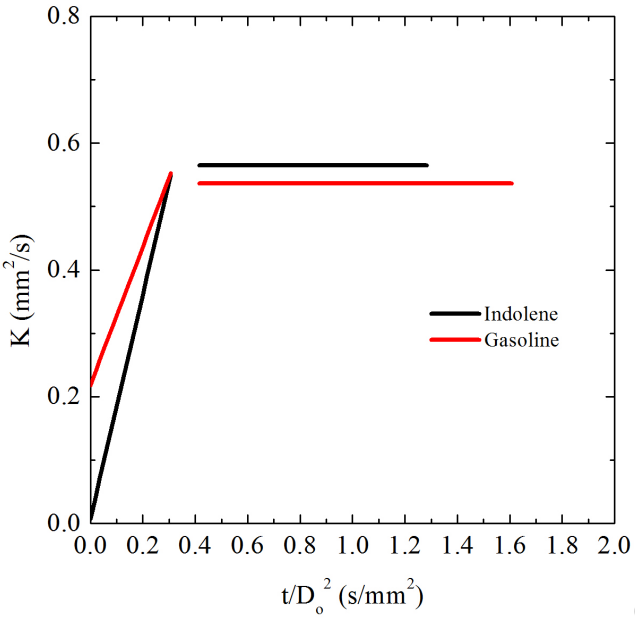

(b)

Fig. 3.21. (a) The D^2 data in Fig. 3.18a fitted with a linear line for the quasi-steady region and a second order polynomial for the transient heating region for the burning rate K (b).

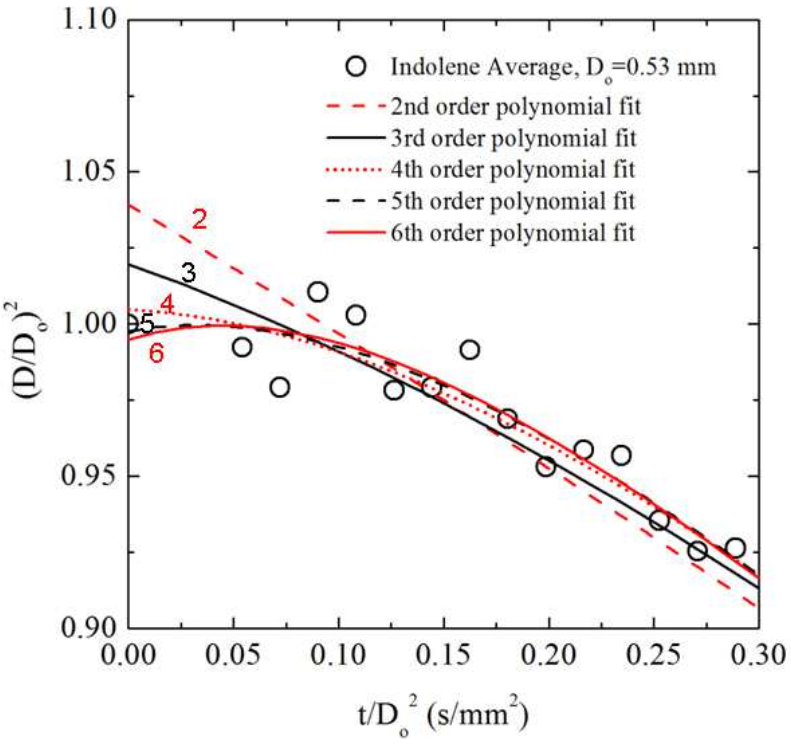

(a)

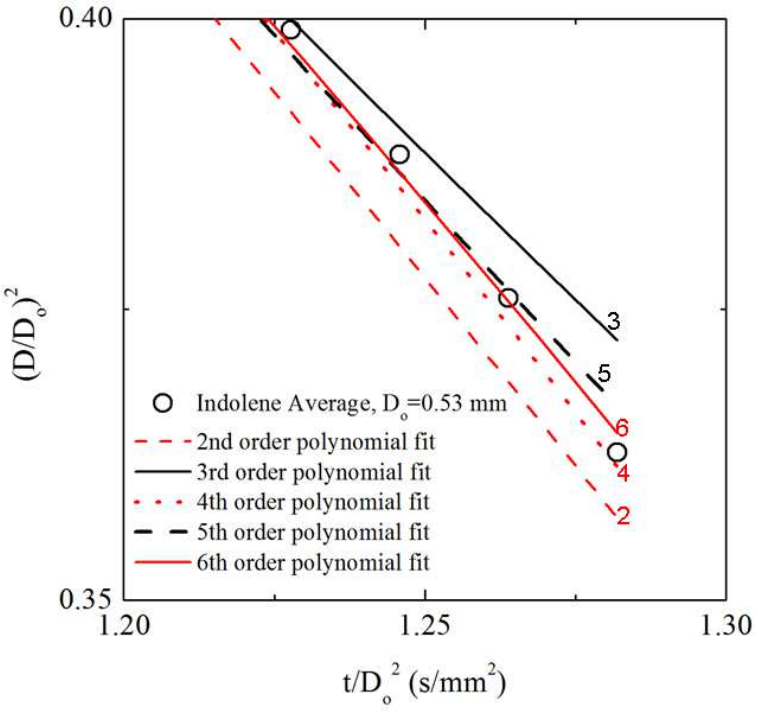

(b)

Fig. 3.22. Various orders of polynomials fitted on the indolene data for (a) $t/D_o^2 < 0.3$ s/mm^2 and (b) $t/D_o^2 > 1.22$ s/mm^2.

polynomial with a higher order better fits the data in a local sense.

Figure 3.23 compares the burning rate curves computed using various order polynomial fits, 2^{nd} (a), 4^{th} (b), 5^{th} (c), and 6^{th} (d), for indolene and gasoline. It is clear that a 2^{nd} order fit does not capture the transient variations (Fig. 3.23a). Figure 3.22b shows that the K determined from a 4^{th} order fit captures more details of the burning rate than does the 2^{nd} order fit. Nonetheless, the drawback of using only one polynomial to fit the entire D^2 data is that the fitted curve will sacrifice the linearity of the data at larger t/D_o^2 in order to accommodate the data at smaller t/D_o^2. This leads to an increase in calculated burning rates at $t/D_o^2 = 1.4$ s/mm^2 (see Figure 3.23b), which is an artifact resulting from the use of this particular polynomial.

Burning rates calculated using 5^{th} and 6^{th} order polynomials for indolene and gasoline are shown in Figs. 3.23c and 3.23d, respectively. It is evident that the higher order polynomial fits are more sensitive to the local evolution of $(D/D_o)^2$. The quasi-steady plateau for the 5^{th} and 6^{th} order fits is realized at $t/D_o^2 \sim 0.4$ s/mm^2 (compared to about 0.5 s/mm^2 for the 4^{th} order fits). Interestingly, the increase of the burning rate after the quasi-steady region seen in the 4^{th} order burning rate curves no longer exists in either the 5^{th} or 6^{th} order burning rate curves. However, a higher order polynomial such as a 6^{th} order fit is more greatly affected by the local fluctuations of $(D/D_o)^2$. It is worth noting that the 5^{th} order burning rates decrease at the end whereas the 4^{th} and 6^{th} order fits behave the opposite. This appears to be caused by the intrinsic concavity of the polynomial and thus does not reflect the real burning rates.

Table 3.1 compares the quasi-steady burning rates obtained from four polynomials shown in Figure 3.23 for indolene and gasoline. Surprisingly, regardless

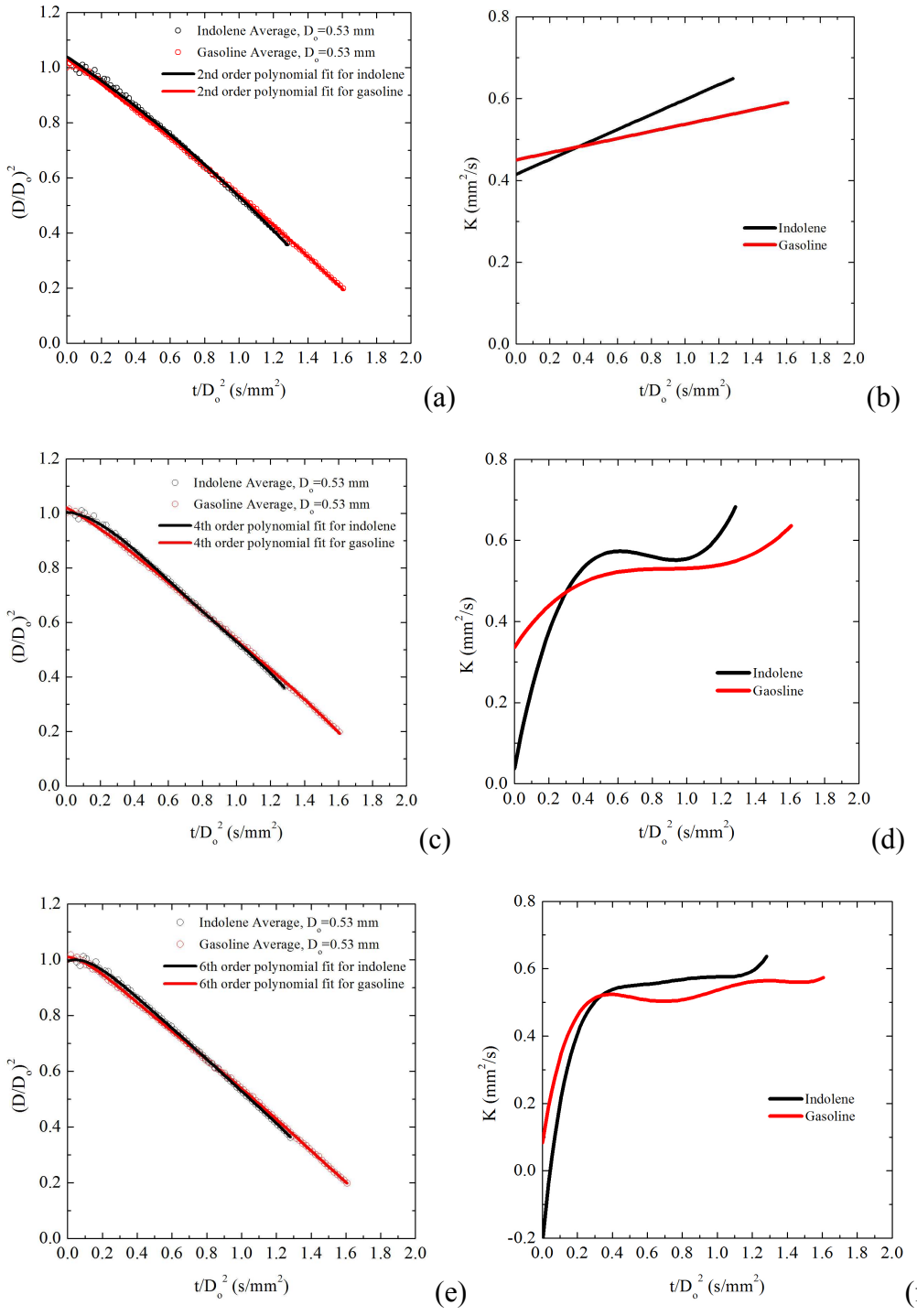

Fig. 3.23. The D^2 data of gasoline and indolene fitted with a 2^{nd} (a), 4^{th} (c), and 6^{th} (e) order polynomial, and the burning rates associated with them 2^{nd} (b), 4^{th} (d), and 6^{th} (f).

Table 3.1. Comparison of the calculated burning rates obtained from various fitting methods. Values in parentheses show the range of t/D_o^2 (s/mm^2) from which the quasi-steady values are computed.

	Quasi-steady burning rate K (mm^2/s)	
	Indolene (D_o=0.53 mm)	Gasoline (D_o=0.53 mm)
Linear	0.565	0.536
2nd order polynomial	0.532	0.520
4th order polynomial	0.565 ($0.56\sim0.90$ s/mm^2)	0.531 ($0.63\sim1.19$ s/mm^2)
5th order polynomial	0.563 ($0.51\sim1.08$ s/mm^2)	0.536 ($0.51\sim1.41$ s/mm^2)
6th order polynomial	0.561 ($0.42\sim0.99$ s/mm^2)	0.534 ($0.42\sim1.50$ s/mm^2)

Note: The burning rate value for linear fit is from the direct derivative of the linear fit; the value for the 2nd order polynomial is computed by averaging the data in the entire burning.

of how accurate a higher order polynomial is able to capture the local variation of data, all of these methods provide very similar quasi-steady burning rates for indolene and gasoline in this comparison. Similar conclusions can be drawn for all the fules studied in the thesis.

3.6. Uncertainty in the Measurements

The measurement precision is dependent on the sharpness and clarity of the images. To estimate the uncertainty, we express it in terms of the number of pixels an image encompasses. For droplet diameter measurements, a 0.5 mm droplet comprised approximately 250 pixels for the high resolution black and white camera used in the GB experiments. This pixel count is measured from what is best judged as the outer edge of the droplet. The droplet surface is a sort of diffuse boundary whose thickness

depends on the sharpness of the image. A value of 5 pixels is approximate for the droplet boundary thickness in images reported in the present study. The uncertainty of the initial droplet diameter expressed as a percent of the pixels it encompasses is then, approximately, ± 2% (i.e., +255/250; -245/250). At the end of burning, the smallest droplet diameter that could be measured is approximately 80 μm which encompasses approximately 40 pixels. Taking again a droplet boundary thickness of 5 pixels, the precision to which the number of pixels a droplet of 80 μm would be known is approximately ± 13%.

For ISS droplet measurements, the thickness of the droplet boundary is also around 5 pixels. For different droplet size conditions examined, the initial pixel value ranges from 172 (for a 5.0 mm droplet) to 44 (for a 1.30 mm droplet). Therefore the uncertainty for the initial droplet diameters ranges approximately from ± 3% (i.e., +177/172; -167/172) to ± 11% (i.e., +49/44; -39/44). For a given burning sequence, the last image analyzed has about 30 pixels. The uncertainty associated with it is 17% (i.e., +35/30; -25/30).

For the soot shell diameter the largest shell diameters measured from GB images encompassed approximately 750 pixels. With a boundary thickness of approximately 20 pixels the uncertainty of the initial soot shell pixel counts, measured from the video images, should be approximately ± 3%. The smallest shell that could be measured encompassed approximately 300 pixels, though it must be emphasized that as burning progressed the shells evolved into irregular shapes and the boundaries were often not contiguous. For a fixed number of boundary pixels, again taken as 20, the approximate uncertainty is ±7%.

For the ISS images, the soot shell has an approximate thickness of 5 pixels. With the soot shell size ranges from 100 to 300 pixels, the soot shell measurements have a ± 5 (i.e., +95/100; 105/100) to ± 2 (i.e., +295/300; 305/300). Note that larger uncertainty for ISS soot shell measurements come from the placement of the AOI when the soot shell is broken (cf. Fig. 3.7f). In this case the uncertainty can be as large as 10 %.

Regarding flame or luminous zone diameter, the largest GB flame image measured comprised approximately 190 pixels and the smallest measured flame consisted of approximately 100 pixels. The luminous zone boundary thickness (as best as could be determined) consisted of approximately 8 pixels. At the upper size, the uncertainty of luminous zone diameter measurements would then be ± 4% (i.e., + 198/190;-182/190). At the lower size, the uncertainty of luminous zone diameter measurements would approximately be ± 9% (i.e., + 108/100;-92/100).

The flame diameters obtained from ISS color images range from 60 to 200 pixels. With the flame boundary thickness of approximately 8 pixels, the uncertainty of ISS flame measurements is ±13% (i.e., +68/60; -52/60) to 4% (i.e., +208/200; -192/200). The LLLUV images has more noise near the flame boundary. The noise area can be as large as 20 pixels for a range of measured flame diameters, 80-200 pixel. Therefore the uncertainty of the flame measurements from LLLUV images range from ± 25% (+100/80; - 60/80) to 10% (+220/200; -180/200).

CHAPTER 4

EFFECTS OF SUPPORT FIBERS ON DROPLET BURNING[1]

4.1 Introduction

This chapter discusses the effects of support fibers on the spherically symmetric droplet flame obtained from our ground-based experiments. The support fibers are speculated to enhance the heat transfer rates from the flame to the droplet surface and the surroundings. 14 μm SiC and 10 μm ceramic fibers are used to investigate the effects of fiber thermal conductivity on the burning processes of heptane and toluene droplets.

As an ultimate comparison, results from fiber-supported experiments are compared with free droplet (no fiber) data. This comparison particularly provides validity of the data obtained from our GB fiber-supported experiments (~ 0.5 mm test droplet anchored on 14 μm SiC fibers) in terms of droplet burning curve, FSR, and SSR, that are used to benchmark droplet burning characteristics of various fuels.

An 80 μm SiC stretched fiber is optional for the droplet combustion experiments on the ISS. Results from ISS free droplet and fiber-supported experiments suggested that when the droplet size is as larger as (4~5 mm), fiber results are almost identical as the free droplet results (with similar droplet size). However, when $D_o < 2$ mm, the fiber appears to induce some vortex that can be traced by soot particles near the fiber-droplet intersection. This local convection enhances the heat transfer into the

[1] This chapter comes from the following publication: Liu, Y.C., Rah, J.K., Trenou, K.T., Hicks, M.C., Avedisian, C.T., "An experimental study of effects of support fiber on droplet burning in a low convection environment," Combustion and Flame (2013).

liquid droplet and significantly increases the evaporation rate.

4.2 Thermal Conductivity of Fiber Materials

Concerning energy transfer through the SiC fiber used in our experiments, an estimate of the conductive transfer through the fiber based on the fiber behaving as a fin insulated on its side with fixed temperatures at its ends was estimated when using a SiC thermal conductivity of 60 W/m-K (Bae and Avedisian (2009)). However, the thermal conductivity of the SiC fibers we used is a matter of speculation. Literature values for bulk SiC range from 490 W/m-K at room temperature to about 60 W/m-K at 1200 K (Incropera and DeWitt (2002)). And for fibrous SiC strands less than 20 μm diameter values of less than 5 W/m-K are reported (Youngblood et al. (1999)). These differences in fiber thermal conductivity will obviously influence the conclusions one may draw about heat transfer to the droplet through the fiber.

We performed some limited tests for heptane and toluene droplets mounted on fibers of a different material with documented thermal conductivity but with the nearly same fiber diameter: 3M Nextel 312 ceramic fibers with k ~ 2 W/m-K (Whittaker et al. (1990)). Figure 4.1 shows the SEM images of these fibers. The fiber sizes obtained from these images are 14.4 ± 2.4 μm for the SiC fibers and 12.4 ± 3.0 μm for the 3M Nextel 312 ceramic fibers. Figure 4.2 compares data from individual (not averaged) runs for the evolution of droplet diameter of heptane (4.1a) and toluene (4.1b).

The results in Fig. 4.2 are similar for the two fuels. From this observation we can at most conclude that the heat transfer effect associated with conduction through

(a)

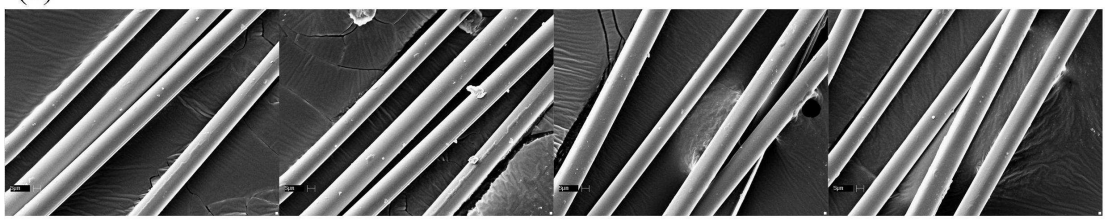

(b)

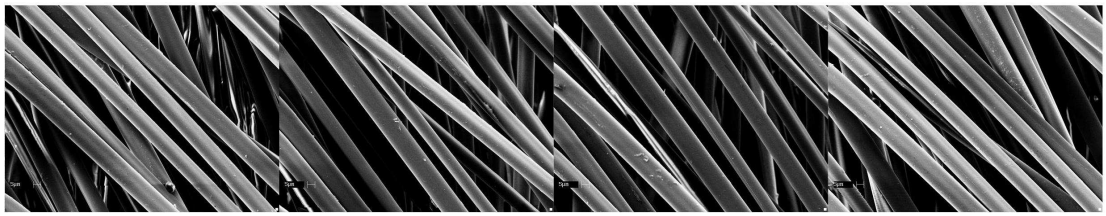

Fig. 4.1. SEM images of SiC fibers (a) and the 3M Nextel 312 ceramic fibers (b) by which the averaged size of the fiber is obtained.

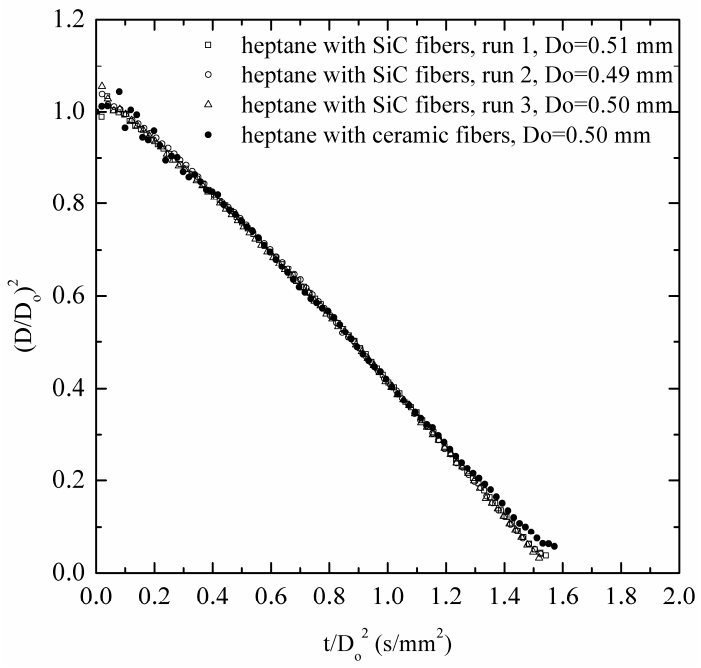

(a)

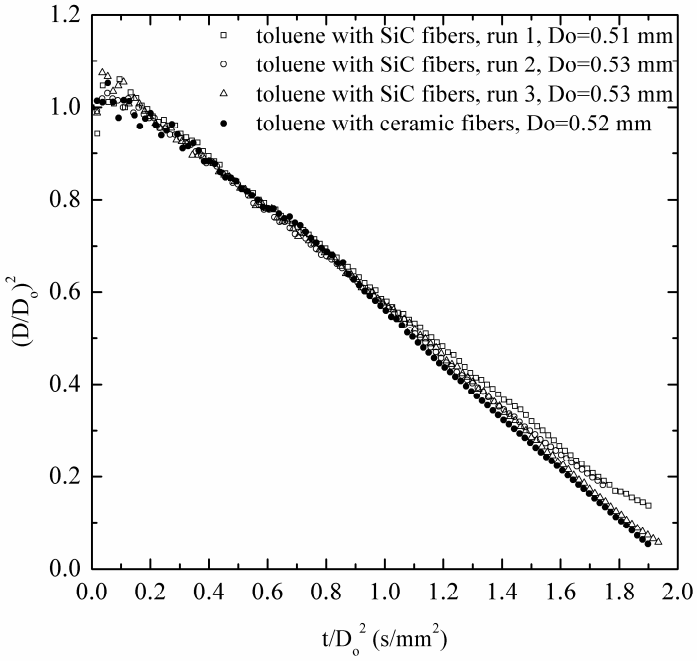

(b)

Fig. 4.2. Comparison of the evolution of scaled droplet diameter burning on SiC and ceramic fibers of approximately 14 μm diameter. (a) heptane; (b) toluene.

these two different fiber materials appears to be similar, suggesting that the fibers either have the same thermal conductivity (since the fiber diameters are close) or that the fibers do not induce a significant heating effect because of their small size except possibly very near the end of burning.

4.3 Fiber-supported vs. Free Droplet Experiments- 14 μm fiber

This section compares the results from the fiber-supported and free droplet experiments for ~0.5 mm n-decane droplets carried out using a drop tower. Figure 4.3 shows the photographic comparison between fiber-supported and free droplet flames. The "corona" effect (see Section 3.4) is seen for the fiber-supported flame (Fig. 4.3a) owing to the fiber glows adding to the total flame intensity. The free droplet flame extinguishes slightly earlier than the fiber-supported because of its smaller initial droplet size (0.51 mm) compared to the fiber-supported (0.54 mm). With the absence of the support fiber, the soot shell around the free droplet is denser compared to the fiber supported droplet. Soot agglomerates are found on the soot shell at 0.2 s for free droplet (cf. Fig. 4.3d). In contrast, Fig. 4.3c shows that the support fiber assists collection of the soot aggregate such that the instantaneous soot shell is less intensive during a burn.

Figure 4.4 shows the D^2 reductions for one run of fiber-supported (red close symbol) and three individual runs of free droplet (white open symbols) burnings. The data from fiber-supported and free droplet experiments look almost identical suggesting that the effects of fiber on the over all burning process is minimal. The free droplet data are slightly scattered in the early burning process compared to the fiber-

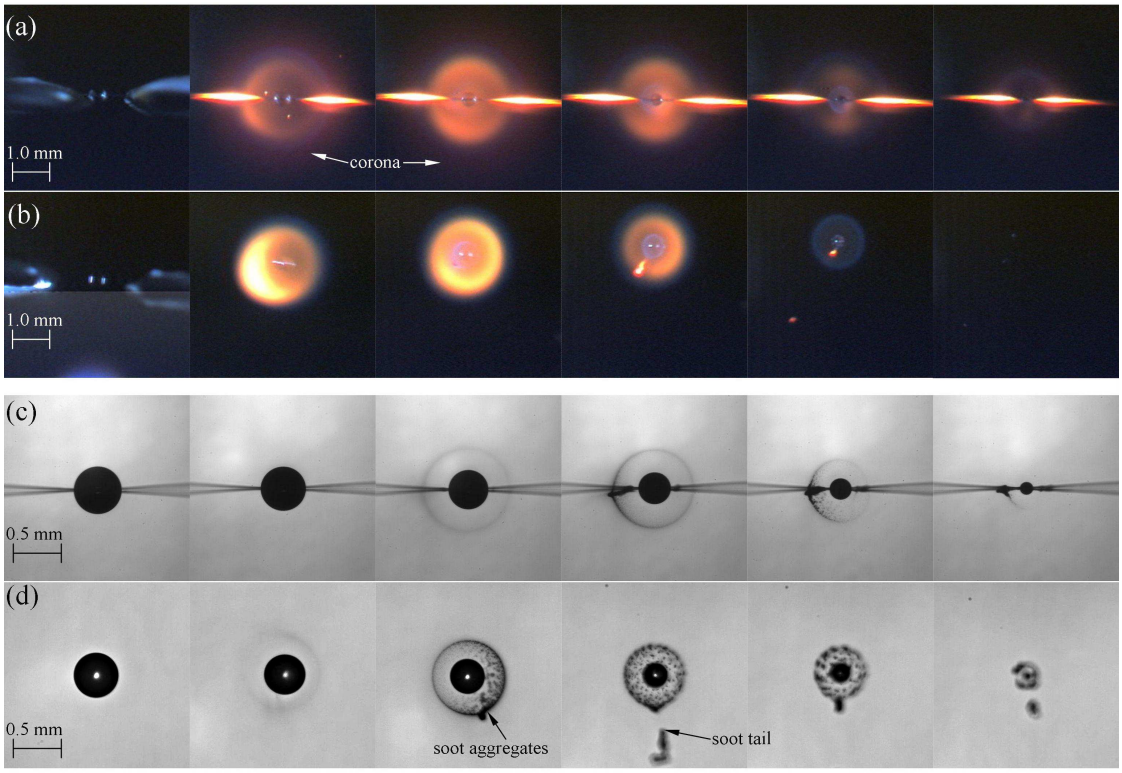

Fig. 4.3. Photographs of n-decane droplet burning (a) with support fibers (color); (b) without support fibers (color); (c) with support fibers (BW); (d) without support fibers (color). The D_o for (a) and (c) is 0.54 mm, for (b) and (d) is 0.51 mm.

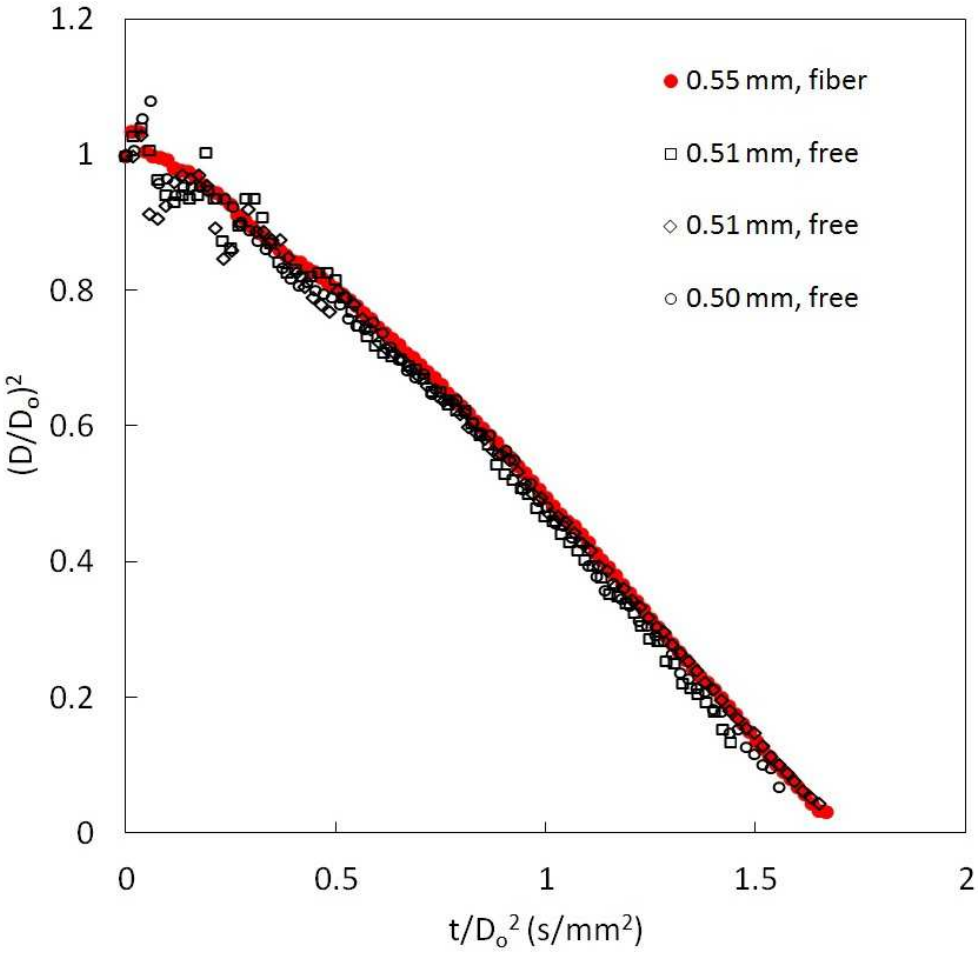

Fig. 4.4. D^2 histories of a fiber-supported droplet and three free-droplet experiments for n-decane droplets showing minimal effects on the burning rate with the use of two crossed 14 μm SiC fibers.

supported data. This is indicative of small motions of the droplet surface without the presence of the fiber due to the physical impacts of sparks. With the presence of the support fiber, droplet distortion due to physical spark impacts quickly dies out. The effect of spark impacts on a free droplet can last until 0.5 s/mm^2.

Figure 4.5 shows the flame standoff ratio (FSR = D_f/D) obtained from fiber-supported and free droplet experiments. The FSR monotonically increases during the burning process, and the fiber-supported data (red close symbols) overlap with the free droplet data (white open symbols) for the entire burning. Results of FSR comparison suggest no difference between the two experimental setups.

Figure 4.6 shows the measured soot standoff ratio (SSR = D_s/D) from both fiber-supported (red close symbols) and free droplet (white open symbols) experiments.

Although all the SSR data look very close to each other, the data for the fiber-supported experiment are found to be slightly higher than the free droplet data when $t/D_o^2 > 1$ s/mm^2. This appears to be due to the soot aggregates remaining on the fiber from the earlier burning, attracting the later formed soot shell. Nonetheless, the SSR results still suggest that the soot shell diameter data produced from fiber-supported droplet flames are representative of the free droplet experiments.

4.4 Fiber-supported vs. Free Droplet Experiments- 80 μm fiber

This section discusses the droplet combustion experiments carried out on the International Space Station with an 80 μm SiC support fiber and without fiber. For the same fiber size, results from large droplets (D_o = 3~5 mm) and small droplets (D_o = 1~

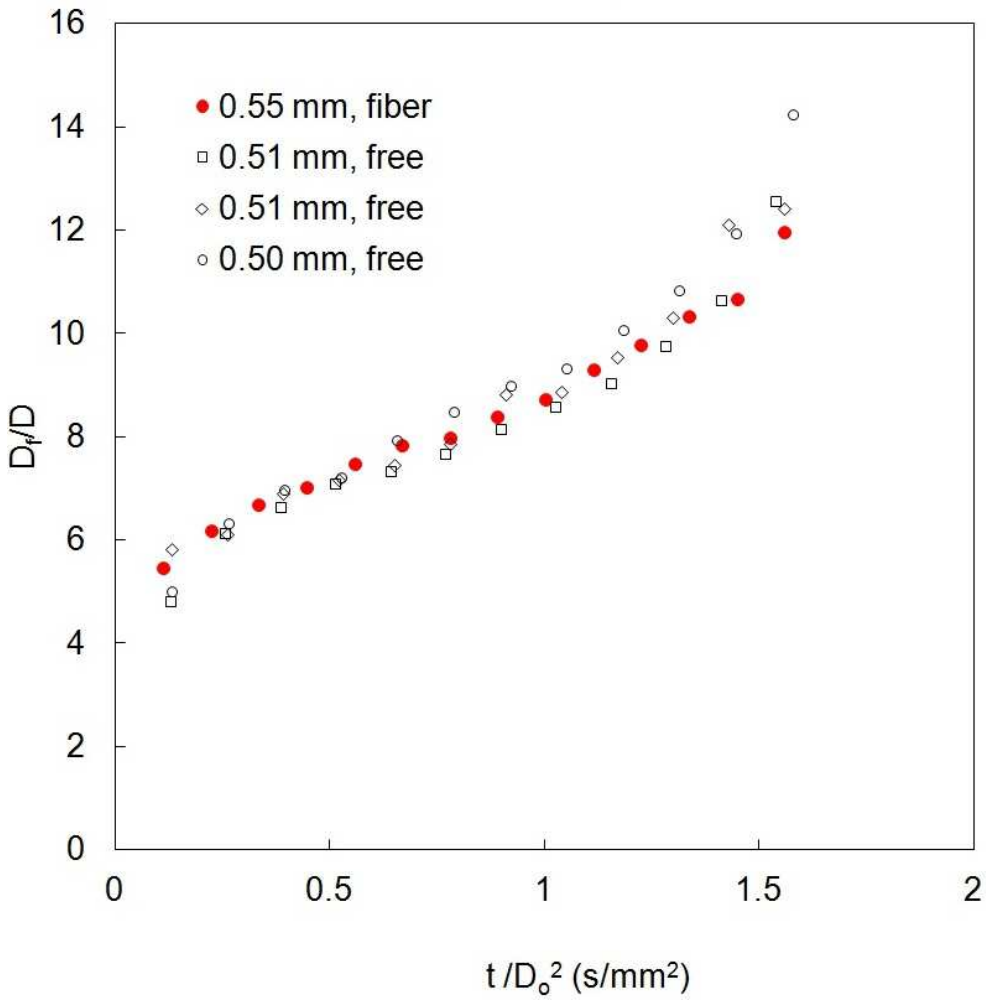

Fig. 4.5. Evolution of flame standoff ratio (FSR) of a fiber-supported droplet and three free-droplet experiments for n-decane droplets showing minimal effects on the burning rate with the use of two crossed 14 μm SiC fibers.

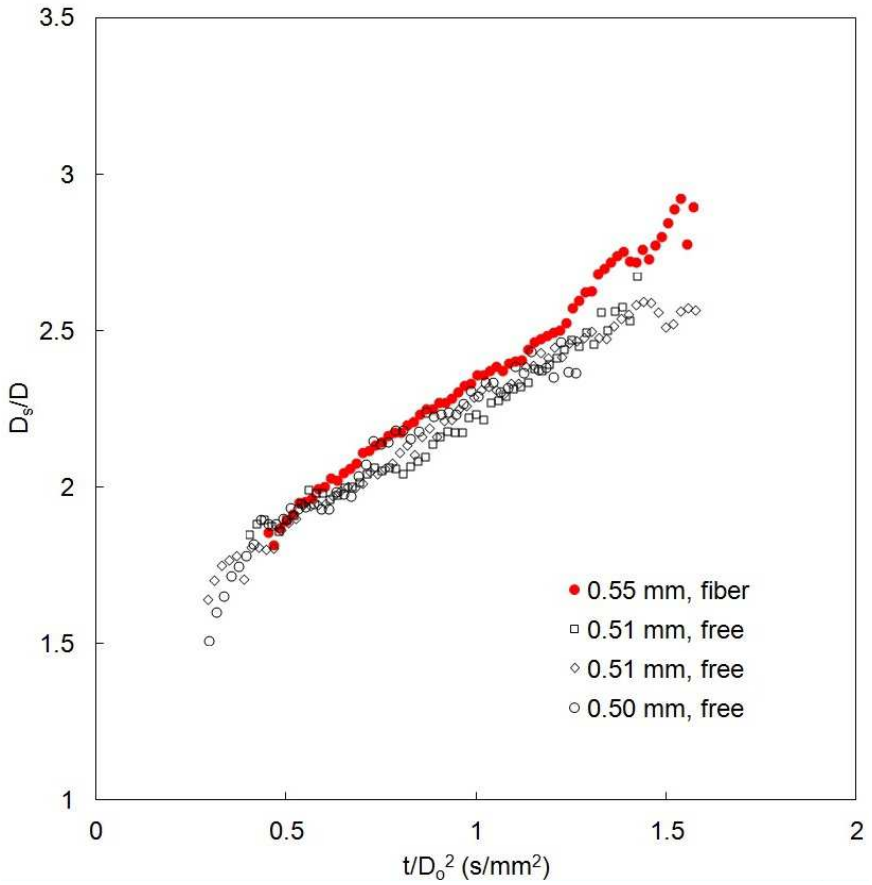

Fig. 4.6. Evolution of soot standoff ratio (SSR) of one fiber-supported droplet and three free-droplet experiments for n-decane droplets showing minimal effects on the burning rate with the use of two crossed 14 μm SiC fibers.

3 mm) are compared to show the effects of the fiber on droplet burning processes. Figure 4.7 shows the photographs from the n-heptane experiments. For D_o = 4.23 mm (with fiber, cf. Fig. 4.7a), though the soot shell in the BW images at 0.2 s/mm^2 is slightly distorted due to the igniter retraction (see Section 3.2), the droplet flame shown in the color image (at 0.2 s/mm^2) maintains spherical symmetry. For D_o = 3.87 mm (free droplet, cf. Fig. 4.7b), due to the small motion of the droplet, the soot shell is slightly expanded in the 10 o'clock direction. The disappearance of the flame between 0.4 and 0.6 s/mm^2 in color images is indicative of flame extinction due to significant radiative heat losses to the surroundings (Marchese et al. (1998), Nayagam et al. (1998), Kazakov et al. (2003), Farouk and Dryer (2012b)) for the large droplets (D_o = 4.23 mm and 3.87 mm, cf. Fig. 4.7a and 4.7b).

For small droplets shown in Fig. 4.7c and 4.7d (D_o = 1.39 mm and 1.30 mm, respectively) it is evident that the flames are brighter than the larger droplets shown in Fig. 4.7a and 4.7b. Chapter 10 discusses the cause of that. More importantly, in the fiber-supported run (see Fig. 4.7c), the soot shell is significantly distorted and pulled in a direction perpendicular to the fiber while the spherical shape of the flame is not affected. When we look more closely, the soot particles that trace the flow direction show a "vortex-like" structure near the droplet-fiber intersection suggesting that additional flows are created due to the presence of the fiber. This fiber-related phenomenon can also be found in Fig. 4.8a for n-octane droplet (D_o = 2.64 mm) where the droplet glided out of the soot shell (at ~ 0.5 s/mm^2) due to momentarily imbalanced forces on the droplet. Figures 4.8b and 4.8c show freely floating n-octane droplets that move slightly upwards while the flame and soot shell are still relatively

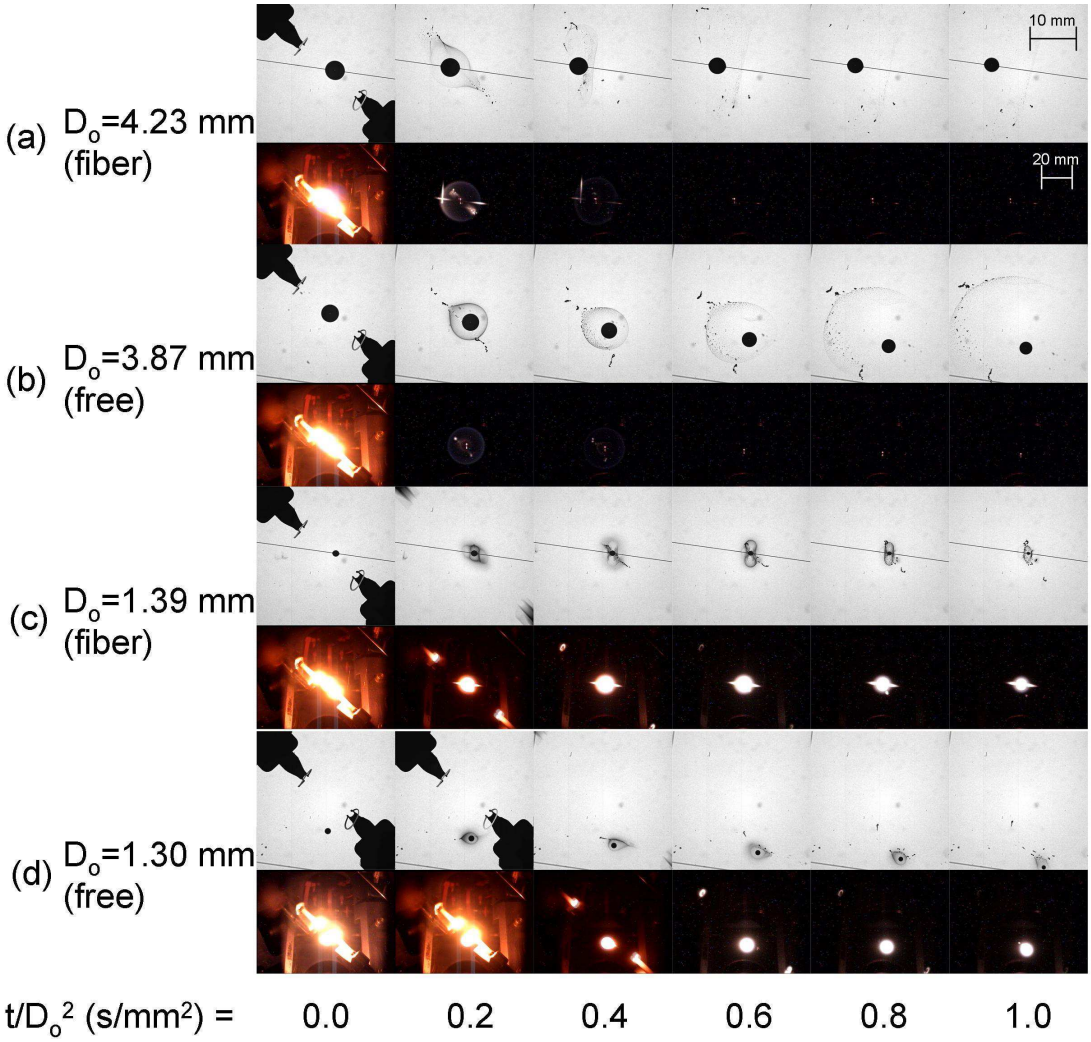

Fig. 4.7. BW and color photographs of n-heptane droplet burning on the ISS: (a) D_o = 4.23 mm with fiber; (b) D_o = 3.87 mm without fiber; (c) D_o = 1.39 mm with fiber; (d) D_o = 1.30 mm without. The fiber material is SiC and it outer diameter is 80 μm.

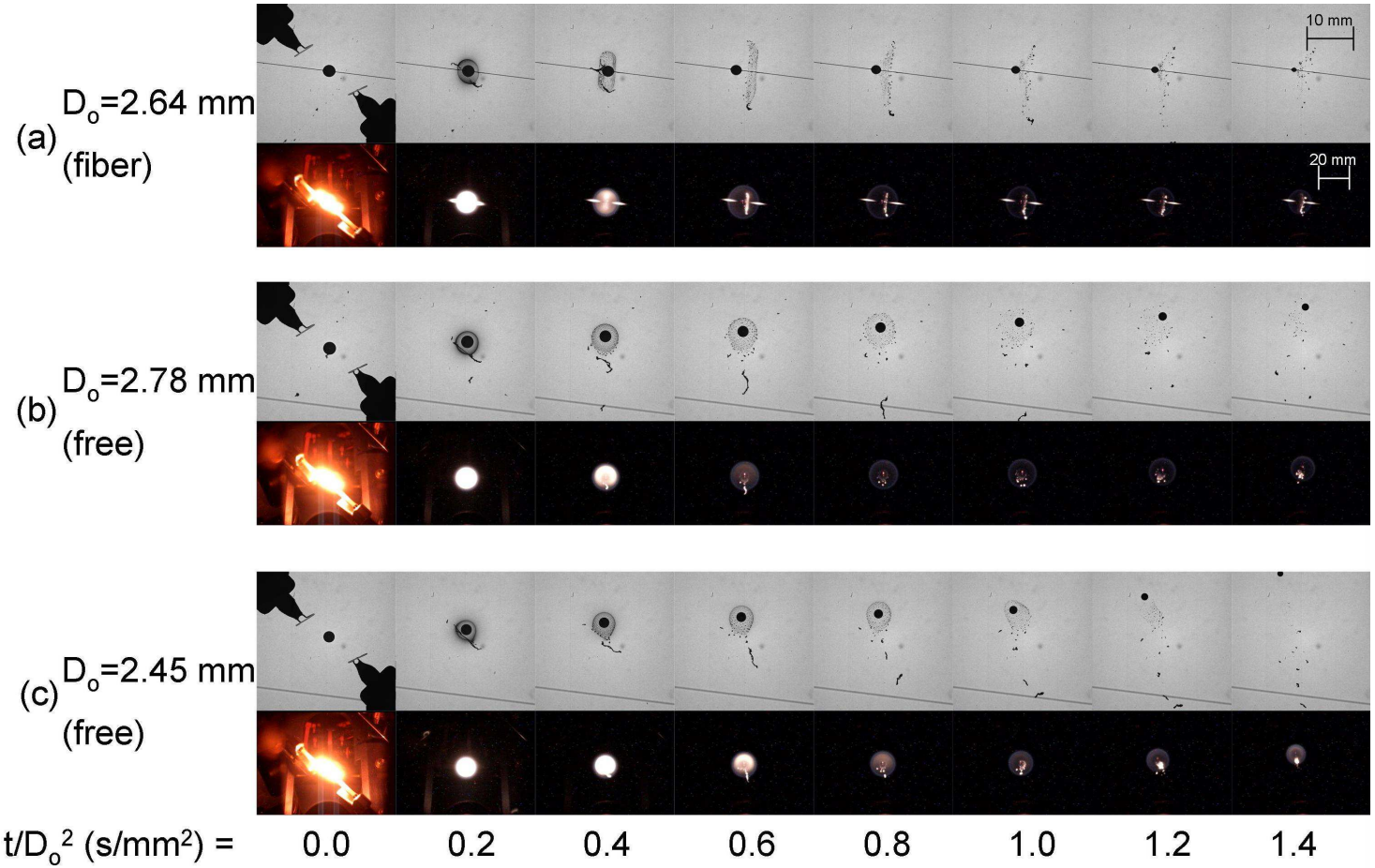

Fig. 4.8. BW and color photographs of n-octane droplet burning on the ISS: (a) D_o = 2.64 mm with fiber; (b) D_o = 2.78 mm without fiber; (c) D_o = 2.45 mm without fiber. The fiber material is SiC and it outer diameter is 80 μm.

spherical.

Figure 4.9 shows the images from n-decane experiments in a similar fashion as Fig. 4.7. It is noted that the fiber barely affects the soot shell structure for the large droplet (cf. Fig. 4.9a and 4.9b). The spherically formed soot shell expands outwardly after flame extinction (between 0.4 and 0.6 s/mm^2) due to the gradually vanishing thermophoretic force that determines the soot shell position. At 1.0 s/mm^2 (cf. Fig. 4.9c), vapor condensation occurs and become visible due to the infrared lighting (Section 2.2). Fiber-induced flows traced by the soot particles are also seen for small n-decane droplet (D_o = 1.82 mm, cf. Fig. 4.9d). Consecutive images in Fig. 4.9e suggest that the spherical symmetry of the soot shell and flame can be well maintained without support fiber for a small droplet (D_o = 1.84 mm).

Figure 4.10 displays "enlarged" images from Fig. 4.7 to 4.9 to show the "vortex-like" flow structure around the fiber-droplet intersection. Though the flow (or the rotational motion of the soot particles) is observed for a large portion of the burning history, images in Fig. 4.10 are selected because they best show the rotational feature of the flow in one image. Figure 4.10a shows symmetrical distortion of a soot shell formed around n-heptane droplet. The flow directions are indicated by the arrows. The inward flows along the fiber squeeze the soot shell and are repelled when they are near the droplet. The flow directions in Figs. 4.10b and 4.10c are identical, but the vortices are shown only on one side of the droplet because the droplet "glided" along the fiber to the left before the images were taken. The flows on the left hand side of the droplet may as well exist for Figs. 4.10b and 4.10c, but a lack of in-situ soot particles prevents the flows from being visualized.

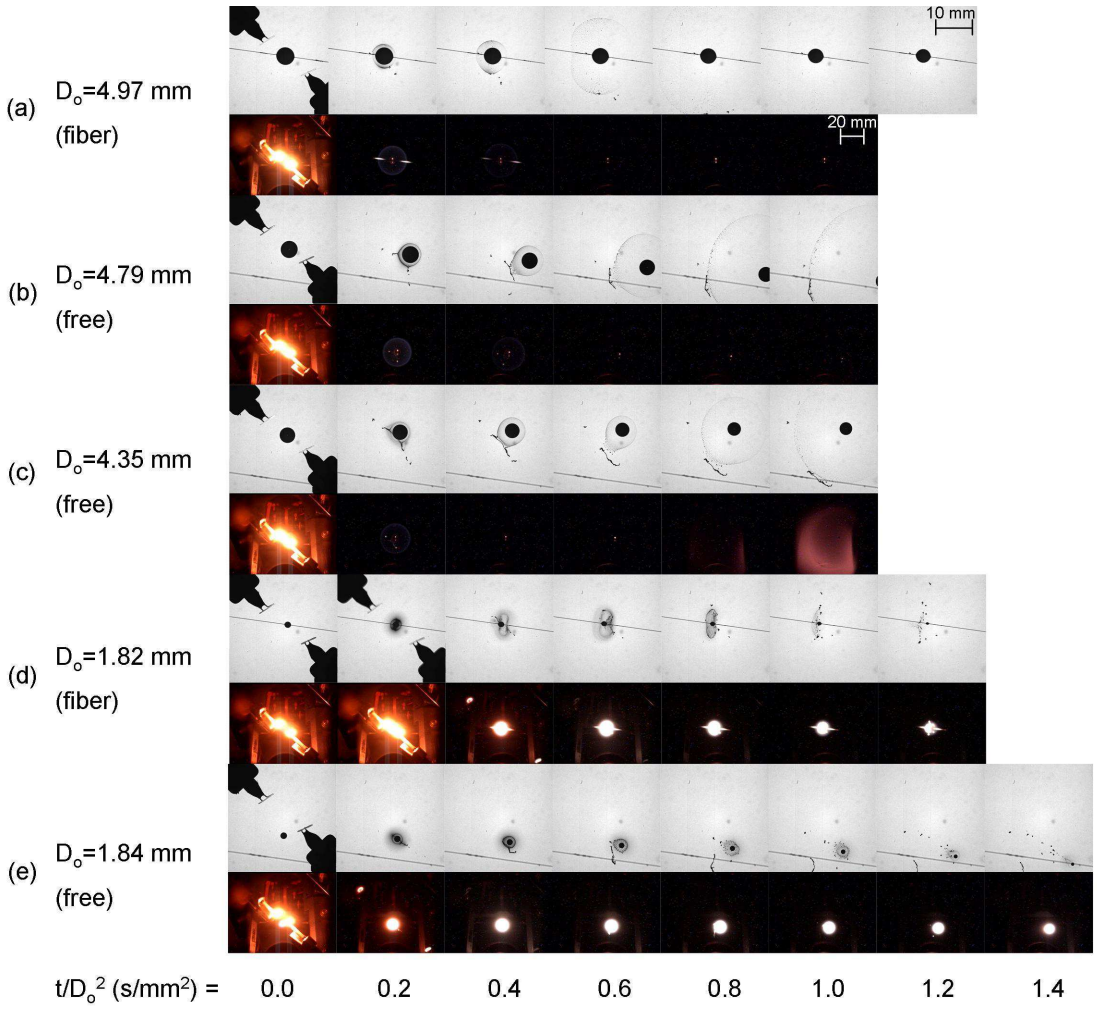

Fig. 4.9. BW and color photographs of n-decane droplet burning on the ISS: (a) D_o = 4.97 mm with fiber; (b) D_o = 4.79 mm without fiber; (c) D_o = 4.35 mm without fiber; (d) D_o = 1.82 mm without fiber; (e) D_o = 1.84 mm without fiber. The fiber material is SiC and it outer diameter is 80 μm.

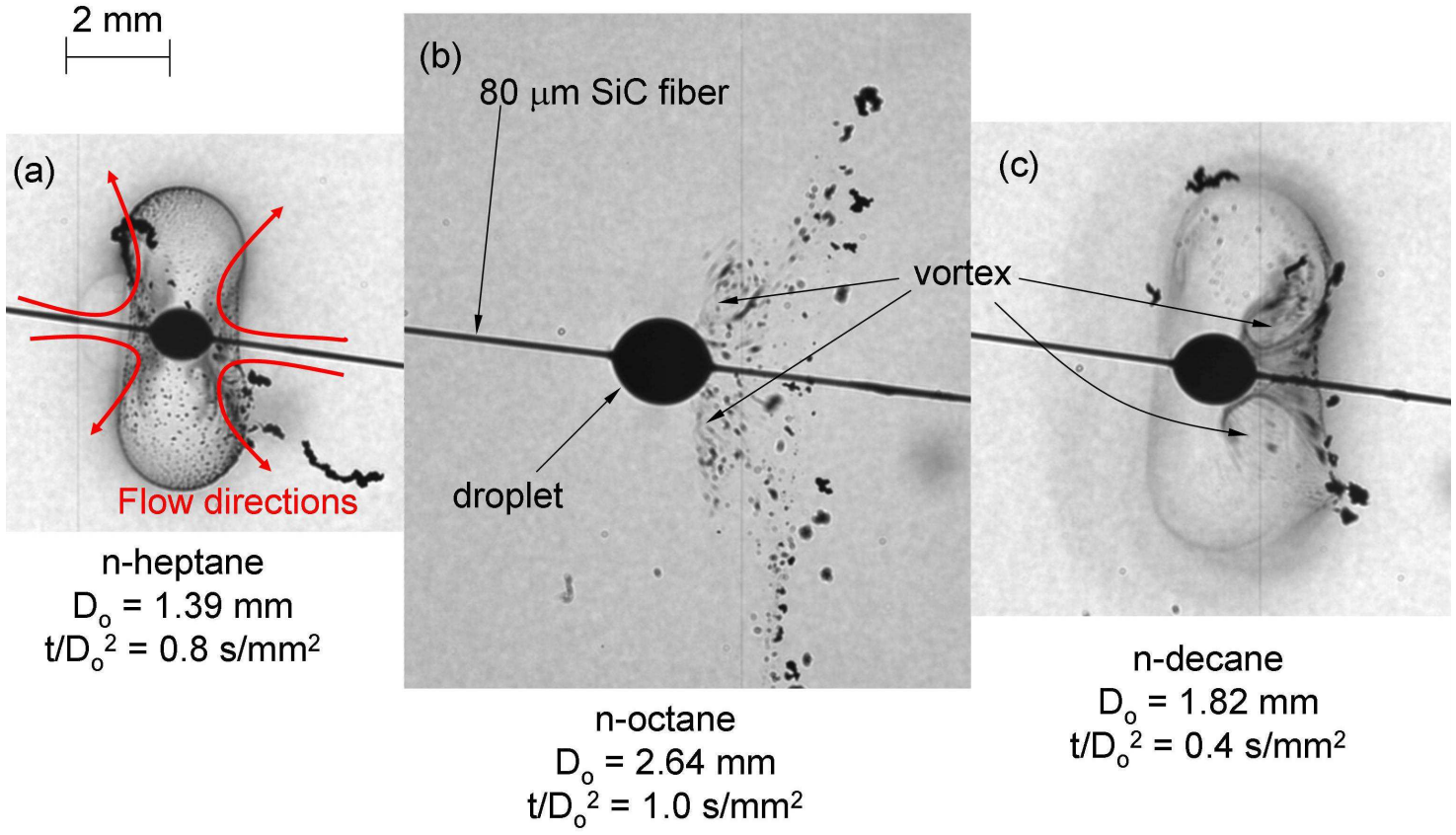

Fig. 4.10. Enlarged images for instantaneous soot particles that visualize the flows induced by the presence of the 80 μm SiC fiber: (a) n-heptane, D_o = 1.39 mm, t/D_o^2 = 0.8 s/mm^2; (b) n-octane, D_o = 2.64 mm, t/D_o^2 = 1.0 s/mm^2; (a) n-decane, D_o = 1.82 mm, t/D_o^2 = 0.4 s/mm^2. Images are selected that best visualize the soot shell distortion (a) and vortices (b) and (c).

Similar soot shell distortion is found in Avedisan and Jackson (2000) for n-heptane with a larger quartz vertical fiber (330 μm). The position of a soot shell is known to be determined by radially outward Stefan drag and diffusion-phoretic force that are balanced by the thermophoresis of the flame. When a fiber is present, the boundary layer of the Stefan flow near the fiber surface weakens the flow itself. The soot particles are then subjected to an imbalanced force towards the droplet that carries the soot particles along. When the soot particles are close to the droplet, the Stefan flow overcomes the weakening thermophoresis and repels the soot particles away from the droplet surface.

Figure 4.11 visualizes the strengths of local Stefan flows that are smaller than the thermophoretic force in the proximity of the fiber leading to the motion of soot particles. The cause of weakened Stefan flow near the fiber is attributed to boundary layer effect. Due to the radial nature of the Stefan flows, the thickness of a boundary layer is related to the local "curvature" of the droplet surface (distortion due to wetting is ignored here). Namely, when the curvature approaches to zero (i.e., infinitely large droplet), the flow becomes purely one-dimensional along the fiber direction. The "far field" velocity U_∞ in this case is exactly the Stefan flow velocity. For an actual droplet (with a non-zero surface curvature near the fiber), the U_∞ must be smaller than the Stefan flow due to the curvature. Reduction of U_∞ is proportional to the curvature so that the fiber induced flow is more significant for smaller droplets (D_o = 2~ 3 mm due to a thicker boundary layer) while it is not visible for the larger droplet (D_o > 4 mm).

Droplet and flame diameters were measured from the images like in Figs. 4.7 to 4.9 using the method discussed in Chapter 3. Figure 4.12 shows the droplet

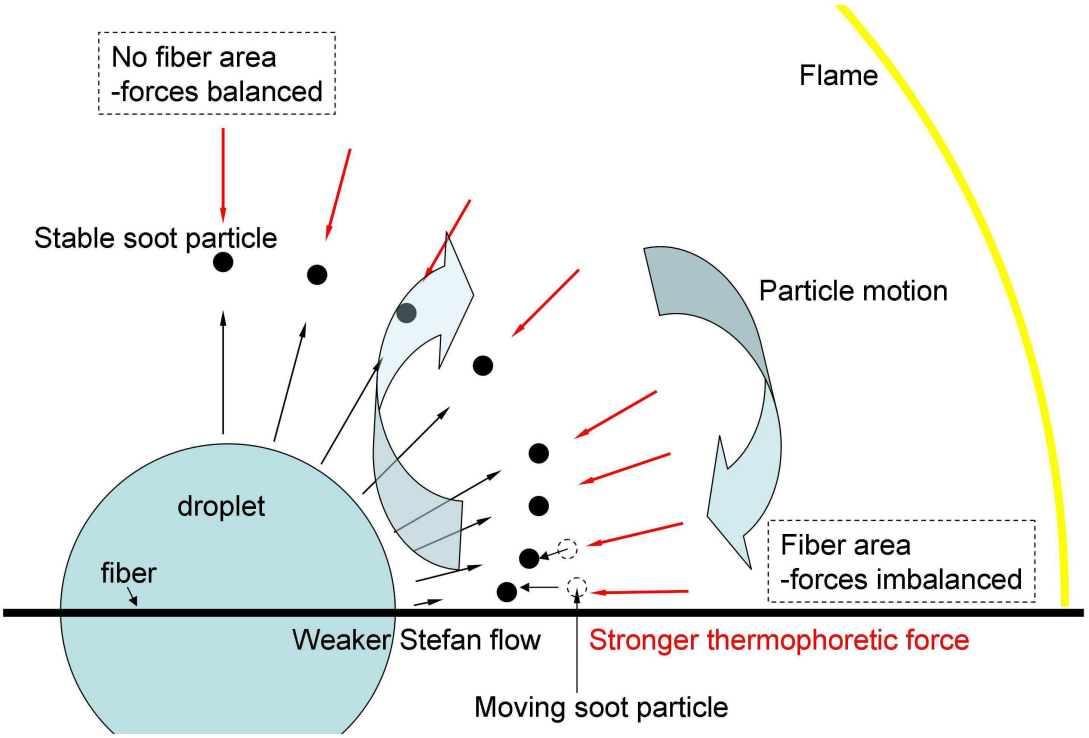

Fig. 4.11 Illustration of soot particle motion near the fiber surface when the Stefan flow is considerably reduced due to boundary layer effect.

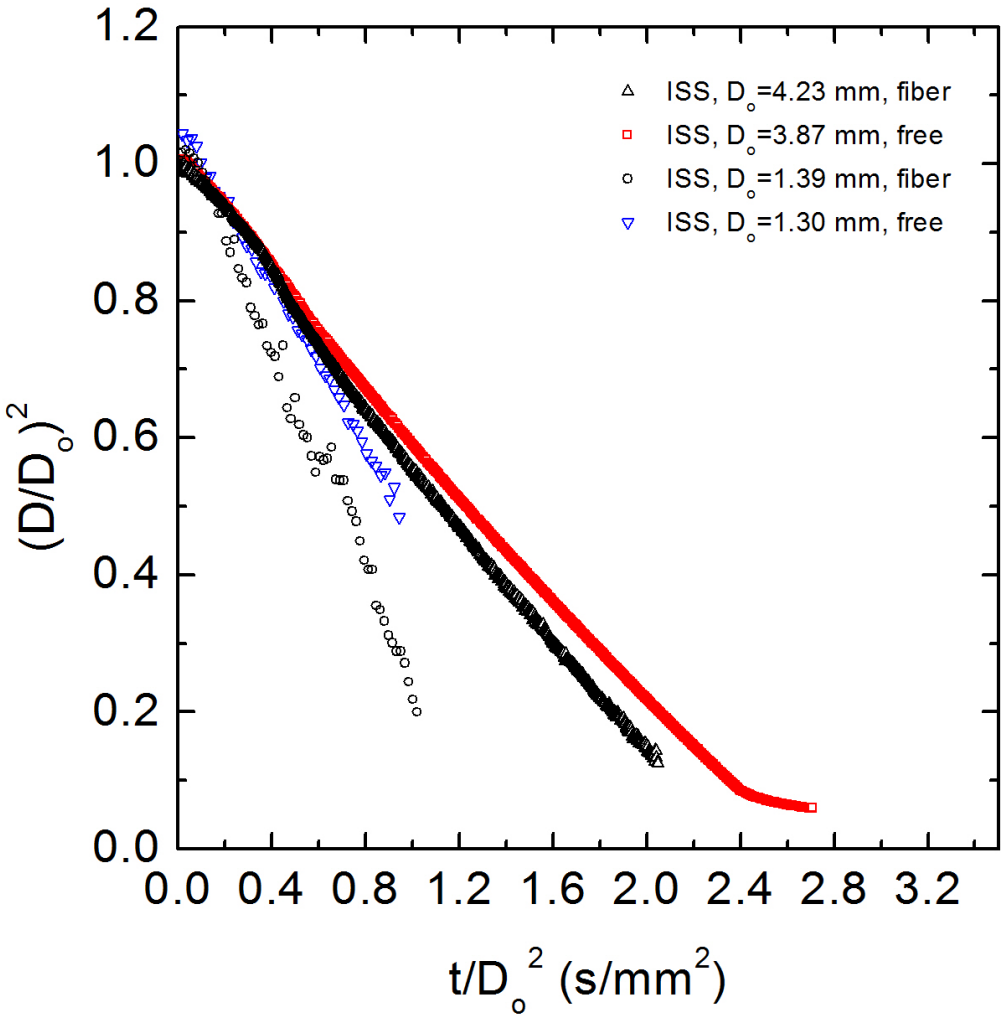

Fig. 4.12. Evolution of droplet diameters for n-heptane droplet burning with and without an 80 μm SiC support fiber.

diameter evolutions using coordinated suggested by the classical D^2 law (Eq. (1.1)), as $(D/D_o)^2$ vs. t/D_o^2. The burning rate ($K = - d((D/D_o)^2)/d(t/D_o^2)$) for D_o = 1.39 mm with fiber is significantly larger than a similar size droplet (D_o = 1.30 mm) without fiber. For larger droplets, K is smaller than those smaller droplets due to radiative heat losses that lower the flame temperature (see Chapter 10). The burning rate with a support fiber (cf. Fig. 4.12, D_o = 4.23 mm) is still slightly larger than a free droplet run (D_o = 3.87 mm). Note that the flame extinguishes before 0.6 s/mm^2 (cf. Fig. 4.7a and 4.7b) for these large droplets so a large portion of the D^2 data are in the "post-extinction" region where the ambient temperature gradually deceases with time. In this region, the soot particles move radially outward (cf. Fig. 4.7a and 4.7b) meaning the thermophoretic forces are diminishing. The evaporation rate of the droplet may be enhanced by the fiber that behaves like a "fin", transferring heat through fiber conduction.

In contrast to many prior speculations regarding how fiber introduces heat to the droplet through fiber conduction, here the burning rates are evidently enhanced via gas phase convection as shown earlier by images. It is believed that the motion of soot particles is caused by the imbalanced forces subjected to them. While the soot particles are moving, they drag the surrounding ambient with them and increase the effective heat transfer coefficient near the droplet surface. Therefore heat is transferred to the droplet at a higher rate leading to a noticeably higher evaporation rate (or burning rate K).

Figures 4.13 and 4.14 show the D^2 evolutions obtained from fiber-supported and free droplet experiments for n-octane and n-decane, respectively. Similar to what

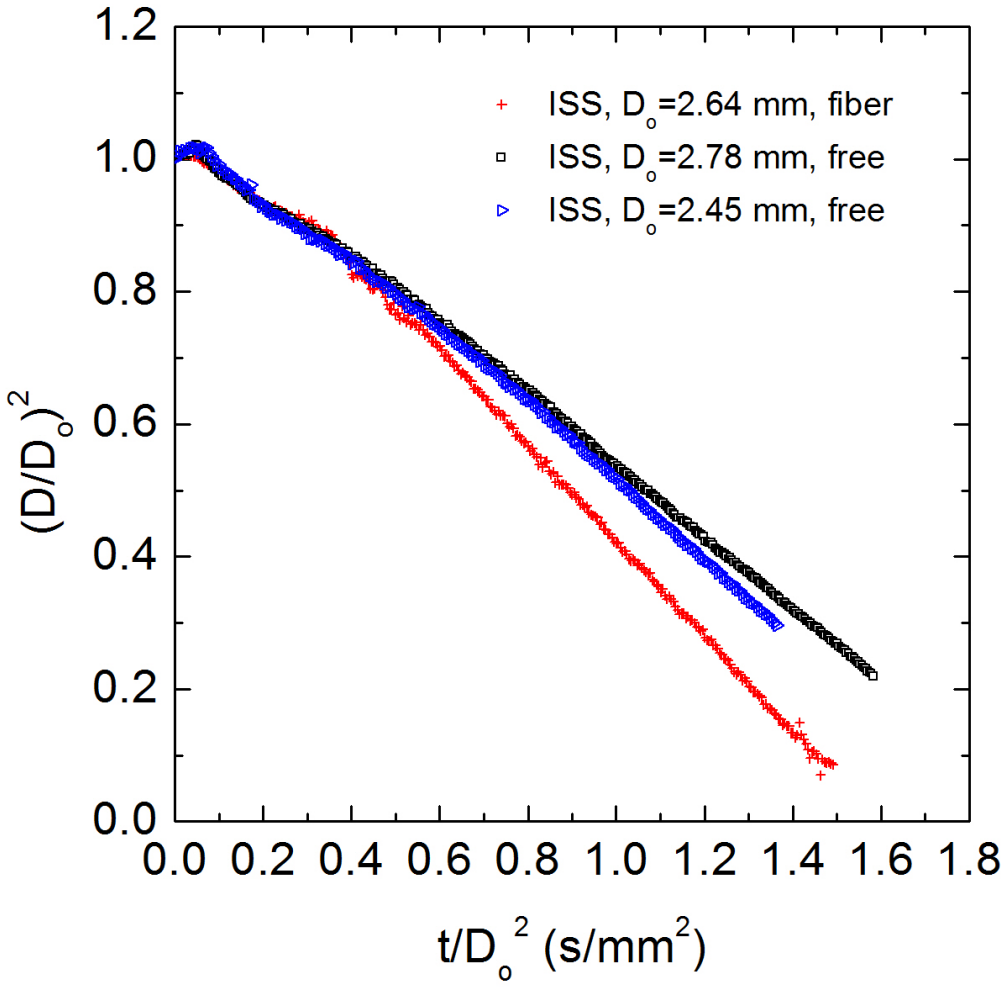

Fig. 4.13. Evolution of droplet diameters for n-octane droplet burning with and without an 80 μm SiC support fiber.

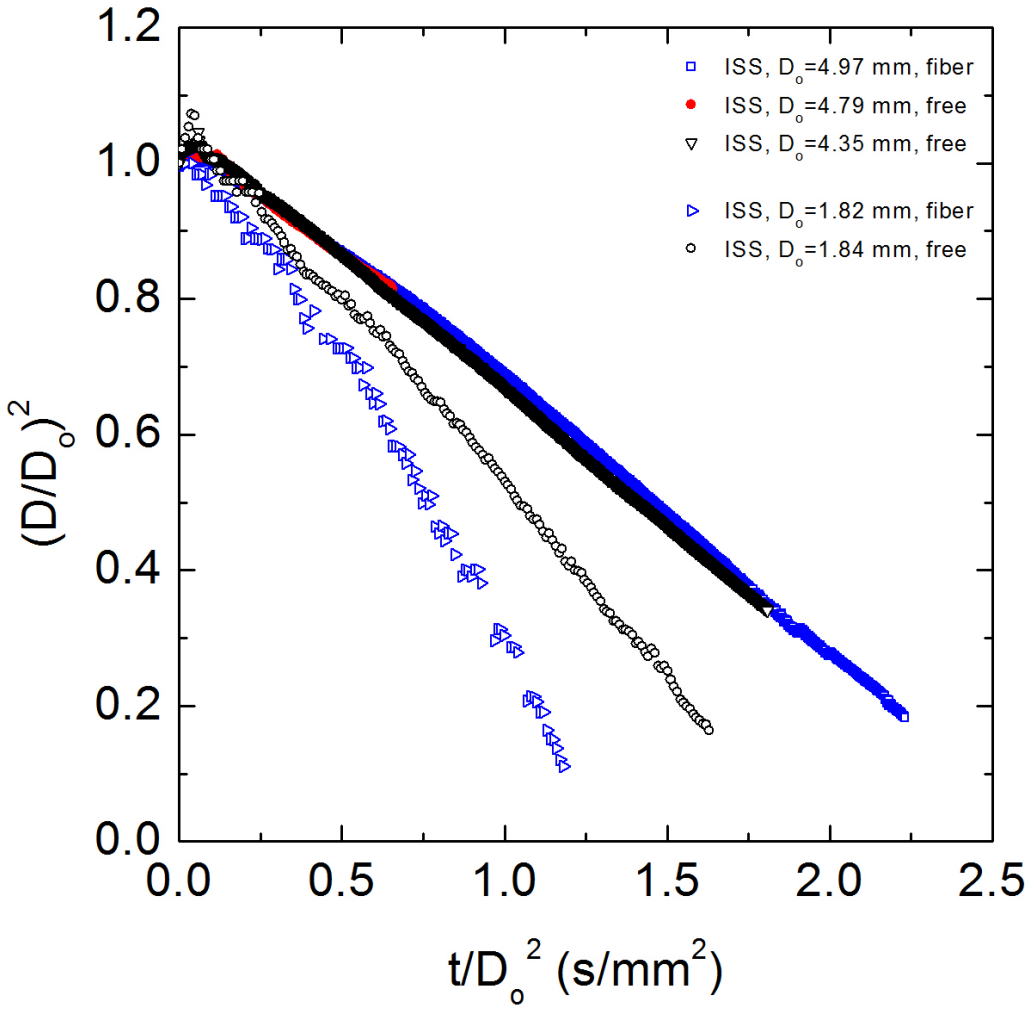

Fig. 4.14. Evolution of droplet diameters for n-decane droplet burning with and without an 80 μm SiC support fiber.

is found in Fig. 4.12, considerably higher burning rates are found for fiber-supported experiments (cf. Fig. 4.13, D_o = 2.45 mm; Fig. 4.14, D_o = 1.82 mm) compared to free droplet experiments with similar D_o. The fiber effects emerge later for a slight larger droplet (D_o = 2.45 mm, at $t/D_o^2 \sim 0.4$ s/mm^2 (Fig. 4.13), compared to D_o = 1.39 mm, at at $t/D_o^2 \sim 0.2$ s/mm^2 (Fig. 4.12)). This is related to the thermal diffusion time $t_h = D_f^2/\alpha$ for the thermophoretic influences to approach inwardly within the gas phase. For large n-decane droplets, the droplet with D_o = 4.79 mm moved out of field of view at ~ 0.6 s/mm^2 (cf. Fig. 4.9b). Up to this point the data for free droplet (D_o = 4.79 mm) fall on top of the fiber data (D_o = 4.97 mm). For the post-extinction region, the fiber results of D_o = 4.97 mm are compared with a free droplet results with a slightly smaller droplet (D_o = 4.35 mm). Note that there might still be fiber effects for the data of D_o = 4.97 mm that slightly increases the burning rate to overlap with the data with slightly smaller D_o.

Figures 4.15 through 4.17 show the flame standoff ratio (FSR = D_f/D) for the data reported in Fig. 4.12 through 4.14 for n-heptane, n-octane, and n-decane, respectively. Note that luminous flame diameter D_f here can only be obtained before the flame disappears due to extinction. Therefore the FSR data for the droplets with flame extinction end earlier (in term of t/D_o^2) compared to smaller droplets. For n-heptane (cf. Fig. 4.15), fiber effects on FSR are not seen for the larger droplets (D_o = 4.23 mm (fiber) and 3.87 mm (free)) and the increase trends of FSR for these two experiments agree very well. In contrast, the FSR of smaller n-heptane droplet flames (D_o = 1.38 mm (fiber) and 1.30 mm (free)) are significantly increased due to fiber. Figure 16 shows evolution of FSR for n-octane droplets. The FSRs for D_o = 2.45 mm

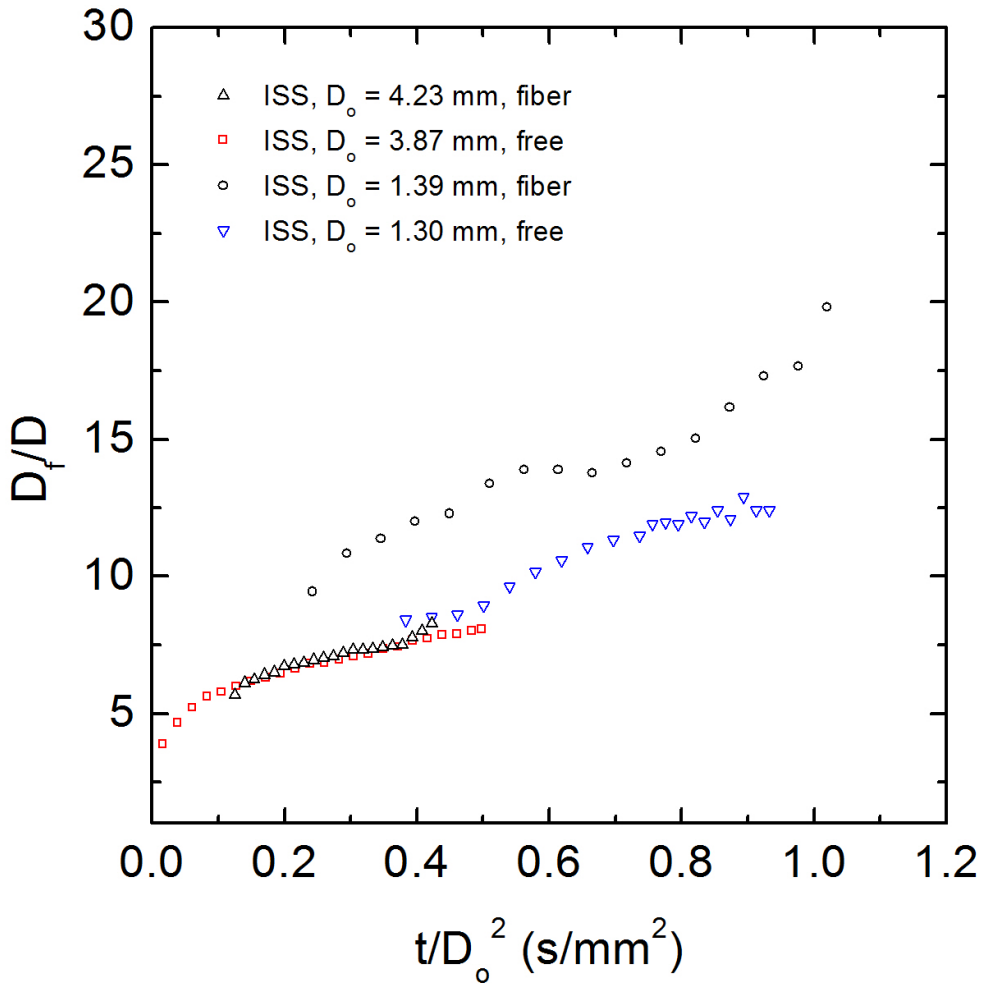

Fig. 4.15. Comparison of FSR for n-heptane droplet flames with and without an 80 μm SiC support fiber.

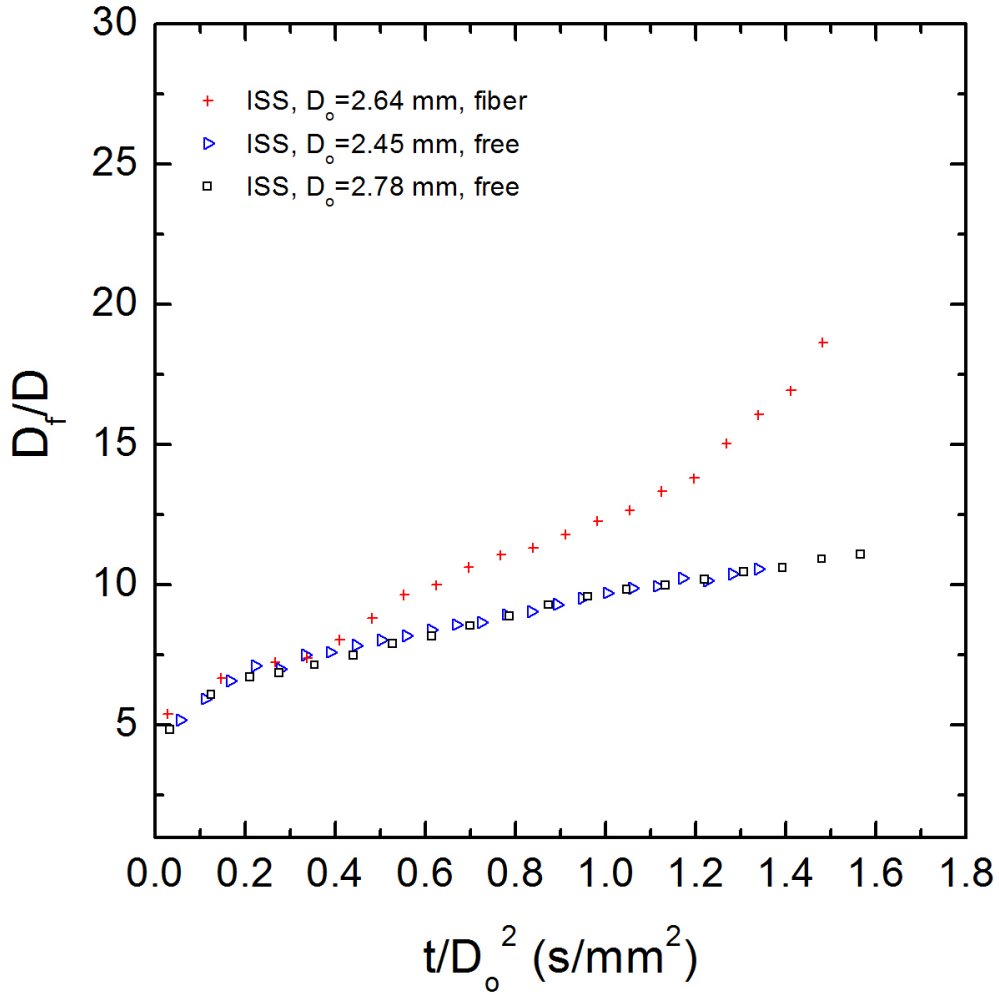

Fig. 4.16. Comparison of FSR for n-octane droplet flames with and without an 80 μm SiC support fiber.

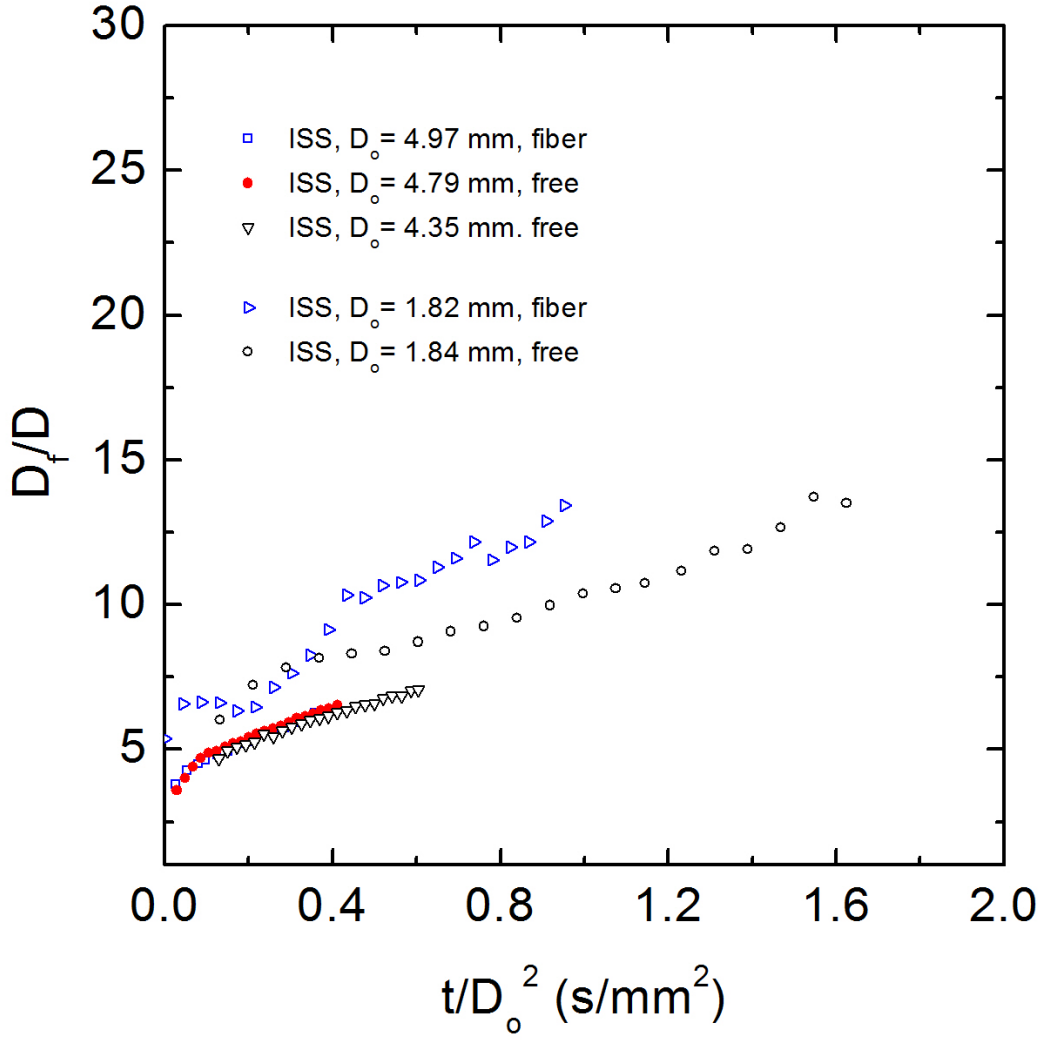

Fig. 4.17. Comparison of FSR for n-decane droplet flames with and without an 80 μm SiC support fiber.

and 2.78 mm are identical while the fiber-supported data for D_o = 2.64 mm (between 2.45 mm and 2.78 mm) show a very different trend after t/D_o^2 = 0.4 s/mm^2. Same conclusion as for n- heptane and n-octane (cf. Figs. 15 and 16) can be drawn from Fig. 17 for n-decane, with significant fiber effects on FSR observed only for the small droplet (D_o = 1.82 mm (fiber), compared to D_o = 1.84 mm (free)). The convection caused by soot particle motions was shown to increase the burning rate in Figs. 4.12 to 4.14. The presence of the fiber increases the value of FSR is not surprising because FSR is proportional to the burning rate K according to Aharon and Shaw (1997). As fuel evaporation is enhanced by convection, the flame (or FSR) is re-positioned to a place further away from the droplet surface due to stronger evaporative flows.

Table 4.1 summarized the D_o and D_{fiber} examined in Sections 4.2 and 4.3. As discussed earlier, for a given size of fiber, the "curvature" of the droplet surface affects the boundary layer thickness of the Stefan flow. To bring in the effect of the absolute fiber size, the curvature of the fiber surface must be considered. We define a "relative curvature ratio" ξ_{rc} as:

$$\xi_{rc} \equiv \frac{\kappa_{fiber}}{\kappa_{droplet}} = \frac{1/r_{fiber}}{1/r_o} = \frac{D_o}{D_{fiber}}. \qquad (4.1)$$

The ξ_{rc} for each condition is also included in Table 4.1.

Figure 4.18 plots the D_o vs. ξ_{rc} using the values in table 4.1. As shown by the dotted line, a threshold value of ξ_{rc} for fiber effects to emerge appears to be around "36" for SiC fibers. Note that what is important is the ratio of the droplet to fiber sizes. The "two-fiber" setup for GB experiments does not alter the ξ_{rc} since the fiber-droplet intersection of one fiber is relatively far away from that of the other fiber (the two

fibers are crossed at a 60^o angle). The criterion for whether or not fiber effects appear can be obtained from single fiber estimate.

Table 4.1. Droplet and fiber diameters and their ratios for the data reported in this chapter.

Fuel	D_o (mm)	D_{fiber} (μm)	$\xi_{rc} = D_o/D_{fiber}$
n-heptane	4.23	80	52.9
	1.39	80	17.4
n-octane	2.64	80	33.0
n-decane	4.97	80	62.1
	1.82	80	22.8
	0.54	14	38.6

4.5 Conclusions

Droplet flames with spherically symmetry are examined with SiC and ceramic support fibers for heptane and toluene (~0.5 mm). Results suggest no difference for using SiC and ceramic fiber due to either their thermal conductivities are very similar or the heat transfer associated with fibers of this size (~14 μm) is negligible.

Fiber-supported and free droplet experiments were carried out for ~0.5 mm n-decane droplets with the fiber setup being two crossed SiC 14 μm fibers using a drop tower facility. Results suggests that no difference is found in terms of the evolutions of D^2, FSR, and SSR during burning except small variation of soot interaction with the

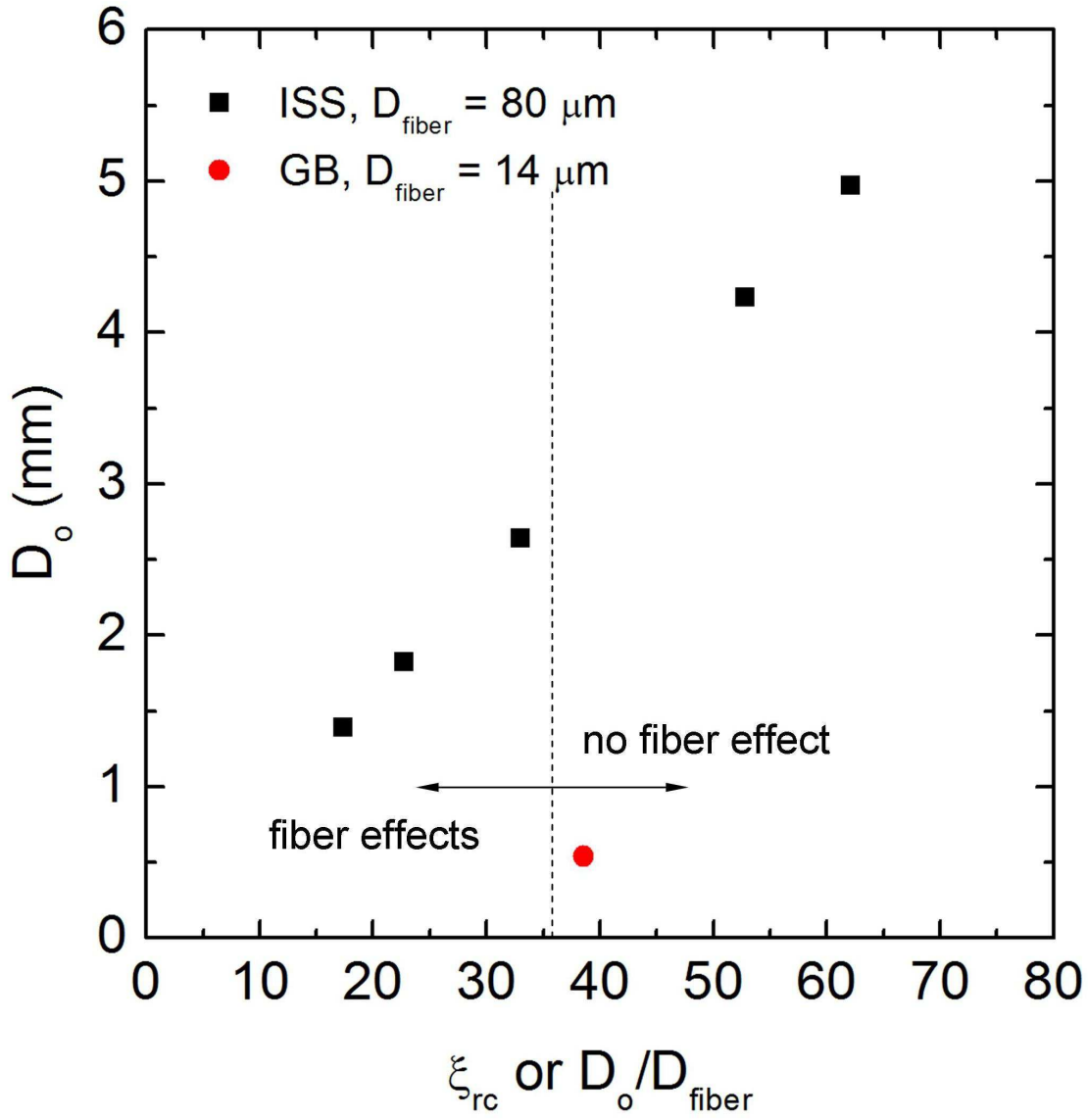

Fig. 4.18. D_o vs. relative curvature ratio ($\xi_{rc} = D_o/D_{fiber}$) for the fiber-supported experiments reported in this Section 4.2 and 4.3.

support fibers that very slightly affects the SSR in the later burning process. These comparisons provide confidence and validity for the fuel benchmark studies with same fiber material and droplet size included in this thesis.

Results from unsupported and fiber-supported droplet combustion experiments on the ISS were for n-heptane, n-octane, and n-decane were reported. It is suggested that the burning rates can be affected by the presence of an 80 μm SiC support fiber through a gas phase convection induced by the soot particle motion for $D_o < 3$ mm. The soot particle motion is believed to be attributed to a relative curvature of the droplet and the fiber that alters the boundary layer thickness of the Stefan flows. FSR is also significantly increased when this fiber is used for $D_o < 3$ mm.

Combining the data from drop tower experiments, a fiber to droplet size ratio of "36" is obtained below which fiber effects is prominent. This result can be used as a guideline for fiber-supported droplet combustion experiments.

CHAPTER 5

BINARY MIXTURES OF N-HEPTANE/ISO-OCTANE AND N-HEPTANE/TOLUENE AND A COMMERCIAL UNLEADED GASOLINE[2]

5.1 Introduction

The droplet burning characteristics of binary blends of iso-octane, n-heptane and toluene reported in this chapter. The results are compared to gasoline (87 octane rating). The initial droplet diameter was fixed at 0.51 ± 0.02 mm and the experiments were carried out in room temperature air.

Selected properties of the fuels reported in this chapter are listed in Table 5.1. The gasoline was a commercial grade purchased from a local service station (Mobil®). It contained no ethanol, and GC/MS analysis of it (discussed in Appendix 5A) indicated no oxygenates. For the binary mixtures, the initial fractional amounts investigated are given in Table 5.2. The mixtures were prepared on a volumetric basis. The volume fractions were converted to the initial mole fraction values listed in Table 5.2.

As a summary observation, measurements of the evolution of droplet diameter show that iso-octane, n-heptane and their mixtures have almost identical burning rates that are significantly higher than gasoline. The pure toluene burning rate matches the gasoline burning rate during the quasi-steady period of the combustion history while it is lower than gasoline in approximately the first quarter and last quarter of the burning history. A small dilution with heptane (heptane (0.05)/toluene (0.95)) raised the

[2] This chapter comes from the following publication: Liu, Y.C., Avedisian, C.T., Combustion and Flame 159 (2012) 770-783.

Table 5.1. Selected Properties of n-heptane, iso-octane, toluene, and gasoline.

property	n-heptane	iso-octane	toluene	gasoline
formula[a]	C_7H_{16}	C_8H_{18}	C_7H_8	$C_{7.76}H_{13.1}$ or $C_{8.26}H_{15.5}$
T_b[b] (K)	372	372	384	297-494[c]
W_F[b] (g/mole)	100.2	114.23	92.14	114.8 or 106.4[a]
ρ_L[d] (@297.7 K, kg/m^3)	680	688	862	731
ρ_L[e] (@ T_b, kg/m^3)	608	638	776	-
K(mm^2/s)[f]	0.72	0.69	0.55	0.53
h_{fg}[b] (@ T_b, J/kg)	31.7×10^4	27.0×10^4	36.0×10^4	-
octane number[g]	0	100	103	87
ν_c[h]	11.0	12.5	9	11.035-12.375

[a] Formula for gasoline is from Turns (2006).
[b] Reid et al. (2987) except for gasoline.
[c] Mobil Oil Corp.
[d] Measured in this study.
[e] Estimated from insets to Figs. 8, 9, and 11 in an approximate quasi-steady period.
[f] Anti-Knocking index (AKI)= (Research Octane Number (RON)+Motor Octane Number (MON))/2.
[g] Assumes one mole of fuel and products of CO_2 and H_2O

Table 5.2. Fractional amounts (of heptane) investigated for the indicated mixture components (actual compositions will differ slightly from the indicated values due to the pre-vaporization process discussed in Appendix 5A of this chapter).

mixture	initial volume fraction	initial mole fraction
heptane/iso-octane	0.5	0.530
heptane/toluene	0.5	0.420
heptane/toluene	0.2	0.154
heptane/toluene	0.05	0.037

mixture burning rate in the last quarter of the history to provide the best overall agreement with gasoline from ignition to burnout. The results show that no combination of the hydrocarbons examined could replicate the flame or soot shell standoff ratios for gasoline.

The sooting propensities inferred from observations of flame brightness and image intensities are in the order toluene > gasoline > n-heptane (0.05)/toluene (0.95) > heptane(0.5)/toluene(0.5) > iso-octane > n-heptane(0.5)/iso-octane (0.5) > n-heptane. For the heptane/toluene system it was found that the burning process of toluene alone was close to gasoline. Adding heptane to toluene allowed for adjusting the composition to better match the burning rate of gasoline.

In addition, three considerations for the experimental arrangement are the following: exposure of the droplet to surrounding air during the set-up time prior to ignition; the potential for heat conduction through the fiber to alter the burning process; the motion of the electrode retraction to induce a flow field that could influence the droplet burning process; and the potential for significant internal liquid motion to exist inside the droplet prior to ignition that could have a demonstrable effect on the droplet burning process.

For a single component liquid the only effect of exposure to air before ignition is to reduce the droplet diameter by evaporation. For mixtures, an added effect not considered in previous studies is the potential of preferential evaporation to change the droplet composition from the initially prepared value. This effect is discussed in Appendix 5A of this Chapter. It is shown that if the droplets are ignited within about 5 s of being deployed on the fiber, the droplet composition at ignition is virtually the

same as at the time of ignition.

5.2 Results and Discussions

5.2.1 Soot and Flame Structure

Figure 5.1 shows selected images of the flame structure for the fuels examined, arranged according to image "brightness". The brightness of the flame is due to the sensitivity of the eye to wavelengths in the visible region of the electromagnetic spectrum created by oxidation of soot aggregates that are transported to the flame (Glassman (1987)). The brightness should qualitatively correlate with the amount of soot formed, being greater with increasing soot formation. Based on this assessment, the sooting propensities (highest to lowest) consistent with Fig. 5.1 would be toluene >heptane/toluene > gasoline > iso-octane >heptane/iso-octane > heptane which is consistent with the ordering given in (Glassman (1987)) based on broad chemical classes.

Selected back-lit images which clearly illustrate the soot structure are shown in Fig. 5.2. The images are again arranged from highest to lowest sooting tendency. It is evident that the heptane and iso-octane flames (Fig. 5.2d-5.2f) are considerably less sooting than the toluene blends (Fig. 5.2a, 5.2b) or gasoline (Fig. 5.2c) and that iso-octane (Fig. 5.2d) appears to produce more soot than n-heptane (Fig. 5.2f) which is consistent with Fig. 5.1. For the toluene flame (Fig. 5.2a) soot formation was so extensive that the aggregates collected and formed a crust that eventually completely obscured the soot shell. Connected soot aggregates are also seen for gasoline (Fig.

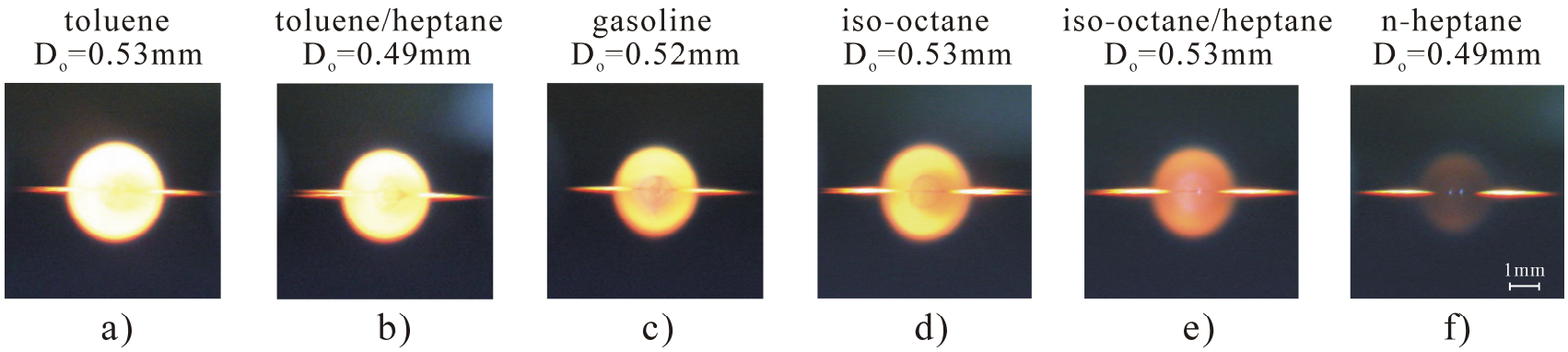

Fig. 5.1. Color video frames of burning droplets (D_o = 0.51 ± 0.02 mm) arranged from highest to lowest intensity: (a) toluene, (b) toluene/heptane (0.5/0.5), (c) gasoline (d) iso-octane, (e) iso-octane/heptane (0.5/0.5), (f) n-heptane. Images were selected from each sequence for maximum qualitative luminosity.

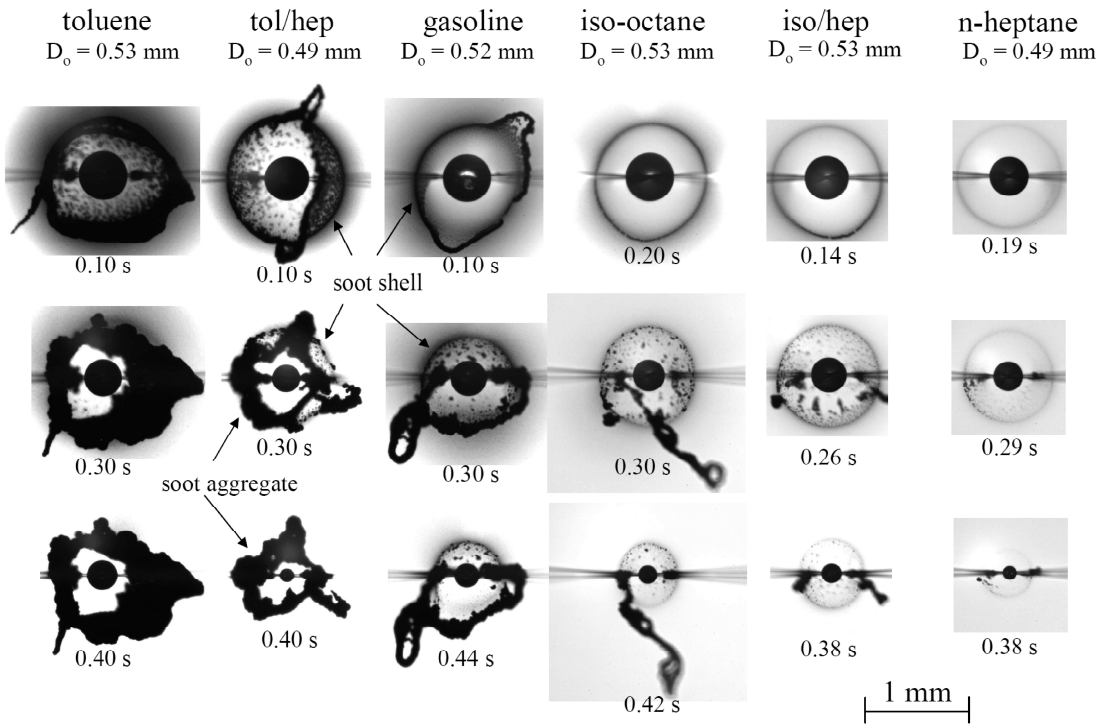

Fig. 5.2. Back-lit high speed digital images of burning droplets (D_o is 0.51 ± 0.02 mm): (a) toluene, (b) toluene/heptane (0.5/0.5), (c) gasoline (d) iso-octane, (e) iso-octane/heptane (0.5/0.5), (f) n-heptane. Images are selected based on intensity.

5.2c) and an equivolume heptane/toluene mixture (Fig. 5.2b).

For some gasoline and toluene droplets, a disruptive effect was observed near the end of burning. This phenomenon could be the result of volatile species being trapped inside the droplet owing to a preferential vaporization effect (Law (1978), Shaw and Williams (1990), Yang et al. (1991)), dissolution of product gases in the droplet during burning (Shaw et al. (1988)), or nonvolatile impurities initially existing inside the liquid. Significant superheating of the primary mixture constituents could not be sustained because of their similar boiling points (Table 5.1) with such impurities being present. Nonvolatile impurities, however small their fractional amount is initially, could affect the burning process near the end of the combustion process and potentially produce this effect.

5.2.2 Quantitative Data

An important task for developing a surrogate is to adjust the fractional amount of constituents to match combustion targets. For droplet burning these targets include the evolution of droplet, soot and flame diameters, and burning rates. A measure of sooting could also be included (e.g., mean or peak soot volume fraction) but was not added in the present study. Figures 5.3 and 5.4 provide such comparisons.

As shown in Fig. 5.3, and from the standpoint of droplet burning, it is clear that heptane and iso-octane are poor surrogates for gasoline. The burning rate K was obtained from a fourth-order polynomial fit of the data in Fig. 5.3 and 5.4 (polynomial fits of different order will produce slightly different trends while the choice of 4^{th} order was considered to be suitable for comparative purposes, see Section 3.6).

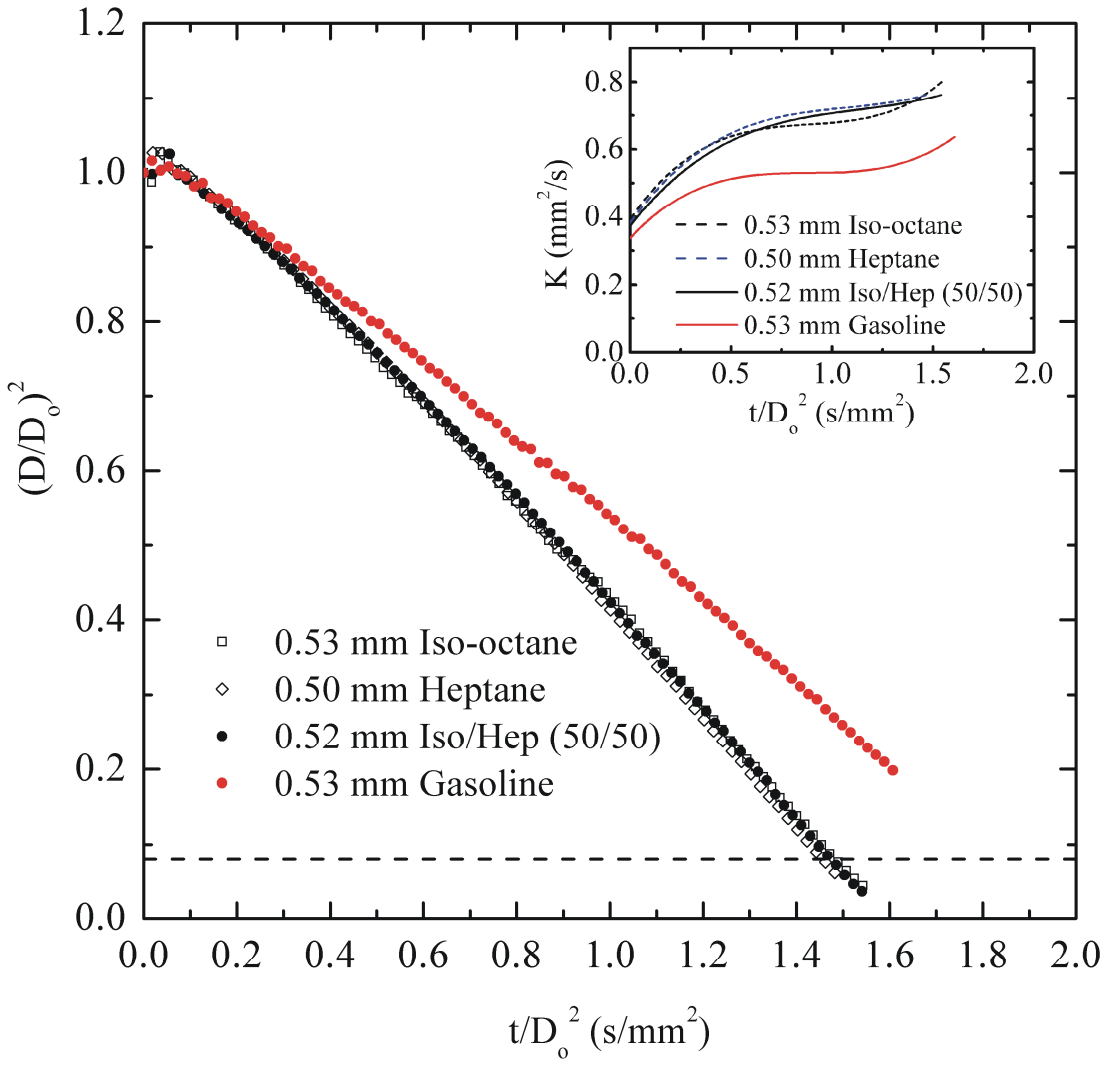

Fig. 5.3. Comparison of the evolutions of scale droplet diameter for iso-octane, n-heptane, gasoline and a iso-octane/heptane (0.5/0.5) mixture. Data are averages of three repetitions for each fuel. Inset shows burning rates based on a 4th order polynomial fit to data. The dashed line indicates where $D \approx 10\ D_{fiber}$.

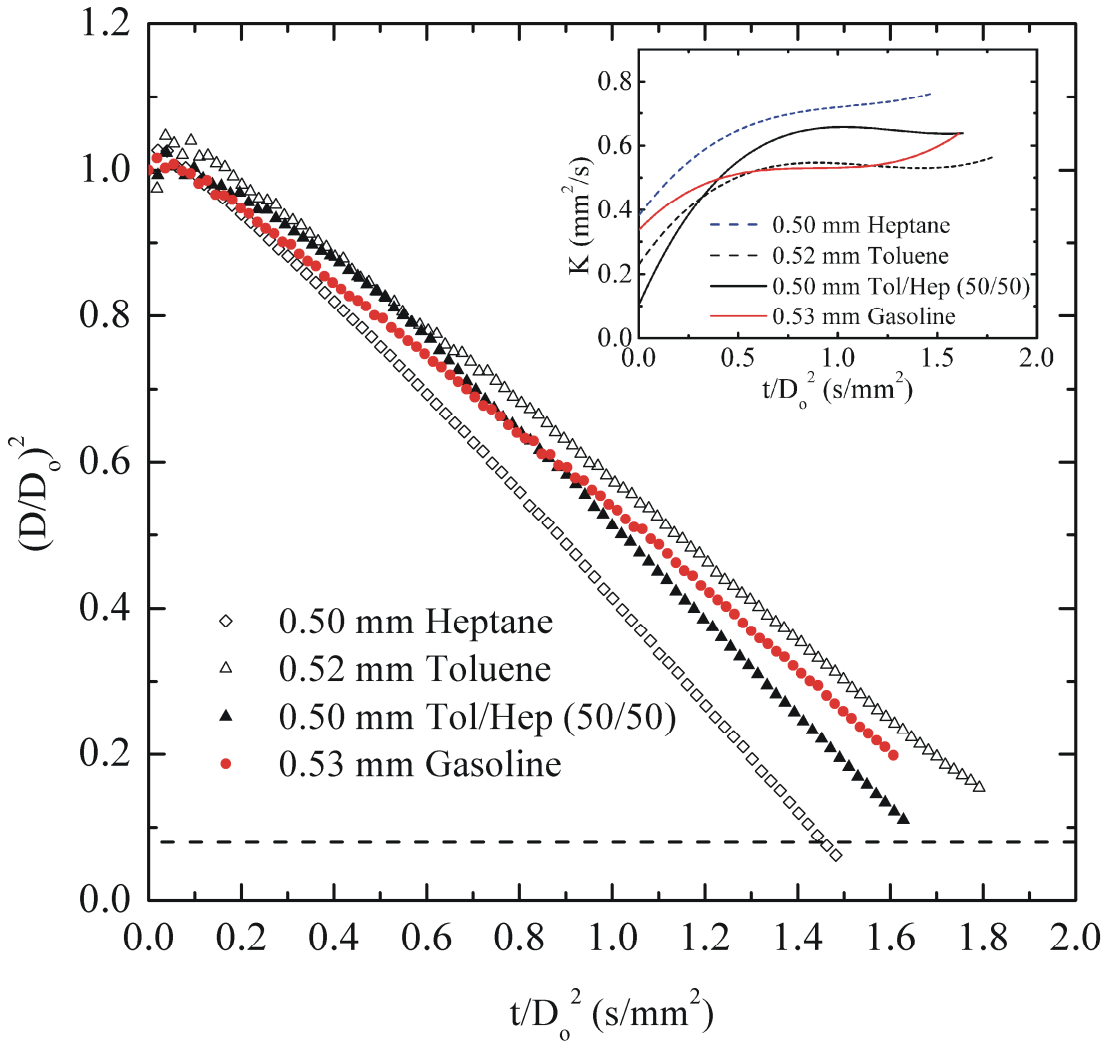

Fig. 5.4. Comparison of the evolutions of droplet diameters for heptane (data from Fig. 5.3), gasoline (data from Fig. 5.3) with toluene, and a toluene/heptane (0.5/0.5) mixture. Data are averages of three repetitions for each fuel. Inset shows burning rates based on a 4th order polynomial fit to data. The dashed line indicates where D ≈ 10 D_{fiber}.

Moreover, the heptane and iso-octane sooting propensities are very different from gasoline as noted previously.

The burning rates, K, are much higher than gasoline as shown in the inset to Fig. 5.3. The burning rates of gasoline, iso-octane, and heptane increase for a portion of the burning history (probably the result of droplet heating that persists throughout burning (Avedisian and Callahan (2007), Shaw and Williams (1990)) followed by a quasi-steady period, 0.7 $s/mm^2 < t/D_o^2 < 1.25$ s/mm^2. The heptane burning rate in this range is close to previous studies for n-heptane droplets of this size (Jackson and Avedisian (1994)). On the other hand, the quasi-steady gasoline burning rate is considerably lower. This shows that there is no mixture fraction for a binary blend of heptane/iso-octane that can replicate the burning rate of gasoline.

It has been shown that toluene can provide a mean for adjusting mixture chemical properties to bring them more in line with gasoline (Chaos et al. (2007)). Regarding the physical process of droplet burning, Fig. 5.4 shows that toluene alone represents well the droplet burning rate of gasoline in the quasi-steady regime, 0.7 $s/mm^2 < t/D_o^2 < 1.2$ s/mm^2. Outside of this range, toluene's burning rate is significantly lower than gasoline. At the same time, considering the range of other combustion properties that might be matched (e.g., flame speed, ignition delay, extinction strain rate, etc.), a potential surrogate might not be able to match all conceivable combustion properties. It depends on what is important to match in a particular application as to labeling a fuel as a surrogate for that application.

As shown in Figs. 5.3 and 5.4, heptane and iso-octane burn in an almost identical way while toluene burns considerably slower. To understand this result, we

draw upon the classical quasi-steady theory of droplet combustion (Turns (2000), Glassman (1987)). This theory (which assumes constant properties, no droplet heating, radiation or soot formation, and a single step reaction) shows that the droplet burning rate is related to properties as

$$K \sim \xi \ln (1+B) \tag{5.1}$$

where

$$\xi \equiv \frac{k_g}{\rho_L c_{pg}} \tag{5.2}$$

For the present study, the quasi-steady theory is not quantitative because the properties depend on temperature and composition while the theory assumes properties are constant. Nonetheless, the physical mechanism responsible for the droplet burning process should still be captured by this analysis.

ξ was estimated using property correlations given in Reid et al. (1987) as listed in Appendix 5B of this chapter. The liquid density in Eq. (5.2) arises from a mass balance on the droplet and it is evaluated at the fuel boiling point. The ratio of gas thermal conductivities to specific heats were evaluated at $T_{p,i} \approx \frac{1}{3}T_{b,i} + \frac{2}{3}T_{f,i}$ as suggested in (Glassman (1987)). Since the flame temperature and a suitable fuel mole fraction are not well established (Law and Williams (1972) suggest x=0.4), ξ was evaluated over $0<x<1$ and for several droplet flame temperatures (we took values ranging from 1400K to 2000K). Figure 5.5 shows the trends of ξ normalized by $\xi_{heptane}$.

It is evident from Fig. 5.5 that $\xi_{heptane} \approx \xi_{iso\text{-}octane}$ over the recommended range

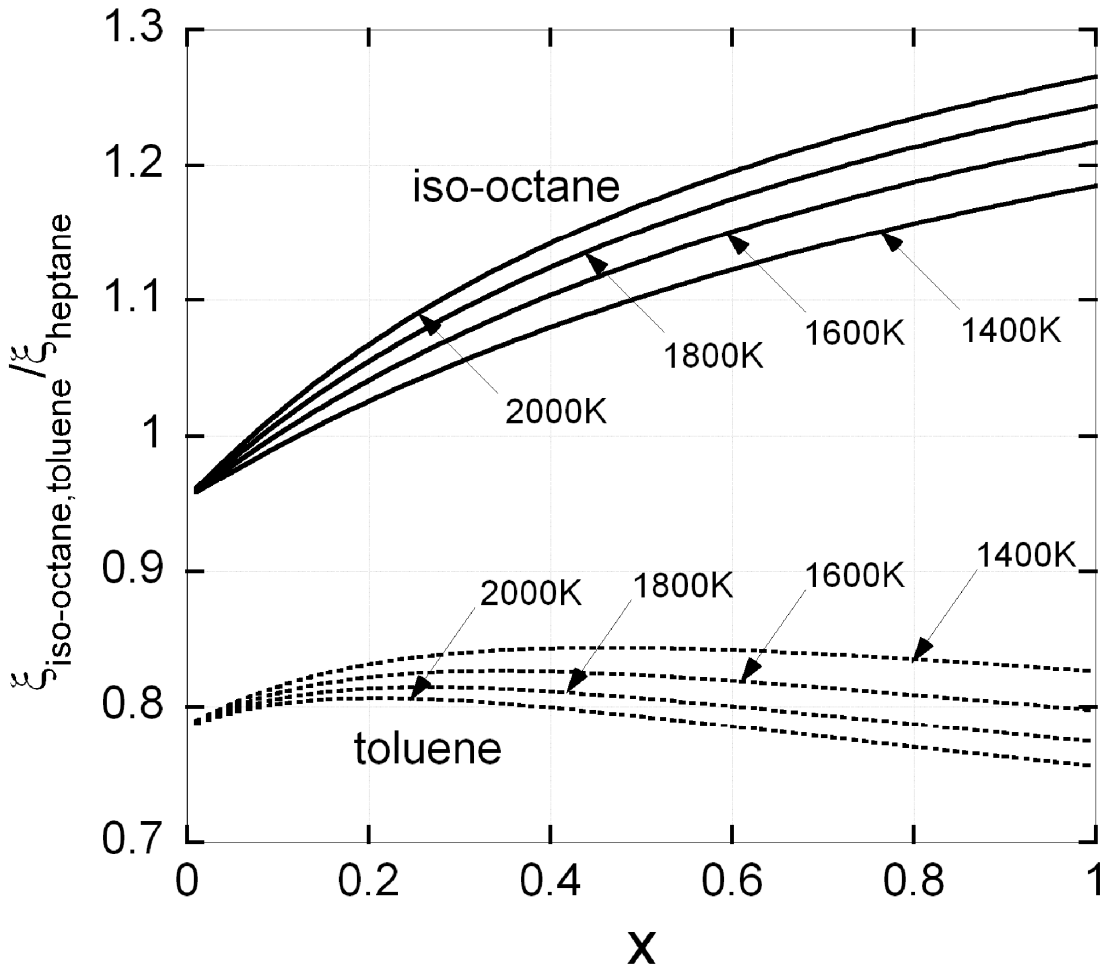

Fig. 5.5. Variation of $\xi_i/\xi_{heptane}$ with hydrocarbon mole fraction evaluated using property correlations in Appendix 5B of this chapter at the indicated flame temperatures ($T_{f,i}$). For all conditions examined, $\xi_{heptane,iso\text{-}octane} > \xi_{toluene}$ which, from the classical theory of droplet burning, would imply that $K_{heptane,\ iso\text{-}octane} > K_{toluene}$.

of x (between 0.2 and 0.4) so that $K_{heptane} \approx K_{iso\text{-}octane}$ while $\xi_{toluene}/\xi_{heptane} < 1$ which implies that $K_{toluene} < K_{heptane}$. These trends are consistent with Figs. 5.3 and 5.4. As such, the physics of the constant property theory are consistent with the experimental results.

There is no obvious indication of preferential vaporization in Figs. 5.3 and 5.4 beyond the gradual change of K shown in the insets to these figures. The mechanisms that could cause K to depend on time include preferential vaporization in which one component evaporates out of the droplet first leaving behind less volatile species (Law (1978)), or a droplet heating process that persists throughout burning (Shaw and William (1990)). The lower heat of vaporization of iso-octane compared to heptane suggests that iso-octane should preferentially vaporize in a heptane/iso-octane mixture. But the fuel boiling points (Table 4.1) and the values of ξ are very close. As a result, an abrupt change of K should not be expected, and it was not observed (Fig. 5.3). The discussions in Appendix 5A of this chapter suggest that preferential vaporization may also be evidenced by the droplet composition changing over time.

Figure 5.6 shows a finer division of mixture fraction at lower heptane loadings for heptane/toluene mixtures that result in an improved match with gasoline. Results for (initial) heptane concentrations of 20% and 5% are illustrated in Fig. 5.6. For both blends, the mixture burning rates are now much closer to gasoline over the entire burning history, especially the 0.05/0.95 heptane/toluene mixture which is almost the same as gasoline (compare insets to Figs. 5.4 and 5.6).

Figure 5.7 shows the flame and soot standoff ratios (i.e., outer luminous zone diameter divided by the droplet diameter at the same time, D_f/D (FSR), and the soot

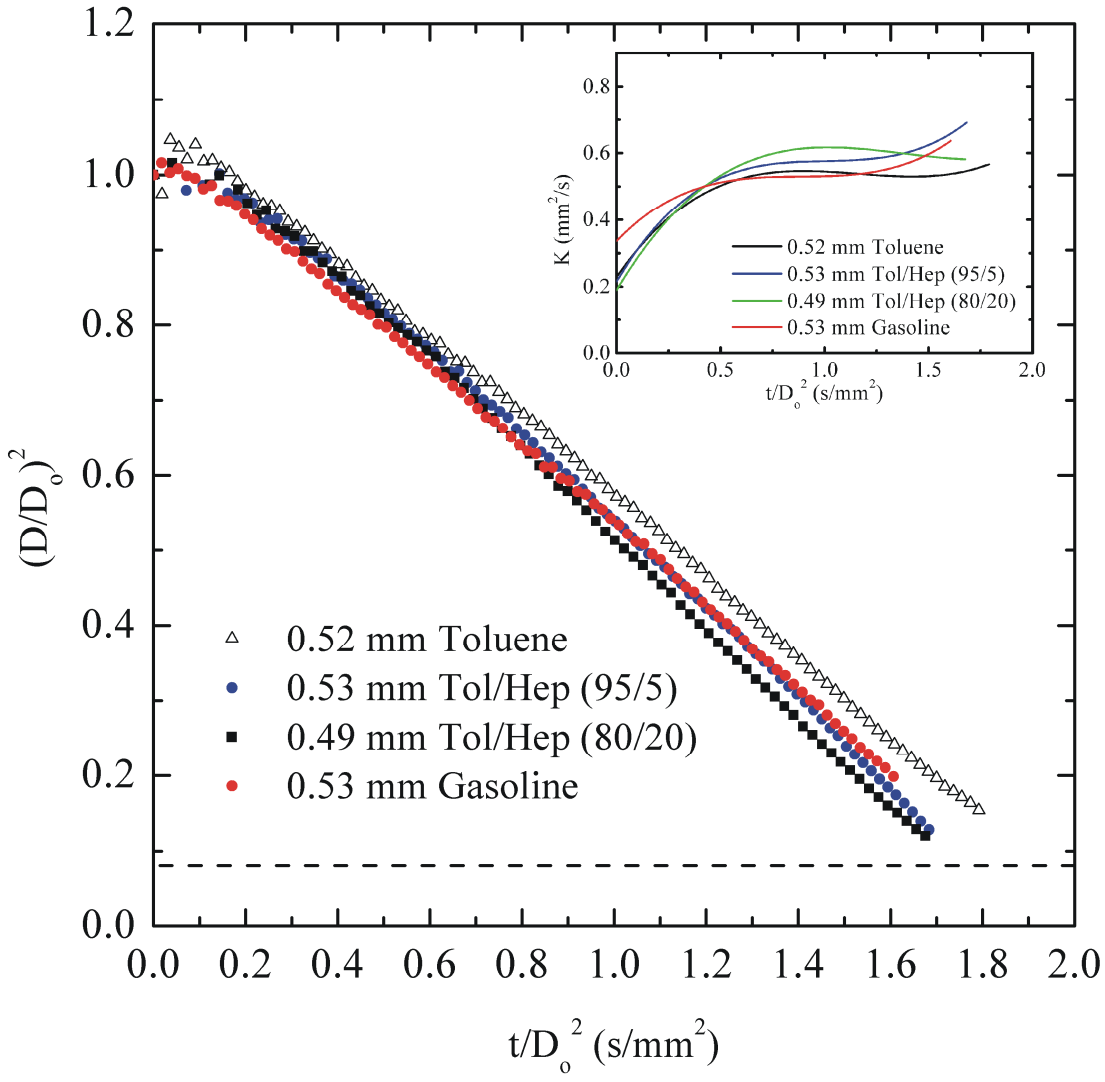

Fig. 5.6. Comparison of the evolutions of droplet diameters for a finer range of compositions for toluene/n-heptane mixtures, (80/20 and 95/5) with toluene (data from Fig. 5.4) and gasoline (data from Fig. 5.3). Inset shows burning rates based on a 4th order polynomial fit to data. Data are averaged three repetitions for each fuel. The dashed line indicates where D ~10 D_{fiber}.

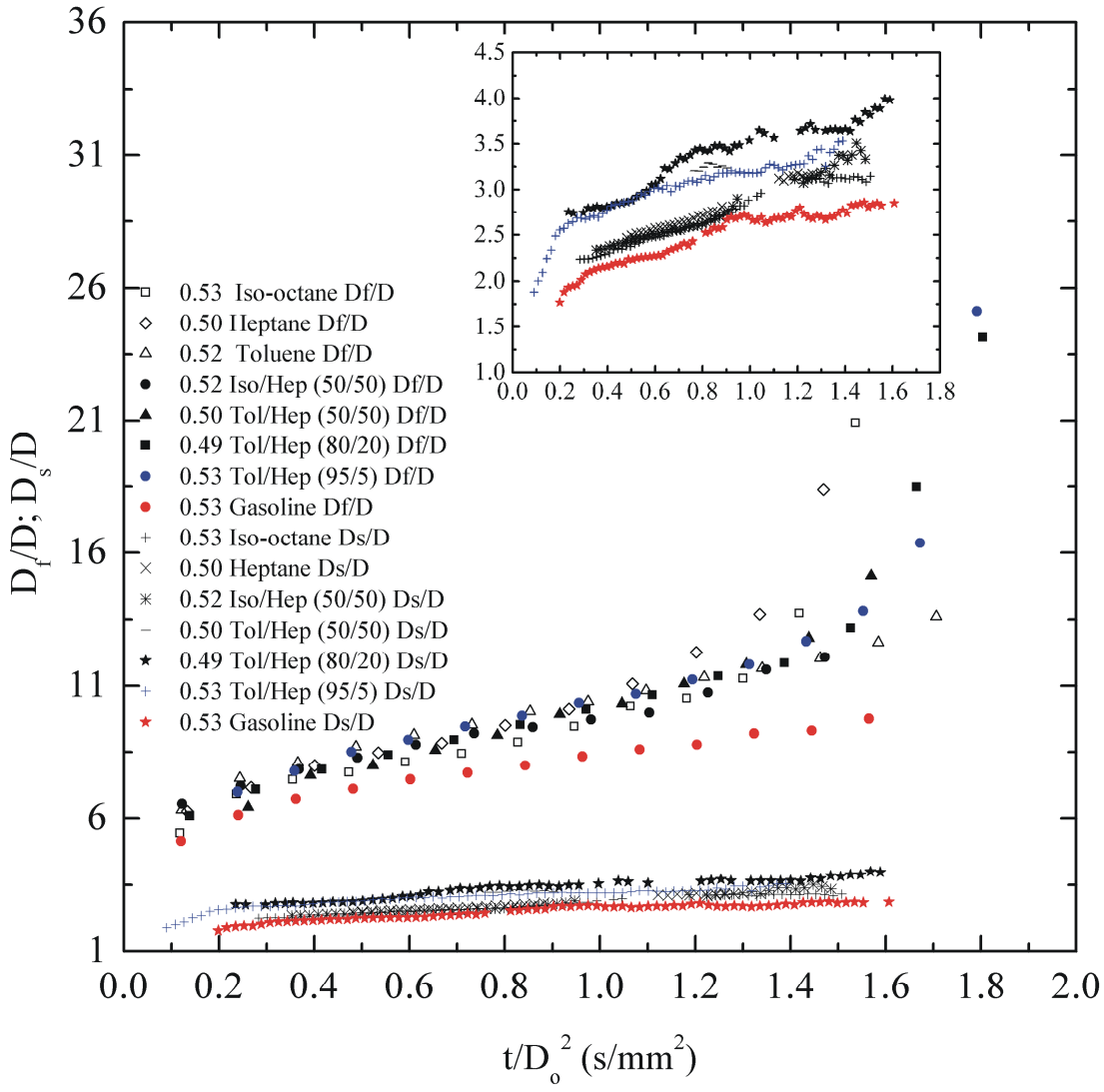

Fig. 5.7. Evolutions of flame and soot standoff ratios (D_f/D, D_s/D) for the fuel systems investigated. Data are averages of three repetitions for each fuel. Numbers in legend are initial droplet diameters in millimeters and compositions are a volume percent. Inset is an enlargement of the soot standoff ratio in terms of the scaled time.

shell diameter divided by the droplet diameter at the same time, D_s/D (SSR), respectively). Unlike the classical theory of droplet burning which shows that D_f/D is constant (Turns (2000), Glassman (1987)), the present results show transient behaviors which are consistent with prior experimental observations and theories that consider fuel vapor accumulation effects and gas flow fields that exhibit quasi-steady and unsteady regions as reviewed in Law and Williams (1972). Heptane, iso-octane and toluene flames are substantially farther from the droplet than gasoline flames.

A simple explanation of the flame standoff ratios shown in Fig. 5.7, relative to each other, can be obtained from the extension of the classical theory developed by Aharon and Shaw (1997) which shows that

$$\frac{D_f}{D} \approx \frac{\rho_L K \nu_c}{8 W_F n \mathcal{D}_{O_2-N_2} x_{O_2,\infty}} \tag{5.3}$$

where a single step stoichiometric reaction is assumed. For present purposes, we want to compare the standoff ratios of heptane, iso-octane and toluene to gasoline. From Eq. (5.3)

$$\Theta \equiv \frac{D_f / D|_i}{D_f / D|_{gasoline}} \approx \left(\frac{\rho_{L,i}}{\rho_{L,gasoline}}\right)\left(\frac{K_i}{K_{gasoline}}\right)\left(\frac{\nu_{c,i}}{\nu_{c,gasoline}}\right)\left(\frac{W_{F,gasoline}}{W_{F,i}}\right) \tag{5.4}$$

where "i" denotes heptane, iso-octane or toluene. Based on the measurements in Fig. 5.7, it is evident that $\Theta > 1$. To estimate Θ from Eq. (5.4) the liquid densities (which are dependent on temperature) and the burning rates, which are time dependent as shown in Figs. 5.3, 5.4, and 5.7, are needed. To simplify the estimates, we use the burning rates in the approximate quasi-steady periods determined from the insets to Figs. 5.3, 5.4, and 5.7; values are listed in Table 5.1. With the data in Table 5.1 $\Theta \approx$

1.31, 1.27, and 1.13 for heptane, iso-octane and toluene, respectively. These trends are qualitatively consistent with the experimental results in Fig. 5.7 which show that gasoline flames are closer to gasoline droplets than the flames of the other fuels examined.

Figure 5.7 shows that the soot standoff ratio is between 1.8 and 2.5 at the low end (beginning from where it could be measured as noted previously). At the upper end it is between 2.9 and 4.0. The inset to Fig. 5.7 shows the SSR on an expanded scale for clarity (the axes labels in the inset are omitted for space but are the same as the major figure). The SSR for gasoline is consistently lower than the hydrocarbons examined which, together with the fact that $\Theta \neq 1$, shows the challenge of simultaneously satisfying a range of droplet combustion properties with a single fractional amount for given mixture components.

5.3 Conclusions

The present study compared the burning histories of spherical droplet flames of an octane 87 grade of gasoline, with n-heptane/iso-octane and n-heptane/toluene mixtures while holding the initial diameter at 0.51 ± 0.02 mm for the base case of droplet burning in an environment that promotes spherical droplet flames while still maintaining significant soot formation. The major observations are the following.

1) An n-heptane/toluene blend in the amount of 5% heptane and 95% toluene replicates the burning rate of gasoline quite well over the entire burning history, while pure toluene is closer to gasoline in the quasi-steady period.

2) None of the mixture fractions examined for heptane/iso-octane or heptane/toluene blends matched the flame standoff or soot standoff ratios of gasoline, with values being consistently higher than gasoline throughout the droplet burning period. The results show that mixture fractions selected to match one droplet burning combustion property may not carry over to another property.

3) Sooting propensities are in the order (low to high) heptane < heptane/iso-octane < iso-octane < gasoline < heptane/toluene < toluene.

4) No significant differences are observed for the burning rates of iso-octane and n-heptane in spite of their significantly different soot propensities.

5) Toluene has a lower burning rate compared to iso-octane, n-heptane, and their mixtures which is believed to be the result of toluene's comparatively higher liquid density.

6) No significant preferential vaporization was detected in the evolution of droplet diameter (squared) for the mixtures examined because the relevant properties (liquid density, gas thermal conductivity and specific heat) are close.

7) A binary blend of an initially prepared composition can experience significant preferential vaporization by exposure of the blend to air prior to ignition that lowers the composition of the volatile component in the droplet. At ignition the mean droplet composition can therefore be different than the initial value. This effect was minimized by limiting exposure of the mixture droplets of the sizes examined (~ 0.5 mm) to ambient air for less than 5 s prior to ignition and the start of burning.

Appendix 5A: Effect of Air Exposure on Droplet Composition

Preferential vaporization of mixture droplets comprised of various species is normally associated with the combustion process. However, this phenomenon can occur during the experimental set-up time when the droplet may be exposed to air from various procedures such as preparing the mixture, forming and deploying the droplet, positioning the instrumentation package prior to release into free-fall and ignition, and/or waiting for a (larger) deployed droplet to reach a (smaller) size of interest. In these cases, the initially prepared mixture fractions may be different at the time of ignition. This section discusses this effect for a representative blend of an initially equivolume mixture of toluene and heptane.

To illustrate this effect, our approach is to first form a “large” droplet of known initial composition and allow it to evaporate in air down to a "small" drop, here being 0.50 mm due to its relevance to the present study. When the droplet reaches the desired size, its mean composition is measured. Figure 5.8 shows the concept. The time to evaporate down to a 0.5 mm droplet is considered to serve as a sort of set-up time in an experiment during which the droplet is exposed to air but has not yet been ignited.

After reaching 0.5 mm, the droplet compositions are measured by gas chromatography/mass spectrometry (GC/MS) analysis. A plot of the average measured composition with evaporation time gives the actual droplet composition that would exist after exposure of the droplet to air for the elapsed time prior to ignition. The time of an initially equivolume toluene/heptane mixture with $D_o > 0.5$ mm to evaporate down to 0.5 mm is measured, as well as the resulting average droplet composition.

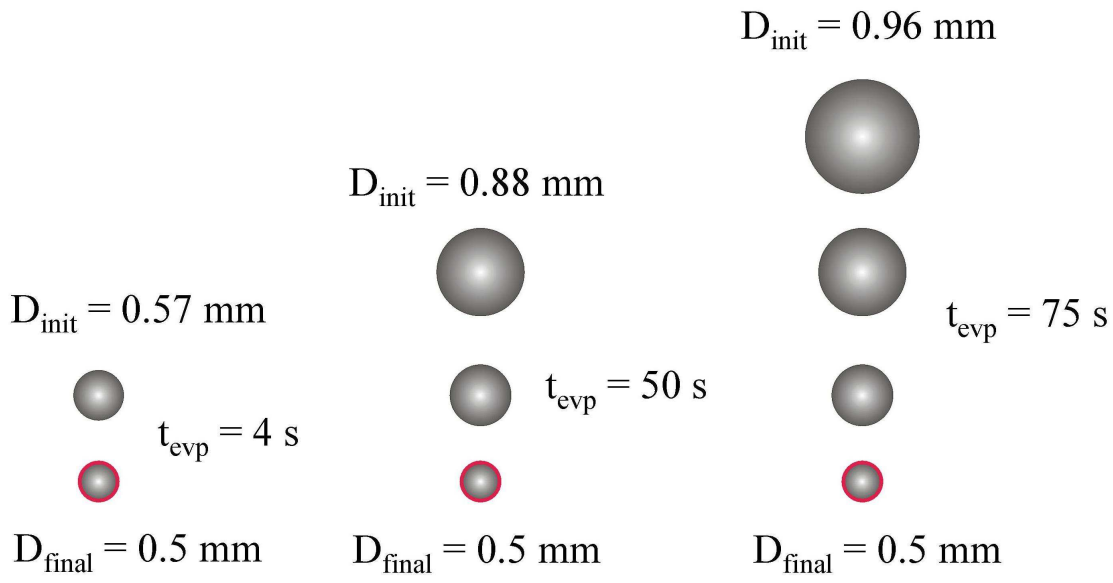

Fig. 5.8. Schematic showing development of droplets of a given size formed by evaporation in air from larger droplets. The indicated times (t_{evp}) are the values associated with evaporation of toluene/n-heptane mixture droplets from D_{init} to D_{final} = 0.5 mm

To measure the evaporation time (which may alternatively be considered the exposure time of the mixture to air), test droplets of a nominally equivolume toluene/heptane mixture were placed on a 14 μm diameter SiC fiber that had been twisted into a loop as schematically illustrated in Fig. 5.9. The time for the droplet to reach 0.5 mm was then recorded by digital video imaging using the same camera as described previously. Equation (5.A1) correlates the time (t_{evp}) of an (initially) equivolume heptane/iso-octane mixture droplet at D_o to evaporate down to 0.5 mm:

$$t_{evp} = 517.11 D_o - 777.55 D_o^2 + 447.1 D_o^3 - 93.803 \qquad (5.A1)$$

where 0.6 mm < D_o < 1 mm. At each value of t_{evp} given by Eq. (5.A1), the droplet concentration was measured by terminating the evaporation process by quickly inserting the droplet into an acetone carrier bath after which the composition was analyzed by a GC/MS.

Figure 5.10a shows representative data from this analysis for heptane/toluene mixtures. The initial state (t_{evp} = 0 s, D_o = 0.88 mm in this case) is the equivolume mixture. The two peaks represent toluene (larger) and heptane (smaller). Though there are heavier non-volatile impurities in the droplet (because the compositions were blended from supplies that contained on the order of 0.5% impurities), they do not show up on the scale of Fig. 5.10a. Figure 5.10b shows the composition change after t_{evp} = 50 s (i.e., corresponding to D_o = 0.79 mm). The different vertical scales are noteworthy. Comparing Figs. 5.10a and 5.10b, evaporation of the droplet (from 0.79 mm to 0.5 mm) has clearly enriched the droplet with toluene. This evaporation effect on droplet composition is far more complex for gasoline.

Figure 5.11 shows GC/MS traces for a gasoline droplet that evaporated down

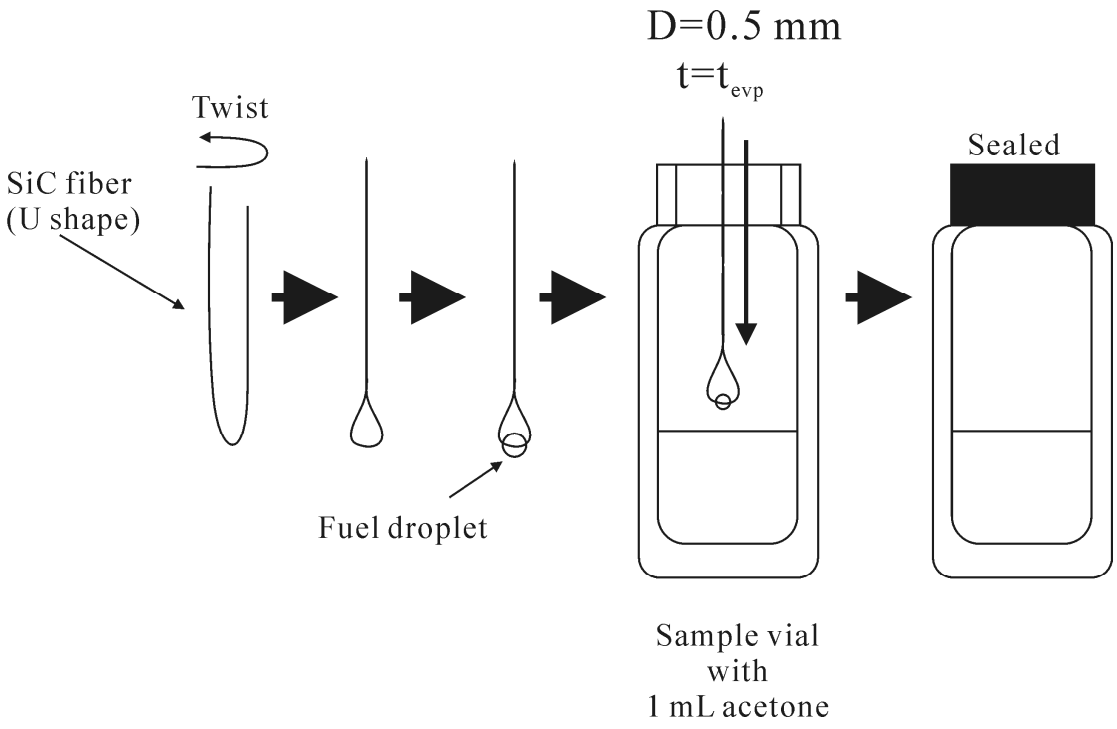

Fig. 5.9. Process for terminating the droplet evaporation process in air and preparation for GC/MS measurements by immersion of the droplet in an acetone bath.

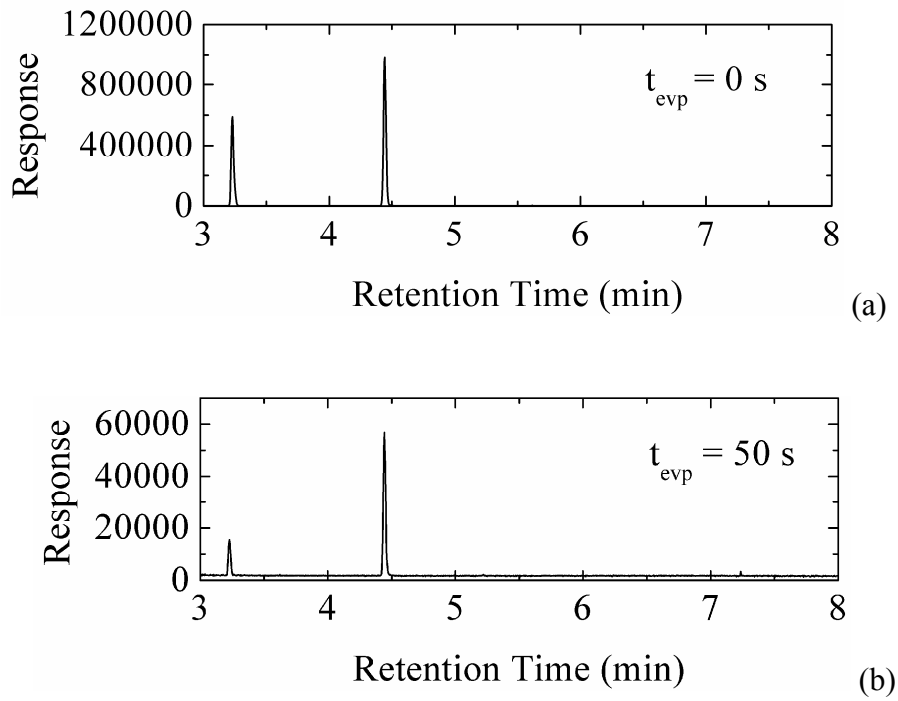

Fig. 5.10. GC/MS traces for a 0.5 mm diameter toluene/n-heptane mixture droplet prior to evaporation in air (a) initially (prior to exposure to air) and (b) after evaporation in air for 50 s. Note different abscissas in (a) and (b). The two peaks shown are for heptane (3.2 min) and toluene (4.4 min).

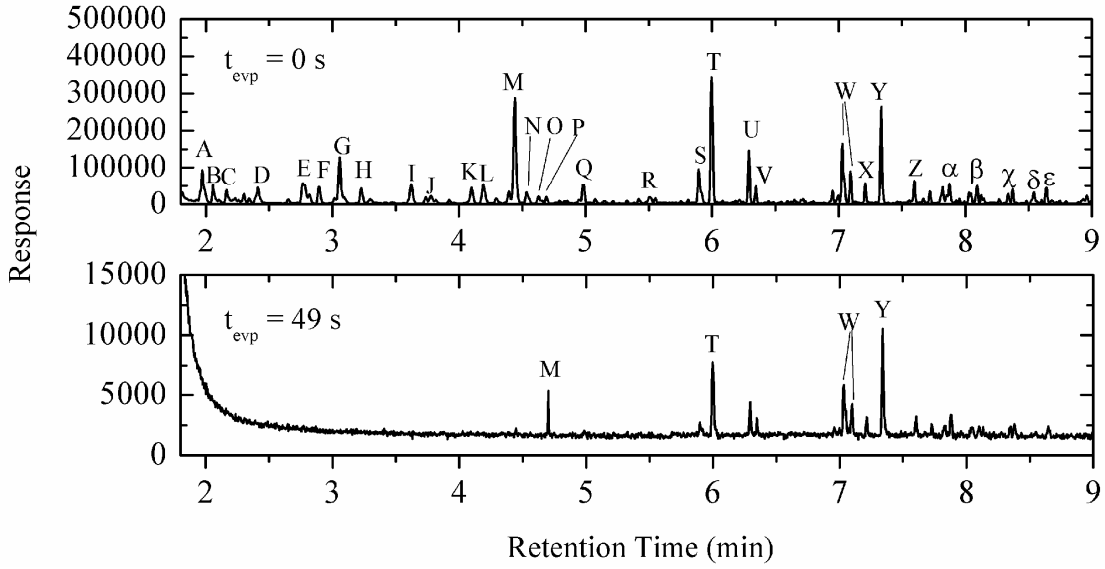

Fig. 5.11. GC/MS measurements for gasoline droplets (a) initially (prior to exposure to air) and (b) after evaporation in air for 49 s. Droplets were diluted with acetone prior to insertion in GC/MS. The peaks are as follows: A, 2-methylpentane; B, 3-methylpentane; C, hexane; D, methylcyclopentane, E, benzene; F, 3-methylhexane; G, iso-octane; H, heptane; I, methylcyclohexane; J, 2,4-dimethylhexane; K, 2,3,4-trimethylpentane; L, 3,3-dimethylhexane; M, toluene; N, 3-methylheptane; O, 1,3-dimethyl-cis-cyclohexane; P, 2,2,5-trimethylhexane; Q, octane; R, ethylcyclohexane; S, ethylbenzene; T, 1,3-dimethylbenzene; U, p-xylene; V, nonane; W, 1-ethyl-2-methyl-benzene; X, 1,2,3-trimethylbenzene; Y, 1,3,5-trimethylbenzene; Z: indane; α, 1-ethyl-3,5-dimethybenzene; β, 1-methyl-2-(1-methylethyl)benzene; χ, 1,2,4,5-tetramethylbenzene; δ, 1-methylindane; ε, 2-ethyl-1,4-dimethylbenzene.

to 0.5 mm from a larger size. The constituents are identified in the figure caption. After exposure to air for 49 s, many of the species initially present have virtually disappeared thereby reducing the highly multi-component nature of the gasoline blend to fewer constituents, primarily toluene, 1.3-dimethylbenzne, 1-ethyl-2-methylbenzene and 1,3,5-trimethylbenzene.

Figure 5.12 shows the variation of measured droplet composition with t_{evp} for heptane/toluene. The mixture is clearly enriched with toluene over time. Thus, for example, a droplet at 0.5 mm that is ignited after being exposed to air for 50 s would now contain approximately 76% toluene and 24% heptane.

The trends in Fig. 5.12 are predicted by considering the evaporation process as proceeding through steps in which an incremental mass of liquid, Δm, is removed from the droplet until the droplet reaches the final specified diameter (0.5 mm). This approach follows the modeling of evaporation of oil spills in ambient air (Okamoto et al. (2010)) though is less detailed than using more rigorous analyses of multi-component droplet evaporation (Law and Law (1982), Sazhin et al. (2010)).

The model is as follows. When a liquid shell of mass Δm surrounding a droplet evaporates, it is assumed to be transformed into a vapor shell of the same incremental mass with mole numbers such that $\Delta N_{1,2v} = \Delta N_{1,2L}$ where

$$\Delta N_{1,2L} = \frac{Y_{1,2}}{Y_1 W_1 + Y_2 W_2} \Delta m \qquad (5.A2)$$

The vapor shell is assumed to be in equilibrium with liquid of a composition that is created by removal of $\Delta N_{1,2L}$ moles, and a simplified vapor/liquid equilibrium relationship is assumed to apply,

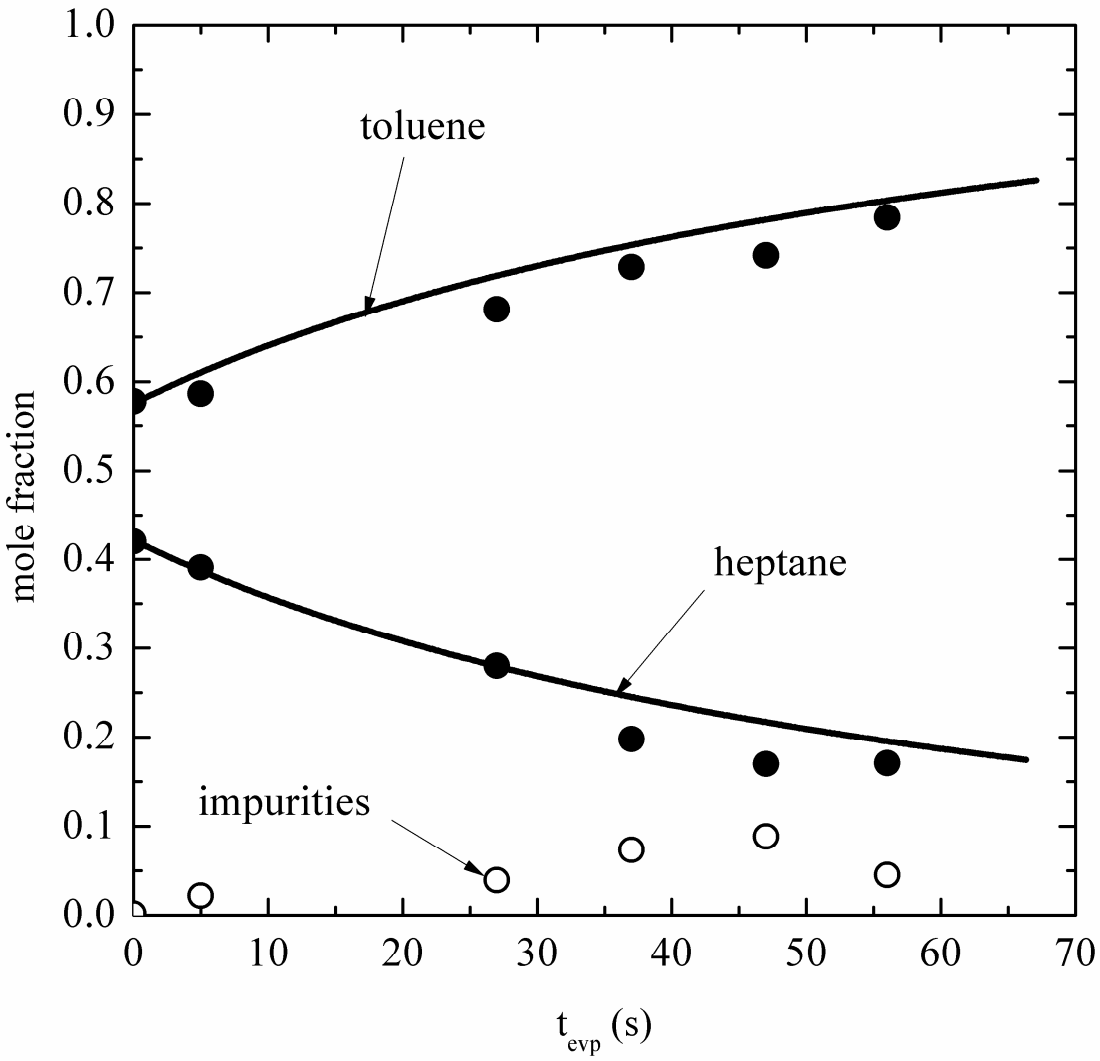

Fig. 5.12. Average concentrations of toluene/heptane mixture droplets after exposure to air for the indicated times (t_{evp}). Data points are measured by GC/MS and the theoretical curves are developed from formulations in Appendix 5A. All data are for droplet diameter D ≈ 0.5 mm.

$$Y_1 = \frac{P_{sat,1}\gamma_1 X_1}{P_{total}} \tag{5.A3}$$

$$Y_2 = \frac{P_{sat,2}\gamma_2 X_2}{P_{total}} \tag{5.A4}$$

where

$$X_1 = \frac{N_1}{N_1 + N_2} \tag{5.A5}$$

$$X_2 = 1 - X_1 \tag{5.A6}$$

The activity coefficients and Antoine constants in Eqs. (5.A3) and (5.A4) were obtained from Myers (1957) and Chien and Null (1972), respectively. P_{total} is the total vapor pressure (1 atm), and $P_{sat,1,2}$ are the saturation of vapor pressures of components 1 and 2). In the far field, the vapor composition will be different because of diffusion but the analysis concerns only the vapor in the immediate vicinity of the droplet surface.

The droplet size decreases incrementally from D_o by $N_{1,2L} - \Delta N_{1,2L}$ as Δm is progressively removed from the droplet. Time is brought into the problem when the droplet diameter reaches a specified diameter, here being 0.5 mm, when Eq. (5.A1) gives the corresponding t_{evp} for the chosen D_o.

In the analysis, $\Delta m = 10^{-7}$ g is much smaller than the mass of a 0.5 mm diameter droplet ($\sim 10^{-5}$ g). This stepwise mass removal process proceeds until the targeted final diameter is reached. At any step in the process,

$$N_{1,2} = \frac{\rho_{1,2} V_{1,2}}{W_{1,2}} \tag{5.A7}$$

where

$$V_{1,2} = \phi_{1,2} \times \frac{\pi(D)^3}{6} \tag{5.A8}$$

and

$$\phi_1 = \frac{X_1}{X_1 + \frac{\rho_1}{\rho_2}\frac{W_1}{W_2}(1 - X_1)} \tag{4.A9}$$

Figure 5.12 shows the variation of predicted toluene and heptane liquid mole fractions with t_{evp} (the corresponding value of D_o comes from Eq. (5.A1)). The agreement with the measured droplet composition is good, considering the simplicity of this model. The Matlab programs that produced the results in Fig. 5.12 are in Appendix F and G.

Figure 5.13 shows the evolution of diameter of gasoline droplets that illustrates the effect of air exposure prior to droplets being ignited. The times shown in the inset represent the period of the droplet on the fiber when it was evaporating in air prior to ignition. The initial diameter of the droplet ($t/D_o^2 = 0$) is also indicated. These initial diameters were the result of larger droplets on the fiber evaporating to the indicated size (Fig. 5.8) before being ignited. The principle differences in the evaporation time appear to reside in the droplet heating period. With prolonged devolitalization of the droplet by air exposure, the effect of heavier components left behind seems to increase the heating period. Once in the relatively steady burning period, there is a slight decrease of burning rate with increased waiting time. However, the gasoline burning rate seems not to be strongly affected by exposure to air in spite of the apparent removal of many constituents from the drop (see Fig. 5.11) at the times indicated in

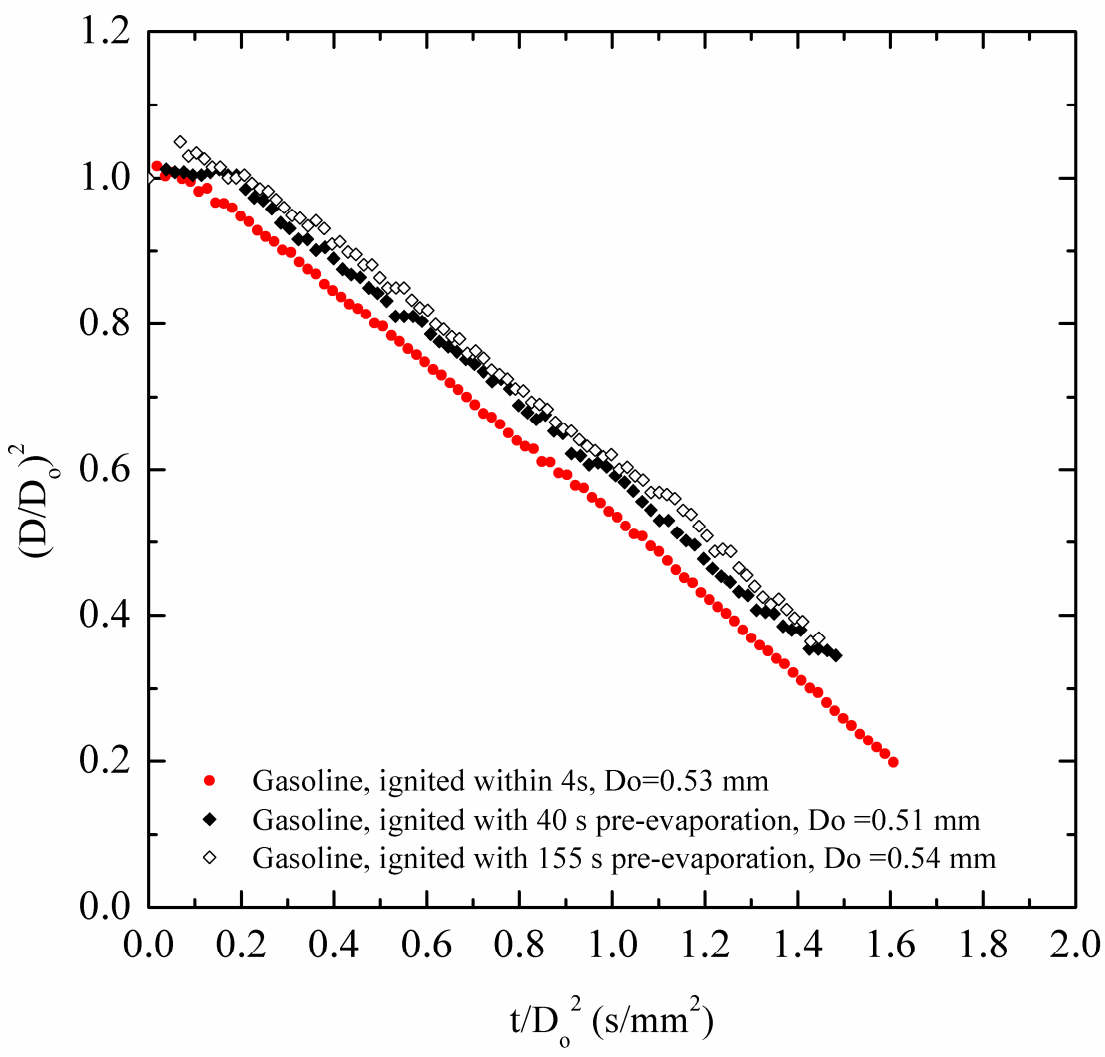

Fig. 5.13. Evolution of diameter of gasoline droplets showing influence of prior exposure to air at the indicated times (t_{evp}).

Fig. 5.13. The effect of pre-vaporization on the droplet composition and hence burning rate is, of course, tied to the thermal properties of the mixture constituents. The aggregate of these properties for gasoline is evident that after 155 s and the associated vaporization that occurs over that time, the droplet composition largely only effects the initial heating period.

Appendix 5B: Property Correlations

The property correlations used to estimate the parameters that factor into ξ for Eq. (5.2), namely the specific heats and thermal conductivities of the hydrocarbon gas, and the liquid densities at the hydrocarbon boiling points, are given in this appendix. The primary source for the correlations is Reid et al. (1987). In what follows, the subscript "i" denotes either heptane, iso-octane or toluene. Since the gas temperature varies over about a thousand degrees from the droplet surface to the flame, a mean temperature is needed to estimate the gas property since the interest is primarily to estimate ξ which comes from a constant property theory. We take the property temperature ($T_{p,i}$) to be

$$T_{p,i} = \frac{1}{3} T_{b,i} + \frac{2}{3} T_{f,i} \tag{5.B1}$$

as suggested in Glassman (1987). The flame temperature is not known so values between 1400 K and 2000 K were thought to be reasonable.

Once the hydrocarbon properties are evaluated, the gas specific heats and thermal conductivities were evaluated using simple mole fraction averages of the gas (assumed to be air) and fuel gas values as

$$k_g = x\, k_{g,i} + (1\text{-}x)\, k_{g,air} \tag{5.B2}$$

and

$$c_{pg} = x\, c_{pg,i} + (1\text{-}x)\, c_{p,air} \tag{5.B3}$$

where "x" is the fuel mole fraction. The linear relationship of Eqs. (5.B2) and (5.B3) are not generally valid. However, according to Law and Williams (1972) the approximation of Eq. (5.B2) allows Eq. (5.1) to predict burning rates. For present purposes we are only using Eq. (5.1) to explain qualitative trends. Furthermore, since the value of x in Eqs. (5.B2) and (5.B3) is not known (Law and Williams (1972) recommends 0.4 for Eq. (5.B2) and 1 for Eq. (5.B3)) it makes no sense to be more precise on mixing rules for gas property predictions when the assumptions of the classical droplet burning theory are questionable in the first place. As a result we evaluated properties over the range $0 < x < 1$.

For the hydrocarbon thermal conductivity (W/m-K), the Roy/Thodos method as recommended by Reid et al. (1987) is used:

$$k_{g,i} = \frac{1}{\Gamma_i}\left(8.757\left(e^{0.0464\,T_{r,i}} - e^{-0.0412\,T_{r,i}}\right) + C_i\, f_i\right) \tag{5.B4}$$

where

$$\Gamma_i = 210\left(\frac{T_{ci}\, W_i^{\,3}}{P_{ci}^{\,4}}\right)^{1/6}, \tag{5.B5}$$

and

$$T_{r,i} = \frac{T_{p,i}}{T_{c,i}}, \tag{5.B6}$$

For iso-octane and heptane,

$$f_i = -0.152T_{r,i} + 1.191T_{r,i}^2 - 0.039T_{r,i}^3 \quad (5.B7)$$

and for toluene,

$$f_i = -0.354T_{r,i} + 1.501T_{r,i}^2 - 0.147T_{r,i}^3. \quad (5.B8)$$

For heptane and toluene

$$C_i = 0.052W_i + 0.00182W_i^2 \quad (5.B9)$$

and for iso-octane, C_i=28.07.

For gas specific heat (J/kg-K) (Reid et al. (1987))

$$c_{pg,heptane} = (-5.146 + 0.6762T_{p,i} - 3.651\times10^{-4}T_{p,i}{}^2 + 7.658\times10^{-8}T_{p,i}{}^3)\frac{1000}{W_i}, \quad (5.B10)$$

$$c_{pg,iso-octane} = (-7.461 + 0.779T_{p,i} - 4.28\times10^{-4}T_{p,i}{}^2 + 9.17\times10^{-8}T_{p,i}{}^3)\frac{1000}{W_i}, \quad (5.B11)$$

and

$$c_{pg,toluene} = (-24.35 + 0.5125T_{p,i} - 2.765\times10^{-4}T_{p,i}{}^2 + 4.911\times10^{-8}T_{p,i}{}^3)\frac{1000}{W_i} \quad (5.B12)$$

The air specific heat (J/kg-K) and thermal conductivity (W/m-K) were computed from correlations developed from data reported in Incropera and DeWitt (2002),

$$c_{pg,air} = 860.68 + 0.04386T_{p,i} + 0.00022465T_{p,i}^2 + 6.2921\times10^{-8}T_{p,i}^3 \quad (5.B13)$$

and

$$k_{g,air} = 0.02408 + 2.7367\times10^{-5}T_{p,i} + 1.4866\times10^{-8}T_{p,i}^2 \quad (5.B14)$$

Liquid density (kg/m^3) at the normal boiling point (1 atm) was determined from the Tyn/Calus correlation (Reid et al (1987)),

$$\rho_{L,i}\,|_{boiling} = 3508.8\frac{W_i}{\upsilon_{c,i}^{1.048}} \quad (5.B15)$$

where $\upsilon_{c,i}$ is the molar volume (in cm^3/mole) at the critical point as determined from values listed in Reid et al. (1987). The above correlations were used to develop Fig. 5.5 from Eq. (5.2).

CHAPTER 6

BURNING CHARACTERISTICS OF A GASOLINE REFERENCE FUEL-INDOLENE AND COMMERCIAL UNLEADED GASOLINE[3]

6.1 Introduction

This chapter discusses the droplet combustion characteristics of indolene and a commercial 87 octane-rated (no ethanol) unleaded gasoline. The tractable flame and sooting dynamics of the spherical flame facilitate comparisons of the burning process while at the same time providing benchmark data that can be useful for model development. The initial droplet diameters ranged from 0.47 mm to 0.59 mm with an average of 0.53 ± 0.05 mm.

The indolene comes from Haltermann Solutions (Houston, TX, Federal Certification Fuel EPA TIER II EEE, HF437). The gasoline used in the experiments was an 87 octane rated unleaded gasoline with no ethanol. It was purchased from a local Mobil station in Ithaca, NY in November 2009. Selected properties for indolene and gasoline are listed in Table 6.1.

Indolene and gasoline were found to display remarkably similar droplet evaporation rates. However, the sooting dynamics were substantially different. Indolene droplets produced soot shells that were somewhat thicker, and which resided farther from the droplet surface, than the soot shells surrounding gasoline droplets. Furthermore, indolene flames were comparatively larger than gasoline flames. The highly multi-component nature of both fuels did not result in noticeable preferential

[3] This chapter comes from the following publication: Liu, Y.C., Savas, A.J., Avedisian, C.T., Energy & Fuels 26 (2012) 5740-5749.

vaporization effects in the evolution of droplet diameter. These results show that indolene replicates some, though not all, of the droplet combustion properties of commercial gasoline.

Table 6.1. Selected properties of indolene and gasoline.

	Indolene	Gasoline (87 octane)
Formula	$C_{9.97}H_{18.42}$[a]	$C_{8.26}H_{15.50}$[b]
ν_c[c]	14.578	12.135
H/C ratio[d]	1.847	1.877
W_F (g/mol)[e]	138.3	114.8
T_b (K)	303-474[f]	297-494[g]
ρ_L (kg/m^3)[h]	739	731
Anti-knocking index[i]	92.75	87
Quasi-steady burning rate K (mm^2/s)[j]	0.57	0.53

[a] calculated from the carbon and hydrogen ratio and carbon weight percent provided by Haltermann Solutions (2010).

[b] obtained from Turns (2006).

[c] $\nu_c = n + m/4$, where n and m come from the formula C_nH_m.

[d] H/C ratio = m/n, where n and m come from the formula C_nH_m.

[e] calculated from the formula.

[f] Haltermann Solutions (2010).

[g] Mobil Oil Corp (<http://ww2.ramapo.edu/libfiles/HR/Environmental_Health_and_Safety/MSDS/Facilities/Plumbing/gasoline.pdf>.)

[h] measured using a digital density meter (Mettler Toledo DA-100M) at 297.7 K.

[i] Anti-knocking Index(AKI) = (Research Octane Number(RON) + Motor Octane Number (MON))/2.

[j] Estimated using the method pertaining to the 4th order polynomial.

6.2 Results and Discussion

6.2.1 Photographic Observations

Figure 6.1 shows the evolution of flame images at 0.1 s intervals for gasoline and indolene droplets. The nearly spherical flames indicate that convection effects were reduced by burning the droplets in a low gravity environment while anchored to the SiC support fibers. The glowing protrusions seen on either side of the flames are a result of the interaction between the flames and SiC fibers.

As shown in Fig. 6.1, the flames are slightly elongated vertically, though the distortion is not especially pronounced. This effect can evidence motion of soot aggregates being restricted by the fiber while in the vertical direction they will be free-floating. As the flame luminosity is due to oxidation of soot, the soot and luminous zone are more able to move freely without a fiber influence, while in the horizontal direction the motion of the luminous zone is more restricted because aggregates cannot move as freely. This effect appears to result in a slightly non-spherical flame (luminous zone).

Also evident in Fig. 6.1 is that indolene flames appear larger and brighter than gasoline flames for similar initial droplet sizes. The flame brightness of the indolene flames persists for a longer period compared to gasoline flames owing to a longer period of soot oxidation.

Flame brightness provides a qualitative measure of the sooting propensity of fuels due to sensitivity of the eye to wavelengths in the visible region of the spectrum. On this basis, Fig. 6.1 would suggest that the brighter indolene flames have more soot

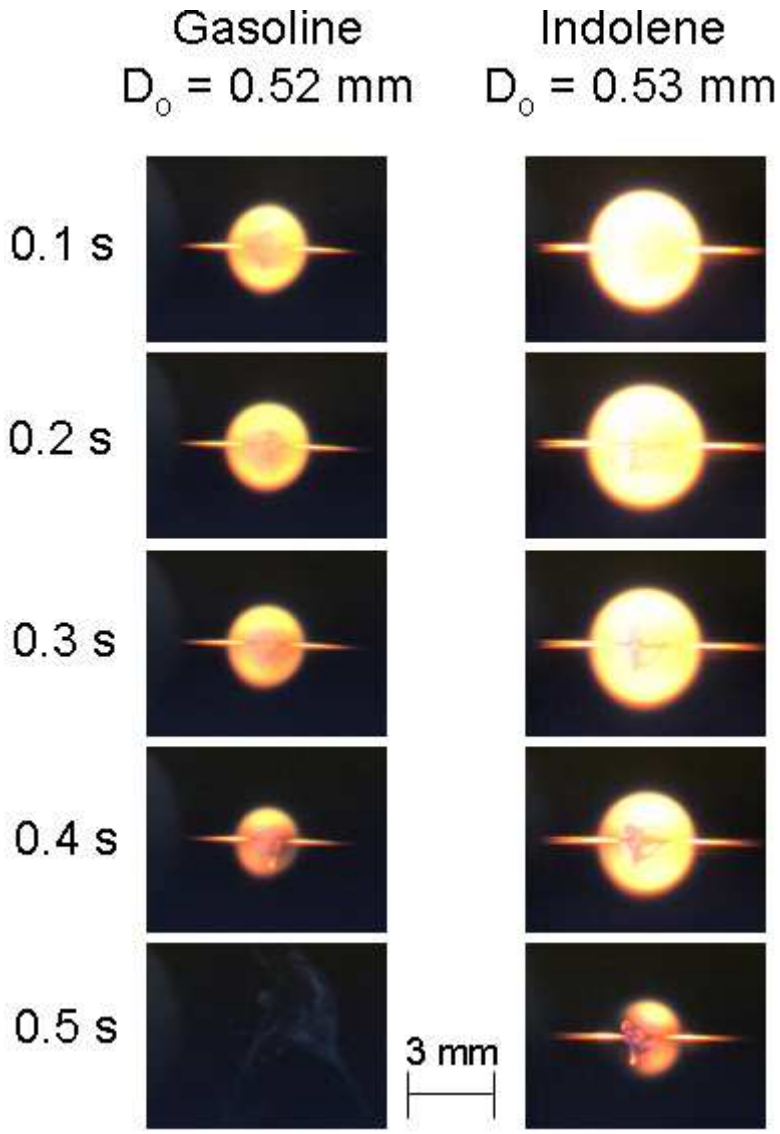

Fig. 6.1. Color images showing the evolution of spherical droplet flames for indolene and gasoline droplets.

formation compared to gasoline. This general trend is consistent with the backlit images shown in Fig. 6.2.

The series of photographs shown in Fig. 6.2 show the evolution of soot formation around gasoline and indolene droplets of similar initial droplet diameter. The soot shells are clearly visible and reside between the droplet and flame as expected (for the backlit image, the flame is not visible in the sequence of Fig. 6.2, as it will be well outside the sooting zone). Indolene droplets tend to form thicker soot shells in the early stages of burning than gasoline flames. Along with the qualitative results of Fig. 6.1, the soot shell images in Fig. 6.2 suggest that indolene is more sooting than gasoline.

The reason for differences of the sooting tendencies of gasoline and indolene is unclear, and hypotheses grounded in the qualitative nature of the experimental results presented in this study (i.e., Figs. 6.1 and 6.2) cannot offer definitive interpretations. Our speculation is that differing aromatic content in the fuels could be responsible for the differing sooting tendencies observed. The indolene examined in the present study had an aromatic (volume) concentration of 28% (Haltermann Solutions (2010). For the gasoline examined in this study, and given the time of year it was purchased, the aromatic content should be about 24% ("The Energy Future Coalition" (2006)). The slightly brighter indolene flames would be consistent with the slightly higher aromatic content of indolene compared to gasoline.

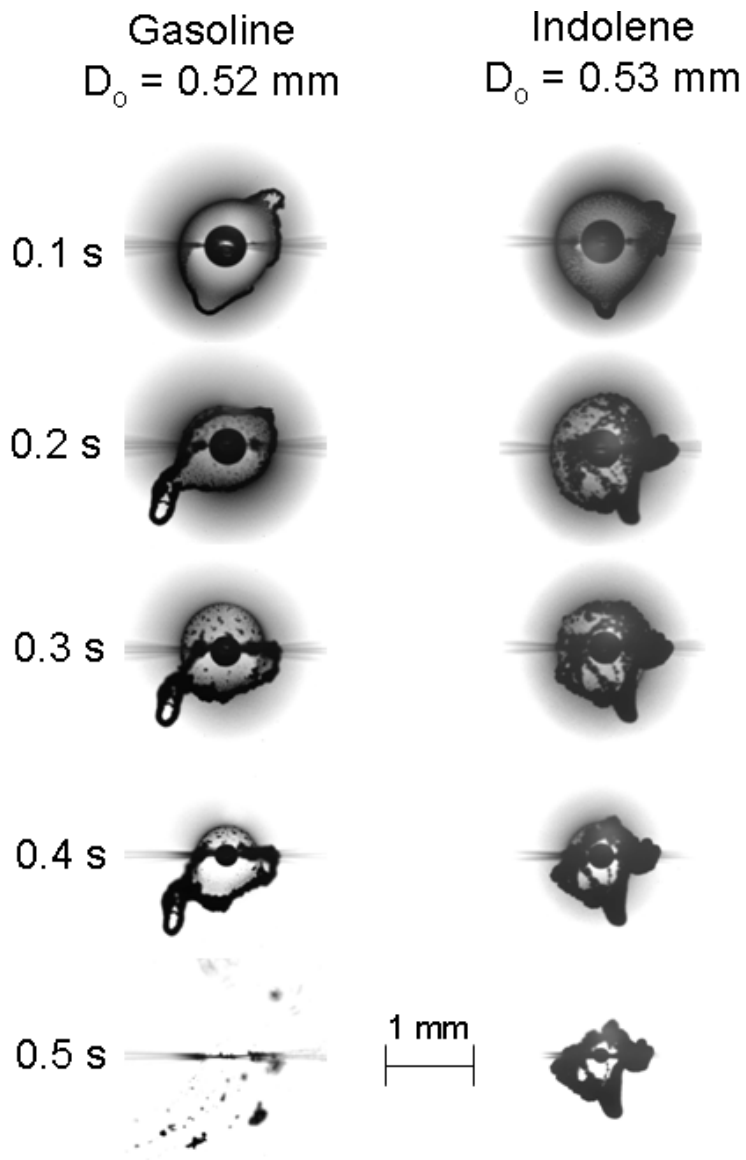

Fig. 6.2. Backlit BW images showing the evolution of droplet size and soot shell dynamics for indolene and gasoline droplets.

6.2.2 Quantitative Data

A quantitative comparison between the droplet, soot, and flame dynamics of gasoline and indolene is shown in this section. Measurements of the droplet diameters are shown using classical scaling from the D-squared law (Turns (2006)) (cf. Eq. (1.1)). The gasoline data shown in Fig. 6.3 are an average of 3 runs (Liu and Avedisian (2012)) and the indolene data are comprised of 4 separate runs. The initial fluctuations seen in the indolene data are from one run (D_o = 0.59 mm) during which the spark energy deformed the droplet at the onset of burning. Data within the first 0.2 s/mm^2 in this run are affected by this droplet deformation. However, this initial disturbance did not affect the remainder of burning, and the other three indolene runs do not have this initial disturbance from the spark.

It is clear that the evolution of droplet diameter for gasoline and indolene shown in Fig. 6.3 is remarkably similar. Figure 6.4 shows the averaged data which was computed by averaging the individual data of Fig. 6.3 at each specific time. The gap in the indolene data at the end (cf. Fig. 6.4) is due to the averaging process among the data sets. The overall trend is the same for both fuels, which is more easily seen by considering just the average data shown in Fig. 6.4. The data show that indolene is an excellent match for gasoline over the range 0.5 s/mm^2 $\leq t/D_o^2 \leq$ 1 s/mm^2, with slight deviations occurring at the beginning and end of burning.

A 6th order polynomial is fitted to the averaged data shown in Fig. 6.4 to give the evolution of burning rate, K (the derivative of the fit), shown in Fig. 6.5. Section 3.5 discusses the impact of using various orders of polynomials on analyzing this type of data. The evolutions of K for indolene and gasoline are nearly identical thus

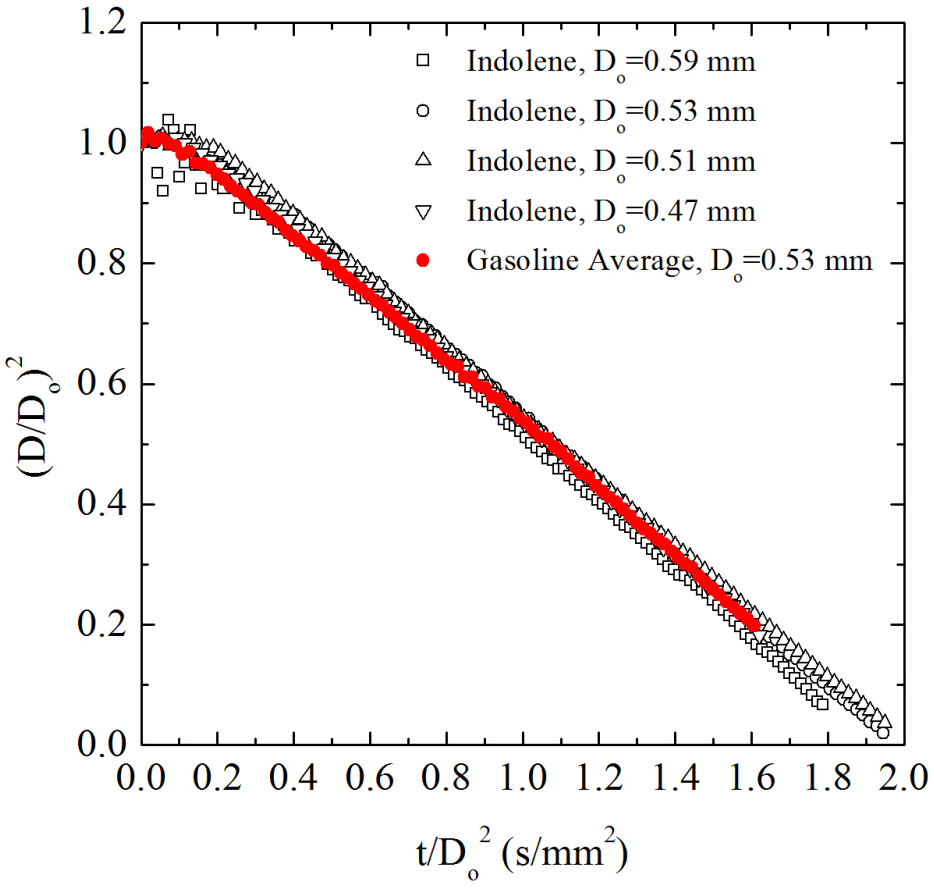

Fig. 6.3. Evolution of droplet diameters for indolene droplet combustion (black open symbols) compared with the averaged gasoline data from Chapter 5 (red data).

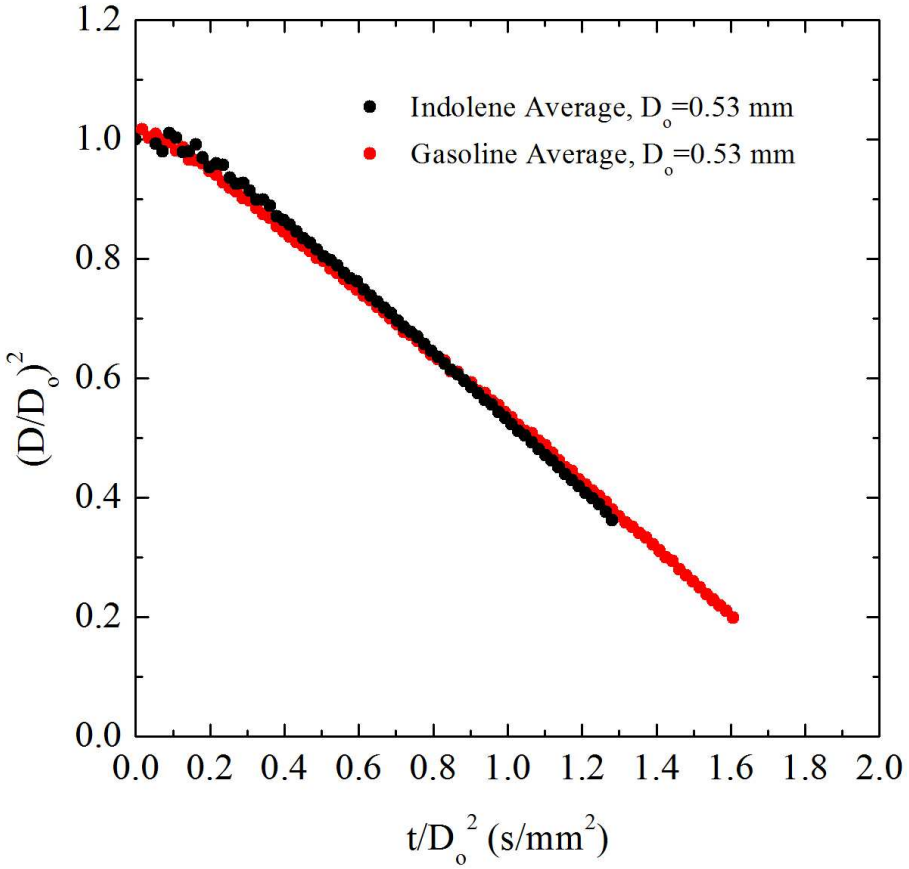

Fig. 6.4. Comparison of averaged droplet size evolution for indolene (black data) and gasoline (red data, from Chapter 5).

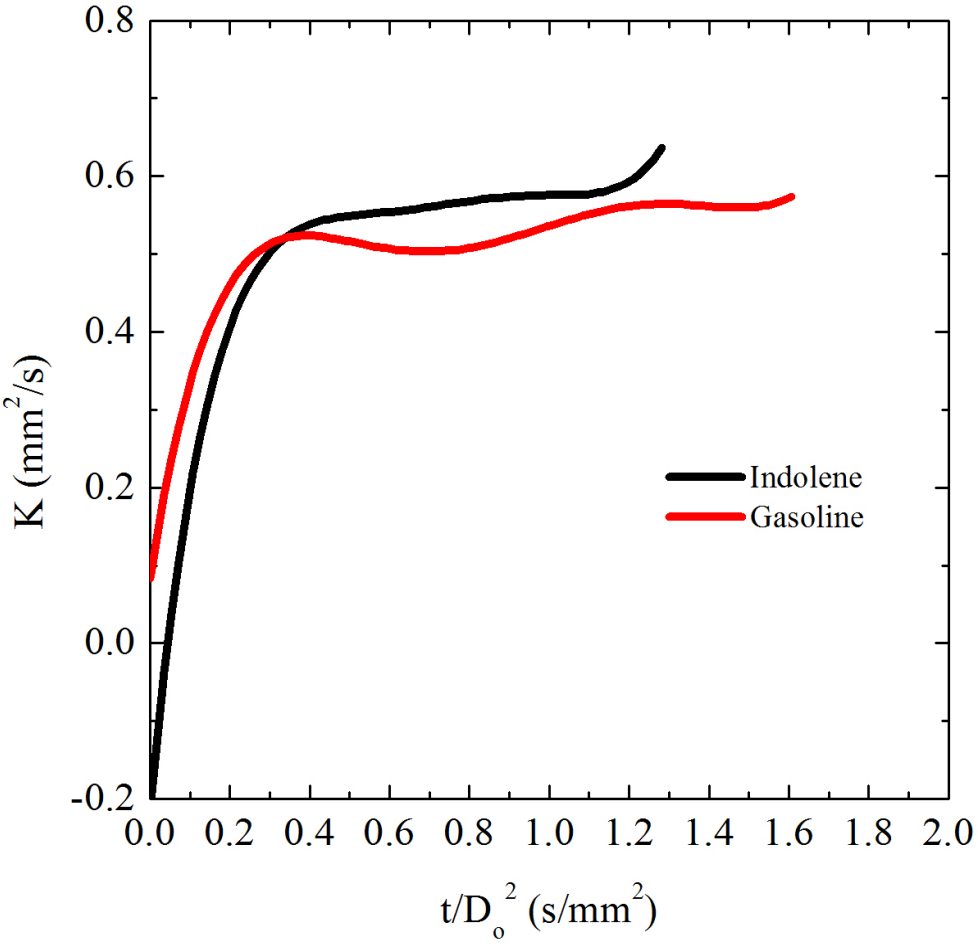

Fig. 6.5. Burning rate curves obtained from the first derivative of a 6th order polynomial fitted to indolene and gasoline (Chapter 5) data.

indicating that both fuels evaporate at almost the same rate during the combustion process. During the early stages of burning indolene appears to have a slightly lower burning rate compared to gasoline, though in fact the burning rates may be considered to be virtually identical within the precision of the data analysis process and photographic quality of the burning history that was recorded in the present investigation. A quasi-steady period is seen for 0.5 $s/mm^2 \leq t/D_o^2 \leq 1$ s/mm^2 as noted above where $K_{indolene} \sim K_{gasoline}$. The final slight increase in burning rate shown in Fig. 6.5 for indolene is most likely an artifact of the 6^{th} order polynomial fit of the data in Fig. 6.4 (see Section 3.5 for more details).

According to Eqs. (5.1) and (5.2) the quasi-steady burning rate is theoretically related to k_g, ρ_L, and c_{pg}. The compositions of indolene and gasoline include hydrocarbon components that have thermal properties which are not substantially different. According to Eq. (5.2), the most important liquid property is density. Since the densities of gasoline and indolene are close, similar burning rates will be expected which is consistent with Fig. 6.5.

The evolutions of flame and soot shell diameter are shown in Figs 6.6 and 6.7, respectively. The flame and soot stand-off ratios (FSR and SSR), defined as D_f/D and D_s/D, respectively, are instantaneous measures of how far the flame and soot shells are positioned from the droplets. Broadly noted, that $D_s/D < D_f/D$ is a consequence of soot forming on the fuel rich side of the flame (Jackson and Avedisian (1992), Avedisian (1997)). As shown in Figs. 6.6 and 6.7, indolene produces flames that are farther away from the droplet compared to gasoline droplet flames, which is consistent with Fig. 6.1 as discussed previously.

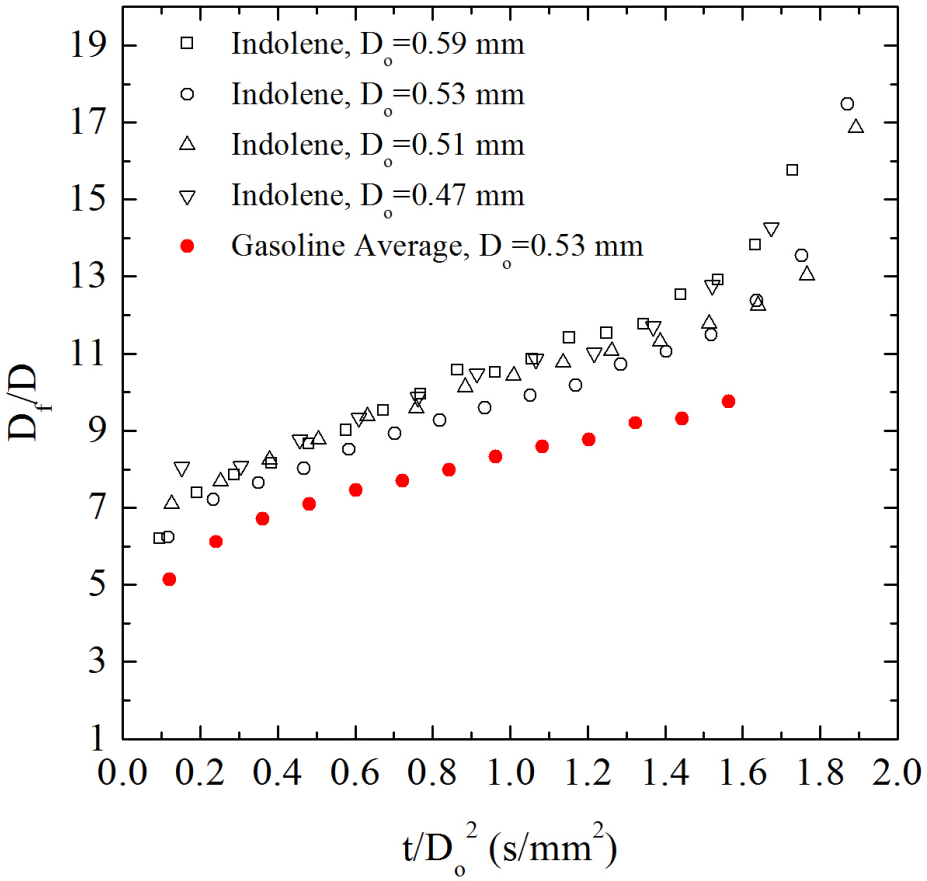

Fig. 6.6. Evolution of flame standoff ratio (FSR, D_f/D) for 4 runs of indolene compared with averaged gasoline data (Chapter 5).

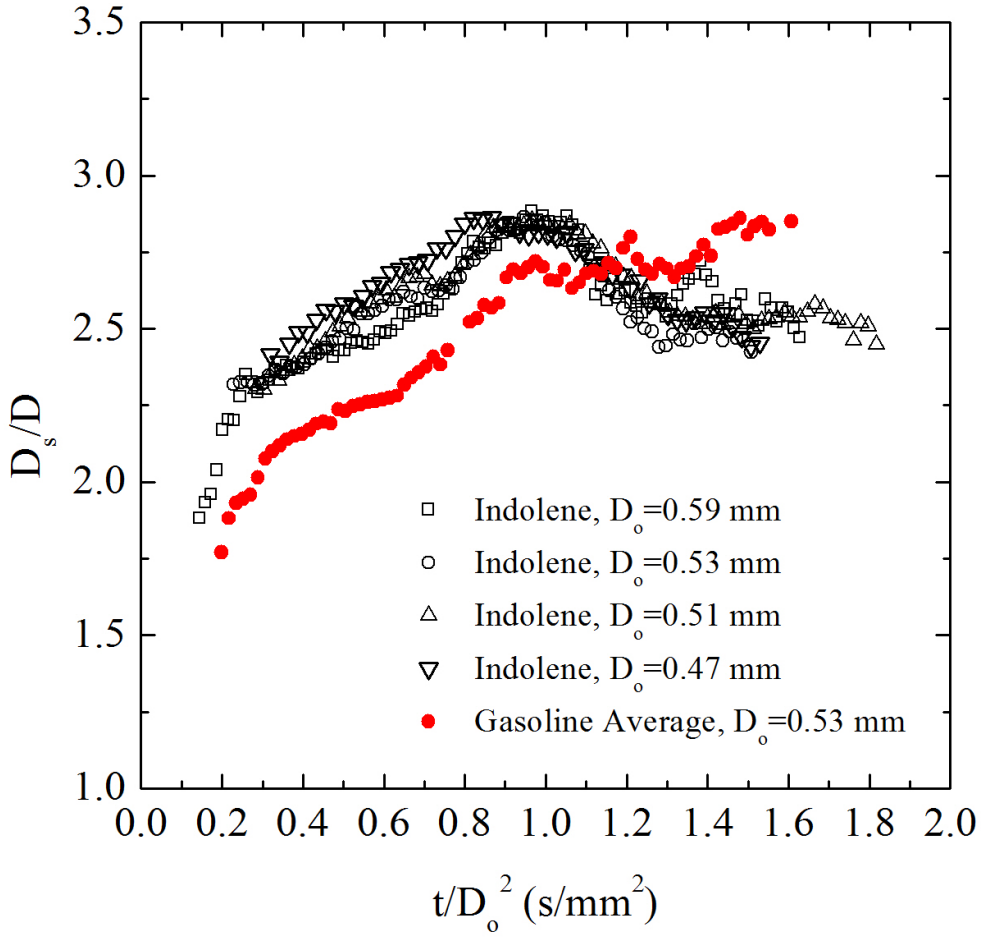

Fig. 6.7. Comparison of soot standoff ratio (SSR, D_s/D) for indolene and gasoline (Chapter 5).

The classical theory of FSR as extended by Aharon and Shaw (1997) results in relative flame position Θ as shown by Eq. (5.4). Values of ρ_L, K, ν_c, and W_F for both indolene and gasoline are provided in Table 6.1, we find that Θ~1.08. This result suggests that indolene should have a slightly higher FSR than gasoline which is consistent with Fig. 6.6, though the differences in Fig. 6.6 are much larger. This may be due to the approximate nature of the theory or uncertainties in estimating the variables for Eq. (5.4).

The SSR for indolene and gasoline are compared in Fig. 6.7. During the early stages of burning, indolene produces soot shells which are comparatively farther from the droplet surface than are gasoline soot shells. At approximately $t/D_o^2 = 1.1$ s/mm^2, the SSRs for the two fuels are equivalent. After this period, the soot shell produced by the indolene droplet is closer to the droplet than is the soot shell produced by the gasoline droplet. This is also seen in Fig. 6.2: between 0.1 s and 0.3 s, the soot shell surrounding the indolene droplet seems to be noticeably farther from the droplet than the soot shell for the gasoline droplet. However, after this point in time the soot shell around the indolene droplet is closer to the droplet, whereas the soot shell surrounding the gasoline droplet does not show this behavior.

It is interesting that the range of chemical compositions that comprise gasoline and indolene which might be expected to produce differing droplet burning characteristics, do not greatly affect all of the indolene and gasoline droplet combustion characteristics. Certainly, the evidence shows that the burning rates (Figs. 6.3-6.5) are not influenced by these compositional differences. However, the FSR and SSR data shown in Figs. 6.6 and 6.7 show differences that cannot be explained solely

on the basis of experimental uncertainty. The FSR is influenced by soot formation (through oxidation of the soot). A definitive explanation of the sooting characteristics of gasoline and indolene droplet flames awaits a more complete examination of soot formed in droplet flames.

6.3 Conclusions

Data are reported for the base case of droplet combustion with spherical symmetry for gasoline and indolene. Results show that some aspects of the combustion process are remarkably similar between the two fuels while others are different: 1) the evolution of droplet diameter (squared) and burning rate of indolene are very close to the commercial grade gasoline employed in the experiments; 2) indolene flames reside farther from the droplet surface than do the flames surrounding gasoline droplets for similar initial droplet diameters; and 3) indolene droplets have a slightly different soot shell dynamic than do gasoline droplets, with the soot shell of indolene droplets being comparatively farther from the droplet initially, then drawing closer to the droplet surface near the end of burning. As a final note, the configuration of spherically symmetric droplet burning is a useful canonical configuration to examine and compare the combustion characteristics of practical fuels.

CHAPTER 7

THREE AND FOUR COMPONENT MISCIBLE MIXTURES AS SURROGATES FOR JET-A[4]

7.1 Introduction

This chapter compares the droplet combustion characteristics of three and four component miscible liquid mixtures and compares the results with an aviation fuel (Jet-A) burning under the same conditions. The configuration used in the comparison is the base case of spherical symmetry whereby the droplet and flame are spherical and concentric. Mixtures consisting of n-decane/iso-octane/toluene (three component surrogate, 3CS) and n-dodecane/iso-octane/1,3,5-trimethylbenzene/n-propylbenzene (four component surrogate, 4CS) in specific molar ratios of 42.67/33.02/24.31 and 40.41/29.48/7.28/22.83, respectively, were previously shown to replicate certain gas phase combustion properties of Jet-A (e.g., ignition delay and extinction strain rate).

Table 7.1 lists representative properties for the surrogate components and their compositions. The lumped properties of surrogates are compared with Jet-A in Table 7.2. These specific blends are assessed here for their ability to replicate combustion properties derived from the spherically symmetric case. The data compared include the evolution of the droplet, flame and soot shell diameters. The initial droplet diameter was fixed at 0.56 ± 0.04 mm in the experiments and combustion was carried out in room temperature air under normal atmospheric pressure.

[4] This chapter comes from the following publication: Liu, Y.C., Savas, A.J., Avedisian, C.T., Proceedings of the Combustion Institute 34 (2013) 1569-1576.

Table 7.1. Selected properties of the pure components in the Jet-A surrogates investigated.

Fuel	Pure component	Formula	ρ_L[a] (g/cm^3)	W_F[b] (g/mol)	ν	T_b[b] (K)	Molar ratio[c]	Volume fraction (%)[d]
3 component surrogate	n-decane	$C_{10}H_{22}$	0.726	142.28	15.5	447.3	0.4267	50.86
	iso-octane	C_8H_{18}	0.688	114.23	12.5	372.4	0.3302	33.34
	toluene	C_7H_8	0.862	92.14	9.0	383.8	0.2431	15.80
4 component surrogate	n-dodecane	$C_{12}H_{26}$	0.745	170.34	18.5	489.5	0.4041	50.36
	iso-octane	C_8H_{18}	0.688	114.23	12.5	372.4	0.2948	26.67
	1,3,5-trimethylbenzene	C_9H_{12}	0.861	120.19	12.0	437.9	0.0728	5.54
	n-propylbenzene	C_9H_{12}	0.858	120.19	12.0	432.4	0.2283	17.43

[a] measured using a digital density meter (Mettler Todelo DA-100M) at 24.6°C.
[b] Reid et al. (1987).
[c] Dooley et al. (2010, 2012a).
[d] obtained from listed densities, molecular weights and molar ratios.

Table 7.2. Comparison of the averaged properties of the surrogates and Jet-A

Fuel	Formula	W_F (g/mol)	ρ_L[e] (g/cm^3)	T_b (K)	ν_c[g]	Δh_c (cal/g-mol)	h_{fg} (cal/g-mol)
3 component surrogate	$C_{8.61}H_{17.28}$[a]	120.83[b]	0.735	120.83[f]	12.93	1.35×10^{6} [h]	8381[j]
4 component surrogate	$C_{9.92}H_{19.43}$[a]	138.70[b]	0.756	138.70[f]	14.77	1.54×10^{6} [h]	9165[j]
Jet-A	$C_{10.17}H_{19.91}$[c]	142.01[c]	0.800	478-573[d]	15.14	1.46×10^{6} [i]	12219[k]

[a] calculated by given molar ratios and the corresponding formula of the constituents.
[b] calculated by taking a molar average on the W_F's for the constituents in Table 6.1.
[c] Dooley et al. (2010).
[d] Colket et al. (2007).
[e] measured using a digital density meter (Mettler Todelo DA-100M) at 24.6°C.
[f] average values by using the molar ratios and T_b's in Table 6.1.
[g] calculated by assuming complete combustion using the averaged chemical formula.
[h] calculated from the Δh_c found in The NIST WebBook (2011) for pure components.
[i] Specification: ASTM D-1655 Jet A, Laboratory Test Report, Department of the Air Force, DET 3, WR-ALC/AFTLA, Wright-Patterson AFB, OH 45433-7632.
[j] calculated from the ΔH_v found in Reid et al. (1987) for pure components.
[k] Polymeropoulos and Ochs (2004).

It was found that both blends do replicate certain features of the droplet burning process of Jet-A, though the four component blend performs slightly better. The 3CS replicated H/C ratio and DCN of Jet-A, but which did not match the MW and TSI. The 4CS matches all four combustion properties (DCN, H/C, MW, and TSI). The sooting propensity and soot standoff ratios are better replicated by the four component blend. Flame standoff ratios and burning rates show a conformance suggested by fuel property variations, and the liquid density is identified as a potentially important property in developing surrogate fuels. The results suggest the potential of combustion properties derived from spherically symmetric droplet combustion to assist with developing surrogates for complex transportation fuels.

7.2 Results and Discussions

Evolutions of the flame and soot structures along the combustion history for each fuel investigated in this study are shown in Fig. 7.1 and Fig. 7.2, respectively. As shown in Fig. 7.1, the flame has a yellow inner core with a dimmer blue zone at the outer periphery. The yellow inner core is a result of soot incandescence whereas the outer blue zone is indicative of CH emission. The two needle-like glows on the sides of the spherical flame are from the interaction of the flame and the supporting fibers.

Figure 7.1 qualitatively shows that Jet-A has the brightest flame among the three fuels. The brightness of the three component surrogate appears to be closer to Jet-A than the four component blend. However, the three component yellow core seems to diminish faster. A better comparison of the sooting tendencies is shown in Fig. 7.2 where the soot dynamics are clearly indicated. The soot aggregates form a

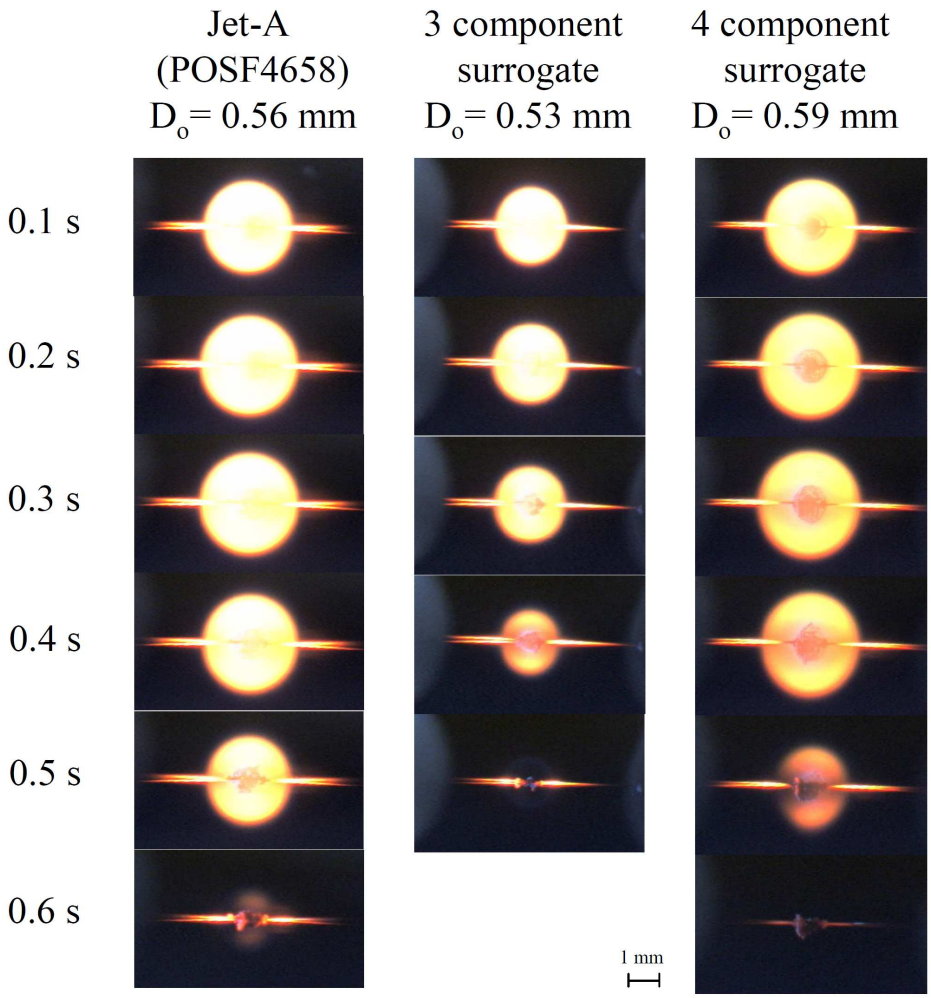

Fig. 7.1. Color flame images of Jet-A and the three and four component surrogates examined.

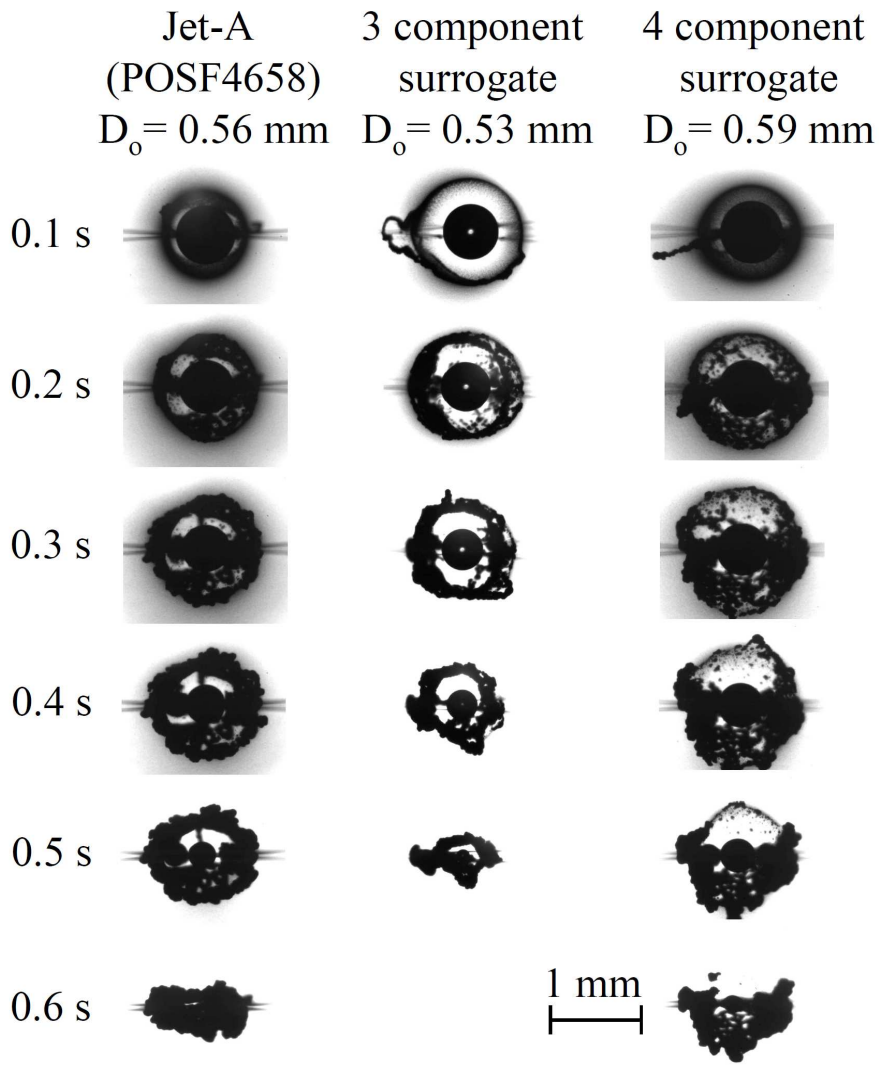

Fig. 7.2. Black and white images of Jet-A and the three and four component surrogates examined showing the evolution of the soot shell.

"shell" structure 0.1 s after ignition. The three component surrogate has a less dense soot shell compared to Jet-A or the four component blend. The four component soot configuration is (qualitatively) remarkably close to Jet-A, which is broadly consistent with this surrogate having matched the TSI of Jet-A (Dooley et al. (2012a)).

A more quantitative comparison of the surrogates with Jet-A is shown by the evolution of D, D_f and D_s presented in the form of the classical theory of droplet combustion (Turns (2006)), $(D/D_o)^2$, (D_f/D), and (D_s/D) with t/D_o^2. The evolution of droplet diameter is a macro-scale expression of how the constituents in a fuel droplet are preferentially vaporized and consumed by the combustion process, and the transient heat transfer associated with the thermal resistances across the liquid and vapor domains.

Figure 7.3 shows the evolution of averaged droplet size measurements made for the three fuels. For each fuel five individual experiments are used for the average. The error bars pertaining to Jet-A data show the standard deviation of the raw data from the five individual experiments. Error bars for the three and four component data are of very similar magnitudes to that of Jet-A. The three component surrogate (black open square) appears to have the shortest burning time, while the four component surrogate (blue solid square) appears to better replicate Jet-A's burning rate. Previous measurements for iso-octane and toluene (Liu and Avedisian (2012)) are also shown for comparison. The trend of the iso-octane data does not resemble either Jet-A or the four component data (nor was it expected to). Toluene is surprisingly close to Jet-A, but it is not suggested that toluene will be a good surrogate for Jet-A overall as it does not replicate other Jet-A targets and its combustion chemistry is different.

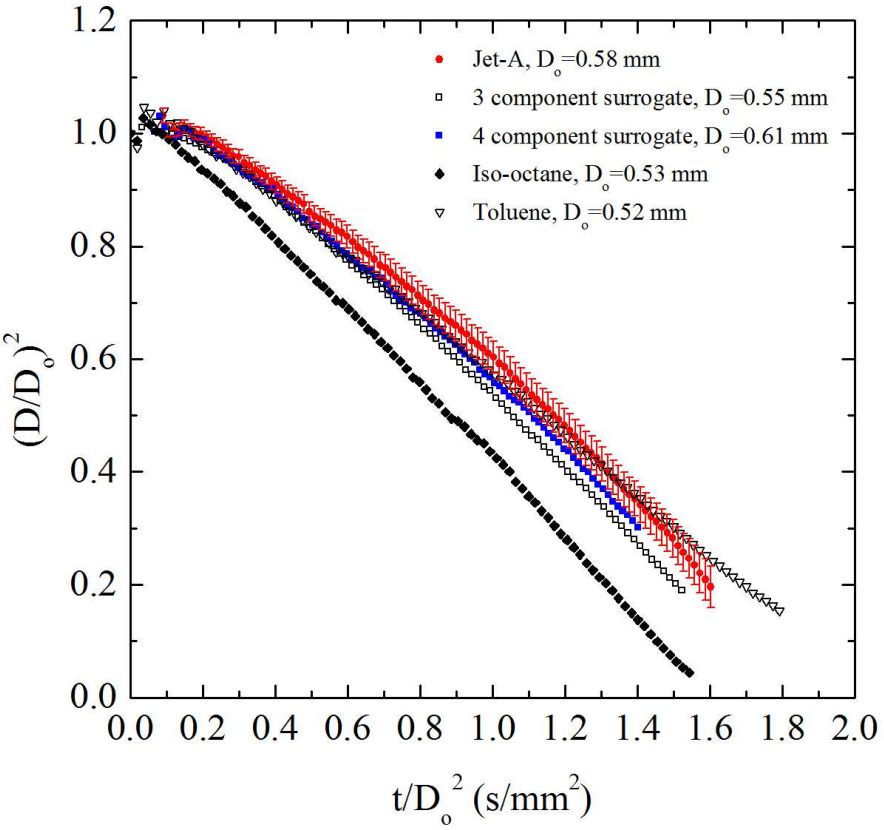

Fig. 7.3. Evolution of droplet diameters for Jet-A and the three and four component surrogates (averaged from five individual runs for each of the three fuels). Also shown are data from Chapter 5 for iso-octane and toluene for comparison.

Figure 7.4 compares the burning rates K, calculated from the first derivative of a 4^{th} order polynomial fit of the data shown in Fig. 7.3. This polynomial is chosen because it better represents the trend of the data compared to other orders. On average, the three component burning rates are close to Jet-A, though the four component blend does a slightly better job in the quasi-steady period, $0.6\ s/mm^2 \le \frac{t}{D_o^2} \le 1.1 s/mm^2$. A fairly large portion of the four component data is within the error bar range of Jet-A data whereas the burning rate of the three component surrogate is consistently higher than that of Jet-A until the very end of burning.

The evolution of flame and soot shell standoff ratios (D_f/D (the FSR) and D_s/D (SSR)) are shown in Fig. 7.5a. The data in Fig. 5a include five individual runs for each fuel. The FSRs of the surrogates are quite close to that of Jet-A, with the three component blend higher than Jet-A and the four component blend lower, though the four component blend appears to better match the Jet-A FSR.

The evolution of the SSR is shown in Fig. 7.5b in an expanded scale. The lines in Fig. 7.5b are included to suggest trends. Jet-A and the four component surrogate appear to have SSRs that follow the same trends as compared to the three component surrogate. The three component surrogate, which does not match Jet-A's TSI, has a much higher SSR from the beginning of burning and gradually crosses over Jet-A's SSR. In this respect, not only the sooting propensity of the four component blend is close to that of Jet-A (cf, Fig. 7.2) but the transport dynamics of the soot cloud appear to be better matched with the four component blend than the three component blend by the consistency of the trends shown in Fig. 7.5b for Jet-A and the four component blend.

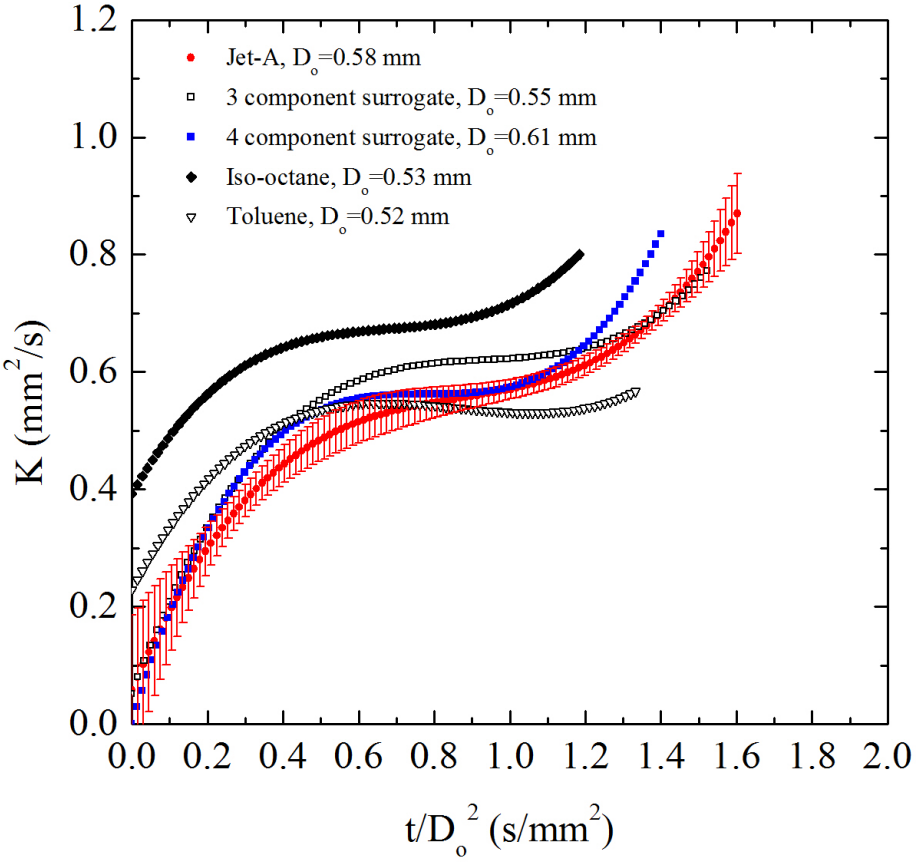

Fig. 7.4. Burning rates as computed from a 4th order polynomial of the data in Fig. 7.3.

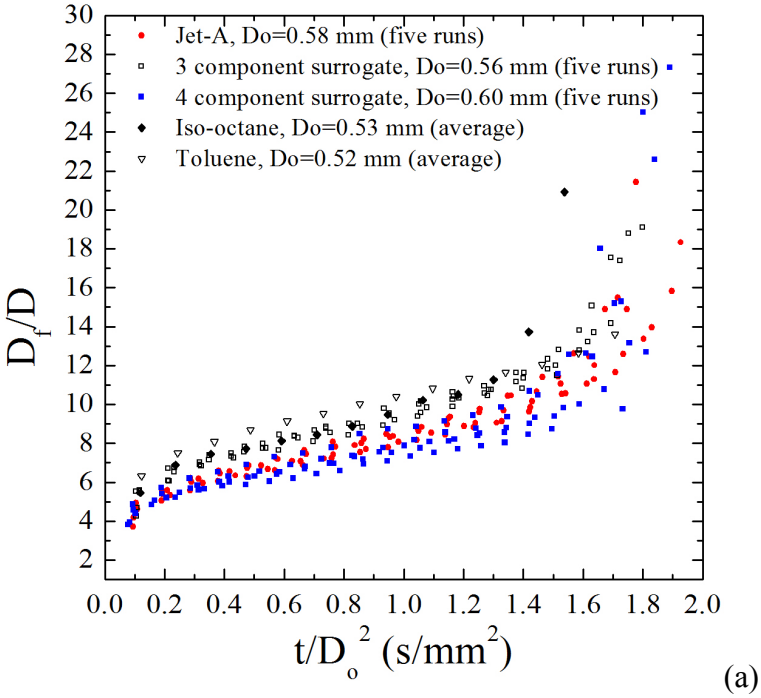

(a)

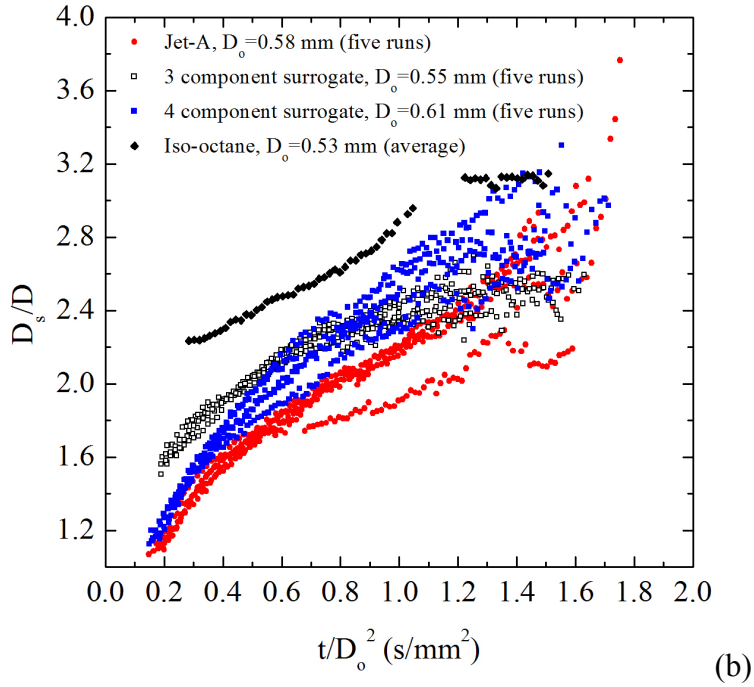

(b)

Fig. 7.5. (a) Evolution of FSR of the fuels investigated comparing to iso-octane and toluene (Chapter 5); (b) SSR for the fuels investigated comparing with iso-octane (Chapter 5).

A comprehensive theory of spherically symmetric droplet combustion of sooting fuel blends as complex as those examined here would be useful to further understand the present experimental trends. Work is being pursued along these lines (Marchese (1999), Kumar et al. (2002), Farouk and Dryer (2012a)). Some insights can be gained from the simpler classical theory (Turns (2006)) to identify important properties for developing surrogates that satisfy droplet flame combustion targets. For example, the variation of burning rate shows the importance of the liquid density, gas specific heat, and thermal conductivity, since $K \sim \frac{k_g}{\rho_L c_{pg}}$ (cf. Eqs. (5.1) and (5.2)) with density being a primary control variable. Similarly, the approximate theory of Aharon and Shaw (1997) shows that $\frac{FSR_{3,4}}{FSR_J} \sim \left(\frac{\rho_{L,3,4}}{\rho_{L,J}}\right)\left(\frac{K_{3,4}}{K_J}\right)\left(\frac{\nu_{3,4}}{\nu_J}\right)\left(\frac{W_{F,J}}{W_{F,3,4}}\right)$ (cf. Eqs. (5.3) and (5.4)) and liquid density is again seen as important (this FSR ratio is approximately unity when using mixture property estimates from Reid et al. (1987), which qualitatively agrees with Fig. 7.5a. Interestingly, molar averages of the densities in Table 7.2 for the three and four component surrogates show that $\rho_{L,3,4}$ and $\rho_{L,J}$ differ by less than 7%, though density was not among the targets used to develop these surrogates.

7.3 Conclusions

Combustion targets derived from the one-dimensional flames of spherically symmetric droplet burning suggest the usefulness of this burning configuration for developing surrogates for real fuels. The surrogates examined, which were developed from combustion properties of gaseous (pre-vaporized) fuels (Dooley et al. (2010, 2012a), capture several droplet combustion properties of Jet-A including the evolution

of droplet diameter, the flame standoff ratio and qualitative features of the sooting dynamics of Jet-A.

The four component surrogate which matches the TSI of Jet-A showed trends for the SSR more consistent with Jet-A throughout the burning process. This blend also had burning rates close to Jet-A in the quasi-period of burning. The SSR for the three component surrogate, which did not match the TSI or MW, exhibits a different trajectory with time. The FSRs for the three fuels were close to each other, with the four component surrogate closer to Jet-A than the three component blend. A simple scaling from the classical theory of droplet combustion is consistent with the trends of the experimental results. Liquid density may be a relevant target in developing surrogates for complex transportation fuels when the flame exists in the two-phase combustion zone.

The results also suggest the relevance of the base case for liquid fuel combustion of spherically symmetric droplet burning as a useful combustion configuration in the development and evaluation of surrogate fuels.

CHAPTER 8

JET-A AND BIO-FUELS DERIVED FROM CAMELINA AND TALLOW[5]

8.1 Introduction

This chapter compares the combustion characteristics of biofuels (or hydroprocessed renewable jet (HRJ)) derived from camelina (CHRJ (POSF6152)) and tallow (THRJ (POSF6308)) with a U.S. domestic aviation fuel (Jet-A, POSF4658) using the spherically symmetric (one-dimensional) droplet flame configuration as the basis of comparison. A blend of camelina biofuel and Jet-A is also examined. The initial droplet diameters were fixed at 0.57±0.03 mm. The biofuels studied have been considered as replacement fuels for conventional jet fuels.

Jet-A is the baseline aviation fuel against which comparisons of performance are made; CHRJ and THRJ were developed specifically for jet propulsion use; and an equal-volume mixture of Jet-A and CHRJ was examined because the equal-volume blend was previously employed in flight tests on production aircraft (Rahmes et al. (2009), Blackey et al. (2011)). The fuels compared in this chapter are all obtained from the Wright Patterson Air Force Base in Dayton, Ohio (USA). The Jet-A data from Chapter 7 are adapted in this chapter for the comparison with biofuels. Three repetitions were carried out for CHRJ and THRJ, and only one experiment is reported for the blend of Jet-A and CHRJ. Selected properties of these fuels are shown in Table 8.1.

Results show that the evolutions of droplet, flame, and soot shell diameters for Jet-A and the bio-fuels are very similar regardless of intrinsic compositional differences

[5] This chapter comes from the following publication: Liu, Y.C., Savas, A.J., Avedisian, C.T., Fuel 108 (2013) 824-832.

among the individual fuels. Sooting behaviors were noted to be different with Jet-A forming significantly thicker soot clouds, most likely due to its higher aromatic content compared to biofuels. The broad similarities shown in this study were consistent with results reported in the literature for performance of the same fuel systems in actual turbine and flight tests where the fuel blends examined were noted to yield essentially indistinguishable differences in overall performance. The results suggest value to the spherical droplet flame configuration to assess performance of real fuels burning under far more complex transport conditions.

Table 8.1. Selective properties of the Jet-A, CHRJ, and THRJ.

	Jet-A (POSF4658)	CHRJ (POSF6152)	THRJ (POSF6308)
Formula	$C_{10.17}H_{19.91}$[a]	$C_{11.27}H_{24.446}$[b]	$C_{12.271}H_{26.412}$[b]
W_F (g/mole)	142[a]	160[b]	174[b]
ρ_L (kg/m^3) @ 24.6 ^oC[c]	800	743	750
$c_{p,L}$ (KJ/kgK)[d]	1.955	2.034	1.978
k_L (W/mK)[d]	0.096	~0.108	~0.124
T_b (^oC)	205-300[f]	151-259[g]	165-255[g]
T_{freeze} (^oC)	<-40[f]	<-77[g]	-62[g]
T_{flash} (^oC)	>38[f]	43[g]	55[g]
Smoke point (mm)[g]	>19	50	>40
H/C ratio[b]	1.957[a]	2.169	2.152
ν_c[e]	15.15	17.38	18.87
Δh_c (MJ/kg)[b]	42.8	44.3	44.1

[a] Dooley et al. (2010).
[b] Hui et al. (2012).
[c] measured using a digital density meter (Toledo Mettler DA-100).
[d] from Bessee et al. (2011) using the value evaluated at 25 ^oC.
[e] calculated from the molecular formula by assuming complete combustion.
[f] Colket et al. (2007).
[g] Corporan et al. (2011).

8.2 Results and Discussions

8.2.1 Flame Structure and Sooting Dynamics

Figure 8.1 compares the flame structures for the HRJs examined with the Jet-A observations from Chapter 7. The times are referenced to the approximate ignition point. The flames consist of the typical inner yellow core enclosed by an outer blue zone. The yellow zone is indicative of incandescence of soot aggregates that reside between the droplet and flame. The two horizontal needle-like glows in each of the images are due to interactions between the flame and support fibers. It is evident that Jet-A droplets have the brightest flames. This effect is consistent with the high aromatic content of Jet-A as noted previously. The HRJs do show some luminosity, though, as they contain soot-producing components (e.g., iso-paraffins). Flames for CHRJ are slightly brighter than THRJ, which is consistent with the fact that CHRJ is comprised of 10% cyclo-paraffins while THRJ has only 2%.

The sooting dynamics are clearly shown in the backlit images of Fig. 8.2. The fiber supports somewhat influence the aggregation, coagulation, and symmetry of the soot shells (cf. Fig. 8.2, note the lower hemisphere of CHRJ and THRJ at 0.2 s and 0.4 s). However, the effect is not as dramatic as for droplets attached to the end of single fibers with much larger fiber diameters (Avedisian and Jackson (2000)).

It is seen that Jet-A forms thicker soot clouds compared to the equal-volume blend or the neat HRJs, which is believed to be due to Jet-A's higher aromatic content as noted previously. With thick soot shells and brighter flames, a droplet can become obscured which will challenge the ability to measure the droplet diameter (D in Fig. 1.2). The lower sooting propensities for the HRJs shown in Fig. 8.2 better reveal the

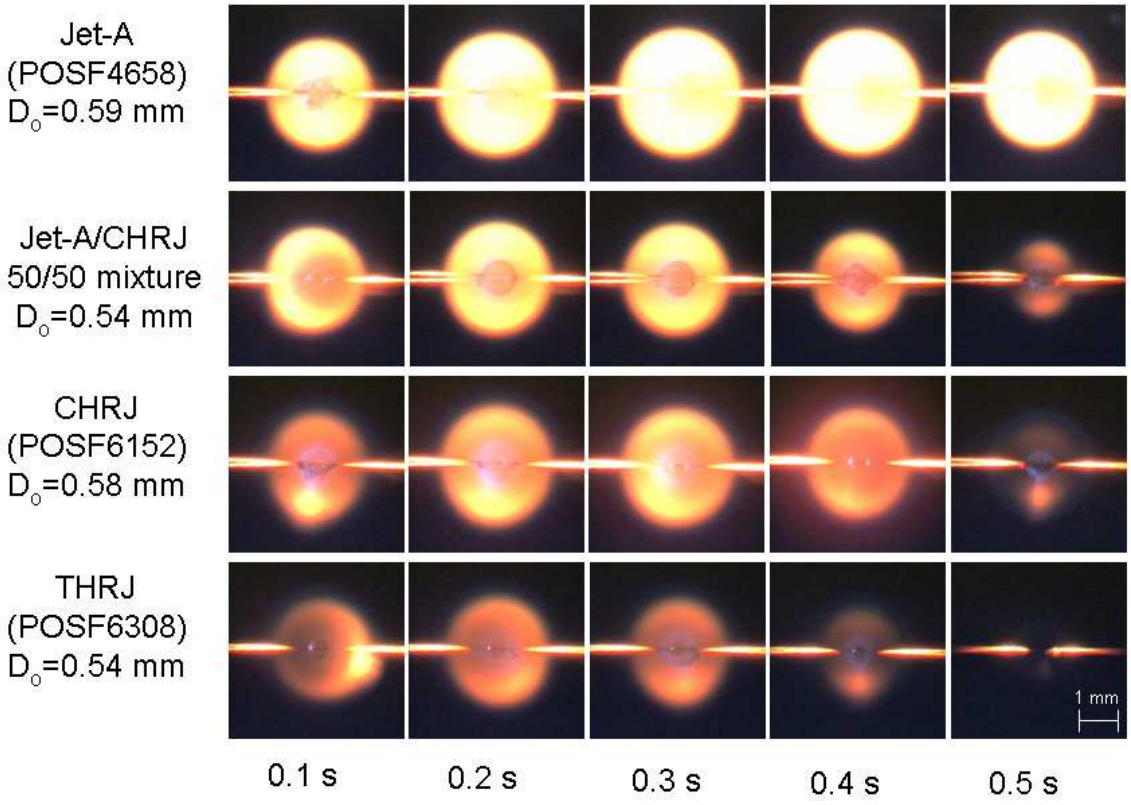

Fig. 8.1. Selected color images showing evolutions of outer appearances of spherical droplet flames for Jet-A (POSF4658) (from Chapter 7), CHRJ (POSF6152), THRJ (POSF6308), and an equal-volume blend.

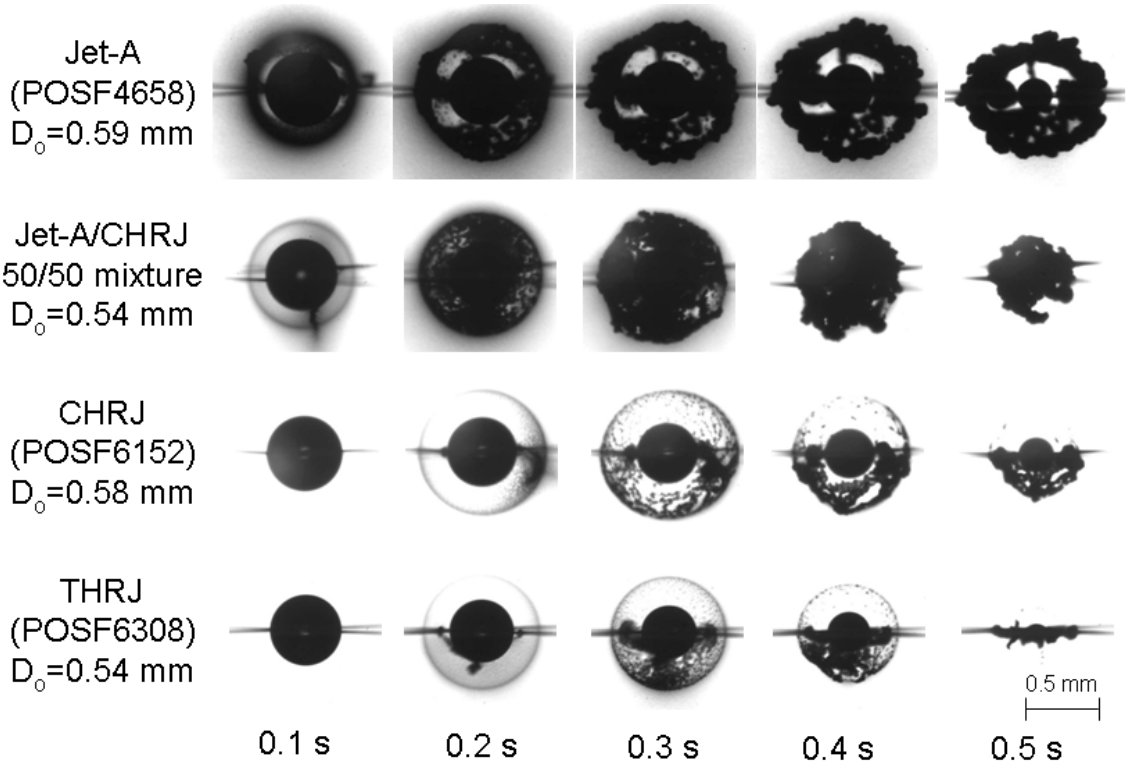

Fig. 8.2. Selected BW images showing evolutions of soot structures in the spherically symmetric flames of Jet-A (POSF4658) (from Chapter 7), the mixture of Jet-A and CHRJ, CHRJ (POSF6152), and THRJ (POSF6308).

evolution of the soot shell that is idealized in Fig. 1.2. Comparisons of sooting propensities for Jet-A and HRJs are found to be qualitatively consistent with the smoke point values provided in Table 8.1 (higher smoke points correspond to lower sooting propensities).

8.2.2 Quantitative Data

The evolution of the droplet diameter is a measure of how fast a liquid fuel is consumed (i.e., its "evaporation" or "burning" rate). The burning rate is an important parameter that characterizes performance of a fuel in a practical engine environment. For the spherically symmetric case, the burning rate is a limit parameter to which the effect of convection must revert when convection effects are eliminated. The influence of the complex swirling and turbulent motion typical of a real engine environment is completely absent under the conditions of the present study which is the base case for liquid fuel burning.

Longstanding theories of droplet burning for the simplified situation shown in Fig. 1.2 related the burning rate, K, to the evolution of droplet diameter, D (or more accurately stated D^2) as (Sirignano (1999), Turns (2006)) (cf. Eq. (1.1)). Figure 8.3 displays all of the measurements of droplet diameter in the coordinates of Eq. (1.1). The HRJs are very close to one another and suggest no substantive differences in burning rates between CHRJ and THRJ. The Jet-A measurements show a slightly slower burning process for some of the runs for this fuel. The lack of data (after $t/D_o^2 = 0.8$ (s/mm^2)) for the one run of the equal-volume mixture (green stars) arises because most of the droplet boundary was obscured by the surrounding thick soot shell in this

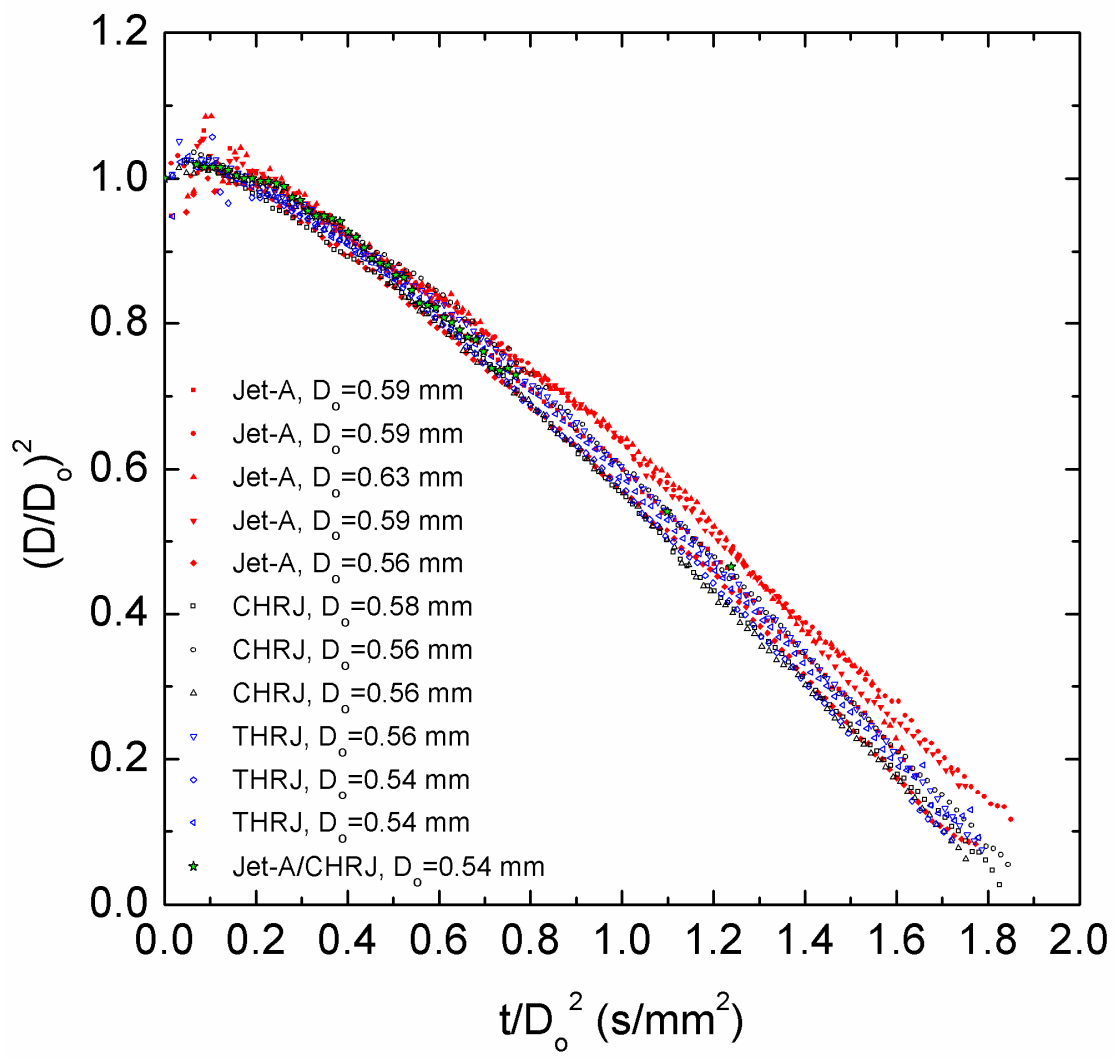

Fig. 8.3. Evolution of measured droplet size (D^2 plot) during combustion for the fuels investigated in this study. This plot includes data from all the individual experiments.

particular experiment.

Figure 8.4 more clearly compares the HRJs examined with Jet-A with the data averaged from Fig. 8.3. No significant differences in the evolution of D^2 over the first 0.8 s/mm^2 are noted. The data for CHRJ and THRJ almost align perfectly throughout the entire combustion process. And for the Jet-A/CHRJ blend the data are almost coincident with Jet-A, indicating that adding HRJ to Jet-A does not appreciably alter the evolution of $(D/D_o)^2$. There are, however, differences in sooting dynamics as noted previously (Fig. 8.2). This may suggest that the formation of soot itself might not exert a strong influence on the thermal and chemical effects on which the evaporation rate depends. Further work is needed to better understand this effect.

Figure 8.5 compares the burning rates among the fuels examined. The data of Fig. 8.5 are correlated with a fourth order polynomial fit from which the derivative is taken to obtain the burning rate (other polynomial fits to data like those shown in Fig. 8.4 have been considered (cf. Section 3.5). The conformance of the burning rates over most of the burning history is evident. The burning rates initially increase during the transient droplet heating process ($t/D_o^2 < 0.8$ (s/mm^2)), then appear to reach a quasi-steady value between 0.8 s/mm^2 $< t/D_o^2 <$1.2 s/mm^2 for each fuel where they are relatively constant. That the burning rates of CHRJ and THRJ are quite close is consistent with their compositions being similar. Interestingly, the burning rate of Jet-A is close to the HRJs during the initial droplet heating period but is noticeably lower in the quasi-steady period. Compounds in Jet-A with higher boiling points (e.g., aromatics or paraffins with large molecular weights) can lead to lower burning rates.

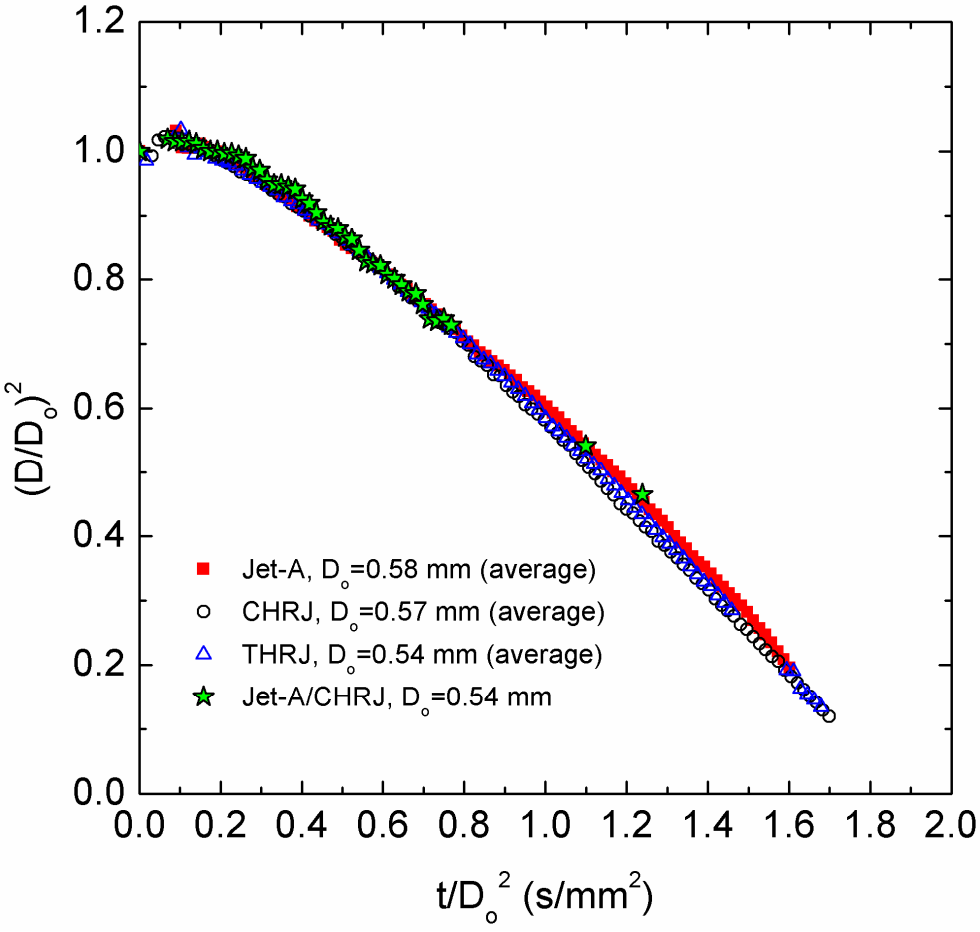

Fig. 8.4. Evolution of averaged D^2 data from Fig. 8.3 for each fuel.

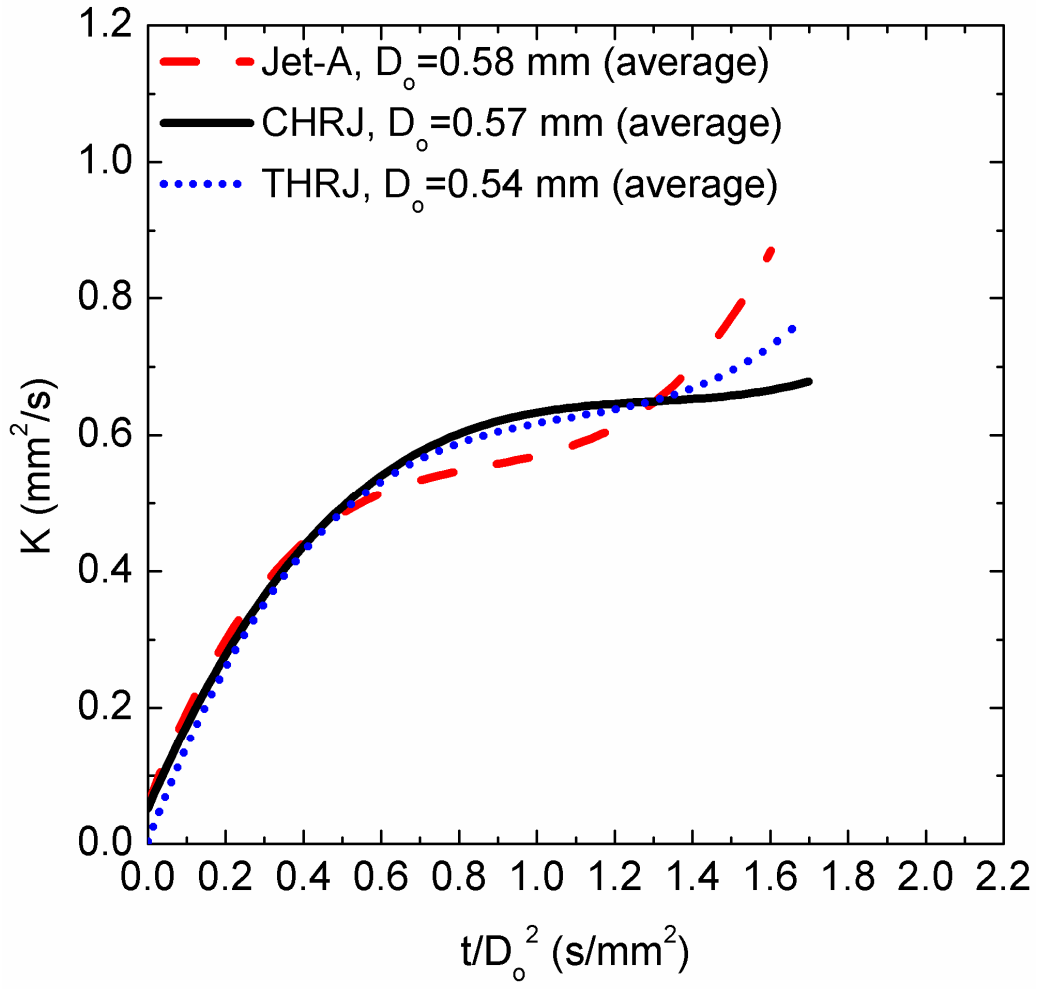

Fig. 8.5. Evolution of burning rate K (mm^2/s) calculated by taking the derivative of a 4th order polynomial fitted to the averaged D^2 data shown in Fig. 8.4.

Figure 8.6 shows evolutions of flame diameters for the fuels investigated. The measurements are scaled with the instantaneous droplet diameter to give a "flame standoff ratio", FSR = D_f/D, which is a measure of the relative position of the flame to the droplet. The classical theory of droplet burning (Sirignano (1999), Turns (2006)) shows that D_f/D should be constant. This is clearly not the case for the data in Fig. 8.6, which reflects an unsteadiness in the burning process that is persistent throughout the burning history. The relative position of the flame to the droplet surface is reasonably close for Jet-A and the biofuels examined, reflecting a thermo/chemical dynamic that is consistent with the conformance of burning rates noted previously (cf. Figs. 8.4 and 8.5).

The relative position of the soot shell to the droplet surface (D_s/D), or the "soot standoff ratio" (SSR), is shown in Fig. 8.7. The SSR is the most difficult quantity to measure especially when the aggregates form thick soot shells (cf. Fig. 8.2). Given this fact, the SSR data in Fig. 8.7 suggest a similar relative position of the soot cloud to the droplet surface. The SSR trends are reasonably close for $t/D_o^2 < 0.9$ s/mm^2, and the SSR for the Jet-A/CHRJ blend is between that of Jet-A and CHRJ reflecting a dilution effect. Near the end of burning it is more challenging to assume a definite geometrical shape to the soot cloud because of the thickening of the cloud and coagulation of aggregates into a contiguous and self-supported structure that is less influenced by the forces acting on the aggregates. Nonetheless, the broad trends for the fuels examined are consistent with each other later in the burning process.

Figure 8.8 shows a bubble inside of a THRJ droplet at 0.45s and 0.46s. At 0.47s, the droplet diameter is noticeably smaller suggesting a sudden escape of the bubble

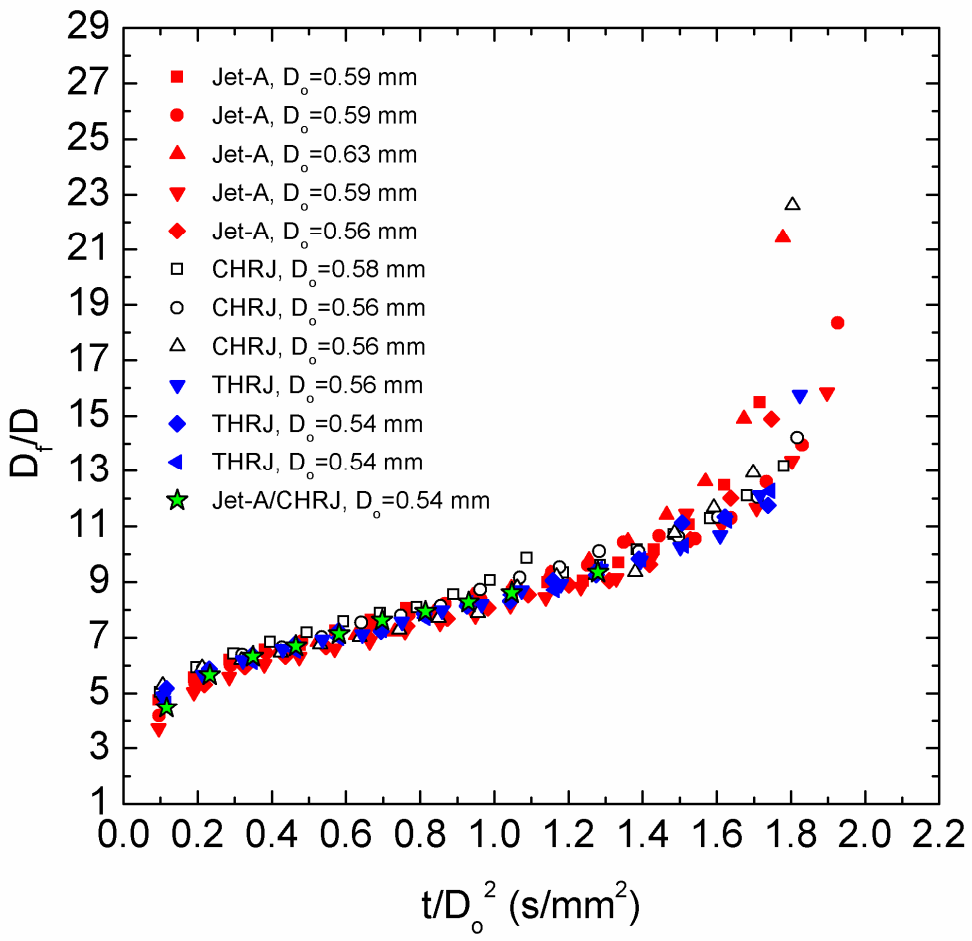

Fig. 8.6. Evolution of flame standoff ratio (FSR = D_f/D) for all the fuels investigated in this study. The arrow indicates expansion of the flame owing to a bubble nucleation event for one of the runs.

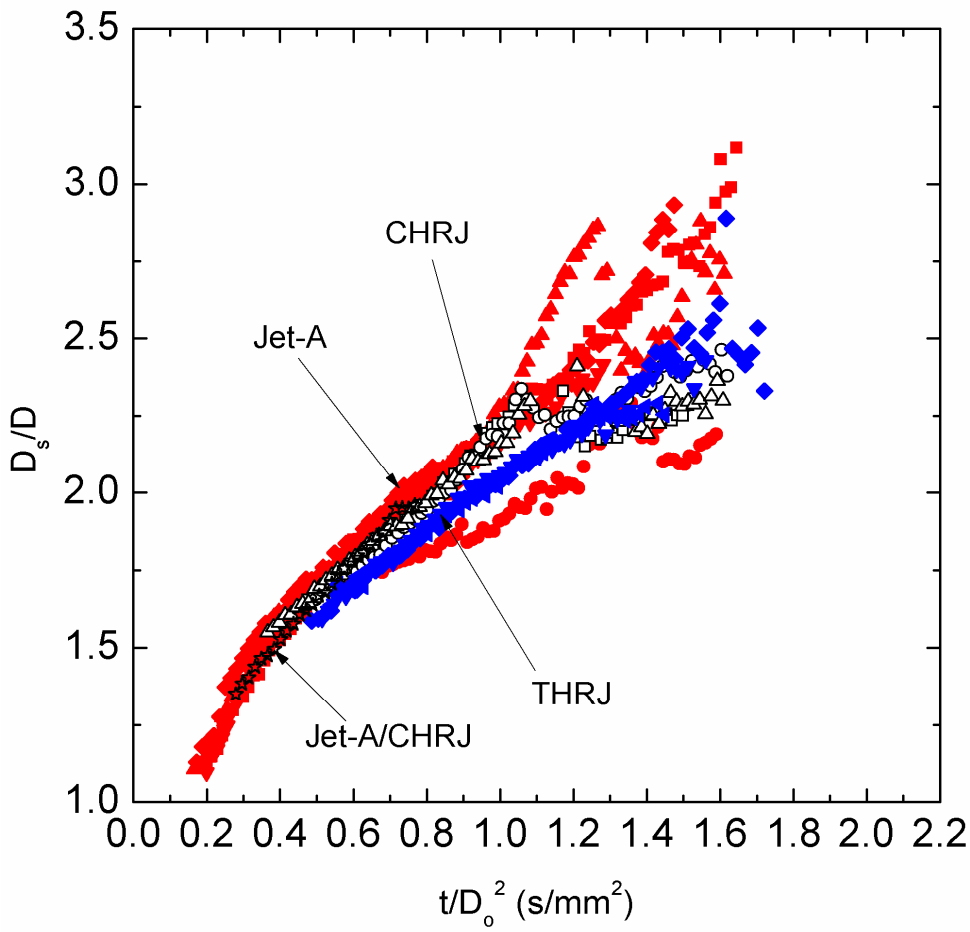

Fig. 8.7. Evolution of soot standoff ratio (SSR = D_s/D) for all the fuels investigated in this study. This plot includes data for all individual runs.

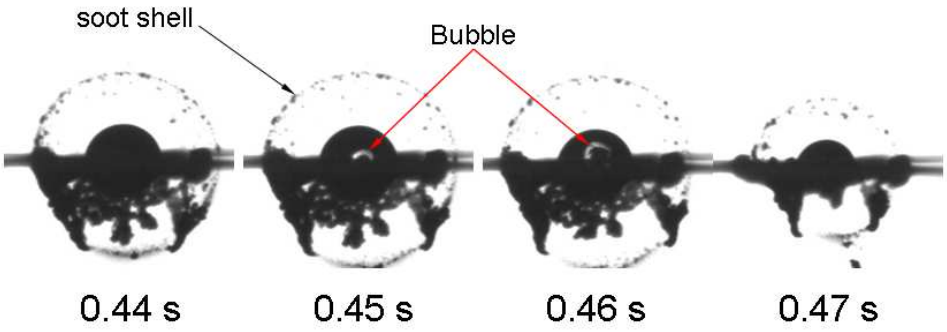

Fig. 8.8. Selected BW images of a THRJ droplet flame showing the effect of internal bubble formation on the flame and soot structure. The bubble is indicated by the red arrow. The droplet at 0.47s is noticeably smaller, most likely because of ejection of a bubble from the liquid droplet.

from the liquid mass over a time interval shorter than 0.005 s. The droplet diameter data during bubble formation are removed from Figs. 8.3 and 8.4 since they do not represent the actual diameter of a "liquid" droplet. Since the droplets were supported by solid (albeit rather small) structures and HRJs are highly multi-component blends with components that have a range of boiling points, the potential for an internal superheating effect that could lead to bubble formation is viable. Furthermore, diffusion of volatile and condensable combustion products to the droplet surface and their subsequent dissolution in the droplet could contribute to this effect of trapping volatile species inside the droplet as the droplet heats up during combustion.

8.2.3 Effect of Fuel Properties on Droplet Burning

Even though the HRJs examined here have different chemical compositions and sooting propensities (Fig. 8.2), their burning rates are similar to Jet-A. Such a result is broadly consistent with full scale turbine tests (Rahmes et al. (2009)) in which HRJs were subjected to a far more complex burning environment than examined here. No significant differences were found in engine performance.

From the perspective of the classic droplet combustion theory (Turns (2006)), the burning rate K (mm^2/s) is predominantly related to k_g, ρ_L, and $c_{p,g}$ (cf. Eqs. (5.1) and (5.2)). The gas properties are not easily estimated for the fuels examined in this study due to the complexity of the compositions. The representative data in Table 8.1 show small differences between the fuels. The difficulty of the classical theory is the assumption of constant properties that necessitates determining suitable average properties for prediction. If it is assumed that the gas phase properties will not vary

significantly, the liquid density in Eq. (5.2) becomes controlling and $K \sim 1/\rho_L$. The liquid density for the Jet-A used in this study (cf. Table 8.1) is slightly higher than the liquid densities for the HRJs, indicating lower burning rates for Jet-A. This prediction is broadly consistent with the burning rates obtained from the experiments during the quasi-steady period ($K_{Jet\text{-}A}/K_{HRJs} \sim 0.92$ compared to $(1/\rho_{L,Jet\text{-}A})/(1/\rho_{L,HRJs}) \sim 0.93$). The lower burning rate for Jet-A in the quasi-steady period can also be attributed to its lower heat of combustion compared to the HRJs. It is also noted that the lower heat of combustion of Jet-A can be related to its higher aromatic content, and the presence of these aromatics leads to soot formation (thus a lower burning rate) which could make Jet-A a less efficient fuel than the HRJs. This observation is also consistent with flight test observations for Jet-A and the HRJs (Rahmes et al. (2009)).

Regarding the FSR, insights into the influence of parameters is obtained from a modification of the classical theory by Aharon and Shaw (1997) (cf. Eqs. (5.3) and (5.4)). Using the FSR of Jet-A as the denominator, with the data from Table 8.1, Θ_{CHRJ} and Θ_{THRJ} are found to be 1.07 and 1.04, respectively, meaning that CHRJ and THRJ flames should be further to the droplet than Jet-A flames. This small difference is consistent with Fig. 8.6.

The results presented here show that the spherically symmetric flame configuration provides a useful quantitative comparison for the combustion performance of complex HRJs. The trends found from the experiments are surprisingly consistent with tests reported in the literature in practical engine systems and flight evaluations of these fuels.

8.3 Conclusions

The droplet combustion characteristics of hydroprocessed biofuels derived from camelina and tallow were studied in an environment that promotes spherical droplet flames, and the results were compared to a conventional aviation fuel, Jet-A. The results are as follows.

a) The biofuels examined have a much lower sooting propensity than Jet-A that tracks with their lower biofuel aromatic content.

b) Despite their sooting and fuel property differences, the biofuels and Jet-A have very similar behaviors in terms of their burning histories, burning rates, and the evolutions of the flame and soot standoff ratios.

c) An equal-volume blend of camelina and Jet-A had sooting propensities intermediate between Jet-A and camelina biofuel showing the effect of dilution.

d) The results presented here that are based on the fundamental spherically symmetric droplet flame configuration are broadly consistent with observations from full scale flight and engine tests that showed similar performances among the fuels examined, thereby suggesting that individual droplets can provide insights into burning under complex transport conditions, with the spherically symmetric configuration being the most basic for liquid fuel combustion.

CHAPTER 9

BIO-DIESEL SURROGATES COMBUSTION-

METHYL BUTANOATE AND METHYL DECANOATE[6]

9.1 Introduction

This chapter presents an experimental effort and detailed numerical simulation of the burning process of an ester-based biodiesel fuel droplet - methyl butanoate (MB) and methyl decanoate (MD). The experiments are carried out using test droplets that are anchored to small SiC support structures (14 μm diameter) and that burn in an ambience subjected to a low gravity level to promote spherical symmetry in the droplet burning process. The initial droplet diameters are 0.53~0.57 mm and the combustion gas is normal atmospheric pressure air. The MB and MD droplets within this size range are found to burn without forming soot shells. The MB results are benchmarked with n-heptane (nH) from Liu and Avedisian (2012).

The experimental results are compared with a detailed numerical simulation that features detailed MB and MD combustion chemistry (Diévart et al. (2012)), radiative heat transfer, species diffusion, and phase change effects to predict the evolution of droplet and flame diameter. The analysis also incorporates a model for heat transfer through the droplet support structure. These comparisons and predictions for multi-phase combustion of MB and MD that have not been seen in the literature provide

[6] This chapter comes from the following publications: Liu, Y.C., Farouk, T., Savas, A.J., Dryer, F.L., Avedisian, C.T., Combust. Flame 160 (2013) 641-655; Farouk, T.I., Liu, Y.C., Savas, A.J., Avedisian, C.T., Dryer, F.L., Proc. Combust. Inst. 34 (2013) 1609-1616.

validation for models associated with chemical kinetics and multi-physics and are therefore valuable for the study of ester-based biodiesel combustion.

9.2 Results and Discussions

9.2.1 Droplet Flame Configuration

The evolution of the MB droplet burning process is shown by the exemplar set of photographs in Fig. 9.1 from the digital video records. Some initial asymmetry of the flame structure exists due to gas motions induced by spark ignition and electrode retractions, though the flame shapes were largely spherical throughout the burning process. As illustrated in Fig. 9.1a soot formation is not observed (i.e., no soot shell). The sequence of color images (Fig. 9.1b) show a faint blue luminosity indicative of CH emissions which is also consistent with no soot formation.

Selected BW and color images of MD droplets are shown in Figs. 9.2 and 9.3, respectively. The spherical flame shapes are maintained throughout burning. The two needle-like glows in Fig. 9.2 are due to the interaction between flame and fibers. The box and circle superimposed on the images at 0.2 s and 0.5 s indicate the means by which the flame diameters were determined as discussed in Section 3.4. As shown in Fig. 9.2, the flame color is almost entirely blue until an inner yellow core is established after 0.1 s which then slightly alters the asymmetry of the inner core.

Figure 9.3 shows a selected set of backlit images that illustrate the evolution of the droplet (the black object) during the burning process. As can be seen, the droplet boundary is fairly sharp. The presence of the fiber does not seem to affect the droplet geometry as the droplet remains nearly spherical (or circular on the 2-D plane), except

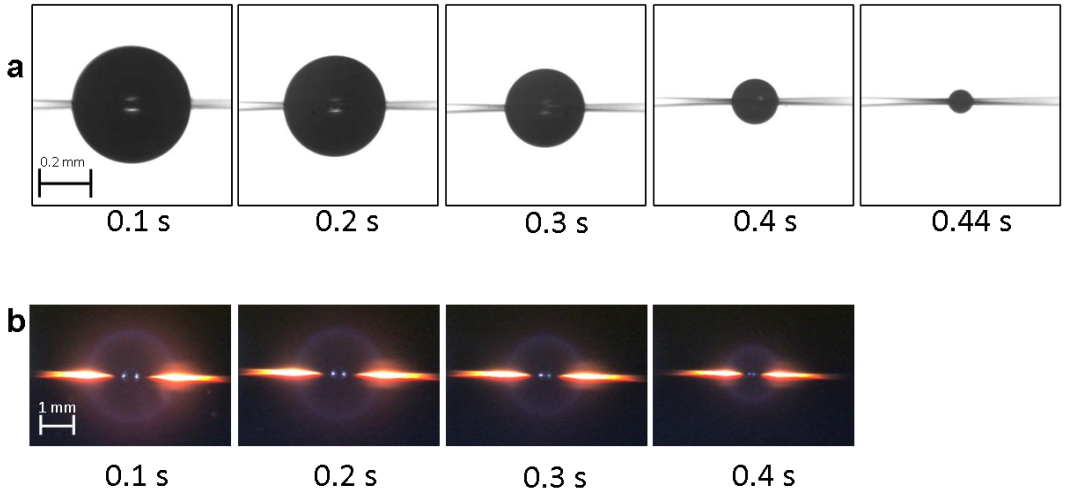

Fig. 9.1. (a) Selection of BW images for a burning MB droplet in atmospheric air. (b) Color images of droplet in "(a)" showing the flame structure (glow is due to flame/fiber interaction). Note the differences in scale between "a" and "b".

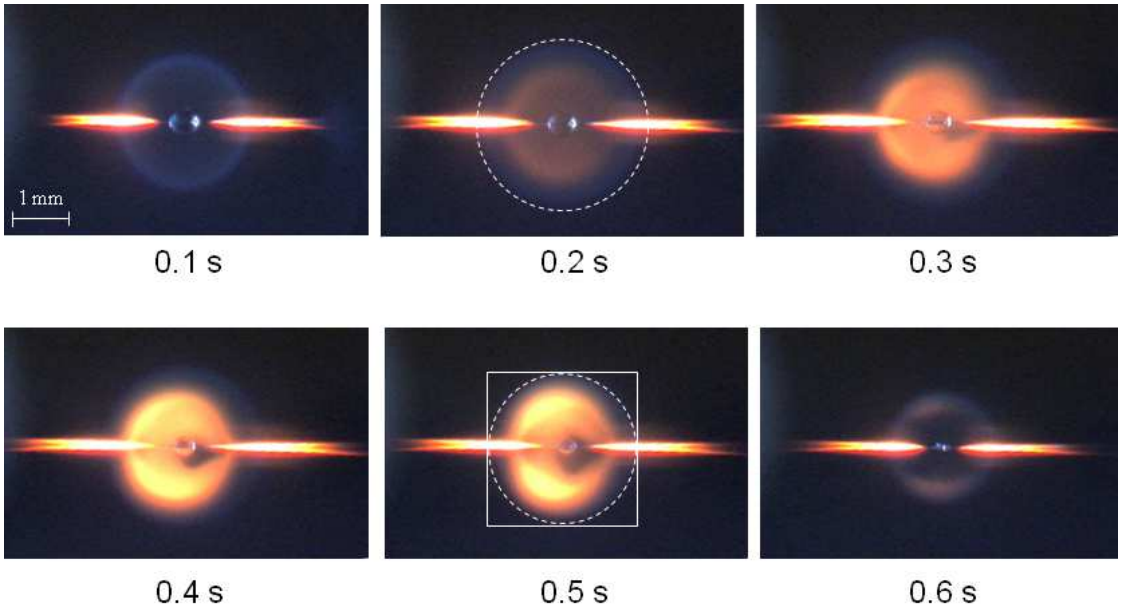

Fig. 9.2. Color images showing evolution of MD droplet flame. The initial diameter D_o of this particular experiment is 0.56 mm. (dotted line show how flames "diameter (as an equivalent ellipse) was determined; outer luminous (blue) zone was used for flame boundary).

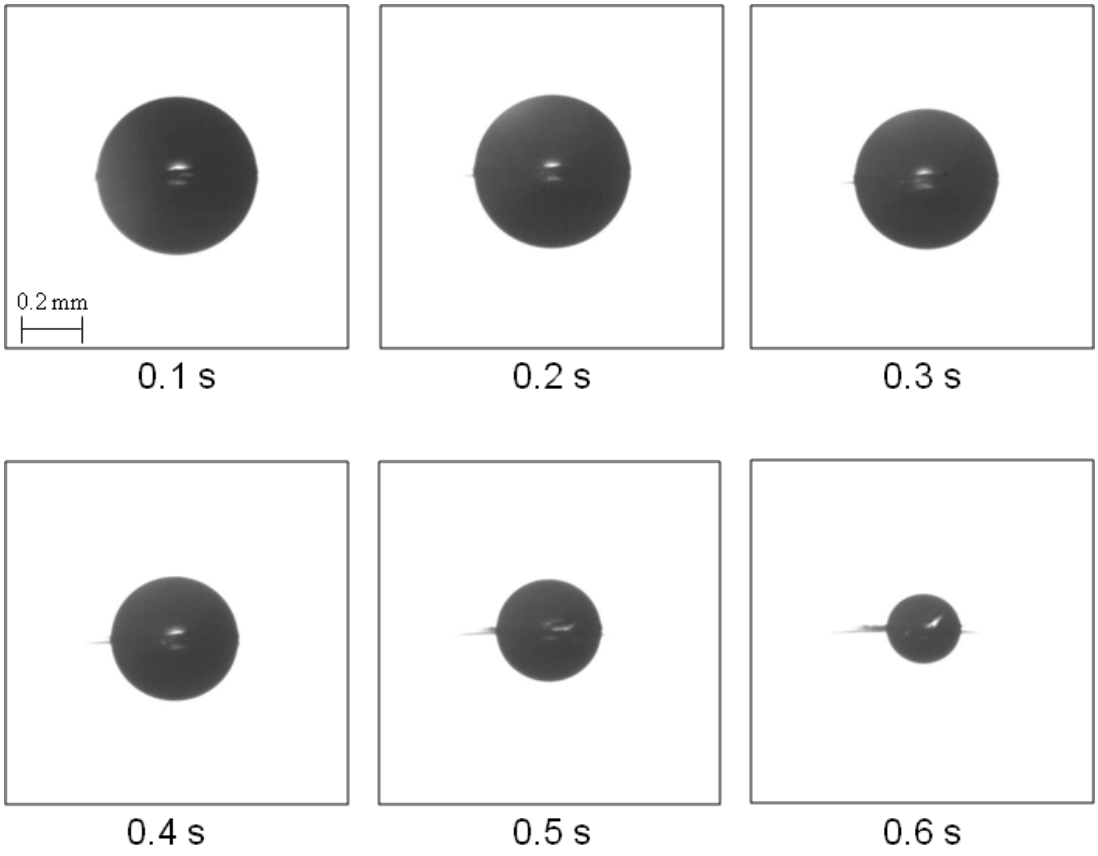

Fig. 9.3. Back-lit images of the droplet (the black object) obtained by the BW high speed camera during the combustion process. The initial diameter of the droplet is D_o = 0.56 mm.

very near the end of the burning process.

Most obvious in Fig. 9.3 is the absence of a soot shell, indicating that MD does not produce enough soot to form a shell structure for the range of initial droplet diameters investigated here. The precise mechanisms for the lack of soot formation for the combustion of methyl ester molecules do not appear to be well understood (Gaïl et al. (2007)). One perspective is that the C-O bonds in the oxygenated molecule remain intact during the ignition process so that there are fewer C atoms available to make soot after ignition (Westbrook et al. (2006)). However, if the oxygen produces CO_2 (which it apparently will for MD (Herbinet et al. (2008))) the bonded oxygen in the ester may not be as effective to reduce soot formation.

9.2.2 Quantitative Data and Comparison with Simulation

Measurements of the droplet diameter (D) obtained from images like those shown in Figs. 9.1a and 9.3 are normalized with the initial diameter (D_o) and presented for MB and MD using the coordinates suggested by the classical droplet combustion theory (Sirignano (1999)) (Eq. (1.1)).

Figures 9.4a and 9.4b compare the predicted evolution of D and K with the experiments for two different ignition energy configurations (see Fig. 9.4 inset) for MB. The ignition energy is prescribed by the energy density ($\rho c_{p,g} \Delta T$) of the initially prescribed temperature profile integrated over the trapezoidal-shaped region depicted in the figures. Both the predicted D and K are in excellent agreement with the measurements for an ignition energy of 0.05 J. For the ignition parameters prescribed earlier for hot wires (2.20 J), the dissipated energy influences a larger volume of the

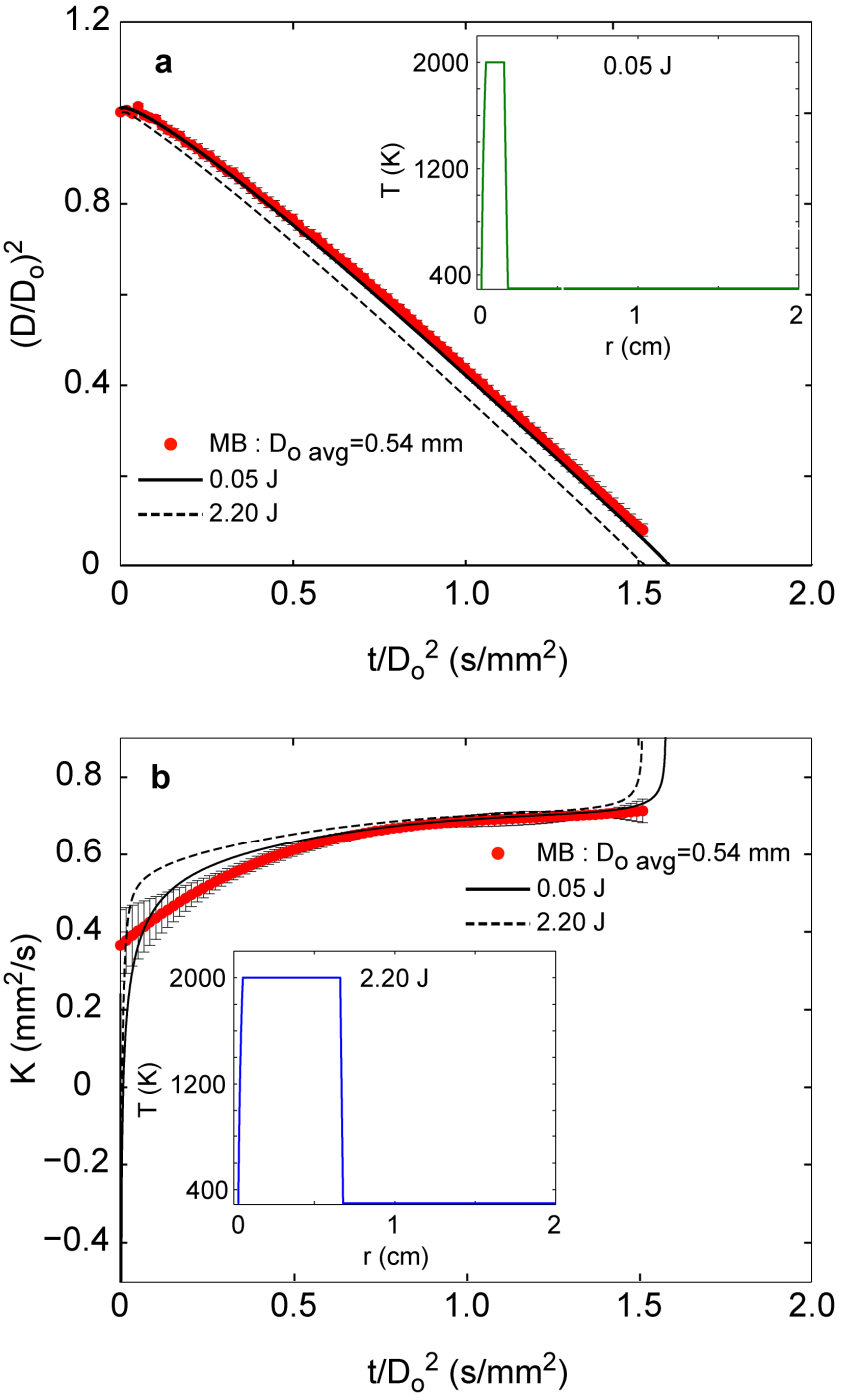

Fig. 9.4. Influence of initial ignition energy on evolution of (a) droplet diameter and (b) burning rate for a MB droplet (D_o = 0.54 mm, 1 atm, 21% O_2/balance N_2). Predictions are compared with measurements. The MB data shown in are the average of 4 individual runs and are identical to that presented later in Fig. 9.5b and Fig. 9.7a.

ambience, enhances initial droplet heating, and substantially affects the initial burning rate behavior (Fig. 9.4b). D^2 regresses linearly almost from the onset of burning for the 2.20 J case, while for the 0.05 J case, the initial stage of gasification and droplet heating approach quasi-steady burning only after about 40% of the total burn time. After achieving quasi-steadiness, the D^2 regression rate is nearly independent of earlier transients.

Figure 9.5a shows quantitative measurements of the evolution of droplet diameter of individual experimental runs in the coordinates of the classical D^2 law for MB. The trends show a transient burning behavior that extends up to 40% of the total burn time after which quasi-steady burning results independent of the earlier transient behavior. This is more clearly seen in Fig. 9.5b which shows the data of Fig. 9.5a averaged over the four individual runs, along with error bars on the measurements (mean and standard deviation). Also included in Fig. 9.5b are measurements from Chapter 5 for nH droplets for D_o = 0.50 mm (average experimental values). The comparison between the measurements and numerical simulations is excellent for both fuels. The predicted diameter evolutions show evidence of early thermal expansion of the droplets, consistent with experimental observations. Both droplets burn to completion as observed experimentally. nH appears to burn at a slightly faster rate (~6%), though nH's heat of combustion (Δh_c) is 40% higher than that of MB (Table 9.1).

The predicted maximum gas temperatures (T_{max}) in Fig. 9.5b show that the T_{max}'s initially decrease due to the initial heating of the droplet, endothermic fuel vapor reactions and heat loss to the ambience. The decrease is greater for MB than for n-

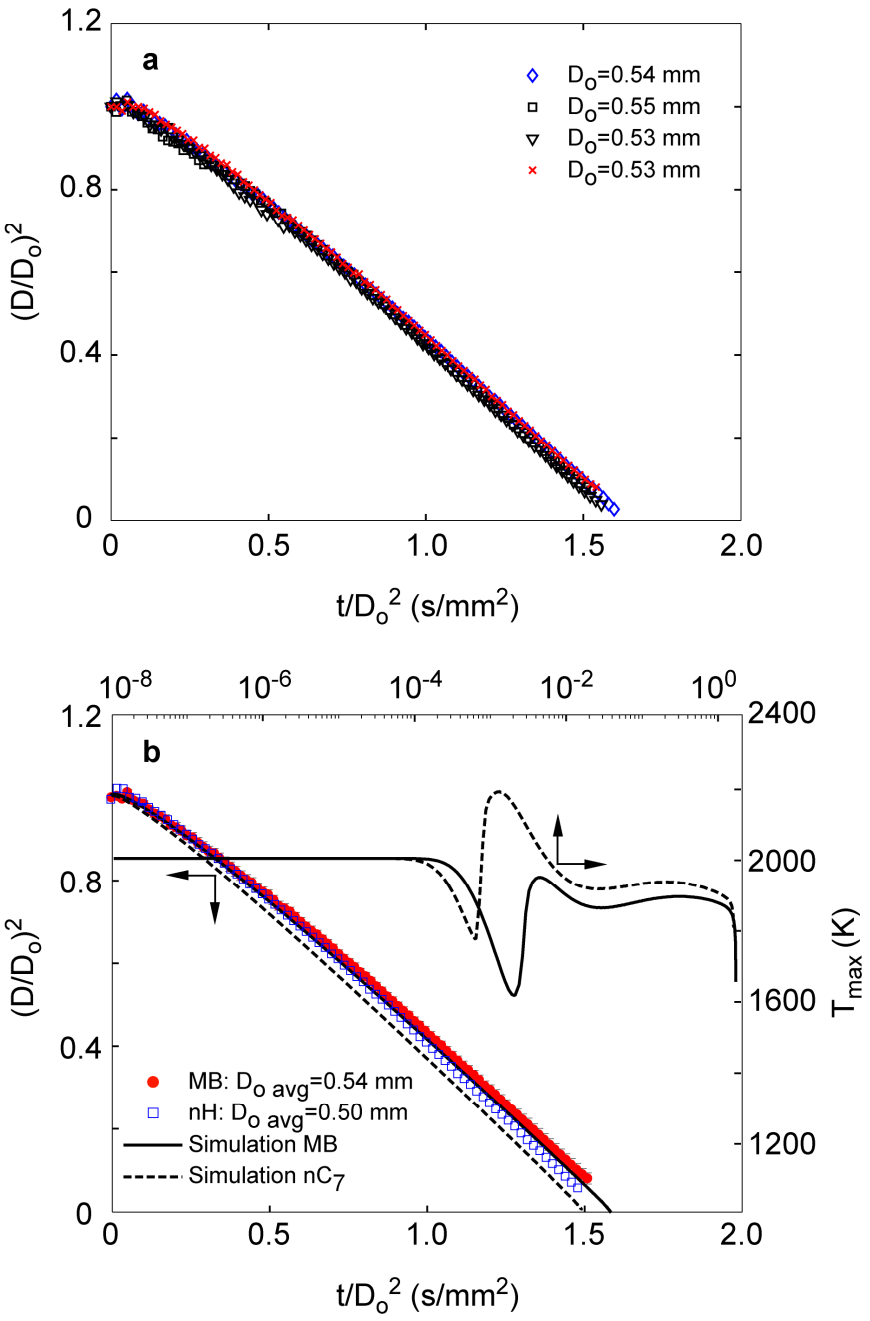

Fig. 9.5. (a) Evolution of MB droplet diameter showing trends for four individual runs (1 atm, 21% O_2/balance N_2), (b) Comparison between measured and predicted droplet diameters and predicted peak temperature evolution for MB and nH (Chapter 5) The MB data shown in "b" are averaged from the data in "a".

Table 9.1. Selected properties of MB and nH.

Property	MB $C_5H_{10}O_2$	nH C_7H_{16}
W_F (g/mol)	102.1	100.2
T_b (K)	376	372
ρ_L* (kg/m^3)	898.4	679.5
$c_{p,L}$ *(J/kg)	1941	2242
h_{fg} @T_b (kJ/mol)	141.4	132.9
Δh_c (kJ/mol)	2945.5	4849.2
Measured average burning rate, $K_{avg\ expt}$ (mm^2/s)	0.64	0.67
Predicted average burning rate, $K_{avg\ sim}$ (mm^2/s)	0.65	0.69
ν_c	7.5	11.0

* Values of density and specific heat are @ 298 K

heptane, mostly because of differences in heat capacity and latent heat of vaporization (Table 9.1). The decreases are followed by sharp increases, indicating ignition of the fuel air vapor mixture surrounding the droplet. Subsequently, the temperatures as the flame structure transitions to that of a quasi-steady burning condition involving sustained liquid fuel vaporization and continued loss of heat through diffusion to the ambience. With similar ignition energy inputs, MB takes longer to ignite, with a quasi-steady flame temperature of only ~ 40 K lower than nH despite the large difference in Δh_c.

Figure 9.6a shows MD data from five repetitions are shown along with the average of these runs. The measurements show good repeatability. There are two aspects of the data in Fig. 9.6a not part of the classical theory: the initial period in which the droplet swells as its density drops due to being heated by the surrounding hot gases from the flame; and the slight curvature of the evolution of droplet diameter which

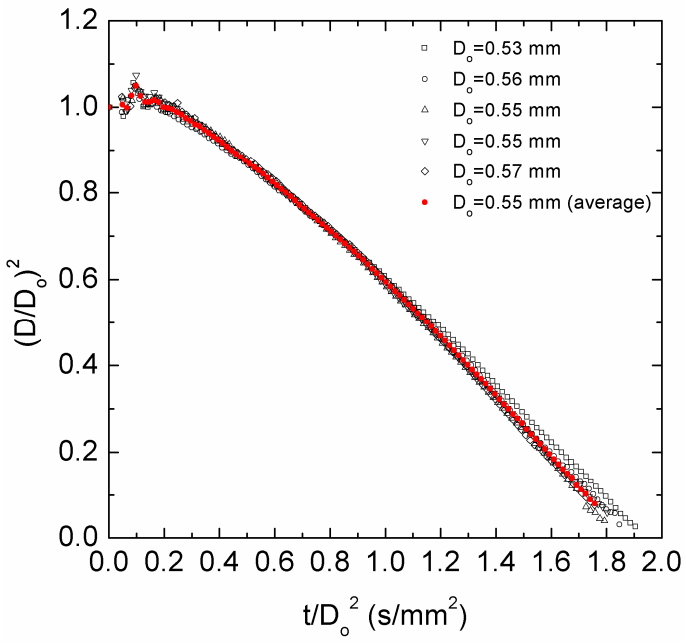

(a)

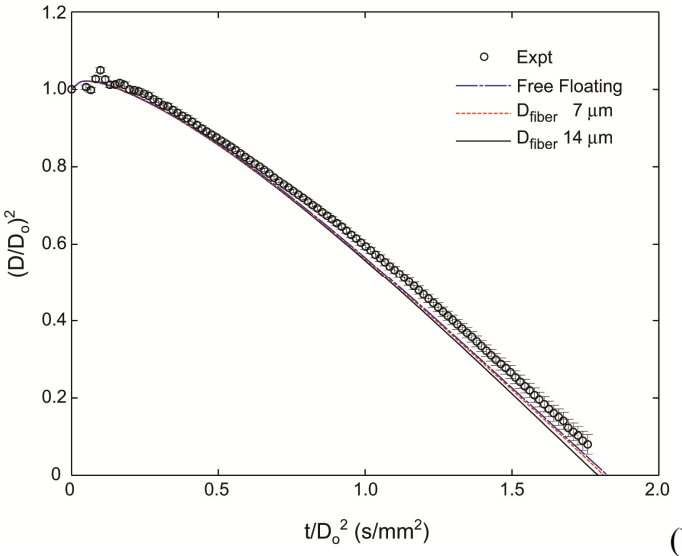

(b)

Fig. 9.6. (a) Evolution of droplet diameters for MD combustion. Black data are the original five individual experiments and the red data are the averaged values from the five runs. (b) Evolution of averaged droplet diameters over the combustion process-compared with simulations of free floating droplet and with various thermal conductivities for the fiber k_{fiber} (the error bars show the standard deviations of the averaged experimental data). D_{fiber} = 14 µm and Nu = 0.36.

indicates a time dependent burning rate (K(t)). In the early period, the droplet heats faster than the fuel evaporates to give the swelling effect. The data are more scattered in this period due to the disturbance attributed to the physical impact of the spark ignition on the droplet. After this initial period, the predicted (and measured) evolution of droplet diameter shows some slight curvature which may be due to unsteady heating that persists throughout burning.

Figure 9.6b compares the simulated evolution of droplet diameter with the experimental values. The standard deviations (vertical bars) pertaining to each averaged data point (black open circle) are calculated from the data for the five individual experiments of Fig. 9.6a. Numerical results are shown for three different fiber sizes: D_{fiber} = 14 μm ; D_{fiber} = 7 μm; and D_{fiber} = 0 ("free floating", where the droplet is not supported by any fiber structure (blue line)).

As shown in Fig. 9.6b, the three numerical results with various fiber conditions are extremely close to one another, with the free floating prediction being closest to the experimental data. This suggests that fibers with such small diameters are not a significant factor to affect the droplet burning history until the very end of burning where the fiber size becomes relatively large compared to the droplet size. Numerical results are very close to the lower limit of the error bars of experimental data though there is still some visible difference at the end of burning. This difference might be caused either by the determination of ignition time for both experimental and numerical cases, by the ignition energy used as the spark energy in the experiments could not be accurately measured and provided for the simulation, or the greater difficulty in obtaining accurate measurements for the small diameters at the end of burning.

However, the final slopes of the predicted burning curve in Fig. 9.6b appear to be consistent with the experimental values.

In the quasi-steady period of burning (the approximate range 0.75 $s/mm^2 < t/D_o^2 < 1.25$ s/mm^2) the simulated droplet diameter is slightly lower than the measured diameter. This difference could be due to the influence of spark energy on the temperature field at the moment of ignition. Employing a larger spark energy in the experiments could reduce the unsteady heating period so that regression begins at an earlier time and shifts the time scale of the experiments to slightly shorter times for a given droplet size.

A comparison of the burning rates is a more stringent test because differentiation amplifies uncertainties in the evolution of droplet diameter. For the data shown, the original droplet diameter data (Figs. 9.5a and 9.6a) were smoothed with a 4^{th} order polynomial and the first derivative was then taken to determine the burning rate from the averaged data. It is important to note that the order of polynomial fit will affect the derivative value. Trends could emerge that are artifacts of the order of the polynomial used to fit the data.

Figure 9.7a shows the evolution of burning rate constants (obtained by fitting the average D^2 profiles shown in Fig. 9.7a and predictions from the detailed numerical model that includes simulations for nH. The predicted K evolution shows a large negative value at the initial state of the burn occurring as the droplet diameter increases due to the thermal expansion. A sharp rise in K occurs as the droplet diameter becomes comparable to the fiber diameter with additional heat flux from the fibers becoming significant. The time-averaged experimental and predicted K's for MB and nH differ by

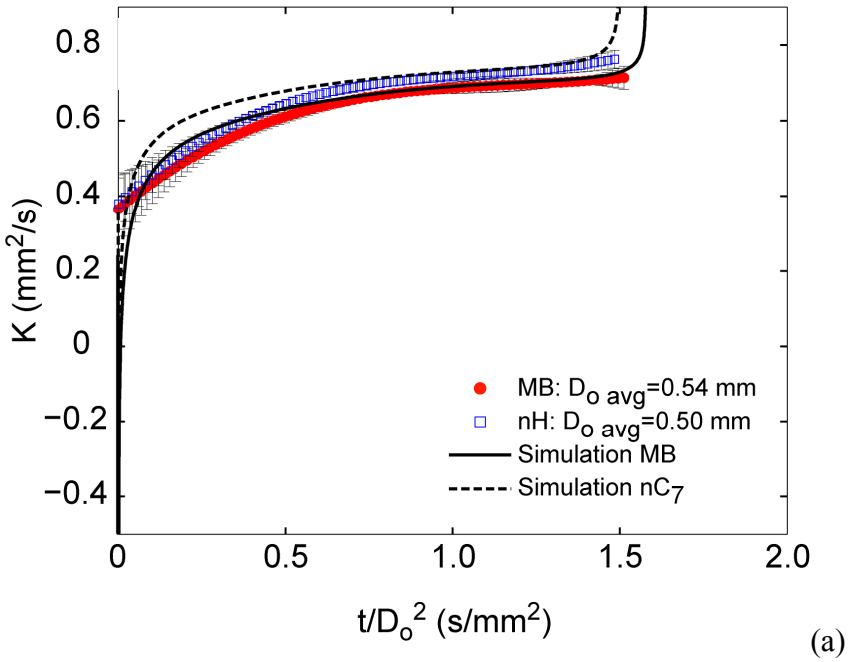

(a)

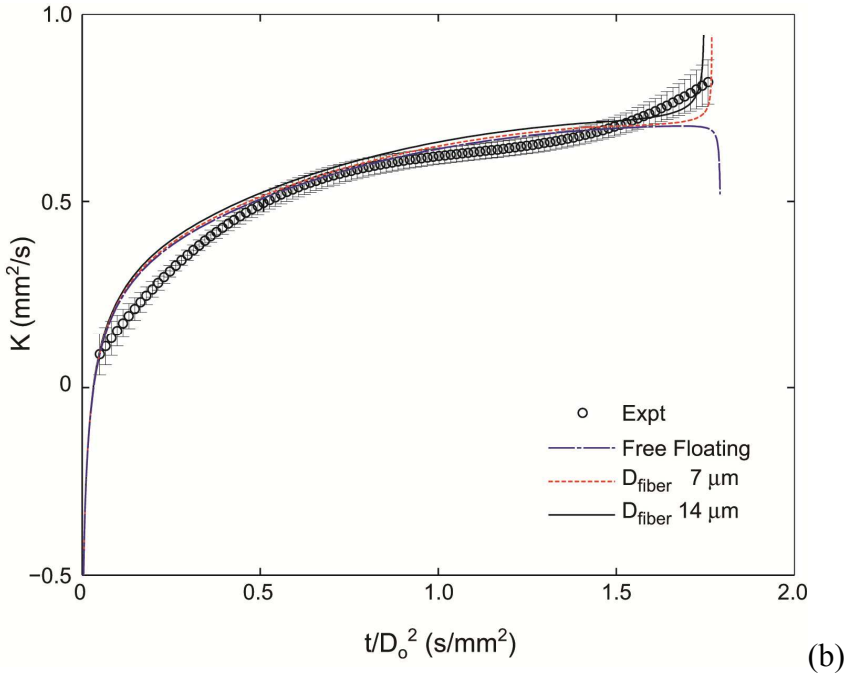

(b)

Fig. 9.7 Comparison of experimentally obtained burning rate and numerical predictions for (a) MB and nH and (b) MD droplets.

less than 3% (averaging was performed for values in between $0.10 \leq t/t_b \leq 0.90$, where t_b is the total burn time).

Figure 9.7b compares the burning rate evolution of a MD droplet obtained from experiments and predictions. The experimental burning rates increase with time, with the increase being significant in the early period of burning, followed by a more gradual (i.e., quasi-steady) period in the mid region of burning (i.e., 0.5 $s/mm^2 < t/D_o^2 < 1.5$ s/mm^2) where the average K is about 0.6 mm^2/s. At the very end of burning, $t/D_o^2 > 1.7$ s/mm^2, K shows a noticeable increase which is suggestive of an extinction-like process. However, as noted above regarding the order of polynomial fit to determine burning rate, the increase of K at the end of burning in Fig. 9.7b could well be an artifact of the order of the polynomial fit to the data in Fig. 9.6a. At the same time, the increase is consistent with an ever increasing influence of the fiber on the burning rate. As the droplet size decreases D_{fiber} remains the same, so there must always be some influence of the fiber even for arbitrarily small fiber sizes.

As shown in Fig. 9.7b, numerically predicted burning rates increase from a negative value beginning with the initial droplet heating period associated with thermally induced expansion of the droplet, and then level off at about $t/D_o^2 \sim 0.5$ s/mm^2. The measured burning rates do not increase as substantially after ignition. However, this trend is influenced by the order of polynomial fit to the data of Fig. 9.6a. As the simulated burning rate increases more quickly than the measured rate in the early period, the extra enthalpy input to the droplet in the simulation might be slightly larger than what is actually transported in the experiments. Unfortunately, the spark energy used in the numerical simulation is the lowest possible energy to trigger chain reactions

for MD combustion. For $t/D_o^2 > 0.5$ s/mm^2, the predicted burning rates agree quite well with the measurements. The simulated burning rate for a fiber-supported droplet is slightly larger than the free floating ($D_{fiber} = 0$) limit due to increased heat transport to the droplet associated with the larger fiber diameter.

Figure 9.8a shows the experimental data of FSR for MB flames and the prediction the flame position marked by the location of T_{max} (Farouk and Dryer (2011)) is shown in Fig. 9.8b along with measurements and prediction for nH (Chapter 5). Error bars are shown to illustrate the uncertainty. The trends show a continually increasing flame standoff ratio due to thermal buffering of the far field that leads to decreased loss of heat from the flame structure and an ever increasing FSR as burning progresses. The model predictions agree well with experimental observations (Fig. 9.8b).

Figure 9.9a shows the FSR of MD from individual experiments. Figure 9.9b compares the numerically predicted flame diameters (D_{flame}), defined as the radial position of maximum temperature in the 1-D simulation domain, for several fiber diameters with the experimental data. The numerical results for various fiber sizes do not differ until 0.3 s into the burn. Clear differences are observed thereafter to the end of combustion where the free floating droplet (D_{fiber}=0) has a slightly larger flame diameter and the flame diameter for D_{fiber}= 14 μm has the smallest flame at the same time. Nonetheless, trends are very consistent with the maximum D_{flame} occurring at 0.22 s for the three simulated fiber diameters and generally show a very good agreement with the measurements.

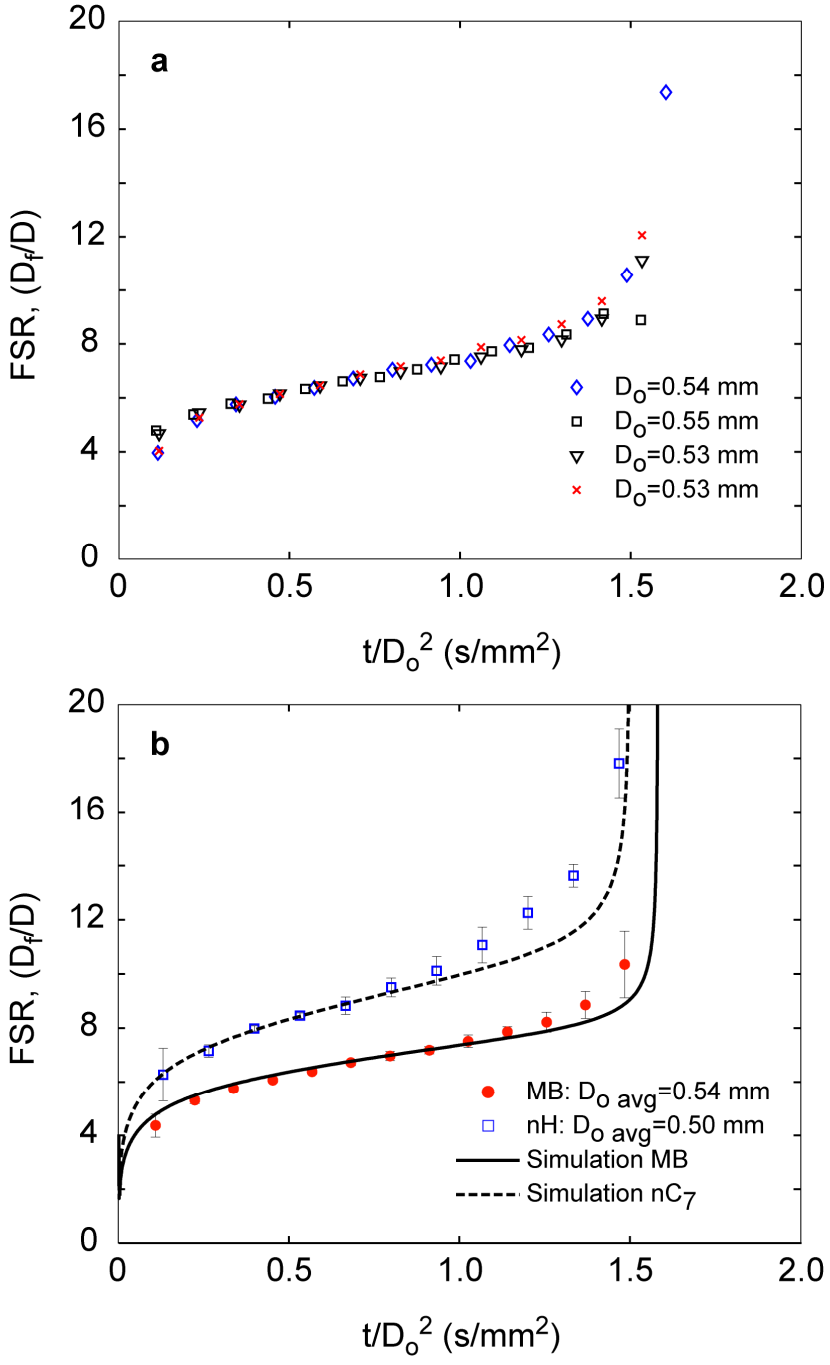

Fig. 9.8. (a) Evolution of FSR for four individual runs of MB droplets for the indicated initial droplet diameters (1 atm, 21% O_2/balance N_2), (b) Comparison of measured and predicted FSR for MB and nH (Chapter 5). The MB data in "b" are averaged from the 4 runs in "a".

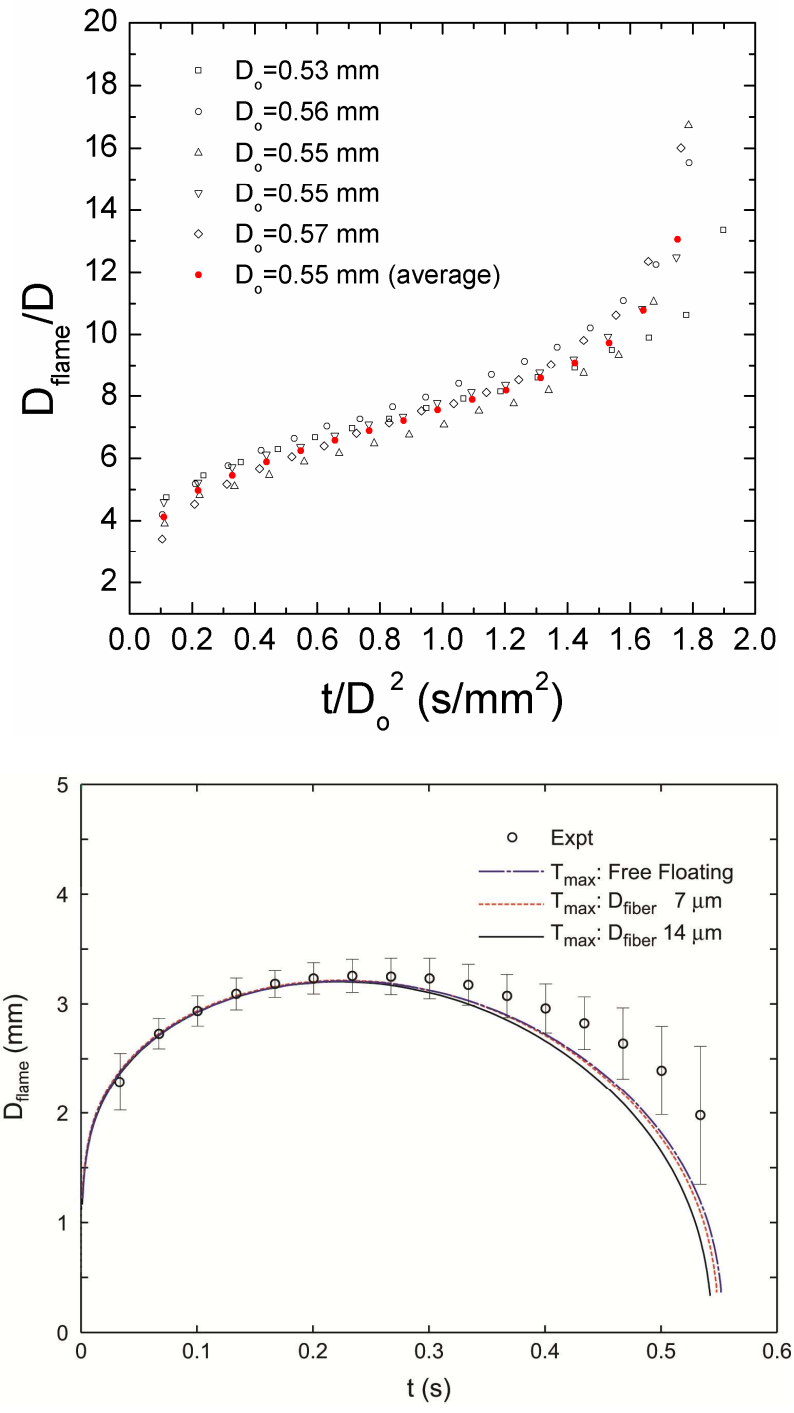

Fig. 9.9 (a) FSR evolution from five individual MD experiments and their averaged values; (b) comparison of predicted FSR with experimental data with various fiber sizes.

The results for the larger fiber (14 μm) show a slightly larger burning rate (cf. Fig. 9.7b) due to the extra source for heat transfer through the fiber, causing the measured D_{flame} to drop earlier at the end of burning. Compared to the experimental data, the general trends are nonetheless very close, with the maximum D_{flame} occurring at 0.22 s. However, at the end of burning the predicted D_{flame} is significantly lower than the averaged experimental data. The large error bars on experimental shown in Fig. 9.9b reflect the lower resolution of the color images and thus a greater challenge to obtain accurate D_{flame} at the end of burning. The lower end of the error bar at the very end of burning is nonetheless close to the predicted data.

The influence of fiber thermal conductivity, k_{fiber}, on droplet burning will depend on the specific values considered for MD droplets. The thermal conductivity of the SiC fibers employed in the present experimental effort was not measured directly. The literature shows a strong temperature dependence, ranging for bulk SiC from several hundred W/mK at room temperature down to 30 W/mK at 1500 K (Incropera and DeWitt (2002)). Fibrous SiC strands of 20 μm diameter have conductivity values of about 5 W/mK (Youngblood et al. (1999)). Comparisons of droplet burning using other fiber materials (i.e., a ceramic fiber) with a known thermal conductivity (i.e., $k_{fiber} \sim 2$ W/mK (Whittaker et al. (1990)) suggests that the lower limits of fiber thermal conductivity may be more relevant to the SiC fibers employed in the present experiments. In this section simulations are reported using $k_{fiber} = 2$ W/mK and 5.2 W/mK.

Figure 9.10a shows the evolution of droplet diameter for a given D_{fiber}. For 2.0 W/mK $< k_{fiber} <$ 5.2 W/mK the results are not substantively affected by the fiber for

k_{fiber} in this range. At the end of burning, it still can be seen that the fiber with higher thermal conductivity starts to act as an extra heat transfer path for the flame to transmit heat into the droplet causing the droplet size to decrease slightly more quickly, but the effect is minimal.

The influence of k_{fiber} on predicted D_{flame} is presented in Fig. 9.10b. Again, the change of k_{fiber} within the range 2.0 W/mK < k_{fiber} < 5.2 W/mK does not appear to strongly affect D_{flame}. The simulation with higher k_{fiber} is consistent with the trend for increasing the fiber diameter as both variations promote heat flow through the fiber thereby increasing the burning rate and reducing D_{flame} slightly more quickly. The free-floating limit shows deviations from the fiber-supported predictions for t > 0.3 s where the difference between numerical and experimental results becomes significant at the end of burning.

To further clarify the influence of fiber thermal conductivity on burning, Fig. 9.11a shows the variation of the ratio of the averaged burning rate to the free-floating limit with fiber thermal conductivity for MD only. As expected, the relative burning rate increases with increasing k_{fiber}, though for k_{fiber} = 5 W/mK the average burning rate deviates from the free-floating limit by only 1.7 %, showing that the fiber does not have a significant influence on the burning rate. From an experimental perspective, a fiber-supported droplet combustion experiment is far easier to perform than a free-floating droplet combustion experiment because the fiber physically anchors the droplet to a fixed position relative to the imaging optics throughout burning. When the fiber has a minimal effect on the combustion process as outlined here, the results are useful for producing data that simulate the ideal configuration of Fig. 1.2.

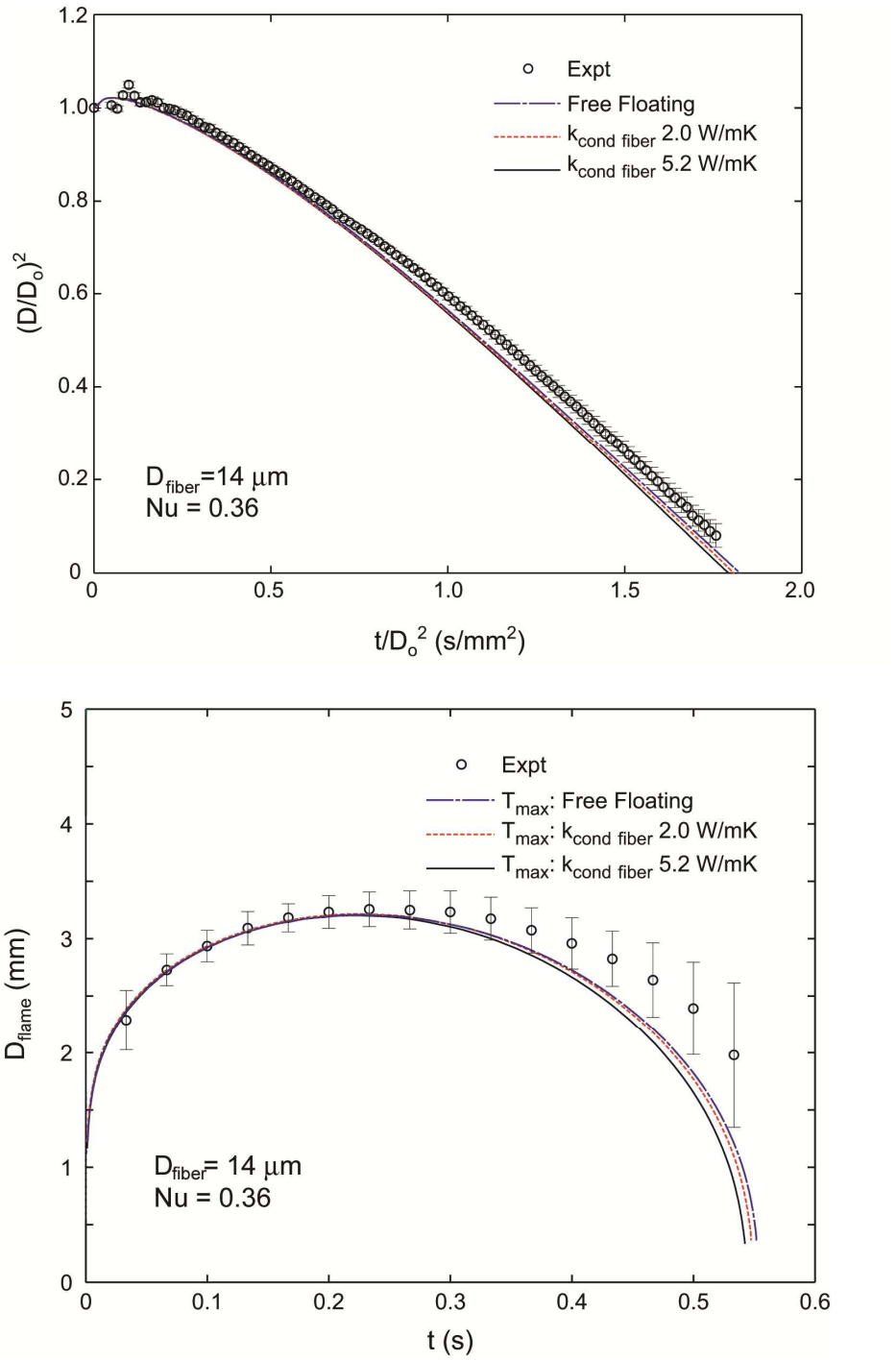

Fig. 9.10. Evolution of averaged MD droplet diameters (a) and flame diameters (b) over the combustion process compared with simulations of free floating droplet and with various thermal conductivities for the fiber k_{fiber} (the error bars show the standard deviations of the averaged experimental data). D_{fiber} = 14 μm and Nu = 0.36.

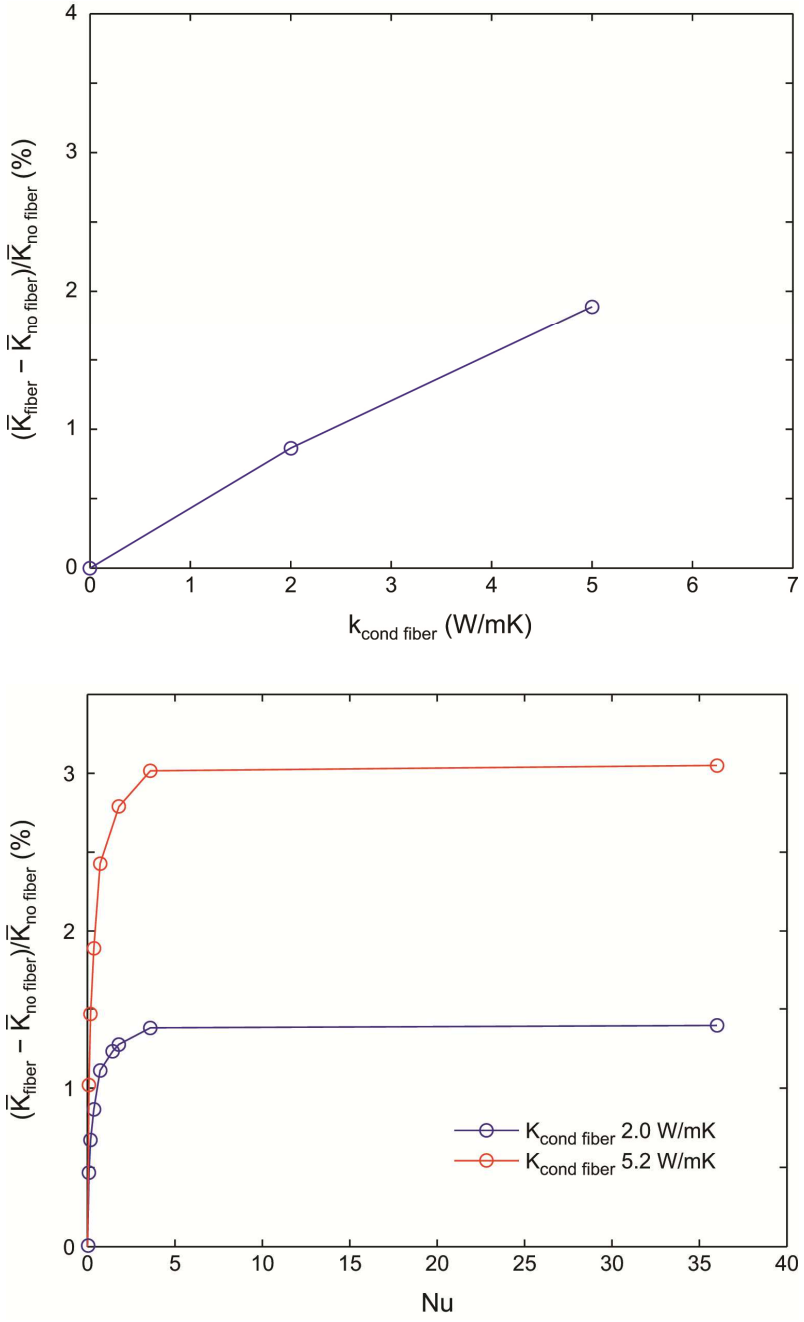

Fig. 9.11. (a) Burning rate evolution for MD droplets: experiments (with error bars showing the standard deviations) vs. simulation with different fiber sizes D_{fiber}. (k_{fiber} = 5.2 W/mK and Nu = 0.36). (b) Numerical results of deviation in burning rate K with various thermal conductivities for the fiber k_{fiber}. (D_{fiber} = 14 μm and Nu =0.36).

The model for heat transfer through the fiber incorporated in the detailed simulation used here requires that the heat transfer coefficient (or Nusselt number) be known to account for convective transport between the tether fiber and surrounding fluid. To show the effect, Fig. 9.11b shows the effect of varying Nu over a wide range on the burning rate relative to the free-floating value. The lower value is the conduction limit, Nu = 0.36 and results for two values of k_{fiber} are shown. As the Nusselt number increases, the burning rate increases due to increased heat transfer from the vapor phase to the tether and levels off above Nu ~ 4 where there is no longer an influence of convection. In the high Nu limit, the convective resistance is small and the vapor temperature around the fiber is close to the fiber temperature. In this case, convection (or radiation) has little influence on heat transfer through the fiber while the fiber is at its maximum temperature.

Figure 9.11b also shows that k_{fiber} does not have a strong influence on the burning rate for the two values simulated regardless of the strength of convection: 3% for k_{fiber} = 5 W/mK and 1.4% for k_{fiber} = 2 W/mK. An influence at this level would be difficult to discern from the experiments of burning rate (Fig. 9.7b) that are determined by differentiating a polynomial fit to the data (e.g., Fig. 9.6a).

9.3 Conclusions

Fiber-supported droplet combustion experiments are carried out in an environment that promotes spherical symmetry for MB and MD droplet with initial diameters of ~0.55 mm. The experimental results agree with the predictions provided by detailed numerical simulations within the error bars.

Measured droplet diameter regression and computed burning rates showed significant nonlinearity, in some cases extending through more than ~40% of the burn time, with an eventual establishment of quasi-steady burning behavior. For atmospheric pressure air, and the droplet size studied, burning of MB and MD droplets occurred without soot formation and to completion. The droplet flame of MB and MD has a clear blue boundary with visible yellow inner core also observed. There is no visible soot shell formation or particulate aggregates visible for this size of MB and MD droplet with the lighting setup of this study.

The comparison between experimental and numerical droplet combustion variables for the spherically symmetric case shown in this study also provided validation for the MB and MD models that involved chemical kinetics proposed previously (Diévart et al. (2012)) and heat and mass transfer associated with multi-phase combustion, which is a corner stone to developing detailed models for multiphase combustion of ester-based bio-fuels. Additional work is needed to expand the database of single droplet combustion under carefully controlled and modelable conditions.

CHAPTER 10

THE INFLUENCE OF INITIAL DIAMETER ON SPHERICAL DROPLET BURNING FOR N-HEPTANE, N-OCTANE, AND N-DEANE: INTERNATIONAL SPACE STATION AND GROUND-BASED EXPERIMENTS[7]

10.1 Introduction

A comprehensive investigation is reported in this chapter on varying the initial droplet diameter (D_o) over a very wide range on the burning characteristics of n-heptane, n-octane and n-decane that are representative of components found in practical fuel systems. Initial droplet diameters ranged from 0.52 mm to 4.4 mm. This wide range influences the importance of radiative transport and sooting dynamics on the droplet burning process, including the droplet burning rate, soot formation and different extinction mechanisms. Table 10.1 includes some properties of the fuels of interest in this chapter.

A low gravity environment was created in a ground-based (drop tower) facility to observe the complete droplet burning history of droplets with $D_o < 1$ mm where the droplet burning times are typically less than one second. For 1.5 mm $< D_o <$ 4.38 mm a space-based facility (the International Space Station (ISS)) was used that provides for essentially unlimited droplet burning times. A unique design aboard the ISS was created near-stationary and free-floating (or unsupported) droplets. The longest measured burning time was 38 s (D_o = 4.38 mm), which is impossible to access with any ground-

[7] This chapter comes from the following paper manuscript: Y.C. Liu, K.N. Trenou, J.K. Rah, M.C. Hicks, C.T. Avedisian, "The influence of initial diameter on convection-free burning in the standard atmosphere for n-heptane, n-octane, and n-decane droplets: International Space Station and ground-based experiments," Combustion and Flame (2013).

Table 10.1. Selected properties for n-heptane, n-octane, and n-decane

	n-heptane	n-octane	n-decane
Chemical formula [a]	C_7H_{16}	C_8H_{18}	$C_{10}H_{22}$
W_F (g/mole) [a]	100.21	114.23	142.29
T_b (K) [a]	371.6	398.8	447.3
T_m (K) [a]	182.6	216.4	243.5
ρ_L at 293 K (kg/m^3) [b]	684	703	730
ρ_b at T_b (kg/m^3) [b]	608	605	609
T_c (K) [a]	540.2	568.8	617.6
P_c (atm) [a]	27	24.5	20.8
h_{fg} (kJ/kg) [c]	316	300	277
HHV (kJ/kg) [c]	48456	48275	48020
LHV (kJ/kg) [c]	44926	44791	44602
T_{ad} (K) [c]	2273	2275	2277

[a]Reid et al. (1977)
[b]from Tyn/Calus Method in Reid et al. (1977).
[c]Turns (2006)

based facility. All experiments reported here in the chapter carried out in the standard atmosphere (room temperature and normal atmospheric pressure).

The results suggest that the burning rate monotonically decreases with increasing D_o. The mechanism is speculated to arise from a transition of a soot-dominated process for small droplets that progressively diminishes in importance as D_o increases to give way to increased radiative losses for large droplets that reduce heat transfer to the droplet surface. The relative position of the flame to the droplet was found to increase with D_o, with generally the flames of smaller droplets residing closer to the droplet surface than the flames of larger droplets. At a given time after ignition, the relative position of the flame to the droplet decreased with increasing D_o. A rather abrupt increase was noted at around $D_o \sim 1$ mm followed by a monotonic decrease with further increases of D_o for all of the fuels examined. The relative position of the soot shell to the droplet increased with time, while the relative position increased with D_o for

a given time after ignition.

For n-heptane in particular, a three-staged burning process was found for $D_o > 3$ mm suggesting several extinction modes. The early extinction mechanism is speculated to be the result of radiation losses from the flame rather than to more diffusively controlled processes. Subsequently, the droplets continued to evaporate until reaching a second limit with a rather abrupt decrease in the droplet burning rate – a so-called "cool-flame" extinction. The imaging system employed in the experiments showed an oscillatory extinction dynamic in which the flame would peel away from the droplet then re-appear before completely disappearing.

10.2 Results and Discussions

We investigated the effects of flame dimension on droplet flames combining GB and ISS data to cover a wide range of droplet diameters. Figure 10.1 shows an overview of droplet flame images from the selected experiments with D_o ranging from 0.52 mm to 3.61 mm for n-octane. Note that the scale factor for GB and ISS images are different (indicated separately below the images in Fig. 10.1). The time stamps showing on the left are the instantaneous burning time t divided by D_o^2 in order to show the entire burning history for various D_o's on the same figure. These experiments are selected because of the completeness of burning histories, i.e. the slightly drifting droplet flames due to no supporting fiber (ISS) stay inside the field of view of both cameras. For the GB experiments, there are two needle-like glows protruding from the flame boundary indicating the presence of the supporting fibers. The use of these fibers (SiC, 14 μm) was proven to have very minimal effects on the burning process of the n-alkanes within

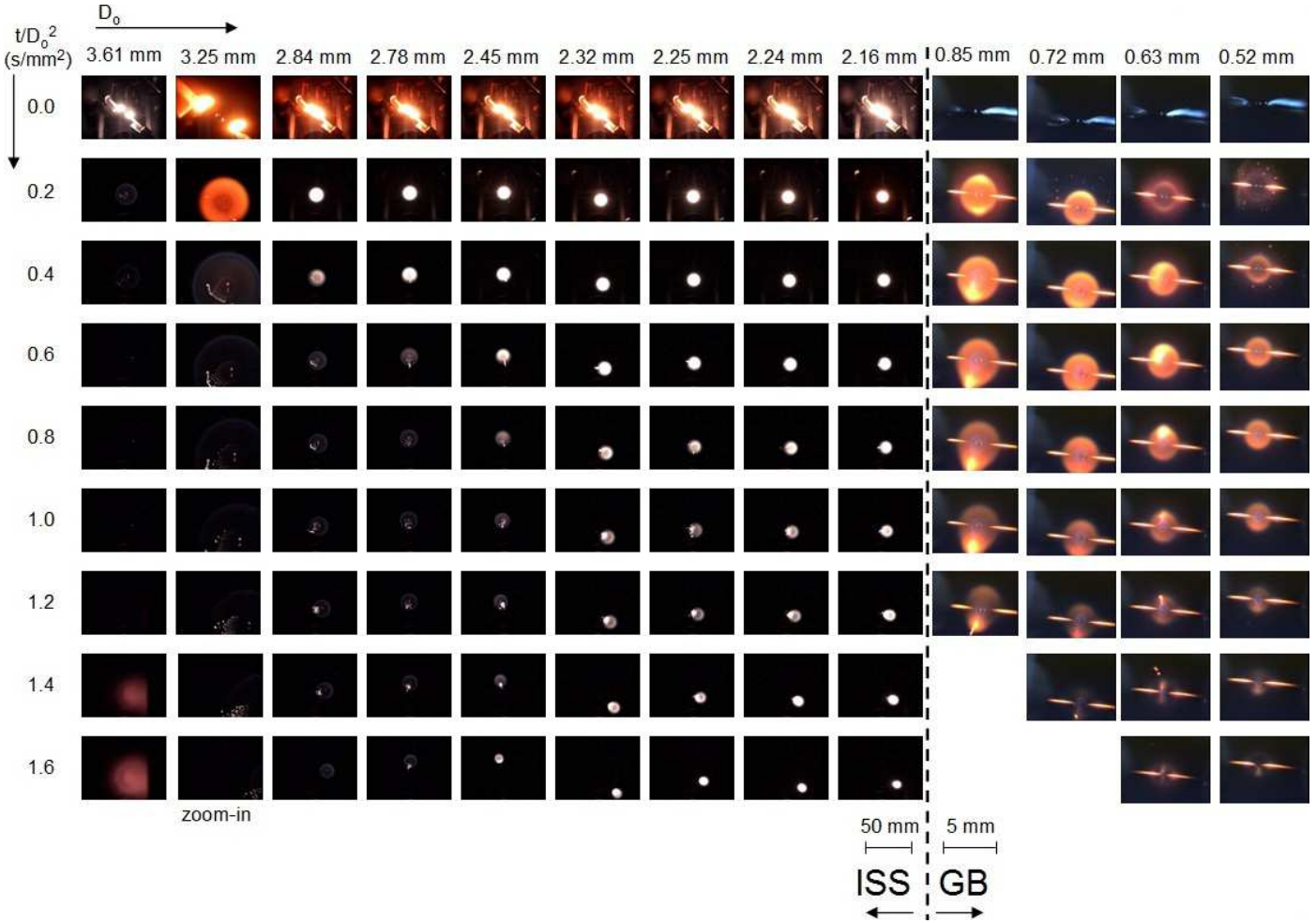

Fig. 10.1. Collection of flame images from the color cameras for both ISS and GB n-octane experiments.

this carbon number and droplet diameter range (Bae and Avedisian (2004), Farouk et al. (2013), Chapter 4). As can be seen in Fig. 10.1, the flame intensity (mainly due to soot incandescence) in the GB range (D_o = 0.52~0.85 mm) increases with increasing droplet diameter. This is an indication of enhanced soot formation due to a longer residence time t_{res} that fuel molecules experience inside the droplet flame.

However, the ISS experiments (D_o = 2.16~3.61 mm, cf. Fig. 10.1) show an opposite trend. When D_o increases the soot incandescence is weakened due to more significant radiative heat losses that inhibit soot formation. The weakening droplet flame (before extinction) gradually proceeds to a stage where only a blue flame is visible (cf. D_o = 2.84 mm, t/D_o^2 = 0.8 s/mm^2). For droplet diameter like D_o = 3.61 mm, radiative extinction that is signified by the disappearance of the flame can be observed. Radiative extinction in a droplet combustion process is caused by excessive radiative heat losses to the surrounding ambient. The radiative heat losses reduce the flame temperature and thus the fuel evaporation rate, so the total heat released from fuel oxidation decreases, which further lower down the flame temperature and finally leads to extinction. This extinction mode is to be contrast to diffusive extinction where the extinction occurs due to depletion of either fuel or oxidizer in a droplet combustion process (Farouk and Dryer (2012b)).

Immediately into the extinction region, some "cloud" structures gradually emerge in the color images (cf. Fig. 10.1, D_o = 3.61, t/D_o^2 = 1.4 and 1.6 s/mm^2). These "clouds" are believed to be the vapor condensation of some combustion products with lower boiling points (e.g. water) due to the transient cooling after radiative extinction. These vapor "clouds" are visible because of the infrared backlight for the BW camera.

Figure 10.2 shows selected BW images from GB and ISS experiments. Again the scale factors for GB and ISS images are different (shown at the bottom of Fig. 10.2). These images are to show qualitative comparison of soot formation and the dynamics of soot shell along the combustion process. In GB images, for $D_o = 0.52$ mm, the soot shell is almost kept intact as a sphere without any soot "tails" breaking the symmetry. This is indicative of less soot formation for smaller droplets (in the GB range) as there are not many soot aggregates that could eventually affect the soot shell symmetry. For $D_o \geq 0.63$ mm, it is evident that the spherically symmetric soot shell is broke by the excessive amount of soot aggregates forming a tail-like structure at an incident angle. Due to the use of supporting fibers, the soot particles at times agglomerate on the fibers (cf. Fig. 10.2, $D_o = 0.72$ mm) so the soot shell symmetry is maintained.

For ISS images (see Fig. 10.2, $D_o = 2.16 \sim 3.61$ mm), though the lighting condition is different, the soot shells are found to be thicker and denser compared to GB images. The soot shells tend to form spherically at every instant but the aggregates shaped as a result of the igniter retraction (in a 4 o'clock and a 10 o'clock direction) retain in the flame and attract the newly formed soot particles. This shape of soot aggregates can be found in all the ISS experiments reported in this study. For larger droplets (e.g., $D_o > 2.84$ mm), soot formation becomes less significant in the later combustion process. This is consistent with the blue faint flame found in Fig. 10.1 for these diameters. Despite the above various dynamics observed for soot shells, they do not appear to affect the spherical symmetry of flames (cf. Fig. 10.1).

Figure 10.3 and 10.4 show the color and BW images, respectively, for n-decane combining ISS and GB experiments. Note that there is only one experiment (with D_o

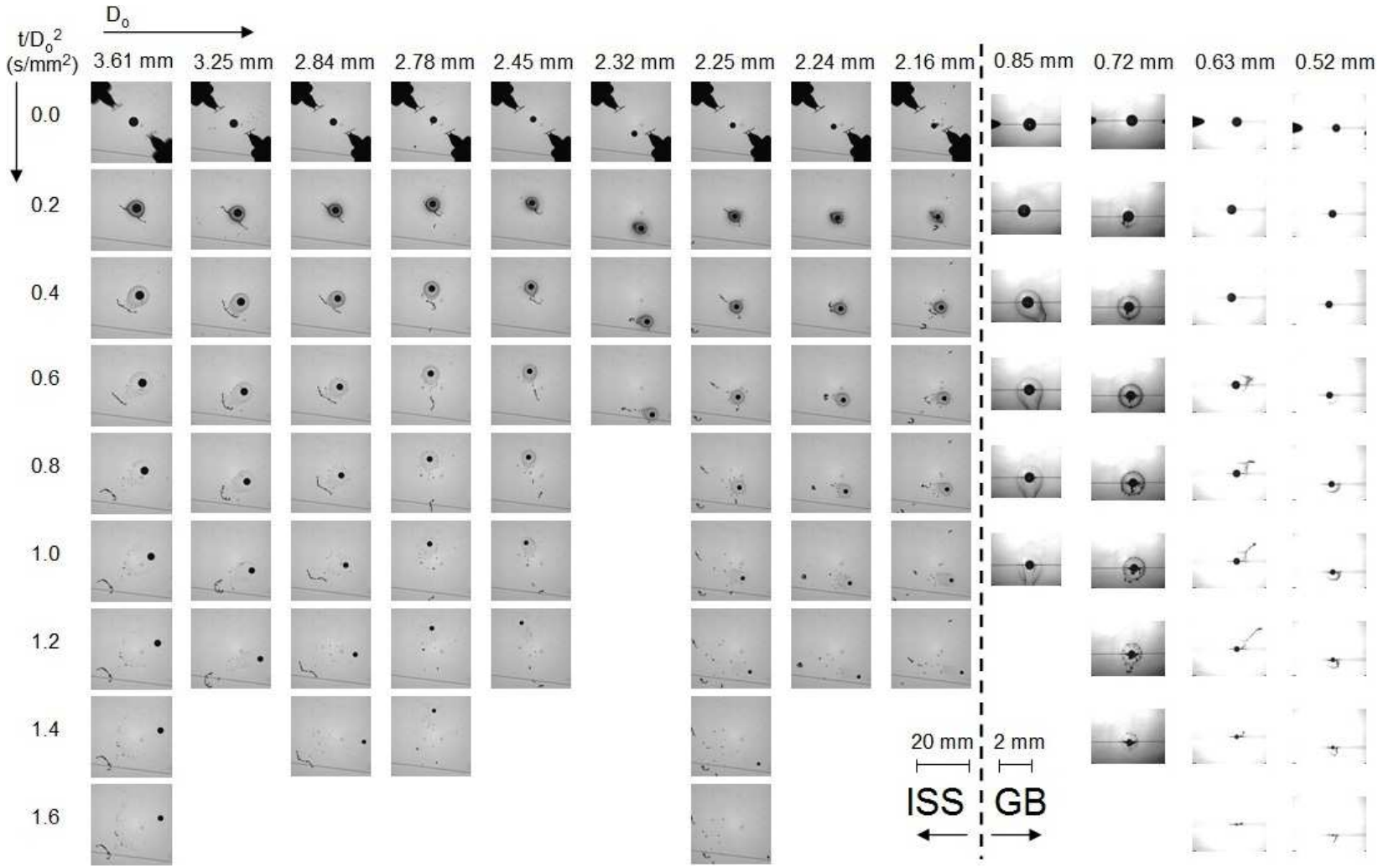

Fig. 10.2. Collection of soot and droplet images from the BW cameras for both ISS and GB n-octane experiments.

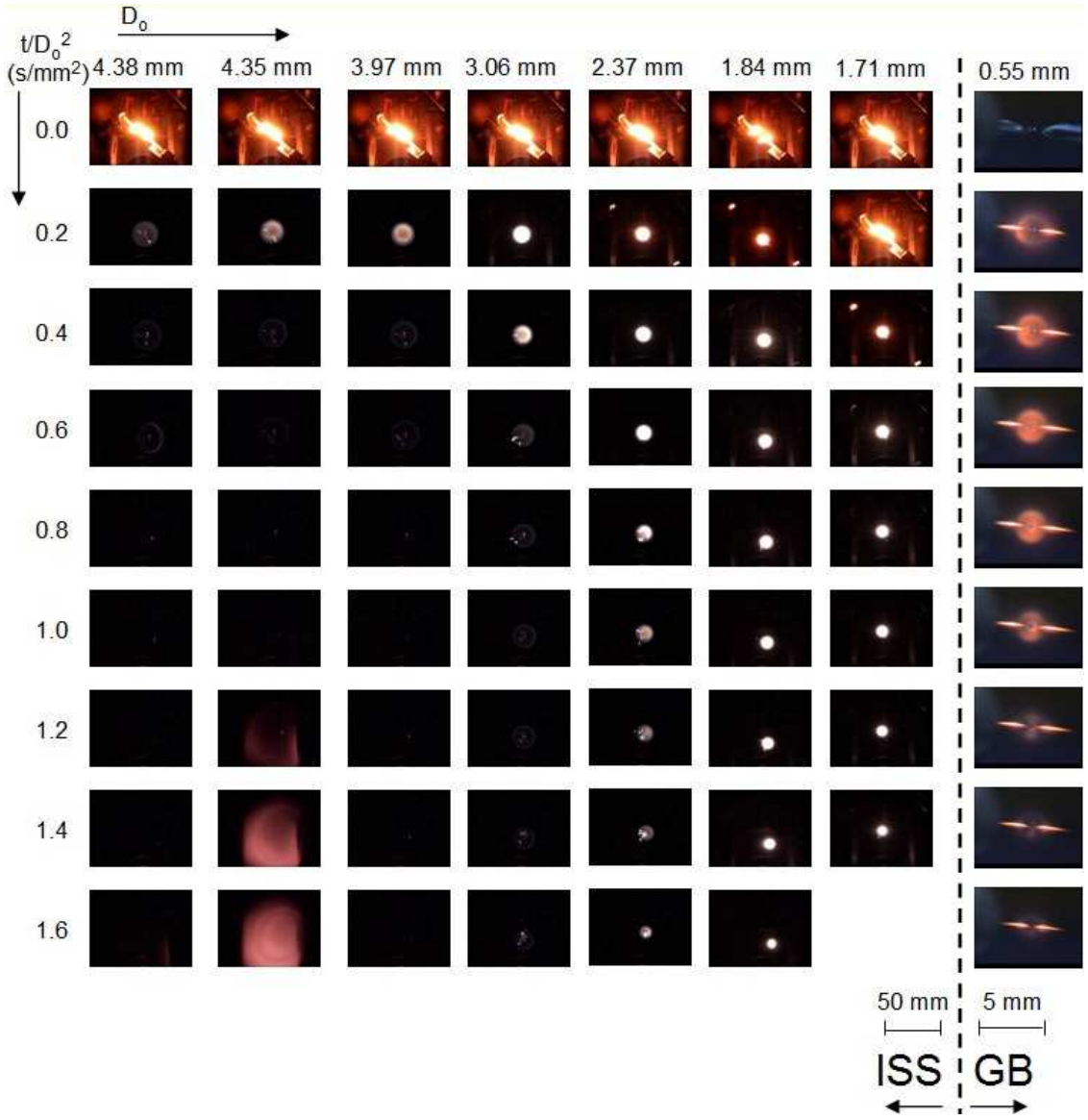

Fig. 10.3. Collection of flame images from the color cameras for both ISS and GB n-decane experiments.

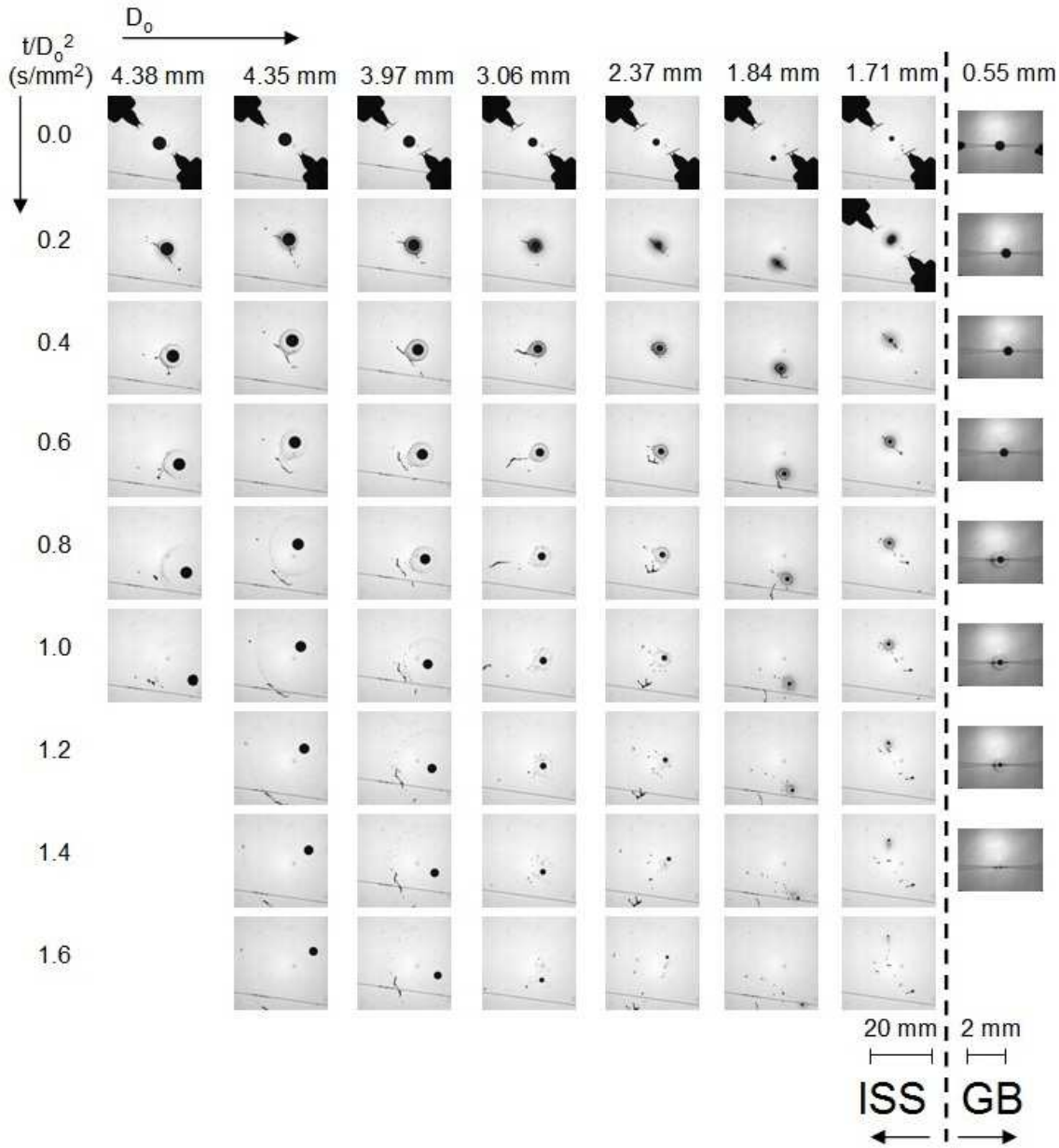

Fig. 10.4. Collection of soot and droplet images from the BW cameras for both ISS and GB n-decane experiments.

=0.55 mm) carried out for GB n-decane, but the diameter conditions for the ISS experiments cover a wider range compared to n-octane (cf. Fig. 10.1 and 10.2). The trend of flame intensity shown in Fig. 10.3 for n-decane is very similar to that for n-octane (Fig. 10.1), with dimmer blue flames for larger droplet diameters. Radiative extinction manifested by the disappearance of the flame is found for n-decane for $D_o \geq$ 3.97 mm with the could-like structure forming (most obvious: D_o =4.35 mm, t/D_o^2 = 1.6 s/mm^2) due to vapor condensation as mentioned for n-octane.

In Fig. 10.4, the only GB n-decane experiment show that the soot shell is very spherical without being affected by the soot aggregates. The amount of soot formation is also qualitatively consistent with the flame intensity shown in Fig. 10.3 for n-decane. Note that for larger n-decane droplets ($D_o \geq$ 3.97 mm) that experience radiative extinction at some point, the soot shell expand radially as a result of a sudden decrease of the thermo-phoretic force due to flame extinction. The soot shell diameter measurements of these images will also be shown later.

Figure 10.5 and 10.6 show the color and BW images for n-heptane droplet combustion from both GB and ISS experiments. Again, there is only one GB experiment (D_o = 0.50 mm, from Chapter 5) included in this comparison. The initial diameter range for ISS experiments tend to cover the 1-2 mm region as well as extend to the radiative extinction region (D_o = 3.32 ~3.87 mm). Similar trends for flame intensity are found for n-heptane as for n-octane (Fig. 10.1) and n-decane (Fig. 10.3)- the flame intensity decreases with increasing D_o due to more significant radiative heat losses that inhibit soot formation for larger droplets. Interestingly, the “cloud-like” structure in Figs. 10.1 and 10.3 for n-octane and n-decane is not found after radiative

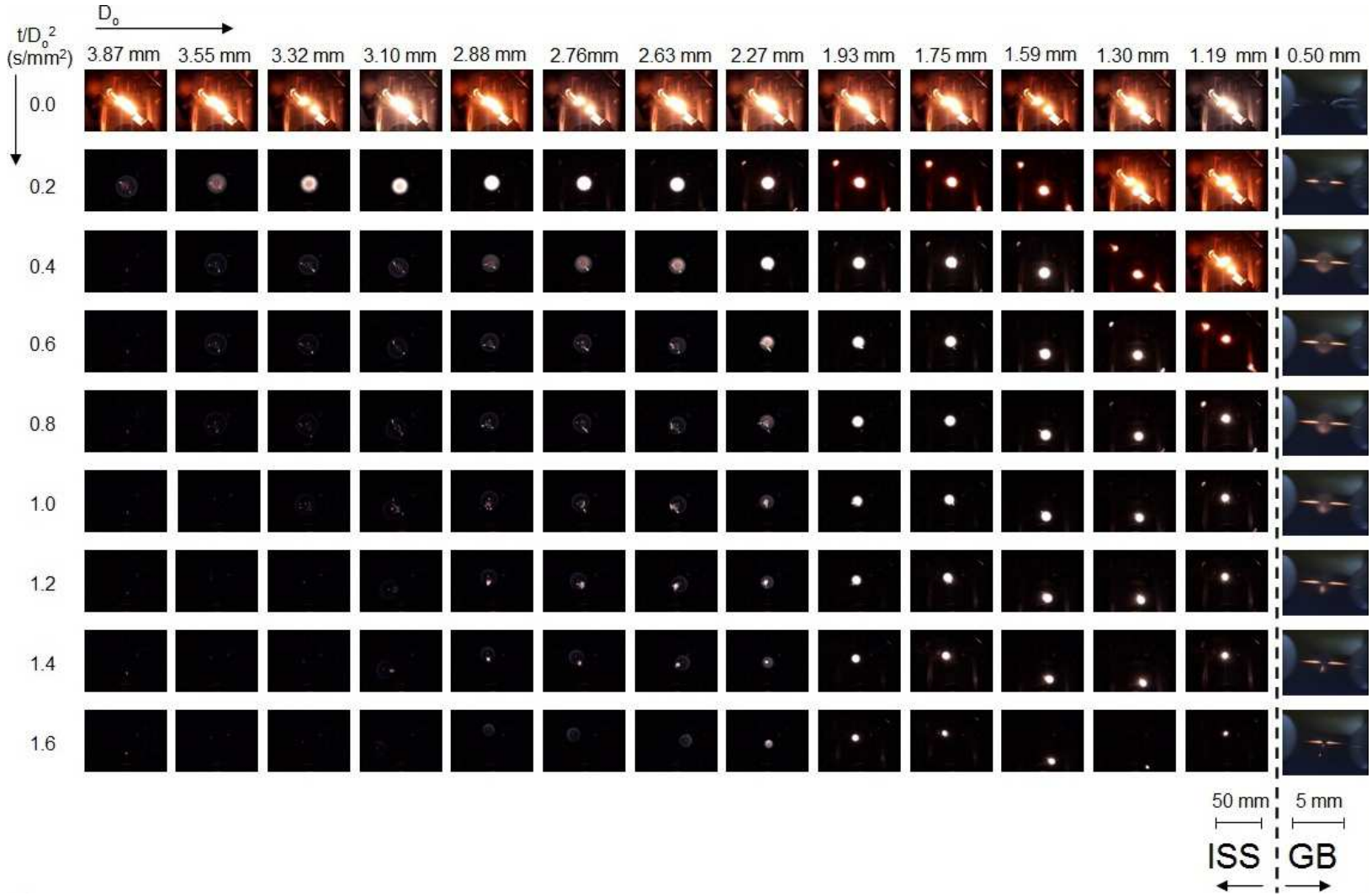

Fig. 10.5. Collection of flame images from the color cameras for both ISS and GB n-heptane experiments.

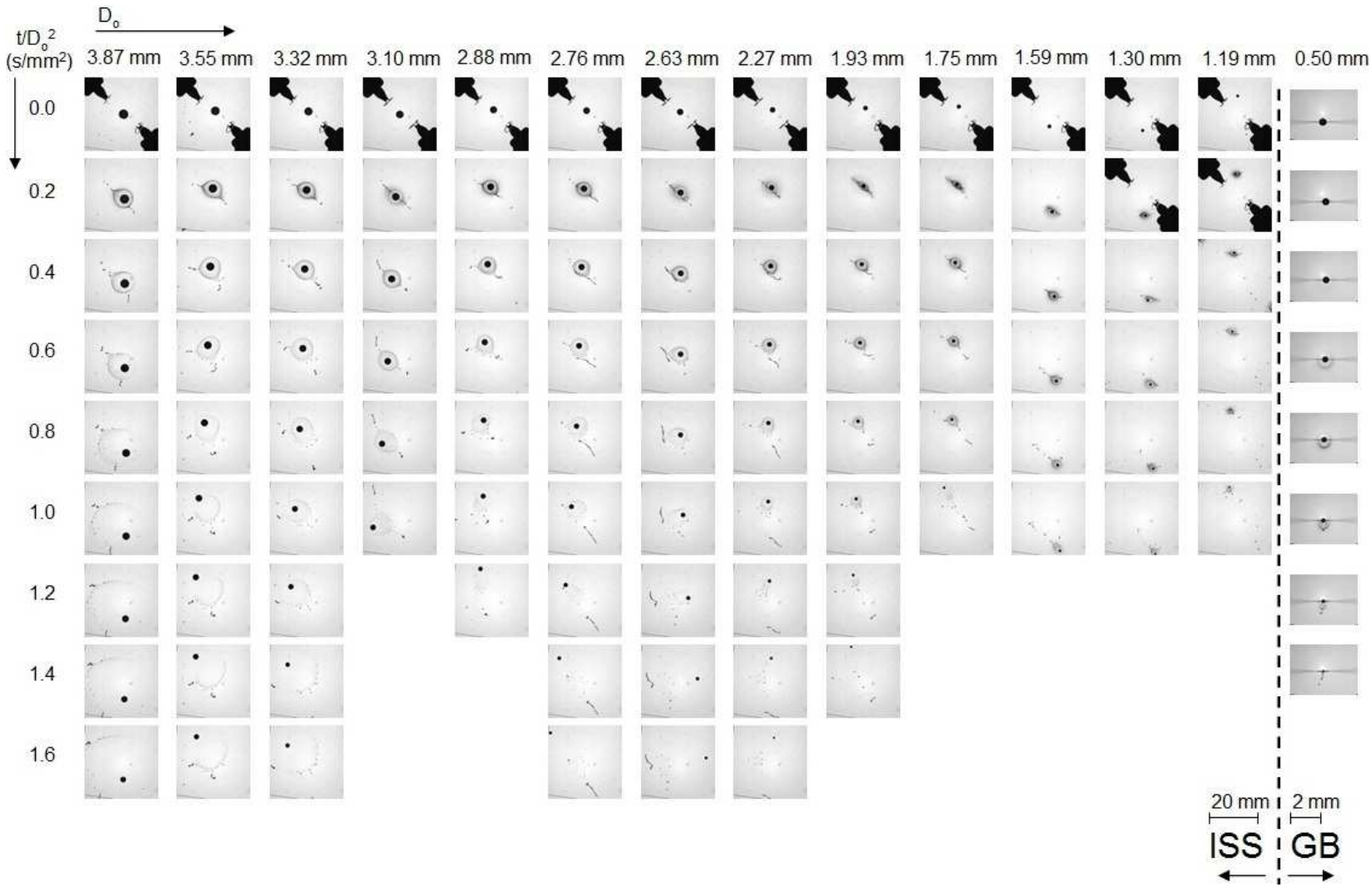

Fig. 10.6. Collection of soot and droplet images from the BW cameras for both ISS and GB n-heptane experiments.

extinction for n-heptane within the imaging period. The reasons are speculated to be the slight higher heat of combustion of n-heptane that allows for a higher flame temperature such that the ambient temperature in the post-extinction period is slight higher compared to for n-octane and n-decane. The vapor condensation might still occur for n-heptane later when the ambient becomes cooler.

The soot dynamics for n-heptane droplet flames are shown in Fig. 10.6. While the n-hetpane droplet flames are spherically symmetric (cf. Fig. 1.2), the soot shells observed from the ISS experiments (shown in Fig. 10.6) are not very stable. We still attempt to extract the soot shell dimension under the assumption of spherically symmetrical soot shells using the method described in Chapter 3.

From the BW images like in Fig. 10.2, the droplet dimension is extract from each of the consecutive images in an experiment. The evolution of D^2 is plotted (as D^2 vs. t) in Fig. 10.7 for n-octane. The significance of Fig. 10.7 is that it shows the capability of the ISS experiments allowing investigations with a much longer low gravity period (~ 27 s for the reported n-octane data) compared to a GB experiment (a vertical dotted line shows the limitation for a GB experiment, 1.2 s, in the present study). The slope of each curve in Fig. 10.7 indicates the burning rate K (mm^2/s). The D^2 evolution for pure evaporation of a 2.8 mm n-octane droplet is also provided (red cross data, with a much smaller slope) in the same figure for comparison. For D_o = 3.61 mm, the radiative extinction point can be identified by the slope change on the D^2 curve meaning the burning rate before and after extinction is different.

In order to better present the D_o effects on the slope of D^2 data, Fig. 10.8a and 10.8b show the D^2 data that are normalized by D_o^2. As shown in Fig. 10.8a, all four GB

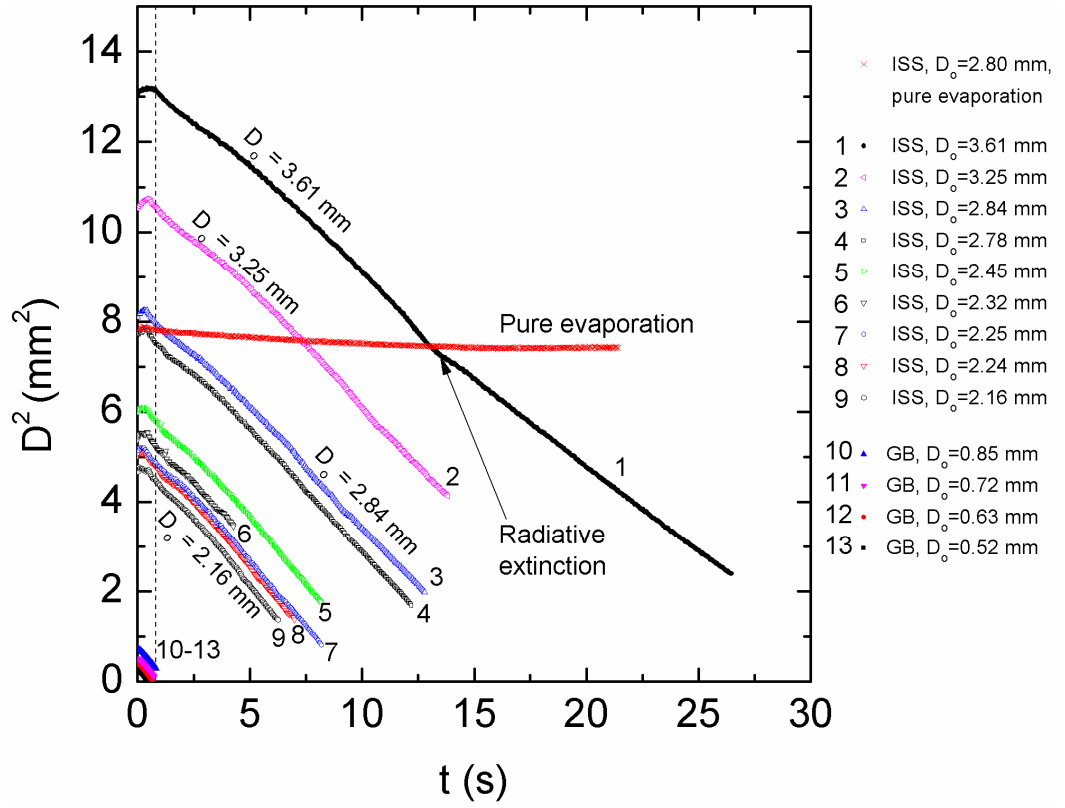

Fig. 10.7. A graph including all the n-octane D^2 real time histories showing the significance of the ISS experiments that allows for a much longer experimentation time compared to GB.

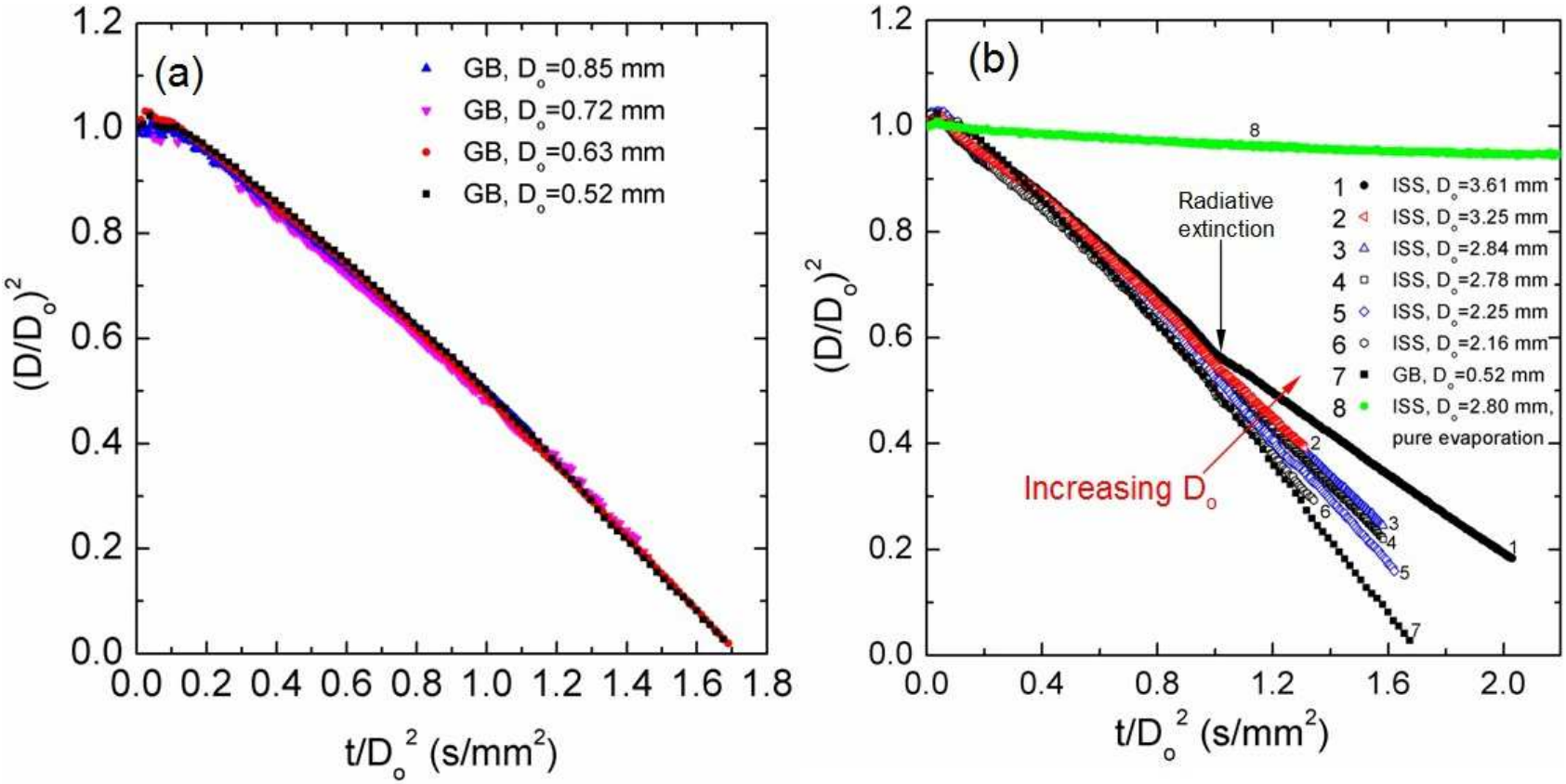

Fig. 10.8. (a) D^2 histories normalized by D_o^2 for the GB n-octane experiments; (b) normalized D^2 data over the D_o range investigated for n-octane.

data (0.52 mm ≤ D_o ≤ 0.85 mm) are very close to one another. Therefore, Fig. 10.8b only includes one condition (D_o = 0.52 mm) from the GB experiments to represent the entire GB data. It is evident in Fig. 10.8b that as D_o increases, the slope of D^2 data decreases indicating a decrease of burning rate due to D_o effects. Again, the data for pure evaporation has a very different slope compared to those burning droplets. The slope change for D_o = 3.61 mm due to radiative extinction is clearer in Fig. 10.6b. Note that the slope in the post-extinction region is still much larger than pure evaporation. Recent investigations suggest that this post-extinction behavior (also termed a "cool flame" (Nayagam et al. (2012)) is caused by the remaining hot ambient still being able to sustain a series of low temperature combustion kinetics after extinction.

Due to the non-linearity of the D^2 curve, it is difficult to obtain one burning rate value for each condition that comprehensively includes the burning characteristics of such a transient process, especially when radiative extinction occurs in some experiments. Figure 10.9a shows how the n-octane D^2 data are divided into four regions (K1 to K4, 0.4 s/mm^2 for each region) in each of these regions a linear fit is used to obtain the burning rate value to be shown in Fig. 10.9b to 10.9e. The black dotted curves indicate the suggested trends for these data, and the black dotted circle outlines the data taken from post-extinction region. As can be seen, the GB data shows very small difference in burning rates except in the K1 region where spark ignition might have slightly distorted the droplet boundary leading to a larger error. The burning rates gradually increase along the burning process for all droplets (by comparing the value in Fig. 10.9b to 10.9e). From Fig. 10.9b to 10.9e, it is evident that in the smaller D_o range (or GB range) the burning rates are nearly constant, but in the larger D_o range (ISS

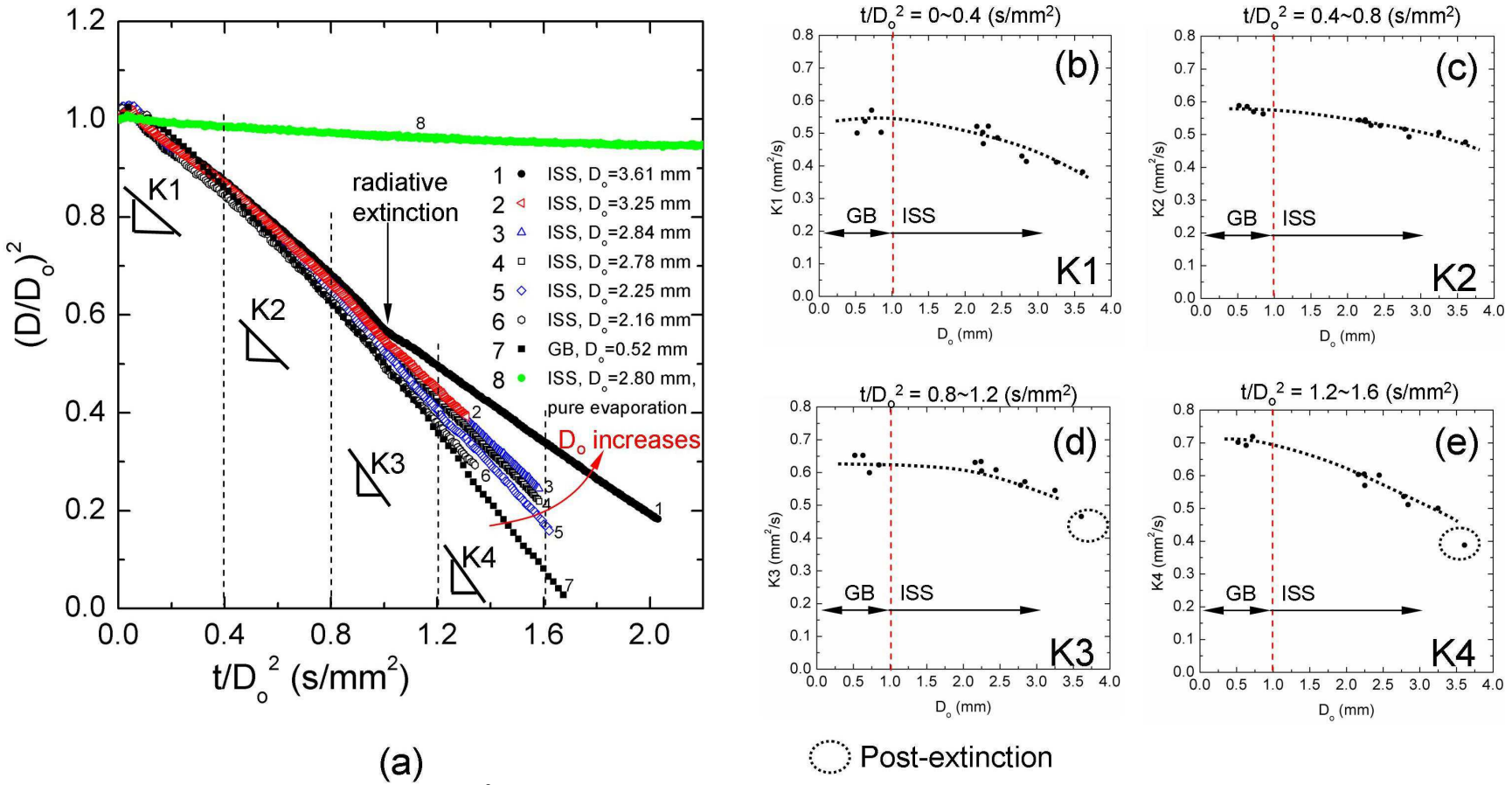

Fig. 10.9. (a) Illustration of dividing the D^2 data (shown in Fig. 10.8) for n-octane into four regions, K1 to K4, for the burning rate analyses; (b) local burning rate K1 vs. D_o; (c) local burning rate K2 vs. D_o; (d) local burning rate K3 vs. D_o; (e) local burning rate K4 vs. D_o.

range) burning rates decrease with increasing D_o. Note that there is a lack of burning rate data for n-octane in the range of D_o ~1-2 mm, but we speculate that the data within this range would not deviate from the suggested trend line (as suggested by the later shown n-decane and n-heptane data, which includes data in this D_o range).

Figure 10.10a shows the D^2 evolution (normalized by D_o^2) for n-decane with various D_o conditions. It is obvious that the slope of the D^2 curves in Fig. 10.10a decreases with increasing D_o, which is similar to the observation for n-octane. Using the same approach as in Fig. 10.9a for n-octane, the D^2 data for n-decane are split into four regions (K1 to K4, with 0.5 s/mm^2 for each region considering the longer burning time of n-decane compared to n-octane). Significant D_o dependency emerges in K2, K3, and K4 regions for n-decane shown in Fig. 10.10c, 10.10d, and 10.10e, respectively. The dotted line shows the suggested trend for each period. It is evident that the burning rate decreases with increasing D_o for n-decane within the D_o range of investigation. Data from the post-extinction region show further lower burning rate compared to that before extinction.

Figure 10.11a shows the D^2 data for n-heptane that are normalized by D_o^2. Similar to n-octane (Fig. 10.9a) and n-decane (Fig. 10.10a), the larger the D_o the smaller the D^2 slope. The entire D^2 data in Fig. 10.11a are divided into "five" regions (with 0.4 s/mm^2 in each region) mainly to cover the considerably amount of data available for post-extinction. The area in which K1 to K5 do not include is a distinct region where the slope of D^2 curve changes at the end of post-extinction region. This is to be discussed later in this section. Figure 10.11b to 10.11f shows the burning rate values in the regions of K1 to K5 (cf. Fig. 10.11a), respectively. The results suggest again, that

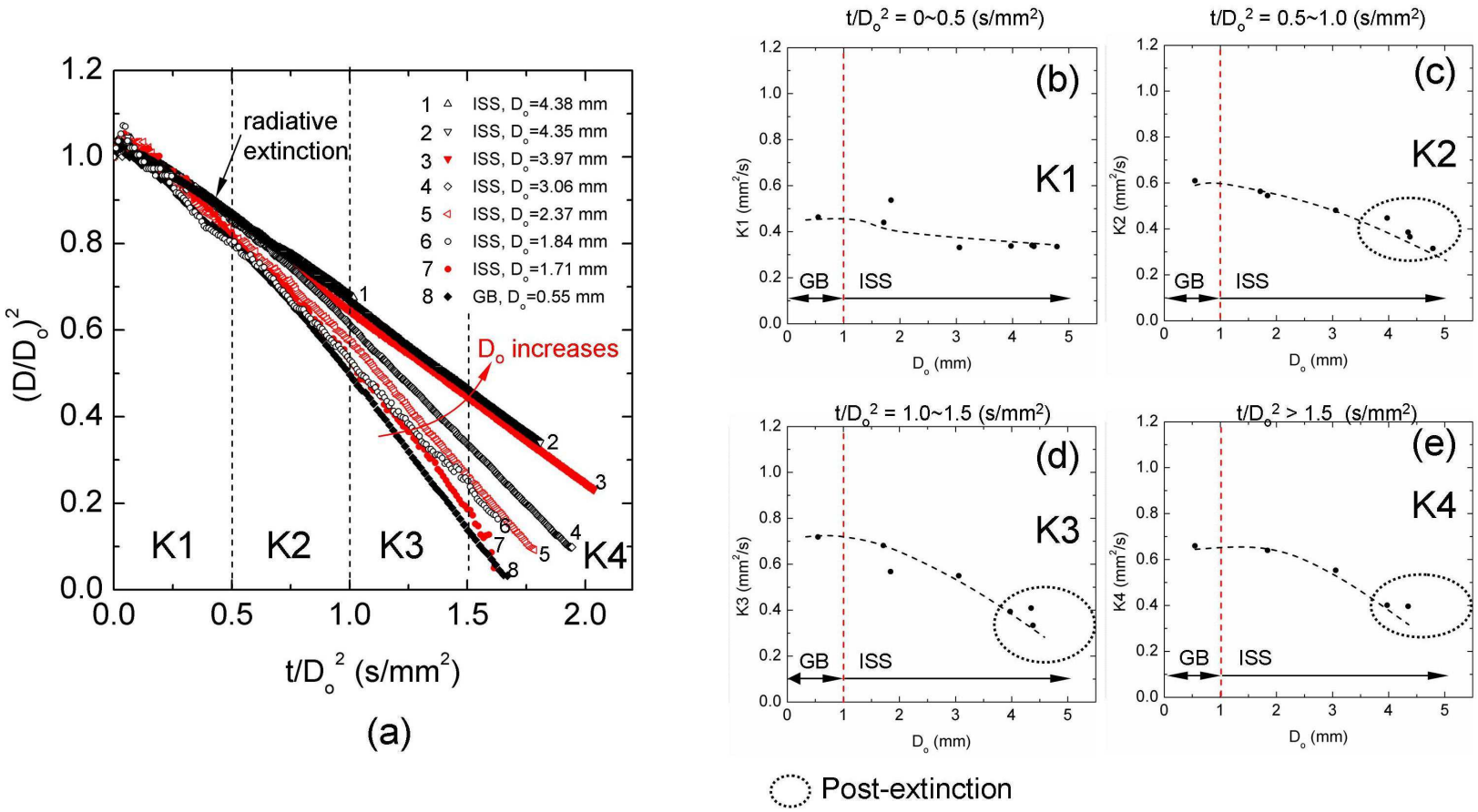

Fig. 10.10. (a) Normalized D^2 histories for n-decane and an illustration of dividing the D^2 data into four regions, K1 to K4, for the burning rate analyses; (b) local burning rate K1 vs. D_o; (c) local burning rate K2 vs. D_o; (d) local burning rate K3 vs. D_o; (e) local burning rate K4 vs. D_o.

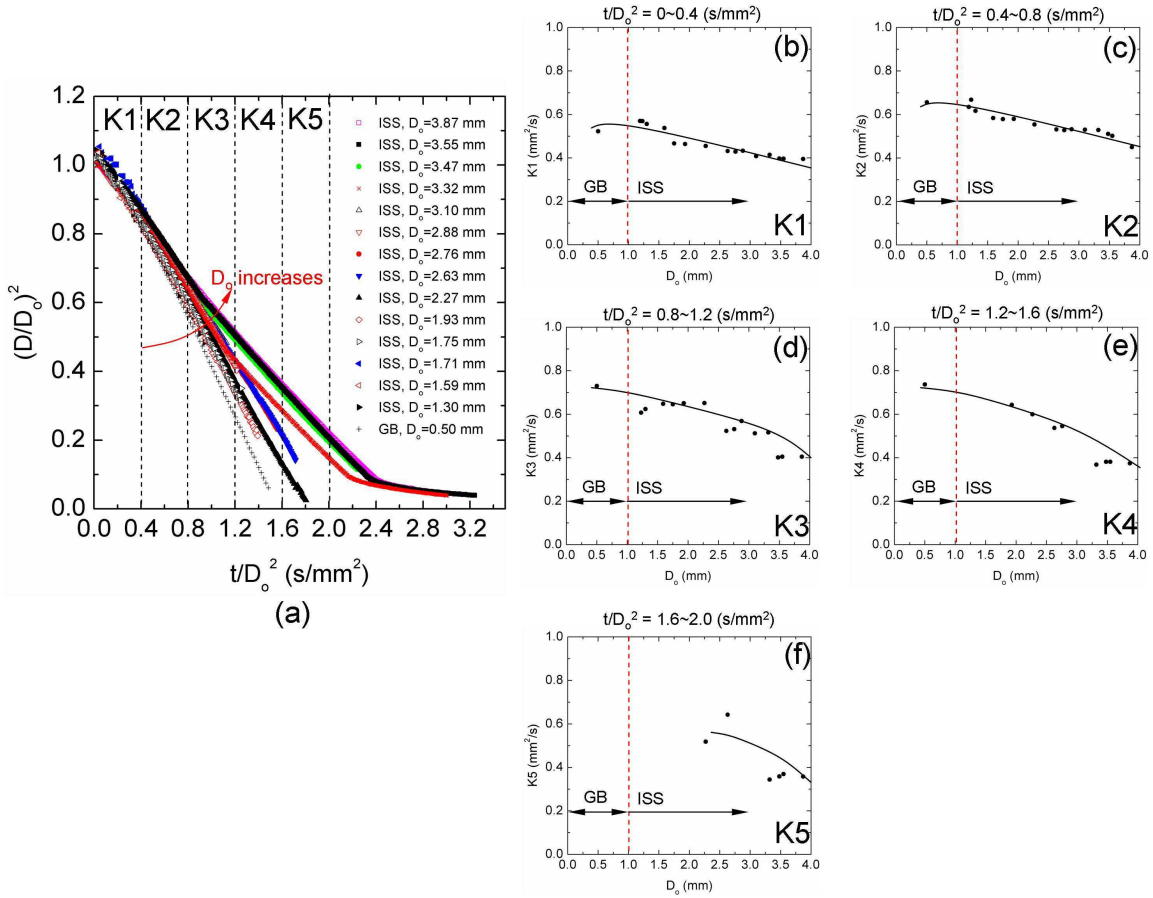

Fig. 10.11. (a) Normalized D^2 histories for n-hepane and an illustration of dividing the D^2 data into four regions, K1 to K5, for the burning rate analyses; (b) local burning rate K1 vs. D_o; (c) local burning rate K2 vs. D_o; (d) local burning rate K3 vs. D_o; (e) local burning rate K4 vs. D_o; (f) local burning rate K5 vs. D_o.

the burning rate decreases with increasing D_o over the regions of K1 to K5.

From the results shown in Fig. 10.9, 10.10, and 10.11, it is conclusive that the burning rate decreases with increasing D_o within the D_o range investigated for the fuel examined. Reviewing the speculated trends for burning rates in Fig. 1.5c, the data reported in this study continue to decrease for $D_o > 1.5$ mm. The experimental results suggest that though soot formation is enhanced due to a larger t_{res} for larger droplet flames, radiative heat losses overwhelmingly lower down the flame temperature for larger droplets (hence inhibit soot formation), leading to a monotonic decrease of burning rate with increasing D_o.

Figure 10.12a shows the flame standoff ratio (FSR ≡ D_f/D) evolution for n-octane. These data are obtained by measuring the size of the blue flame from the images shown in Fig. 10.1. Only 20 data points are measured for each D_o condition regardless the total number of images available from the ISS experiments while all GB flame images are measured and shown in Fig. 10.12a. The FSR values for n-octane monotonically increase with time and all the FSR data are cluttered in Fig. 10.12a. In order to examine the D_o effects on FSR, the data extracted from the three sampling lines (t/D_o^2 = 0.4, 0.8, and 1.2 s/mm^2, respectively) indicated in Fig. 10.12a are plotted in Fig. 10.12b. As can be seen, the FSR for n-octane decreases with increasing D_o in the GB range, and the FSR data in the ISS region decreases from a larger value than for D_o = 0.85 mm. Although there is a gap (D_o = 1.0~ 2.0 mm) where no data is currently available, the black dotted line in Fig. 10.12b indicates a "three-stage" trend for FSR at t/D_o^2 = 0.8 s/mm^2. This suggested trend is also applicable for the data with t/D_o^2 = 0.4 and 1.2 s/mm^2 in Fig. 10.12b.

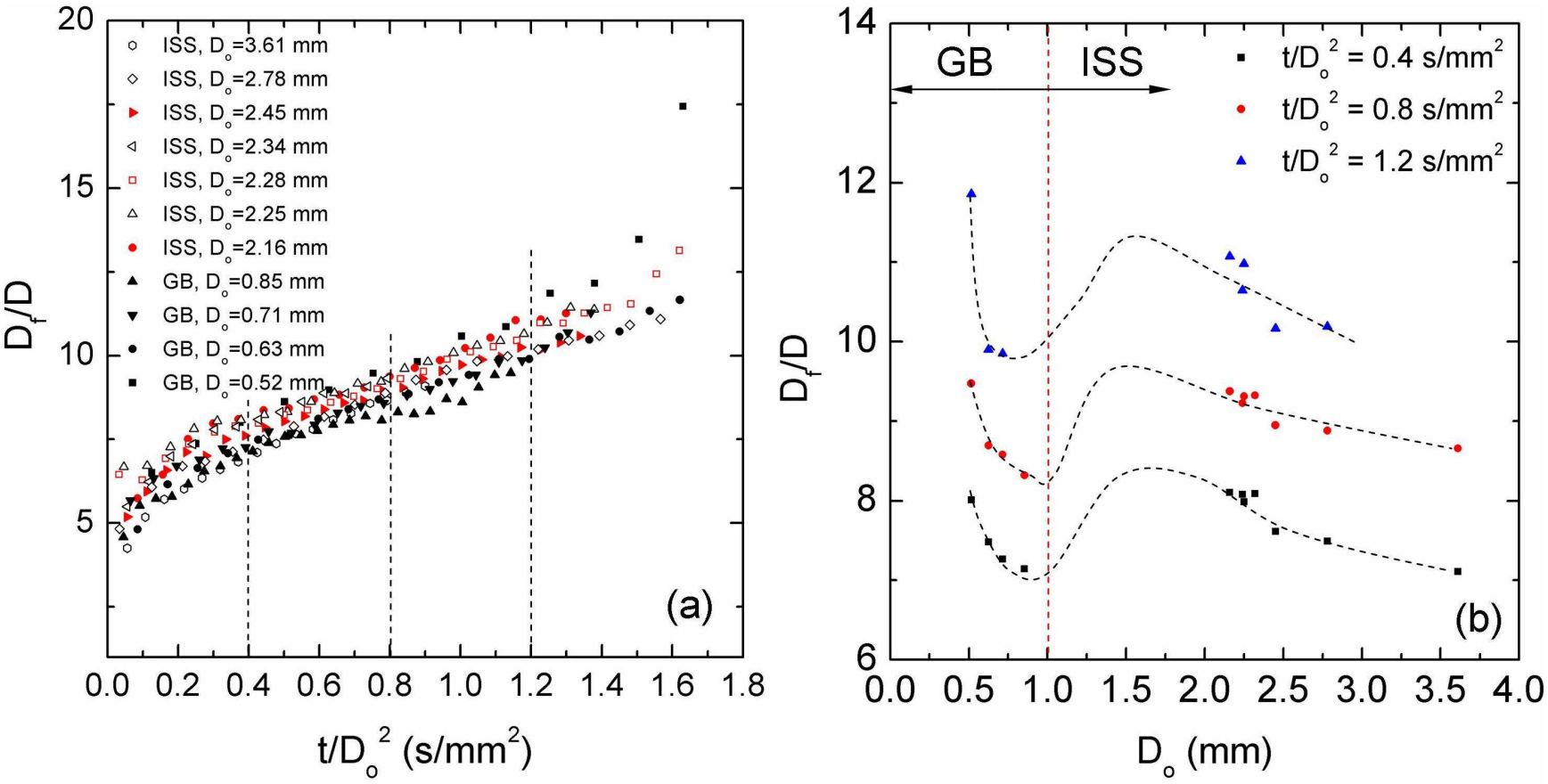

Fig. 10.12. (a) Flame standoff ratio (FSR) for n-octane over the D_o range investigated; (b) FSR vs. D_o for the data extracted from the three dotted lines in (a) for t/D_o^2 = 0.4, 0.8 and 1.2 s/mm^2.

Similar analyses as shown in Fig. 10.12a and 10.12b are also performed for n-decane and n-heptane and shown in Fig. 10.13a, 10.13b, 10.14a and 10.14b, respectively. Again, FSRs for n-decane and n-heptane increase with time (see Fig. 10.13a and 10.14a). For the extracted FSR data from n-decane experiments (cf. Fig. 10.13b), though there is only one experiment from the GB range, we suspect that the trend (shown by the black dotted line in Fig. 10.13b) to be similar as for n-octane (cf. Fig. 10.12b) due to the fact that the FSRs in the ISS range decrease with increasing D_o, and, these FSR values are all larger than the GB value at the same t/D_o^2. Figure 10.14a shows similar increasing trend for FSR over time. The "three-stage" trend for the FSR is also found in n-heptane data (see Fig. 10.14b). Note that the n-heptane data better cover the range of D_o = 1~2 mm in which the trend of "increasing FSRs" as suggested by the black dotted line is confirmed for n-heptane.

Figure 10.15 illustrates the observed "three-stage" curve in the FSR vs. D_o graphs for the fuel examined in this study, with the three stages labeled as I, II, and III (stage I represents the region where FSRs decrease with increasing D_o; stage II is the increasing FSR region; stage III is the other region where FSRs also decrease with increasing D_o). Combining the observations for soot formation and radiative heat losses from all the results in the present study, we attempt to provide explanations for this "three-stage" behavior of FSR. In stage I, the FSR values are greatly affected by soot formation. The decrease of FSR observed in this stage is due to the enhanced soot formation when D_o increases in this small D_o region (also observed in Fig. 10.1 for n-octane). The larger t_{res} with negligible radiative heat losses to the surroundings cause fuel molecules to convert to soot particles that could potentially reduce the effective

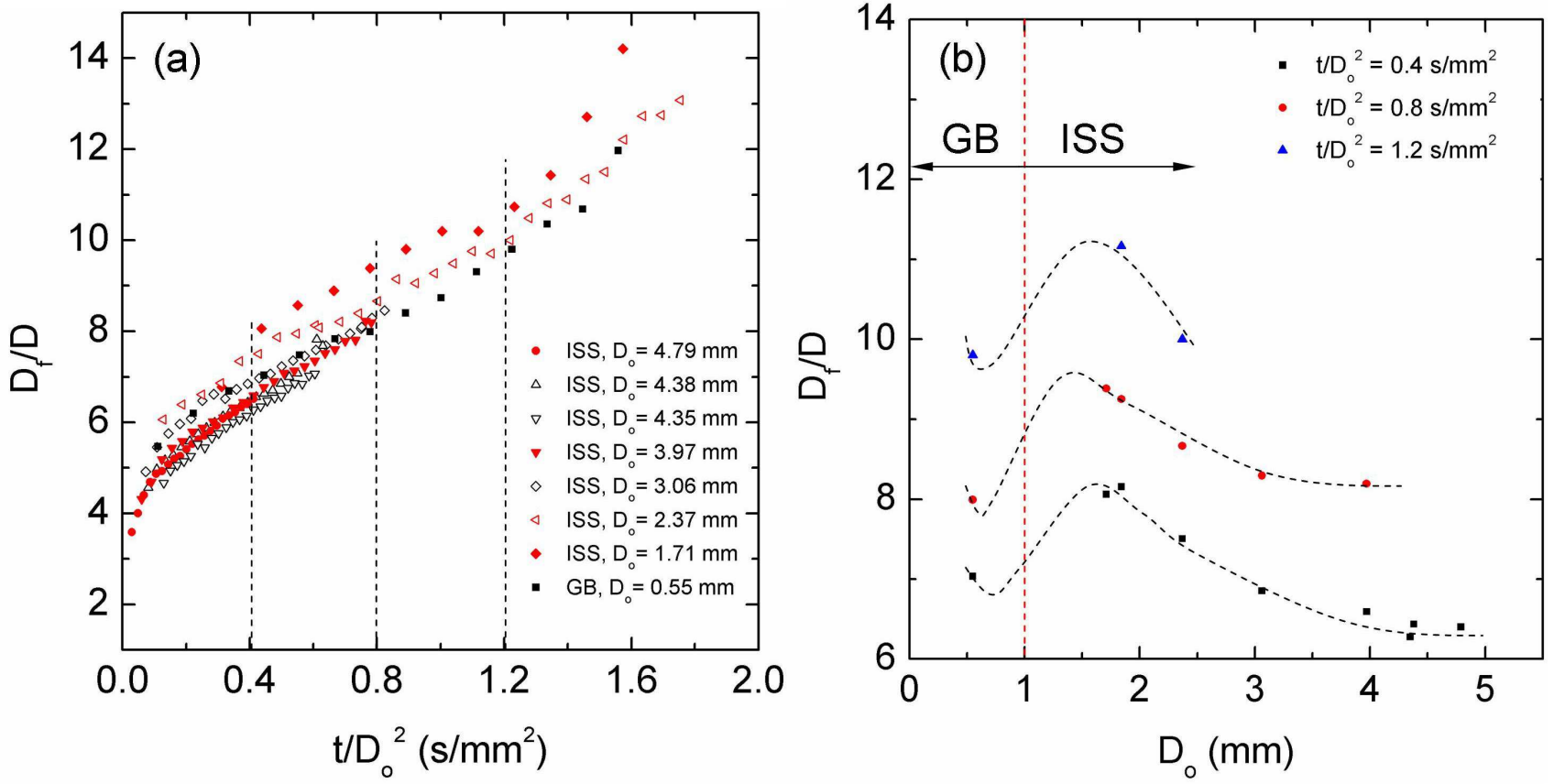

Fig. 10.13 (a) Flame standoff ratio (FSR) for n-decane over the D_o range investigated; (b) FSR vs. D_o for the data extracted from the three dotted lines in (a) for t/D_o^2 = 0.4, 0.8 and 1.2 s/mm^2.

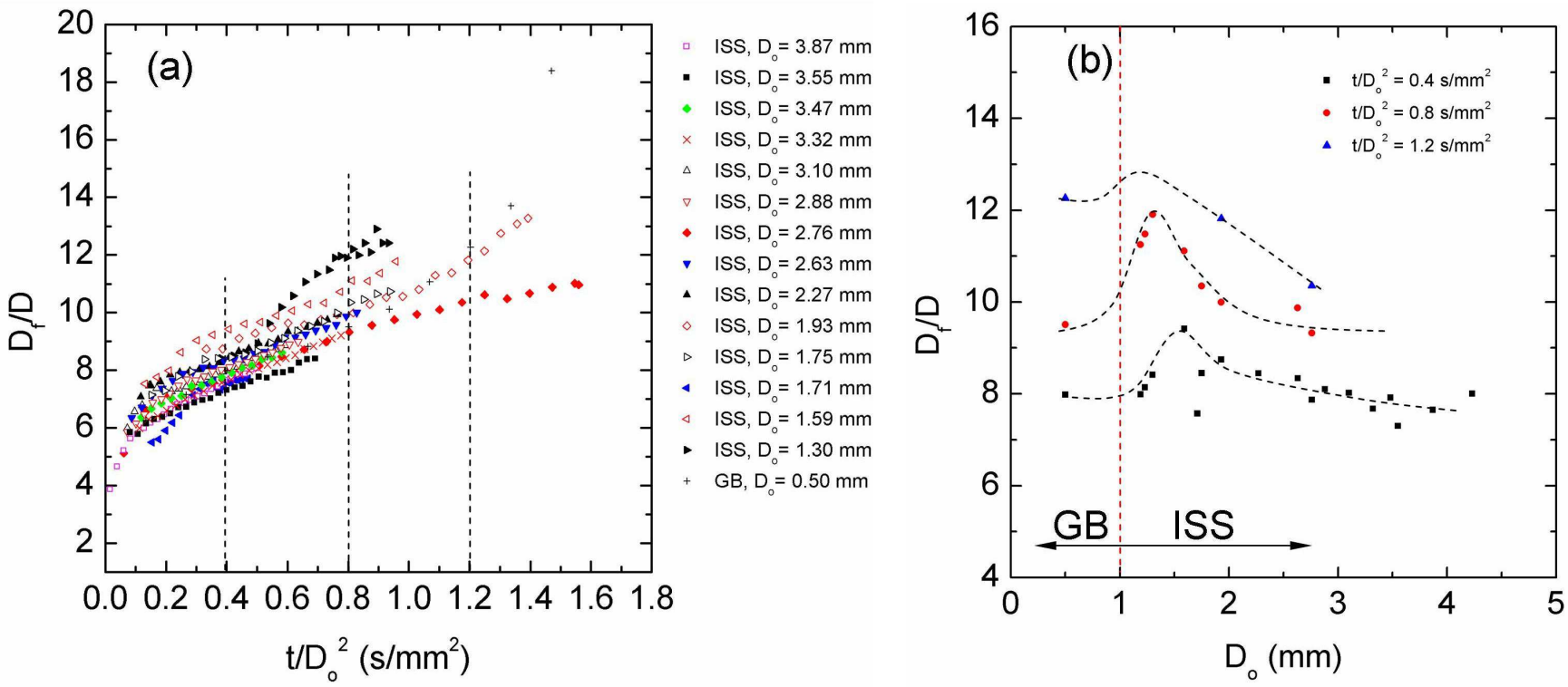

Fig. 10.14. (a) Flame standoff ratio (FSR) for n-hepane over the D_o range investigated; (b) FSR vs. D_o for the data extracted from the three dotted lines in (a) for t/D_o^2 = 0.4, 0.8 and 1.2 s/mm^2.

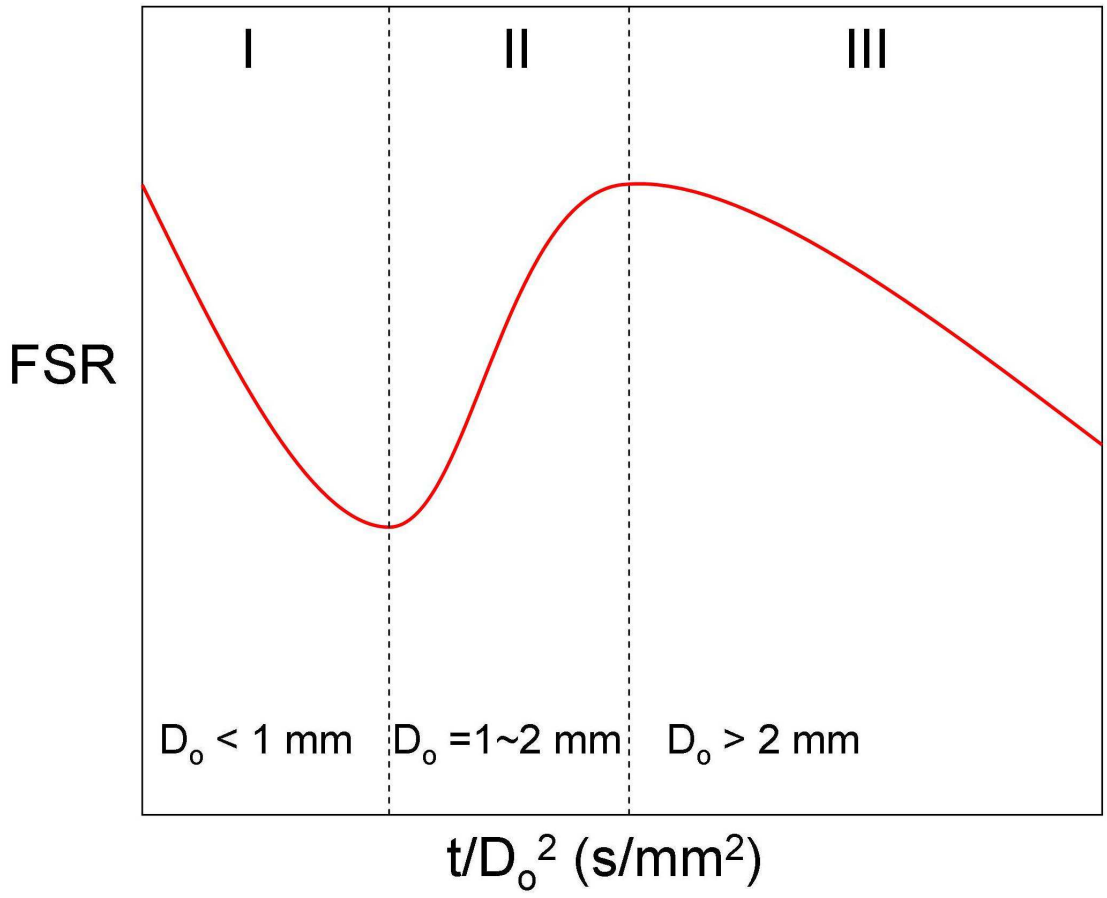

Fig. 10.15. Schematic of the "three-stage" curve suggested in the plots of FSR vs. D_o in Fig. 10.12b, 10.13b and 10.14b.

diffusion coefficient in the gas phase (Nayagam et al. (2008)). The reduction of the effective diffusion coefficient would lower the fuel diffusion rate, thus causing the flame retreat (i.e. smaller FSR).

For stage II shown in Fig. 10.15, this is when the radiative heat losses become significant (D_o ~ 1 mm (Marchese and Dryer (1997))). Compared to stage I, soot formation is slightly inhibited due to substantial radiative heat losses that begin to cool down the flame, but the radiation effects are still not too much to affect the burning rate (fuel evaporation rate), as evident in Fig. 10.9, 10.10, and 10.11. The effectively diffusion coefficient increases with increasing D_o in this narrow region resulting increasing FSRs.

Stage III is where radiative losses created by large droplet flames dominate the burning process (particular burning rate, see Fig. 10.9, 10.10, and 10.11). The flame temperature is cooled down to a point where soot formation is no longer prominent. The FSR decreases with increasing D_o in this region simply because the burning rate is greatly reduced due to significant radiative heat losses, as the FSR depends partially on the burning rate K (Aharon and Shaw (1997)).

Figure 10.16 shows the FSRs obtained from the color and LLLUV images from the ISS experiments. Three D_o conditions are selected for comparison as these conditions are the smallest, intermediate, and the largest D_o among all the ISS n-octane experiments. The FSRs measured from LLLUV images (open symbols) are found to be consistently larger compared to those obtained from color images (close symbols). When the flame is larger (D_o = 3.61 mm), the difference between two measurements become more obvious. The inset photos are the flame images recorded by the LLLUV

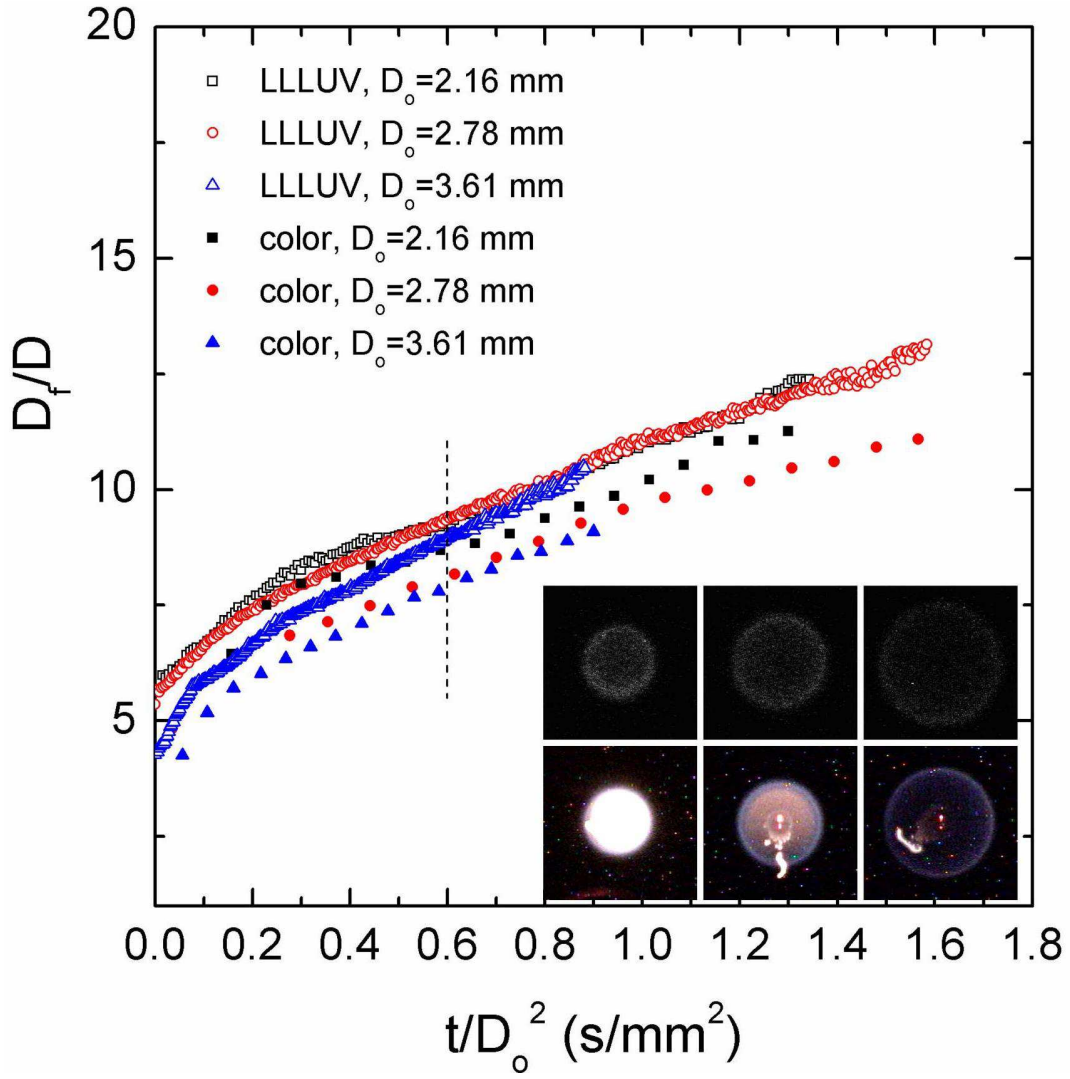

Fig. 10.16. FSR obtained from color and LLLUV images. The inset images correspond to the data on the dotted line.

camera (the upper row) and the color camera (the lower row) at $t/D_o^2 = 0.6$ s/mm^2 (the black dotted line in the Fig. 10.16) for the three D_o conditions. These images are with the same scale for the comparison of the real flame sizes. As mentioned earlier, the LLLUV camera records the OH narrow band emission while the color camera documents the emission in the range of visible lights. OH flames appear to be consistently larger than the outer boundary of the visible flames. Therefore, the FSR discussions pertaining to OH flames should be qualitative the same as for color flames in terms of D_o effects.

Figure 10.17 shows the evolution of soot standoff ratio, SSR ≡ D_s/D, for n-octane with the D_s and D measured from the BW images. The results suggest that SSR of n-octane increases with increasing D_o. Similar trends are also found for n-decane (Fig. 10.18) and n-heptane (Fig. 10.19). Note that for the larger D_o data in Fig. 10.18, SSR values are reported for the post-extinction region where the soot shell expands due to weakening thermophoresis leading to the dramatic increase of SSRs. The slight scatter of data in Fig. 10.19 (n-heptane) is due to less stable soot shells observed in all the n-heptane experiments. Except for the outliners (D_o =1.30 and 1.71 mm), most data exhibit a similar trend as found for n-octane and n-decane.

For all the fuels examined in this chapter, radiative extinction occurs when D_o reaches a certain value (usually above 3 mm, depending on the fuel). A spherical droplet flame usually extinguishes from one “point” on the flame shell. Then the flame boundary moves towards the opposite point on the shell until the entire flame disappears. For sooting fuels tested in this study, this extinction process is initiated due to the presence of soot aggregates. Figure 10.20a shows consecutive images (recorded

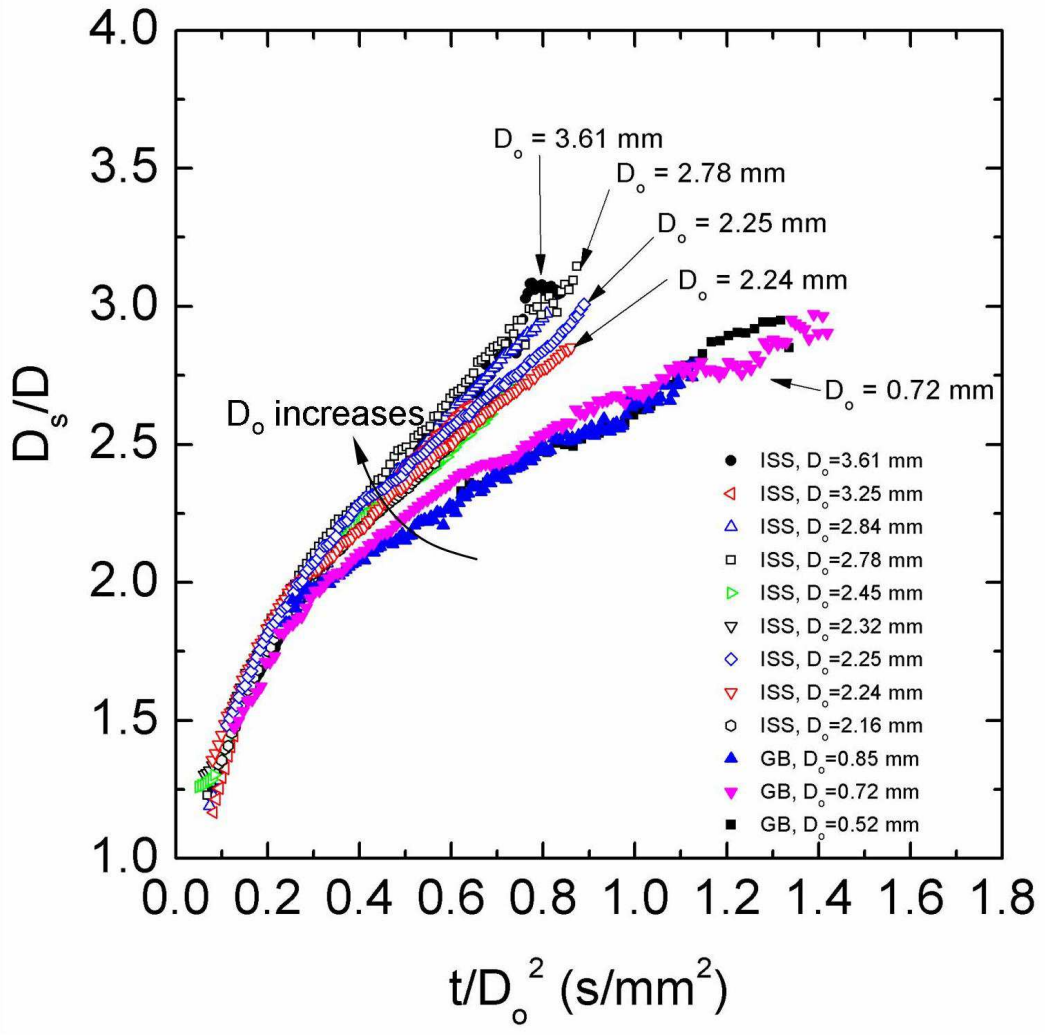

Fig. 10.17. Evolution of soot standoff ratio (SSR) for n-octane droplet flames over the D_o range investigated.

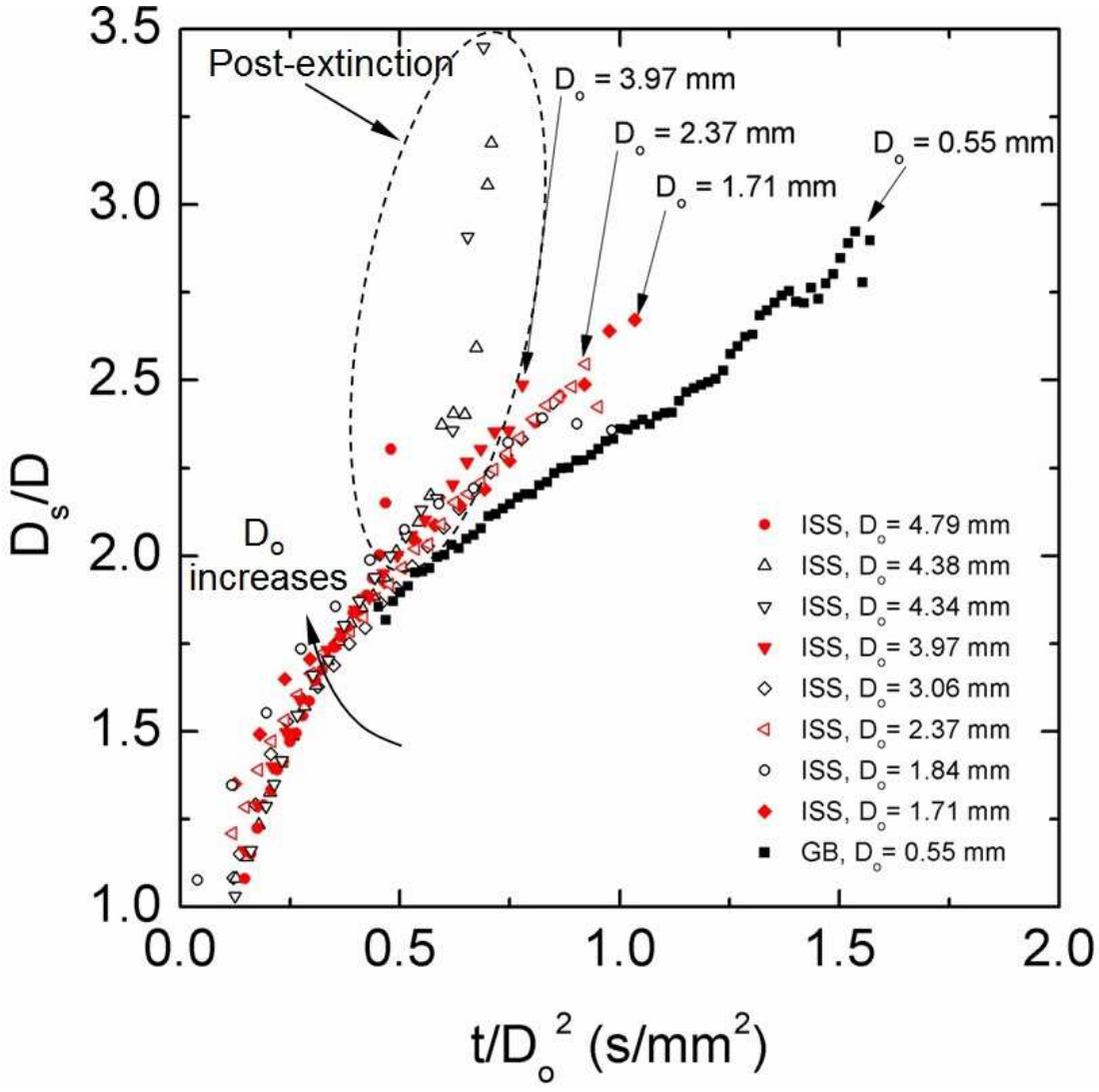

Fig. 10.18. Evolution of soot standoff ratio (SSR) for n-decane droplet flames over the D_o range investigated.

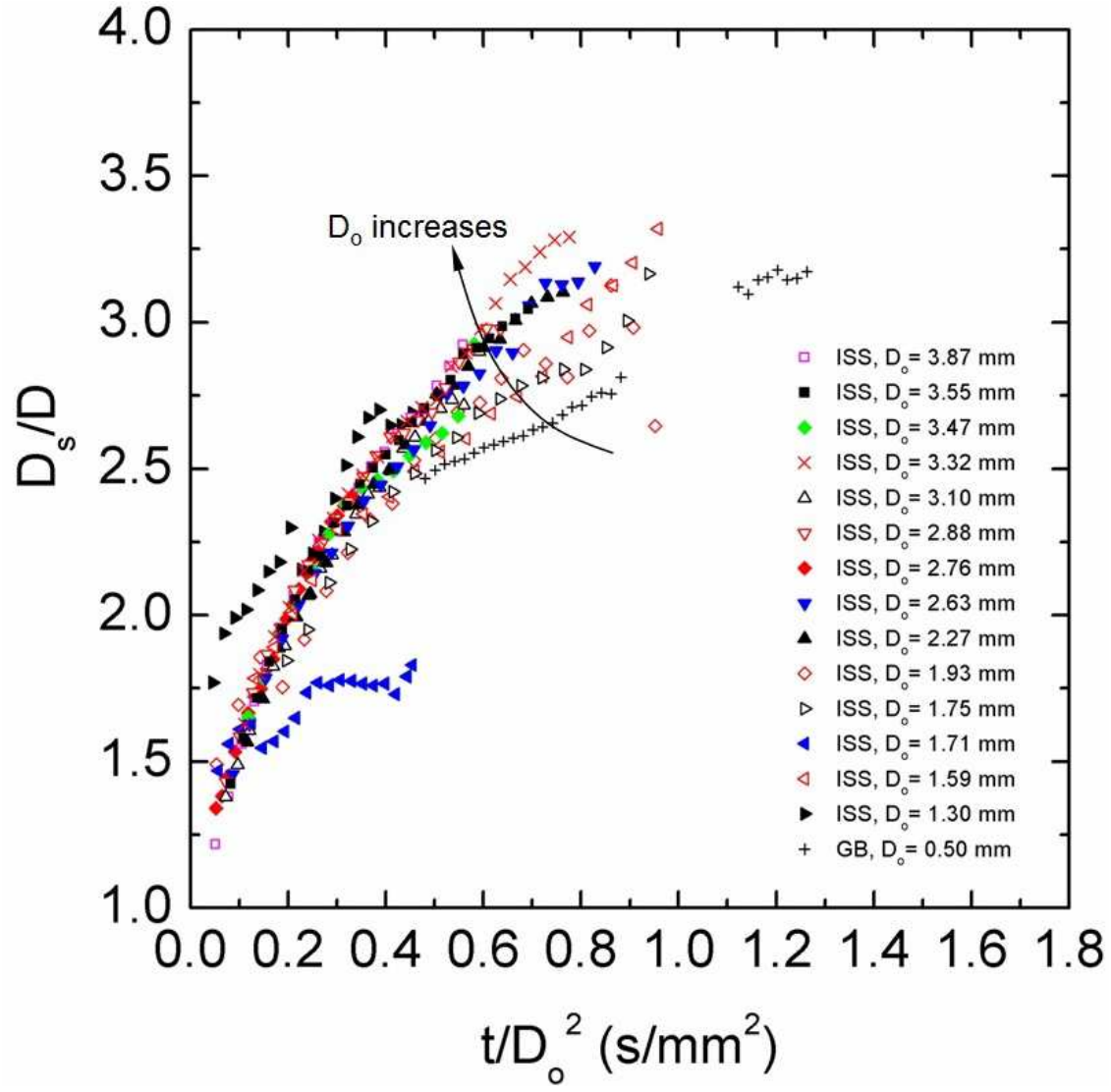

Fig. 10.19. Evolution of soot standoff ratio (SSR) for n-hepane droplet flames over the D_o range investigated.

at 30 fps) for such a transient process of radiative extinction. As shown, the bright "tail" at five o'clock inside the flame is the soot aggregates making contact with the flame. This contact affects the local heat transfer because soot aggregates act like a heat sink with a higher thermal conductivity than the ambient inside the flame. So the unevenly distributed heat from the flame sheet triggers the extinction from that particular angle (five o'clock).

For non-sooty fuel, the flame would just completely extinguish once the flame shell is open. On the contrary, due to the presence of the "hot" soot aggregates produced by sooty fuels, the extinguishing flame can grow back to the position where the extinction is triggered. Figure 10.20b shows such a process. And, once the close-back flame touch the soot aggregates, the flame open up again (cf. Fig. 10.20a).

The reciprocal flame extinction process assembles the motion of a "jellyfish." This "jellyfish" motion can be manifested by showing the evolution of flame angle (how much the visible flame occupies a sphere; full spherical flame: 360^o; no flame: 0^o) before the flame completely disappears. Figure 10.20c shows such a graph for n-decane and n-heptane experiments in which more than one jelly fish motion is observed in a radiative extinction event. The inset to Fig. 10.20c shows how the flame angle is defined and measured. The black solid squares in Fig. 10.20c show that a n-decane droplet flame (D_o = 5.1 mm) experiences three reciprocal jellyfish motion, with a larger flame opening in each time, until the fourth open-up motion where the flame completely extinguishes. The "a" and "b" inserted in Fig. 10.20c indicate the data corresponding to the images shown in Fig. 10.20a and 10.20b, respectively. For the red solid circles (n-heptane, D_o = 3.55 mm), only one complete cycle of jellyfish motion is seen before the

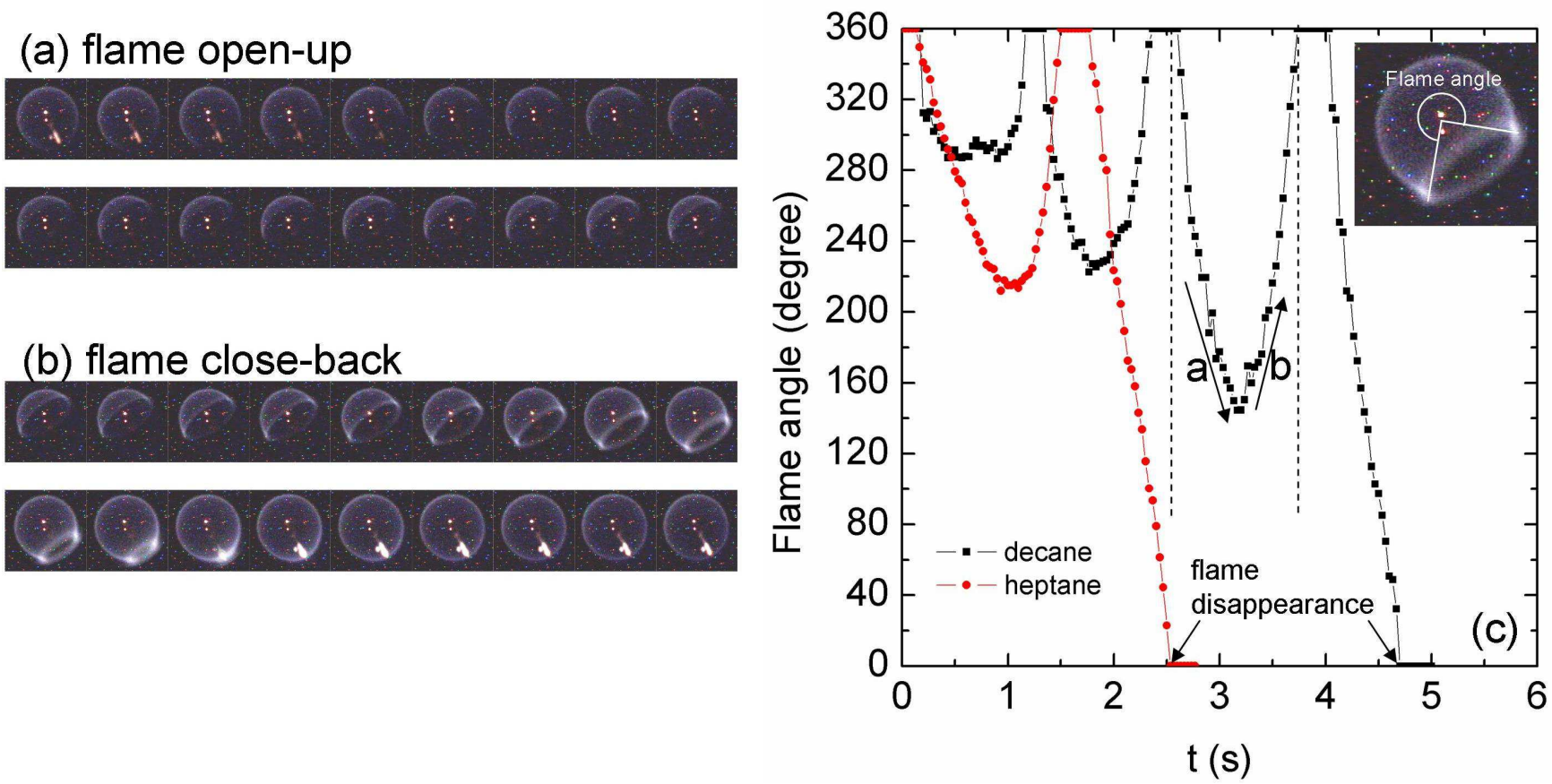

Fig. 10.20. Photographs showing the flame open-up (a) and close-back (b) motion during the radiative extinction process as well as the flame angle evolution for n-decane and n-heptane flames (c) with an inset image demonstrating the flame angle measurement (the a and b in the plot correspond to the photographs shown in (a) and (b).

flame completely disappears.

As mentioned earlier, radiative extinction changes the slope of the D^2 curve. Figure 10.21a and 10.21b show the D^2 data near radiative extinction for n-decane (3 runs) and n-heptane (4 runs), respectively. The arrows in these figures point at the time where the flame completely disappears in the color images. It is evident from Fig. 10.21a and 10.21b that larger D_o's allow earlier radiative extinction. This D_o effect on radiative extinction is better shown in Fig. 10.22a and 10.22b for the time (t/D_o^2) at which the extinction occurs and the droplet diameter at extinction (D_{ext}), respectively.

As shown in Fig. 10.22a, the t/D_o^2 at extinction appears to linearly decrease with increasing D_o, though the slope is different for various alkanes (shown in black dotted lines for n-decane and n-heptane). Radiative extinction for n-heptane occurs for smaller D_o's compared to n-decane. For the similar D_o conditions (3.75 mm < D_o < 4.0 mm, in Fig. 10.22a), n-heptane flames extinguish at an earlier time than does n-decane. This might be due to the slightly higher burning rates intrinsic to n-heptane compared to n-decane, so n-heptane has a shorter burning time (if burnt to completion) compared to n-decane with the same D_o condition. Nonetheless, it is difficult to scale the time with the total burning time t_b (i.e. t/t_b) since these droplets did not burn to completion so the t_b is uncertain. Figure 10.22b shows that droplet flames with large D_o's extinguish at a larger D_{ext}, and the data appear to have a linear trend (suggested trend line is shown by the black dotted line).

Figure 10.23a shows the D^2 data from two n-heptane experiments that exhibit three various regions (recognized by their very different slopes) in their burning histories: visible flame region; cool flame region; and post cool flame region (as

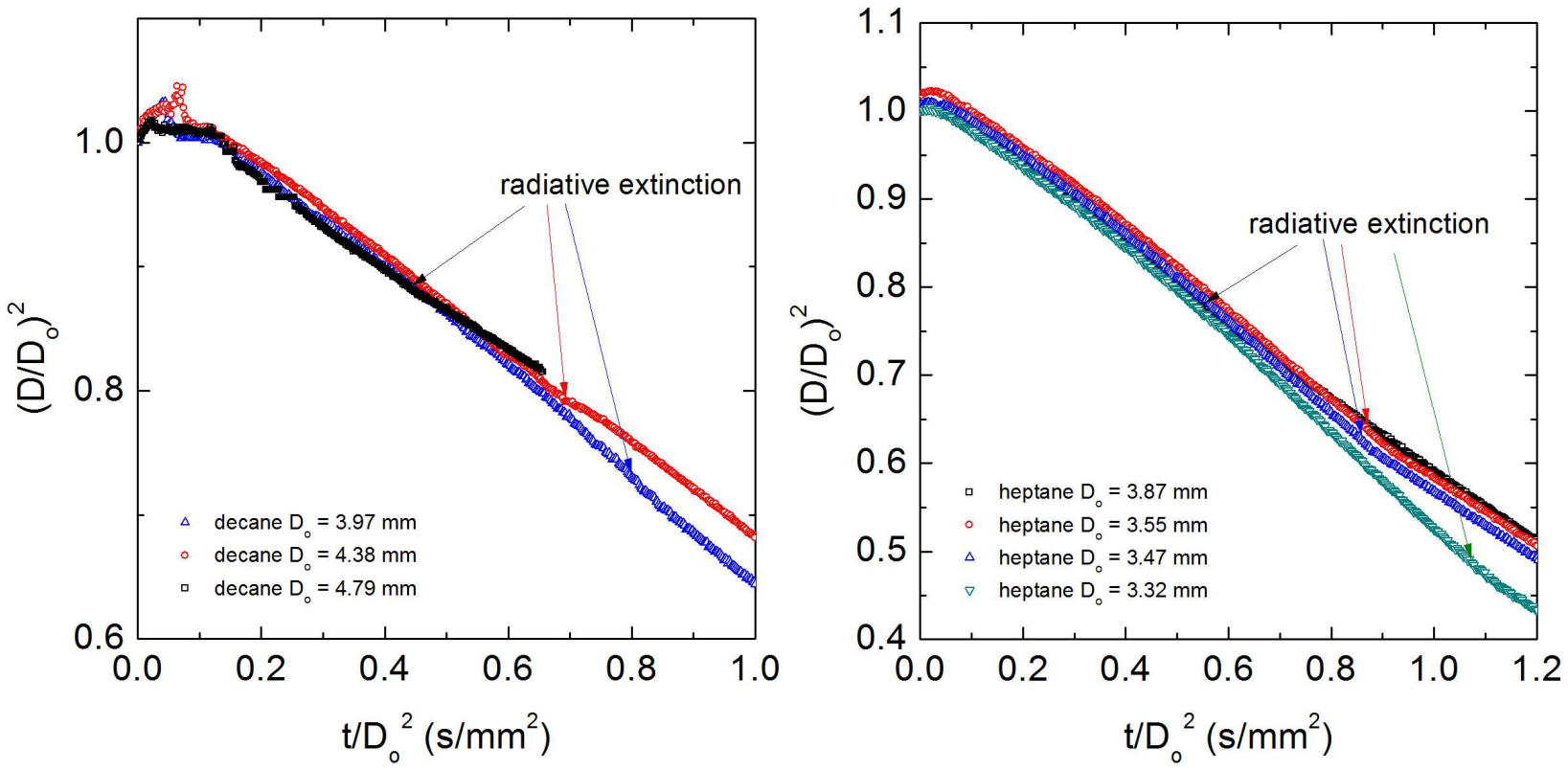

Fig. 10.21. Normalized D^2 histories near the radiative extinction point for (a) n-decane and (b) n-heptane.

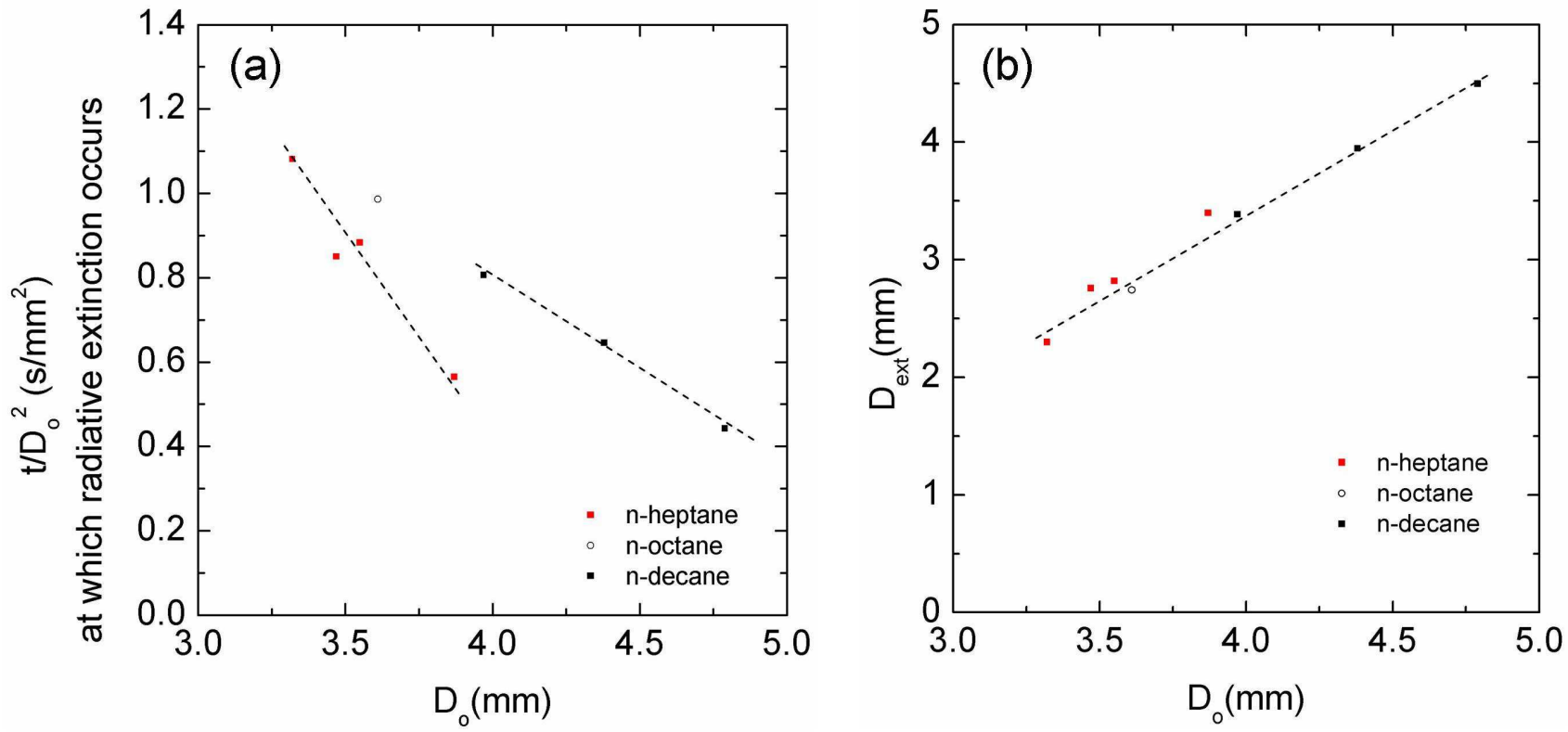

Fig. 10.22. (a) t/D_o^2 at which radiative extinction occurs vs. D_o; (b) extinction diameter D_{ext} vs. D_o with dotted lines suggesting the linear trends for n-octane, n-decane, and h-heptane expe

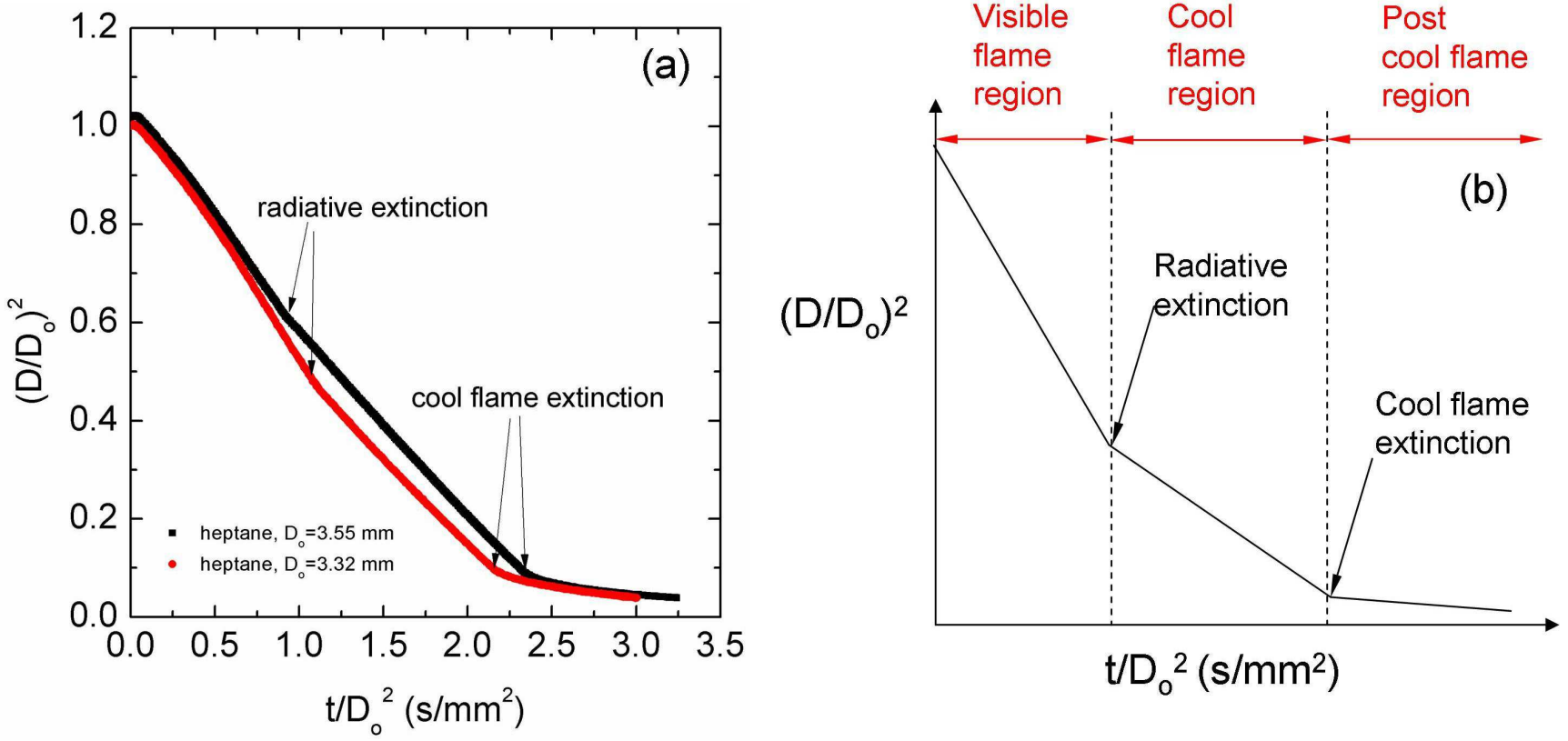

Fig. 10.23. (a) Normalized D^2 histories for n-heptane showing radiative extinction and cool flame extinction that cause slope change on the curve; (b) schematic of the three-staged D^2 curve observed in (a).

illustrated by Fig. 10.23b). It is because of n-heptane's higher burning rate that the third slope region can be capture within the limited data storage on ISS for an experiment. The boundary between earlier two regions shown in Fig. 10.23b is radiative extinction for which the mechanisms are provided along the discussions. We speculate that the second slope change found at the end of D^2 data is attributed to "cool flame extinction" where the low temperature oxidation kinetics (Nayagam et al. (2012)) are no longer sustained due to continuing heat dissipation. This slope change is only obvious in D^2 data. There is no significant difference (not in the visible light range) found in both BW and color images at the instant of slope change.

10.3 Conclusions

Experimental data of n-ocane, n-decane, and n-heptane droplet flames with spherical symmetry over a wide range of initial droplet diameters provide better understanding for the dimension effects on the combustion physics. These dimension effects are attributed to the interplay of soot formation and radiative heat losses with different D_o ranges. Main findings in the present study are itemized as follows:

1. The D^2 evolution along the burning histories of n-octane, n-decane, and n-heptane is significantly dependent on D_o, with the burning rate (the slope of the D^2 curve) decreasing with increasing D_o. This is to be contrast to the prediction from the classical droplet combustion theory with burning rate being a constant for all D_o and time.
2. Radiative extinction signified by the disappearance of the visible flame and the slope change of the D^2 curve is found for droplets larger than 3 mm.

Followed by the radiative extinction, a post-extinction region that has a droplet evaporation rate larger than that for pure evaporation suggest low temperature kinetics occurring in the period.

3. Results suggest that the FSR increases throughout the burning history. A "three-stage" behavior is found on the plot of FSR vs. D_o. This "three-stage" curve is attributed to subtle variation of soot formation (and thus the effective diffusion coefficient in the gas phase) due to the interplay of fuel residence time t_{res} and radiative heat losses in various D_o ranges.
4. Results suggest that SSR also increase over the burning history. SSR values increase with increasing D_o due to weakening thermophoresis caused by radiative heat losses.
5. A reciprocal "jellyfish-like" flame motion is recognized in the transient process of radiative extinction. This jellyfish motion is triggered by the presence of soot aggregates being a heat sink to locally cool down the flame, and a heat source that assist flame propagation in a cycle of a jellyfish motion.
6. D_o effects on the extinction time and extinction droplet diameter are also observed. Results suggest that larger droplets extinguish earlier with a larger droplet diameter.
7. D^2 data from n-heptane reveal that after radiative extinction, there is another slope change point near the end signifying the extinction of the "cool flame."

CHAPTER 11

CONCLUDING REMARKS

We have demonstrated that low gravity experiments that promote spherical symmetry of droplet flames is a useful one-dimensional experimental platform for assessing the efficacy of surrogate fuels that are designed to replicate combustion properties of complex real fuels, e.g., Jet-A and gasoline. While most experimental setups considered in surrogate development are gas phase configurations, the one-dimensional droplet flame configuration is more similar to the real engine environment- multi-phase combustion, thus providing combustion characteristics related to condensed phase fuels.

Results from aviation biofuels (derived from camelina and tallow) that have shown comparable performances as Jet-A suggests that the droplet burning characteristics observed in our experiments is similar as the results seen in the actual engine and flight tests, but droplet combustion experiments provide more quantitative and fundamental information that is tailored to the intrinsic differences between jet fuel and the biofuels. The data generated from this specific flame configuration also validate the numerical model developed with reduced oxidation kinetics and combustion physics.

By comparing the results from free droplet and fiber-supported experiments, we concluded that the 14 μm SiC fibers used for the above studies show minimal effects on droplet burning parameters. It provides confidence towards pursuing the spherically symmetric droplet flame configuration with the assistance of support

fibers. However, a 80 μm SiC fiber used on the ISS increases the droplet burning rate and FSR when the D_o/D_{fiber} ratio is smaller than "36".

Combining the experimental results for n-heptane, n-octane, and n-decane obtained from our 1.2 s drop tower and from the ISS, combustion physics related to the droplet/flame length scale (0.5 mm < D_o < 5 mm, a wider range of D_o compared to literature) are revealed. The burning rates of these fuels monotonically decrease with increasing D_o, Results of FSR and SSR show significant dependency on D_o suggesting the subtle interplay between soot formation and radiation in various D_o regimes can cause noticeable differences in the combustion transport. Radiative droplet flame extinctions were identified for D_o > 3 mm for all the examined n-alkanes followed by a "cool flame" region in which the droplet evaporation rate is found to be much higher than pure evaporation.

APPENDIX A

Drop Tower Operations and Troubleshooting

A.1 Fiber-supported Experiments

In the fiber-supported configuration for the present study, SiC fibers (~14 μm diameter) are positioned by hand and taped onto support posts on the plane where the spark electrodes are mounted. The fibers are crossed and have an angle of 60 degrees at the intersection. The fiber cross point has equal distances from the tips of the four spark electrodes. Figure A1 is a photograph showing the above described configuration for fibers and spark electrodes.

Fibers should be installed with appropriate "tension." This tension is preferable because it helps to maintain the position of the fiber intersection and, thus, the position of the burning droplet during free-fall.

To install a fiber, all four electrodes should first be positioned (like in Fig. A1) in order to know the exact position to create the fiber intersection. Then, a piece of single fiber filament with an appropriate length (usually 10 to 15 cm) is separated from the fiber bundle (see Fig. A2) using scissors. The fiber usually floats around and is difficult to "see." One can take a small piece of tape and put one end of the fiber across the center of the tape (see Fig. A3a, shown with a red wire for visibility). Then the tape (with a piece of fiber on it) is fastened on one of the four posts on the fixture ring (see Fig. A3b) with the fiber protruding from one side of the tape and from the center of the support (see Fig. A3b). The fiber then is "pulled" slightly to reach the other post (Fig. A3c). With one hand pulling the fiber with slight tension, another

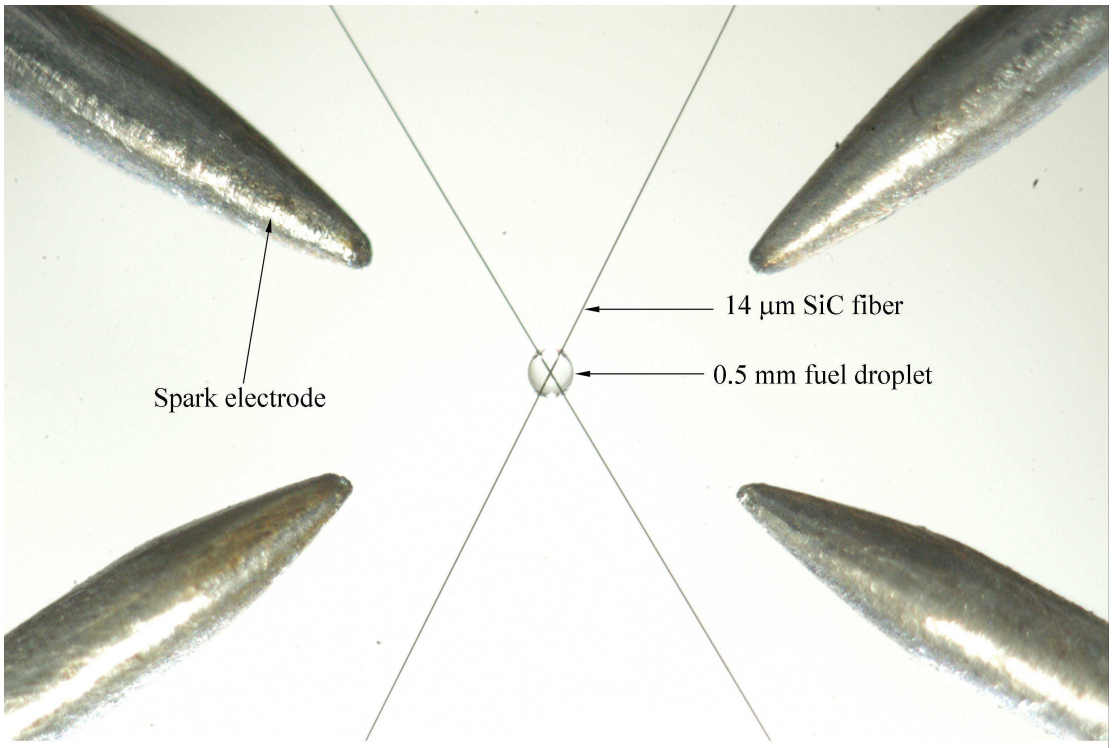

Figure A1. A photograph showing the equal distances between each spark electrode and the fuel droplet as well as the tow fibers intersecting at an angle of 60 degrees.

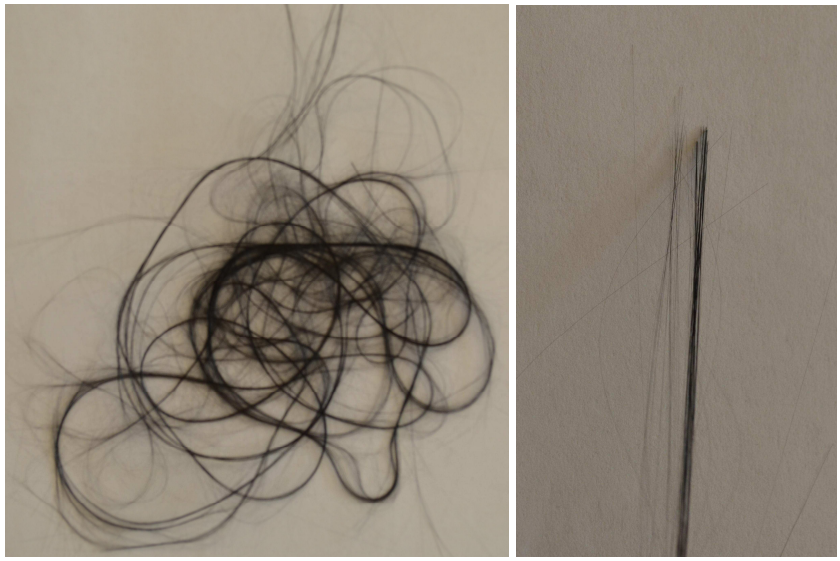

(a) (b)

Fig. A2. (a) the SiC fibers as a whole bundle; (b) an isolated bundle from which one filament can be cut and separated.

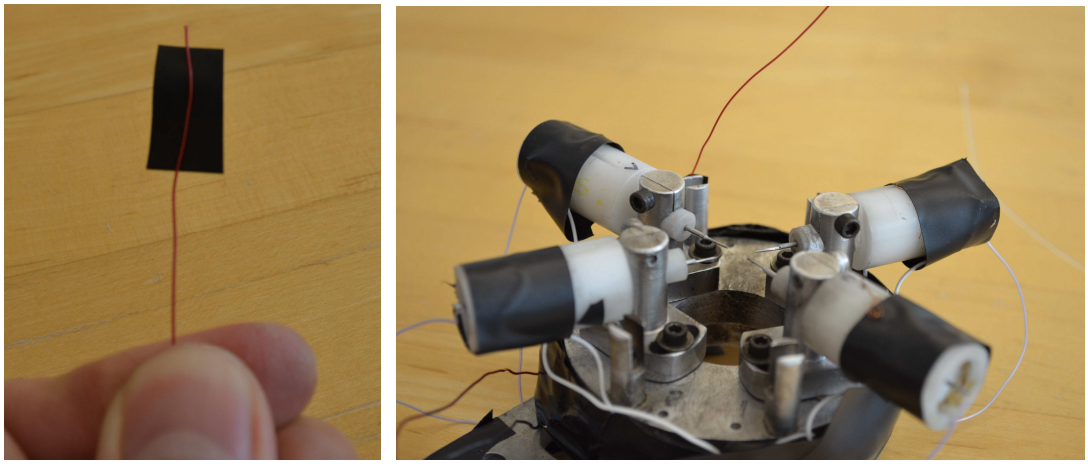

(a) (b)

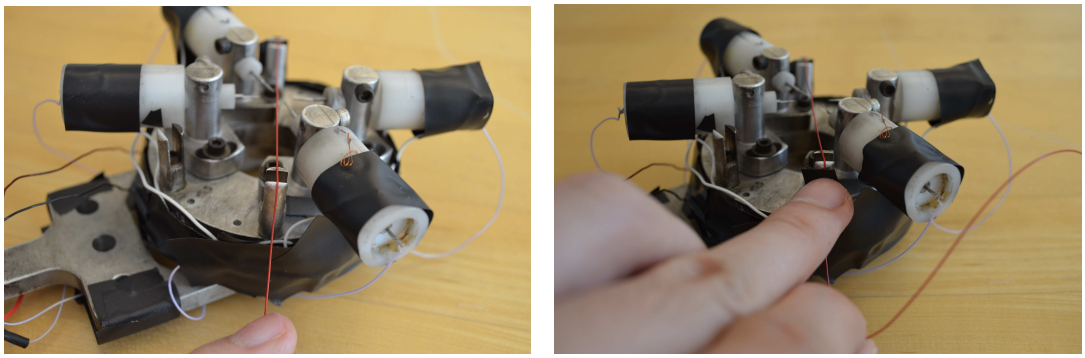

(c) (d)

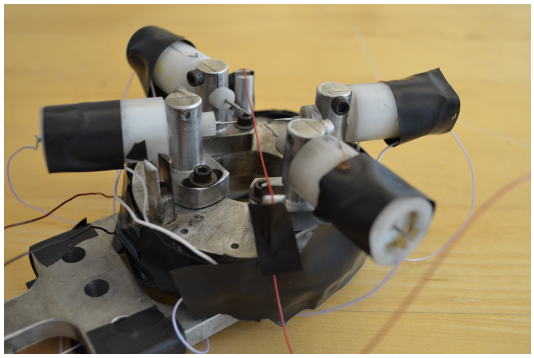

(e)

Fig. A3. Demonstration of how to install a fiber filament (shown with a red wire for visibility here) on the post: (a) put the fiber on a piece of tape; (b) tape the fiber on one post; (c) pull the fiber towards the other post; (d) tape the other end of the fiber on the post with a little fiber tension; (e) final look of the installed fiber.

hand uses a small piece of tape to fasten this end of fiber (Fig. A3d and A3e). While taping the other end of the fiber, it is necessary that the fiber passes through the plane where the droplet will be anchored (cf. Fig. A1). To install the remaining one fiber, similar techniques are applied.

When the fibers are installed, the BW camera (see Section 2.1.8.1) is used to view the cross of two fibers. It should be horizontally in line with the spark electrodes. A loose fiber might lead to a lower position of the fiber cross. If the two fibers are installed with appropriate tension but the fiber cross is still not in the same plane as spark electrodes, the position of the electrodes should be repositioned.

As described in Section 2.1.3, to successfully deploy a droplet to the desired position, the droplet trajectory (namely, angle and height) is controlled by the voltage and width of a pulse that actives the piezoelectric plate and the orientation of the droplet generator. In a fiber-supported droplet combustion experiment, the droplet trajectory can be arbitrary as long as the droplet lands at the cross of the two fibers. If it requires more than one droplet generation (e.g. for a droplet larger than 0.7 mm) to form a droplet with the desirable size, the droplet trajectory should be adjusted such that the droplet lands from the side of the fiber cross (see Fig. A4). This particular shooting angle would facilitate the merging of a flying droplet with a droplet already attached to the fiber cross.

When a test droplet is mounted at an exact position, it is very easy to obtain excellent focus and contrast for the droplet boundary prior to an experiment. In particular, as the plane of fiber cross represents the center of the droplet in an experiment, one can focus the BW camera at the fiber cross (without a droplet sitting

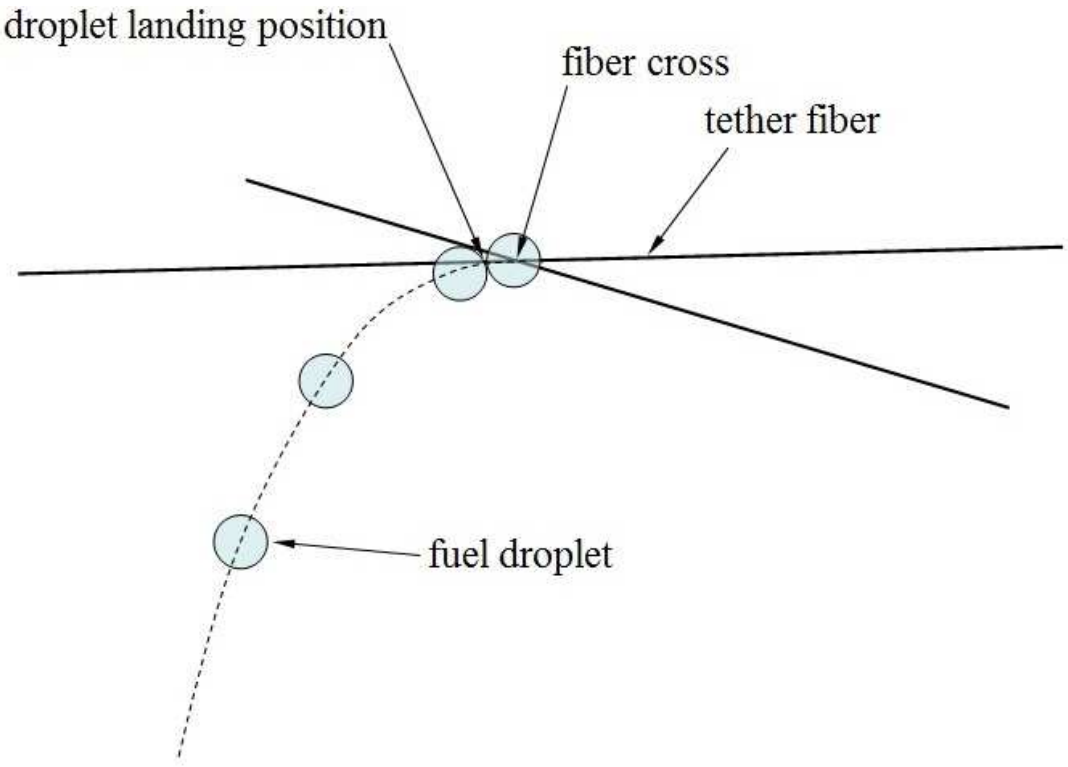

Fig. A4. Droplet trajectory and droplet landing position for fiber-supported droplet experiments.

on it).

The entire 0 g experiment is controlled by the signals pre-programmed in the QC9618. The signals designated for a fiber-supported experiment is shown in Fig. 2.31. Only the first three channels that control magnet delay (Channel 1), spark ignition (Channel 2) and electrode retraction (Channel 3) are used in fiber-support experiments. Figure A5 to A7 shows how to actually set the parameters on the QC-9618 to generate the signals shown in Fig. 2.31. A detailed step-by-step procedure for implemented a fiber-supported droplet combustion experiment with drop tower facilities is as follows.

Preparation

1. Remove the spark electrode set from the combustion chamber.

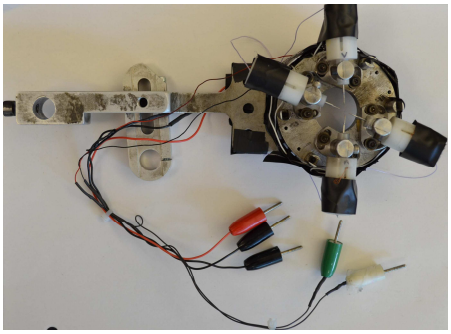

2. Check if the droplet generator and the traverse stage underneath it are working and in correct position.
3. Remove and discard the used fibers on the spark electrode set.
4. Remove soot particles from the tips of four electrodes by slightly scratching them using a blade until they look shiningly polished.
5. Place two new fibers on the spark electrode set.

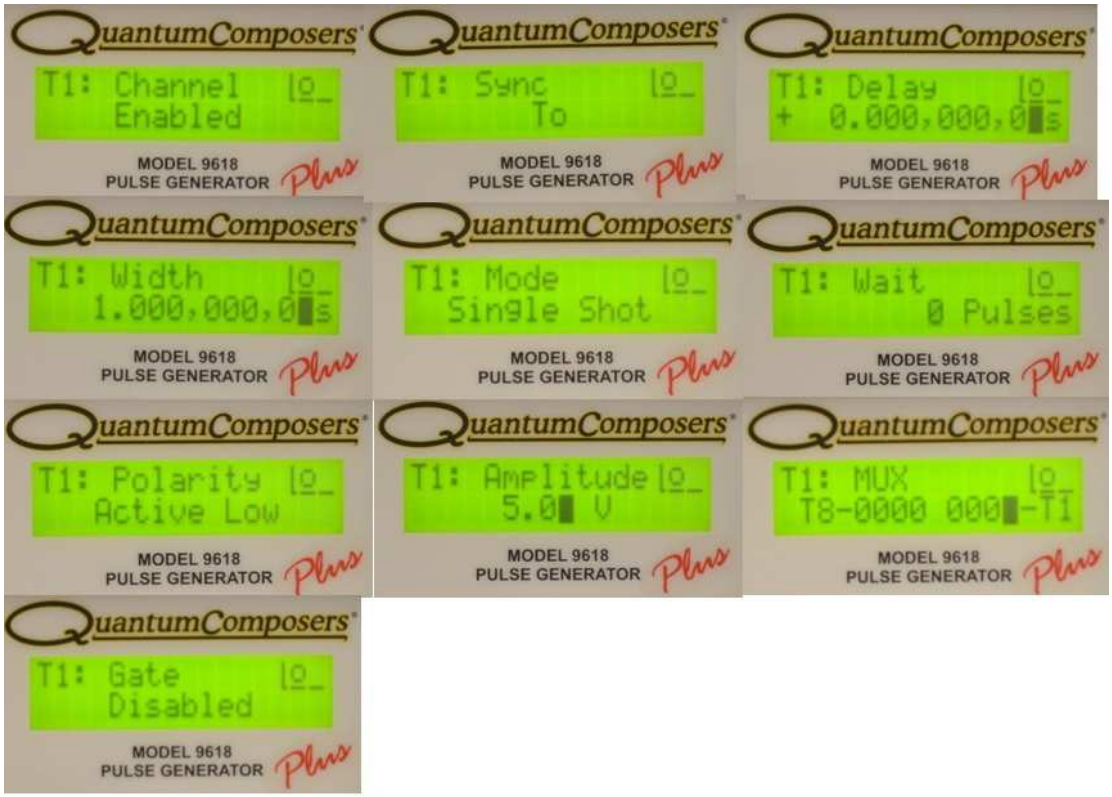

Fig. A5. Detailed settings on the QC-9618 that generates the signal shown in Fig. 2.31 for Channel 1: magnet.

Fig. A6. Detailed settings on the QC-9618 that generates the signal shown in Fig. 2.31 for Channel 2: spark.

Fig. A7. Detailed settings on the QC-9618 that generates the signal shown in Fig. 2.31 for Channel 3: retraction.

6. Turn on the main power for the drop package.

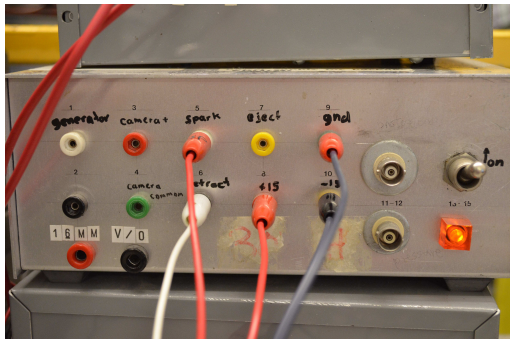

7. Open the software “Camera Control” for the BW camera and “Pinnacle Studio 12” for the color camera on the desktop of the PC.

8. In the BW camera software, go to “setting” by pressing the yellow wrench button  on the tab, set the exposure time to around 100 μs (settings might differ from fuel to fuel) and recoding speed at 200 fps.

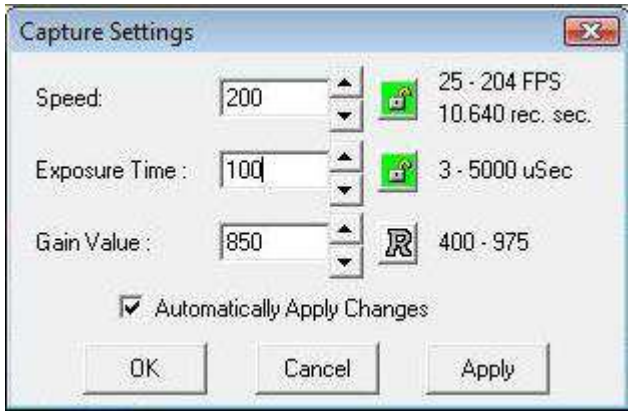

9. Start recoding BW images by pressing the green light green on the tab. 

10. Place the LED backlight in position by taping the LED light bulb on the

combustion chamber wall against the BW camera.

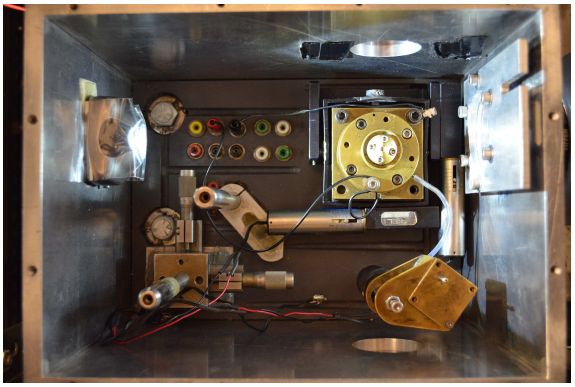

11. Fine tune the LED position until the background intensity for the BW camera view is uniform.
12. Put the spark electrode set back to the combustion chamber and make sure the electrodes are at the center of BW camera view.

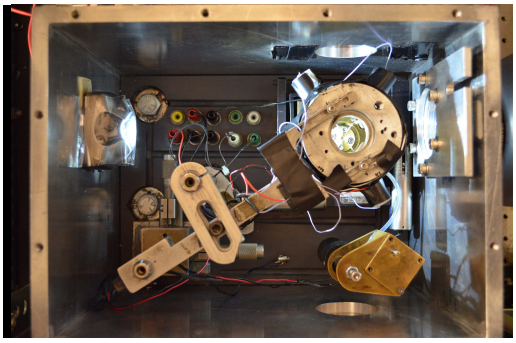

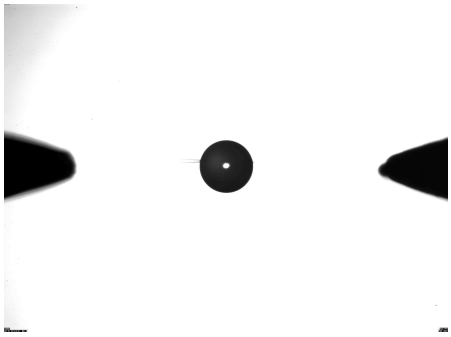

13. Connect the wires for droplet generation, spark ignition, and electrode reaction inside the combustion chamber (see the connections in the above photo).
14. Adjust the traverse for the BW camera to focus the fiber cross (thus the future droplet).

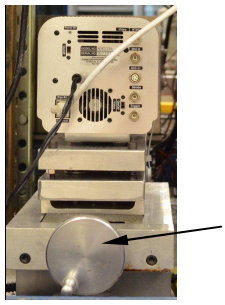

15. Adjust the two traverses underneath the droplet generator for the best droplet trajectory.

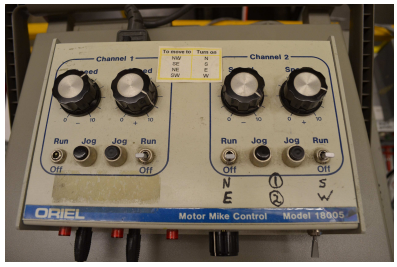

16. Generate droplets on the fiber cross by pressing the “man” button on the HP 214B.

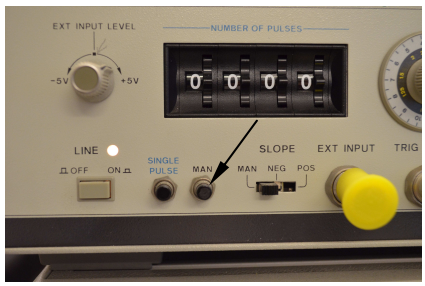

17. Extract the droplet size from the recorded BW images (a scaling factor comes from the recorded images of a calibration ball, tungsten carbide, 0.794 mm, see Section 3.4).
18. Check how many droplets are needed to form a droplet with the desirable size (a 0.5 mm droplet usually requires only one shot, but a 0.8 mm droplet requires more than on shot).
19. When there is a droplet on the fiber, adjust the traverse for color camera to obtain good contrast/focus for the droplet boundary.

20. Check the “sustain” signal from the low voltage circuit box using the HP 54603B oscilloscope, replace 4853 if the signal does not go from -15 V to 12 V with the spark signal from QC-9618.

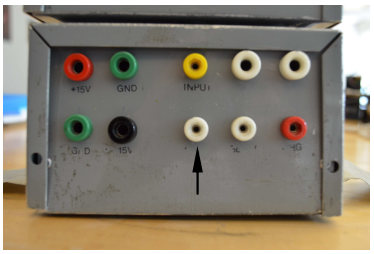

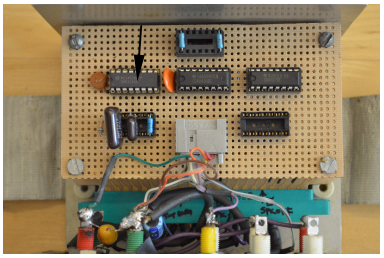

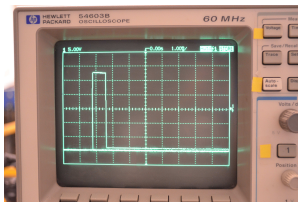

(a healthy “sustain” signal from the low energy box should go from -15 V to 12 V with a width of the designated spark duration: 800 μs here)

21. Perform some 1 g droplet burning tests to find the lowest energy to ignite the droplet (the energy of sparks is adjusted from the two dials on the high voltage box, and the energy settings required for various fuels is very different, see Section 2.1.5).

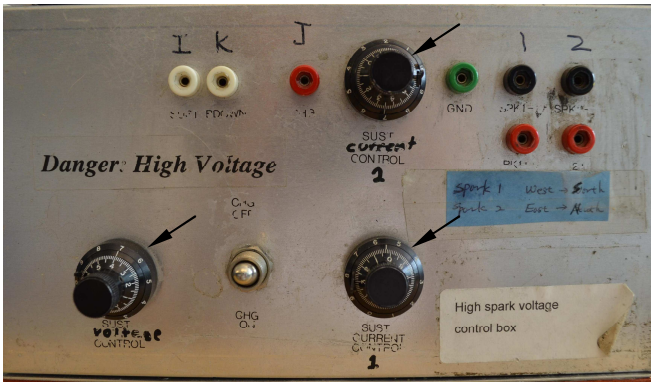

22. Replace the fiber and repeat 21 until the lowest ignition energy is found.

Low gravity experiments

1. Bolt the chamber lid on to close the chamber.
2. Double check all the connections between the 30 V power supply, low voltage circuit box and high voltage orange box, and the chamber.
3. Switch on the 30V power supply inside the drop package and the charging for the high voltage orange box.

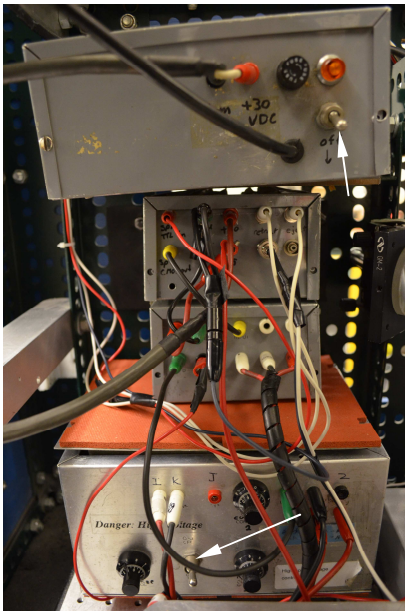

4. Place the transparent side plates on the outer package.

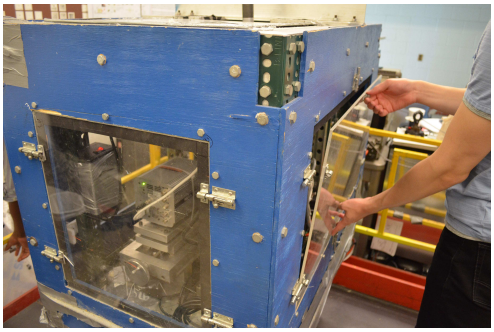
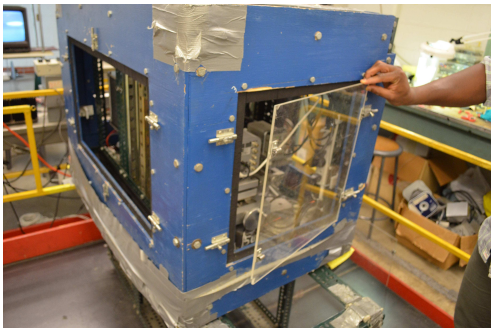

5. Release a bit more the strand metal wire from the winch and remove the eyebolt that is screwed on the upper center metal plate of the inner package.
6. Clean the upper center metal plate as well as the bottom of the electro-magnet by paper towel, just to make sure there is no dust that could affect the performance of the magnet.
7. Place the electro-magnet on the center metal plate of the inner package.
8. Line up the magnet with the two aluminum plates on the center metal plate.

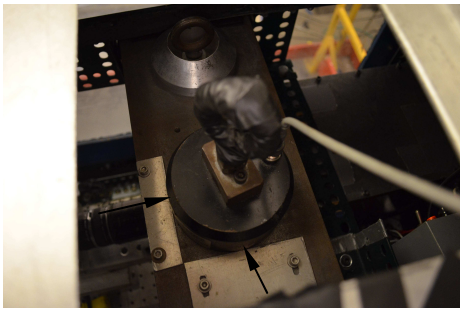

9. Double check if the cable for the magnet is tangled in a way that would catch the drop package at release.

10. Turn on QC9618 to activate the 5 V signal for the magnet.

11. Adjust the voltage to 100 V (for safety concern) on the HP 6010A for the electro-magnet.

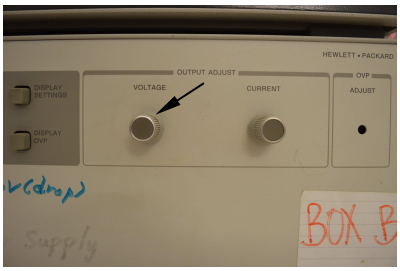

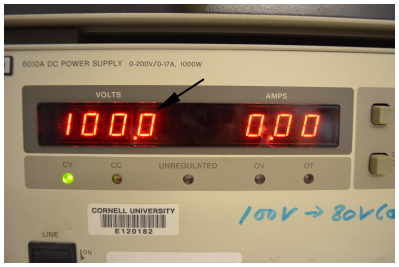

12. Wait around 10 seconds for the magnet to complete grip the drop package.

13. Turn on the power box for the winch.

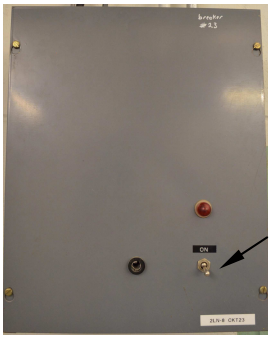

14. Flip the winch controller to UP.

15. Very slowly raise the inner drop package by adjusting the voltage on the variac to around 10 V (the voltage on the variac determine the speed). (the package might be detached from the magnet if more than 30 V is used)

16. Make sure the two safety eyebolts and the cone-shaped metal on the inner package are perfectly aligned with the two holes on the outer package.

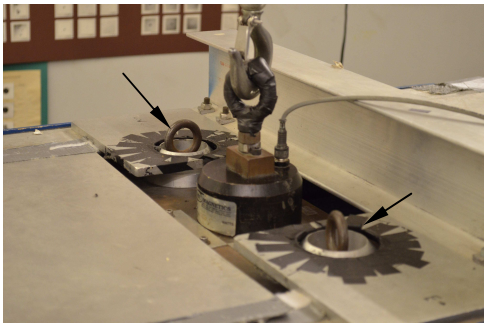

17. Raise the entire package about 2 inches above the cart, turn the variac to 0V to stop the winch.

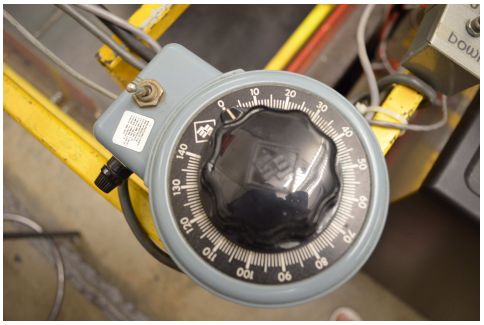

18. Count to three, roll the floor from the bottom of the hung package as fast as possible.

    (DANGER!!!! The package is now positioned over the free-fall shaft)

19. Arrange the long cable to hang down straight from the bottom of the package; part of the long cable should sit on the side wall of the deceleration tank.

20. Stabilize the package.

21. Lower the magnet voltage (on HP 6010A) to 50 V.

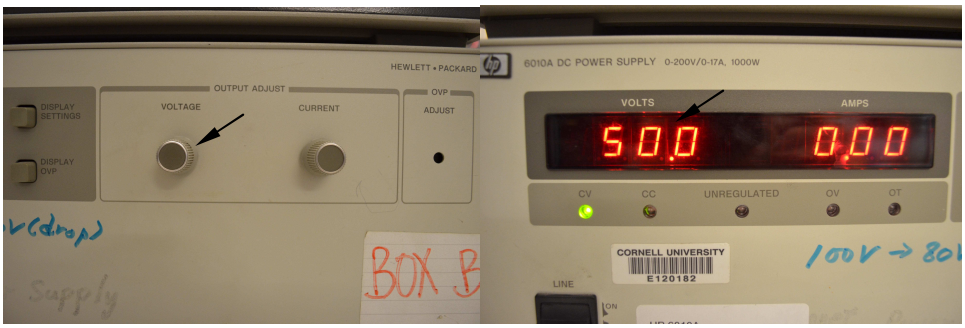

22. Switch on the ± 15 V power supply on the control desk and start charging the spark capacitors for 7 minutes.

23. Double check if all the timing settings are correctly programmed in the QC-9618 for channel 1: magnet, channel 2: spark, channel 3: retraction.

24. Make sure the BW camera is not stopped by the default 10 minute recording termination in the software.

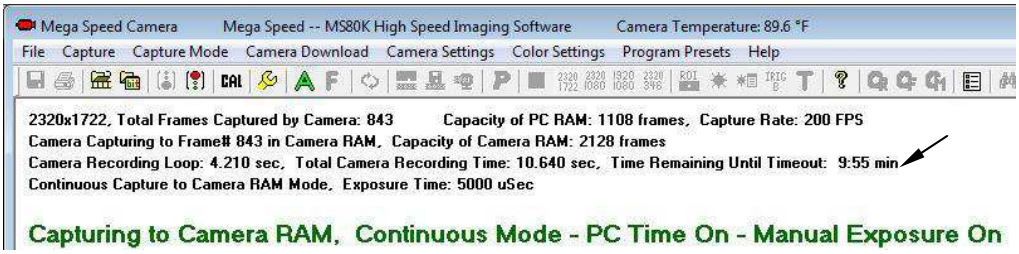

25. In Pinnacle Studio 12, go to the “Capture” tab, press “Start Capture”, type the file name save the color video.

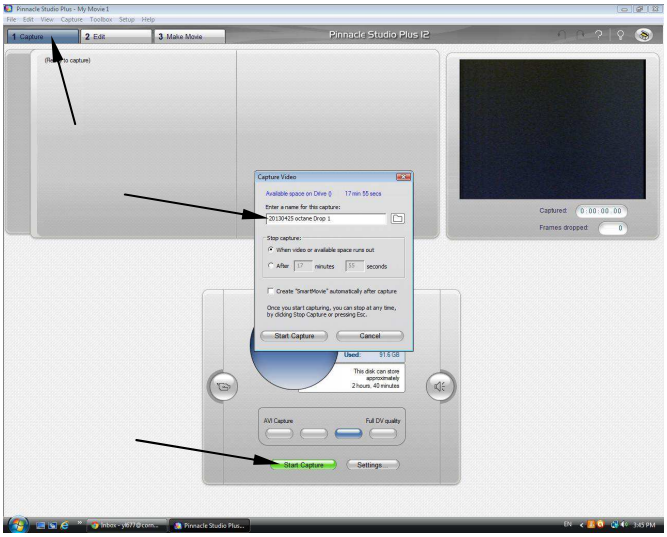

26. Start saving the color video by pressing the grey “start capture” button on the file name window.

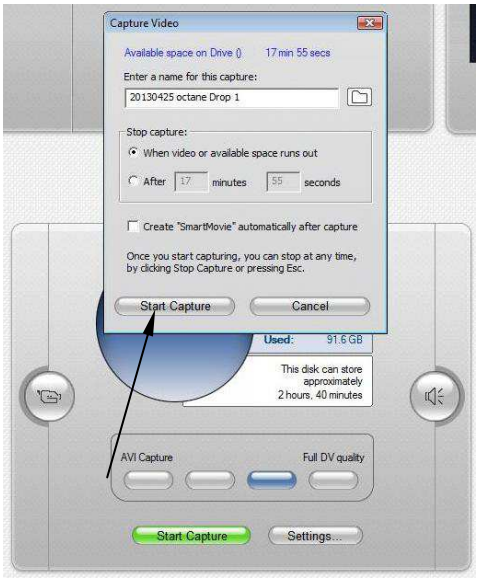

27. Shoot droplets (press the “man” button on the HP 214B) and adjust the voltage dial on the HP 214B (to fine tune the height of the droplet trajectory) until the droplets can land on the fiber intersection (can be seen in the views of both cameras).

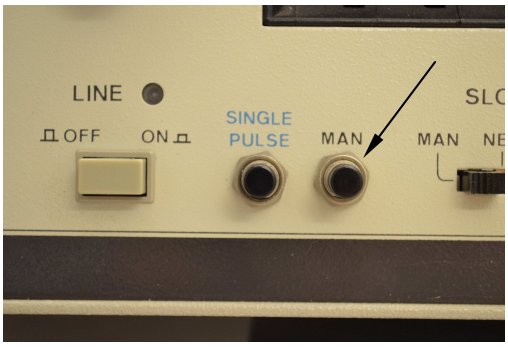

28. Keep shooting droplets until the droplet on the fibers is with the desirable size.
29. For single component fuels, a droplet with desirable size is obtained by evaporating a slightly bigger droplet down. For multi-component fuels, it is preferable to anchor only one droplet on the fiber and proceed to the next step as

soon as possible to prevent preferential evaporation and change of the fuel composition.

30. Click “run” on QC-9618 to initiate the drop experiment.

31. Immediately after the drop package landed the deceleration tank, quickly “stop” recording color and BW images from the computer.

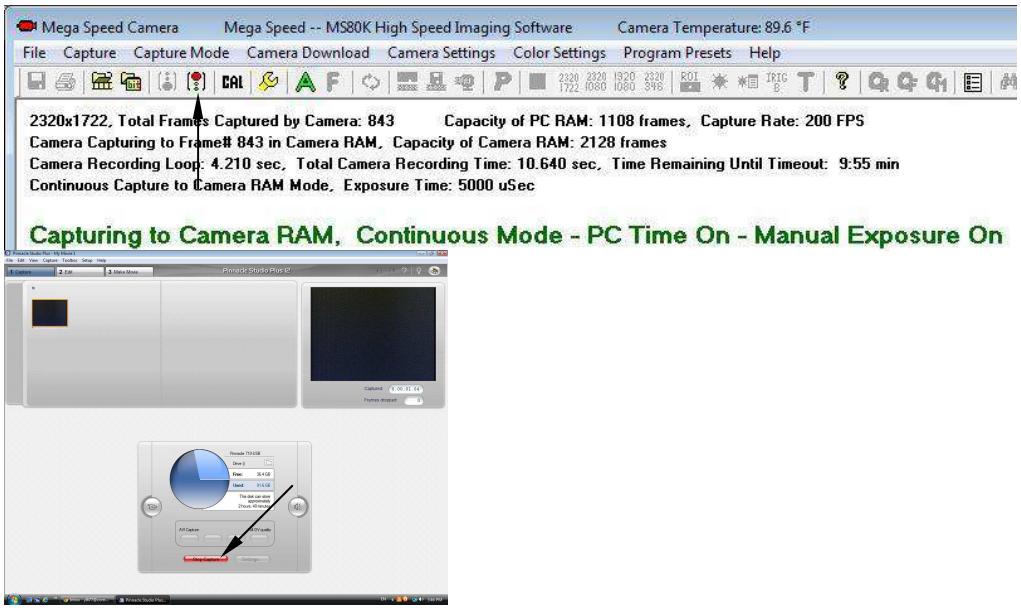

32. Switch off the HP 6010A, HP 214B, ± 15 V power supply, QC-9618. Make sure the main power of the package is still "ON" for the drop package.

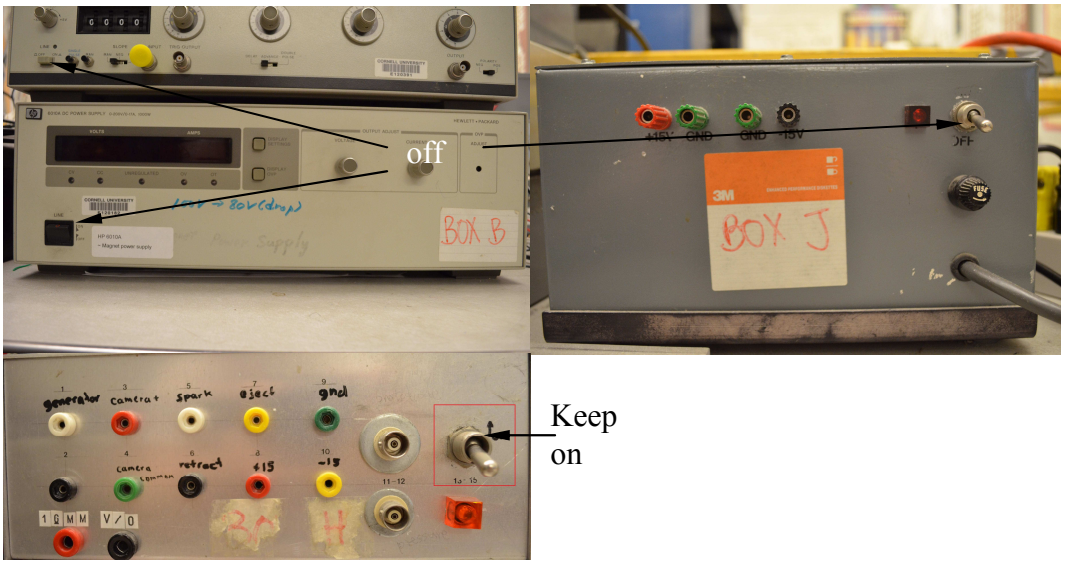

33. Start downloading BW images from the temporary memory onboard the BW camera by pressing the "download button"  ; select "To Hard Drive As JPEG" at the bottom and input the image destination/directory; input the "start frame" and "end frame" (images can be "previewed" from the right small preview window); choose the minimum downloading speed (5 fps). (See Section 2.1.8.1 for more details).

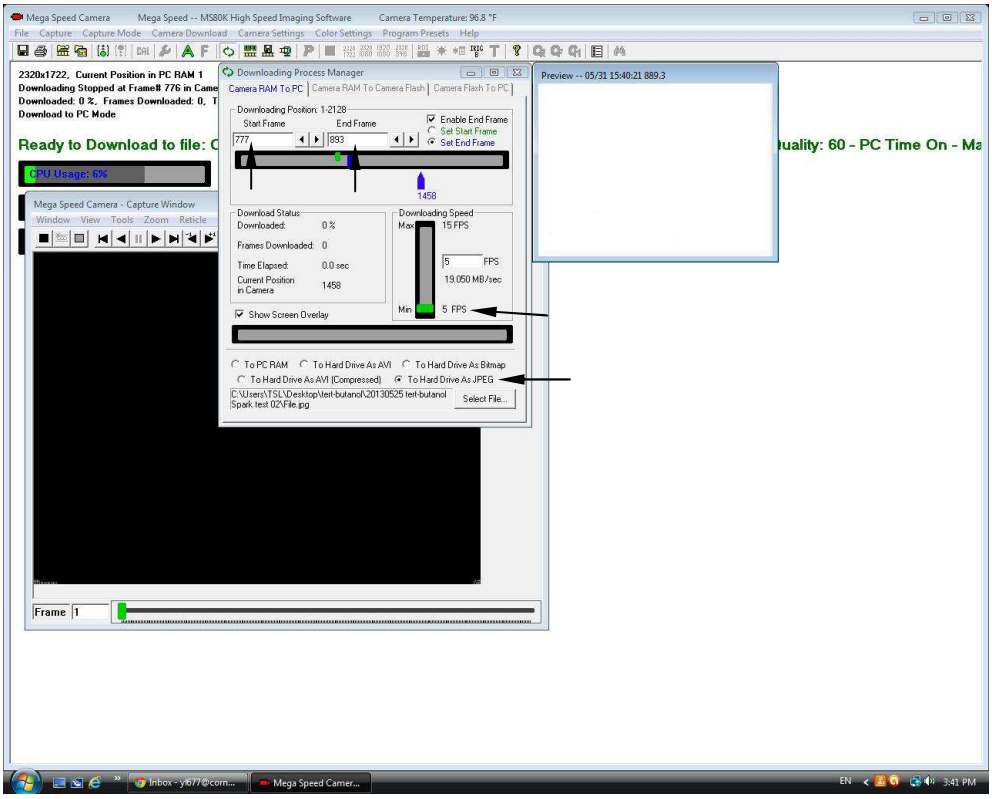

34. Make sure both color and BW images are saved by checking the images in the folder just created by the software on PC.
35. Close the camera software window (Camera Control and Pinnacle Studio 12) on PC.
36. Switch off the main power of the drop package.

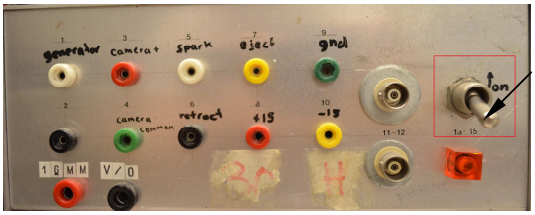

37. Lower down the magnet and take it off the hook.
38. Lower down the hook to the top of the drop package downstairs using maximum speed (variac at 140 V).

39. Zero the variac to stop the winch un the hook reaches the package.

40. Flip the direction controller to “neutral” for the winch.

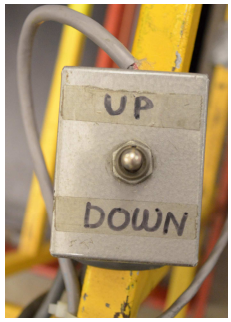

41. Put 80 V on the variac – a moderate speed for raising the package when it is sitting in the deceleration tank.

42. Bring the eyebolt down to the package and screw it back on the upper center plate of the inner package.

43. Make sure the long cable and winch wire are not tangled.

44. Use the direction controller downstairs to raise the inner package, with the speed set on the variac upstairs (80 V).

45. Adjust the position of the outer package while the inner package is lifted up until the two cone-shaped metal pieces are perfectly aligned with the two holes on the outer package.
46. Double check is there is any scratch on the long cable.
47. Stop the winch from the downstairs winch direction controller when the package is lifted around 5 ft above the deceleration tank.
48. Put all the foam boards and the blanket back to their original positions and make sure the deceleration tank is in a good shape for the next drop experiment.
49. Go back upstairs and switch “UP” the winch direction controller there.

50. Use maximum speed (140 V on variac) to raise the package.

51. When the package is lifted up to the “drop” position, zero the variac.

52. Switch the winch direction controller to “neutral”.

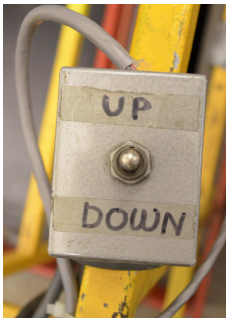

53. Close the sliding floor and make sure the floor does not jam the long cable from the gap.
54. Slowly lower down the package, adjust the position of the cart to let the package sit squarely on it.
55. Very slowly lower down the inner package until it sits on the outer package.
56. Take off the side plates from the outer package.
57. Switch off the 30 V power supply and discharge the capacitors in the high voltage orange box.

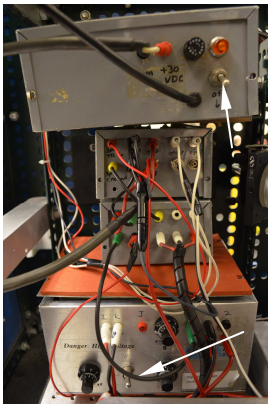

58. Remove the metal beam that fastens the combustion chamber.
59. Unbolt the chamber lip and open the chamber.
60. Use a fan to flush fresh air into the chamber.

61. Switch off the LED light.

62. Get ready for the next drop experiment.

A.2 Free Droplet Experiments:

A.2.1 Introduction

Free droplet experiments are far more challenging than fiber-supported experiments due to delicate tuning issues involved. Detailed prior free droplet experiments were given by Yang (1990), Jackson (1993) and Callahan (2000). Here we offer some current considerations of the droplet deployment mode.

Free droplet experiments are implemented by shooting a single droplet vertical upwards and when the droplet reaches the apex of its trajectory, the instrumentation package is released. The accurate timing of package release is followed by spark ignition and retraction of spark electrodes. There are several challenges involved in the series of the above events. The biggest challenge is that we want the droplet to stay in the field of view and focused for both BW and color camera views

To perform a successful free droplet burning experiment, the following requirements must be met as discussed in the next section.

A.2.2 Vertical Droplet Trajectory and Repeatably Accurate Droplet Apex

When the drop package is accelerating along the direction of gravity during a free fall, the droplet moves in the same direction such that the relative velocity of the droplet to the falling package is zero in any direction. Since the droplet trajectory determines the initial velocity of the droplet, a droplet with essentially "zero" velocity in any direction at its apex is necessary to achieve.

Assuming the apex of the droplet trajectory is always at the same height as the spark electrodes, a low gravity environment must be created right at the instant the

droplet reaches the apex. Figure A8 shows trajectories which do not allow for a "zero" initial droplet velocity when the droplet reach the height of the electrodes. For example, when the droplet trajectory is not perfectly vertical (Fig. A8a), the droplet is going to move laterally. Figure A8b shows an apex that is too high such that when the package is released the droplet will move upwards. When the apex of the droplet trajectory is too low (Fig. A8c), the droplet would then move downwards relative to the package during free fall because of its initially downward velocity.

In order to achieve a vertical droplet trajectory, droplet generation tests, along with some fine tuning, are required prior to an experiment. The level and balance of the package is critical for these tests. To emulate balancing a freely hung package just prior to release, the droplet shooting tests should be performed when the package is hung (use of electro-magnet is not necessary here, an eyebolt can be used instead).

The rolling floor should not be opened during droplet generation tests due to crew operations. When the floor is closed the long (and heavy) signal cable will exert forces on the hung package (see Fig. A9a). The long cable should be pulled up and set on the floor in order to remove tension on the package. An ideal arrangement for the cable is shown in Fig. A9b. During all the droplet generation tests prior to an experiment the cover of the combustion chamber and all elements associated with an experiment should be in place in order to achieve similar balance for the package and thus the droplet trajectory as when an experiment is initiated.

The direction of the droplet generated is mainly controlled by the 2-D traverse stage with two motors (Oriel Motor Mike Control, Model: 18005) underneath the droplet generator (see Fig. A10). The apex of the droplet trajectory is controlled by HP

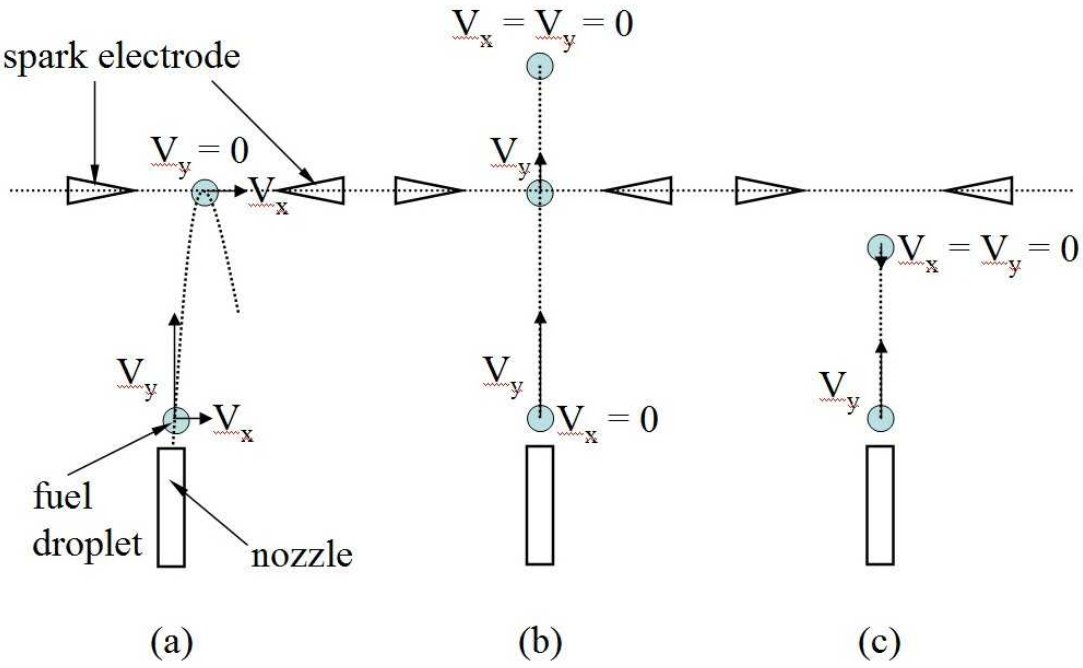

Fig. A8. Failure modes for droplet shooting in free-droplet experiments: (a) the trajectory is not purely vertical; (b) the trajectory apex is too high; (c) the trajectory apex is too low.

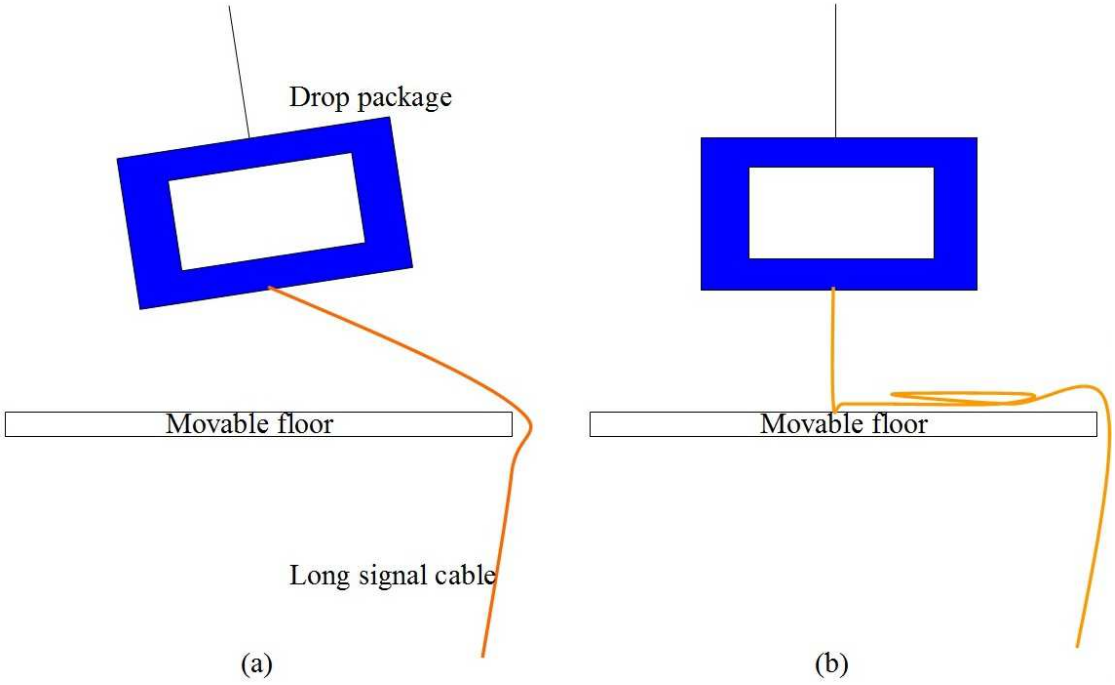

Fig. A9. Illustration of (a) unleveled package due to cable pulling; (b) leveled package ready for 1 g droplet trajectory tests.

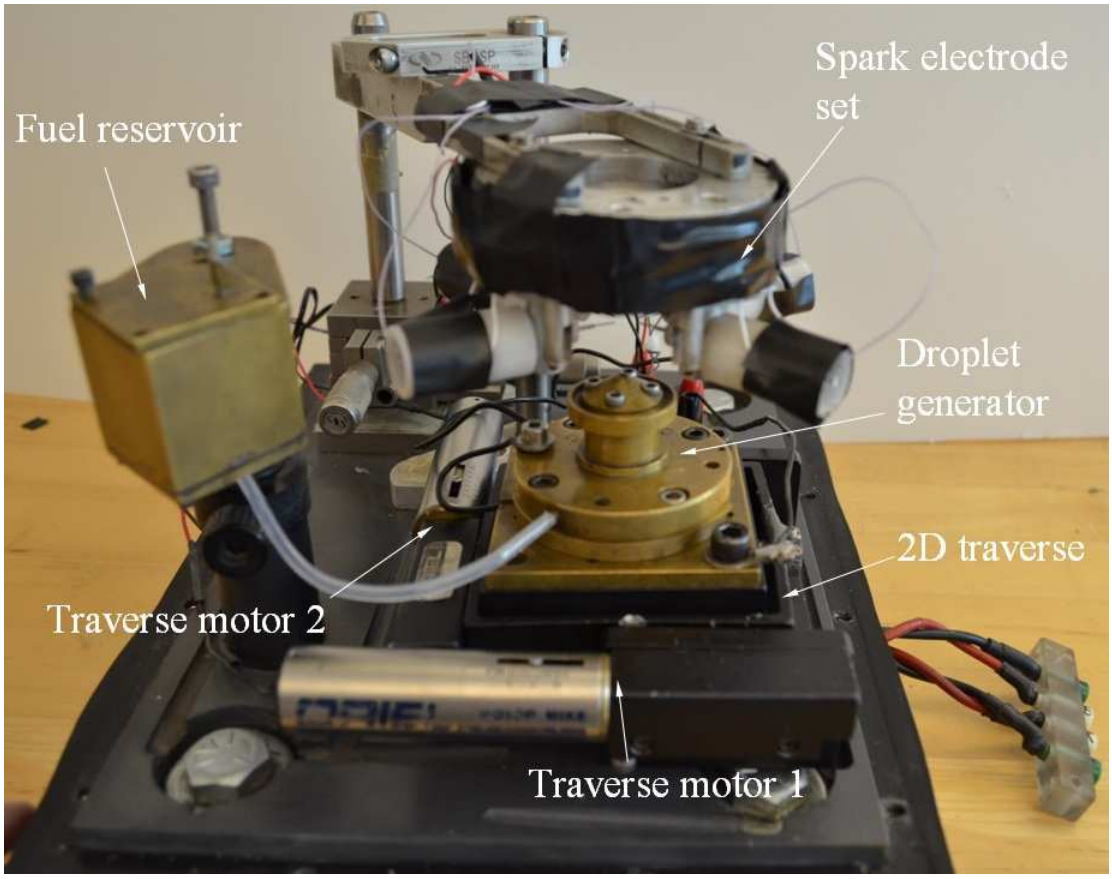

Fig. A10. Photograph showing the relative position of the droplet generator, 2D traverse with two motors to change the orientation of the droplet generator.

214B. In order to obtain a vertical droplet trajectory, the traverse stage should be adjusted until the droplet trajectory from the nozzle is vertical and the droplet falls back right on the nozzle tip. The trajectory of the droplet should be recorded by the BW camera at 200 fps. The droplet is marked on the PC screen where it first appears in the field of view, then its position is compared with that of a droplet leaving the field of view (both at the bottom of BW images). Due to the deformation of droplet boundary (cf. Fig. A11) during the flight, the position of the droplet is better determined by its center of mass. Here we can use the reflection (white dot, see Fig. A11) as the representative droplet center.

The droplet trajectory also needs to look vertical in the view of the color camera. Due to the low framing rate of the color camera, it is difficult to ensure a vertical droplet trajectory using recorded color videos. To get an estimate for the droplet trajectory in the view of the color camera, we can eyeball the trajectory from a TV screen that displays the real time color video of nozzle tip while generating droplets. If the droplet travels back down following its way up and finally splash the center of the nozzle, the droplet trajectory should be vertical for the color camera.

There are three main parameters that control the height of the droplet apex: pulse voltage (on HP 214B), pulse amplitude (on HP 214B), and the liquid level in the fuel reservoir. The pulse amplitude is usually fixed (for fixed a droplet size) and voltage is adjusted to achieve the desired droplet apex (the exact height of spark electrodes). Liquid level in the fuel reservoir is also very critical to the quality of the droplet generation. Recommended liquid level is about one half of the reservoir, which makes the liquid level about 2 cm above the nozzle tip. When the liquid level is too

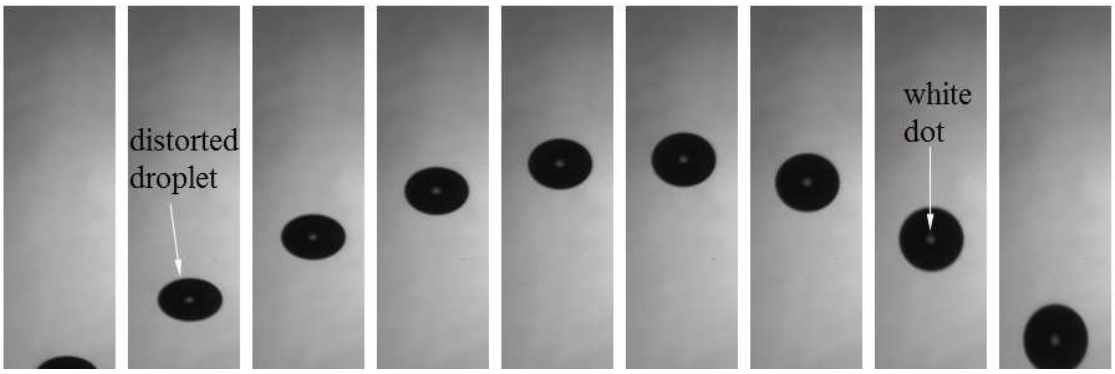

Fig. A11. A series of n-decane droplet images (from left to right, recorded at 200 fps) showing the distortion of a moving droplet and the white dot at the center of droplets that can be used as a reference to see the droplet trajectory regardless distorted droplet boundary.

low the droplet trajectory could vary for different shots in a series.

When the liquid level is too high, fuel will start to leak from the nozzle tip, which is very undesirable because the liquid spill might burn in an experiment. The fuel leakage from the nozzle tip will quickly reduce the liquid level (to around one half) hence it is difficult to maintain constant liquid level for droplet generation. The droplet apex and droplet size are also slightly influenced by the fuel liquid level. A consistent liquid level must be maintained before an experiment. "Satellite" droplets are sometimes generated along with the main droplet. Adequate reservoir liquid level and the pulse amplitude also help to improve it (see Section 2.1.3).

The spark electrodes should be positioned such that the droplet (at the apex) is right at the center of the spark gap on both cameras. Once the droplet trajectory and the electrodes are positioned for an experiment, the traverses attached to the bottom of the cameras must be adjusted for best focusing of the droplet.

A.2.3 Magnet Delay

Power to the electro-magnet used to hold the instrumentation package is controlled by the HP 6010A while the signal to release the package is programmed in the QC-9618 signal generator. A 5V voltage is constantly maintained in channel 1 of QC-9618 to activate the magnet and grab the package. Once deactivated, the magnetic power disappears and the package is released into free fall. However, there exists a noticeable "delay," Δt_{magnet} (see Section 2.1.6), between the time of terminating power to the magnet and when the package is actually separated from the magnet. This magnet delay is critical to know for free droplet experiments. The package should be

separated from the magnet at the exact instant when the droplet reaches the apex of its trajectory. Figures A12 to A14 show the parameters set on the QC-9618 for a free-droplet experiment (cf. Fig. 2.33).

A.2.4 Spark Energy

Unlike fiber-support experiments, a free droplet is ignited while freely floating in the ambient at its apex. Due to the fact that the droplet is travelling upward before ignition, the fuel vapor concentration around a free droplet is lower compared to a fiber supported droplet. Difficulty with igniting a free droplet will hence lead to use of slightly a higher spark energy (than in a fiber-supported experiment). This might potentially result the spark exerting a greater physical impact on a free droplet. With an appropriate spark energy, a free droplet should be ignited without its trajectory being altered (otherwise the free droplet could fly out of the view or lose good contrast).

In order to find the appropriate spark energy to ignite free droplets, ignition tests are performed in normal gravity prior to an experiment. Guidelines to obtaining good ignition for a free droplet include: clean spark electrodes; no droplet distortion observed after ignition; and droplet should stay in focus after ignition.

Provided here is a step-by-step preparation prior to a free droplet experiment.

Fig. A12. Detailed settings on the QC-9618 that generates the signal shown in Fig. 2.33 for Channel 1: magnet.

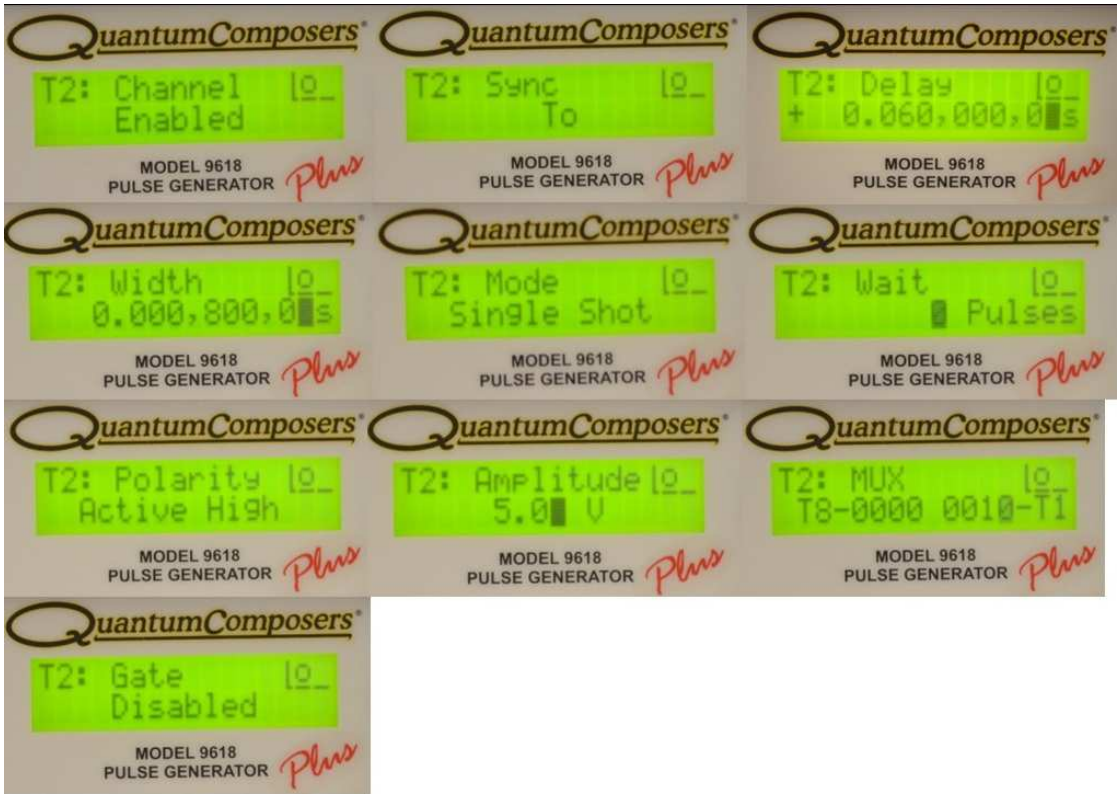

Fig. A13. Detailed settings on the QC-9618 that generates the signal shown in Fig. 2.33 for Channel 2: spark.

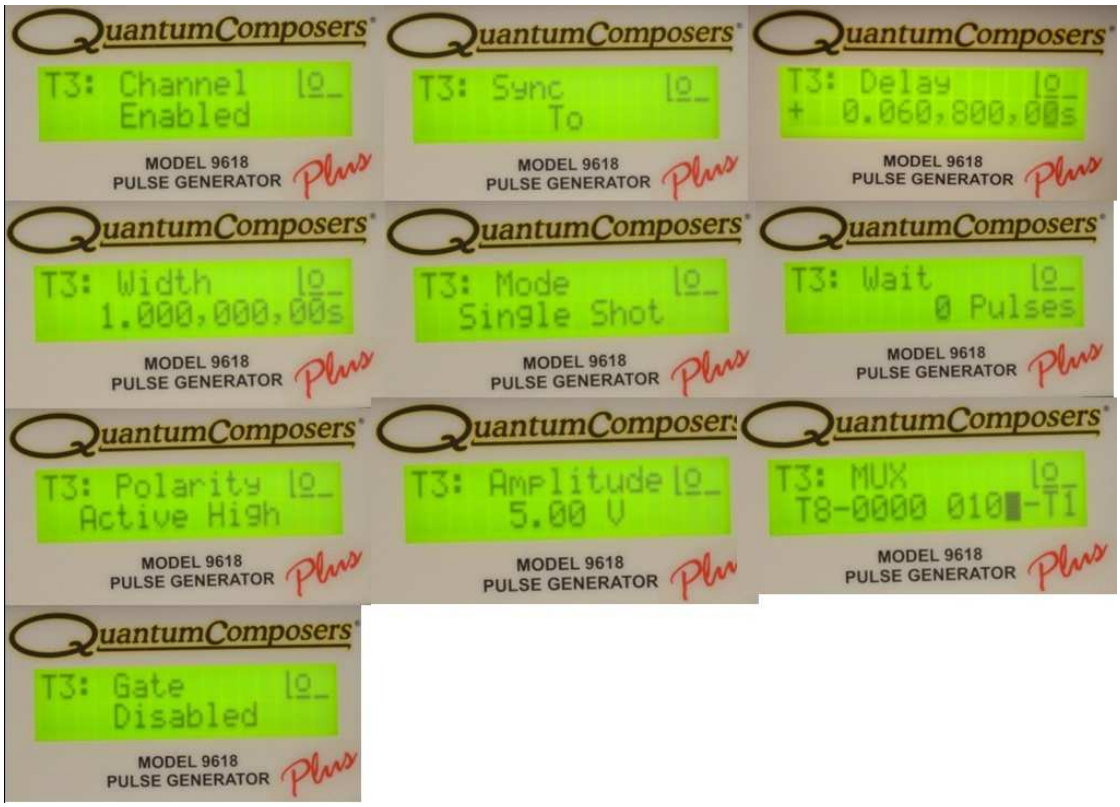

Fig. A14. Detailed settings on the QC-9618 that generates the signal shown in Fig. 2.33 for Channel 3: retraction.

Preparation

1. Check the "sustain" signal after a drop. The signal should be ~-15 V in normal state and a square wave with amplitude of ~12 V should be generated when the spark is triggered. Failure of component 4548 in the low energy grey box usually lead to a signal with ~0 V when spark is triggered.

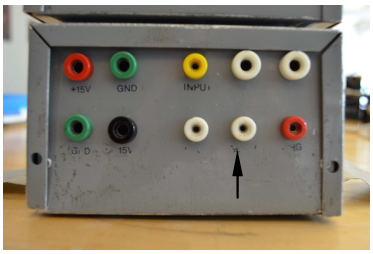

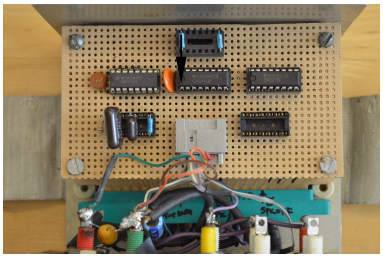
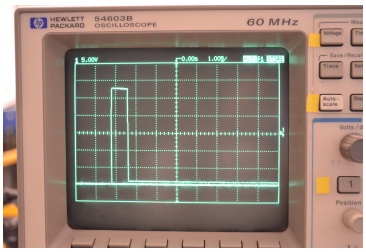

2. Remove carbon particle deposition on the tips of four spark electrodes by slightly scratching the tips using a blade until the tips look shiningly polished.
3. Refill the fuel reservoir to one half of the full reservoir.
4. Open the camera software for both camera on the PC desktop ("Camera Control" for the BW camera and "Pinnacle Studio 12" for the color camera.

5. In the BW camera software, go to "setting" by pressing the yellow wrench button  on the tab, set the exposure time to around 100 μs (settings might differ from

fuel to fuel) and recoding speed at 200 fps.

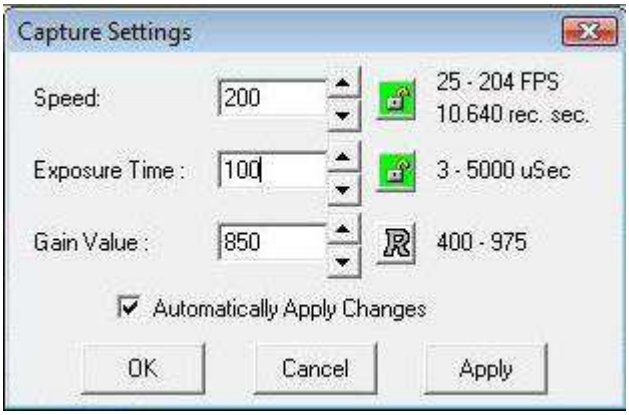

6. Start recoding BW images by pressing the green light green on the tab.
7. Put the spark electrode set back to the combustion chamber and make sure the electrodes are at the center of BW camera view.

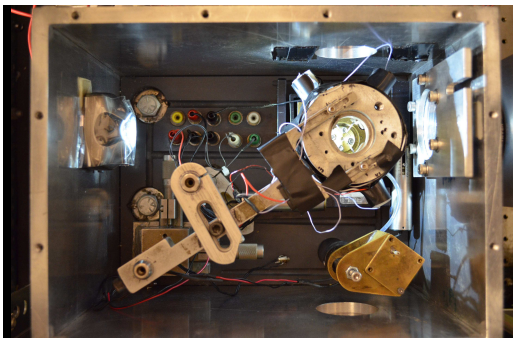

8. Fine tune the LED position until the background intensity for the BW camera view is uniform.
9. Hang the entire package using an eyebolt and remove the cart underneath it (just the cart, not the rolling floor).
10. Pull part of the long signal cable up and set it one the floor, in order to emulate the balance of the package before a drop (cf. Fig. A9).
11. Connect the controller (Oriel Motor Mike Control, Model 18005) of the two traverse motors for the droplet generator "inside the combustion chamber."

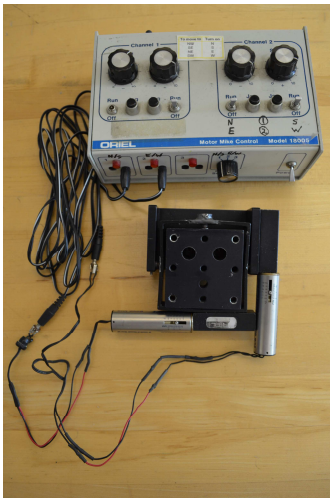

12. Turn on the pulse generator for droplet generation (HP 214B).

13. Place the chamber lid on the chamber, as well as the metal beam and metal cover for the outer package to emulate the balance for an experiment.
14. Start generating droplets by pushing the “man” button on the HP 214B, use appropriate voltage and amplitude (see Section 2.1.3) of the pulse to obtain a good height of droplet trajectory.

15. Use the Oriel controller (shown below) to drive the two traverses and adjust the tilting angle of the droplet generator to obtain a vertical trajectory for the droplet.

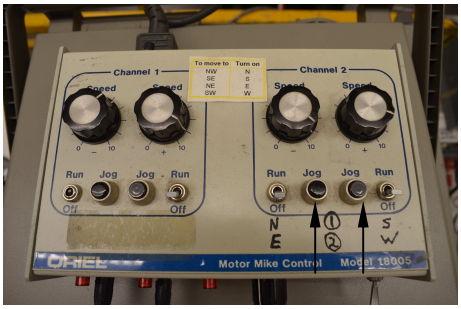

16. Record and review the droplet trajectory using the BW camera with its software.
17. Repeat step 14-16 until the droplet trajectory appears “vertical” in the view of the BW camera.
18. After a vertical droplet trajectory is obtained, use the traverse underneath the combustion chamber to position the droplet right at the center of the BW camera view.

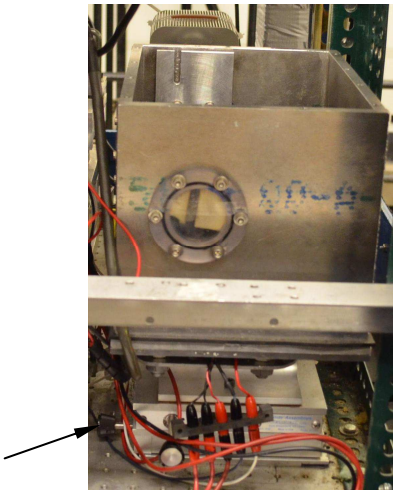

19. Adjust the position of the spark electrode set on the support by changing where it is bolted on the U-shaped fixture to accommodate the droplet apex in the view of both cameras.

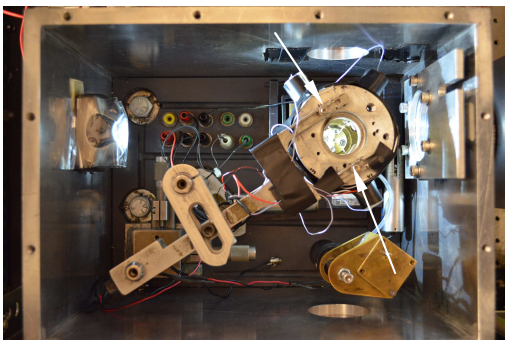

20. Adjust the traverse underneath the cameras for optical contrast/focus of the droplet boundary (view the recorded images of both cameras to see).

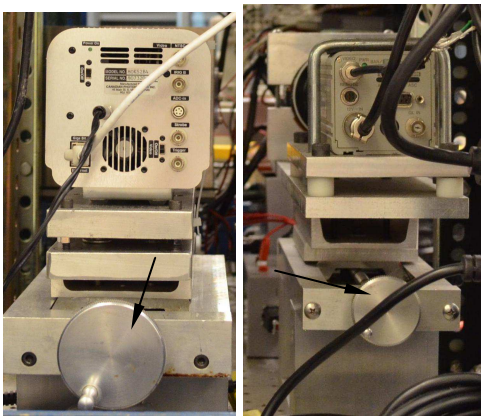

21. Refill the fuel reservoir to one half of the full reservoir.

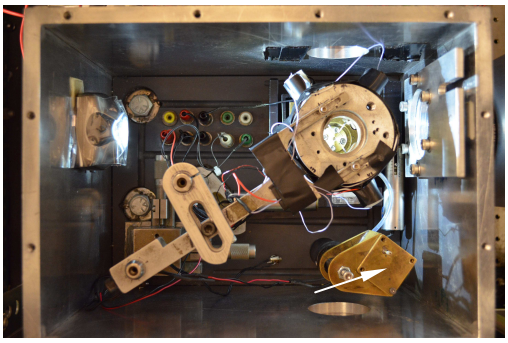

22. Generate some droplet and record them with the BW camera.

23. Determine if the droplet trajectory is vertical from the recorded BW images.

24. When done, gently put the drop package back on the cart.

Low gravity experiment

1. Replace batteries for LED if the light intensity is low (view from the BW images).
2. Push the spark electrodes to the position that allows spark to occur (basically push them towards the droplet position until the end).
3. Disconnect the wires between the traverse controller and the two traverses inside the combustion chamber.
4. Double check the connections for droplet generation, spark, and retraction inside the chamber.
5. Gently bolt the lid on top of the combustion chamber.
6. Bolt the crossing metal bar to the inner package frames- on near the color camera mirror and one on the opposite side of the inner package.

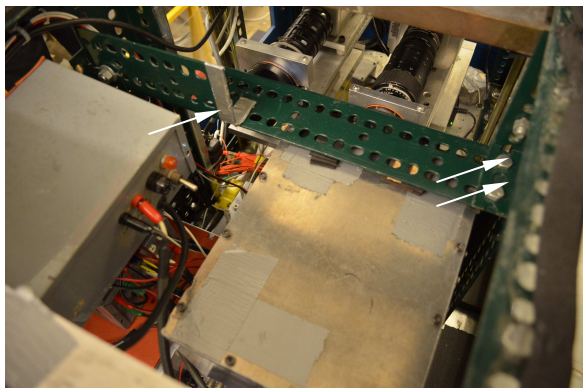

7. Re-adjust the mirror if the electrodes look displaced from the color camera (bolting the metal beam in step 6 might slightly bend the frame on which the mirror is fastened).

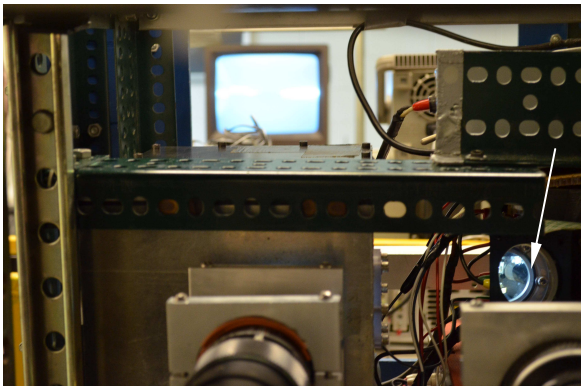

8. Double check all the electrical connections (e.g. the 30 V power supply; low voltage grey box; high voltage orange box; and wiring between the high voltage box and the combustion chamber, as well as the connection for spark electrode retraction).
9. Switch on the 30V power supply inside the drop package and the charging for the high voltage orange box.

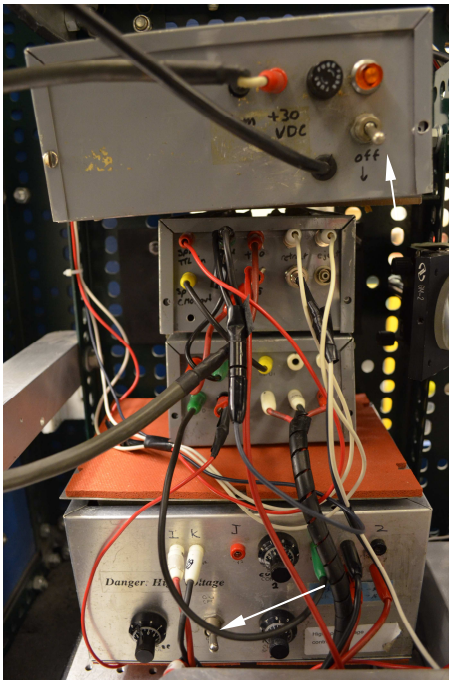

10. Gently put the transparent plates on the four sides of the outer package.

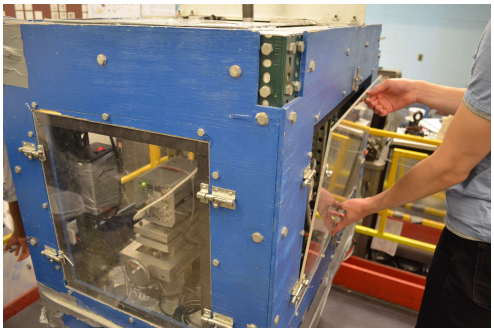
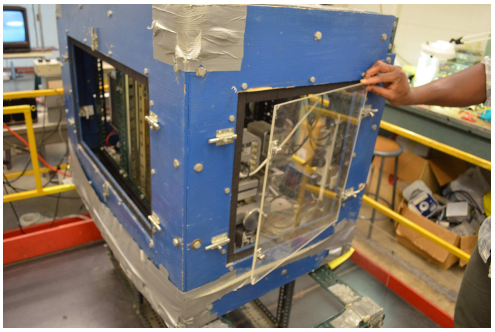

11. Release a bit more the strand metal wire from the winch and remove the eyebolt that is screwed on the upper center metal plate of the inner package.
12. Clean the upper center metal plate as well as the bottom of the electro-magnet using paper towel by wiping down all the dusts that could potentially affect the magnet performance.
13. Place the electro-magnet on the center metal plate of the inner package.
14. Line up the magnet with the two aluminum plates on the center metal plate.

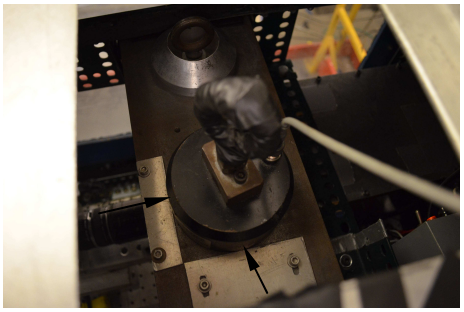

15. Double check if the cable for the magnet is tangled in a way that would catch the drop package at release.
16. Turn on QC9618 to activate the 5 V signal for the magnet.

17. Adjust the voltage to 100 V (for safety concern) on the HP 6010A for the electro-magnet.

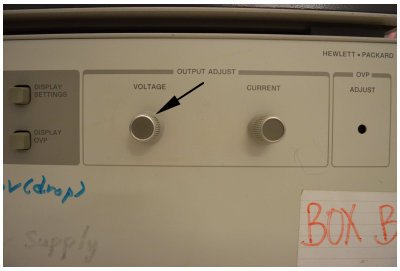

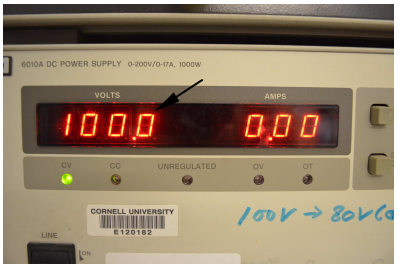

18. Wait around 10 seconds for the magnet to complete grip the drop package.

19. Turn on the power box for the winch.

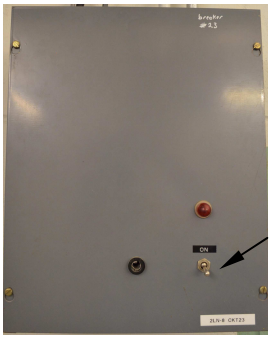

20. Flip the winch controller to UP.

21. Very slowly raise the inner drop package by adjusting the voltage on the variac to around 10 V (the voltage on the variac determine the speed). (the package might be detached from the magnet if more than 30 V is used)

22. Make sure the two safety eyebolts and the cone-shaped metal on the inner package are perfectly aligned with the two holes on the outer package.

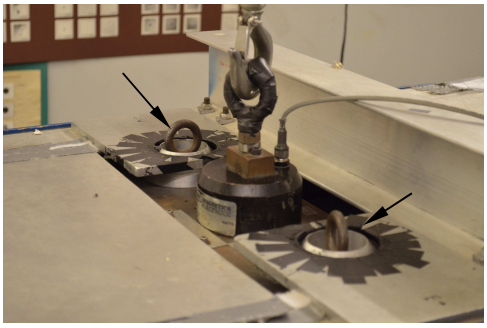

23. Raise the entire package about 2 inches above the cart, turn the variac to 0V to stop the winch.

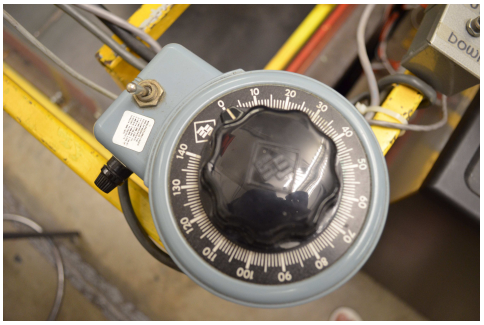

24. Count to three, roll the floor from the bottom of the hung package as fast as possible.

(DANGER!!!! The package is now positioned over the free-fall shaft)

25. Arrange the long cable to hang down straight from the bottom of the package; part of the long cable should sit on the side wall of the deceleration tank.

26. Stabilize the package.

27. Lower the magnet voltage (on HP 6010A) to 50 V.

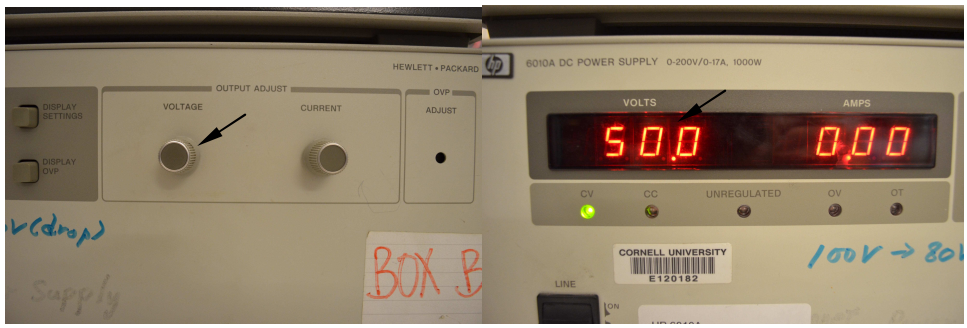

28. Switch on the ± 15 V power supply on the control desk and start charging the spark capacitors for 7 minutes.

29. During this 7 minutes, disconnect the trigger cable from the output of the HP 214B to the EXT/ GATE port of QC-9618.

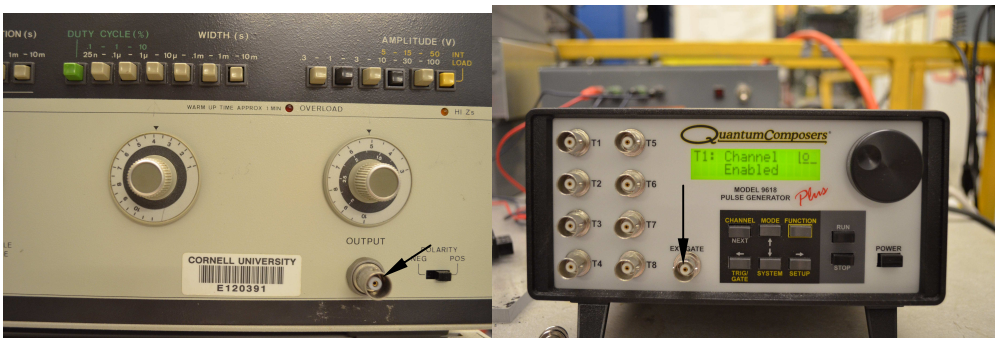

30. Generate droplets (press the “man” button on the HP pulse generator) and adjust the voltage dial on the HP pulse generator until the desired apex is achieved.

31. Reconnect the trigger cable between the HP pulse generator and QC-9618.

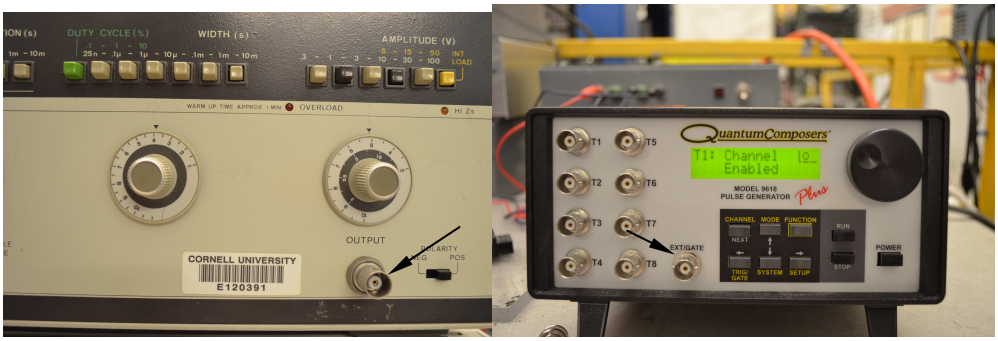

32. Select “triggered” mode on the QC-9618.

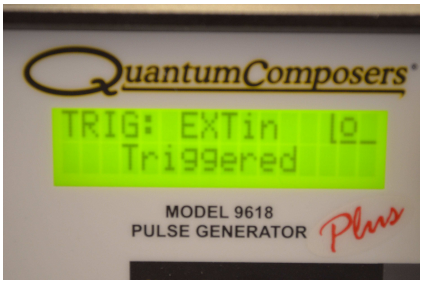

33. Make sure the BW camera is not stopped by the default 10 minute recording termination in the software.

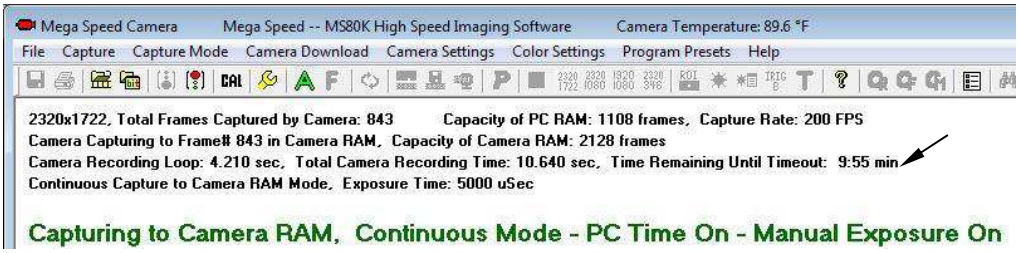

34. In Pinnacle Studio 12, go to the "Capture" tab, press "Start Capture", type the file name save the color video.

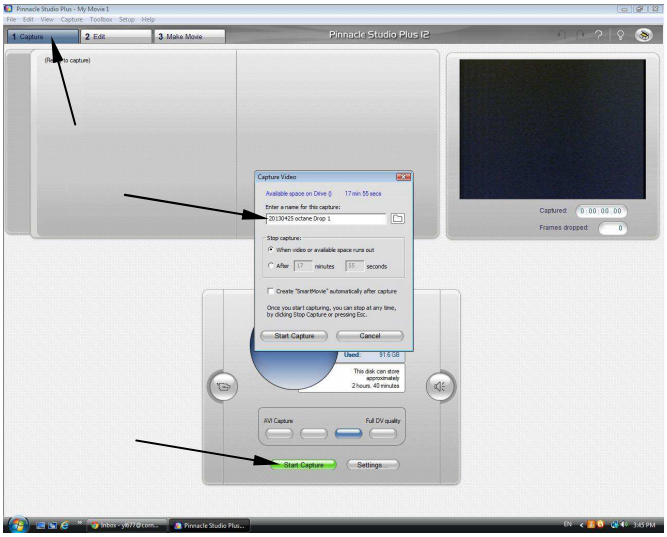

35. From the computer, start saving the color video by pressing the grey "start capture" button on the file name window.

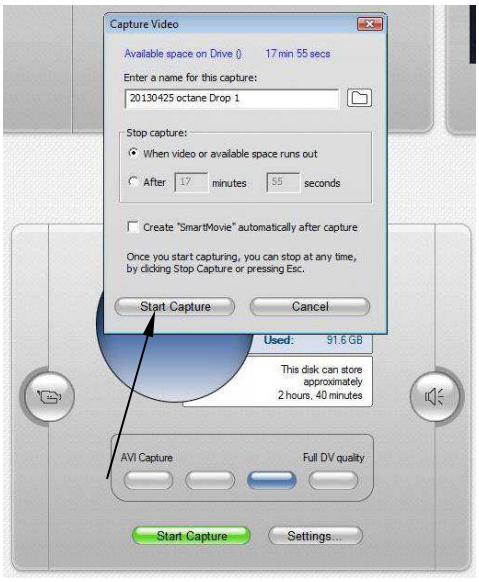

36. Wait a few second, when the color video time starts to "tick," press the "man" button on the HP 214B to initiate the entire drop experiment.

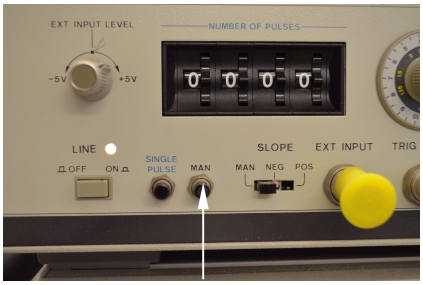

37. After the drop package landed the deceleration tank, quickly "stop" recording color and BW images from the computer.

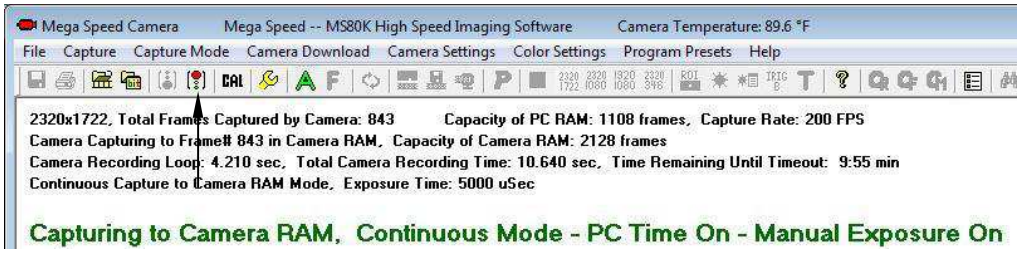

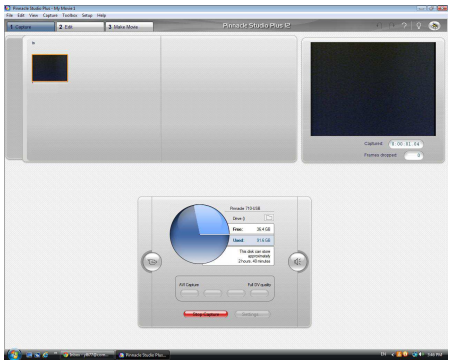

38. Switch off the HP 6010A, HP 214B, ± 15 V power supply, QC-9618. Make sure the main power of the package is still "ON" for the drop package.

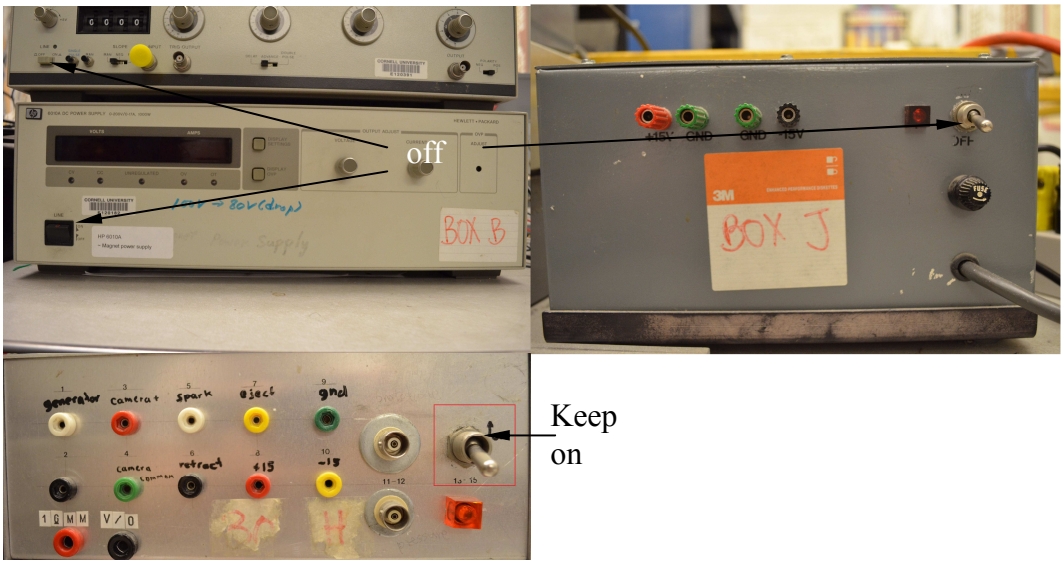

39. Start downloading BW images from the temporary memory onboard the BW camera by pressing the "download button"  ; select "To Hard Drive As JPEG" at the bottom and input the image destination/directory; input the "start frame" and "end frame" (images can be "previewed" from the right small preview window); choose the minimum downloading speed (5 fps). (See Section 2.1.8.1 for more details).

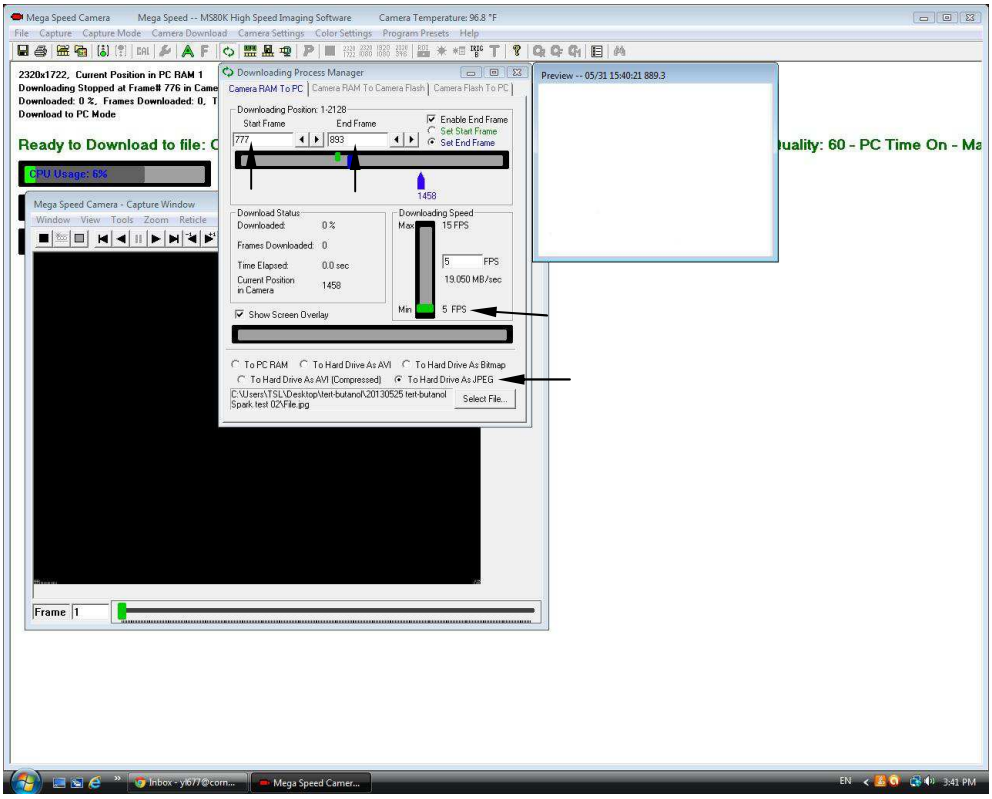

40. Make sure both color and BW images are saved by checking the images in the folder just created by the software on PC.
41. Close the camera software window (Camera Control and Pinnacle Studio 12) on PC.
42. Switch off the main power of the drop package.

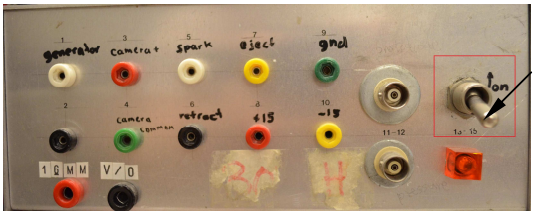

43. Lower down the magnet and take it off the hook.
44. Lower down the hook to the top of the drop package downstairs using maximum speed (variac at 140 V).

45. Zero the variac to stop the winch un the hook reaches the package.

46. Flip the direction controller to “neutral” for the winch.

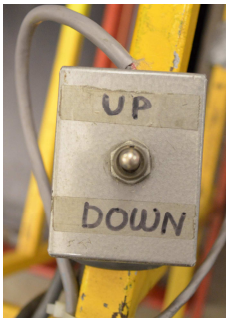

47. Put 80 V on the variac – a moderate speed for raising the package when it is sitting in the deceleration tank.

48. Bring the eyebolt down to the package and screw it back on the upper center plate of the inner package.

49. Make sure the long cable and winch wire are not tangled.

50. Use the direction controller downstairs to raise the inner package, with the speed set on the variac upstairs (80 V).

51. Adjust the position of the outer package while the inner package is lifted up until the two cone-shaped metal pieces are perfectly aligned with the two holes on the outer package.
52. Double check is there is any scratch on the long cable.
53. Stop the winch from the downstairs winch direction controller when the package is lifted around 5 ft above the deceleration tank.
54. Put all the foam boards and the blanket back to their original positions and make sure the deceleration tank is in a good shape for the next drop experiment.
55. Go back upstairs and switch “UP” the winch direction controller there.

56. Use maximum speed (140 V on variac) to raise the package.

57. When the package is lifted up to the “drop” position, zero the variac.

58. Switch the winch direction controller to “neutral”.

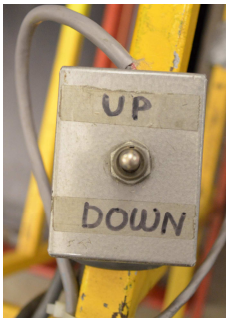

59. Close the sliding floor and make sure the floor does not jam the long cable from the gap.
60. Slowly lower down the package, adjust the position of the cart to let the package sit squarely on it.
61. Very slowly lower down the inner package until it sits on the outer package.
62. Take off the side plates from the outer package.
63. Switch off the 30 V power supply and discharge the capacitors in the high voltage orange box.

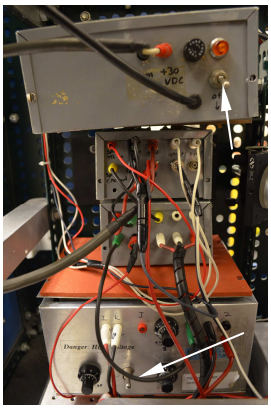

64. Remove the metal beam that fastens the combustion chamber.

65. Unbolt the chamber lip and open the chamber.

66. Use a fan to flush fresh air into the chamber.

67. Switch off the LED light.

68. Get ready for the next drop experiment.

APPENDIX B

Troubleshooting for the Spark Ignition Systems

For the ground-based experiments reported in this study, the fuel droplet is ignited by two symmetric sparks. The energy of these two sparks is controlled by the spark circuitry developed since Jackson (1994) with some minor modifications by Callahan (2000). As mentioned in Appendix A, to obtain useful data from a ground-based experiment, droplet generation, fiber support, spark firing, electrode retraction, electromagnet, as well as recording of the BW and color camera must work with minimal error. Among all these individual operations during an experiment, failure of spark ignition is the most frequently seen problem and the most complicated problem for troubleshooting. This appendix aims to include all the failure modes of spark ignition and the tests to confirm the source of failure as well as how to fix it. Jackson (1994) provided some insightful troubleshooting procedures for the spark circuit. The following produces are developed based on his methodology with some current considerations.

The failure of spark ignition can be divided into four categories: (I) sparks do not appear across the electrode gaps, (II) sparks appear but being unable to ignite the droplet, (III) sparks are two strong and loud even with low energy settings, and (IV) the sparks are unexpected fired without a signal. From here mode (I) to (IV) are used to refer these various modes of spark problems. When mode (I) is encountered, it means either the “breakdown” voltage is not large enough to create the first conductive channel across the electrodes or the breakdown voltage is not properly

generated at all. The logical troubleshooting for mode (I) is as follows. As mentioned as part of the experimental procedure in Appendix A, the part needs most frequent replacement is the MCI4358 in the low voltage spark circuit (see Fig. B1, and Fig. 2.25). The correct signal of sustain spark from the output of the low voltage spark circuit is shown as the signal "f" in Fig. 2.27. This should be the very first thing to check due to its potential to burn out after an experiment regardless the failure modes. If a new MCI4358 is used but the sustain signal is still different than the signal "f" shown in Fig. 2.27, the two CD4049 inverters in the low voltage circuit box should be replaced (see Fig. B1 and Fig. 2.17).

Sometimes the soot aggregates or oxides that stick on the electrode tips can become impedance for the breakdown voltage. So when mode (I) is identified, the tip of each spark electrode should be cleaned by sanding it using a piece of sand paper and polishing the tip by scratching it using a blade. Note that though the breakdown voltage is controlled from the high voltage spark circuit, the gradually blunting electrode tips can also significantly decrease the eventual voltage and in turn affect the breakdown spark. If the electrode tips are very clean but there are still no sparks, all the connections from the back of the electrodes to the high voltage spark circuit should be checked. The simplest way is to test the connectivity between the electrode tip and the connection that goes into the high voltage box. Sometimes when the spark wires are exposed and making contact with metal materials (e.g. the body of the spark electrode set) or the surface of the threaded laser board, the connectivity between spark electrodes and the upstream pin connection looks alright but the sparks can be directed to this lower resistance to ground leading to no spark across the electrodes.

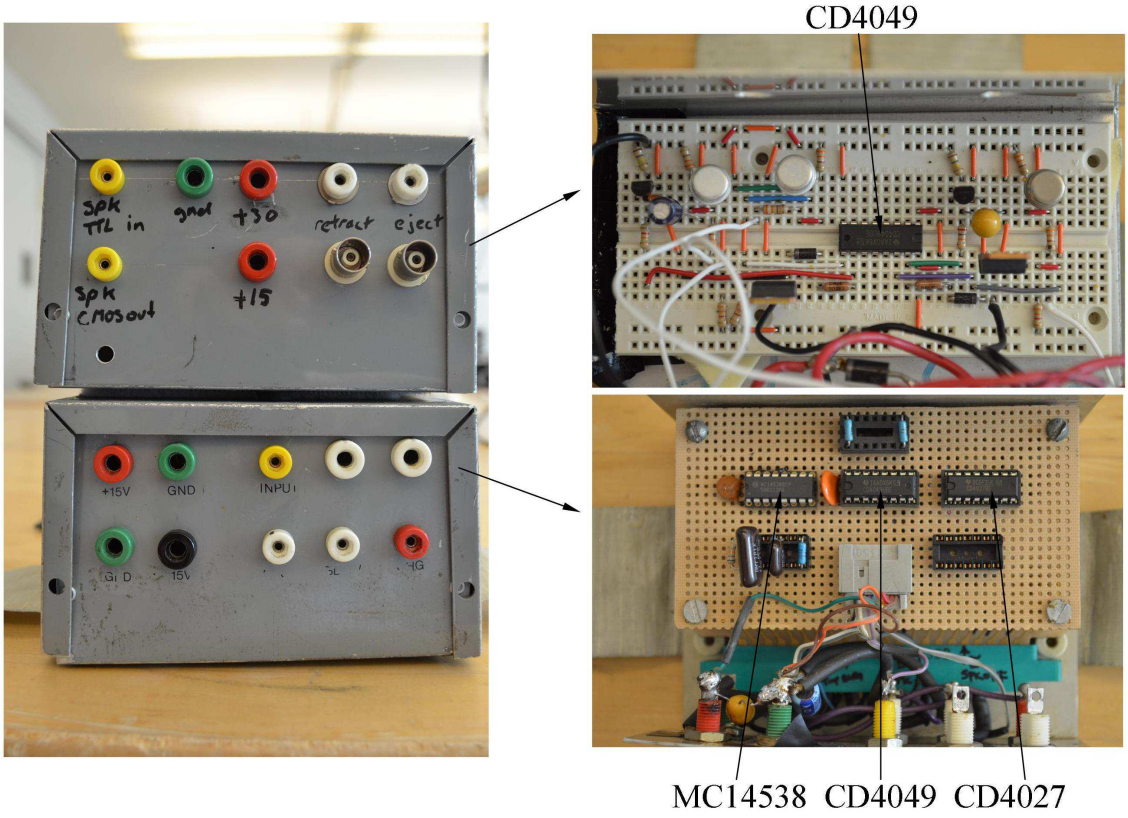

Fig. B1. Components in the low voltage spark circuit (cf. Fig. 2.17) that are considered in the troubleshooting process for spark ignition.

If everything above was tested and there is still no spark, it suggests that the problem is from the spark circuit box. The thyristor 2N6404 (see Fig. B2 and Fig. 2.18) in the high voltage spark circuit that controls the breakdown sparks should be checked. The "diode" mode on a potentiometer can be used to test this component. Figure B3 shows this component and the correct readings on the potentiometer between the pins. Other components in the breakdown circuit appear to be very endurable and have not been replaced during the course of study.

Mode (II) is identified when only very weak light blue sparks appear across the electrode gaps. The weak sparks can be indicative of either the sustaining spark is not working at all or the sustaining spark is triggered with an improper voltage such that the droplet is not ignited. There are two components in the high voltage spark circuit needed to be checked when the spark is weak. The MJ12005 transistor (see Fig. B2 and Fig. 2.18) controls the release of two individual sustaining sparks from the 20 μF capacitors. If the MJ12005 transistor fails to properly work, the sustaining sparks will not be fired from the two transistors MJE5852 (see Fig. B2 and Fig. 2.18) even when the 20 μF capacitors are fully charged. Note that the malfunction of the downstream transistors MJE5852 will cause mode (III) of spark failure (see later discussions). Figure B3 illustrates a simply test for the MJ12005 using the "diode" mode on the potentiometer and the corresponding readings. If the MJ12005 works properly but the sparks still look weak, the LM350 (see Fig. B2 and Fig. 2.18) should be replaced because it controls the charging voltage for the two 20 μF capacitors and thus the voltage of the sustaining sparks.

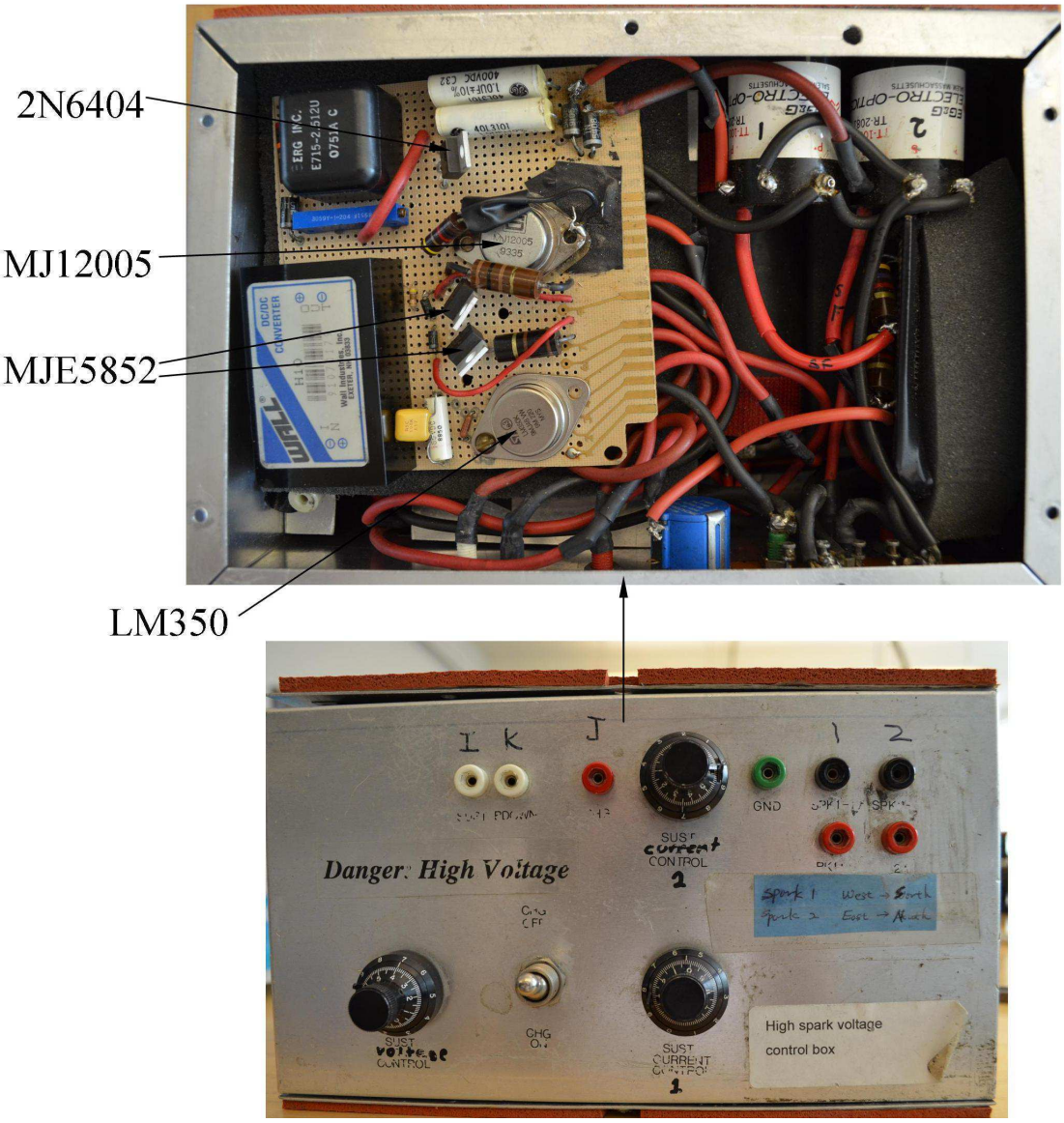

Fig. B2. Components in the high voltage spark circuit (cf. Fig. 2.18) that are considered in the troubleshooting process for spark ignition.

Fig. B3. Illustration of testing a MJ12005 transistor using the “diode” function of a potentiometer and the corresponding readings.

When mode (III) is encountered, the spark energy is not controlled by the high voltage box leading to very bright and loud sparks. This is due to the burn-out MJE5852 being unable to replicate the spark duration from the upstream transistor MJ12005. When a MJE5852 is burned, it is still able to open the gate according to the signal from MJ12005, but it is unable to close the gate leading to a continuing current flowing out from the capacitor. This leads to a much longer (so bright and loud) spark than desired. Note that the MJE5852 usually burns out one at a time, and it can be easily recognized by seeing one spark that is much stronger than the other. A simple test for the MJE5852 transistors can be performed using the diode function on a potentiometer. Figure B4 illustrates the connections for the test as well as the corresponding readings on the meter. When a burned out MJE5852 transistor is measured, the reading on the meter displays "O.L." (overload) instead of 0.56 V meaning the transistor has become a pure "conductor".

When mode (IV) of failure is met, weak sparks jump over the electrodes without any signal inputs. Provided that the sustaining spark voltage is not high enough to create the first conductive channel in the air, this problem must be due to malfunction of the thyristor 2N6404. When the 2N6404 is not working properly, the breakdown current can not be held in the capacitors such that once they are charged to certain energy level, current leakage occurs leading to the unexpected sparks. Replacing the old 2N6404 with a new one shall resolve this problem.

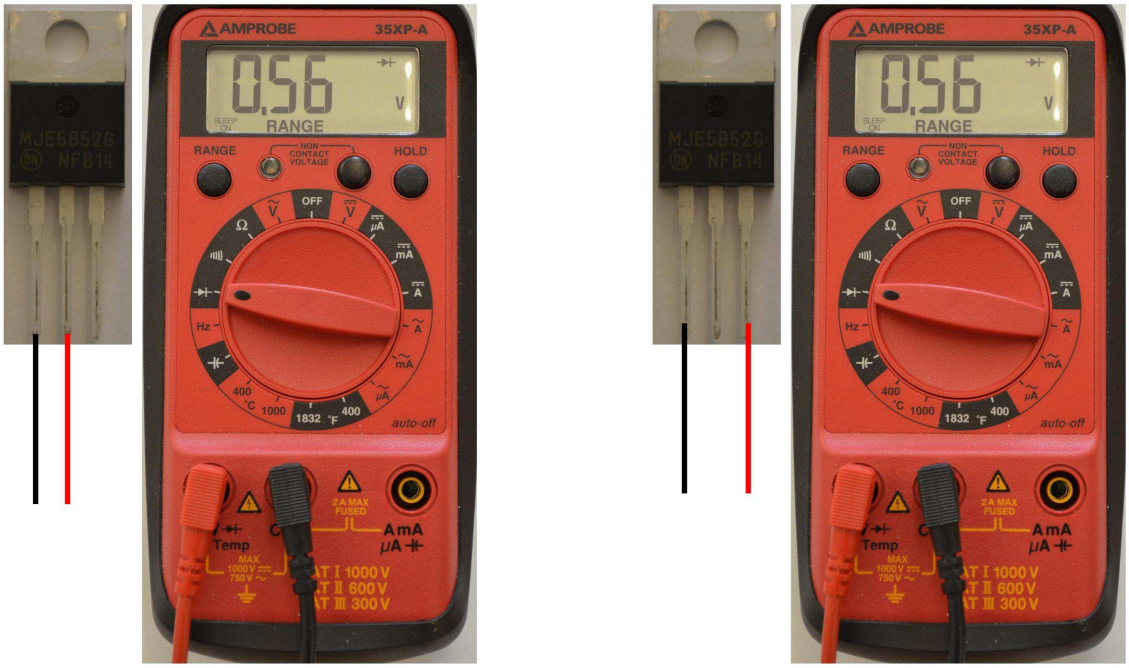

Fig. B4. Illustration of testing a MJE5852 transistor using the "diode" function of a potentiometer and the corresponding readings. Note that the values on the meter can vary from 0.54 V to 0.57 V.

APPENDIX C

Automation of Droplet Diameter Measurements for Consecutive Images from a Droplet Burning Process[8]

C.1 Introduction

Extracting physical dimensions from consecutive digital images of a transient event is a fundamental problem in image analysis. This task is especially important in the study of droplet combustion in which droplet and flame diameter histories are determined from analyses of consecutive digital images. Such data provide the rate of combustion that relates to the performance of practical liquid-fueled propulsion systems. The data analysis problem for droplet burning is often complicated by the formation of soot around the droplet that introduces background noise that must be filtered out in order to ensure accurate diameter measurements. Individual images may be analyzed by manual processes using commercial software that require subjective judgments about which regions to omit from an image. Several hundreds of consecutive frames from high speed imaging devices (film and video) must typically be analyzed individually to extract the droplet diameter history, which can be time-intensive. For example, the time to manually analyze between 50 and 100 frames typically takes several hours. A process that could reduce the analysis time by a factor of ten would significantly improve the efficiency of data analysis and allow for study of a wider range of fuel systems within a specified period of time.

[8] This appendix comes from the following publication: Dembia, C.L., Liu, Y.C., Avedisian, C.T., Image Analysis and Stereology 31 (2012) 137-148.

The ability to use planar images, which provide only two-dimensional information, for the analysis of droplet combustion experiments relies on the assumption that the droplets and their flames are volumes of revolution. Only then can a two-dimensional description of the droplet and its flame provide sufficient information to determine their shape and size. This assumption is valid when gas phase spherical symmetry prevails, as is achieved by removing all forms of convection around the droplet, which is accomplished by burning "small" droplets in a low gravity environment (Dietrich et al. (1996), Avedisian (2000) Bae and Avedisian (2004a), Hicks et al. (2010). Figure C1a illustrates the resulting configuration. The spherical droplet is concentric with its spherical flame, which in turn is concentric with a soot "shell" that may develop as a result of the formation of particulates during the burning process (the physics of soot shell development is discussed in Jackson and Avedisian (1994), Choi and Lee (1996), Avedisian (1997). The planar image is then truly a volume of revolution of the planar circular image. This situation is well suited to the application of an automated image analysis algorithm that can detect an edge of interest (e.g., droplet boundary), determine an effective diameter from it, and advance through a sequence of images.

Figures C1 to C3 are representative of the images that are encountered in droplet combustion experimentation carried out in a low gravity environment. From such images, physical dimensions must be extracted to provide quantitative data of the burning process. Figure C1b (Jackson and Avedisian (1994)) depicts a free-floating burning droplet from one frame of a sequence for an n-heptane droplet (C_7H_{16}, boiling point of 98^{o}C) obtained from a high speed 16 mm LOCAM II movie camera operated

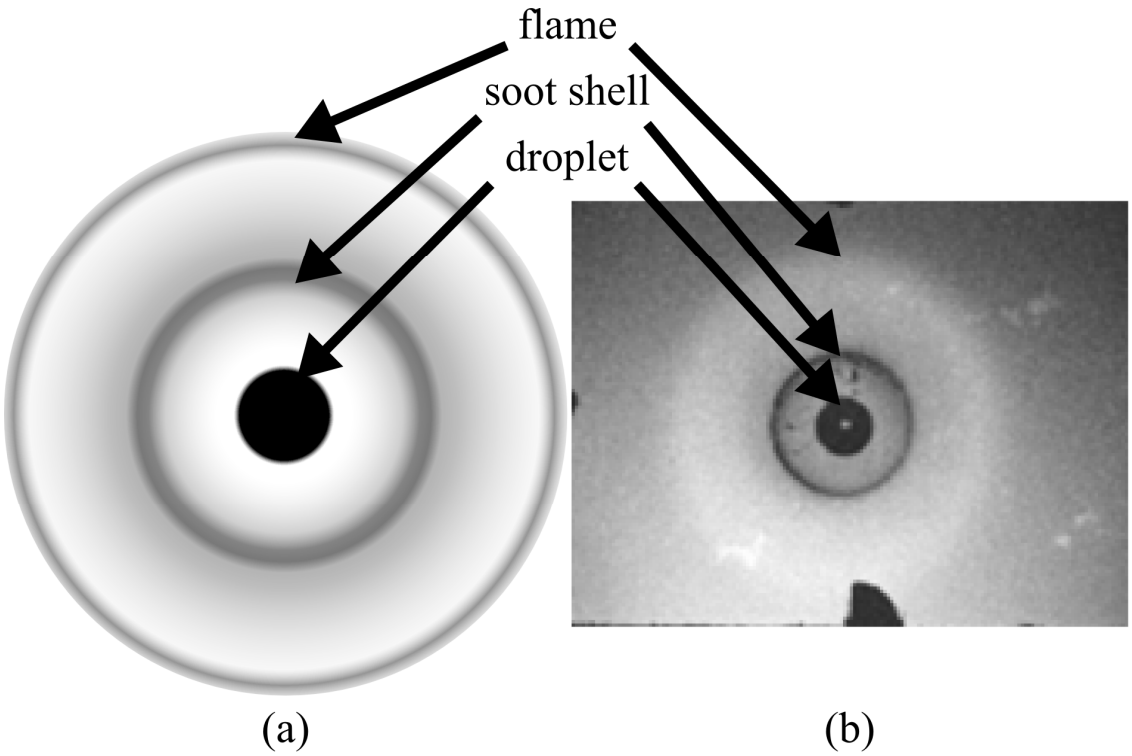

Fig. C1. (a) Idealization and (b) film photo of a spherically symmetric droplet, showing the flame and soot shell (Jackson and Avedisian (1994)).

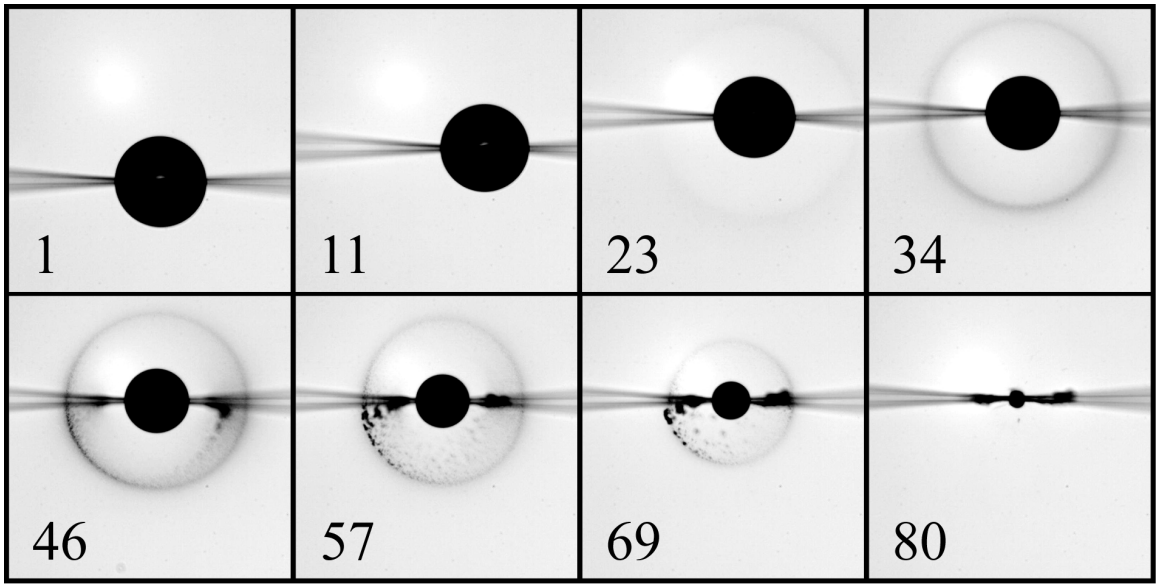

Fig. C2. Selected images from a fiber-supported heptane droplet burning experiment.

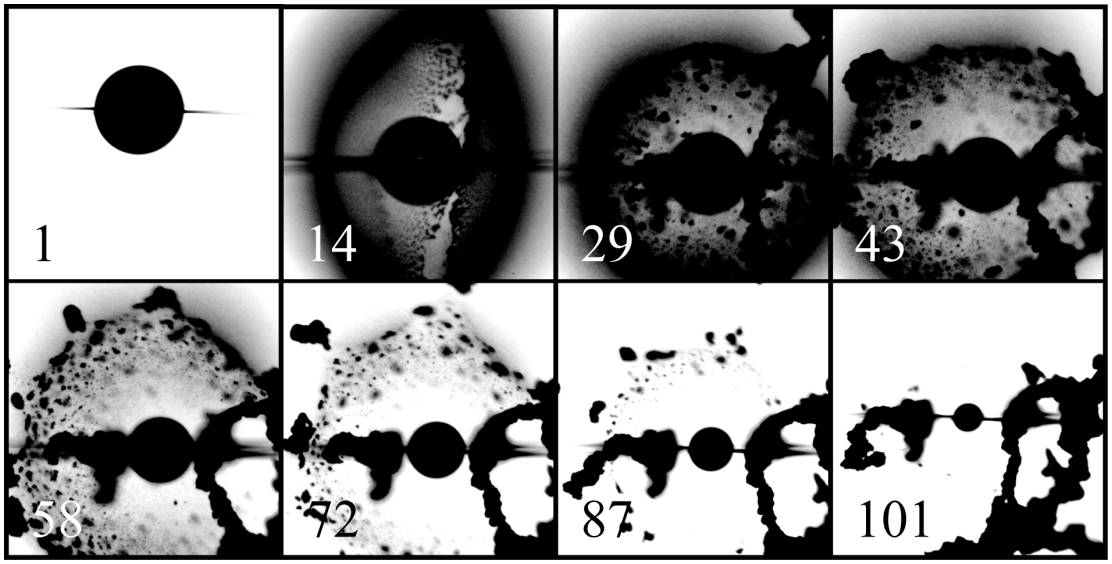

Fig. C3. Selected images from a fiber-supported toluene droplet burning experiment.

at 200 frames per second. Fig. C2 (Liu and Avedisian (2012)) shows 8 selected images from the burning history of an n-heptane droplet as captured with a 3.9 megapixel digital video camera operated at 200 frames per second with the droplet held by two crossed SiC support fibers (14 μm diameter). The initial diameter of the heptane droplet is 0.52 mm. In all these experiments the droplet is ignited by high voltage sparks formed across two electrode pairs on either side of the droplet. The outer luminous zone in Fig. 1b is the droplet's flame. The horizontal bands in Fig. C2 are support fibers. The thin black circle that develops around the droplet in Fig. C2 is a soot shell. The diameter of the soot shell is of interest because of its relevance to environmental air quality.

Early image processing techniques used for analog films of droplet combustion studies involved first manually digitizing each image using a Vanguard Motion Analyzer and tracing the boundary of the droplet with a digitizing pen on a Thomson plotting table (Stewart et al. (1969), Law and Williams (1972)). This method was also commonly used in studies of the dynamic motions associated with biological activities (Stewart et al. (1969), Carpenter and Duvall (1983)). A variation of this approach for droplet analysis was developed by Choi (1992) and Choi et al. (1988b). This variation involved using a micro-processor to detect the droplet boundary from digitized images using mean filtering and intensity thresholding methods. Commercial software now exists to accomplish tasks such as tracking boundaries, measuring diameters, and advancing images in a sequence (e.g., Image-Pro, ImageWarp, CLEMEX, SigmaScan, and PAX-it, etc.).

There are several issues to consider in the analysis of droplet combustion

images. Even though the droplet boundary may be in sharp focus and, accordingly, can be easily detected (e.g., Fig. C2), the soot cloud that surrounds it may obscure parts of the droplet's boundary. Figure C3 shows selected frames from a 102-frame burning sequence of a fiber-supported toluene droplet (C_7H_8, boiling point of 111 ^oC) with an initial diameter of 0.52 mm. The droplet before ignition, shown is in sharp focus with high contrast. However, soon into the burning history the soot forms thick and contiguous structures that attach to the fiber and obscure parts of the droplet boundary. An automated analysis routine can ideally detect a boundary when only part of it is visible (*e.g.*, determining a circle using only a few points on an arc). This task is facilitated, in the case of droplet combustion, by the knowledge that the droplet should have a spherical shape.

In this paper we describe an algorithm for automatically determining the dimensions of droplets when only partial information about the droplet's boundary is available. The algorithm is written in MATLAB and the full program is provided in the "supplementary material" section of the Journal. The algorithm is tailored to the case of near-spherical droplet symmetry so that the droplet's cross section can be approximated by a circle or an ellipse.

The paper is organized as follows. The next section reviews a manual approach to the analysis of droplet burning histories using a commercial software package. We then describe the DROPLETD algorithm in detail, and we subsequently compare results of the automated analysis to a manual analysis approach.

C.2 Manual Data Analysis with Commercial Software

As a base case for comparison we used the package Image-Pro Plus v.6.3 as our prior droplet burning studies (Bae and Avedisian (2004a,2009), Liu and Avedisian (2012)) employed this package for image analysis. A typical procedure for manually obtaining droplet diameter measurements includes the following steps: (1) the droplet image is loaded into the software; (2) a threshold value of grayscale intensity is selected to convert the original grayscale image (with intensity values ranging from 0 to 255) into a black and white (black=0, white=255) binary image; (3) an elliptical "area of interest" (AOI) tool is activated and the AOI is manually placed on what is perceived to be the droplet boundary based on the assigned threshold value; (4) the pixel readings for the width W and height H of the elliptical AOI are recorded; (5) the effective droplet diameter (D), in units of pixels, is calculated by taking a geometric average of the width (W) and height (H) of the ellipse (i.e., $D=(W\times H)^{0.5}$); and (6) the process is repeated for each frame in the sequence.

The intensity threshold and AOI tool of Image Pro is illustrated in Fig. C4. The points in the red areas have an intensity below the threshold. The grayscale intensity threshold that correctly reveals the droplet boundary may vary from image to image. Image-Pro has an automatic threshold feature that attempts to automatically determine an appropriate intensity threshold. Figure C4a-1 is taken from the heptane sequence of Fig. C2. For a droplet image with little background noise, such as for heptane, this feature succeeds at differentiating the droplet from a uniform background (Fig. C4a-2). Alternatively, the threshold may be adjusted manually, as is done for Fig. C4a-3 and Fig. C4a-4. Fig. C4a-3 shows the result of a threshold of 20, which poorly

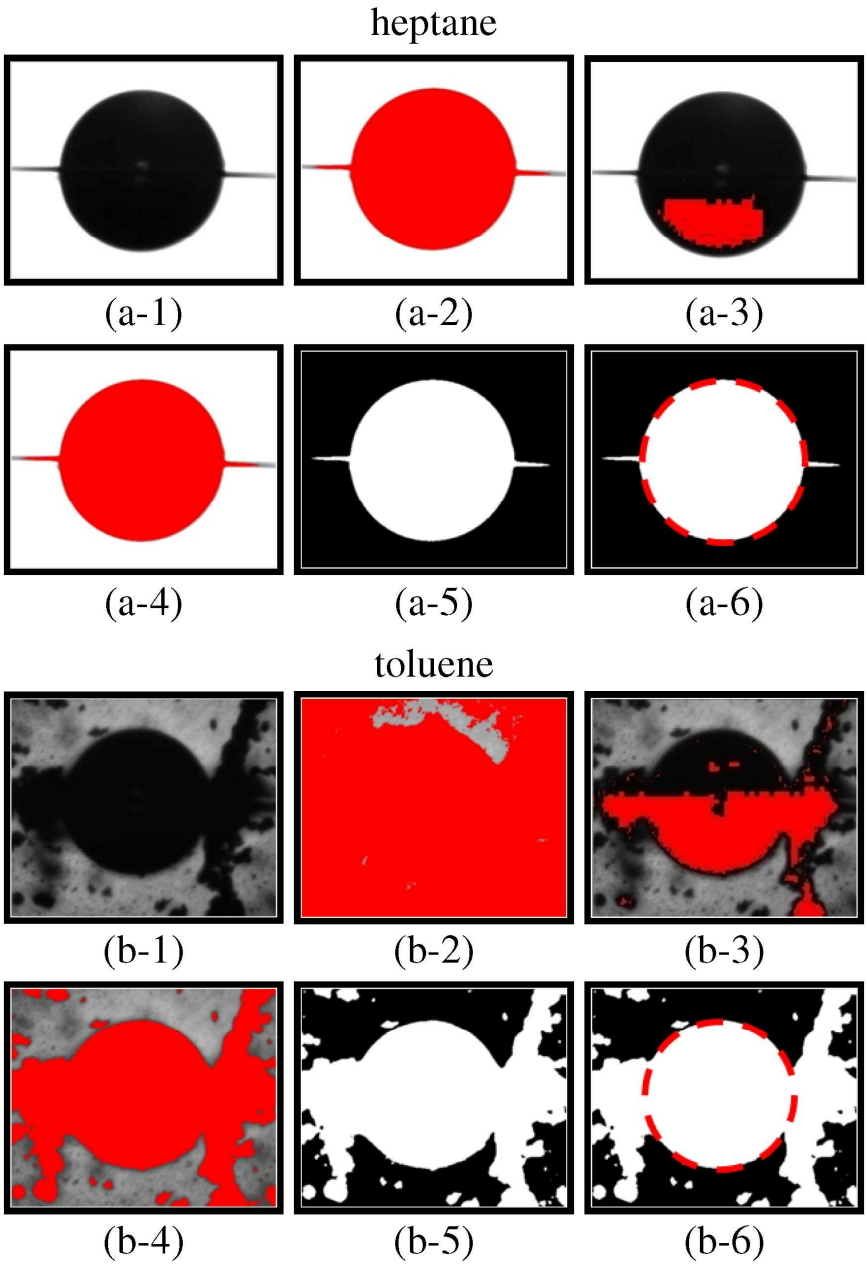

Fig. C4. Steps in a manual Image-Pro analysis, for both heptane and toluene droplets.

distinguishes the droplet from its surroundings. Figure C4a-4, on the other hand, shows the success of a threshold of 160. Ideally the threshold value should generate a region that just blocks the droplet but does not cover the actual droplet boundary. Figure C4a-5 shows that after a threshold is chosen, whether automatically or manually, Image-Pro converts the droplet image into a black and white image. Figure C4a-6 shows a manual fitting of an AOI, represented by the dashed line, to the droplet boundary that is now clearly evident in the black and white image.

Figure C4b-1 through Fig. C4b-6 illustrate the challenge of applying the same procedure to a droplet image with considerable background noise from soot formation, in this case from the toluene sequence of Fig. C3. The original image is shown in Fig. C4b-1. Figure C4b-2 shows the result of using Image-Pro's automatic threshold feature to distinguish the droplet from its surroundings. Clearly, the automatic threshold feature is not successful. In this case, the user must find a threshold manually. Figure C4b-3 and Fig. C4b-4 show the results of two different thresholds found manually. The threshold used in Fig. C4b-4 satisfactorily distinguishes the droplet from its surroundings. Figure C4b-6 shows an AOI that is sized with some operator judgment to manage the irrelevant information of the fiber support and soot surrounding the droplet.

The procedure outlined above provides droplet diameters in units of pixels, which must be converted to physical units (e.g., millimeters). The conversion is accomplished using a conversion factor obtained from the analysis of an image of a calibration ball (a 0.79 mm tungsten carbide ball bearing) that is recorded under the same lighting conditions and with the same focal distance as are used for the droplet

images. Since the correct intensity threshold may vary from image to image, it would seem that the conversion factor may also vary from image to image. However, in the calibration image the ball is so opaque and the ball's boundary is so sharp that the entire range of intensity threshold values that is relevant in the analysis of droplet images yield the same conversion factor. Therefore, the calibration factor is conveniently independent of intensity threshold in the range that is relevant.

The above steps are often laborious and time-consuming when analyzing many images (e.g., analyses can take several hours for a 100 frame sequence). In the next section we describe an algorithm that automates these steps.

C.3 The Matlab Algorithm: DROPLETD

An algorithm termed "DROPLETD" is described by the flowchart in Fig. C5, and a MATLAB implementation of the algorithm is provided as supplementary material. The algorithm consists primarily of two operations: edge detection and shape fitting. The edge detection step provides a collection of candidate boundary points that may be on the droplet boundary and to which an assumed droplet shape may be fit. The shape fitting step is used to obtain an effective diameter of the droplet, which is the quantity desired from each image. Candidate boundary points are iteratively removed from the collection of candidate boundary points until the resulting fit provides an effective droplet diameter that falls below a specified error bound.

Edge detection may be performed in one of two ways: with a constant intensity threshold; or with an adaptive intensity threshold. Edge detection is described in detail later in this section. The shape fitting process is also performed in one of two ways: as

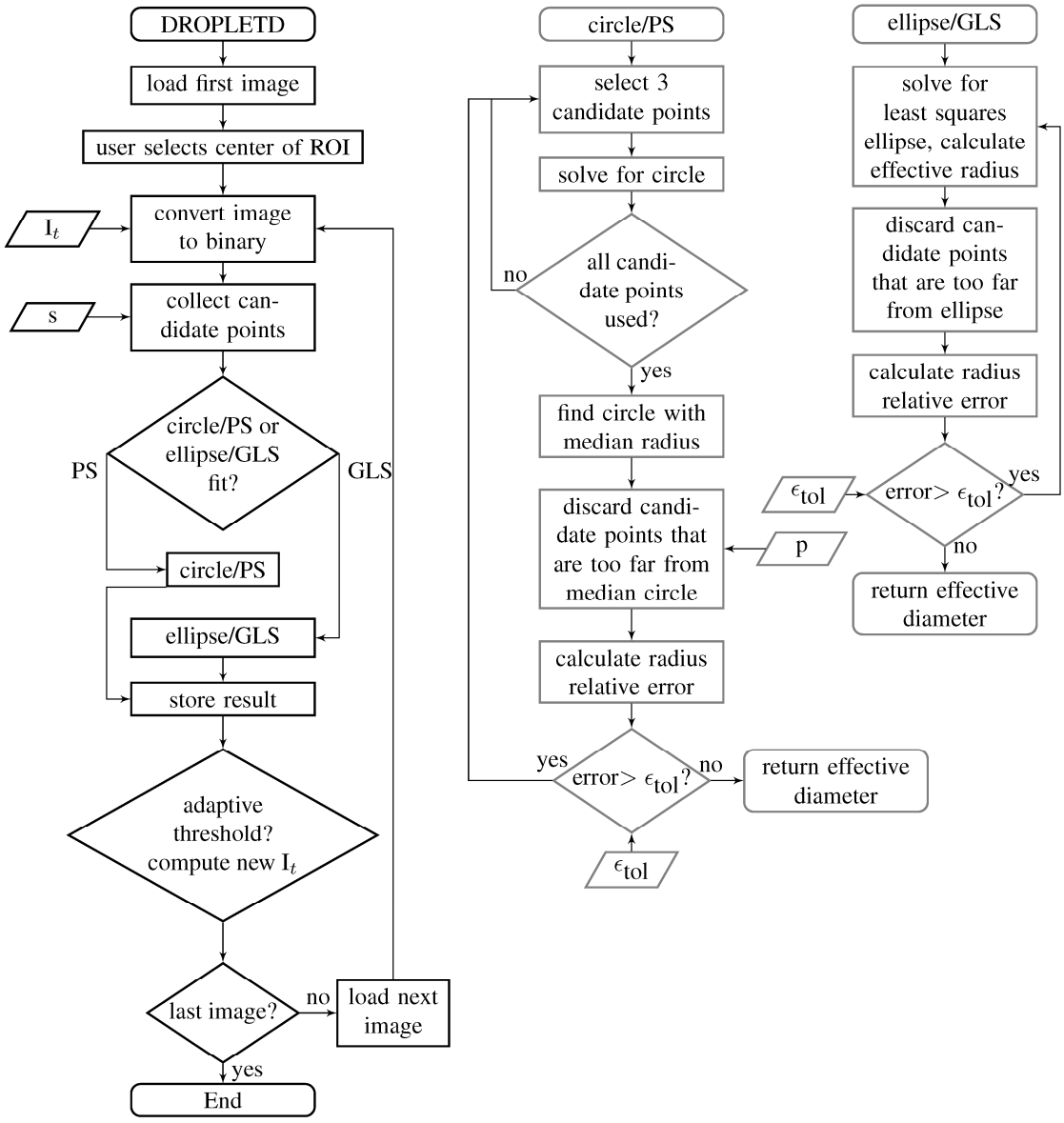

Fig. C5. Flowchart for the DROPLETD automated analysis.

a circle fit or as an ellipse fit. Furthermore, there are two different methods by which a circle or ellipse can be fit to the boundary points: the so-called "point sampling" (PS) method or the "global least squares" (GLS) method. In this implementation, circle fits are tied to the PS method, and ellipse fits are tied to the GLS method for reasons discussed later. The shape fitting methods are described further in the supplemental material at the end of this appendix.

The algorithm starts by displaying to the user the first image in the sequence of images. The user selects a point on the interior of the droplet to specify the center of a region of interest (ROI). The ROI is a square with side length 2s in which the algorithm will search for droplet boundary points. The value of s for the first image in the sequence, s_1, is a parameter of the algorithm. In the present study, a value of 300 pixels is used for s_1, which was found to work well for droplets whose initial diameter is about 250 pixels. For all subsequent images, s is set to be slightly larger than the diameter computed for the droplet in the previous image. A key aspect of the automated nature of this algorithm is that for all frames after the first, it is not necessary for the user to specify the center of the ROI. Instead, the center of the ROI for subsequent images is taken to be the center of the droplet in the previous image. For the algorithm to function properly, the center of the ROI must be within the droplet boundary, and s must always be larger than the droplet's radius. Thus, the droplet in one frame is allowed to have a displacement from its location in the previous frame of about 2s in order for the center of the ROI to remain within the droplet boundary.

The edge detection method used in the algorithm is an intensity threshold

method in which a grayscale image is converted into a black and white image with the use of a grayscale intensity threshold, I_t. Then, a collection of boundary points is created from the points in the ROI, when scanning from the center of the droplet outwards, at which the color transitions from black to white.

The constant intensity threshold method operates by using a single value of I_t for all images in the sequence. The appropriate value for a sequence depends on the fuel being studied and on lighting conditions. For an adaptive intensity threshold, I_t is calculated for each image using data from the previous image in the sequence. The value of I_t is found to be proportional to the average intensity value of certain points across the droplet and its surroundings. Three scan lines that are 45 degrees apart and across the droplet center (shown in Fig. C6) are used to sample the intensity values for the droplet and the background. While more scan lines could be used to compute the adaptive intensity threshold, the use of three scan lines was found to be sufficient for obtaining accurate results. It is important, however, that none of the scan lines are aligned with the support fiber, as this would incorrectly decrease the value computed for I_t.

In order to weight the droplet and its boundary equally in this averaging, the lines have a length that is twice the diameter of the droplet from the previous image. The average intensity value of these sampled points is then used to determine I_t,

$$I_t = f\frac{\sum_k I_k}{N} \tag{C.1}$$

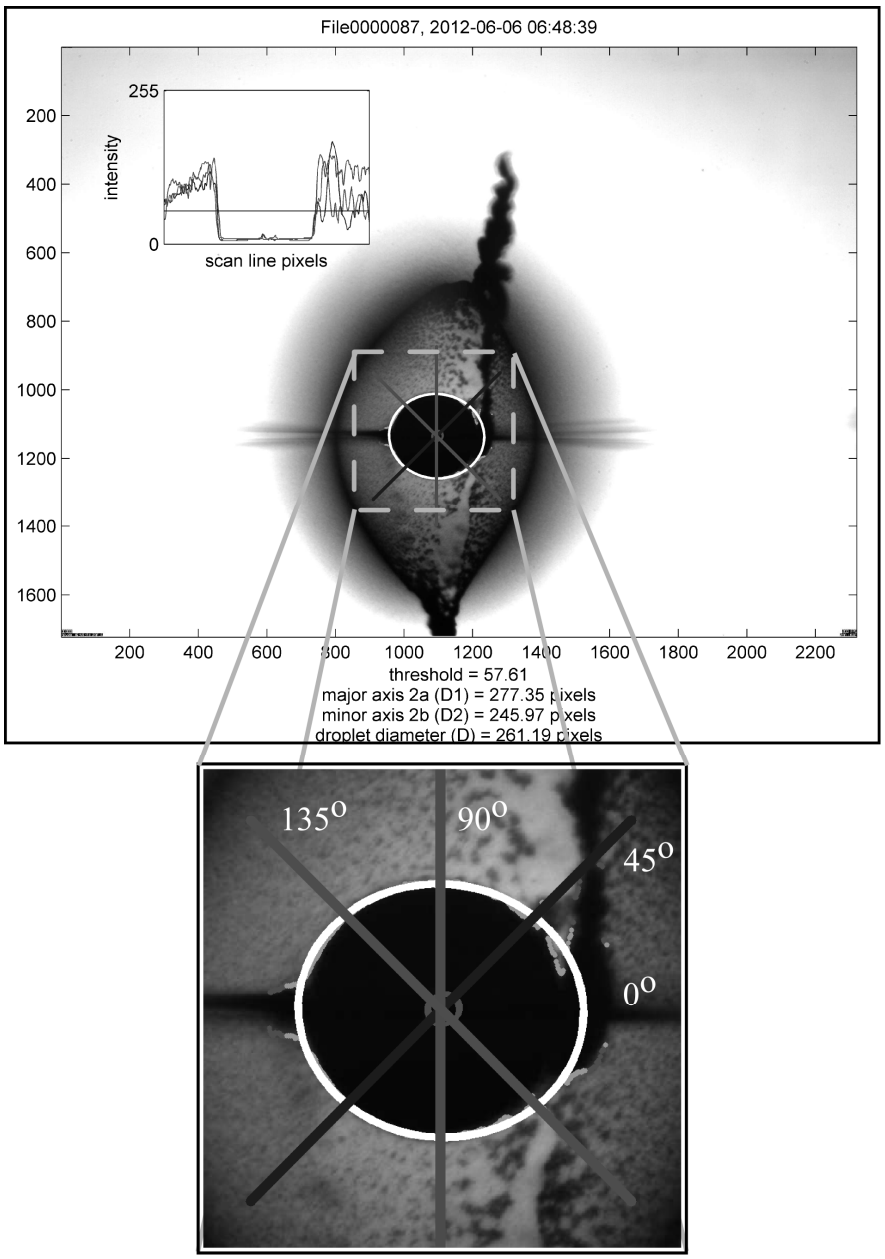

Fig. C6. Output of DROPLETD analysis of the 15th frame of the toluene experiment.

where f is a proportionality constant, I_k is the intensity of the k-th point along the three scan lines, and N is the total number of points along all three scan lines. The threshold defined by Eq. (C.1) is applied to the next image in the sequence.

The value for f depends on the fuel being studied and on lighting conditions, as well as on other parts of the algorithm (e.g. the shape fitting method used). A small value for f favors a darker threshold and thus tends to underestimate the droplet diameter, and is accordingly appropriate for droplets with bright surroundings. In the present study, values for f were selected by examining the values that generally minimize the error between DRPOLETD and a manual analysis. It was found that the error reached a minimum plateau for $0.67 < f < 1.0$.

Two other edge detection methods were also explored. The first of these is a "gradient" threshold method in which the gradient of the grayscale intensity determines the droplet boundary (i.e., inflection point). Thus, a collection of candidate boundary points could potentially be gathered from the points at which the gradient of the intensity exceeds some threshold. This method, however, typically inaccurately predicted large droplet diameters. Edge following methods, which attempt to follow a trail of high gradient values (Pitas (2006)), were also considered. However, such methods were derailed by the presence of the support fiber and were not considered further.

Once equipped with a collection of candidate boundary points, the algorithm fits a shape to the boundary points in an attempt to determine the droplet's effective radius or diameter. The details of the procedure to fit a prescribed shape (circle or ellipse) to the boundary points are discussed in the Appendix. In the case of an ellipse

fit, the effective droplet radius is the geometric mean of the fitted ellipse's semi-major and semi-minor axis lengths.

In a typical analysis, a fraction of the candidate boundary points are fairly distant from the actual droplet boundary. In order to obtain accurate results, it is important that these points are discarded and that a new fit is performed with only the remaining candidate boundary points. This is especially important when the presence of a large amount of soot causes the algorithm to incorrectly detect the boundary of the soot to be boundary of the droplet. This iteration continues until the effective droplet radius falls below a specified error bound.

The discarding of boundary points is controlled with an iterative process whereby the condition

$$\frac{\left|\Delta_i - r_i\right|}{r_i} > p \tag{C.2}$$

where Δ_i is the distance between the boundary point and the center of the droplet and r_i is the radius of the circle fit in the i-th iteration. In the present study, p= 0.1 is used (*i.e.*, the distance between the boundary point and the center of the circle fit must be within 10% of r_i to survive an iteration). For ellipse fits, any candidate boundary point that satisfies

$$\Delta_i > (1+p)a_e \tag{C.3}$$

or

$$\Delta_i < (1-p)b_e \tag{C.4}$$

is discarded, where a is the ellipse's semi-major axis length, b is the ellipse's semi-

minor axis length, and the value of 0.1 is still used for p. A new fit is found with the remaining boundary points, and a new radius r_{i+1} is computed. This process continues until the condition

$$\frac{\left|r_{i+1} - r_i\right|}{r_{i+1}} < \varepsilon_{tol} \tag{C.5}$$

is met, where ε_{tol} is the error tolerance for shape fitting iterations and a value of 10^{-4} has been used in the present study. The method typically requires 2 to 15 iterations for the error to fall below this tolerance. This procedure is performed for each image in the sequence to provide a history of the effective droplet diameter. A summary of the parameters that control the operation of DROPLETD is given in Table C1.

As with the manual analysis, the droplet diameters computed by the algorithm are in units of pixels. In order to obtain the diameter of the droplet in physical units, a conversion factor must be obtained by using DROPLETD to analyze a calibration image using the same edge detection and shape fitting methods used for the droplet images.

The user can choose which of the two edge detection or shape fitting methods to use. The choice of which of these methods to use depends on the nature of the burning sequence. For fuels that generate minimal soot, a constant intensity threshold was found to give accurate droplet diameter results. However, for fuels that generate so much soot that the surrounding intensity changes throughout the burning, an adaptive intensity threshold is often necessary. The determination of whether a circle fit or an ellipse fit is more appropriate is not as straightforward, though a circle fit can be more resilient in cases where soot blocks part of the droplet's boundary.

Table C1. The parameters that control the operation of DROPLETD, and their default values.

parameter	description	default
s_1	Half the side length of the region of interest for edge detection (in pixels).	300
I_t	Grayscale intensity threshold (integer between 0 and 255). More relevant for a constant threshold.	100
ε_{tol}	Error tolerance for the convergence on a droplet's radius.	10^{-4}
p	Affects how candidate points are discarded. A larger value is more allowing.	0.1
f	Proportionality constant in the calculation of the adaptive intensity threshold.	1.0

C.4 Comparisons between Manual and Automated Analyses

In this section, we present comparisons between the automated (DROPLETD) and manual (Image-Pro) analysis of droplet combustion experiments. We employ the heptane and toluene burning sequence of Figs. C2 and C3, respectively, for these comparisons. The DROPLETD results are compared to the Image-Pro results for a variety of the options available in DROPLETD. These include the use of a constant or adaptive intensity threshold, selecting the value of f (Eq. (C.1)), imposing circle or ellipse fits to the droplet shape, and considering the effect of the PS or GLS methods for using boundary points to obtain a fit.

The success of the automated analysis is judged with figures that display the evolution of the square of droplet diameter, D^2, based on the classical theory of droplet

combustion (Turns, (2006)). From this theory, the evolution of D^2 is predicted to be linear though in practice this is often not the case (Liu and Avedisian (2012)). The difference between D obtained from the automated analysis algorithm presented here (D_{auto}) and the manual (D_{man}) analysis for each frame in a sequence is defined as

$$\varepsilon_{auto} = \frac{D_{auto} - D_{man}}{D_{man}} \tag{C.6}$$

A negative error indicates that DROPLETD underestimated the D relative to the D_{man}. The output from DROPLETD is converted to physical units (e.g. mm) as discussed in the previous section.

Figure C7 compares various DROPLETD analyses with an Image-Pro analysis for heptane. The images were analyzed in four ways: a circle fit to the droplet shape using the PS method and an ellipse fit to the droplet shape using the GLS method, for both adaptive and constant thresholds. For the adaptive threshold, f=1.0 in Eq. (C.1) was used. Fig. C7a shows that all four methods successfully approximate the evolution of D^2 from the manual analysis. Only data for every fourth frame are shown to avoid clutter. An adaptive threshold with an ellipse fit is the only method that overestimates the droplet's diameter, as this method is able to accommodate more distance candidate boundary points. The maximum relative error consistently occurs at the end of the burning because the thickness of the droplet boundary becomes relatively large compared to the smaller droplet at the end of burning, and a larger fraction of the boundary is obfuscated by the support fiber and surrounding soot.

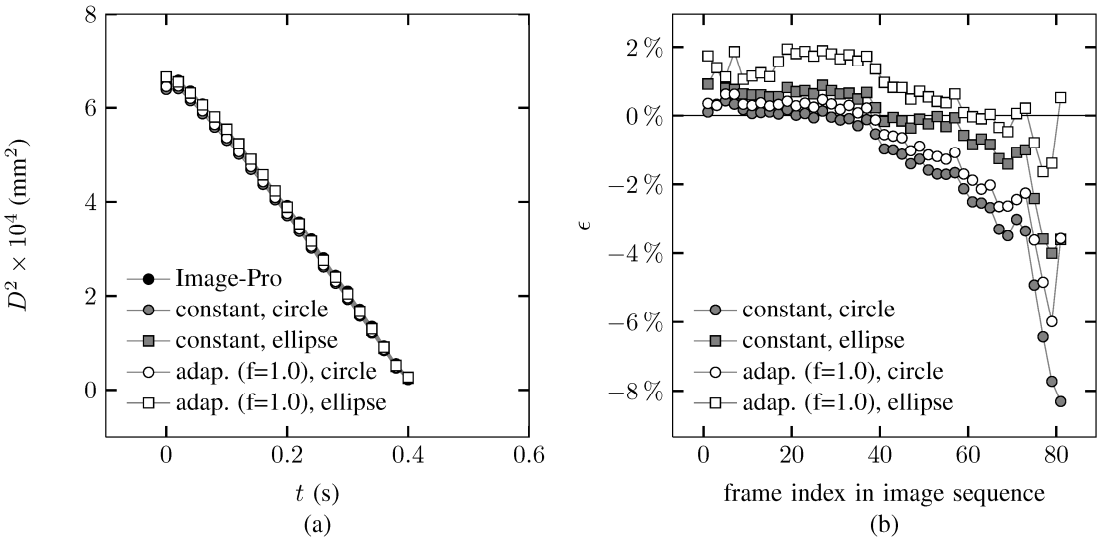

Fig. C7. (a) Evolution of D^2 and (b) error (Eq. (C.6)) for heptane (cf. Fig. C2).

Figure C7b shows that the evolution of the error (Eq. (C.6)) for every other image in the sequence. After frame 40 the constant method underestimates the droplet diameters. Holding the threshold constant does not provide for an adaptation to the slightly changing surrounding intensity as the soot shell forms and evolves. An adaptive intensity threshold corrects for this effect. A value for f of 1.0 with the adaptive threshold appears to reduce the error by a factor of approximately two compared to the use of f = 0.67. For both types of thresholds for heptane, the ellipse fit is more successful than the circle fit because it is more adaptive to the droplet's shape: the average eccentricity of the ellipses is about 0.32.

Figure C8 compares the evolution of D^2 for toluene obtained using constant and adaptive thresholds (and with the PS method for a circle fit and the GLS method for the ellipse fit to the droplet shape). Figure C8a with f=1 shows that for $t < 0.25$ s, the automated analysis results using a constant threshold deviate substantially from the manual analysis results. This initial difference is attributed to excessive soot formation that, compared to the heptane experiment, produces a more pronounced change in the surrounding intensity early in the burning process. A constant threshold cannot adapt to such changes in surrounding intensity, and such an analysis does not succeed at reproducing the results obtained with Image-Pro. An adaptive threshold is necessary for these images. For $t > 0.25$ s all four analyses are consistent. Figure C8b compares the relative errors for the adaptive threshold method for toluene for two different values of f. The results show that f = 1.0 produces a smaller error compared to f = 0.67, as the larger value provides a looser fit.

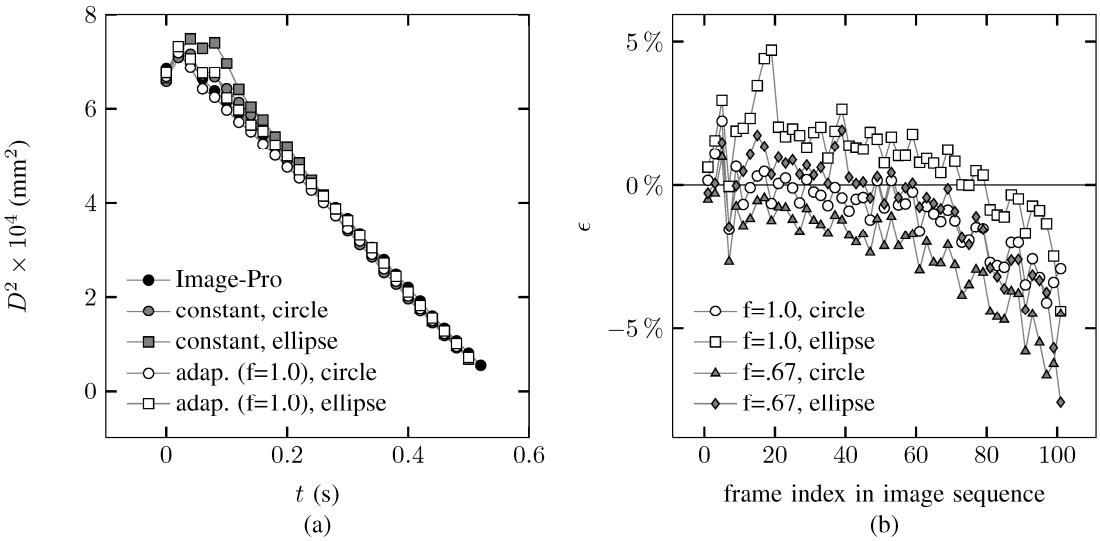

Fig. C8. (a) Evolution of D^2 and (b) error (Eq. (C.6)) for toluene (cf. Fig. C3).

The results of two adaptive threshold analyses for toluene are shown in Fig. C9 using the GLS method of detecting boundary points. In this case, the droplet shape is assumed to be a circle, though this combination is not an option in the distributed version of the algorithm (for reasons explained here). Results for f=0.67 and f=1.0 are compared. The results show significant divergence of the droplet diameter for $t > 0.2$ s which also coincides with a large amount of soot forming on the support fiber that blocked a portion of the droplet boundary (i.e., the impact of the fiber on sooting configuration was discussed in Avedisian and Jackson (2000)). The GLS method in combination with a circle fit is too accommodating to erroneous boundary points from soot, and the algorithm incorrectly determines D. This result motivates tying the circle fit for the droplet shape to the PS method instead of the GLS method. By changing f from 1.0 to the smaller value of 0.67, the algorithm detects the candidate boundary points to be closer to the dark center of the droplet.

As is evident in Figs. C7 to C9 the automated method tends to underestimate the droplet diameter. This effect is less noticeable when plotting $(D/D_0)^2$ versus t/D_0^2 as per the classical theory of droplet burning (Turns (2006)), where D_0 is the initial droplet diameter. In these coordinates, constant differences across methods are suppressed.

Figure C10 summarizes the automated analysis of a representative frame of the toluene burning history (cf. Fig. C3) for a variety of settings. The white curve is the shape that is fitted to the droplet, the red dots are candidate boundary points that were discarded, and the green dots are points that are used in the final fit. A constant I_t leads to the creation of an initial collection of candidate boundary points that are too far from the droplet boundary. In subsequent iterations, these points are discarded from

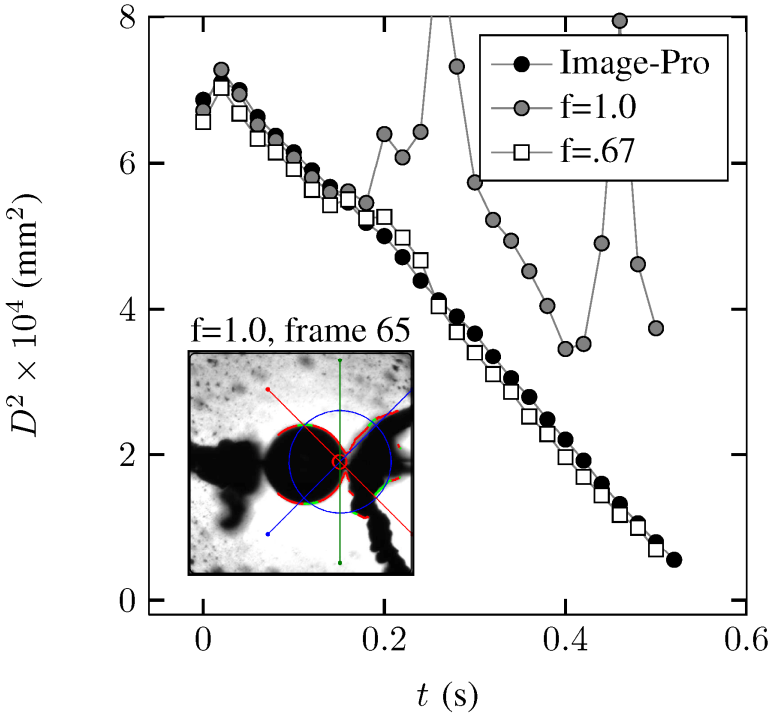

Fig. C9. Evolution of D^2 plot for toluene using circle fits with the GLS method.

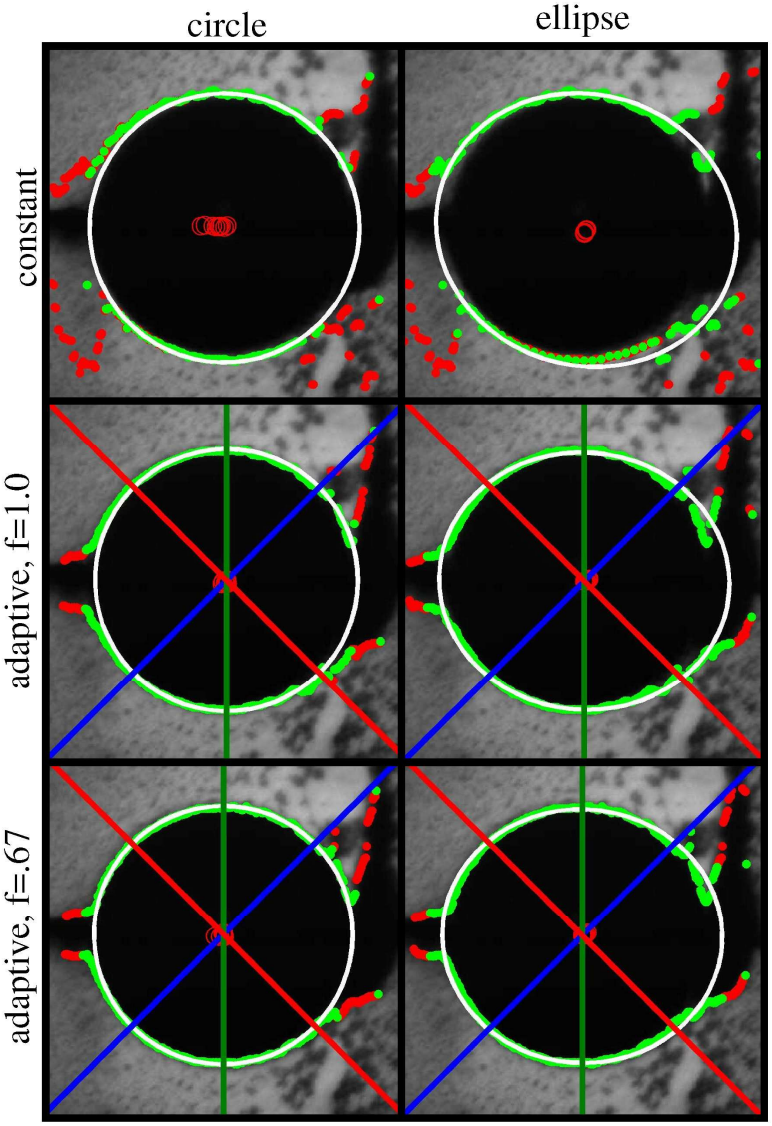

Fig. C10. Comparison of edge detection and shape fitting settings for the 15th frame of the toluene burning sequence from Fig. C3.

the collection. However, with an ellipse fit, enough of these points remain in the collection that the resulting ellipse is clearly too large. This corresponds to the initial large error seen in Fig. C8a for the constant ellipse analysis. Figure C10 also shows that an adaptive threshold prevents the algorithm from considering points far from the droplet boundary, but that an ellipse can be more accommodating to boundary points that actually belong to soot.

C.5 Conclusions

An algorithm has been developed that successfully extracts droplet diameters from digital images of burning droplets of sooting fuels in an automated manner with minimal error. This results in a saving of time in the analysis process by almost a factor of ten compared to the typical manual method of analysis.

The proper selection of the various options in the algorithm depends on the nature of the data being analyzed. For images with low noise or less soot (e.g., heptane), a constant intensity threshold is sufficient for analysis. For fuels in which the droplet's surroundings are changing due to soot formation (e.g., toluene), an adaptive intensity threshold is necessary. Generally, f=1.0 provides more accurate results compared to setting f=0.67. However, under certain conditions a lower value of f can prevent the algorithm from diverging. Additionally, a circle fit is often preferred instead of an ellipse fit if the droplet boundary is blocked by the formation of large amounts of soot.

C.6 Supplemental Material

This section describes the methods used to fit a collection of points to a circle or ellipse. The objective of fitting a circle or ellipse to the collection of points is to obtain the effective diameter of the shape that the points describe. The use of an ellipse fit is considered since it is a more general shape and the shape of a droplet's cross-section may deviate from a circle due to motion of the droplet at the start of its free fall, and disturbance from the spark at the time of ignition. An effective droplet diameter is calculated as the geometric mean of the ellipse's major and minor axis lengths. The choice of whether to use a circle or ellipse depends on the burning sequence. Indeed, the presence of soot in the images sometimes derails an ellipse fit, and a circle fit is more appropriate in such cases.

There are two ways by which the algorithm can use its collection of candidate boundary points to obtain a circle or ellipse that approximates the candidate boundary points. The first of these is the "point-sampling" (PS) method, which operates by generating many different exact fits and choosing the one with the median effective radius. The second of these is the global least squares (GLS) method, which generates a single approximate fit to obtain an effective radius. In practice, circle fits are more successful with the PS method, and ellipse fits are more successful with the GLS method (cf. Fig. C12). Therefore, the PS method is presented only in the context of circle fits, and the GLS method is presented only in the context of ellipse fits.

The first step in the PS method is to divide the collection of candidate points into three groups, as labeled by the Roman numerals I, II, and III in Fig. C11. Then, the algorithm selects the first point from each of these groups and finds the circle that

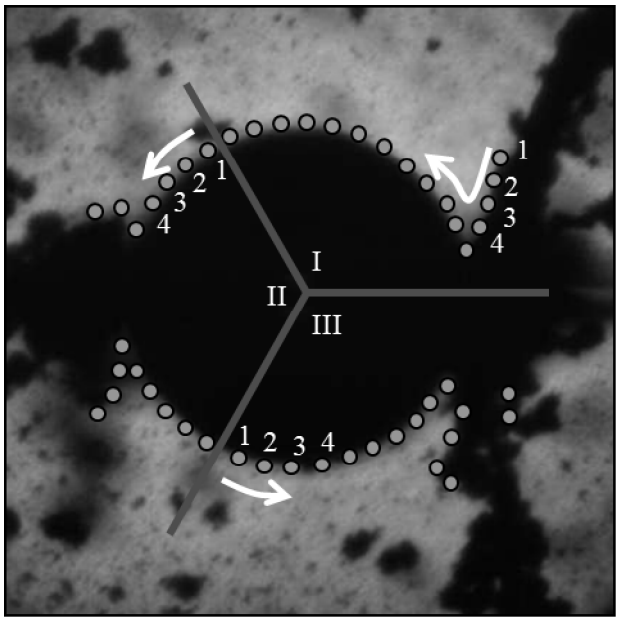

Fig. C11. Illustration of the point sampling (PS) method for circle fits.

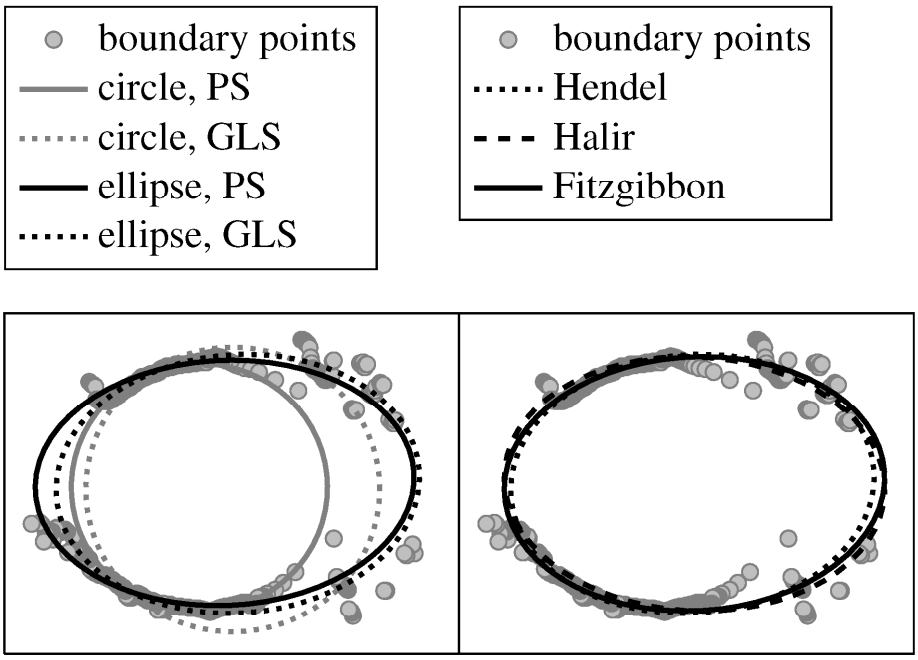

(a) comparison of shape fitting methods in DROPLETD

(b) comparison of various ellipse GLS fits

Fig. C12. Comparison of various shape fitting methods for the 19th frame of the toluene droplet burning sequence of Fig. C3.

contains them. This requires the solution of the simultaneous equations

$$\begin{aligned}(x_1 - x_c)^2 + (y_1 - y_c)^2 &= r^2 \\ (x_2 - x_c)^2 + (y_2 - y_c)^2 &= r^2 \\ (x_3 - x_c)^2 + (y_3 - y_c)^2 &= r^2\end{aligned} \tag{C.7}$$

where (x_c, y_c) is the location of the circle's center and r is its radius. The points (x_1, y_1), (x_2, y_2), and (x_3, y_3) represent the points taken from group I, II, and III, respectively. The solution to the set of equations above provides an exact circle fit to these three points. The algorithm creates an array of such circles by moving sequentially through the groups in this manner, as illustrated in Fig. C11. The circle with the median radius is used to represent the droplet boundary.

The GLS method determines the ellipse that best fits the collection of all candidate points in a least-squares sense. The equation for an ellipse can be expressed as

$$x^2 + c_1 xy + c_2 y^2 + c_3 x + c_4 y + c_5 = 0 \tag{C.8}$$

If an ellipse is to be fit to only five points, a set of five equations of the form of Eq. (C.8) can be solved simultaneously to obtain the coefficients c_1 through c_5 that describe this ellipse. If an ellipse is to be fit to N > 5 points, the system of equations in Eq. (C.9) must be solved.

$$\begin{bmatrix} x_1 y_1 & y_1^2 & x_1 & y_1 & 1 \\ x_2 y_2 & y_2^2 & x_2 & y_2 & 1 \\ \vdots & \vdots & \vdots & \vdots & \vdots \\ x_N y_N & y_N^2 & x_N & y_N & 1 \end{bmatrix} \begin{bmatrix} c_1 \\ c_2 \\ c_3 \\ c_4 \\ c_5 \end{bmatrix} = \begin{bmatrix} x_1^2 \\ x_2^2 \\ \vdots \\ x_N^2 \end{bmatrix} \tag{C.9}$$

where (x_i, y_i) (i=1 to N) represents a candidate point. This set of equations is solved in

a least squares sense to determine the values of c_1 through c_5 that can then be used to obtain the center (x_{ce}, y_{ce}) and effective radius r_e of the ellipse (Hendel (2010), Weisstein (2012)).

The coordinates for the center of the ellipse are

$$x_{ce} = \frac{c_2 c_1 - c_1 c_4}{c_1^2 - c_2} \tag{C.10}$$

and

$$y_{ce} = \frac{c_4 - c_1 c_3}{c_1^2 - c_2} \tag{C.11}$$

The effective radius of the ellipse is $r_e = (a_e b_e)^{0.5}$, where a_e and b_e are the semi-major and semi-minor axis lengths given by Eqs. (C.12) and (C.13).

$$a_e = \sqrt{\frac{2(c_4^2 + c_2 c_3^2 + c_5 c_1^2 - 2c_1 c_3 c_4 - c_2 c_5}{(c_1^2 - c_2)[\sqrt{(1-c_2)^2 + 4c_1^2} - (1+c_2)]}} \tag{C.12}$$

$$b_e = \sqrt{\frac{2(c_4^2 + c_2 c_3^2 + c_5 c_1^2 - 2c_1 c_3 c_4 - c_2 c_5}{(c_1^2 - c_2)[-\sqrt{(1-c_2)^2 + 4c_1^2} - (1+c_2)]}} \tag{C.13}$$

The PS method is not used with ellipse fits for the following reason. Since an ellipse is defined by five points, the PS method would require the candidate boundary points to be divided into five groups. It is possible, however, that an entire fifth of the droplet boundary is disrupted by the presence of soot. Thus, dividing the boundary points into so many groups can introduce large errors.

Figure C12 summarizes the various shape fitting options using the candidate boundary points that were detected for the 19th frame of the toluene burning sequence of Fig. C3. Most of the candidate boundary points on the right side of these figures

come from soot and not the droplet boundary. Figure C12a compares circle and ellipse fits with both the PS and the GLS methods. It is evident from this figure that the circle fit does not work well with the GLS method, as the fit is too susceptible to the boundary points on the soot. The circle fit with the PS method, on the other hand, succeeds at avoiding those points. The ellipse fit is also too accommodating to the boundary points on the soot. Thus, one must be careful when using an ellipse fit. For the ellipse fit, there is a slight difference between the PS and GLS methods; most notably the GLS method provides a less eccentric fit. For this reason, the ellipse fit is tied to the GLS method. Figure C12b compares various other ellipse fits using the GLS method, (i.e., solving Eq. (C.9)) as given by the formulations of Hendel (2010), Halir and Flusser (1998), and Fitzgibbon et al. (1999). As the Hendel fit is slightly less eccentric than the others, the DROPLETD algorithm implements Hendel's formulation.

APPENDIX D

Matlab Program for Droplet Diameter Measurements: DROPLETD.m

D.1 Overview

The MATLAB function DROPLETD.m determines the diameter of a circular or elliptical object as it evolves over the course of a series of consecutive images. The function has been developed for use with the images produced in the experiments performed in Cornell University's droplet combustion laboratory, but with slight modification it can be used in general for similar purposes. This document assumes that the program is being used to determine the diameter of a nearly spherical droplet. The text below describes how the function works, and describes the inputs and outputs of the function. The code is provided as well. For an understanding of the algorithm, refer to the related paper.

D.2 How it works

After DROPLETD is called, the program prompts the user to select a point within the droplet in the first image in the series (this particular behavior can be changed, see below). For each image, the function performs two steps to determine the droplet's diameter. The first step is edge detection. Based on the current value of the parameter `thresh`, the function converts the input image into a black and white image (pixels with an intensity value greater than `thresh` are given a value of 255, or white, and those equal to or below are given a value of 0, or black). The pixels where the function finds the transition from white to black are considered to be on the edge of

the droplet. The function creates a list of these boundary points. The second step is to fit either a circle or an ellipse to the collected edge points. This fitting is done iteratively: the function continually recalculates the fit until two consecutive fits produce a sufficiently similar diameter for the droplet, as determined by the parameter "tolerance". The function performs these operations for each image in the sequence, and the analysis of one image on a typical personal computer takes about 1 second.

D.3 Input

The function is called by executing lines like any of the following:

[diameters, varargout] = dropletd(imgdir, fileNameBase, firstImage, lastImage, ... threshType, shapeType)

[diameters, threshes] = dropletd(imgdir, fileNameBase, firstImage, lastImage, ...'dynamic', shapeType)

[diameters, semiMajor, semiMinor threshes] = dropletd(imgdir, fileNameBase, firstImage, lastImage, threshType, 'ellipse')

[diameters, semiMajor, semiMinor threshes] = dropletd(imgdir, fileNameBase, firstImage, lastImage, 'dynamic', 'ellipse')

"Imgdir" is the directory in which the images are contained. The images are expected to be of format JPG. "fileNameBase" describes how the images are named.

They must be numbered, and the filename must end in zeros that represent where this number occurs in the filename. The user does not include the file extension in "fileNameBase". The following are valid values of "fileNameBase": 'File0000', 'experiment3_00000'. The files, then, would have names such as 'File0030.jpg' or 'experiment3_00100.jpg'. The value 'experiment03_00000' is not valid: all zeros must appear together, and must be at the end of the string.

"firstImage" is the number in the image's filename for the first image to be used for the analysis. "lastImage" is the number of the last image to be used for the analysis. To analyze images from File0015.jpg to File0030.jpg, firstImage is 15 and lastImage is 30.

"threshType" and "shapeType" are strings that specify which of the two edge detection methods and shape fitting methods are used. "threshType" can be either 'static' or 'dynamic', while "shapeType" can be either 'circle' or 'ellipse'. For "threshType" as 'dynamic', the value of threshold is updated for each image based on average intensities in and around the droplet in the previous image (for the first image, a dynamic threshold is achieved by analyzing the first image twice).

Once DROPLETD is called, it creates a figure window containing the first image in the series. The function prompts the user to select a point inside the droplet. For subsequent images the function assumes that the center of the droplet in the next images is close to the center of the droplet in the previous image.

D.4 Options and Parameters

saveImages: The function will , for each input image, save an image showing

the results of the fit. By default, this is set to false.

initialCenter: If the user would rather not specify the center of the first droplet interactively, as is done by default, the user can specify this point with this option. This may be useful if the user intends to run a batch of analyses, and would rather not provide a mouse input every so often.

increment: For a value of 1, the function analyzes each image between firstImage and lastImage. For a value of 2, the function analyzes only every other image between firstImage and lastImage, etc. The default value is 1.

searchlimInit: This is the initial value for the variable searchlim. This parameter determines the number of pixels the function should search in the horizontal and vertical directions from the initial mouse-clicked input for the "center" of the droplet. A value that is too large might deceive the function into thinking that extraneous objects in the images are part of the droplet (the algorithm looks too far out). A value that is too small will prevent the algorithm from finding the edge of the droplet. The user must only choose this parameter for the first image analyzed, as the function determines an appropriate value to use for searchlim for subsequent images in the series. The default is 300. In the paper, this parameter is given the symbol s.

threshInit: This is the initial value for the variable thresh, which separates the points into either black or white. A thresh value of 100 means that a point with a grayscale intensity between 101 and 255 is converted into a white point (255) and a point with a grayscale intensity between 0 and 100 is converted into a black pixel (0). This parameter is more important when threshType is 'static'. The default is 100. In the paper, the thresh variable is given the symbol I_k.

tolerance: For a given image, the function iteratively fits a circle or ellipse to the collected edge points. After calculating a fit, the function discards points that are far from the fit. Then the function performs the fit again using the edge points that were not discarded. The iterations stop when two consecutive fits provide diameters that are within the error tolerance given by the parameter tolerance. This convergence usually requires 2-15 iterations. The default value is 10^{-4}. In the paper, this parameter is given the symbol ε_{tol}.

discardFrac: This parameter determines how far a collected edge point must be from a circle or ellipse fit to be discarded. A larger fractional value is more allowing. The default value is 0.1. In the paper, this parameter is given the symbol p.

threshFrac: This parameter is only significant with a dynamic threshold. It is a proportionality constant in the calculation of thresh, which is determined by an average of the grayscale intensities across the droplet and the region around the droplet. When threshFrac = 1, thresh is set as exactly the average of the grayscale intensities picked across the droplet boundary. The value of threshFrac that provides the most accurate results varies with the nature of the images being analyzed and the other parameters. In the paper, this parameter is given the symbol f.

D.5 Ouput

The function produces three types of outputs: data arrays, a text file output, and images.

diameters: An array of droplet diameters in pixels.

semiMajors: An array of the semi-major axis lengths used in each image when

using an ellipse fit.

semiMinors: An array of the semi-minor axis lengths used in each image when using an ellipse fit.

threshes: An array of the grayscale intensity threshold used in each image when using a dynamic threshold.

The function produces a text file, saved in a subdirectory of the user's specified imgdir, that contains information about the inputs and the values of the various parameters, as well as the data arrays described above. The user has the option of having the function produce an image for each input image that shows all the candidate boundary points, and the resulting fit. To enable this, the user can set the option saveImages to true. These files are then located next to the text file output.

The Matlab code of the program described above is as follows:

```
------------------------------------------------------------------------------------------------------
--
function D = dropletd2(fit,dct,imgdir,first,last)
%DROPLETD Determine diameter evolution for spherical droplet combustion.
%   [D] = DROPLETD(IMGDIR,FIRST,LAST) analyzes all photos in directory
%   IMGDIR with filenames of the format File0000000.jpg between indices
%   FIRST and LAST (inclusive), where FIRST and LAST are scalars, according
%   to a circular (FIT = 1) or elliptical (FIT = 2) fit. For FIT = 1, D is
%   a column vector containing the diameter (in pixels) for the droplet in
%   each photo between FIRST and LAST. For FIT = 2, D is a 3-column array
%   containing the geometric mean of semimajor and semiminor axis lengths,
%   the semimajor axis lengths, and semiminor axis lengths (all doubled).
%   DCT toggles dynamic color thresholding, and is only needed for sooty
%   experiments. If DCT = 0, the same color threshold value will be used
%   for edge detection for all images. If DCT = 1, the program will use the
%   average color across the droplet boundary to constantly update the
%   color threshold.
%
%
```

```
% INPUTS
% fit     (int) 1 for circular least squares fit, 2 for elliptical least
%         squares fit.
% dct     (int) 1 for dynamic color threshold (slower), 0 for constant
%         threshold.
% imgdir  (string) the full pathname containing JPG images for consideration.
% first   (int) index of the first image of interest
%         for example: the image with filename File0000078.jpg contains the
%         image of the droplet at the moment of ignition.
% last    (int) index of the last image of interest
%
% OUTPUTS
% D       (array) droplet diameter in pixels, size (last-first+1,1), for
%         fit = 1. geometric mean of semiaxis lengths, semimajor axis
%         lengths, semiminor axis lengths (all doubled), size
%         (last-first+1,3), for fit = 2.
% (JPG) for each photo analyzed, (last-first+1) many, image indicating the
%         detected droplet boundary and least squares fitted conic section
%         and diameter (semiaxis) result.
% (TXT) containing a timestamp, program runtime, parameter values used
%         (searchlimit1, threshold, tolerance, eliminator) and array D
%         (comma delimited for fit = 2).
%
% SAMPLE FUNCTION CALL
%  D = dropletd2(2,1,'C:\20100228\02v',72,105)
%
% LIMITATIONS
% At least half of a droplet must be visible in an image for the image to
% be analyzed.
% The code is somewhat less successful for sooty experiments.
% INTERNAL VARIABLES (sorted by first use)
% r DUAL USES (EDGE DETECTION ROWINDEX AND FITTING RADIUS)
% c
% count
% imgrgb plotted for the first iteration
% img grayscale version of imgrgb, used in the actual analysis
% searchlimit
% threshold
% tolerance
% eliminator
% increment
% interval
% theta
% xc
% yc
```

```
% rmed
% isEdge

% PARAMETERS
% searchlimit1  initial, dynamic
% threshold1    initial, can be dynamic
% tolerance     decides when a radius (diameter) estimate is sufficient
% eliminator    decides which points are discarded

%check the last COUNT iteration to reduce the search range (300)
%and to change 80 to be more rigid (check the last 5 iterations)
searchlimit1 = 300;
searchlimit = searchlimit1;
threshold1 = 100;
threshold = threshold1; %0 is black, 255 is white
tolerance = 10^(-4);
eliminator = .1;
dctfraction = 1/3;
increment = 1;

%% CHECK FOR INPUT ERRORS

if fit ~= 1 && fit ~= 2
   error('Input FIT must be either 1 for circle fit or 2 for ellipse fit')
end
% dir is a string, the rest are int's, first and last are less than 10^7.

%% INITIALIZE

% If dir does not end in a backslash, add a backslash.
% but don't do it if the dir string is null (')
if imgdir(end) ~= '\' &&  ~isempty(imgdir)
   imgdir = [imgdir '\'];
end

% Set up the filename of the images to be analyzed.
filename = 'File0000000';
filename(end-length(num2str(first))+1:end) = num2str(first);

% Obtain the first image.
imgrgb = imread([imgdir filename '.jpg']);

[N, M, P] = size(imgrgb); % we assume all images have the same dimensions.

% Determine if input image is 1-D (grayscale) or 3-D.
```

```
% Typically the input images are 3-D despite being grayscale.
if P == 3
   img = rgb2gray(imgrgb);
else % P = 1
   img = imgrgb;
end

%% OUTPUT PREPARATION
% Create output directory.
outputdir = ['output' datestr(now,30) '_' num2str(first) '-' num2str(last)];
mkdir(imgdir,outputdir) % create dir where outputs will go.

% Output run-identifying information, parameters, and diameter array.
% File is saved in outputdir as a .txt, can be imported by at least Excel
% and MATLAB.
fid = fopen([imgdir outputdir '\output.txt'],'w+');
if fit == 1
   fprintf(fid,'%s\n',['Droplet Circle Fit (least squares): ' datestr(now,31)]);
else
   fprintf(fid,'%s\n',['Droplet Ellipse Fit (least squares): ' datestr(now,31)]);
end
fprintf(fid,'%s\n',[imgdir ' files ' num2str(first) ' to ' num2str(last)]);
fprintf(fid,'%s\n',sprintf('searchlimit1: %d',searchlimit1));
fprintf(fid,'%s\n',sprintf('threshold1: %d',threshold));
fprintf(fid,'%s\n',sprintf('tolerance: %1f',tolerance));
fprintf(fid,'%s\n',sprintf('eliminator: %1f',eliminator));
if fit == 1 % Put a header thing in the output file.
   if dct == 0
      fprintf(fid,'%s\n',sprintf('D'));
   else
      fprintf(fid,'%s\n',sprintf('D,threshold'));
   end
else
   if dct == 0
      fprintf(fid,'%s\n',sprintf('D,D1,D2'));
   else
      fprintf(fid,'%s\n',sprintf('D,D1,D2,threshold'));
   end
end
% Diameters are added to the file as they are calculated.

% Initialize a little bit more.
theta = 0:.1:2*pi; % This will help plot a circle/ellipse on each output jpg.

% Output matrix. If fit = 1, dct = 0, then only diameters are output.
```

```
% If fit = 1, dct = 1, then diameters and threshold values are output.
% If fit = 2, dct = 0, then diameters, 2*semimajor, 2*semiminor are output.
% If fit = 2, dct = 1, then threshold values are also output.
D = zeros(last-first+1,2*fit-1+dct);

%% PROMPT USER FOR INITIAL DROPLET LOCATION

% Set up the first figure.
h = figure('Name','DROPLETD2.m: Choose a point within the droplet');
figure(h)
image(imgrgb) % Plot image.
title([filename ', ' datestr(now,31)])
xlabel('Use the mouse to click a point inside the droplet.')
axis image;
hold on

% Intake initial values of r and c, the row and column coordinates.
[xg, yg] = ginput(1); % we want to start somewhere inside the droplet.
tic % and we're off!
xc = round(xg); % these don't need to be near the center of the droplet.
yc = round(yg);

set(h,'Visible','off')
plot(xg,yg,'o') % the ginput point

% Loop through all images.
count = first;
while count <= last

   % Initialize output figure.
   if count ~= first
      h = figure('Visible','off','Name','DROPLETD2.m');
      image(imgrgb)
      title([filename ', ' datestr(now,31)])
      axis image
      hold on
   end

   % Image Conditioning.
   % Examine each "quadrant" of the droplet as specified by the initial input.
   % Convert grayscale image to a black-and-white image according to the
   % threshold parameter.
   img2 = 255*(img > threshold);

   % Coarse Coordinate Gathering.
```

```
% Initialize the arrays that will house the parameterized points of the circle.
X = [];
Y = [];

if xc > M || yc > N
   error('The fit has diverged. Sorry.')
end

% QUADRANT I
c = min(xc + searchlimit,M);
while c > xc
   isEdge = 0;
   r = yc;
   while r > 1 && abs(r - yc) < searchlimit && ~isEdge
      isEdge = (img2(r,c,1) == 0) && ~(img2(r-1,c,1) == 0);
      if isEdge
         X = [X c];
         Y = [Y r];
      end
      r = r - 1;
   end
   c = c - 1;
end

% QUADRANT II
c = xc;
while c > 1 && abs(c - xc) < searchlimit
   isEdge = 0;
   r = yc;
   while r > 1 && abs(r - yc) < searchlimit && ~isEdge
      isEdge = (img2(r,c,1) == 0) && ~(img2(r-1,c,1) == 0);
      if isEdge
         X = [X c];
         Y = [Y r];
      end
      r = r - 1;
   end
   c = c - 1;
end

% QUADRANT III
c = max(xc - searchlimit,0);
while c < xc
   isEdge = 0;
   r = yc;
```

```
    while r < N && abs(r - yc) < searchlimit && ~isEdge
        isEdge = (img2(r,c,1) == 0) && ~(img2(r+1,c,1) == 0);
        if isEdge
            X = [X c];
            Y = [Y r];
        end
        r = r + 1;
    end
    c = c + 1;
end

% QUADRANT IV
c = xc;
while c < M && abs(c - xc) < searchlimit
    isEdge = 0;
    r = yc;
    while r < N && abs(r - yc) < searchlimit && ~isEdge
        isEdge = (img2(r,c,1) == 0) && ~(img2(r+1,c,1) == 0);
        if isEdge
            X = [X c];
            Y = [Y r];
        end
        r = r + 1;
    end
    c = c + 1;
end

%% CIRCLE OR ELLIPSE? Execute fit for current image
if fit == 1 % Circle

    % Recalculate radius until we're below some error threshold.
    k = 0;
    r_last = inf; %the first err will thus always be infinity.
    err = inf; %the loop must run at least once.

    while err > tolerance %tolerance is a parameter
        if length(X) < 3
            error('Data is not clean enough; need at least 3 good points for a circle.')
        end
        L = floor(length(X)/3);
        xc = zeros(L,1);
        yc = zeros(L,1);
        r  = zeros(L,1);

        for i = 1:L
```

```
        xin = [X(i); X(i+L); X(i+2*L)];
        yin = [Y(i); Y(i+L); Y(i+2*L)];

        [xc(i), yc(i), r(i)] = circlelsq(xin,yin);

    end
    %need an error message here b/c sometimes r has zero size
    [r, I] = sort(r);
    r = r(max(ceil(L/2),1));
    I = I(max(ceil(L/2)));
    xc = xc(I); %choose the corresponding center.
    yc = yc(I);

    plot(xc,yc,'ro')

    % Eliminate bad boys.
    i = 1;
    while i <= length(X)
        dist = sqrt((X(i) - xc)^2 + (Y(i) - yc)^2);
        if abs(dist - r) > eliminator*r
            plot(X(i),Y(i),'r.','MarkerSize',3)
            X = [X(1:max(1,i-1)) X(min(i+1,end):end)];
            Y = [Y(1:max(1,i-1)) Y(min(i+1,end):end)];
        end
        i = i + 1;
    end
    k = k + 1;

    err = abs(r-r_last)/r;
    r_last = r;

end

% Diameter achieved, clean up & prepare for tomorrow.

% the center of the current circle become the interior starting point
% for the next image.
xc = round(xc);
yc = round(yc);

idx = count - first + 1;
D(idx,1) = 2*r;

% Plot all collected data points that survived.
plot(X,Y,'g.','MarkerSize',3)
```

```
    x = xc + r*cos(theta);
    y = yc + r*sin(theta);
    plot(x,y,'b-')

    if dct == 0
       % Send the diameter information to the output file.
       fprintf(fid,'%s\n',sprintf('%f',D(idx,1)));
       xlabel(sprintf('droplet diameter (D) = %.2f pixels',D(idx,1)))
    else % Also threshold information.
       D(idx,2) = threshold;
       fprintf(fid,'%s\n',sprintf('%f,%f',D(idx,1),D(idx,2)));
       xlabel({sprintf('threshold = %.2f',D(idx,2)),...
             sprintf('droplet diameter (D) = %.2f pixels',D(idx,1))})
    end

    searchlimit = round(1.2*r); %don't look too far out.

    if dct == 1
       [Section1, xg1, yg1] = ddsection2(img,xc,yc,D(idx,1),pi/4);
       [Section2, xg2, yg2] = ddsection2(img,xc,yc,D(idx,1),pi/2);
       [Section3, xg3, yg3] = ddsection2(img,xc,yc,D(idx,1),pi/2+pi/4);
       threshold = dctfraction*2*mean([Section1; Section2; Section3]);

       plot([xg1 xg2 xg3],[yg1 yg2 yg3],'.-')
       axes('Position',[.2 .65 .2 .2],'Layer','top','Box','on','XTick',[],'YTick',[0 255]);
       hold on
       plot(1:length(Section1),Section1,...
          (1:length(Section2))*length(Section1)/length(Section2),Section2,...
          (1:length(Section3))*length(Section1)/length(Section3),Section3)
       plot([1 length(Section1)],threshold*[1 1])
       axis([-inf inf 0 255])
    end

    saveas(h,[imgdir outputdir '\' filename '_1.jpg'])
    set(h,'Visible','on')
    close(h)

elseif fit == 2 % Ellipse

    k = 0;
    r_last = inf;
    err = inf;

    while err > tolerance
       if length(X) < 5
```

```
      error('Data is not clean enough; need at least 5 good points for an ellipse.')
   end

   [a,b,xc,yc,phi] = ellipselsq(X,Y);
   r = sqrt(a*b);

   plot(xc,yc,'ro')

   % Eliminate bad boys.
   i = 1;
   while i <= length(X)
      dist = sqrt((X(i) - xc)^2 + (Y(i) - yc)^2);
      if dist > (1 + eliminator)*a || dist < (1 - eliminator)*b
         plot(X(i),Y(i),'r.','MarkerSize',3)
         X = [X(1:max(1,i-1)) X(min(i+1,end):end)];
         Y = [Y(1:max(1,i-1)) Y(min(i+1,end):end)];
      end
      i = i + 1;
   end
   k = k + 1;

   err = abs(r-r_last)/r;
   r_last = r;

end

% Diameter achieved, clean up & prepare for tomorrow.

idx = count - first + 1;
xc = round(xc);
yc = round(yc);
D(idx,1) = 2*r;
D(idx,2) = 2*a;
D(idx,3) = 2*b;

% Plot all collected datapoints that survived.
plot(X,Y,'g.','MarkerSize',3)
x = xc + a*cos(theta)*cos(phi) - b*sin(theta)*sin(phi);
y = yc + a*cos(theta)*sin(phi) + b*sin(theta)*cos(phi);
plot(x,y,'b-') % the fitted conic section.

if dct == 0
   % Send the diameter information to the output file.
   fprintf(fid,'%s\n',sprintf('%f,%f,%f',D(idx,1),D(idx,2),D(idx,3)));
   xlabel({sprintf('semimajor axis 2a (D1) = %.2f pixels',D(idx,2)),...
```

```
            sprintf('semiminor axis 2b (D2) = %.2f pixels',D(idx,3)),...
            sprintf('droplet diameter (D) = %.2f pixels',D(idx,1))})
    else
        D(idx,4) = threshold;
        % Send the diameter information to the output file.
        fprintf(fid,'%s\n',sprintf('%f,%f,%f,%f',D(idx,1),D(idx,2),D(idx,3),D(idx,4)));
        xlabel({sprintf('threshold = %.2f',D(idx,4)),...
            sprintf('semimajor axis 2a (D1) = %.2f pixels',D(idx,2)),...
            sprintf('semiminor axis 2b (D2) = %.2f pixels',D(idx,3)),...
            sprintf('droplet diameter (D) = %.2f pixels',D(idx,1))})
    end

    searchlimit = round(1.2*a); %don't look too far out.

    if dct == 1
        [Section1, xg1, yg1] = ddsection2(img,xc,yc,D(idx,1),pi/4);
        [Section2, xg2, yg2] = ddsection2(img,xc,yc,D(idx,1),pi/2);
        [Section3, xg3, yg3] = ddsection2(img,xc,yc,D(idx,1),pi/2+pi/4);
        threshold = dctfraction*2*mean([Section1; Section2; Section3]);

        plot([xg1 xg2 xg3],[yg1 yg2 yg3],'.-')
        axes('Position',[.2 .65 .2 .2],'Layer','top','Box','on','XTick',[],'YTick',[0 255]);
        hold on
        plot(1:length(Section1),Section1,...
            (1:length(Section2))*length(Section1)/length(Section2),Section2,...
            (1:length(Section3))*length(Section1)/length(Section3),Section3)
        plot([1 length(Section1)],threshold*[1 1])

    end

    saveas(h,[imgdir outputdir '\' filename '_1.jpg'])
    set(h,'Visible','on')
    close(h)
end

fprintf([filename ' processed; converged in %d iterations.\n'],k)
count = count + increment;
if count <= last
    filename(end-length(num2str(count))+1:end) = num2str(count);
    imgrgb = imread([imgdir filename '.jpg']);
    if P == 3
        img = rgb2gray(imgrgb);
    else
        img = imgrgb;
    end
```

```
   end
end % have gone through all images

%% OUTPUT

% Display total runtime of the program & close out output file.
runtime = toc;
if runtime < 60
   fprintf('EXECUTION COMPLETE. Runtime: %.2f seconds\n',runtime)
else
   fprintf('EXECUTION COMPLETE. Runtime: %d min and %.2f seconds\n',...
      floor(runtime/60),mod(runtime,60))
end
fprintf(fid,'\n%s\n',sprintf('Runtime: %.2f seconds',runtime));
fclose(fid);


end

function [xc, yc, r] = circlelsq(X,Y)

%http://www.infogoaround.org/JBook/LSQ_Circle.html

L = length(X);

A = [2*sum(X.^2) 2*sum(X.*Y) sum(X);
   2*sum(X.*Y) 2*sum(Y.^2) sum(Y);
   2*sum(X)    2*sum(Y)    L    ];
b = -[sum((X.^2 + Y.^2).*X);
   sum((X.^2 + Y.^2).*Y);
   sum( X.^2 + Y.^2)   ];

parameters = A\b;
xc = -parameters(1);
yc = -parameters(2);
r = sqrt(xc^2 + yc^2 - parameters(3));

end

function [semimajor_axis, semiminor_axis, x0, y0, phi] = ellipselsq(x, y)
%
% ellipse_fit - Given a set of points (x,y), ellipse_fit returns the
% best-fit ellipse (in the Least Squares sense)
%
% Input:
```

```
%                   x - a vector of x measurements
%                   y - a vector of y measurements
%
% Output:
%
%               semimajor_axis - Magnitude of ellipse longer axis
%               semiminor_axis - Magnitude of ellipse shorter axis
%               x0 - x coordinate of ellipse center
%               y0-  y coordinate of ellipse center
%               phi - Angle of rotation in radians with respect to
%               the x-axis
%
% Algorithm used:
%
% Given the quadratic form of an ellipse:
%
%      a*x^2 + 2*b*x*y + c*y^2  + 2*d*x + 2*f*y + g = 0   (1)
%
%  we need to find the best (in the Least Square sense) parameters a,b,c,d,f,g.
%  To transform this into the usual way in which such estimation problems are
presented,
%  divide both sides of equation (1) by a and then move x^2 to the
% other side. This gives us:
%
%      2*b'*x*y + c'*y^2  + 2*d'*x + 2*f'*y + g' = -x^2          (2)
%
%   where the primed parameters are the original ones divided by a.
%  Now the usual estimation technique is used where the problem is
%  presented as:
%
%    M * p = b,  where M = [2*x*y y^2 2*x 2*y ones(size(x))],
%    p = [b c d e f g], and b = -x^2. We seek the vector p, given by:
%
%    p = pseudoinverse(M) * b.
%
%    From here on I used formulas (19) - (24) in Wolfram Mathworld:
%    http://mathworld.wolfram.com/Ellipse.html
%
%
% Programmed by: Tal Hendel <thendel@tx.technion.ac.il>
% Faculty of Biomedical Engineering, Technion- Israel Institute of Technology
% 12-Dec-2008
%
% CHRIS DEMBIA STOLE THIS CODE FROM THE INTERNET
%--------------------------------------------------------------------------
```

```
x = x(:);
y = y(:);

%Construct M
M = [2*x.*y y.^2 2*x 2*y ones(size(x))];

% Multiply (-X.^2) by pseudoinverse(M)
e = M\(-x.^2);

%Extract parameters from vector e
a = 1;
b = e(1);
c = e(2);
d = e(3);
f = e(4);
g = e(5);

%Use Formulas from Mathworld to find semimajor_axis, semiminor_axis, x0, y0
%, and phi

delta = b^2-a*c;

x0 = (c*d - b*f)/delta;
y0 = (a*f - b*d)/delta;

phi = 0.5 * acot((c - a)/(2*b));

nom = 2 * (a*f^2 + c*d^2 + g*b^2 - 2*b*d*f - a*c*g);
s = sqrt(1 + (4*b^2)/(a-c)^2);

a_prime = sqrt(nom/(delta* ( (c-a)*s -(c+a))));

b_prime = sqrt(nom/(delta* ( (a-c)*s -(c+a))));

semimajor_axis = max(a_prime, b_prime);
semiminor_axis = min(a_prime, b_prime);

if (a_prime < b_prime)
   phi = pi/2 - phi;
end


if abs(phi) < pi/4
   phi = -phi;
```

```
end

end

% function [a, b, xc, yc, phi] = ellipselsqw(X,Y)
%
% X = X(:);
% Y = Y(:);
% W = ones(size(X));
%
% %online method
% for i = 1:5
%     %Construct M
% M = [2*X.*Y.*W W.*Y.^2 2*W.*X 2*W.*Y W.*ones(size(X))];
%
% % Multiply (-X.^2) by pseudoinverse(M)
% e = M\(-W.*X.^2);
% %
% % M = [2*X.*Y Y.^2 2*X 2*Y ones(size(X))];
% %
% % % Multiply (-X.^2) by pseudoinverse(M)
% % e = M\(-X.^2)
% %Extract parameters from vector e
% a = 1;
% b = e(1);
% c = e(2);
% d = e(3);
% f = e(4);
% g = e(5);
%
% delta = b^2-a*c;
%
% xc = (c*d - b*f)/delta;
% yc = (a*f - b*d)/delta;
%
% phi = 0.5 * acot((c - a)/(2*b));
%
% nom = 2 * (a*f^2 + c*d^2 + g*b^2 - 2*b*d*f - a*c*g);
% s = sqrt(1 + (4*b^2)/(a-c)^2);
%
% a_prime = sqrt(nom/(delta* ( (c-a)*s -(c+a))));
%
% b_prime = sqrt(nom/(delta* ( (a-c)*s -(c+a))));
%
% a = max(a_prime, b_prime);
```

```
% b = min(a_prime, b_prime);
%
% if (a_prime < b_prime)
%     phi = pi/2 - phi;
% end
%
% if abs(phi) < pi/4
%     phi = -phi;
% end
%
% if i < 5
%
% SLOPE = (Y-yc)./(X-xc);
%
% % if xg < xc
% %     thetaintersect = pi + atan(a/b*(m*cos(phi)-sin(phi))/(m*sin(phi)+cos(phi)));
% % else
%
% thetaintersect = atan(a/b*(SLOPE*cos(phi)-sin(phi))./(SLOPE*sin(phi)+cos(phi)));
%
% % end
% PX = xc + a*cos(thetaintersect)*cos(phi) - b*sin(thetaintersect)*sin(phi);
% PY = yc + a*cos(thetaintersect)*sin(phi) + b*sin(thetaintersect)*cos(phi);
% %plot(PX,-PY,'*')
% % for j = 1:length(PX)
% % plot([xc PX(j)],[-yc -PY(j)])
% % end
% W = ((PX-xc).^2 + (PY - yc).^2).^(-3);
% end
% end
% end

function [Section,xg,yg] = ddsection2(img,xc,yc,D,theta)

xg = zeros(2,1);
yg = zeros(2,1);

xg(1) = xc - D*cos(theta);
xg(2) = xc + D*cos(theta);
yg(1) = yc + D*sin(theta);
yg(2) = yc - D*sin(theta);

height = abs(yg(2)-yg(1));
width = abs(xg(2)-xg(1));
```

```
if sqrt(width^2 + height^2) < 5
   error('points are too close!')
end

xg = round(xg);
yg = round(yg);

if xg(2) < xg(1)
   xg = [xg(2); xg(1)];
   yg = [yg(2); yg(1)];
end

m = (yg(2) - yg(1))/(xg(2) - xg(1));
b = -xg(1)*m + yg(1);

% maximus = max(height,width);
% Section = zeros([maximus,1]);

if m == Inf

   Section = img(yg(1):yg(2),xg(1));

elseif m == 0

   Section = img(yg(1),xg(1):xg(2));

elseif m > 1/2 %more vertical than horizontal, positive
   %each row only has one img point extracted
   Section = img(yg(1),xg(1));

   xC = xg(1);

   for yC = yg(1) + 1:yg(2)

      xR = xC + .5;
      yR = m*xR + b;
      if yR < yC
         xC = xC + 1;
      end
      Section = [Section; img(yC,xC)];
   end

elseif m > 0 %more horizontal than vertical, positive
   %each column only has one img point extracted
   Section = img(yg(1),xg(1));
```

```
    yC = yg(1);

    for xC = xg(1) + 1:xg(2)

        yT = yC + .5;
        xT = (yT - b)/m;
        if xT < xC %cell (xC,yC+1) is chosen.
            yC = yC + 1;
        end
        Section = [Section; img(yC,xC)];
    end

elseif m >= -1/2 %more horizontal than vertical, negative
    %each column only has one img point extracted
    Section = img(yg(1),xg(1));

    yC = yg(1);

    for xC = xg(1) + 1:xg(2)
        yB = yC - .5;
        xB = (yB - b)/m;
        if xB < xC
            yC = yC - 1;
        end
        Section = [Section; img(yC,xC)];
    end
elseif m < -1/2 %more vertical than horizontal, negative
    %each row only has one img point extracted
    Section = img(yg(1),xg(1));

    xC = xg(1);

    for yC = yg(1) + 1:-1:yg(2)

        xR = xC + .5;
        yR = m*xR + b;
        if yR > yC
            xC = xC + 1;
        end
        Section = [Section; img(yC,xC)];
    end

end
end
```

APPENDIX E

Modified Matlab Program for Droplet Diameter Measurements for the ISS Images

The algorithm and the steps to run this program are identical as the program in Appendix D. Some modifications are made to incorporate the differences in file names and image format between drop tower and ISS images. Before running this program, the "filename" in the "INITIALIZE" algorithm should be change to the file name of the images from the particular ISS experiment of interest.

```
function D = dropletd3(fit,dct,imgdir,first,last)
%DROPLETD Determine diameter evolution for spherical droplet combustion.
%   [D] = DROPLETD3(FIT,DCT,IMGDIR,FIRST,LAST) analyzes all photos in
directory
%   IMGDIR with filenames of the format File0000000.tif between indices
%   FIRST and LAST (inclusive), where FIRST and LAST are integer scalars,
%   according to a circular (FIT = 1) or elliptical (FIT = 2) fit.
%   For FIT = 1, D is a column vector containing the diameter (in pixels)
%   for the droplet in each photo between FIRST and LAST. For FIT = 2, D is
%   a 3-column array containing the geometric mean of major and mminor axis
%   lengths, the major axis lengths, and minor axis lengths. DCT toggles
%   dynamic color thresholding, and is only needed for sooty data. If
%   DCT = 0, the same color threshold value will be used for edge detection
%   for all images. If DCT = 1, the program will use an average color
%   across the droplet boundary to constantly update the color threshold.
%
% INPUTS
% fit     (int) 1 for circular least squares fit, 2 for elliptical least
%         squares fit.
% dct     (int) 0 for constant threshold, 1 for dynamic color threshold.
% imgdir  (string) the full pathname containing JPG images for consideration.
% first   (int) index of the first image of interest.
%         for example: the image with filename File0000078.jpg contains the
%         image of the droplet at the moment of ignition.
% last    (int) index of the last image of interest.
%
% OUTPUTS
% D       (array) droplet diameter in pixels, size (last-first+1,1), for
```

```
%       fit = 1, dct = 0. geometric mean of major and minor axis lengths,
%       major axis lengths, minor axis lengths (all doubled), size
%       (last-first+1,3), for fit = 2, dct = 0. additional column if
%       dct = 1.
% (JPG) for each photo analyzed, (last-first+1) many, image indicating the
%       detected droplet boundary and least squares fitted conic section
%       and diameter (semiaxis) result.
% (TXT) containing a timestamp, program runtime, parameter values used
%       (searchlimit1, threshold, tolerance, eliminator) and matrix D
%       (comma delimited for fit = 2 or dct ~= 0).
%
% SAMPLE FUNCTION CALL
%  D = dropletd3(2,1,'C:\20100228\02v',72,105)
%
% LIMITATIONS
% The position of the droplet must overlap between consecutive images or
% the function will have trouble determining where the droplet is.
% At least half of a droplet must be visible in an image for the image to
% be analyzed.
%
% CALIBRATION
% For the output of this program to mean anything useful, a calibration
% image must be run through the program to obtain a conversion between
% pixel units and physical units. The calibration image is specific to the
% experimental setup. The calibration run should use the same settings
% (fit, dct, and all parameter values) as those used to analyze data from
% an experiment.
%
% PARAMETERS
% increment     interval of images to skip between first and last image (5
%               if only every 5th image between first and last are to be
%               analyzed).
% searchlimit1  how far to look for a droplet boundary for the first image.
% threshold1    the approximate value of the color (0 to 255) at the
%               droplet's edge in the first image.
% tolerance     decides when a radius (diameter) estimate is sufficient.
% eliminator    decides which points in vectors X, Y are discarded.
% dctfraction   fraction between 0 and 1. affects how the dynamic threshold
%               is chosen.
%
% This function has been developed by Chris Dembia (cld72@cornell.edu) and
% Frank Liu (yl677@cornell.edu) tailored for data produced at the ISS drop
% lab.

increment = 1;
```

```
searchlimit1 = 80;
searchlimit = searchlimit1;
threshold1 = 100;
threshold = threshold1; % 0 is black, 255 is white
tolerance = 10^(-4);
eliminator = .1;
dctfraction = 2/3;

%% CHECK FOR INPUT ERRORS

if fit ~= 1 && fit ~= 2
   error('Input FIT must be either 1 for circle fit or 2 for ellipse fit.')
end
if dct ~=0 && dct ~= 1
   error('Input DCT must either be 0 for static threshold or 1 for DCT.')
end
if round(first) ~= first
   error('Input FIRST must be an integer.')
end
if round(last) ~= last
   error('Input LAST must be an integer.')
end

%% INITIALIZE

% If dir does not end in a backslash, add a backslash.
% but don't do it if the imgdir string is null ('')
if imgdir(end) ~= '\' &&  ~isempty(imgdir)
   imgdir = [imgdir '\'];
end

% Set up the filename of the images to be analyzed.
filename = 'E159F06A_00000';
filename(end-length(num2str(first))+1:end) = num2str(first);

% Obtain the first image.
imgrgb = im2uint8(imread([imgdir filename '.tif']));
imgrgb = cat(3,imgrgb,imgrgb,imgrgb);

[N, M, P] = size(imgrgb); % We assume all images have the same dimensions.

% Determine if input image is 1-D (grayscale) or 3-D.
% Typically the input images are 3-D despite being grayscale.
if P == 3
   img = rgb2gray(imgrgb);
```

```
else % P = 1
    img = imgrgb;
end

%% OUTPUT PREPARATION
% Create output directory.
outputdir = ['output' datestr(now,30) '_' num2str(first) '-' num2str(last)];
mkdir(imgdir,outputdir) % create dir where outputs will go.

% Output run-identifying information, parameters, and diameter array.
% File is saved in outputdir as a .txt, can be imported by at least Excel
% and MATLAB.
fid = fopen([imgdir outputdir '\output.txt'],'w+');
if fit == 1
    fprintf(fid,'%s\n',['Droplet Circle Fit (least squares): ' datestr(now,31)]);
else
    fprintf(fid,'%s\n',['Droplet Ellipse Fit (least squares): ' datestr(now,31)]);
end
fprintf(fid,'%s\n',[imgdir ' files ' num2str(first) ' to ' num2str(last)]);
fprintf(fid,'%s\n',sprintf('searchlimit1: %d',searchlimit1));
fprintf(fid,'%s\n',sprintf('threshold1: %d',threshold));
fprintf(fid,'%s\n',sprintf('tolerance: %1f',tolerance));
fprintf(fid,'%s\n',sprintf('eliminator: %1f',eliminator));
fprintf(fid,'%s\n',sprintf('dctfraction: %1f',dctfraction));
if fit == 1 % Put a header in the output file.
    if dct == 0
        fprintf(fid,'%s\n',sprintf('D'));
    else
        fprintf(fid,'%s\n',sprintf('D,threshold'));
    end
else
    if dct == 0
        fprintf(fid,'%s\n',sprintf('D,D1,D2'));
    else
        fprintf(fid,'%s\n',sprintf('D,D1,D2,threshold'));
    end
end
% Diameters are added to the file as they are calculated.

% Initialize a little bit more.
theta = 0:.1:2.01*pi; % This will help plot a circle/ellipse on each output jpg.

% Output matrix. If fit = 1, dct = 0, then only diameters are output.
% If fit = 1, dct = 1, then diameters and threshold values are output.
% If fit = 2, dct = 0, then diameters, 2*semimajor, 2*semiminor are output.
```

```
% If fit = 2, dct = 1, then threshold values are also output.
D = zeros(last-first+1,2*fit-1+dct);

%% PROMPT USER FOR INITIAL DROPLET LOCATION

% Set up the first figure.
h = figure('Name','DROPLETD3.m: Choose a point within the droplet');
figure(h)
image(imgrgb) % Plot image.
title([filename ', ' datestr(now,31)],'Interpreter','none')
xlabel('Use the mouse to click a point inside the droplet.')
axis image
hold on

% Intake initial values of r and c, the row and column coordinates.
[xg, yg] = ginput(1); % we want to start somewhere inside the droplet.
tic % and we're off!
xc = round(xg); % these don't need to be near the center of the droplet.
yc = round(yg);

set(h,'Visible','off')
plot(xg,yg,'o') % the ginput point

% Loop through all images.
scrap = 1; % the first run-through is scrapped.
loopvector = [first first:increment:last];
for count = loopvector

   % Initialize output (unless it's the first iteration).
   if ~scrap
      filename(end-length(num2str(count))+1:end) = num2str(count);
      imgrgb = im2uint8(imread([imgdir filename '.tif']));
      imgrgb = cat(3,imgrgb,imgrgb,imgrgb);
      if P == 3
         img = rgb2gray(imgrgb);
      else
         img = imgrgb;
      end
      h = figure('Visible','off','Name','DROPLETD3.m');
      image(imgrgb)
      title([filename ', ' datestr(now,31)],'Interpreter','none')
      axis image
      hold on
   end
```

```
% Image Conditioning.
% Examine each "quadrant" of the droplet as specified by the initial input.
% Convert grayscale image to a black-and-white image according to the
% threshold parameter.
img2 = 255*(img > threshold);

% Coarse Coordinate Gathering of droplet edge.
% Initialize the arrays that will house the parameterized points of the circle.
X = [];
Y = [];

if xc > M || yc > N % The center of the droplet must be within the image.
   error('The fit has diverged. Sorry.')
end

% QUADRANT I
c = min(xc + searchlimit,M); % column index.
while c > xc
   isEdge = 0;
   r = yc; % row index.
   while r > 1 && abs(r - yc) < searchlimit && ~isEdge
      isEdge = (img2(r,c,1) == 0) && ~(img2(r-1,c,1) == 0);
      if isEdge % concatenate these points onto our list.
         X = [X c];
         Y = [Y r];
      end
      r = r - 1; % Step upward.
   end
   c = c - 1; % Step leftward.
end

% QUADRANT II
c = xc;
while c > 1 && abs(c - xc) < searchlimit
   isEdge = 0;
   r = yc;
   while r > 1 && abs(r - yc) < searchlimit && ~isEdge
      isEdge = (img2(r,c,1) == 0) && ~(img2(r-1,c,1) == 0);
      if isEdge
         X = [X c];
         Y = [Y r];
      end
      r = r - 1; % Step upward.
   end
   c = c - 1; % Step leftward.
```

```
end

% QUADRANT III
c = max(xc - searchlimit,0);
while c < xc
   isEdge = 0;
   r = yc;
   while r < N && abs(r - yc) < searchlimit && ~isEdge
      isEdge = (img2(r,c,1) == 0) && ~(img2(r+1,c,1) == 0);
      if isEdge
         X = [X c];
         Y = [Y r];
      end
      r = r + 1; % Step downward.
   end
   c = c + 1; % Step rightward.
end

% QUADRANT IV
c = xc;
while c < M && abs(c - xc) < searchlimit
   isEdge = 0;
   r = yc;
   while r < N && abs(r - yc) < searchlimit && ~isEdge
      isEdge = (img2(r,c,1) == 0) && ~(img2(r+1,c,1) == 0);
      if isEdge
         X = [X c];
         Y = [Y r];
      end
      r = r + 1; % Step downward.
   end
   c = c + 1; % Step rightward.
end

%% CIRCLE OR ELLIPSE? Execute fit for current image
if fit == 1 % Circle

   % Recalculate radius until we're below the error tolerance.
   k = 0;
   err = inf; % The loop must run at least once.
   r_last = inf; % The first err will thus always be infinity.

   while err > tolerance % tolerance is a parameter
      if length(X) < 3
         error('Data is not clean enough; need at least 3 good points for a circle.')
```

```
end

% Local Iteration fit.
L = floor(length(X)/3);
xc = zeros(L,1);
yc = zeros(L,1);
r  = zeros(L,1);

% Partition the collected edge point into 3 bins and fit a
% circle to many sets of three points, one point taken from each bin in
% order.
for i = 1:L
   xin = [X(i); X(i+L); X(i+2*L)];
   yin = [Y(i); Y(i+L); Y(i+2*L)];

   [xc(i), yc(i), r(i)] = circlelsq(xin,yin);

end

if isempty(r)
   error('Not enough data collected to generate a circle fit.')
end

[r, I] = sort(r); % Take the circle with the median radius.
r = r(max(ceil(L/2),1));
I = I(max(ceil(L/2)));
xc = xc(I); % Choose the corresponding circle center.
yc = yc(I);

plot(xc,yc,'ro') % Plot the center of the circle from this iteration.

% Eliminate bad boys.
i = 1;
while i <= length(X)
   dist = sqrt((X(i) - xc)^2 + (Y(i) - yc)^2);
   if abs(dist - r) > eliminator*r
      plot(X(i),Y(i),'r.','MarkerSize',3)
      X = [X(1:max(1,i-1)) X(min(i+1,end):end)];
      Y = [Y(1:max(1,i-1)) Y(min(i+1,end):end)];
   end
   i = i + 1;
end
k = k + 1;

err = abs(r-r_last)/r;
```

```
    r_last = r;

end

% Diameter achieved, clean up & prepare for the next image.

% The center of the current circle becomes the interior starting point
% for the next image.
xc = round(xc);
yc = round(yc);

idx = count - first + 1;
D(idx,1) = 2*r;

% Plot all collected datapoints that survived.
plot(X,Y,'g.','MarkerSize',3)
x = xc + r*cos(theta);
y = yc + r*sin(theta);
plot(x,y,'b-')

if ~scrap % Don't execute this for the first run-through.
    if dct == 0
        % Send the diameter information to the output file.
        fprintf(fid,'%s\n',sprintf('%f',D(idx,1)));
        xlabel(sprintf('droplet diameter (D) = %.2f pixels',D(idx,1)))
    else % Also output threshold information.
        D(idx,2) = threshold;
        fprintf(fid,'%s\n',sprintf('%f,%f',D(idx,1),D(idx,2)));
        xlabel({sprintf('threshold = %.2f',D(idx,2)),...
            sprintf('droplet diameter (D) = %.2f pixels',D(idx,1))})
    end
end

searchlimit = round(1.1*r); % Don't look too far out next time.

if dct == 1 % dynamic color threshold
    % Extract the color values (0 to 255) along a 45, 90 and 135
    % degree line through the center of the droplet.
    [Section1, xg1, yg1] = ddsection2(img,xc,yc,D(idx,1),pi/4);
    [Section2, xg2, yg2] = ddsection2(img,xc,yc,D(idx,1),pi/2);
    [Section3, xg3, yg3] = ddsection2(img,xc,yc,D(idx,1),pi/2+pi/4);
    threshold = dctfraction*2*mean([Section1; Section2; Section3]);

    % Plot the lines along which color values are sampled.
    plot([xg1 xg2 xg3],[yg1 yg2 yg3],'.-')
```

```
        % Make a cute inset plot of the color values along the plotted lines.
        % 'Position' determines inset plot's location in the figure.
        axes('Position',[.27 .70 .2 .2],'Layer','top','Box','on',...
             'XTick',[],'YTick',[0 255]);
        hold on
        plot(1:length(Section1),Section1,...
           (1:length(Section2))*length(Section1)/length(Section2),Section2,...
           (1:length(Section3))*length(Section1)/length(Section3),Section3)
        plot([1 length(Section1)],threshold*[1 1])
        axis([-inf inf 0 256])
    end

    if ~scrap % The first iteration is scrapped.
        saveas(h,[imgdir outputdir '\' filename '_1.jpg'])
    end
    set(h,'Visible','on')
    close(h)

elseif fit == 2 % Ellipse

    k = 0;
    err = inf;
    r_last = inf;

    while err > tolerance
        if length(X) < 5
            error('Data is not clean enough; need at least 5 good points for an ellipse.')
        end

        % Calculate ellipse fit using a subfuction with least squares
        % stuff.
        [a,b,xc,yc,phi] = ellipselsq(X,Y);
        r = sqrt(a*b);

        plot(xc,yc,'ro')

        % Eliminate bad boys.
        i = 1;
        while i <= length(X)
            dist = sqrt((X(i) - xc)^2 + (Y(i) - yc)^2);
            if dist > (1 + eliminator)*a || dist < (1 - eliminator)*b
                plot(X(i),Y(i),'r.','MarkerSize',3)
                X = [X(1:max(1,i-1)) X(min(i+1,end):end)];
                Y = [Y(1:max(1,i-1)) Y(min(i+1,end):end)];
            end
```

```
        i = i + 1;
      end
      k = k + 1;

      err = abs(r-r_last)/r;
      r_last = r;

    end

    % Diameter achieved, clean up & prepare for tomorrow.

    idx = count - first + 1;
    xc = round(xc);
    yc = round(yc);
    D(idx,1) = 2*r;
    D(idx,2) = 2*a;
    D(idx,3) = 2*b;

    % Plot all collected datapoints that survived.
    plot(X,Y,'g.','MarkerSize',3)
    x = xc + a*cos(theta)*cos(phi) - b*sin(theta)*sin(phi);
    y = yc + a*cos(theta)*sin(phi) + b*sin(theta)*cos(phi);
    plot(x,y,'b-') % the fitted conic section.

    if ~scrap
      if dct == 0
        % Send the diameter information to the output file.
        fprintf(fid,'%s\n',sprintf('%f,%f,%f',D(idx,1),D(idx,2),D(idx,3)));
        xlabel({sprintf('major axis 2a (D1) = %.2f pixels',D(idx,2)),...
          sprintf('minor axis 2b (D2) = %.2f pixels',D(idx,3)),...
          sprintf('droplet diameter (D) = %.2f pixels',D(idx,1))})
      else
        D(idx,4) = threshold;
        % Send the diameter information to the output file.

fprintf(fid,'%s\n',sprintf('%f,%f,%f,%f',D(idx,1),D(idx,2),D(idx,3),D(idx,4)));
        xlabel({sprintf('threshold = %.2f',D(idx,4)),...
          sprintf('semimajor axis 2a (D1) = %.2f pixels',D(idx,2)),...
          sprintf('semiminor axis 2b (D2) = %.2f pixels',D(idx,3)),...
          sprintf('droplet diameter (D) = %.2f pixels',D(idx,1))})
      end
    end

    searchlimit = round(1.2*a); % Don't look too far out next time.
```

```
        if dct == 1
            [Section1, xg1, yg1] = ddsection2(img,xc,yc,D(idx,1),pi/4);
            [Section2, xg2, yg2] = ddsection2(img,xc,yc,D(idx,1),pi/2);
            [Section3, xg3, yg3] = ddsection2(img,xc,yc,D(idx,1),pi/2+pi/4);
            threshold = dctfraction*2*mean([Section1; Section2; Section3]);

            plot([xg1 xg2 xg3],[yg1 yg2 yg3],'.-')
            axes('Position',[.27 .70 .2 .2],'Layer','top','Box','on',...
                'XTick',[],'YTick',[0 255]);
            hold on
            plot(1:length(Section1),Section1,...
               (1:length(Section2))*length(Section1)/length(Section2),Section2,...
               (1:length(Section3))*length(Section1)/length(Section3),Section3)
            plot([1 length(Section1)],threshold*[1 1])
            axis([-inf inf 0 255])
        end

        if ~scrap
            saveas(h,[imgdir outputdir '\' filename '_1.jpg'])
        end
        set(h,'Visible','on')
        close(h)

    end

    fprintf([filename ' processed; converged in %d iterations.\n'],k)

    scrap = 0; % Done with the first loop.
end % Have gone through all images.

%% OUTPUT

% Display total runtime of the program & close out of output file.
runtime = toc;
if runtime < 60
    fprintf('EXECUTION COMPLETE. Runtime: %.2f seconds\n',runtime)
else
    fprintf('EXECUTION COMPLETE. Runtime: %d min and %.2f seconds\n',...
        floor(runtime/60),mod(runtime,60))
end
fprintf(fid,'\n%s\n',sprintf('Runtime: %.2f seconds',runtime));
fclose(fid);

end
```

```
function [xc, yc, r] = circlelsq(X,Y)

% This least squares solution for a circle comes from the internet.
% http://www.infogoaround.org/JBook/LSQ_Circle.html

L = length(X);

A = [2*sum(X.^2) 2*sum(X.*Y) sum(X);
   2*sum(X.*Y) 2*sum(Y.^2) sum(Y);
   2*sum(X)    2*sum(Y)    L    ];
b = -[sum((X.^2 + Y.^2).*X);
   sum((X.^2 + Y.^2).*Y);
   sum( X.^2 + Y.^2)   ];

parameters = A\b;
xc = -parameters(1);
yc = -parameters(2);
r = sqrt(xc^2 + yc^2 - parameters(3));

end

function [semimajor_axis, semiminor_axis, x0, y0, phi] = ellipselsq(x, y)
%
% This least squares solution for a circle comes from the Mathworks
% website.
% http://www.mathworks.com
% ellipse_fit - Given a set of points (x,y), ellipse_fit returns the
% best-fit ellipse (in the Least Squares sense)
%
% Input:
%                   x - a vector of x measurements
%                   y - a vector of y measurements
%
% Output:
%
%               semimajor_axis - Magnitude of ellipse longer axis
%               semiminor_axis - Magnitude of ellipse shorter axis
%               x0 - x coordinate of ellipse center
%               y0-  y coordinate of ellipse center
%               phi - Angle of rotation in radians with respect to
%               the x-axis
%
% Algorithm used:
%
% Given the quadratic form of an ellipse:
```

```
%
%       a*x^2 + 2*b*x*y + c*y^2  + 2*d*x + 2*f*y + g = 0   (1)
%
%  we need to find the best (in the Least Square sense) parameters a,b,c,d,f,g.
%  To transform this into the usual way in which such estimation problems are
presented,
%  divide both sides of equation (1) by a and then move x^2 to the
% other side. This gives us:
%
%       2*b'*x*y + c'*y^2  + 2*d'*x + 2*f'*y + g' = -x^2           (2)
%
%   where the primed parametes are the original ones divided by a.
%  Now the usual estimation technique is used where the problem is
%  presented as:
%
%    M * p = b,  where M = [2*x*y y^2 2*x 2*y ones(size(x))],
%    p = [b c d e f g], and b = -x^2. We seek the vector p, given by:
%
%    p = pseudoinverse(M) * b.
%
%    From here on I used formulas (19) - (24) in Wolfram Mathworld:
%    http://mathworld.wolfram.com/Ellipse.html
%
%
% Programmed by: Tal Hendel <thendel@tx.technion.ac.il>
% Faculty of Biomedical Engineering, Technion- Israel Institute of Technology
% 12-Dec-2008
%
%------------------------------------------------------------------------

x = x(:);
y = y(:);

%Construct M
M = [2*x.*y y.^2 2*x 2*y ones(size(x))];

% Multiply (-X.^2) by pseudoinverse(M)
e = M\(-x.^2);

%Extract parameters from vector e
a = 1;
b = e(1);
c = e(2);
d = e(3);
f = e(4);
```

```
g = e(5);

%Use Formulas from Mathworld to find semimajor_axis, semiminor_axis, x0, y0
%, and phi

delta = b^2-a*c;

x0 = (c*d - b*f)/delta;
y0 = (a*f - b*d)/delta;

phi = 0.5 * acot((c - a)/(2*b));

nom = 2 * (a*f^2 + c*d^2 + g*b^2 - 2*b*d*f - a*c*g);
s = sqrt(1 + (4*b^2)/(a-c)^2);

a_prime = sqrt(nom/(delta* ( (c-a)*s -(c+a))));

b_prime = sqrt(nom/(delta* ( (a-c)*s -(c+a))));

semimajor_axis = max(a_prime, b_prime);
semiminor_axis = min(a_prime, b_prime);

if (a_prime < b_prime)
   phi = pi/2 - phi;
end

if abs(phi) < pi/4
   phi = -phi;
end

end

function [Section,xg,yg] = ddsection2(img,xc,yc,D,theta)
xg = zeros(2,1);
yg = zeros(2,1);

xg(1) = xc - D*cos(theta);
xg(2) = xc + D*cos(theta);
yg(1) = yc + D*sin(theta);
yg(2) = yc - D*sin(theta);

height = abs(yg(2)-yg(1));
width = abs(xg(2)-xg(1));

if sqrt(width^2 + height^2) < 5
```

```
    error('points are too close!')
end

xg = round(xg);
yg = round(yg);

if xg(2) < xg(1)
    xg = [xg(2); xg(1)];
    yg = [yg(2); yg(1)];
end

m = (yg(2) - yg(1))/(xg(2) - xg(1));
b = -xg(1)*m + yg(1);

% maximus = max(height,width);
% Section = zeros([maximus,1]);

if m == Inf
    Section = img(yg(1):yg(2),xg(1));
elseif m == 0
    Section = img(yg(1),xg(1):xg(2));
elseif m > 1/2 %more vertical than horizontal, positive
    %each row only has one img point extracted
    Section = img(yg(1),xg(1));

    xC = xg(1);

    for yC = yg(1) + 1:yg(2)

        xR = xC + .5;
        yR = m*xR + b;
        if yR < yC
            xC = xC + 1;
        end
        Section = [Section; img(yC,xC)];
    end

elseif m > 0 %more horizontal than vertical, positive
    %each column only has one img point extracted
    Section = img(yg(1),xg(1));

    yC = yg(1);

    for xC = xg(1) + 1:xg(2)
```

```
        yT = yC + .5;
        xT = (yT - b)/m;
        if xT < xC %cell (xC,yC+1) is chosen.
            yC = yC + 1;
        end
        Section = [Section; img(yC,xC)];
    end

elseif m >= -1/2 %more horizontal than vertical, negative
    %each column only has one img point extracted
    Section = img(yg(1),xg(1));

    yC = yg(1);

    for xC = xg(1) + 1:xg(2)
        yB = yC - .5;
        xB = (yB - b)/m;

        if xB < xC
            yC = yC - 1;
        end
        Section = [Section; img(yC,xC)];
    end

elseif m < -1/2 %more vertical than horizontal, negative
    %each row only has one img point extracted
    Section = img(yg(1),xg(1));

    xC = xg(1);

    for yC = yg(1) + 1:-1:yg(2)

        xR = xC + .5;
        yR = m*xR + b;
        if yR > yC
            xC = xC + 1;
        end
        Section = [Section; img(yC,xC)];
    end

end
end
```

APPENDIX F

Matlab Program for Prediction of Concentration During

Preferential Evaporation of A Binary Mixture Droplet: Heptane and iso-Octane

Detailed description of this program is given in Appendix 5A in Chapter 5. The following is the body of the Matlab code that executes iterations with phase equilibrium information obtained from literature for heptane and iso-octane.

```
% This is a program for calculating the concentration of a binary mixture
% droplet evaporating from different initial diameters.

% The calculation employs activity coefficients that describe quasi-steady
% equilibrium of the liquid and vapor.

% 1. heptane
% 2. iso-octane

% parameters (densities in g/cm3, molecular weight in g/mole)
p1 = 0.680; % measured from DDM at 24.6 oC
p2 = 0.688; % measured from DDM at 24.6 oC
MW1 = 100.21;
MW2 = 114.23;
A12 = 1.288549;
A21 = 0.801811;
dw = 1e-7;

% initial conditions
dinitial = 0.9565; %initial droplet diameter
dfinal = 0.5; % final droplet diameter
dd = 0.001; % diameter decrease for each loop
V1percent = 50;
V2percent = 100- V1percent;

% Saturation Pressure (mmHg)for the two species, by Antonie Equation
T = 24.6;          % celsius
A1 = 9.0273;
B1 = 1268.115;
C1 = 216.9;
```

```
A2 = 8.9368;
B2 = 1257.84;
C2 = 220.735;

P1sat = 10^(A1-B1/(T+C1));
P2sat = 10^(A2-B2/(T+C2));
d=dinitial;
d0=dinitial;
j=1;
while (d0 > dfinal);

% droplet volume
V0 = pi/6*d0^3/1000;
V1 = V0*V1percent/100;
V2= V0-V1;

% droplet weight
w1 = V1*p1;
w2 = V2*p2;
w0 = w1 + w2;

% mole number
N1 = w1/MW1;
N2 = w2/MW2;
d = d0;
i=0;

while(d > dfinal);

% mole fraction in liquid phase
x1 = N1/(N1+N2);
x2 = N2/(N1+N2);

% Wilson Equation for the activity coefficients
r1 = exp(-log(x1+x2*A12)+x2*(A12/(x1+x2*A12)-A21/(A21*x1+x2)));
r2 = exp(-log(x2+A21*x1)-x1*(A12/(x1+x2*A12)-A21/(A21*x1+x2)));

% mole fraction in vapor phase
y1 = r1*x1*P1sat/760;
y2 = r2*x2*P2sat/760;

% mole change to proceed evaporation
dN1 = y1*dw/(y1*MW1+y2*MW2);
dN2 = y2*dw/(y1*MW1+y2*MW2);
Vt = N1*MW1/p1+N2*MW2/p2;
```

```
V1 = N1*MW1/p1;
V2 = N2*MW2/p2;
d = (6*Vt/pi)^(1/3)*10;

N1old = N1;
N2old = N2;
N1 = N1-dN1;
N2 = N2-dN2;

i=i+1;
end

% D (mm) and t (s) relation obtained from experimental data
t=517.11*d0^3-777.55*d0^2+447.1*d0-93.803;
plot(t, x1)
hold all
plot(t,x2)
hold all
G(j,1)=t;
G(j,2)=x1;
d0=d0-dd ;
j=j+1;

end
```

APPENDIX G

Matlab Program for Prediction of Concentration During

Preferential Evaporation of A Binary Mixture Droplet: Toluene and Heptane

Detailed description of this program is given in Appendix 5A in Chapter 5. The following is the body of the Matlab code that executes iterations with phase equilibrium information obtained from literature for toluene and heptane.

```
% This is a program for calculating the concentration of a binary mixture
% droplet evaporating from different initial diameters.

% The calculation employs activity coefficients that describe quasi-steady
% equilibrium of the liquid and vapor.

% 1. toluene
% 2. heptane

% parameters (densities in g/cm3, molecular weight in g/mole)
p1 = 0.862;
p2 = 0.68;
MW1 = 92.14;
MW2 = 100.21;
A12 = 0.138121751;
A21 = 0.183266812;
dw = 1e-8;

% initial conditions
dinitial = 0.9565; %initial droplet diameter
dfinal = 0.5; % final droplet diameter
dd = 0.001; % diameter decrease for each loop
V1percent = 50.d0; %58.92d0 ;% measured concentration at t= 0s (shooting droplets
into the vials);
V2percent = 100- V1percent;

% Saturation Pressure (mmHg)for the two species, by Antonie Equation
T = 24.6;          % celsius
A1 = 6.95464;
B1 = 1344.8;
```

```
C1 = 219.482;
A2 = 6.9024;
B2 = 1268.115;
C2 = 216.9;

P1sat = 10^(A1-B1/(T+C1));
P2sat = 10^(A2-B2/(T+C2));
d=dinitial;
d0=dinitial;
j=1;
while (d0 > dfinal);

% droplet volume
V0 = pi/6*d0^3/1000;
V1 = V0*V1percent/100;
V2= V0-V1;

% droplet weight
w1 = V1*p1;
w2 = V2*p2;
w0 = w1 + w2;

% mole number
N1 = w1/MW1;
N2 = w2/MW2;
d = d0;
i=1;

while(d > dfinal);

% mole fraction in liquid phase
x1 = N1/(N1+N2);
x2 = N2/(N1+N2);

% polynomial fit for the activity coefficients
r1 = 0.3182*x2^2-0.0027*x2+1.0036;
r2 = 0.4312*x2^2-0.7758*x2+1.3542;

% mole fraction in vapor phase
y1 = r1*x1*P1sat/760;
y2 = r2*x2*P2sat/760;

% mole change to proceed evaporation
dN1 = y1*dw/(y1*MW1+y2*MW2);
dN2 = y2*dw/(y1*MW1+y2*MW2);
```

```
Vt = N1*MW1/p1+N2*MW2/p2;
V1 = N1*MW1/p1;
V2 = N2*MW2/p2;
phi1=V1/(V1+V2);
phi2=1-phi1;
d = (6*Vt/pi)^(1/3)*10;

N1old = N1;
N2old = N2;
N1 = N1-dN1;
N2 = N2-dN2;

if(j==1)
   phi1_(i,j)=phi1;
end

i=i+1;

end

% D (mm) and t (s) relation obtained from experimental data
t=99.062*d0^2+1.3362*d0-24.83;
%t=-10.406*d0^2+144.54*d0-69.988;
plot(t, x1)
hold all
plot(t,x2)
hold all
G(j,1)=t;
G(j,2)=x1;
G(j,3)=phi1;
G(j,4)=d0;
d0=d0-dd ;
j=j+1;

end
```

APPENDIX H

Matlab Program for OH Flame Image Measurements

This is the Matlab program used to automate a series of consecutive flame images from the LLLUV camera in the ISS experiments. This program utilizes manual measurements for selected images in a given experiment and generates a fitting of those manual measurements. This fitting is then used to create measuring parameters to mimic the manual measurements for all the images the entire experiments. More details can be found in the notes within the body of the code.

```
function [diam, Df,t,m] = flame4(imgdir,f_name,f_start,f_end)
% This program is developed to automate the flame diameter measurements from the
ISS OH flame images by Eric Ching and Frank Liu
% The measurement is performed based on the inputs of manually measured value.
%This program used the image calling function in the droplet diameter measurement
program % , DROPLETD, developed by Chris Dembia and Frank Liu.

diam = cell(f_end-f_start+1,2);

% If dir does not end in a backslash, add a backslash.
% but don't do it if the imgdir string is null (')
if imgdir(end) ~= '\' &&  ~isempty(imgdir)
   imgdir = [imgdir '\'];
end

% %for Inputs from manual measurements for E061A02
thresh=1300;
w = 9; % length of test region
mean_val
=[5957.79006147060;4073.95774014686;2507.93544687474;2310.10165224233;218
6.45601315179;2144.69691605329;2148.01679123579;2163.85168230716;2206.123
45679012;2230.17042739581;]';
thresh3_val = [68;42;23;24;30;23;24;19;20;23;];

plot(mean_val,thresh3_val,'--rs')

pp = splinefit(mean_val,thresh3_val,length(mean_val)-1,2); % best fit
```

```
% polyfit, spline, splinefit

for idx = f_start:f_end
   % Make f_start and f_end 5 digits if they are not already
   z = '00000';
   f_idx = num2str(idx);
   f_idx = ['_' z(1:5-length(f_idx)) f_idx];

   % Read the image and store into a variable
   filename = [f_name f_idx];
   fmt='.tif';
   Df=imread([imgdir filename fmt]);

   % Set up the first figure.
   if idx==f_start
   h = figure('Name','flame4.m');
   figure(h)
   imshow(Df) % Plot image. Cannot use image function since image is a tif file.
   title([filename ', ' datestr(now,31)],'Interpreter','none')
   xlabel('Click a point near the center of the droplet.')
   axis image
   end

   % Take a square region surrounding the circle, letting the user input the
   % center of the region. The square should be noticeably bigger than the droplet.

   % Some initializations
   if idx ~= f_start % if not the first iteration
      ic = round(rc);
      jc = round(cc);
   else
      [jc, ic] = ginput(1); % center of square region
      tic % and we're off!
      ic = round(ic); % row
      jc = round(jc); % column
      [nr, nc] = size(Df); % dimensions of whole figure (should be 512 x 512)
                           % should be the same for all figures
      l = 256; % length of region
      d = l/2;
      % In reality, the dimensions are (l + 1) by (l + 1)

   end

   % Start at top left corner of region. Check rows initially and note all the
```

```
    % rows ("significant row") that contain at least a certain number of elements whose
values are
    % greater than the value of a "black" control pixel by a certain amount. To
    % find this control pixel, take a 5x5 square in the top left corner of the
    % figure and take the median value. Do the same for columns. Later, take
    % the average of all the significant rows and columns and that will be the
    % center of the circle.

    % Find control pixel. Note that here, a 5x5 square region in the top left
    % corner of the figure was taken to find the control pixel value. It is
    % important that the droplet does not enter this square region throughout
    % its movement, so the user may need to check all relevant droplet images
    % and change the location of the square region accordingly.
    %cp = [Df(1:5,1); Df(1:5,2); Df(1:5,3); Df(1:5,4); Df(1:5,5)];
    %cp = double(median(cp));

    % Pick a threshold
    diffs = zeros(1,min([l+1,ic+d,nr-(ic-d)+1])*min([l+1,jc+d,nc-(jc-d)+1]));
        % vector to contain the differences between all values in the
        % region and the control pixel value
    z = 0; % index for diffs
    t = []; % vector to contain the values in diffs greater than thresh
    v = 0; % index for t
    for i = max(ic-d,1):min(nr,ic+d) % rows
        for j = max(1,jc-d):min(nc,jc+d) % columns
            z = z + 1;
            %diffs(z) = double(Df(i,j)) - cp;
            diffs(z) = double(Df(i,j)) ;
            if diffs(z) > thresh
                v = v + 1;
                t(v) = diffs(z);
            end
        end
    end
    diffs = sort(diffs);
    t = sort(t);

    r_sig = []; % vector to contain the row number of each significant row
    c_sig = []; % vector to contain the column number of each significant column
    r_edge = [];
    c_edge = [];

    s = floor(w/2);

    % Find thresh3
```

```
m = mean(t);

thresh2 = 15; % number of differences greater than thresh for a significant row
%thresh3 = ppval(pp,idx);
thresh3 = ppval(pp,m);

%thresh3 = 1;

% Check rows
for i = max(ic-d,1):min(nr,ic+d) % rows
   %diff = double(Df(i,j)) - cp;
   diff = double(Df(i,j));
   n = 0; % number of differences greater than thresh in specific row
   isEdge = 0;
   for j = max(1,jc-d):min(nc,jc+d) % columns
      %diff = double(Df(i,j)) - cp; % difference
      diff = double(Df(i,j));
      if diff >= thresh
         n = n + 1;
         if ~isEdge
            % Test differences between control pixel and other points w/in test region
            k = 0; % number of differences greater than thresh3 in test region
            for r = max([i-s,1,ic-d]):min([i+s,nr,ic+d])  % test region
               for c = max([j-s,1,jc-d]):min([j+s,nc,jc+d])
                  %test = double(Df(r,c)) - cp;
                  test = double(Df(r,c));
                  if test > thresh
                     k = k + 1;
                  end
               end
            end
            if k > thresh3
               isEdge = 1;
               r_edge = [r_edge i];
               c_edge = [c_edge j];
            end
         end
      end
   end

   if n >= thresh2
      r_sig = [r_sig i];
   end
end
```

```
% Test other side of circle for experimental radii
for i = max(ic-d,1):min(nr,ic+d) % rows
   j = min(nc,jc+d);
   isEdge = 0;
   while ~isEdge &&  j >= max(1,jc-d)
      %diff = double(Df(i,j)) - cp; % difference
      diff = double(Df(i,j));
      if diff >= thresh
         k = 0;
         for r = max([i-s,1,ic-d]):min([i+s,nr,ic+d])  % test region
            for c = max([j-s,1,jc-d]):min([j+s,nc,jc+d])
               %test = double(Df(r,c)) - cp;
               test = double(Df(r,c));
               if test > thresh
                  k = k + 1;
               end
            end
         end
         if k > thresh3
            isEdge = 1;
            r_edge = [r_edge i];
            c_edge = [c_edge j];
         end
      end
      j = j - 1;
   end
end

% Check columns
for j = max(1,jc-d):min(nc,jc+d) % columns
   n = 0; % number of differences greater than thresh in specific column
   for i = max(1,ic-d):min(nr,ic+d) % rows
      %diff = double(Df(i,j)) - cp; % difference
      diff = double(Df(i,j));
      if diff >= thresh
         n = n + 1;
      end
   end

   if n >= thresh2
      c_sig = [c_sig j];
   end
end
```

```
    rc = mean(r_sig); % row number of center
    cc = mean(c_sig); % column number of center
    x0 = cc; % x-coordinate of center
    y0 = rc; % y-coordinate of center

    %hold on
    %plot(x0,y0,'w')

    % Find radius. Check row and column of center.
    rad = zeros(1,length(r_edge)); % vector to contain the values of all experimental
radii
    for k = 1:length(rad)
        rad(k) = dist(rc,cc,r_edge(k),c_edge(k));
    end

    rad = sort(rad); % sort in ascending order

    % Take radius to be median of experimental radii
    r = median(rad);

    diam{idx-f_start+1,2} = 2*r; % diameter
    diam{idx-f_start+1,1} = filename;
    %DrawCircle(x0,y0,r,'w')
    %msg = sprintf('The diameter of the droplet is approximately %.3f pixels', 2*r);
    %xlabel(msg)

    %if idx~=f_start
%     theta = linspace(0,2*pi);
%     cosVals = cos(theta);
%     sinVals = sin(theta);
%
%     %q = figure('Name','flame4.m','visible','off');
%     imshow(Df); % Plot image. Cannot use image function since image is a tif file.
%     title([filename ', ' datestr(now,31)],'Interpreter','none');
%     msg = sprintf('The diameter of the droplet is approximately %.3f pixels', 2*r);
%     xlabel(msg);
%     axis image;
%
%     hold on
%
%     plot(x0+r*cosVals,y0+r*sinVals,'color','w','Linewidth', 1);

    %f = getframe(h);              %# Capture the current window
    %imwrite(f.cdata,([num2str(filename) '.jpg']));  %# Save the frame data
```

```
    %print(f,[imgdir outputdir '\' filename],'-djpeg');
    %hold off
    %end
    idx
%     figure(2)
%     plot(mean_val, thresh3_val)
end
```

REFERNECES

Abu-Isa, I.A., Rubber Chem. Technol. 56(1) (1983) 169-196.

Ackerman, M.D., Nayagam, V., Hicks, M.C., Williams, F.A., 43rd AIAA Aerospace Sciences Meeting and Exhibit, Reno, Nevada, USA, Jan. 10-13, 2005, AIAA 2005-1139.

Ackerman, M., Williams, F.A., Combust. Flame 143 (2005) 599-612.

Agarwal, A.K., Prog. Energy Combust. Sci. 33 (2007) 233-271.

Aharon, I., Shaw, B.D., Microgravity Sci. Technol. X/2 (1997) 75-85.

Aharon, I., Shaw, B.D., Combust. Flame 113 (1998) 507-518.

Aharon, I., Tam, V.K.., Shaw, B.D., J. Combust. 2013 (2013) Article ID 154202, 6 pages.

Air Transport Action Group, "Powering the future of flight, the six easy steps to growing a viable aviation biofuels industry," March 2012. <http://atag.org/component/downloads/downloads/152.html>

Anand, K., Ra, Y., Reitz, R.D., Bunting, B., Energy Fuels 25 (2011) 1474-1484.

Andersen V.F., Anderson, J.E., Wallington, T.J., Mueller, S.A., Nielsen, O.J., Energy Fuels 24 (2010a) 2683-2691.

Andersen V.F.; Anderson, J.E.; Wallington, T.J.; Mueller, S.A.; Nielsen, O.J.; Energy Fuels 24 (2010b) 3647-3654.

Avedisian, C.T., Yang, J.C., Wang, C.H., Proc. R. Soc. Lond. A 420 (1988) 183-200.

Avedisian, C.T., "Soot Formation in Spherically Symmetric Droplet Combustion," in "Physical and Chemical Aspects of Combustion," Gordon and Breach Publ., 1997, Chapter 6, pp. 135-160.

Avedisian, C.T, Jackson, G.S., J. Prop. Power. 16 (2000) 974-979.

Avedisian, C.T., Callahan, B.J., Proc. Combust. Inst. 28 (2000) 991-997.

Avedisian, C.T., J. Propul. Power 16 (2000) 628-635.

Avedisian, C.T., Bae, J.H., 6th International Microgravity Combustion Workshop, 2001, NASA/CP-2001-210826, Paper No. 63, p. 249-252.

Bae, J.H., Avedisian, C.T., Proceedings of International Mechanical Engineering Congress & Exposition, IMECE2001/HTD-24237, New York, NT, 2001a.

Bae, J.H., Avedisian, C.T., Technical Meeting of the Eastern States Section of the Combustion Institute, Hilton Head, 2001b, Paper No. 47, p.223-226.

Bae, J.H., Avedisian, C.T., 37th Intersociety Energy Conversion Engineering Conference (IECEC), Washington, DC, Jul. 29-31, 2002, paper no. 20101.

Bae, J.H., Avedisian, C.T., Eastern State Section of Combustion Institute Fall Technical Meeting, Washington, University Park, PA, 2003a, Paper No. 94, p. 373-376.

Bae, J.H., Avedisian, C.T., 41st Aerospace Science Meeting & Exhibit, Reno, NV, 2003b, AIAA 2003-1148.

Bae, J.H., Avedisian, C.T., 7th International Workshop on Microgravity Combustion & Chemical Reacting Systems, Cleveland, OH, 2003c, NASA/CP-2003-212376, Paper No. 29, p. 113-116.

Bae, J.H., Avedisian, C.T., Proceedings of International Mechanical Engineering Congress & Exposition, IMECE2003-42019, Washington, D.C., 2003d.

Bae, J.H., Avedisian, C.T., Combust. Flame 137 (2004a) 148-162.

Bae, J.H., Avedisian, C.T., 2nd International Energy Conversion Engineering Conference, Providence, Rhode Island, Aug. 16-19, 2004b, AIAA 2004-5690

Bae, J.H., *"Experimental Observations and Analyses on the Dynamics of Isolated Spherical Droplet Flames Burning in Various Ambient Gases and Pressures,"* Ph.D. Thesis, Sibley School of Mechanical and Aerospace Engineering, Cornell University, Ithaca, NY, USA, 2005.

Bae, J.H., C.T. Avedisian, Environ. Sci. Technol. 39 (2005) 8008-8013.

Bae, J.H., C.T. Avedisian, Combust. Flame 145 (2006) 607-620.

Bae, J.H., Avedisian, C.T., Proc. Combust. Inst. 31 (2007) 2157-2164.

Bae, J.H., Avedisian, C.T., Proc. Combust. Inst. 32 (2009) 2231-2238.

Ben-Dor, G., Elperin, T., Krasovitov, B., Proc. R. Soc. Lond. A 459 (2003) 766-703.

Bessee, G.B., Hutzler, S.A., Wilson, G.R., "Propulsion and power rapid response

research and development (R&D) support," Delivery Order 0011: Analysis of Synthetic Fuels, Interim Report, Southwest Research Institute (SwRI), April, 2011, AFRL-RZ-WP-TR-2011-2084.

Bieleveld, T., Frassoldati, A., Cuoci, A., Faravelli, T., Ranzi, E., Niemann, U., Seshadri, K., Proc. Combust. Inst. 32 (2009) 493-500.

Blackey, S., Rye, L., Wilson, C.W., Proc. Comb. Inst. 33 (2011) 2863-2885.

Blackwell, K.E., "The Department of Defense: Reducing its reliance on fossil-based aviation fuel- Issues for Congress," CRS Report for Congress, Order Code RL34062, Jun. 15, 2007.

Bolik, T., Konig, J., Eigenbrod, Ch., Rath, H.J., Microgravity Sci. Technol. 13 (2001) 14-19.

Brzustowski, T.A., Twardus, E.M., Wojcicki, S., Sobiesiak, A., AIAA J. 17 (1979) 1234-1242.

Brzustowski, T.A., Sobiesiak, A., Wojcicki, S., Sump. (Int.) Combust. 18 (1981) 265-273.

Bykowski, B.B., Garbe, R.J., Ind. Eng. Chem. Prod. Res. Dev. 20 (1981) 726-734.

Callahan, B.J., Avedisian, C.T., AIAA (1999) Paper No. 99-1077.

Callahan, B.J., "*Droplet Combustion of Nonane, Hexanol, and Their Mixtures in Reduced Gravity*," Master Thesis, Mechanical and Aerospace Engineering, Cornell University, Ithaca, NY, USA, 2000.

Chakravarthy, K., McFarlane, J., Daw, S., Ra, Y., Reitz, R., Griffin, J., SAE Paper (2007) 2007-01-4030.

Chandra, S., Avedisian, C.T., Proc. Roy. Soc. London A 429 (1990) 481-504.

Chao, B.H., Law, C.K., Symp. (Int.) Combust. 23 (1991) 523-531.

Chaos, M., Zhao, Z., Kazakov, A., Gokulakrishnan, P., Angioletti, M., Dryer, F.L., 5th US National Combustion Meeting, San Diego, CA, March 25-28, 2007, Paper# E26.

Card, J.M., Choi, M.Y., 23rd Fall Technical Meeting, Eatern States Section: The Combustion Institute, Dec. 3-5, 1990, paper no. 86.

Carpenter, G.C., Duvall, D., How-to-do-it: motion picture and videotape analysis of

behavior, The American Biology Teacher 45 (1983) 349-52.

Chauveau, C., Gökalp, I., Proc. 7th European Symp. Materials Fluids Sci. Microgravity, Oxford, UK,, 1989, pp. 467-472.

Chauveau, C., Monsallier, G., Acta Astronaut. 20 (1989) 223-228.

Chauveau, C., Chesneau, X., Gökalp, I., AIAA (1993) Paper No. 93-0824.

Chauveau, C., Chesneau, X., Gökalp, I., Adv. Space Res. 16 (1995) 157-160.

Chauveau, C., Chesneau, X., Vieille, B., Deide, A., Gökalp, I., Materials and Fluids Under Low Gravity, Lecture Notes in Physics 464 (1996) 415-424.

Chauveau, C., Gökalp, I., Segawa, D., Kadota, T., Enomoto, H., Proc. Combust. Inst. 28 (2000) 1071-1077.

Chen, A.G., Shaw, B.D., Combust. Sci. Technol., 150 (2000) 59-75.

Chien H.H.Y., and Null, H.R., AIChE J. 18 (1972) 1177-1183.

Choi, M.Y., Dryer, F.L. Haggard Jr., J.B., Brace, M.H., 21st Fall Technical Meeting, Eastern States Section: The Combustion Institute, Dec. 7-9, 1988a, paper no. 98.

Choi, M.Y., Dryer, F.L., Haggard Jr., J.B., Brace, M.H., AIP Conference Proc. 197 (1988b) 338-361.

Choi, M.Y., Dryer, F.L., Haggard, J.B., AIP Conference Proc.: Drops and Bubbles, American Institute of Physics 197 (1989) 338-361.

Choi, M.Y., Dryer, F.L. Haggard Jr., J.B., Symp. (Int.) Combust. 23 (1990) 1597-1604.

Choi, M.Y., "*Droplet combustion characteristics under microgravity and normal-gravity conditions*," Ph.D. Thesis, Department of Mechanical and Aerospace Engineering, Princeton University, Princeton, N.J., 1992.

Choi, M.Y., Dryer, F.L., Card, J.M., Williams, F.A., Haggard, J.B., Borowski, B.A., AIAA (1992) Paper No. 92-0242.

Choi, M.Y., Dyer, F.L., Green, G.J., Sangiovanni, J.J., AIAA (1993) Paper No. 92-0242.

Choi, M.Y., Lee, K.-O., Symp. (Int.) Combust. 26 (1996) 1243-1249.

Choi, M.Y., Yozgatligil, A., Kazakov, A., Dryer, F.L., Ferkul, P., Conference & Exhibit on International Space Station Utilization, Cape Canaveral, FL, 2001, AIAA 2001-5045

Choi, B.C., Choi, S.K., Chung, S.H., Proc. Combust. Inst. 33 (2011) 609-616.

CLEMEX intelligent microscopy, <www.clemex.com>.

Colket, M., Edwards, T., Williams, S., Cernansky, N.P., Miller, D.L., Egolfopoulos, F., Lindstedt, P., Seshadri, K., Dryer, F.L., Law, C.K., Friend, D., Lenhert, D.B., Pitsch, H., Sarofim, A., Smooke, M., Tsang, W., AIAA paper (2007) AIAA-2007-0770.

Cooke, J.A., Bellucci, M., Smooke, M.D., Gomez, A., Violi, A., Faravelli, T., Ranzi, E., Proc. Combust. Inst. 30 (2005) 439-446.

Cooper, C.D., Alley, F.C., Air Pollution Control- A Design Approach, 3rd edi., Waveland Press Inc., Illinois, 2002, Chap. 1, p. 2, 50, 541.

Corporan, E., Edwards, T., Shafer, L., DeWitt, M.J., Klingshirn, C., Zabarnick, S. West, Z., Striebich, R., Graham, J., Klein, J., Energy Fuels 25 (2011) 955-966.

Cromas, J., "*Particulate Matter Formation Mechanisms in a Direct-Injection Gasoline Engine*," Master Thesis, Mechanical Engineering, University of Wisconsin-Madison, 2003.

Curran, H.J., Pitz, W.J., Westbrook, C.K., Callahan, C.V., Dryer, F.L., Proc. Comb. Inst. 27 (1998) 379-387.

Dagaut, P., Gaïl, S., J. Phys. Chem. A 111 (2007) 3992-4000.

Dagaut, P., Gaïl, S., Sahasrabudhe, M., Proc. Combust. Inst. 31 (2007) 2955-2961.

Dagaut, P., Togbé, C., Fuel 87 (2008) 3313-3321.

Dakka, S.M., Shaw, B.D., the Spring Meeting of the Western States Section of the Combustion Institute, UC Davis, Mar. 29-30, 2004, paper 04S-46.

Dakka, S.M., Shaw, B.D., Microgravity Sci. Technol. 18 (2006) 5-13.

Dattarajan, S., Lutomirski, A., Lobbia, R., Smith, O.I., Karagozian, A.R., 42nd AIAA Aerospace Sciences Meeting and Exhibit, Reno, Neveda, Jan. 5-8, 2004, AIAA 2004-955.

Dattarajan, S., Lutomirski, A., Lobbia, R., Smith, O.I., Karagozian, A.R., Combust.

Flame 144 (2006) 299-317.

Daw, C.S., Edwards, K.D., Wagner, R.M., Green, Jr., J.B., J. Eng. Gas Turbines Power 130 (2008) 052801.

Dee, V., Shaw, B.D., 39th Aerospace Sciences Meeting and Exhibit, Reno, Nevada, Jan. 8-11, 2001, AIAA 2001-0468.

Dee, V., Shaw, B.D., Int. J. Heat Mass Trans. 47 (2004) 4857-4867.

Dembia, C.L., Liu, Y.C., Avedisian, C.T., Image Anal. Stereol. 31 (2012) 137-148.

Dietrich, D.L., Haggard Jr., J.B. Second International Microgravity Combuston Workshop, CP-10113, NASA (1992) 317-323.

Dietrich, D.L., Haggard Jr., J.B., Dryer, F.L., Nayagam, V., Shaw, B.D., Williams, F.A., Symp. (Int.) Combust. 26 (1996) 1201-1207.

Dietrich, D.L., Struck, P.M., Ikegami, M., Xu, G., Combust. Theory Model. 9 (2005) 569-585.

Diévart, P., Won, S.H., Dooley, S., Dryer, F.L., Ju, Y., Combust. Flame 159 (2012) 1793-1805.

Dimou, I.; "*Particulate Matter Emissions from a DISI Engine under Cold-Fast-Idle Conditions for Ethanol-Gasoline Blends*," Master Thesis, Mechanical Engineering and Naval Engineer at the Massachusetts Institute of Technology, 2011

Dobbins, R.A., Combust. Flame 130 (2002) 204-214.

Dooley, S., Won, S.H., Chaos, M., Heyne, J., Ju, Y., Dryer, F.L., Kumar, K., Sung, C.J., Wang, H., Oehlschlaeger, M.A., Santoro, R.J., Litzinger, T.A., Combust. Flame 157 (2010) 2333-2339.

Dooley, S., Won, S.H., Heyne, J., Farouk, T.I., Ju, Y., Dryer, F.L., Kumar, K., Hui, X., Sung, C.-J., Wang, H., Oehlschlaeger, M.A., Iyer, V., Iyer, S., Litzginer, T.A., Santoro, R.J., Malewicki, T., Brezinsky, K., Combust. Flame 159 (2012a) 1444-1466.

Dooley, S., Won, S.H., Jahangirian, S., Ju, Y., Dryer, F.L., Wang, H., Oehlschlaeger, M.A., Combust. Flame 159 (2012b) 3014-3020.

Dzik, J., Nayagam, V., Williams, F.A., Int. Comm. Heat Mass Trans. 37 (2010) 211-225.

Edwards, T., Maurice, L.Q., J. Propul. Power 17 (2001) 461-466.

Edwards, T.F., AIAA J. Propul. Power 19 (2003)1089-1107.

Faeth, G.M., Olson, D.R., SAE Tans. 77 (1968) 1793-1802.

Faeth, G.M., Dominicis, D.P., Tulpinsky, J.F., Olson, D.R., Symp. (Int.) Combust. 12 (1969) 9-18.

Farouk, T.I., Dryer, F.L., Combust. Theory Model. 15 (2011) 487-515.

Farouk, T.I., Dryer, F.L., Combust. Flame 159 (2012a) 200-209.

Farouk, T.I., Dryer, F.L., Combust. Flame 159 (2012b) 3208-3223.

Farouk, T.I., Liu, Y.C., Savas, A.J., Avedisian, C.T., Dryer, F.L., Proc. Combust. Inst. 34 (2013) 1609-1616.

Farrell, J.T., Bunting, B.G., SAE Paper (2006) 2006-01-3275.

Farrell, J.T., Cernansky, N.P., Dryer, F.L., Friend, D.G., Hergart, C.A., Law, C.K., McDavid, R.M., Mueller, C.J., Patel, A.K., Pitsch, H., Society of Automotive Engineers paper (2007) SAE-2007-01-0201.

Fisher, E.M., Pitz, W.J., Curran, H.J., Westbrook, C.K., Proc. Combust. Inst. 28 (2000) 1579-1586.

Fitzgibbon, A., Pilu, M., Fisher, R., IEEE Trans. Pattern Anal. Mach. Intell. 21(1999) 476-80.

Gaïl, S., Thomson, M.J., Sarathy, S.M., Syed, S.A., Dagaut, P., Diévart, P., Marchese, A.J., Dryer, F.L., Proc. Combust. Inst. 31 (2007) 305-311.

Ganley, J.T., Springer, G.S., Environ. Sci. Technol. 8 (1974) 340-347.

Gauthier, B.M., Davidson, D.F., Hanson, R.K., Combust. Flame 139 (2004) 300–311.

Ghassemi, H., Baek, S.W., Khan, Q.S., 31th KOSCO Symp., (2005) 110-119

Glassman, I., *Combustion*, 3rd ed., Academic Press, San Diego, 1987, pp. 270, 303, 307-309, 403.

Glassman, I., Yetter, R.A., *Combustion*, 4th edi., Academic Press, Burlington, MA, 2008, Ch. 8, pp. 457-483.

Godsave, G.A.E., Proc. Combust. Inst. 4 (1953) 818-830.

Gökalp, I., Chauveau, C., Richard, J.R., Symp. (Int.) Combust. 22 (1988) 2027-2035.

Gökalp, I., Chauveau, C., Monsallier, G., AIP Conference Proc.: Drops and Bubbles, American Institute of Physics 197 (1989) 362-372.

Haggard, J.B., Kropp, J.L., AIAA (1987) paper no. 87-0576.

Haggard, J.B., Brace, M.H., Kropp, J.L., Dryer, F.L., AIAA (1989) Paper No. 89-0501

Haggard, J.B., Brace, M.H., Dryer, F.L., Choi, M.Y., Williams, F.A., Card, J.M., AIAA (1990) Paper No. 90-0649.

Haggard, J.B., Borowski, B.A., Dryer, F.L., Choi, M.Y., Williams, F.A., Card, J.M., AIAA (1991) Paper No. 91-0720.

Halir, R., Flusser, J., Proc WSCG'98 (1998) 125-132.

Hara, H., Kumagai, S., 22nd Symp. (Int.) Combust. (1988) Poster No. P257

Hara, H., Kumagai, S., Paper presented at the 12th Int. Colloquium on Dynamics of Explosions & Reactive Systems, Univ. Michigan, Ann Arbor, Jul. 23-28, 1989.

Hara, H., Kumagai, S., Symp. (Int.) Combust. 23 (1991) 1605-1610.

Hara, H., Kumagai, S., Symp. (Int.) Combust. 25 (1994) 423-430.

Hakansson, A., Stromberg, K., Pedersen, J., Olsson, J.O., Chemosphere 44 (2001) 1243–1252.

Haltermann Solutions, Product Information of EPA TIER II EEE Federal Register HF437, Haltermann Solutions, Houston, TX, 2010.

Hendel, T. <http://www.mathworks.com/matlabcentral/fileexchange/22423ellipse-fit>, 18 May 2010.

Hibert, D., Subcontract Report (2011) NREL/SR-5400-52909.

Herbinet, O., Pitz, W.J., Westbrook, C.K., Combust. Flame 154 (2008) 507-528.

Herbinet, O., Pitz, W.J., Westbrook, C.K., Combust. Flame 157 (2010) 893-908.

Hicks, M.C., Nayagam, V., Williams, F.A., 5th US Combustion Meeting, UC San Diego, Mar. 25-28, 2007, paper # G18.

Hicks, M.C., Nayagam, V., Williams, F.A., Combust. Flame 157 (2010) 1439–1445.

Holley, A.T., You, X.Q., Dames, E., Wang, H., Egolfopoulos, F.N., Proc. Combust. Inst. 32 (2009) 1157-1163.

Hubbard, G.L., Denny, V.E., Mills, A.F., Int. J. Heat Mass Transfer 18 (1975) 1003-1008.

Hui, X., Kumar, K., Sung, C.-J., Edwards, T., Gardner, D., Fuel 98 (2012) 176-182.

Humer, S., Seiser, R., Seshadri, K., J. Propul. Power 27 (2011) 847-855.

IATA 2010 Report on Alternative Fuels, 5th ed., 2010 International Air Transport Association, Montreal-Geneva. Ref. No: 9709-03.

Image-Pro Plus Version 6.3 for Windows Start-Up Guide, Media Cybernetics, Inc., Bethesda, MD, 2008

ImageWarp, <www.imagewarp.com>.

Imamura, O., Kuno, Y., Osaka, J., Sato, J., Tsue, M., Kono, M., Proc. Combust. Inst. 30 (2005a) 1949-1956.

Imamura, O., Kubo, Y., Osaka, J., Sato, J., Tsue, M., Kono., Microgravity Sci. Technol. 17 (2005b) 13-17.

Imamura, O., Kume, I., Osaka, J., Sato, J., Tsue, M., Kono, M., 56th Int. Astronaut. Cong, Kukuoka, Japan, Oct. 17-21, 2005c, IAC-05-A2.7.07

Imamura, O., Chen, B,. Nishida, S., Yamashita, K., Tsue, M., Kono, M., Proc. Combust. Inst. 33 (2011a) 2005-2011.

Imamura, O., Chen, B., Yamashita, K., Nishida, S., Tsue, M., Kono., M., J. Environ. Eng. 6 (2011b) 211-219.

Imamura, O., Yamashita, K., Nishida, S., Ianus, G., Tsue, M., Kono, M., Combust. Sci. Technol. 183 (2011c) 755-763.

Incropera, F.P., DeWitt, D.P., *Introduction to Heat Transfer*, 4th ed., Wiley, New York, 2002, pp. 824, 831, 910.

Instruction Manual, High-Speed B/W & Color CMOS Camera Model # MS80K S2, v. 2.4.

Isoda, H., Kumagai, S., Symp. (Int.) Combust. 7 (1959) 523-531.

Jackson, G.S., Avedisian, C.T., Yang, J.C., 23rd Fall Technical Meeting, Eastern States Section: The Combustion Institute, Dec. 3-5, 1990, paper no. 85.

Jackson, G.S., Avedisian, C.T., Yang, J.C., Proc. Roy. Soc. London A435 (1991) 259-369.

Jackson, G.S., Avedisian, C.T., Yang, J.C., Int. J. Heat Mass. Trans. 35 (1992) 2017-2033.

Jackson, G.S., Avedisian, C.T., Proc. R. Soc. Lond. A 446 (1994) 255-276.

Jackson, G.S., *"Spherically Symmetric Droplet Combustion of Sooting and Multi-component Fuels,"* Ph.D. Thesis, Sibley School of Mechanical and Aerospace Engineering, Cornell University, Ithaca, NY, USA, 1994.

Jackson, G.S., Avedisian, C.T., Int. J. Heat Mass Transf., 41 (1998) 2503-2515.

Jackson, G.S., Avedisian, C.T., J. Propulsion and Power 16 (2000) 974-979.

Jangi, M., Sakurai, S., Ogami, Y., Kobayashi, H., Combust. Flame 156 (2009) 99-105.

Jangi, M., Kobayashi, H., Combust. Flame 157 (2010) 91-105.

Johnson, R.T., Riley, R.K., "Feasibility of Methanol/Gasoline Blends for Automotive Use," in Evaporation-Combustion of Fuels; *Advances in Chemistry*: American Chemical Society, Washington, DC, 1978, pp 245-266.

Kadota, T., Satoh, K., Segawa, D., Sato, J., Marutani, Y., Symp. (Int.) Combust. 27 (1998) 2595-2601.

Kar, K., Cheng, W., SAE Paper (2011) paper no. 2011-01-1159.

Kayes, D., Hochgreb, S., Environ. Sci. Technol. 33 (1999) 3968-3977.

Kazakov, A., Conley, J., Dryer, F.L., Combust. Flame 134 (2003) 301-314.

Knight, B., Williams, F.A., Combust. Flame 38 (1980) 111-119.

Kikuchi, M., Yamamoto, S., Yoda, S., Wakashima, Y., Mikami, M., 56th Int. Astronaut. Cong, Kukuoka, Japan, Oct. 17-21, 2005, IAC-05-A2.7.04.

Kikuchi, M., Yamamoto, S., Yoda, S., Mikami, M., Nomura, H., Moriue, O., Umemura, A., Hisashi, Y., Sugano, N., Moesl, K., Sattelmayer, T., Eigenbrod, C.,

Minster, O., Proc. 20th RSA Symp. On European Rocket and Ballon Programmes and Related Research, Hyére, France, May 22 -26, 2011, ESA SP-700.

Kimura, M., Ihara, H., Okajima, S., Iwama, A., Combust. Sci. Technol. 44 (1986) 289-306.

Kinder, J.D., Rahmes, T., "Evaluation of bio-derived synthetic paraffinic kerosene (Bio-SPK)." The Boeing Company, Sustainable Biofuels Research & Technology Program, 2009; http://www.ascension-publishing.com/BIZ/Bio-SPK.pdf

Knight, B., Williams, F.A., Combust. Falme 38 (1980) 111-119.

Kobayashi, H., Park, J., Iwahashi, T., Niioka, T., Proc. Combust. Inst. 29 (2002) 2603-2610.

Kobayashi, H., Mitsuya, M., Hanai, H., Sakurai, S., Ogami, Y., 56th Int. Astronaut. Cong, Kukuoka, Japan, Oct. 17-21, 2005, IAC-05-A2.7.06.

Kumagai, S., Jet Propulsion 26 (1956) 786.

Kumagai, S., Isoda, H., Symp. (Int.) Combust. 6 (1957) 726-731.

Kumagai, S., Sakai, T., Okajima, S., Sympo. (Int.) Combust. 13 (1971) 779-785.

Kumar, S., Ray, A., Kale, S.R., Combust. Sci. Technol. 174 (2002) 67–102.

Kyne, A.G., Patterson, P.M., Pourkashanian, M., Williams, A., Wilson, C.W., Proc. International Symposium on Air Breathing Engines, 14th, Florence, Italy (1999) 377–387.

Law, C.K., Williams F.A., Combust. Flame 19 (1972) 393-405.

Law, C.K., AIChE J. 24 (1978) 626-632.

Law, C.K., Law, H.K., AIAA J. 20 (1982) 522-527.

Lebedev, O.N., Marchenko, V.N., Heat Trans. Sov. Res. 11 (1979) 92-98.

Lee, K.-O., Manzello, S.L., Choi, M.Y., Combust. Sci. Technol. 132 (1998) 139-156.

Liu, Y.C., Avedisian, C.T., Combust. Flame 159 (2012) 770-783.

Liu, Y.C., Savas, A.J., Avedisian, C.T., Energy Fuels 26 (2012a) 5740-5749.

Liu, Y.C., Savas, A.J., Avedisian, C.T., 50th AIAA Aerospace Sciences Meeting, Nashville, Tennessee, Jan, 09-12, 2012b, AIAA 2012-1253.

Liu, Y.C., Savas, A.J., Avedisian, C.T., Proc. Combust. Inst. 34 (2013a) 1569-1576.

Liu, Y.C., Farouk, T., Savas, A.J., Dryer, F.L., Avedisian, C.T., Combust. Flame 160 (2013b) 641-655.

Liu, Y.C., Savas, A.J., Avedisian, C.T., Fuel 108 (2013c) 824-832.

Manzello, S. L., Hua, M., Choi, M. Y., & Dryer, F. L., Proceedings of the Fifth International Microgravity Combustion Workshop (1999) pp. 241-244.

Manzello, S.L., Choi, M.Y., Kazakov, A., Dryer, F.L., Dobashi, R., Hirano, T., Proc. Combust. Inst. 28 (2000) 1079-1086.

Manzello, S.L., Yozgatligil, A., Choi, M.Y., Int. J. Heat Mass Trans. 47 (2004) 5381-5385.

Manzello, S.L., Park, S.-H., Yozgatligil, A., Choi, M.Y., Enegry Fuels 23 (2009) 3586-3591.

Marchese, A.J., Dryer, F.L., Colantonio, R.O., Nayagam, V., Symp. (Int.) Combust. 26 (1996) 1209-1217.

Marchese, A.J., Dryer, F.L., Combust. Sci. Technol. 124 (1997) 371-402.

Marchese, A.J., Dryer, F.L. Colantonio, R.O., Symp. (Int.) Combust. 27 (1998) 2627-2634.

Marchese, A.J., Dryer, F.L., Nayagam, V., Combust. Flame 116 (1999) 432-459.

Metghalchi, M., Keck, J.C., Combust. Flame 48 (1982) 191-210.

Mikami, M., Kono, M., Sato, J., Dietrich, D.L., Williams, F.A., Combust. Sci. Technol. 90 (1993) 111-123.

Mikami, M., Habara, O., Kono, M., Sato, J., Dietrich, D.L., Williams, F.A., Combust. Sci. Technol. 124 (1997) 295-309.

Mikami, M., Kono, M., Sato, J., Dietrich, D.L., Symp. (Int.) Combust. 27 (1998) 2643-2649.

Mikami, M., Oyagi, H., Kojima, N., Kikuchi, M., Wakashima, Y., Yoda, S., Combust. Flame 141 (2005) 241-252.

Mikami, M., Oyagi, H., Kojima, N., Wakashima, Y., Kikuchi, M., Yoda, S., Combust Flame 146 (2006) 391-406.

Mitsuya, M., Hanai, H., Sakurai, S., Ogami, Y., Kobayashi, H., Int. J. Heat Fluid Flow 26 (2005) 914-921.

Mobil Oil Corp.,Automotive Gasolines, report no. 9130-00-142-9457, [also see http://ww2.ramapo.edu/libfiles/HR/Environmental_Health_and_Safety/MSDS/Facilities/Plumbing/gasoline.pdf].

Moesl, K.G., Sattelmayer, T., Kikuchi, M., Yoda, S., Proc. 19th ESA Symp. On European Rockers and Ballon Programmes and Related Research, Rad Reichenhall, Germany, Jun. 7-11, 2009, ESA SP-671.

Moesl, K.G., Sattelmayer, T., Eigenbrod, C., Kikuchi, M., Yamamoto, S., Yoda, S., Mikami, M., Monura, H., Moriue, O., Umemura, A., Hisashi, Y., Sugano, N., Proc. 20th ESA Symp. On European Rocket and Ballon Programmes and Related Research, Hyére, France, May 22-26, 2011, ESA SP-700.

Mueller, C.J., Cannella, W.J., Bruno, T.J., Bunting, B., Dettman, H.D., Franz, J.A., Huber, M.L., Natarajan, M., Pitz, W.J., Ratcliff, M.A., Wright, K., Energy Fuels 26 (2012) 3284-3303.

Myers, H.S., AIChE J. 3 (1957) 467-472.

Nakaya, S., Segawa, D., Kadota, T., Nagashima, Y., Furuta, T., Proc. Combust. Inst. 33 (2011) 2031-2038.

Nakaya, S., Fujishima, K., Tsue, M., Kono, M., Segawa, D., Proc. Combust. Inst. 34 (2013) 1601-1608.

Nayagam, V., Haggard Jr., J.B., Colantonio, R.O., Marchese, A.J., Dryer, F.L., Zhang, B.L., Williams, F.A., AIAA J. 36 (1998) 1369-1378.

Nayagam, V., Marchese, A.J., Sacksteder, K.R., Prog. Scale Model. (2008) 169-178.

Nayagam, V., Dietrich, D.L., Ferkul, P.V., Hicks, M.C., Williams, F.A., Combust. Flame 159 (2012) 3583-3588.

Nomura, H., Suganuma, Y., Setani, A., Takahashi, M., Mikami, M., Hara, H., Proc. Combust. Inst. 32 (2009) 2163-2169.

Nomura, H., Iwasaki, H., Suganuma, Y., Mikami, M., Kikuchi, M., Proc. Combust.

Inst. 33 (2011) 2013-2020.

Nomura, H., Takahashi, H., Suganuma, Y., Kikuchi, M., Proc. Combust. Inst. 34 (2013) 1593-1600.

Nunome, T., Kato, S., Maruta, K., Kobayashi, H., Niioka, T., Proc. Combust. Inst. 29 (2002) 2621-2626.

Okai, K., Tsue, M., Kono, M., Mikami, M., Sato, J., Dietrich, D.L., Williams, F.A., Symp. (Int.) Combust. 27 (1998) 2651-2657.

Okai, K., Ono, Y., Moriue, O., Kato, H., Tsue, M., Kono, M., Sato, J., Dietrich, D.L., Williams, F.A., JSME Int. J. Series B 43 (2000a) 485-490.

Okai, K., Moriue, O., Araki, M., Tsue, M., Kono, M., Sato, J., Dietrich, D.L., Williams, F.A., 121 (2000b) 501-512.

Okajima, S., Kumagai, S., Symp. (Int.) Combust. 15 (1975) 401-407.

Okajima, S., Kumagai, S., Archivum Termodynamiki I Spalanis 7 (1976) 267-277.

Okajima, S., Kumagai, S., Symp. (Int.) Combust. 19 (1982) 1021-1027.

Okajima, S., Kanno, H., Kumagai, S., Acta Astronaut. 12 (1985) 555-563.

Okajima, S., Archivum Combustionis 5 (1985) 267-277.

Okajima, S., Hara, H., Prog. Astronaut. Aeronaut. 113 (1988) 151-167.

Okamoto, K., Watanabe, N., Hagimoto, Y., Miwa, K., Ohtani, H., J. Loss Prevent. Proc. 23 (2010) 89-97.

Oyagi, H., Shigeno, H., Mikami, M., Kojima, N., Combust. Flame 156 (2009) 763-770.

Pagliaro, M., Rossi, M., *The Future of Glycerol*, RSC Publishing, Cambridge, 2010, p. 11.

Pan, K.L., Li, J.W., Chen, C.P., Wang, C.H., Combust. Flame 156 (2009) 1926-1936.

Pan and Chiu, "Droplet combustion of blended fuels with alcohol and biodiesel/diesel in microgravity conditions," Fuel (2013), in press. http://dx.doi.org/10.1016/j.fuel.2013.03.029

Park, S.-H., Choi, S.-C., Choi, M.Y., Yozgatligil, A., Combust. Sci. Technol. 180

(2008) 631-651.

Park, S.-H., Choi, N.Y., Yozgatligil, A., Combust. Sci. Technol. 181 (2009) 1164-1186.

Park, S.-H., Choi, M.Y., Energy Fuels 23 (2009) 4395-4403.

PAX-it Image Database Software, <http://www.paxit.com/index.asp>.

Pitas, I., Digital image processing algorithms and applications, John Wiley & Sons, New York, New York, 2006.

Pitz, W.J., Cernansky, N.P., Dryer, F.L., Egolfopoulos, F.N., Farrell, J.T., Friend, D.G., Pitsch, H. Society of Automotive Engineers paper (2007) SAE-2007-01-0175.

Ra, Y., Reitz, R.D., McFarlane, J., Daw, C.S., SAE Int. J. Fuels Lubr. 1 (2008) 703-718 (SAE paper no. 2008-01-1379)

Rahmes, T.F., Kinder, J.D., Henry, T.M., Crenfeldt, G., LeDuc, G.F., Zombanakis, G.P., Abe, Y., Lambert, D.M., Lewis, C., Juenger, J.A., Andac, M.G., Reilly, K.R., Holmgren, J.R., McCall, M.J., Bozzano, A.G., AIAA Paper no. 2009-7002, 9th AIAA Aviation Technology, Integration, and Operations Conference (ATIO), 21-23 Sep., 2009, Hilton Head, South Carolina.

Ramanathan, V., Carmichael, G., Nature Geoscience 1 (2008) 222-227.

Randolph, A.L., Law, C.K., Combust. Flame 64 (1986) 267-284.

Reid, R.C., Prausnitz, J.M., Poling, B.E., *The Properties of Gases and Liquids*, 4th ed., McGraw-Hill, New York, 1987.

Reitz, R.D., Combust. Flame 160 (2013) 1-8.

Ristau, R., Igsleder, H., Rath, H.J., Proc. 7th European Symp. Materials Fluids Sci. Microgravity, Oxford, UK, 1989, pp. 437-477.

Sato, J., Tsue, M., Niwa, M., Kono, M., AIP Conefernece Proc.: Drops and Bubbles 197 (1989) 387-393.

Sato, J., Tsue, M., Niwa, M., Kono, M., Combust. Flame 82 (1990) 142- 150.

Sato, J., AIAA (1993) Paper No. 93-0813.

Sazhin, S.S., Elwardany, A., Krutitskii, P.A., Castanet, G., Lemoine, F., Sazhina,

E.M., Heikal, M.R., Int. J. Heat Mass Transfer 53 (2010) 4495-4505.

Segawa, D., Kadota, T., Nakainkyo, A., Hirota, S., Enomoto, H., Proc. Combust. Inst. 28 (2000a) 1063-1069.

Segawa, D., Yamasaki, H., Kadota, T., Tanaka, H., Emonoto, H., Tsue, M., Proc. Combust. Inst. 28 (2000b) 985-990.

Segawa, D., Kajikawa, T., Hirota, S., Nakaya, S., Kadota, T., 56th Int. Astronaut. Cong, Kukuoka, Japan, Oct. 17-21, 2005a, IAC-05-A2.7.03.

Segawa, D., Yoshida, M., Nakaya, S., Kadoka, T., Microgravity Sci. Technol. 17 (2005b) 23-30.

Segawa, D., Yoshida, M., Nakaya, S., Kadoka, T., Proc. Combust. Inst. 31 (2007) 2149-2156.

Service, R.F., Science 319 (2008) 1745.

Seshadri, K., Lu, T., Herbinet, O., Humer, S., Niemann, U., Pitz, W.J., Seiser, R., Law, C.K., Proc. Combust. Inst. 32 (2009) 1067-1074.

Shaw, B.D., Dryer, F.L., Williams, F.A., Gat, N., 19th Fall Technical Meeting Eastern States Section: The Combustion Institute, Dec. 15-17, 1986, paper no. 54.

Shaw, B.D., Dryer, F.L., Williams, F.A., Haggard Jr., J.B., Acta Astronaut 17 (1988) 1195-2102.

Shaw, B.D., Williams, F.A., Int. J. Heat Mass Trans. 33 (1990) 301-317.

Shaw, B.D., Clark, B.D., Wang, D.F., AIAA J. 39 (2001a) 2327-2335.

Shaw, B.D., Aharon, I., Lenhart, D., Dietrich, D.L., Williams, F.A., Combust. Sci. Technol. 167 (2001b) 29-56.

Shaw, B.D., Harrison, M.J., Microgravity Sci. Technol. 13 (2002) 30-40.

Shaw, B.D., Dee, V., Microgravity Sci. Technol. 16 (2005) 26-34.

Shaw, B.D., Wei, J.B., Combust. Sci. Technol. 179 (2007) 1205-1223.

Shaw, B.D., Wei, J.B., Combust. Sci. Technol. 183 (2011) 969-983.

Shaw, B.D., Wei, J.B., J. Combust. 2012 (2012) Article ID 587987, 8 pages.

SigmaScan, Systat Software Inc., <www.sigmaplot.com/index.php>.

Sirignano, W.A., Fluid Dynamics and Transport of Droplets and Sprays, Cambridge University Press, 1999, pp. 23-76.

Smith, R.A., Wood, C.P., Samuelsen, G.S., AIAA/SAE/ASME/ASEE 21st Joint Propulsion Conference, Monterey CA, July 8-10, 1985, paper no. AIAA-85-1311

Spalding, D.B., Symp. (Int.) Combust. 4 (1953) 847-864.

Specification of UTG 96, Chevron Phillips Chemical Company LP, The Woodlands, TX, 2008.

Stewart, G.H., Lynch, P.R., Gimenez, J.L., Med. Biol. Eng. Comput. 7 (1969) 435-438.

Struk, P.M., Dietrich, D.L., Tien, J.S., Micrograv. Sci. Technol. 9 (1996) 106-116.

Struk, P.M., Dietrich, D.L., Sims, C., Picot, B., Kitano, K., Honma, S., Ikeda, K., Ikegami, M., 1st Joint Meeting of U.S. Sections of the Combustion Institute, Washington D.C., 1999, Paper No. 170

Struk, P.M., Dietrich, D.L., Ikegami, M., Xu, G., Proc. Combust. Inst. 29 (2002) 609-615.

Sung, C.J., Wang, C.H., Paper presented at 6th Nat. Conf. on Mech. Eng., Chinese Soc. Mech. Eng., Dec. 8, 1989.

Tanabe, M., Kuwahara, T., Satoh, K., Fujimori, T., Sato, J., Kono, M., Proc. Combust. Inst. 30 (2005) 1957-1964.

Tanabe, M., Microgravity Sci. Technol. 22 (2010) 507-515.

Tsue, M., Segawa, D., Kadota, T., Symp. (Int.) Combust. 26 (1996) 1251-1258.

"Transforming Combustion Research Through Cyberinfrastructure", Committee on Building Cyberinfrastructure for Combustion Research, National Research Council, The National Academies Press, April 2011 (http://www.nap.edu/catalog.php?record_id=13049), ISBN 978-0-309-16387-3.

Turns, S.R., *An Introduction to Combustion*, 2nd ed. McGraw-Hill, New York, 2006.

Ueda, T., Imamura, O., Okai, K., Tsue, M., Kono, M., Sato, J., Proc. Combust. Inst. 29 (2002) 2595-2601.

United States Patent and Trademark Office, Trademark Serial number: 71225514, Mark: Indolene, 1926. <http://assignments.uspto.gov/assignments/q?db=tm&sno=71225514>

Urban, B.D., Kroenlein, K., Kazakov, A., Dryer, F.L., Yozgatiligil, A., Choi, M.Y., Manzello, S.L., Lee, K.O., Dobashi, R., Microgravity Sci. Technol. 15 (2004) 12-18.

Vaughn, T., Wessel, M., Marchese, A.J., 45th AIAA Aerospace Sciences Meeting and Exhibit, Reno, Nevada, Jan. 8-11, 2007, AIAA 2007-741.

Vieille, B., Chauveau, C., Chesneau, X., Odëide, A., Gökalp, I., Symp. (Int.) Combust. 26 (1996) 1259-1265.

Violi, A., Yan, S., Eddings, E.G., Sarofim, A.F., Granata, S., Faravelli, T., Ranzi, E., Combust. Sci. Technol. 174 (2002) 399-417.

Vranos, A., Liscinsky, D.S., Combust. Sci. Technol. 38 (2007) 145-160.

Wakashima, Y., Yamamoto, S., Kikuchi, M., Yoda, S., Mikami, M., Umemura, A., Microgravity Sci. Technol. 16 (2005) 338-341.

Wei, J.B., Shaw, B.D., the 2004 Spring Meeting of the Western States Section of the Combustion Institute, UC Davis, Mar. 29-30, 2004, paper 04S-44.

Wei, J.B., Shaw, B.D., Combust. Flame 146 (2006) 484-492.

Wei, J.B., Shaw, B.D., Combust. Sci. Technol. 181 (2009) 1480-1494.

Weisstein EW (2012), "Ellipse." From MathWorld--A Wolfram Web Resource. <http://mathworld.wolfram.com/Ellipse.html> last access on July 05, 2012.

Williams, B.A., Combust. Flame 124 (2001) 330-333.

Williams, F.A., Hicks, M.C., Nayagam, V., Choi, M.Y., Dryer, F.L., Shaw, B.D., Research Requirements Document- Droplet Flame Extinguishment in Microgravity (FLEX), Nov. 4, 2005.

Whittaker, A.J., Allitt, M.L., Onn, D.G., Bolt, J.D., Thermal Conductivity 21 (C.J. Cremers and H.A. Fine, eds.) (1990) 187-198.

Xu, G., Ikegami, M., Honma, S., Ikeda, K., Nagaishi, H., Dietrich, D.L., Takeshita, Y., Energy Fuels 16 (2002) 366-378.

Xu, G., Ikegami, M., Honma, S., Ikeda, K., Ma, X., Nagaishi, H., Dietrich, D., Struk, P.M., Int. J. Heat Mass Trans. 46 (2003) 1155-1169.

Xu, G., Ikegami, M., Honma, S., Ikeda, K., Dietrich, D.L., Struk, P.M., Int. J. Heat Mass Trans. 47 (2004a) 5807-5821.

Xu, G., Ikegami, M., Honma, S., Ikeda, K., Dietrich, D.L., Struk, P.M., Int. J. Heat Mass Trans. 47 (2004b) 2029-2035.

Yamashita, K., Imamura, O., Osaka, J., Tsue, M., Kono, M., Combust. Sci. Technol. 180 (2008a) 652-673.

Yamashita, K., Imamura, O., Osaka, Nakaya, S., J., Tsue, M., Kono, M.,46th AIAA Aerospace Sciences Meeting and Exhibit, Reno, Nevada, Jan. 7-10, 2008b, AIAA 2008-965.

Yahyaoui, M.; Djebaïli-Chaumeix, N.; Dagaut, P.; Paillard, C.-E.; Gail, S.; Proc. Combust. Inst. 31 (2007) 385-391.

Yang, J.C., Avedisian, C.T., Wang, C.H., 29th Fall Technical Meeting, Eatern Section: The Combustion Institute, Nov. 2-5, 1987, paper no. 43.

Yang, J.C., Avedisian, C.T., Symp. (Int.) Combust. 22 (1988) 2037-2044.

Yang. J.C., Jackson, G.S., Avedisian, C.T., AIP Conference Proc.: Drops and Bubbles, American Institute of Physics 197 (1989) 1619-1625.

Yang, J.C., *"An Experimental Method for Studying Combustion of An Unsupported Fuel Droplet at Reduced Gravity,"* Ph.D. Thesis, Sibley School of Mechanical and Aerospace Engineering, Cornell University, Ithaca, NY, USA, 1990.

Yang, J.C., Jackson, G.S., Avedisian, C.T., Proc. Combust. Inst. 23 (1991) 1619-1625.

Youngblood, G.E., Senor, D.J., Kowbel, W., Webb, J., Kohyama, A., "Thermal conductivity of SiC and C fibers", In *Fusion Materials: Semi-Annual Progress Report Ending December 31, 1999*, vol. 27, ed. Rowcliffe, A.F., pp. 113-118. US Department of Energy, Office of Fusion Energy Sciences, Washington DC.

Yozgatligil, A., Choi, M.Y., Kazakov, A., Dryer, F.L., Manzello, S.L., Dobashi, R., 41st Aerospace Sciences Meeting and Exhibit, Reno, Nevada, Jan. 6-9, 2003, AIAA 2003-1147.

Yozgatligil, A., Park, S.-H., Choi, M.Y., Kazakov, A., Dryer, F.L., Combust. Sci. Technol. 176 (2004) 1985-1999.

Zhang, H.R., Eddings, E.G., Sarofim, A.F., Proc. Combust. Inst. 31 (2007) 401-409.

Zigler, B.T., Walton, S.M., Assanis, D., Perez, E., Wooldridge, M.S., Wooldridge, S.T., J. Eng. Gas turbines Power 130 (2008) 052803.

VENDORS

3M Energy Markets & Advanced Materials Division
3M Corporate Headquarters, St. Paul, MN 55144-1000
Phone: (651) 283-0458

AEC Magnetics
4699 Interstate Drive, Cincinnati, OH 45246
Phone: (800) 635-3954

American Piezo Ceramics Inc.
213 Duck Run Rd Mackeyville, PA 17750
Phone: (570) 726-6961

Black Diamond Equipment, Ltd.
2084 E 3900 S, Salt Lake City, UT 84124
Phone: (801) 278-5533

Canadian Photonic Labs
45 Main St., P.O. Box 1560, Minnedosa, Manitoba, Canada, R0J 1E0
Phone: (204) 867-3141

Corel Inc., Mountain View
385 Ravendale Dr Mountain View, CA 94043
Phone: (650) 930-5800

Dirtz, Prym Consumer USA Inc.
950 Brisack Road, Spartanburg, SC 29303-4709
Phone: (864) 576-5050

Electrohome Electronics LTD (Now acquired by Bluelectronics Group)
4080 Montrose Road, Niagara Falls, ON, Canada, L2H 1J9
Phone: (905) 353-0732

Formosa Plastic Corporation, Taiwan
No.201, Dunhua N. Rd., Songshan Dist., Taipei City 105, Taiwan (R.O.C.)
Phone：886-2-27122211

HP (Agilent Technologies, Inc.)
5301 Stevens Creek Blvd, Santa Clara, CA 95051
Phone: (877) 424-4536

Hitachi Kokusai Corporate
150 Crossways Park Drive, Woodbury, New York 11797 USA
Phone: (516) 682-4431

McCrone Microscopes & Accessories
850 Pasquinelli Drive, Westmont, IL 60559-5539
Phone: (630) 887-7100

Media Cybernetics, Inc.
401 N Washington St #350 Rockville, MD 20850
Phone: (301) 495-3305

Quantum Composer Inc.
212 Discovery Drive, Bozeman, MT 59718
Phone: (800) 510-6530

Salem Specialty Ball Company
259 Albany Turnpike, Canton, CT 06019
Phone: (877) 844-4885
Schott Process Systems, Inc.
1160 Sunnyside St SW, Hartville, OH 44632
Phone: (330) 877-2350
Sentech (Intertest)
303 State Route 94, Columbia, NJ 07832
Phone: (800) 535-3626
Small Parts, Inc.
600 Humphrey St., Logansport, IN 46947
Phone: (574) 753-6323
Teledyne LeCroy,
700 Chestnut Ridge Rd Chestnut Ridge, NY 10977
Phone: (845) 425-2000